



**THE SCALING OF LOSS PATHWAYS AND HEAT TRANSFER IN SMALL  
SCALE INTERNAL COMBUSTION ENGINES**

DISSERTATION

Joseph K. Ausserer, Captain, USAF

AFIT-ENY-DS-16-S-055

**DEPARTMENT OF THE AIR FORCE  
AIR UNIVERSITY  
AIR FORCE INSTITUTE OF TECHNOLOGY**

---

---

**Wright-Patterson Air Force Base, Ohio**

**DISTRIBUTION STATEMENT A.**  
APPROVED FOR PUBLIC RELEASE; DISTRIBUTION UNLIMITED.

The views expressed in this dissertation are those of the author and do not reflect the official policy or position of the United States Air Force, Department of Defense, or the United States Government. This material is declared a work of the U.S. Government and is not subject to copyright protection in the United States.



AFIT-ENY-DS-16-S-055

**THE SCALING OF LOSS PATHWAYS AND HEAT TRANSFER IN SMALL  
SCALE INTERNAL COMBUSTION ENGINES**

DISSERTATION

Presented to the Faculty

Department of Aeronautics and Astronautics

Graduate School of Engineering and Management

Air Force Institute of Technology

Air University

Air Education and Training Command

In Partial Fulfillment of the Requirements for  
Candidacy for the Degree of Doctor of Philosophy

Joseph K. Ausserer, MS

Captain, USAF

August 2016

**DISTRIBUTION STATEMENT A.**  
APPROVED FOR PUBLIC RELEASE; DISTRIBUTION UNLIMITED.

AFIT-ENY-DS-16-S-055

**THE SCALING OF LOSS PATHWAYS AND HEAT TRANSFER IN SMALL SCALE  
INTERNAL COMBUSTION ENGINES**

Joseph K. Ausserer, MS  
Captain, USAF

Committee Membership:

Marc D. Polanka, PhD  
Chairman

Mark F. Reeder, PhD  
Member

David R. Jacques, PhD  
Member

Fred R. Schauer, PhD  
Member

ADEDEJI B. BADIRU, PhD  
Dean, Graduate School of Engineering and Management

### **Abstract**

The rapid expansion of the remotely piloted aircraft market includes an interest in 10 kg to 25 kg vehicles (Group 2) for monitoring, surveillance, and reconnaissance. Power plant options for those aircraft are often 10 cm<sup>3</sup> to 100 cm<sup>3</sup> displacement internal combustion engines. Both power and fuel conversion efficiency decrease increasingly rapidly in the aforementioned size range, with fuel conversion efficiency falling from approximately 30% for automotive and larger scale engines (greater than 100 cm<sup>3</sup> displacement) to less than 5% for micro glow fuel engines (less than 10 cm<sup>3</sup> displacement). Based on the literature, it was unclear which loss mechanisms were responsible for the increasing rate of decreasing performance. Moreover, predictive models for losses such as friction, heat transfer, and short-circuiting (scavenging) were unavailable for ICEs in the stated size range. Previous research also indicated that these losses could cause an inherent relaxation in an engine's fuel octane requirement, possibly allowing small ICEs below a certain size to be converted from gasoline to JP-8 or diesel with little to no modification. To investigate these issues, three research objectives were proposed addressing the scaling of loss pathways, the modelling of heat transfer, friction losses, and gas exchange, and the determination of fuel anti-knock requirements for engines in the 10 cm<sup>3</sup> to 100 cm<sup>3</sup> displacement size range.

Objective 1 addressed the relative importance of loss pathways. The Small Engine Research Bench was constructed to measure the energy pathways in a family of geometrically similar, commercially available engines with 28 cm<sup>3</sup>, 55 cm<sup>3</sup>, and 85 cm<sup>3</sup>

displacements. At peak power, the loss pathways ranked by relative magnitude were: short-circuiting (40%-50%), sensible exhaust enthalpy (14%-18%), incomplete combustion (11%-17%), brake power (14%-15%), and heat loss from the cylinder (10%-11%). The measured losses were compared to balances for large and smaller engines, showing that the primary losses driving efficiency in 10 cm<sup>3</sup> to 100 cm<sup>3</sup> displacement two-stroke engines is short-circuiting and incomplete combustion and that thermal losses do not begin to increase substantially until engine displacement decreases below 10 cm<sup>3</sup>. The objective concluded with a parametric study describing the interactions between engine operating parameters, engine performance metrics, and the loss pathways that identified ways to improve engine performance over current commercial-off-the-shelf configurations.

Objective 2 examined models for heat transfer, friction, and gas exchange. Data from the engines were fit to Taylor and Toong's spatially and temporally averaged heat flux model. Compared to fits developed for larger compression-ignition and spark-ignition engines, the engines tested herein had substantially lower values for the Reynold's number exponent, 0.3-0.4 instead of 0.7-0.75 as was common in the literature. The results showed that the Taylor and Toong model was not formulated to handle the observed variations in throttle, speed, and cooling flow rate and was highly sensitive to the trapped mass used to calculate in-cylinder temperature. A model for engine friction was developed that predicts friction for similar two-stroke engines less than 100 cm<sup>3</sup> displacement using the surface area to volume ratio, engine rotational speed, and delivery ratio. Engine performance data was compared to the perfect isothermal mixing and perfect isothermal displacement models and indicates that the perfect isothermal mixing model using the trapped volume to

calculate delivery ratio predicts engine scavenging performance within  $\pm 5\%$  (absolute) at most points and  $\pm 10\%$  (absolute) over the whole operational range.

Objective 3 investigated the conversion of  $10 \text{ cm}^3$  to  $100 \text{ cm}^3$  displacement two-stroke, SI engines to low anti-knock index fuel. The knock limit was defined as the more conservative of 5 bar maximum amplitude of pressure oscillations or 5 bar/deg peak pressure rise rate for 1% of 400 consecutive cycles. Knock was strongly dependent on rotational speed. Generally, once knock occurred the knock-limited speed range increased by 500 rpm for every 10 octane number (ON) decrease. The results also showed a dependence on engine size, with the  $55 \text{ cm}^3$  and  $85 \text{ cm}^3$  engines being knock-limited about 500 rpm and 1000 rpm faster (or 10 ON and 20 ON higher) than the  $28 \text{ cm}^3$  engine, respectively. Switching from 98 ON fuel (manufacturer recommended) to 20 ON (JP-8, diesel equivalent) fuel led to a 2%-3% increase in power at non knock-limited conditions. Changing from 98 ON fuel to 20 ON fuel improved fuel conversion efficiency by 0.5%-1%, which translates to an approximately 6% increase in range or endurance. Of the three parameters investigated, combustion phasing had the greatest potential for controlling/ increasing knock-limited power, and offered the most control authority relative to its impact on fuel conversion efficiency.

## **Acknowledgements**

First and foremost I would like to thank Dr. Marc Polanka, my advisor, and Mr. Paul Litke from the Air Force Research Laboratory (AFRL), the project sponsor, for their mentorship and guidance on this project. I would also like to thank everyone at AFRL's Small Engine Research Laboratory, especially Rich Ryman, Jacob Baranski, Ben Naguy, JR Groenewegen, and Adam Brown, as well as all of the other student's that helped with the construction of the bench, especially Capt Alex Rowton, Capt Joshua Rittenhouse, Capt Kevin Horn, and Capt Matthew Deutsch. Similarly, I would like to thank all of the individuals in the various laboratories that collaborated on the project, especially Keith Grinstead, Rich Striebich, Linda Schaffer, and Dr. Keith Rein. Finally, I would like to thank my wife and family for their support and encouragement and for their perpetual belief that the project would succeed.

## Table of Contents

	Page
Abstract .....	iv
Acknowledgements .....	vii
Table of Contents .....	viii
List of Figures .....	xv
List of Tables .....	xxix
Abbreviations .....	xxxix
Nomenclature .....	xxxiii
I Introduction .....	1
1. General Issue .....	1
1.1. Loss Pathways and Efficiency .....	3
1.2. Loss Models .....	5
1.3. Fuel .....	5
2. Problem Statements .....	7
2.1. Scaling of Loss Pathways .....	7
2.2. Loss Models .....	8
2.3. Inherent Relaxation of Fuel AKI Requirement with Engine Size .....	10
3. Research Objectives and Scope .....	11
3.1. Objective 1 .....	11
3.2. Objective 2 .....	12
3.3. Objective 3 .....	13
3.4. Project Scope .....	14
4. Uniqueness .....	15
5. Organization .....	15

II	Literature Review .....	17
1.	Chapter Overview .....	17
2.	The Two-Stroke, Spark-Ignition Engine .....	17
2.1.	Context for the Two-Stroke Engine .....	18
2.2.	Ignition Type.....	22
2.3.	Fuel Delivery .....	25
2.4.	Cooling Types .....	36
2.5.	Gas Exchange and Scavenging .....	36
2.6.	Normal and Abnormal Combustion.....	45
2.7.	Friction.....	62
2.8.	Other Engine Performance Metrics .....	65
2.9.	Summary .....	67
3.	Small Engine Literature and Testing.....	68
3.1.	Introduction to Small Engine Testing .....	68
3.2.	1950-1980 – Early Testing Efforts .....	69
3.3.	Cadou, Menon, and Moulton: Micro Glow Fuel Engines: 2002-2013 .....	71
3.4.	Small Engines from a Teaching Standpoint: Raine et al: 2002-2004.....	72
3.5.	Other Relevant Engine Testing (2000-Present) .....	73
3.6.	Small Engines at AFRL (2010-2014) .....	76
4.	Engine Scaling and Loss Pathways.....	81
4.1.	Why Loss Pathways in ICEs Scale .....	82
4.2.	Scaling Studies on Losses in Internal Combustion Engines.....	86
4.3.	Review of Objective 1: Engine Loss Scaling Study .....	94



5.	Models and Measurements.....	95
5.1.	Heat Transfer .....	95
5.2.	Friction.....	136
5.3.	Gas Exchange: Scavenging and Short-Circuiting.....	142
5.4.	Review of Objective 2: Models for Small Engines .....	170
6.	Operation on Heavy Fuel .....	171
6.1.	Heavy Fuel Conversion: Benefits and Obstacles.....	172
6.2.	Early Efforts (1970-2000).....	173
6.3.	Turn of the Millennium (2000-2010).....	174
6.4.	Expanding Interest in Heavy Fuel Conversion (2011-Present) .....	177
6.5.	Review of Objective 3: Relaxation of AKI Requirement with Engine Size	183
III	Methodology .....	184
1.	Chapter Overview .....	184
2.	Facility: Small Engine Research Bench .....	185
2.1.	Drivetrain and Dynamometer System.....	186
2.2.	Intake Air System .....	189
2.3.	Combustion Analysis System .....	193
2.4.	Engine Control System .....	196
2.5.	Computer Control and Instrumentation Systems.....	198
2.6.	Summary: Facility.....	200
3.	Objective 1: The Scaling of Loss Pathways and Engine Performance .....	201
3.1.	Engine Selection .....	202
3.2.	Thermal Loss Measurements .....	204

3.3. Engine Friction Measurements .....	205
3.4. Short-Circuiting and Exhaust Enthalpy Measurements .....	207
3.5. Summary: Objective 1 .....	226
4. Objective 2: Heat Transfer, Friction, and Gas Exchange Modelling .....	226
4.1. Heat Transfer .....	227
4.2. Friction .....	238
4.3. Gas Exchange and Scavenging .....	239
4.4. Summary: Objective 2 .....	240
5. Objective 3: Fuel AKI Relaxation.....	241
5.1. Defining and Detecting Knock .....	242
5.2. Determination of Fuel AKI Requirement .....	244
5.3. Parametric Study of Engine Controls .....	246
5.4. Summary: Objective 3 .....	247
IV Objective I: The Scaling of Loss Pathways and Engine Performance .....	249
1. Chapter Overview .....	249
2. Energy Balances and Scaling Trends .....	250
2.1. Introduction.....	250
2.2. Comparison to Manufacturer Data (COTS Configuration) .....	250
2.3. Energy Balances on 3W Modellmotoren Engines & Speed Parametric Study .....	256
2.4. Scaling of Loss Pathways .....	263
2.5. Section Summary and Conclusions .....	281
3. Parametric Engine Studies .....	282

3.1. Equivalence Ratio .....	284
3.2. Combustion Phasing .....	289
3.3. Engine Cooling and Head Temperature.....	299
3.4. Throttle.....	306
3.5. Thermodynamic Loss Angle.....	312
3.6. Section Summary and Conclusions .....	316
4. Summary: Objective 1 .....	317
V Objective 2: Heat Transfer, Friction Loss, and Gas Exchange Modelling .....	320
1. Chapter Overview .....	320
2. Heat Transfer Modeling .....	320
2.1. In-cylinder Temperature Results.....	322
2.2. Heat Transfer Modelling Results .....	362
2.3. Heat Transfer Modelling Summary .....	374
3. Friction Loss Modelling .....	376
3.1. Speed Results .....	377
3.2. Throttle Results.....	389
3.3. Friction Modelling Summary.....	392
4. Gas Exchange Modelling .....	393
4.1. Speed.....	394
4.2. Throttle.....	398
4.3. Equivalence Ratio, Combustion Phasing, & Engine Head Temperature & Cooling.....	400
4.4. Gas Exchange Modelling Summary .....	404

5.	Summary: Objective 2.....	405
VI	Objective 3: Fuel AKI Relaxation.....	410
1.	Chapter Overview .....	410
2.	Impact of Fuel AKI on KLIMEP, Power, and Burn Angle: All ONs .....	411
3.	Comparison of 98 ON and 20 ON PRF: KLIMEP, Burn Angle and Efficiency: .....	422
4.	Parametric Study of Engine Controls.....	435
4.1.	Equivalence Ratio .....	436
4.2.	Combustion Phasing .....	441
4.3.	Engine Head Temperature & Cooling .....	445
5.	Summary: Objective 3.....	449
VII	Conclusions and Suggestions for Future Work.....	454
1.	Chapter Overview .....	454
2.	Research Objectives and Key Conclusions.....	455
2.1.	Objective 1 .....	455
2.2.	Objective 2 .....	459
2.3.	Objective 3 .....	464
3.	Problems Statements and Answers .....	467
3.1.	Scaling of Loss Pathways .....	468
3.2.	Loss Models .....	468
3.3.	Inherent Relaxation of Fuel AKI Requirement with Engines Size.....	470
3.4.	Answers beyond the Original Questions.....	471
4.	Final Thoughts and Future Work .....	472
	Appendix A.....	473

Appendix B .....	488
Appendix C .....	502
Appendix D .....	516
Appendix E .....	529
Appendix F .....	544
Appendix G .....	561
Bibliography .....	570
Vita .....	591

## List of Figures

	Page
Figure 1: Generalized heat engine, adapted from [30]. .....	19
Figure 2: Four-stroke engine cycle, reprinted from Heywood [21:10] with permission from McGraw Hill Education. ....	21
Figure 3: Two-stroke engine cycle, reprinted from Heywood [21:11] with permission from McGraw Hill Education. ....	22
Figure 4: Schematic of simple air carburetor, reprinted from Heywood [21:283] with permission from McGraw Hill Education. ....	26
Figure 5: Schematic of a Modern Carburetor, reprinted from Heywood [21:288] with permission from McGraw Hill Education. ....	27
Figure 6: Equivalence ratio for a 3W Modellmotoren 55i engine based on measured values of intake air and fuel flow rates, data from Ausserer <i>et al.</i> [10]. ....	28
Figure 7: Generic cross section of a modern fuel injector, reprinted from [48]. ....	31
Figure 8: Schematic of a UEGO sensor applied to determine the equivalence ratio of an engine by measuring oxygen concentration in the exhaust from Zhao and Ladommatos [56:48]. Reprinted with permission from SAE International. ....	35
Figure 9: Phasing of a two-stroke engine with crankcase compression, reprinted from Heywood and Sher [21:11] with permission from Taylor & Francis Ltd. ....	37
Figure 10: Two-stroke scavenging methods, reprinted from Heywood and Sher [22:47] with permission from Taylor & Francis Ltd. ....	41
Figure 11: Illustration of normal combustion process, reprinted with permission from Baranski [53:8]. ....	46
Figure 12: Combustion regimes where automotive and larger scale ICEs as well as micro glow engines operate. Reprinted from Menon and Cadou [71] with permission from Taylor & Francis Ltd. ....	52
Figure 13: Knocking cycle on a Rotax 914 engine showing (a) light, (b) medium, and (c) heavy knock. Reprinted with permission from Baranski [53:17]. ....	58
Figure 14: Friction regimes and Stribeck curve as applicable to friction in an ICE, reprinted from Heywood and Sher [22:366] with permission from Taylor and Francis Ltd. ...	63
Figure 15: Typical fuel conversion efficiencies of various sizes of engines, reprinted with permission from Edwards <i>et al.</i> [100]. ....	67

Figure 16: Schematic of Homemade engine Test setup by Gierke [106].	70
Figure 17: In-cylinder pressure traces from a Fuji IMVAC 34-EI showing the faster, earlier, and shorter combustion phasing of n-heptane relative to iso-octane, reprinted from Wilson [43:49].	79
Figure 18: In-cylinder pressure trace for n-heptane in a Fuji IMVAC engine at full throttle showing knock, reprinted from Wilson [43:51].	80
Figure 19: Scaling of engine power with surface area to volume ratio, reprinted from Rowton <i>et al.</i> [5].	84
Figure 20: Relationship between displaced volume, surface area to volume ratio, and bore to stroke ratio showing that bore to stroke ratio has a smaller impact on geometry than the surface are to volume ratio, reprinted from Rowton <i>et al.</i> [5].	85
Figure 21: ICE energy pathways from Heywood [21:674], reprinted with permission from McGraw Hill Education.	90
Figure 22: Energy accounting on a General Motors 1.9 L Diesel engine at road load power and peak efficiency, with and without energy recovery options, reprinted with permission from Edwards <i>et al.</i> [100].	91
Figure 23: Energy pathway breakdown for a) a 0.16 cm <sup>3</sup> Cox 010 glow fuel engine, b) a 7.54 cm <sup>3</sup> OS 46 FX engine, c) an automotive SI engine, and d) and automotive CI engine. The charts are reprinted with permission from Menon and Cadou [16] with data from Heywood for c) and d) [21:674].	92
Figure 24: Energy pathways in 3W Modellmotoren engines at wide open throttle and 6.5 m/s mean piston speed as determined by Rowton [135:116].	94
Figure 25: Heat transfer network for an ICE cylinder with the cylinder gas on the left and the coolant on the right, adapted from Franco and Martorano [140].	99
Figure 26: Temporally and spatially averaged Reynolds and Nusselt number correlation, reprinted from Taylor and Toong [138] with permission from ASME.	103
Figure 27: Taylor's data [138] as reinterpreted by Annand [17], reprinted with permission from SAGE Publications.	104
Figure 28: Comparison of instantaneous, spatially averaged heat transfer models to 125 cm <sup>3</sup> displacement four-stroke engine data, reprinted with permission from Wu <i>et al.</i> [66].	115
Figure 29: Fit of Wu <i>et al.</i> 's heat transfer model to data from a 125 cm <sup>3</sup> displacement, four-stroke engine, reprinted with permission from Wu <i>et al.</i> [66].	117

Figure 30: Left: 3W-55i engine installed in insulated enclosure. Right: Insulated enclosure showing cooling air path. Figure reprinted from Rittenhouse <i>et al.</i> [121].	121
Figure 31: Schematic of a heat flux gauge, reprinted from Chang <i>et al.</i> [35], reprinted with permission from SAE International.	122
Figure 32: Thin film heat flux gauges installed by Rittenhouse <i>et al.</i> on a Modellmotoren 3W-55i engine, reprinted from Rittenhouse <i>et al.</i> [121].	123
Figure 33: Sample infrared image of a Modellmotoren 3W-55i engine, reprinted from Rittenhouse <i>et al.</i> [121].	125
Figure 34: Schematic of a FTIR spectroscopy unit, reprinted from [167].	130
Figure 35: Mid infrared spectrum for gaseous CO <sub>2</sub> collected by Dow Chemical Company, raw data obtained from NIST [180].	132
Figure 36: Idealized scavenging models. Left: Perfect displacement model. Right: Perfect mixing model. Reprinted from Heywood and Sher [22:123] with permission from Taylor & Francis Ltd.	144
Figure 37: The three zones of the Maekawa scavenging model, reprinted from Heywood and Sher [22:127] with permission from Taylor & Francis Ltd.	148
Figure 38: Tracking of gases during scavenging. The dotted lines denote a control volume. Figure reprinted from Heywood and Sher [22:93] with permission from Taylor & Francis Ltd.	156
Figure 39: Operation schematic of an FID, from Zhao and Ladommatos [56:114], reprinted with permission from SAE International.	163
Figure 40: Schematic of a GC-MSD system for emissions measurements, reprinted with permission from the University of Colorado - Boulder [239].	165
Figure 41: Raw gas chromatogram using HP-5ms column to separate exhaust gas from a small two-stroke, gasoline engine. Time is in minutes and abundance is molecular counts at the mass selective detector.	166
Figure 42: Electron ionization mass spectrum of iso-octane (2,2,4 tri methyl pentane), data from the National Institute of Standards and Technology [248].	169
Figure 43: Fuel consumption for the FlexDI® system compared to the stock carburetor on a 50 cm <sup>3</sup> two-stroke engine, reprinted from Cathcart <i>et al.</i> [15] with permission from SAE International.	175
Figure 44: Fuel consumption of a 3W-28i two-stroke engine converted from gasoline to heavy fuel, data from the 3W International website [252].	182



Figure 45: Specific fuel consumption of a 3W-28i two-stroke engine converted from gasoline to heavy fuel, data from the 3W International website [252]. .....	182
Figure 46: Layout of Small Engine Research Bench as of April 2016 during data collection for Objectives 1, 2, & 3. ....	185
Figure 47: Photograph of SERB drivetrain as of July 2015. The optics tower is not installed in this view. ....	186
Figure 48: Schematic of SERB drivetrain components. ....	187
Figure 49: Connection diagram for Magtrol Dynamometer system consisting of a 2 WB 65 Eddy Current Dynamometer, a DES 311 Power supply, a TSC401 Signal Conditioning Unit, and a DSP6001 High-Speed Dynamometer Controller [264]. ....	188
Figure 50: Schematic of SERB intake air system components. ....	190
Figure 51: Photograph of SERB showing the intake air system. ....	191
Figure 52: Top Left: Custom Kistler Measuring spark plug with copper spacer washer installed. Top Right: Stock CM-6 spark plug. Bottom: Kistler Flush Mount Pressure Transducer. ....	194
Figure 53: Schematic of SERB fuel system components. ....	198
Figure 54: Schematic of SERB cooling air system components. ....	204
Figure 55: Schematic of SERB friction testing setup and drivetrain. ....	205
Figure 56: Power dissipation by SETB drivetrain measured as the difference between power delivered at the electric motor cradle and power dissipated at the dynamometer. For the fit, $R^2=0.96$ . ....	207
Figure 57: SERB exhaust system schematic showing sampling port locations. Diagram is not drawn to scale. ....	209
Figure 58: Exhaust sampling probe for the Small Engine Research Bench. ....	210
Figure 59: Schematic of the SERB exhaust sampling system. ....	211
Figure 60: Calibration curve for the GC-MS. SIM mode was used to quantify the argon 40 AMU/e <sup>-</sup> ion and the iso-octane 99 AMU/e <sup>-</sup> ion. ....	215
Figure 61: Calibration of TCD O <sub>2</sub> response for a 100 $\mu$ L sample of air and hydrogen. ....	218
Figure 62: Calibration of TCD N <sub>2</sub> response for a 100 $\mu$ L sample of air and hydrogen. ....	219
Figure 63: Calibration of TCD H <sub>2</sub> response for a 100 $\mu$ L sample of air and hydrogen. ....	219

Figure 64: Calibration of TCD CO response for a 100 $\mu$ L sample of carbon monoxide and nitrogen. ....	220
Figure 65: Oxygen in Exhaust Sample as a function of sampling port. For exhaust geometry and sampling port location see Figure 57. ....	225
Figure 66: Left: Schematic of optical probe assembly and installation [167]. Right: Photograph of optical probe and sapphire rod. ....	233
Figure 67: Schematic of optical path in 3W-XXi engines. ....	234
Figure 68: Optical access for the SERB. ....	235
Figure 69: Schematic of TLAS setup used on the SERB. ....	236
Figure 70: Comparison of brake power produced by a 3W-28i with heavy fuel injection system and banana muffler to a 3W-28i engine as tested on the SERB. ....	252
Figure 71: Comparison of brake specific fuel consumption on a 3W-28i with heavy fuel injection system and banana muffler to a 3W-28i engine as tested on the SERB. ..	254
Figure 72: Energy balances at WOT, $\phi=1.06\pm0.02$ , $CA_{50}=8\pm0.5^\circ$ aTDC, & $CHT=130\pm2^\circ$ C for the 3W-28i, 3W-55i, and 3W-85Xi engines. Uncertainty bars are for a 95% confidence interval. ....	257
Figure 73: Trapped energy balances at WOT, $\phi=1.06\pm0.02$ , $CA_{50}=8\pm0.5^\circ$ aTDC, & $CHT=130\pm2^\circ$ C for the 3W-28i, 3W-55i, and 3W-85Xi engines. Uncertainty bars are for a 95% confidence interval. ....	261
Figure 74: Relationship between fuel conversion efficiency and engine displacement grouped by type of engine. Adapted (including fit) with permission from a similar plot by Menon and Cadou [6]. Data for glow fuel engines collected by Menon and Cadou [6]. Data for small vehicle, highway, and large diesel engines based on manufacturer specifications compiled by Menon and Cadou [6]. ....	264
Figure 75: Complete energy balances for seven engines. Data for automotive engines was compiled from Heywood [21:674]. Data for the mirco glow fuel engines was collected by Menon and Cadou [16]. Friction losses from the 3W engines are part of the cooling load and sensible exhaust enthalpy. Deviations in chart totals from 100% are due to roning errors during normaliztion of the data. ....	267
Figure 76: Energy balances on trapped fuel energy for five engines showing trends in loss pathways with surface area to volume ratio. Friction losses from the 3W engines are part of the cooling load and sensible exhaust enthalpy. The data for automotive engines was compiled from Heywood [21:674]. Deviations in chart totals from 100% are due to roning errors during normaliztion of the data. ....	269

Figure 77: Energy balances on released fuel energy for seven engines, showing trends in loss mechanisms with surface area to volume ratio. Friction losses from the 3W engines, rejected as heat, are part of the cooling load and sensible exhaust enthalpy. The data for automotive engines was compiled from Heywood [21:674]. Data for the micro glow fuel engines was collected by Menon and Cadou [16]. Deviations in chart totals from 100% are due to rounding errors during normalization of the data.....	272
Figure 78: Relationship between internal combustion engine BMEP and engine displacement grouped by type of engine. Adapted (including fit) with permission from a similar plot by Menon and Cadou [6]. Data for glow fuel engines collected by Menon and Cadou [6]. Data for small vehicle, highway, and large diesel engines based on manufacturer specifications compiled by Menon and Cadou [6]. .....	274
Figure 79: Charging efficiency at WOT, $\phi=1.06\pm0.02$ , $CA_{50}=8\pm0.5^\circ\text{aTDC}$ , & $CHT=130\pm2^\circ\text{C}$ for the 3W-28i, 3W-55i, and 3W-85Xi engines. ....	278
Figure 80: BMEP at WOT, $\phi=1.06\pm0.02$ , $CA_{50}=8\pm0.5^\circ\text{aTDC}$ , & $CHT=130\pm2^\circ\text{C}$ for the 3W-28i, 3W-55i, and 3W-85Xi engines. ....	278
Figure 81: Intake air flow at WOT, $\phi=1.06\pm0.02$ , $CA_{50}=8\pm0.5^\circ\text{aTDC}$ , & $CHT=130\pm2^\circ\text{C}$ for the 3W-28i, 3W-55i, and 3W-85Xi engines.....	280
Figure 82: Effect of equivalence ratio on fuel conversion efficiency. The engines were operated at 6000 rpm, WOT, $CA_{50}=8\pm0.5^\circ\text{aTDC}$ , & $CHT=130\pm2^\circ\text{C}$ . ....	284
Figure 83: Effect of equivalence ratio on engine power, normalized as MEP. The engines were operated at 6000 rpm, WOT, $CA_{50}=8\pm0.5^\circ\text{aTDC}$ , & $CHT=130\pm2^\circ\text{C}$ .....	285
Figure 84: Effect of equivalence ratio on COV of IMEP. The engines were operated at 6000 rpm, WOT, $CA_{50}=8\pm0.5^\circ\text{aTDC}$ , & $CHT=130\pm2^\circ\text{C}$ . ....	286
Figure 85: Effect of equivalence ratio on energy pathways & balances. The engines were operated at 6000 rpm, WOT, $CA_{50}=8\pm0.5^\circ\text{aTDC}$ , & $CHT=130\pm2^\circ\text{C}$ . Uncertainty bars are for a 95% confidence interval.....	288
Figure 86: Effect of combustion phasing on fuel conversion efficiency. The engines were operated at 6000 rpm, WOT, $\phi=1.06\pm0.02$ , & $CHT=130\pm2^\circ\text{C}$ .....	290
Figure 87: Impact of combustion phasing on IMEP. The engines were operated at 6000 rpm, WOT, $\phi=1.06\pm0.02$ , & $CHT=130\pm2^\circ\text{C}$ . ....	291
Figure 88: Effect of combustion phasing on IMEP. The engines were operated at 6000 rpm, WOT, $\phi=1.06\pm0.02$ , & $CHT=130\pm2^\circ\text{C}$ .....	292
Figure 89: Comparison of manufacturer timing curve and MBT timing curve. The engines were operated at 6000 rpm, WOT, $\phi=1.06\pm0.02$ , & $CHT=130\pm2^\circ\text{C}$ .....	293

Figure 90: Effect of combustion phasing on energy pathways & balances. The engines were operated at 6000 rpm, WOT, $\phi=1.06\pm0.02$ , & $CHT=130\pm2^{\circ}C$ . Uncertainty bars are for a 95% confidence interval. ....	295
Figure 91: Effect of combustion phasing on intake air and fuel flow rate. The engines were operated at 6000 rpm, WOT, $\phi=1.06\pm0.02$ , & $CHT=130\pm2^{\circ}C$ .....	296
Figure 92: Effect of combustion phasing on measured emissions. The engines were operated at 6000 rpm, WOT, $\phi=1.06\pm0.02$ , & $CHT=130\pm2^{\circ}C$ .....	297
Figure 93: Effect of combustion phasing on EGT. The engines were operated at 6000 rpm, WOT, $\phi=1.06\pm0.02$ , & $CHT=130\pm2^{\circ}C$ .....	298
Figure 94: Effect of cooling air speed on engine head temperature. The engines were operated at 6000 rpm, WOT, $\phi=1.06\pm0.02$ , & $CA50=8^{\circ}aTDC$ . ....	300
Figure 95: Effect of cooling air speed on engine cooling load. The engines were operated at 6000 rpm, WOT, $\phi=1.06\pm0.02$ , & $CA50=8^{\circ}aTDC$ . ....	302
Figure 96: Effect of cooling air speed on fuel conversion efficiency. The engines were operated at 6000 rpm, WOT, $\phi=1.06\pm0.02$ , & $CA50=8^{\circ}aTDC$ . ....	302
Figure 97: Effect of cooling air speed on IMEP. The engines were operated at 6000 rpm, WOT, $\phi=1.06\pm0.02$ , & $CA50=8^{\circ}aTDC$ . ....	303
Figure 98: Effect of cooling air speed on charging efficiency. The engines were operated at 6000 rpm, WOT, $\phi=1.06\pm0.02$ , & $CA50=8^{\circ}aTDC$ . ....	304
Figure 99: Effect of cooling air speed on energy pathways & balances. The engines were operated at 6000 rpm, WOT, $\phi=1.06\pm0.02$ , & $CA50=8^{\circ}aTDC$ . Uncertainty bars are for a 95% confidence interval. ....	305
Figure 100: Effect of delivery ratio (throttle) on IMEP. The engines were operated at 6000 rpm, $\phi=1.06\pm0.02$ , $CA50=8^{\circ}aTDC$ , & $CHT=130\pm2^{\circ}C$ . ....	306
Figure 101: Effect of delivery ratio (throttle) on energy pathways & balances. The engines were operated at 6000 rpm, $\phi=1.06\pm0.02$ , $CA50=8^{\circ}aTDC$ , & $CHT=130\pm2^{\circ}C$ . Uncertainty bars are for a 95% confidence interval. ....	308
Figure 102: Effect of delivery ratio (throttle) on charging and trapping efficiencies. The engines were operated at 6000 rpm, $\phi=1.06\pm0.02$ , $CA50=8^{\circ}aTDC$ , & $CHT=130\pm2^{\circ}C$ . ....	309
Figure 103: Effect of delivery ratio (throttle) on trapped energy pathways & balances. The engines were operated at 6000 rpm, $\phi=1.06\pm0.02$ , & $CA50=8^{\circ}aTDC$ , & $CHT=130\pm2^{\circ}C$ . Uncertainty bars are for a 95% confidence interval. ....	310

Figure 104: Effect of delivery ratio (throttle) on fuel conversion efficiency. The engines were operated at 6000 rpm, $\phi=1.06\pm0.02$ , & CA50=8°aTDC, & CHT=130±2°C..	311
Figure 105: Thermodynamic loss angles under motored conditions determined using two methodologies. ....	314
Figure 106: Thermodynamic loss angle on 3W Modellmotoren engine compared to tabulated loss angles for conventional engines documented in [73:188].....	315
Figure 107: Impact of speed on in-cylinder temperature (TLAS) and pressure. The engines were operated at WOT, $\phi=1.06\pm0.02$ , CA50=8±0.5°aTDC, & CHT=130±2°C. Pressure is a 400 cycle average, temperature is a 500 ms average. ....	323
Figure 108: Comparison of 50 cycles of pressure and temperature data to the average pressure and temperature trace. Data collected on the 3W-55i engine at 6000 rpm, WOT, $\phi=1.06\pm0.02$ , CA50=8±0.5°aTDC, & CHT=130±2°C. ....	324
Figure 109: Comparison of the average in-cylinder pressure trace as measured by the AVL Indismart to the trace measured by the TLAS system. Data collected on the 3W-55i engine at 6000 rpm, WOT, $\phi=1.06\pm0.02$ , CA50=8±0.5°aTDC, & CHT=130±2°C. ....	326
Figure 110: 95% confidence interval on measured temperature and pressure expressed in absolute units for the speed sweep results in Figure 107. ....	327
Figure 111: 95% confidence interval on measured temperature and pressure expressed as a percentage for the speed sweep results in Figure 107. ....	328
Figure 112: In-cylinder temperature calculated using the variable mass model for the speed sweep. Trapped mass was calculated using cylinder temperature and pressure at exhaust port close. Gas exchange temperature was set equal to TLAS temperature at port close. ....	329
Figure 113: Mass of cylinder contents calculated using the ideal gas law and the in-cylinder pressure and temperature for the speed sweep. The engines were operated at WOT, $\phi=1.06\pm0.02$ , CA50=8±0.5°aTDC, & CHT=130±2°C. ....	331
Figure 114: In-cylinder temperature calculated using the average mass model for the speed sweep. Trapped mass was calculated as the average trapped mass for all points, calculated using cylinder temperature and pressure at exhaust port close. Gas exchange temperature was set equal to the calculated temperature at port close. ....	334
Figure 115: Average temperature summary statistics for the speed sweep. The engines were operated at WOT, $\phi=1.06\pm0.02$ , CA50=8±0.5°aTDC, & CHT=130±2°C. ....	336

Figure 116: Pressure and peak temperature summary statistics for the speed sweep. The engines were operated at WOT, $\phi=1.06\pm0.02$ , $CA50=8\pm0.5^\circ\text{aTDC}$ , & $CHT=130\pm2^\circ\text{C}$ . .....	337
Figure 117: Impact of equivalence ratio on in-cylinder temperature (TLAS) and pressure. The engines were operated at 6000 rpm, WOT, $CA50=8\pm0.5^\circ\text{aTDC}$ , & $CHT=130\pm2^\circ\text{C}$ . Pressure is a 400 cycle average, temperature is a 500 ms average. ....	338
Figure 118: Mass of cylinder contents calculated using the ideal gas law and the in-cylinder pressure and temperature for the equivalence ratio sweep. The engines were operated at 6000 rpm, WOT, $CA50=8\pm0.5^\circ\text{aTDC}$ , & $CHT=130\pm2^\circ\text{C}$ . ....	339
Figure 119: In-cylinder temperature calculated using the variable and average mass models for the equivalence ratio sweep. Trapped mass was calculated at exhaust port close. Gas exchange temperature was set equal to model temperature at port close. ....	340
Figure 120: Average temperature summary statistics for the equivalence ratio sweep. The engines were operated at 6000 rpm, WOT, $CA50=8\pm0.5^\circ\text{aTDC}$ , & $CHT=130\pm2^\circ\text{C}$ . ....	341
Figure 121: Pressure and peak temperature summary statistics for the equivalence ratio sweep. The engines were operated at 6000 rpm, WOT, $CA50=8\pm0.5^\circ\text{aTDC}$ , & $CHT=130\pm2^\circ\text{C}$ . ....	342
Figure 122: Impact of combustion phasing on in-cylinder temperature (TLAS) and pressure. The engines were operated at 6000 rpm, WOT, $\phi=1.06\pm0.02$ , & $CHT=130\pm2^\circ\text{C}$ . Pressure is a 400 cycle average, temperature is a 500 ms average. ....	343
Figure 123: Mass of cylinder contents calculated using the ideal gas law and the in-cylinder pressure and temperature for the combustion phasing sweep. The engines were operated at 6000 rpm, WOT, $\phi=1.06\pm0.02$ , & $CHT=130\pm2^\circ\text{C}$ . ....	344
Figure 124: In-cylinder temperature calculated using the trapped and average mass models for the combustion phasing sweep. Trapped mass was calculated at exhaust port close. Gas exchange temperature was set equal to model temperature at port close. ....	345
Figure 125: Average temperature summary statistics for the combustion phasing sweep. The engines were operated at 6000 rpm, WOT, $\phi=1.06\pm0.02$ , & $CHT=130\pm2^\circ\text{C}$ . ....	347
Figure 126: Pressure and peak temperature summary statistics for the combustion phasing sweep. The engines were operated at 6000 rpm, WOT, $\phi=1.06\pm0.02$ , & $CHT=130\pm2^\circ\text{C}$ . ....	348

Figure 127: Impact of engine cooling on in-cylinder temperature (TLAS) and pressure. The engines were operated at 6000 rpm, WOT, $\phi=1.06\pm0.02$ , & $CA50=8\pm0.5^\circ\text{aTDC}$ . Pressure is a 400 cycle average, temperature is a 500 ms average.....	349
Figure 128: Mass of cylinder contents calculated using the ideal gas law and the in-cylinder pressure and temperature for the cooling sweep. The engines were operated at 6000 rpm, WOT, $CA50=8\pm0.5^\circ\text{aTDC}$ , & $\phi=1.06\pm0.02$ .....	350
Figure 129: In-cylinder temperature calculated using the trapped and average mass models for the cooling sweep. Trapped mass was calculated at exhaust port close. Gas exchange temperature was set equal to model temperature at port close.....	351
Figure 130: Average temperature summary statistics for the cooling sweep. The engines were operated at 6000 rpm, WOT, $CA50=8\pm0.5^\circ\text{aTDC}$ , & $\phi=1.06\pm0.02$ . ....	353
Figure 131: Pressure and peak temperature summary statistics for the cooling sweep. The engines were operated at 6000 rpm, WOT, $CA50=8\pm0.5^\circ\text{aTDC}$ , & $\phi=1.06\pm0.02$ . ..	354
Figure 132: Impact of throttle (normalized as delivery ratio) on in-cylinder temperature (TLAS) and pressure. The engines were operated at 6000 rpm, $\phi=1.06\pm0.02$ , $CA50=8\pm0.5^\circ\text{aTDC}$ , & $CHT=130\pm2^\circ\text{C}$ .....	355
Figure 133: Mass of cylinder contents calculated using the ideal gas law, in-cylinder pressure and temperature for the throttle sweep. The engines were operated at 6000 rpm, $\phi=1.06\pm0.02$ , $CA50=8\pm0.5^\circ\text{aTDC}$ , & $CHT=130\pm2^\circ\text{C}$ . ....	356
Figure 134: In-cylinder temperature calculated using the trapped and average mass models for the throttle sweep. Trapped mass was calculated at exhaust port close. Gas exchange temperature was set equal to model temperature at port close.....	357
Figure 135: Average temperature summary statistics for the throttle sweep. The engines were operated at 6000 rpm, $\phi=1.06\pm0.02$ , $CA50=8\pm0.5^\circ\text{aTDC}$ , & $CHT=130\pm2^\circ\text{C}$ . ....	358
Figure 136: Pressure and peak temperature summary statistics for the throttle sweep. The engines were operated at 6000 rpm, $\phi=1.06\pm0.02$ , $CA50=8\pm0.5^\circ\text{aTDC}$ , & $CHT=130\pm2^\circ\text{C}$ . ....	359
Figure 137: Nusselt and Reynolds numbers calculated for the Taylor and Toong model. Large, filled points represent the baseline condition of 6000 rpm, WOT, $\phi=1.06\pm0.02$ , $CA50=8\pm0.5^\circ\text{aTDC}$ , & $CHT=130\pm2^\circ\text{C}$ .....	364
Figure 138: Inputs to the Nusselt and Reynolds numbers for the Taylor and Toong model collected on the LSDAQ. Large, filled points represent the baseline condition of 6000 rpm, WOT, $\phi=1.06\pm0.02$ , $CA50=8\pm0.5^\circ\text{aTDC}$ , & $CHT=130\pm2^\circ\text{C}$ . ....	365

Figure 139: Gas temperature used to calculate the Nusselt number for the Taylor and Toong model. Large, filled points represent the baseline condition of 6000 rpm, WOT, $\phi=1.06\pm0.02$ , $CA50=8\pm0.5^\circ\text{aTDC}$ , & $CHT=130\pm2^\circ\text{C}$ . .....	367
Figure 140: Thermal conductivity used to calculate the Nusselt number for the Taylor and Toong model. Large, filled points represent the baseline condition of 6000 rpm, WOT, $\phi=1.06\pm0.02$ , $CA50=8\pm0.5^\circ\text{aTDC}$ , & $CHT=130\pm2^\circ\text{C}$ . .....	368
Figure 141: Dynamic viscosity used to calculate the Nusselt number for the Taylor and Toong model. Large, filled points represent the baseline condition of 6000 rpm, WOT, $\phi=1.06\pm0.02$ , $CA50=8\pm0.5^\circ\text{aTDC}$ , & $CHT=130\pm2^\circ\text{C}$ . .....	369
Figure 142: Fits of Taylor and Toong's model to data collected on the 3W-28i and 3W-55i engines. Large, filled points represent the baseline condition of 6000 rpm, WOT, $\phi=1.06\pm0.02$ , $CA50=8\pm0.5^\circ\text{aTDC}$ , & $CHT=130\pm2^\circ\text{C}$ . .....	370
Figure 143: Comparison of fits to Taylor and Toong model for the studied 3W engines to literature models from Taylor and Toong [138] and Annand [17] for automotive and larger scale engines. ....	374
Figure 144: Engine friction loss testing results as a function of speed. Fits created using linear least squares regression to the (linearized) three term model. ....	378
Figure 145: Comparison of linear friction loss model fits for 3W engines to literature models for automotive and larger scale engines and micro glow fuel engines in terms of power density and FMEP. Literature data collected from Heywood [21:722], Heywood and Sher [22:368], and Menon and Cadou [16]. ....	379
Figure 146: Comparison of cubic friction loss model fits for 3W engines to literature models for automotive and larger scale engines and micro glow fuel engines in terms of power density and FMEP. Literature data collected from Heywood [21:722], Heywood and Sher [22:368], and Menon and Cadou [16]. ....	381
Figure 147: Engine friction loss testing results as a function of mean piston speed. Fits created using linear least squares regression to Blair's model [27:379]. ....	384
Figure 148: Comparison of friction loss model fits for 3W engines to literature models for conventional two-stroke engines in terms FMEP. Literature data collected from Blair [27:379]. ....	386
Figure 149: Scaling of FMEP (normalized friction losses) with surface area to volume ratio at WOT for small two-stroke engines less than $100\text{ cm}^3$ displacement. Literature data based on friction testing results reported by Menon and Cadou [16]. ....	388
Figure 150: Influence of throttle setting (normalized as delivery ratio) on engine friction losses at 6000 rpm. Fits created using linear least squares regression. ....	390



Figure 151: Normalized friction results for the 3W-28i, 3W-55i, and 3W-85Xi engines and the resulting linear fits. Also included is a line of average slope describing the general relationship between friction power and delivery ratio.....	391
Figure 152: Impact of speed on scavenging behavior for WOT, $\phi=1.06\pm0.02$ , $CA50=8\pm0.5^\circ\text{aTDC}$ , $CHT=130\pm2^\circ\text{C}$ , for the 3W-28i, 3W-55i, and 3W-85Xi engines compared to perfect isothermal mixing and displacement models. ....	395
Figure 153: Impact of throttle on scavenging behavior for 6000 rpm, $\phi=1.06\pm0.02$ , $CA50=8\pm0.5^\circ\text{aTDC}$ , $CHT=130\pm2^\circ\text{C}$ , for the 3W-28i, 3W-55i, and 3W-85Xi engines compared to perfect isothermal mixing and displacement models. ....	399
Figure 154: Impact of equivalence ratio on scavenging behavior for 6000 rpm, WOT, $CA50=8\pm0.5^\circ\text{aTDC}$ , $CHT=130\pm2^\circ\text{C}$ , for the 3W-28i, 3W-55i, and 3W-85Xi engines compared to perfect isothermal mixing and displacement models. ....	401
Figure 155: Impact of combustion phasing on scavenging behavior for 6000 rpm, WOT, $\phi=1.06\pm0.02$ , $CHT=130\pm2^\circ\text{C}$ , for the 3W-28i, 3W-55i, and 3W-85Xi engines compared to perfect isothermal mixing and displacement models. ....	402
Figure 156: Impact of cooling air speed on scavenging behavior for 6000 rpm, WOT, $\phi=1.06\pm0.02$ , $CA50=8\pm0.5^\circ\text{aTDC}$ , for the 3W-28i, 3W-55i, and 3W-85Xi engines compared to perfect isothermal mixing and displacement models. ....	403
Figure 157: Knock-limited IMEP for $\phi=1.06\pm0.02$ , $CA50=8\pm0.5^\circ\text{aTDC}$ , & $CHT=130\pm2^\circ\text{C}$ . Red points were knock-limited. Orange points indicate the presence of abnormal combustion.....	412
Figure 158: Idealized autoignition criteria based on temperature, density (pressure), and induction time for two fuel air mixtures. Autoignition will occur for conditions above the surface for the fuel air mixture. Adapted from Obert [282:105].....	413
Figure 159: Knock-limited indicated power for $\phi=1.06\pm0.02$ , $CA50=8\pm0.5^\circ\text{aTDC}$ , & $CHT=130\pm2^\circ\text{C}$ . Red points were knock-limited. Orange points indicate the presence of abnormal combustion.....	415
Figure 160: Total burn angle ( $CA0-CA90$ ) in CAD for $\phi=1.06\pm0.02$ , $CHT=130\pm2^\circ\text{C}$ , & $CA50=8\pm0.5^\circ\text{aTDC}$ . Red points were knock-limited. Orange points indicate the presence of abnormal combustion.....	418
Figure 161: Total burn angle ( $CA0-CA90$ ) in milliseconds for $\phi=1.06\pm0.02$ , $CHT=130\pm2^\circ\text{C}$ , & $CA50=8\pm0.5^\circ\text{aTDC}$ . Red points were knock-limited. Orange points indicate the presence of abnormal combustion. ....	419
Figure 162: Total burn angle ( $CA0-CA90$ ) in CAD for 7900 rpm, $\phi=1.06\pm0.02$ , $CHT=130\pm2^\circ\text{C}$ , & $CA50=8\pm0.5^\circ\text{aTDC}$ . Red points were knock-limited. Orange points indicate the presence of abnormal combustion. ....	420

Figure 163: KLIMEP for $\phi=1.06\pm0.02$ , $CA50=8\pm0.5^\circ\text{aTDC}$ , & $CHT=130\pm2^\circ\text{C}$ . Red points were knock-limited. Orange points indicate the presence of abnormal combustion. ....	423
Figure 164: Total burn angle ( $CA0-CA90$ ) for $\phi=1.06\pm0.02$ , $CA50=8\pm0.5^\circ\text{aTDC}$ , & $CHT=130\pm2^\circ\text{C}$ . Red points were knock-limited. Orange points indicate the presence of abnormal combustion.....	424
Figure 165: Comparison of 400 cycle average in-cylinder pressure curves for the 3W-85Xi engine operating abnormal combustion free on 20 ON PRF and 98 ON PRF. Operating conditions: 7900 rpm, $\phi=1.06\pm0.02$ , $CA50=8\pm0.5^\circ\text{aTDC}$ , & $CHT=130\pm2^\circ\text{C}$ . .....	425
Figure 166: Spark timing and mass fraction burned angles for $\phi=1.06\pm0.02$ , $CA50=8\pm0.5^\circ\text{aTDC}$ , & $CHT=130\pm2^\circ\text{C}$ . Filled points were knock-limited. ....	426
Figure 167: Delivery ratio for $\phi=1.06\pm0.02$ , $CA50=8\pm0.5^\circ\text{aTDC}$ , & $CHT=130\pm2^\circ\text{C}$ . Red points were knock-limited. Orange points indicate the presence of abnormal combustion. ....	431
Figure 168: Reeds and reed carries for the 3W-28i (left), 3W-55i (middle) and 3W-85Xi (right) engines. ....	432
Figure 169: Fuel conversion efficiency for $\phi=1.06\pm0.02$ , $CA50=8\pm0.5^\circ\text{aTDC}$ , & $CHT=130\pm2^\circ\text{C}$ . Red points were knock-limited. Orange points indicate the presence of abnormal combustion.....	434
Figure 170: Effect of equivalence ratio on knock and KLIMEP for $CA50=8\pm0.5^\circ\text{aTDC}$ , $CHT=130\pm2^\circ\text{C}$ , & 20 ON PRF blend. Red points were knock-limited. Orange points indicate the presence of abnormal combustion. ....	437
Figure 171: Effect of equivalence ratio on delivery ratio, fuel conversion efficiency, and knock running on 20 ON PRF blend. The engines were operated at $CA50=8\pm0.5^\circ\text{aTDC}$ , & $CHT=130\pm2^\circ\text{C}$ . Red points were knock-limited. Orange points indicate the presence of abnormal combustion. ....	438
Figure 172: Effect of combustion phasing on knock and KLIMEP for $\phi=1.06\pm0.02$ , $CHT=130\pm2^\circ\text{C}$ , & 20 ON PRF blend. Red points were knock-limited. Orange points indicate the presence of abnormal combustion. ....	442
Figure 173: Effect of combustion phasing on delivery ratio, fuel conversion efficiency, and knock running on 20 ON PRF blend. The engines were operated at $\phi=1.06\pm0.02$ , $CHT=130\pm2^\circ\text{C}$ . Red points were knock-limited. Orange points indicate the presence of abnormal combustion.....	443
Figure 174: Effect of head temperature and engine cooling on knock and KLIMEP for $\phi=1.06\pm0.02$ , $CA50=8\pm0.5^\circ\text{aTDC}$ , & 20 ON PRF blend. Red points were knock-limited. Orange points indicate the presence of abnormal combustion. ....	446

Figure 175: Effect of head temperature on delivery ratio, fuel conversion efficiency, and knock running on 20 ON PRF blend. The engines were operated at $\phi=1.06\pm0.02$ , $CA50=8\pm0.5^\circ\text{aTDC}$ , & 20 ON PRF blend. Red points were knock-limited. Orange points indicate the presence of abnormal combustion. ....	447
Figure 176: Effect of engine cooling on delivery ratio, fuel conversion efficiency, and knock running on 20 ON PRF blend. The engines were operated at $\phi=1.06\pm0.02$ , $CA50=8\pm0.5^\circ\text{aTDC}$ , & 20 ON PRF blend. Red points were knock-limited. Orange points indicate the presence of abnormal combustion. ....	448
Figure 177: 95% confidence interval on measured temperature and pressure expressed in absolute units for equivalence ratio sweep results in Figure 117.....	562
Figure 178: 95% confidence interval on measured temperature and pressure expressed as a percentage for equivalence ratio sweep results in Figure 117.....	563
Figure 179: 95% confidence interval on measured temperature and pressure expressed in absolute units for combustion phasing sweep results in Figure 122.....	564
Figure 180: 95% confidence interval on measured temperature and pressure expressed as a percentage for combustion phasing sweep results in Figure 122.....	565
Figure 181: 95% confidence interval on measured temperature and pressure expressed in absolute units for cooling sweep results in Figure 127.....	566
Figure 182: 95% confidence interval on measured temperature and pressure expressed as a percentage for cooling sweep results in Figure 127.....	567
Figure 183: 95% confidence interval on measured temperature and pressure expressed in absolute units for throttle sweep results in Figure 132. ....	568
Figure 184: 95% confidence interval on measured temperature and pressure expressed as a percentage for throttle sweep results in Figure 132. ....	569

## List of Tables

	Page
Table 1: Knock Modes and Corresponding Zeros of the Derivative of the Bessel Function of the First Kind, adapted from Baranski [53:14] and Galloni [81].....	57
Table 2: Knock Mitigation Strategies, Adapted from Attard [85] and Baranski [53:25].	60
Table 3: Preliminary AFRL and AFIT Papers on Engine Scaling.....	81
Table 4: MIT Similar Engine Geometry Information [9:178].....	86
Table 5: ICE Energy Pathways [21:674].	90
Table 6: Non-dimensional Parameters for ICEs, Adapted from Annand [17] .....	100
Table 7: Models and the Correlation Coefficient for Time Averaged Heat Transfer from a 125 cm <sup>3</sup> displacement, Four-Stroke Engine at 1-7 bar BMEP and 3000 to 6000 rpm from Wu <i>et al.</i> [66].....	115
Table 8: In-Cylinder Gas Temperature Measurement Techniques, Adapted and Augmented from Zhao and Ladommatos [56:640].	128
Table 9: Constants for Equations (72) and (73).....	138
Table 10: Constants for Equation (74) as compiled by Blair [27:379].....	139
Table 11: Tracer Gas Methods, Adapted and Augmented from Heywood and Sher [22:89-90] .....	158
Table 12: Listing of Temperature Measurement Names and Locations.....	192
Table 13: Pressure Measurements Installed on the SETB .....	193
Table 14: Design Characteristics of 3W Modellmotoren Engines Selected for Loss Study to Complete Objective 1.....	203
Table 15: Engine Control Limits For a Stable Operating Condition. ....	212
Table 16: GC-MS Parameters for Iso-Octane and Argon Separation and Quantification .....	214
Table 17: GC-TCD Parameters for Oxygen and Nitrogen Separation and Quantification .....	217
Table 18: GC-FID Parameters for Iso-Octane and Argon Separation and Quantification .....	222

Table 19: FID Sensitivity Relative to Hydrocarbon Family as Compiled by Zhao and Ladommatos [56:118]. .....	223
Table 20: Evaluation of Measurement Availability for Heat Transfer Modelling .....	228
Table 21: Optical Path Characteristics.....	234
Table 22: Knock Frequency Characteristics of 3W Modellmotoren Engines .....	244
Table 23: Control of Knock Influence Parameters on the SERB .....	245
Table 24: Base Case for Parametric Engine Studies.....	283
Table 25: Comparison of In-Cylinder Temperature Modelling Results to TLAS Measurement in the Combustion Dome.....	361
Table 26: Best Fit Coefficients for Equation (128), Nusselt Number as a Function of Reynolds Number for Characteristic Values Suggested by Taylor and Toong .....	371
Table 27: Literature Coefficients for Equation (128), Nusselt Number as a Function of Reynolds Number for Characteristic Values Suggested by Taylor and Toong .....	373
Table 28: Best Fit Coefficients for Equations (133) and (134), Friction Losses as Linear, Quadratic, and Cubic Functions of Engine Rotational Speed.....	377
Table 29: Constants for Equations (133) and (134).....	380
Table 30: Best Fit Coefficients for Equations (135) and (136), Friction Losses as a Function of Mean Piston Speed.....	383
Table 31: Constants for Equations (135) and (136) Compiled by Blair [27:379] .....	385
Table 32: Best Fit Coefficients for Equation (138), Friction Losses as a Function of Surface Area to Volume Ratio .....	387
Table 33: Best Fit Coefficients for Equation (139), Friction as a Linear Function of Delivery Ratio .....	391
Table 34: Best Fit Coefficients for Equation (140), Friction as a Linear Function of Delivery Ratio .....	392

## Abbreviations

AFIT	Air Force Institute of Technology
AFRL	Air Force Research Laboratory
AKI	Anti-knock index
ANSI	American National Standards Institute
ASL	Above sea level
ATC	After top center
aTDC	After top dead center
BDC	Bottom dead center
BSFC	Brake specific fuel consumption
BTC	Before top center
bTDC	Before top dead center
CA	Crank angle
CFD	Computation fluid dynamics
CHT	Cylinder head temperature
CI	Confidence interval
COV	Coefficient of variance
COTS	Commercial off the shelf
DoD	Department of Defense
ECU	Engine control unit
EGT	Exhaust gas temperature
FID	Flame ionization detector
FMEP	Friction mean effective pressure (Pa)
FTIR	Fourier Transform Infrared (Spectroscopy)
GC	Gas chromatography/ gas chromatograph
GPIB	General Purpose Interface Bus
HCCI	Homogenous charge compression-ignition
HID	Helium ionization detector
ICE	Internal combustion engine
KLIMEP	Knock-limited indicated mean effective pressure
LDV	Laser Doppler Velocimetry
LSDAC	Low Speed Data Acquisition and Control
MAPO	Maximum amplitude of pressure oscillations
MEMS	Microelectromechanical systems
MFB	Mass fraction burned
MS	Mass spectrometry
MSD	Mass selective detector
NDIR	Nondispersive infrared (spectroscopy)
NI	National Instruments

NMR	Nuclear magnetic resonance
OEM	Original equipment manufacturer
ON	Octane number
ONR	Octane number requirement
PIV	Particle image velocimetry
PRF	Primary reference fuel
RPA	Remotely piloted aircraft
RTD	Resistance temperature detector
UEGO	Universal exhaust gas oxygen
UHC	Unburned hydrocarbon
VCSEL	Vertical-cavity surface-emitting laser
SBIR	Small Business Innovative Research
SERB	Small Engine Research Bench
SERL	Small Engine Research Laboratory
SFC	Specific fuel consumption
TCD	Thermal conductivity detector
TDC	Top dead center
TLAS	Tunable laser absorption spectroscopy
UHC	Unburned hydrocarbons
WOT	Wide open throttle

## Nomenclature

$\%i$	Percent of species ‘i’
$A$	Area (m <sup>2</sup> )
	Absorbance
$(A_i)_{SIM}$	Mass spectrometer detector peak area, ‘i’
$(A_i)_{TCD}$	Thermal conductivity detector peak area, ‘i’
$A_n$	Fourier coefficient
$\frac{A}{F}$	Air to fuel ratio
$B$	Engine bore (m)
$B_n$	Fourier coefficient
$c$	Speed of sound (m/s)
	Speed of light (m/s)
$C_{\#}$	Number of carbon atoms in molecule
$C_d$	Discharge coefficient
$C_1$	Generic constant
$C_2$	Generic constant
$C_3$	Generic constant
$C_p$	Specific heat, constant pressure (J/kg-K)
$CR$	Compression ratio
$D$	Characteristic length (m)
$\dot{E}_{e,k}$	Exhaust kinetic energy (W)
$E_p$	Energy, a photon (J or eV)
$f$	Frequency, Hz
	Friction coefficient
$f_p$	Frequency, primary knock (Hz)
$h$	Heat transfer coefficient (W/m <sup>2</sup> -K)
	Planck’s constant (m <sup>2</sup> /kg-s)
$h_c$	Heat transfer coefficient, coolant (W/m <sup>2</sup> -K)
$\dot{H}_{e,ic}$	Enthalpy loss, incomplete combustion
$\dot{H}_{e,s,a}$	Enthalpy loss, to atmosphere (kW)
$h_g$	Heat transfer coefficient, cylinder gas (W/m <sup>2</sup> -K)
$h_o$	Convection coefficient, overall (W/m <sup>2</sup> -K)
$H_p$	Enthalpy, products (J/kg)
$H_r$	Enthalpy, reactants (J/kg)
$I$	Current (A)
$J_{m,n}$	Zero of the derivative of the Bessel function of the first kind
$k$	Thermal conductivity (W/m-K)



$k_g$	Thermal conductivity, gas (W/m-K)
$K$	Short-circuiting parameter
$l$	Path length (m)
$L$	Stroke (m)
$m_0$	Reference mass (kg)
$\dot{m}_a$	Mass flow rate, air (kg/s)
$m_{ch}$	Mass of fresh charge (kg)
$m_{cyl}$	Mass of cylinder contents (kg)
$\dot{m}_{ex}$	Mass flow rate of charge exhausted from the engine (kg/s)
$\dot{m}_{ch}$	Mass flow rate of fresh charge into the engine (kg/s)
$m_f$	Mass of fuel (kg)
$\dot{m}_f$	Mass flow rate of fuel (kg/s)
$\dot{m}_g$	Mass flow rate, gas (kg/s)
$\dot{m}_i$	Mass flow rate of species 'i' (kg/s)
$m_{ret}$	Retained mass (kg)
$MW_{ex}$	Molecular weight, exhaust (kg/kmol)
$MW_{fc}$	Molecular weight, fresh charge (kg/kmol)
$MW_i$	Molecular weight, species 'i' (kg/kmol)
$n$	Concentration (mol/L)
$n_r$	Engine type constant (2 for four-stroke, 1 for two-stroke)
$N$	Engine speed (rpm)
$N_{HC}$	Hydrocarbon sensitivity
$Nu$	Nusselt number
$P$	Power (kW)
$p$	Pressure, generic (Pa)
$p_0$	Pressure, reference conditions (Pa)
$p_1$	Pressure, cylinder contents at exhaust port close (Pa)
$p_b$	Pressure, burnt gas (Pa)
$P_b$	Power, brake (W)
$p_{cyl}$	In-cylinder pressure (Pa)
$P_f$	Power, friction (W)
$P_i$	Power, indicated (W)
$p_{im}(\theta)$	Pressure, intake manifold (Pa)
$p_{mot}$	Pressure, motored (Pa)
$P_{pf}$	Power, piston friction (W)
$p_{ref}$	Pressure, reference (Pa)
$P_{tf}$	Power, friction (W)
$P_{SL}$	Power, sea level (W)

$Pr$	Prandtl number
$q$	Mixing parameter
$Q^*$	Energy released per unit working fluid (J/mol-K or J/kg-K)
$\dot{Q}_{c,e}$	Heat transfer rate, to coolant from exhaust ports (W)
$\dot{Q}_{comb}$	Heat release rate, combustion (W)
$\dot{Q}_{cool}$	Heat transfer rate, to coolant (W)
$Q_{cyl}$	Heat released to cylinder gas during combustion (J)
$Q_{cyl,loss}$	Heat transfer from the cylinder (J)
$\dot{Q}_{cyl,loss}$	Heat transfer rate from the cylinder (W)
$\dot{Q}_{e,r}$	Heat transfer rate, radiated from the exhaust (W)
$Q_H$	Heat transfer, high reservoir (J)
$Q_{LHV}$	Lower heating value (J/kg)
$Q_{HV}$	Heating value (J/kg)
$Q_L$	Heat transfer, low reservoir (J)
$\dot{Q}_{misc}$	Heat transfer, miscellaneous (W)
$\dot{Q}_w$	Heat transfer rate, to combustion chamber wall (W)
$r$	Radial distance from bore axis (m)
$R$	Gas constant (J/mol-K (universal) or J/kg-k)
$Re$	Reynolds number
$SA$	Surface area (m <sup>2</sup> )
$SC_{\Lambda>1}$	Short-circuiting guaranteed by excess fresh charge
$SC_{scavenging}$	Short-circuiting directly attributable to poor scavenging
$S_p$	Piston speed (m/s)
$\bar{S}_p$	Mean piston speed (m/s)
$St$	Stanton number
$t$	Time (s)
$T$	Temperature, generic (K)
$T_0$	Temperature, reference (K)
$T_1$	Temperature, cylinder contents at exhaust port close (K)
$T_b$	Temperature, burnt gas (K)
$T_c$	Temperature, coolant (K)
$t_{cyl}$	Cylinder wall thickness (m)
$T_{g,cyl}$	Temperature, gas in-cylinder (K)
$T_H$	Temperature, high reservoir (K)
$T_i$	Temperature, fresh charge (K)
$T_L$	Temperature, low reservoir (K)
$T_{ref}$	Temperature, reference (K)
$T_s$	Temperature, cylinder wall (exterior) (K)

$T_w$	Temperature, cylinder wall (interior) (K)
$V$	Velocity (m/s)
$V^*$	Non-dimensional velocity
$V_g$	Velocity, gas (m/s)
$V_b$	Volume, burnt gas (m <sup>3</sup> )
$V_{ch}$	Volume, fresh charge (m <sup>3</sup> )
$V_{cyl}$	Volume, cylinder (m <sup>3</sup> )
$V_d$	Volume, displacement (m <sup>3</sup> )
$V_{ref}$	Volume, reference (m <sup>3</sup> )
$V_{tr}$	Volume, trapped (m <sup>3</sup> )
$w$	Humidity, relative (%)
$w_{SL}$	Humidity, relative, sea level (%)
$W$	work (J)
$x_b$	Mass fraction, burned
$x_i$	Mass fraction, species 'i'
$x_r$	Mass fraction, residuals
$y_{i,a}$	Mole fraction, species 'i', ambient
$y_{i,b}$	Mole fraction, species 'i', burnt charge
$y_{i,ex}$	Mole fraction, species 'i', exhaust
$y_{i,fc}$	Mole fraction, species 'i', fresh charge
$y_{i,u}$	Mole fraction, species 'i', unburnt charge

### Greek

$Y^*$	Non-dimensional length scale
$\alpha$	Absorptivity
$\gamma$	Ratio of specific heats
$\Delta E$	Change in energy level (eV or J)
$\Delta P$	Pressure drop (Pa)
$\lambda$	Wavelength (m)
$\Lambda$	Delivery ratio
$\varepsilon_g$	Emissivity, gas
$\varepsilon_w$	Emissivity, wall
$\eta_c$	Combustion efficiency
$\eta_{ch}$	Charging efficiency
$\eta_{fc}$	Fuel conversion efficiency
$\eta_m$	Mechanical efficiency
$\eta_{ret}$	Retaining efficiency
$\eta_{scv}$	Scavenging efficiency
$\eta_{th}$	Thermal efficiency

$\eta_{tr}$	Trapping efficiency
$\eta_v$	Volumetric efficiency
$\theta$	Crank angle (CAD)
$\theta_{sc}$	Crank angle, scavenge close (CAD)
$\theta_{so}$	Crank angle, scavenge open (CAD)
$\mu$	Viscosity (m <sup>2</sup> /s)
$\rho$	Density (kg/m <sup>3</sup> )
$\rho_0$	Density, reference conditions (kg/m <sup>3</sup> )
$\rho_b$	Density, burnt gas (kg/m <sup>3</sup> )
$\rho_i$	Density, fresh charge (kg/m <sup>3</sup> )
$\rho_{pwr}$	Density, power (W/cm <sup>3</sup> )
$\rho_{SL}$	Density, sea level (kg/m <sup>3</sup> )
$\sigma$	Stefan-Boltzmann constant (W/m <sup>2</sup> -K <sup>4</sup> )
	Normal pressure (Pa)
$\tau$	Extent of process progression
$\omega_g$	Swirl velocity, gas (rad/s)
$\zeta$	Sensitivity factor

# **THE SCALING OF LOSS PATHWAYS AND HEAT TRANSFER IN SMALL SCALE INTERNAL COMBUSTION ENGINES**

## **I Introduction**

This work addresses shortcomings in the current understanding of the relative importance of and predictive correlations for loss pathways in small internal combustion engines (ICEs) for Group 2 remotely piloted aircraft. This chapter covers the introduction for the project. Section 1 outlines the three specific issues with using small ICEs for remotely piloted aircraft that will be addressed in this dissertation: the relative importance of loss pathways, the availability of predictive models for loss pathways, and the ability to run the engines on logistically supported fuel. Section 2 translates these general issues into a set of corresponding problem statements. Then, Section 3 develops the problem statements into a cohesive set of research objectives. Next, Section 4 comments on the uniqueness of the research. The final section, Section 5, provides an overview of the remainder of the document.

### **1. General Issue**

In September 2014, the Air Force Research Laboratory's (AFRL) Small Engine Research Laboratory (SERL) was approached to select commercial-off-the-shelf (COTS) components to construct a motor-generator set for a remotely piloted aircraft (RPA) with the following requirements: the finished system was required to produce 4 kW of power, achieve a brake specific fuel consumption of 0.5 kg/kW-hr, have a specific power greater than 1.25 kW/kg, and be ready for initial testing in less than three weeks. Sifting through manufacturer data on commercially available engines, laboratory personnel easily found maximum power ratings and masses for most engines. However, comparisons of

manufacturer power with test data collected on engines at SERL revealed that, as tested, most engines delivered less power than the manufacturer rating and some delivered as little as 60% of the manufacturers' claims. Furthermore, researchers struggled to find relevant fuel consumption data, quantitative thermal cooling requirements, and torque-speed curves for developing the required motor-generator set.

Despite the sparse data and poor thermal efficiencies of small internal combustion engines, the small unmanned aircraft market continues to experience explosive growth. In 2013, a report release by AUVSI estimated that between 2015 and 2025, remotely piloted systems could create over 100,000 new jobs and \$82 billion in economic activity [1]. Of the remotely piloted aircraft (RPAs) tasked with surveillance and reconnaissance type missions (which range from military applications, to border patrol, precision agriculture, and wildfire observation), the majority are electric powered [2, 3], and hydrocarbon fueled aircraft remain, by total number, the minority.

However, hydrocarbon fueled RPAs enjoy a distinct advantage over electrically powered vehicles. Even with the best battery and electric motor technology on the market, hydrocarbon fueled RPAs offer superior range and endurance due to the high specific energy of hydrocarbons relative to batteries [4]. For instance, one of the best rechargeable battery chemistries available on the market, lithium sulfur, offers a specific energy of 600 W-hr/kg while the average hydrocarbon offers nearly 13,000 W-hr/kg. Theoretically, this offers hydrocarbon fueled vehicles a 20:1 range or endurance margin over a comparable electric propulsion systems. In practice, the margin is smaller. Compared to electric power plants which have efficiencies from 80% to 90%, automotive scale internal combustion engines (ICEs) typically have fuel conversion efficiencies of ~30%. The

10 cm<sup>3</sup> to 100 cm<sup>3</sup> (1-7 kW, mfg. rated) engines used in Group 2 remotely piloted aircraft (RPAs) have lower efficiencies of 4%-15% [5, 6]. For an 85% efficient electric motor, a 5% ICE fuel conversion efficiency is the breakeven point [7], where both produce the same power for an equivalent weight. Therefore, ICE propulsion still offers an advantage over electric propulsion for current (at the time of writing) COTS, 1-7 kW (10-100 cm<sup>3</sup> displacement) power plants.

### **1.1. Loss Pathways and Efficiency**

When working with small hydrocarbon engines, the practically achievable fuel conversion efficiency as the engine becomes smaller remains unknown. In theory efficiency drops with engine size due to the increasing magnitude of losses *relative* to the amount of energy released during combustion. As such, there likely exists a point where the electric motor system becomes desirable. There is some question in literature about how much the efficiency truly scales with engine size in practice. There are a number of variables that can quantify ‘engine size’, although typically displaced volume, bore diameter, or power is implied. In this work, ‘engine size’ is primarily used to indicate displaced volume unless otherwise indicated.

The answer is not as clear cut as looking up efficiency as a function of displaced volume. One study found that the efficiencies of nine micro engines with 8-650 W power output had fuel conversion efficiencies ranging from 4%-9%. The variation was tied more to equivalence ratio than to displaced volume [2, 6, 8]. Another study of three engines from 2.5–6.8 kW found that as engine size decreased from the largest to the smallest engine, efficiency decreased from 16% to 9% [5]. A third set of test data taken on automotive and larger scale engines and compiled by Taylor [9:401-11] indicated that for

large engines (bores from 5 cm to 30 cm), engine size has little impact on efficiency. When taken as a group, the test data showed indicated thermal efficiencies (as opposed to brake efficiency reported above) of 30-50% for these engines. However, if broken out by engine type, the efficiencies were scattered about a group mean (48% for two-stroke engines, 44% for four-stroke engines) with an absolute deviation of  $\pm 4\%$ , and showed no trend with bore diameter. Nevertheless, Taylor also noted that in the case of very small engines, poor fuel conversion efficiency (values not provided) is common due to high heat losses and inadequate mixture preparation [9:409]. Taylor did indicate that there is a decrease in efficiency as engine size decreases, although the majority of the decrease may occur in a limited range of engine sizes. The discussion in Rowton *et al.* [5] and Ausserer *et al.* [10], discussed in greater detail in Chapter II, Section 4, suggests displaced volumes from 10 cm<sup>3</sup> to 100 cm<sup>3</sup> (1-7 kW, manufacturer rated power) for the engine style considered herein is where the sharp decrease in fuel conversion efficiency begins. Literature sources also disagree on the dominant loss pathways responsible for this efficiency drop. Despite the disagreement, there are three consistent themes throughout the surveyed literature:

- Engines with displaced volumes from 10-100 cm<sup>3</sup> [5] have lower fuel conversion efficiencies than conventional size engines and higher fuel conversion efficiencies than engines with displacements less than 10 cm<sup>3</sup> [2, 6, 8], and there is a definite trend of lower efficiency with decreasing engine size.
- Thermal losses play a significant role in engine efficiency, coupled with other important mechanisms such as friction, quenching, incomplete combustion, and short-circuiting of fresh charge.



- The relative importance of these loss pathways and how that order changes with engine size across the 10-100 cm<sup>3</sup> displaced volume range is unquantified.

## **1.2. Loss Models**

A model for each of these losses would be far more useful than a set of empirical measurements on one or two engines, and models for these losses are sometimes available for conventional engines. They are not, however, available for 10 cm<sup>3</sup> to 100 cm<sup>3</sup> displacement engines. In all instances encountered in the literature, models for heat transfer and friction losses were adapted from models for larger engines, often with little validation to demonstrate their applicability at the small scale. Of all of the loss pathways, the models for the following would be the most useful.

- 1) A model for the overall heat transfer from the engine. Preferably this model would be in terms of easily measured engine parameters.
- 2) A model for friction losses that captures both speed and engine size effects.

## **1.3. Fuel**

In addition to the challenges of poorly quantified losses and a lack of appropriate models for design calculations, the small engines considered herein also face a third challenge: fuel. Until the last two to three decades, most engines with displaced volumes less than 100 cm<sup>3</sup> operated on a mixture of nitromethane, methanol, and castor oil, called glow fuel. Glow fuel has a low air to fuel ratio (6.42:1 compared to ~15:1 for gasoline) and a low heating value (16.5 kJ/kg compared to 35.5 kJ/kg for gasoline) [10, 11]. Thus, the introduction of small gasoline powered, spark-ignition engines improved performance (range, endurance) by a factor of four. Compared to glow fuel engines that ran significantly rich, were difficult to start, and tended to coat their surroundings with castor oil and unburnt

fuel, small gasoline powered spark-ignition engines were a giant technological leap forward despite their inferior performance relative to larger engines.

For military applications, fuel technology must take an additional step forward. DoD Directive 4140.25 [12] encourages the movement towards a single battle field fuel. For the Air Force and Army, this means JP-8 and in the future Jet A/Jet A-1. The Navy may still use JP-5, which is very similar to JP-8, although it has a slightly higher flash point [12]. In either case, there are three primary challenges to running a small internal combustion engine on heavy fuels such as diesel or jet fuel. First, the low vapor pressure of heavy fuel makes it difficult to form a combustible mixture, especially in air carbureted engines. Second, the low lubricity of heavy fuel relative to gasoline requires special attention to lubrication to prevent wear on engine components. Third, the low anti-knock index (AKI) of jet fuel (approximately 20 [13]) makes it prone to knock in ICEs, which can lead to engine damage and failure.

At least one source has suggested that increased losses (specifically thermal losses) relative to the energy released during combustion may relax the AKI requirement as engine size decreases [9:409]. A relative increase in thermal losses would also lower the fuel conversion efficiency. Yet, it remains unclear if increasing thermal losses are actually the dominant loss pathway. In any case, it may be possible to manage the dominant loss mechanisms to both obtain better efficiency and run a low AKI fuel. Additionally, there are conflicting reports on how the specific fuel consumption and efficiency of a small engine are impacted by running heavy fuel [14, 15]. Further research is warranted to determine the performance benefits of low AKI fuels and how engine size affects those benefits and the feasibility of conversion. Clearly there are opportunities to enhance the

understanding of small ICEs with respect to the scaling of losses, heat transfer and friction models, and the interaction of engine size, loss pathways, and loss mechanisms, and fuel anti-knock requirements.

## **2. Problem Statements**

Aircraft and ground power applications of ICEs with displaced volumes from 10 cm<sup>3</sup> to 100 cm<sup>3</sup> would benefit from an enhanced understanding of loss pathways, and in turn that understanding could be leveraged to improve the overall efficiencies of these engines. Thus, this work will focus on three interrelated problems targeted at understanding the drop in efficiency with engine size. These problems, defined in this section, will be translated into research objectives in the next section.

### **2.1. Scaling of Loss Pathways**

Research in conventional sized engines (larger than 100 cm<sup>3</sup> displaced volume) and micro engines (less than 10 cm<sup>3</sup> displaced volume) indicates that the relative importance of the four primary loss pathways in ICEs almost completely reverses between automotive and larger scale and micro scale engines. Cadou *et al.* [16] report the following losses in order of decreasing importance for nine micro engines: incomplete combustion, heat transfer, sensible enthalpy in the exhaust, and friction losses, which is reversed from automotive scale engines. Moreover, the literature indicates that this reversal may occur between 10 cm<sup>3</sup> and 100 cm<sup>3</sup> displaced volume. An understanding of how these loss pathways change with engine size is crucial to improving the fuel conversion efficiency and to determining if the mechanisms responsible for the efficiency drop permit an inherent (and useful) relaxation of fuel AKI requirement with engine size.

## 2.2. Loss Models

For predicting loss behaviors in small engines there is a lack of available data to indicate whether or not models for conventional engines are valid. For example, Menon and Cadou employed a heat transfer model proposed by Annand [17] in their study of glow engines. In their results, Menon and Cadou acknowledge that the model was developed for large compression-ignition (CI) and spark-ignition engines [16], and as a result, the model may not have been appropriate for the engines investigated in their work. In fact, many of the heat transfer models in literature were developed for large scale CI engines, many of which are water cooled. In contrast, the engines considered herein have displaced volumes between 10 cm<sup>3</sup> and 100 cm<sup>3</sup> and are spark-ignited, air-cooled engines. The differences in engine pressures, temperatures, and flow patterns make it improbable that the existing models can simply be applied to these small ICEs without adaptation. Two losses, heat transfer and friction, have readily available models proposed for automotive and larger scale engines that remain untested on the engine size considered here.

### 2.2.1. Heat Transfer Model

Essentially all heat transfer models used for ICEs date to a steady state analysis of a constant volume sphere performed by Nusselt [18] in 1923. The model was refined by Taylor and Toong in 1957 into the following form, where  $a$  and  $m$  are constants,  $Nu$  is the Nusselt number, and  $Re$  is the Reynolds number. Originally developed for turbulent flow over a flat plate, this form is common to many heat transfer applications, and it suggests that the heat transfer with the engine is primarily due to convection.

$$Nu = aRe^m \tag{1}$$

Taylor and Toong suggested that  $m = 0.75$  and that  $a$  is a function of engine geometry and type, and may also be influenced by heat transfer (especially radiation) that is not directly related to the Reynolds number. Other authors have added additional terms to capture other engine physics and parameters such as radiation, surface area, and gas swirl induced by the intake. A discussion of the more notable models is reserved for Chapter II, Section 5.1. Even with the simple model in Equation (1), there remains debate about the appropriate characteristic length scales, fluid properties, and velocity. Despite entire references devoted to heat transfer studies and correlations for automotive and larger scale engines (example [19, 20] and several textbook chapters [9:266-311, 21:668-711]), an evaluation of the available models for small engines has not been accomplished. Thus, there is no validated model for predicting heat transfer in 10-100 cm<sup>3</sup> displacement ICEs.

### 2.2.2. Friction Model

Heywood's book, *Internal Combustion Engine Fundamentals* [21:719-20], considered one of the authoritative sources on engines, presents the following friction correlation, which has been well studied for automotive and larger scale, four-stroke ICEs. In Equation (2),  $FMEP$  is the friction mean effective pressure,  $N$  is the rotational speed of the engine, and  $a$ ,  $b$ , and  $c$  are empirically determined constants.

$$FMEP = a \left( +b \left( \frac{N}{1000} \right) + c \left( \frac{N}{1000} \right)^2 \right) \quad (2)$$

The fit implies that the friction power normalized by engine volume consists of three types of losses, and that those losses are proportional to engine speed. The coefficients are typically valid for a given type (spark-ignition, compression-ignition) and design (valve type, bearing type) of engine. However, the appropriate coefficients and the validity of the

correlation are not well studied for two-stroke engines [22:369]. Heywood and Sher also note that the coefficients are not well studied for small engines [22:369].

### **2.3. Inherent Relaxation of Fuel AKI Requirement with Engine Size**

For engines where heat transfer as a percentage of released energy increases as the engine size decreases, it has been shown that the knock-limited fuel AKI requirement also decreases [9:409]. However, previous work on small engines indicates that the relative heat transfer losses may not actually increase as rapidly as other losses [5]. It is well established that losses relative to the energy released during combustion increase with decreasing displaced volume, as indicated by the fuel conversion efficiency of engines smaller than 10 cm<sup>3</sup> displacement [6], 10 cm<sup>3</sup> to 100 cm<sup>3</sup> displacement [5], and conventional size engines [21:674]. The exact mechanism(s) responsible for the increase in losses will determine whether a measureable increase in knock resistance with decreasing engine size exists. For example, a mechanism reducing the thermal loading of the in-chamber gases, such as heat transfer from the cylinder head or quenching of combustion in crevice volumes, will reduce the potential for knock and in turn the required fuel AKI. However, any mechanism that increases gas and engine temperatures, such as sensible exhaust enthalpy losses and friction, will increase the propensity to knock and in turn the fuel AKI requirement.

In addition to conversion to a logistically supported fuel, advocates for heavy fuel conversion of small engines have claimed the lower AKI fuels will provide improved fuel conversion efficiency relative to higher AKI fuels. The argument is based on higher laminar flame speeds, and thus higher turbulent flame speeds for low AKI fuels. Previous investigations indicate that the laminar flame speed of n-heptane (a 0 octane number (ON),

low AKI fuel) is 5-10 cm/s faster than iso-octane (a 100 ON, high AKI fuel) [23]. However, while Wilson *et al.* [14] concluded that this difference in flame speed translates to an improvement in efficiency, data taken by Cathcart *et al.* [15] indicated that the improvement in efficiency was more a function of the fuel preparation technique and that for the same fuel preparation method, the low AKI fuel actually delivered a lower fuel conversion efficiency. Thus, it is unclear if the use of a low AKI fuel in a small engine will provide a benefit outside of meeting the requirements set forth in DoD 4140.25 [12].

### **3. Research Objectives and Scope**

The problems outlined in Section 2 provided a number of exciting research opportunities to improve the engineering community's understanding of small engines and its ability to leverage those small engines for a wide variety of applications to include RPAs. The objectives for this research have been divided into three subsections each corresponding to one of the problems described in Section 2. Following the research objectives is a subsection (Section 3.4), bounding the scope for this effort.

#### **3.1. Objective 1**

*Investigate how loss pathways scale in 10-100 cm<sup>3</sup> displacement ICEs.*

This first objective addresses the issues posed in Section 2.1, establishing the order of importance for losses and how that order changes with engine size. This first objective may be broken down into the following high level tasks:

- 1) Determine the relative contributions of the following losses in a family of geometrically similar, commercially available engines with displaced volumes ranging from 10-100 cm<sup>3</sup> (1-7 kW, manufacturer rated power):
  - a. Heat transfer from the cylinder (also referred to as cooling load)

- b. Short-circuiting of fresh charge (unburnt fuel) to the exhaust
  - c. Sensible enthalpy in the exhaust gases
  - d. Incomplete combustion
  - e. Brake power (not a loss, but an energy pathway necessary for a full energy accounting)
  - f. Friction losses, including pumping work (sometimes lumped with heat transfer and sensible exhaust enthalpy due to measurement methodology)
- 2) Determine which losses are responsible for the observed decrease in fuel conversion efficiency as engine size decreases.
  - 3) Perform a parametric study of engine controls (speed, throttle, equivalence ratio, combustion phasing, and cylinder head temperature) to link losses with the mechanisms that cause them.

### 3.2. Objective 2

*Develop models/ correlations for thermal and friction losses  
for 10-100 cm<sup>3</sup> displacement ICEs.*

As established in Section 2.2, there are no established models for overall thermal losses (convection to the cooling flow) or friction losses (within the engine) for 10-100 cm<sup>3</sup> displacement ICEs. Therefore, this objective aims to fill that void by employing the loss data collected for Objective 1 and developing appropriate overall heat transfer and friction loss models or correlations for 10-100 cm<sup>3</sup> displacement ICEs. This objective may also be expressed in terms of the following high level tasks:

- 1) Determine if the overall heat flux model proposed by Taylor and Toong [21:677-80] is appropriate for 10-100 cm<sup>3</sup> displacement, two-stroke, spark-ignition engines,



and identify an appropriate exponent relating Nusselt number and Reynolds number.

- 2) Evaluate other quantities for inclusion in the model for the Nusselt number.
- 3) Compare friction loss data from the tested engines to the proposed friction loss correlation presented in Section 2.2.2.
- 4) Identify which coefficient(s) in the friction loss model scale with engine size and reconcile that information with engine design.

### **3.3. Objective 3**

*Quantify the relationship between engine size, loss mechanisms, performance, and fuel AKI requirements in 10-100 cm<sup>3</sup> displacement ICEs.*

The third and final objective satisfies the Department of Defense's (DoD) primary motivation for this research: enabling heavy fuel for Group 2 RPAs. This objective will determine if the mechanisms that cause losses to increase relative to fuel energy with decreasing engine size, identified in Section 3.1, provide an inherent relaxation in the fuel AKI requirement. Note that these mechanisms may be factors that control losses or the losses themselves. Thus, there is distinction between “losses pathways”, which are the energy pathways measured for Objective 1, and “loss mechanisms”, which are the underlying processes that drive those losses. For example, reducing the compression ratio is a “loss mechanism” that increases the heat transfer and exhaust enthalpy “loss pathways”. Objective 3 may be expressed in terms of the following high level tasks:

- 1) Map the knock-limited indicated mean effective pressure for a family of geometrically similar 10-100 cm<sup>3</sup> displacement engines, running primary reference blend fuels ranging from 0-100 ON.

- 2) Evaluate the performance impact (power, efficiency) of converting from 98 ON fuel to 20 ON fuel.
- 3) Quantify the impact of engine control variables (speed, equivalence ratio, combustion phasing, and head temperature) on the knock limit. Link changes in losses and loss mechanisms (identified in Objective 1) and engine size to the observed trends in the fuel AKI requirement.

### **3.4. Project Scope**

Internal combustion engines encompass a vast field that has received significant attention over the past century. Consequently, a definition of scope is necessary to create a feasible, meaningful project. As per the propulsive requirements of Group 2 RPAs, this project will focus on engines with displaced volumes from 10 cm<sup>3</sup> to 100 cm<sup>3</sup> (1-7 kW, manufacturer rated power). Due to the focus on aircraft applications, the engine type will be constrained to two-stroke engines. Most small commercial two-stroke ICEs are spark-ignited, offering improved performance over glow fuel (catalyzed compression-ignition) engines through control of combustion phasing. Thus this study will also be constrained to spark-ignition engines.

The RPA market thrives on inexpensive, commercially available components (as do other markets, such as lawn tools), and thus the study will be restricted to commercially obtainable engines. In order to reduce the impact of geometry (other than size) as a confounding variable, the engines will be kept as similar as feasible within the constraints of commercially available products. Remaining geometrical differences will be noted. With these constraints, the results will provide relevant, scientific insight for the improvement of Group 2 RPA propulsion systems.

#### **4. Uniqueness**

This effort is unique and distinct from past efforts for several reasons. First, the objective to order the relative importance of losses has not been examined in detail for 10 cm<sup>3</sup> to 100 cm<sup>3</sup> displacement engines. Moreover, unlike previous studies of small ICEs, this study will close the energy balances instead of using an unmeasured pathways to make up the difference between input fuel energy and the measured pathways. Second, models for heat transfer and friction losses, examined in Objective 2, have not been developed, tested, or validated for 10 cm<sup>3</sup> to 100 cm<sup>3</sup> displacement engines. Finally, while there have been a number of one-off heavy fuel conversions of small engines in the literature, Objective 3 proposes a systematic study to determine how the mechanisms that enable such conversions scale with engine size and whether or not a general conclusion may be drawn about the relationship between AKI relaxation and engine size.

#### **5. Organization**

The remainder of the document is organized as follows. Chapter II provides a literature review. The first three sections provide overviews of the chapter (Section 1), two-stroke (Section 2) engines, and small engine testing (Section 3). The following three sections provide background on engine scaling (Section 4), heat transfer (Section 5), and heavy fuel operation (Section 6), as relevant to Objectives 1, 2, and 3, respectively. Chapter II was written for readers who may not have extensive two-stroke engine testing background. For readers primarily interested in the methodology and results, Chapter II may be used as a reference (relevant sections of Chapter II are identified for reference in later chapters). Chapter III describes the proposed research methodology. The first section provides an overview of the chapter. Section 2 describes the laboratory facility. The remaining three

sections (Sections 3-5) discuss the methodology for accomplishing each of the research objectives.

Chapter IV-VI describes the results of each objective. Each chapter begins with an overview (Section 1) and ends with a summary and conclusions section. Chapter IV describes the results of Objective 1, and consists of two main parts. The first part (Section 2) examines scaling and loss pathways. The second part (Section 3) explores the impact of the four main engine control variables: equivalence ratio, combustion phasing, head temperature, and throttle on the loss pathways. Chapter V addresses the modelling goals of Objective 2 and is split into three sections. Each section addresses one of the modelled pathways: heat transfer (Section 2), friction (Section 3), and gas exchange (Section 4). Chapter VI explains the results of the fuel AKI requirement study and is also divided into three parts. The first two parts (Section 2 and Section 3) examine knock limits, power, burn angle, and efficiency for reference fuel blends ranging from 0 ON to 98 ON. Section 3 focusses specifically on the conversion from 98 ON fuel (manufacturer recommended) to 20 ON fuel (JP-8 and diesel equivalent). The third part (Section 4) examines the impact of combustion phasing, equivalence ratio, and head temperature on the knock limit and ties those impacts back to changes in the energy pathways observed during Objective 1. Lastly, Chapter VII provides a summary of this work and outlines suggestions for future efforts.

## II Literature Review

### 1. Chapter Overview

This chapter is intended to orient the reader with the aspects of two-stroke engines and engine testing relevant to the proposed work. It also provides an overview of relevant, prior art in the field. The remainder of this chapter is split into five sections. Section 2 discusses the two-stroke engine, how it compares to other internal combustion engines, and its key operational aspects. Section 3 summarizes prior small engine testing that provided insight for the development of the Small Engine Research Bench (SERB), described in Chapter III. Section 4 discusses engine scaling and provides a proposed energy balance for tracking the loss pathways that are the focus of Objective 1. Section 5 covers loss models and measurement techniques for conventional size engines. For the models considered for Objective 2 (heat transfer and friction) the relevant sub-sections also discuss the models in additional depth including what terms might improve the fidelity for 10-100 cm<sup>3</sup> displacement, SI, two-stroke engines. Finally, Section 6 provides an overview of the obstacles to and attempts at heavy fuel conversion of small ICEs, forming a foundation for Objective 3.

### 2. The Two-Stroke, Spark-Ignition Engine

A comprehensive discussion of ICE topics is well beyond the scope of this document, and there are numerous textbooks available on the subject. *Internal Combustion Engine Fundamentals* by Heywood is an excellent source for general information on conventional engine topics [21]. A somewhat more modern text applicable specifically to two-stroke engines was written by Heywood and Sher [22]. A pair of texts by Taylor offer one of the

most extensive collections of actual engine data, although that data is somewhat dated [9, 24]. Other useful texts on engines include those by Pulkrabeck [25], Stone [26], Blair [27], and Ferguson and Kirkpatrick [28]. This discussion of ICEs will focus on those aspects most relevant to the current effort. The first section (Section 2.1) will address how two-stroke engines fit within the context of internal combustion engines and what advantages two-stroke engines offer. The following sections address ignition types (Section 2.2), fuel delivery (Section 2.3), cooling (Section 2.4), gas exchange and scavenging (Section 2.5), combustion (Section 2.6), and friction (Section 2.7). The last section (Section 2.8) presents several other engine performance metrics necessary for the study of small engines that did not fit conveniently into one of the other sections.

## **2.1. Context for the Two-Stroke Engine**

Two-stroke spark-ignition engines are a subset of internal combustion engines. Generally speaking, an engine is any device that converts the chemical energy in a fuel into useful work. A combustion engine achieves that conversion through oxidation of the fuel at high temperature. The fuel may be oxidized inside the working fluid or external to the working fluid, leading to the distinction between internal and external combustion engines. The steam engine is a common example of an external combustion engine, where the heat from combusting the fuel vaporizes water (the working fluid) to create steam that is then used to drive a turbine and do useful work. In an internal combustion engine, the fuel is introduced into the working fluid and combusted. Examples include jet turbine engines (Brayton cycle), large diesel truck engines (Diesel cycle) and automobile engines (typically Otto cycle). Internal combustion engines have one key advantage over external combustion engines: they do not require a large heat exchanger to move energy from the

combustion products to the working fluid [21:1-2]. This allows internal combustion engines to be significantly lighter (higher specific power) than external combustion engines.

### 2.1.1. Types of Internal Combustion Engines

There are several types of internal combustion engines. Some engines, like jet turbines and gas fired power generation turbines, which nominally follow a Brayton cycle, operate at a steady state condition where air is continuously ingested, compressed, mixed with fuel, combusted, and expanded through a turbine and nozzle to produce power and/ or thrust. Because Brayton cycle engines operate at a steady state, their performance is limited by the maximum temperature that the materials can withstand. Typically, this translates to limits on the maximum combustion temperature to restrict the turbine inlet temperature [29].

Figure 1, adapted from [30], shows a notional heat engine where the maximum possible thermal efficiency is governed by the first and second laws of thermodynamics. At maximum efficiency, the process must be reversible (no net production of entropy) and the thermal efficiency ( $\eta_{th}$ ) becomes a direct function of the temperature of the hot ( $T_H$ ) and cold ( $T_L$ ) reservoirs as shown in Equation (3). Since the hot reservoir is limited in a turbine

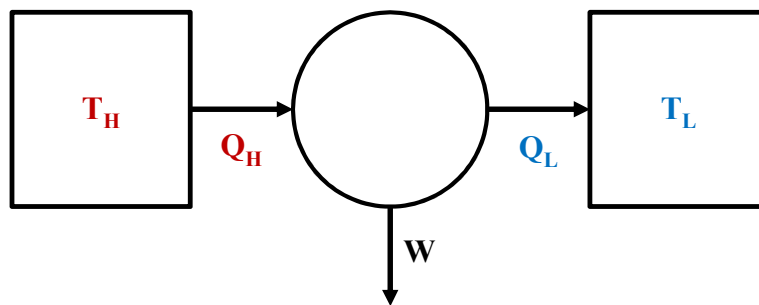


**Figure 1: Generalized heat engine, adapted from [30].**

engine due to material limits at steady state operation, the maximum potential efficiencies of such engines suffer. Turbine engines are often throttled by controlling the turbine inlet temperature, and throttled performance directly decreases the fuel conversion efficiency and increases the specific fuel consumption.

$$\eta_{th} = 1 - \frac{T_L}{T_H} \quad (3)$$

Reciprocating engines overcome these limitations through cyclical operation. Since combustion only occurs for a portion of each cycle, the engine must only withstand the peak pressures and temperatures during a fraction of the operation, and thus reciprocating ICEs can run at higher peak temperatures and pressures. Additionally, the efficiency and fuel consumption of reciprocating engines degrades more slowly under throttled conditions. Turbine engine efficiency is also directly related to the compressor efficiency, which degrades with decreasing corrected mass flow and in turn decreasing engine size. Reciprocating engines do not have this limitation. Thus, because of their superior throttling characteristics, higher allowable peak pressures, temperatures, and theoretical thermal efficiencies, reciprocating ICEs are ideal for small aircraft applications. For clarity, in the remainder of this document ICE will refer specifically to reciprocating engines.

### **2.1.2. Engine Cycle: Two-Stroke vs Four-Stroke**

Both the two-stroke and four-stroke engine cycles follow the same general process. Fresh air and fuel is inducted into the engine. The fuel is compressed, ignited, and then it combusts, creating a high pressure working fluid. That high pressure working fluid pushes on a piston. The connecting rod and crankshaft convert that linear motion into rotational motion which is transmitted out the engine and used to accomplish useful work. The hot exhaust gases are then purged from the cylinder.



As shown in Figure 2, reprinted from Heywood [21:10], and Figure 3, also reprinted from Heywood [21:11], the two engine types are dramatically different in how they accomplish the process. In the four-stroke engine, each step has its own stroke of the piston: intake, compression, expansion, exhaust. In the two-stroke engine, the intake and compression stroke and the expansion (power) and exhaust stroke are combined. Thus, the two-stroke engine produces one power stroke per revolution, instead of a power stroke every other revolution. This difference is key for aeronautical applications, since the two-stroke engine theoretically produces twice as much power per revolution.

The elimination of a revolution dedicated to the exchange of exhaust gases for fresh charge, referred to as scavenging in two-stroke engines, forces charge intake and exhaust removal to overlap significantly. This reduces how effectively the engine can fill the combustion volume with fresh charge, and results in two-stroke engines only producing

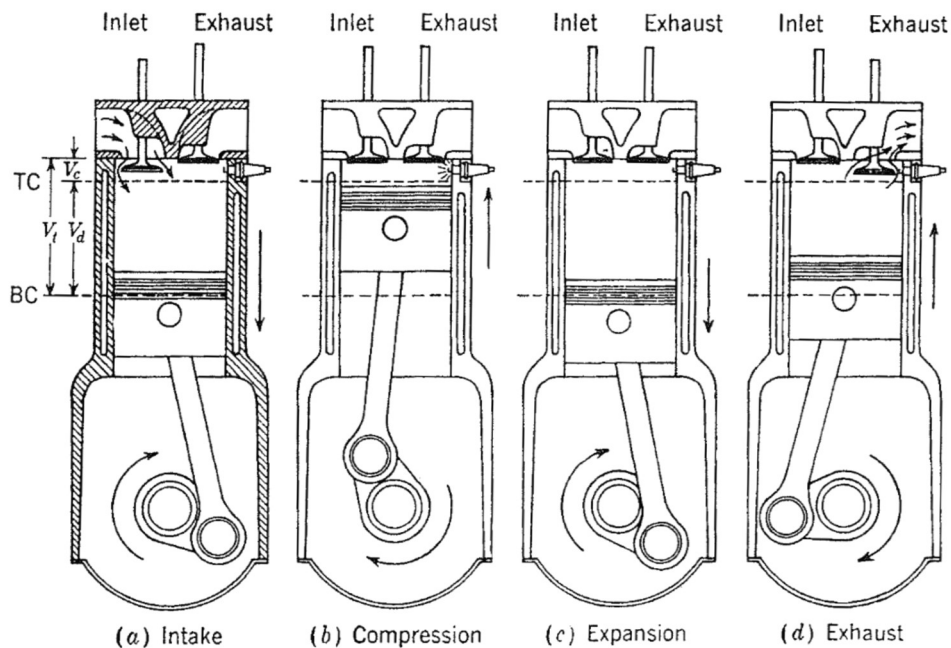


**Figure 2: Four-stroke engine cycle, reprinted from Heywood [21:10] with permission from McGraw Hill Education.**

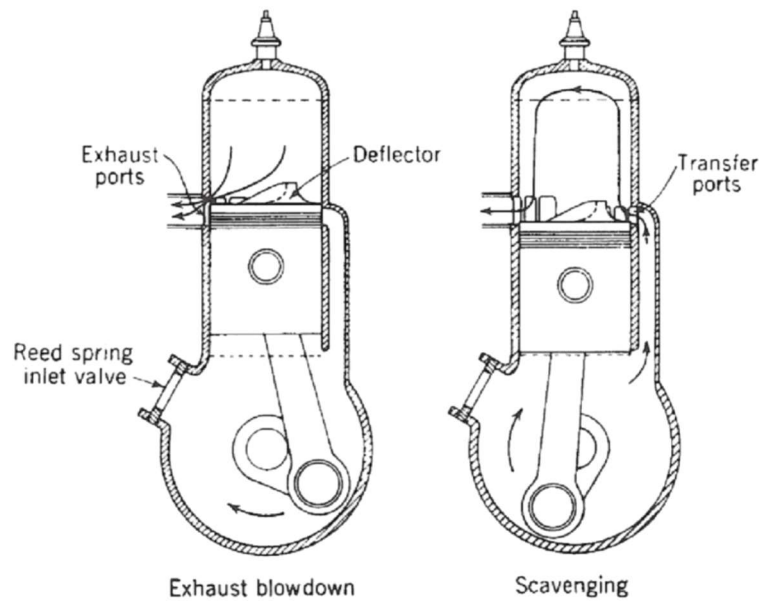


**Figure 3: Two-stroke engine cycle, reprinted from Heywood [21:11] with permission from McGraw Hill Education.**

about 50% more power than a four-stroke engine of comparable size [22:11-12]. Still, this serves as a key advantage to the two-stroke engine in applications where weight is critical, such as aircraft and handheld power tools.

## **2.2. Ignition Type**

A primary classification of ICEs is the method used to initiate combustion. Traditionally, there have been two methods of igniting the fuel air mixture in an ICE: a spark event and compression-ignition. Another more modern method of ignition is homogenous charge compression ignition (HCCI). This section will cover these types of ignition and some of the consequences of the ignition type for engine design.

### **2.2.1. Compression Ignition (CI)**

In a CI engine, the air is inducted into the cylinder and compressed. The fuel is then injected and when the engine reaches the autoignition temperature of the fuel and air

mixture, combustion occurs. The amount of fuel injected into the cylinder is used to throttle the engine, and the localized concentration of the injected spray significantly extends the lean limit of the CI engine. Thus compression-ignition engines can run globally lean, offering excellent specific fuel consumption (SFC) as low as 200 g/kW-hr [21:52].

The primary disadvantage of the CI engine is mass. To achieve the pressure and temperature necessary for autoignition, typical CI engines run at compression ratios of 18-22, compared to 6-10 for spark-ignition (SI) engines. The lower compression ratios in SI engines limits the in-cylinder temperature and prevents autoignition and knock, which are undesirable and can cause damage in an SI engine. While higher compression ratios inherently lead to higher theoretical thermal efficiencies, they also require more engine structure to withstand the greater cycle pressures and more cooling to handle the increased cycle temperatures. The result is that CI engines have lower power to weight ratios than SI engines (assuming both are equally turbocharged or naturally aspirated) [21:58]. The result is that for lightweight aeronautical applications, SI engines, especially two-stroke engines, have a distinct advantage.

### **2.2.2. Spark-Ignition**

In an SI engine, the fuel and air is mixed in the intake runner or the crankcase and then inducted into the cylinder. The combustion process is initiated using a high voltage electrical discharge, which forms a spark. The spark timing is controlled using an engine control unit (ECU), and precise combustion phasing to achieve maximum power is a distinct advantage of the SI engine. The spark timing to achieve the maximum engine power is the maximum brake torque (MBT) timing. When the air and fuel are mixed outside of the cylinder, the in-cylinder mixture is nominally homogenous. The mixture

must also be sufficiently rich to sustain combustion, and thus an SI engine cannot run significantly globally lean. For automotive and larger scale engines combustion typically becomes unstable at an equivalence ratio near 0.85 [21:831]).

Since the 1920s, researchers have investigated stratified charge methods to extend the operability limits of SI engines [21:37-40]. In a stratified charge design, the fuel is injected directly into the cylinder as in a CI engine. The injection is directed to promote the desired equivalence ratio at the spark plug, while allowing the engine to run globally lean, improving fuel consumption especially under throttled conditions. Recently, stratified charge methods have been investigated for extending the knock limit of SI engines to low AKI fuels [31, 32].

### **2.2.3. Homogenous Charge Compression Ignition (HCCI)**

The HCCI engine is a relatively new concept that combines the fuel air mixture strategies common in SI engines with compression-ignition. Whereas CI engines use direct injection and by default a stratified charge to control combustion phasing, the HCCI engine inducts a combustible mixture of fuel and air and relies on chemistry and cooling to control the combustion phasing. The mixture in HCCI engines combusts simultaneously throughout the combustion volume, giving the concept two distinct advantages over SI engines. First, it is widely believed that the high surface area to volume area ratio in small SI engines leads to thermal quenching of the propagating flame, limiting the practical size of an SI engine [33]. HCCI operation does not involve a propagating flame. Rather, the entire charge is heated to the autoignition temperature. Thus, HCCI engines become limited in size by the piston cylinder clearance gap, which is a function of manufacturing technology [33]. Second, HCCI engines may operate at increased compression ratios of

12-15, leading to higher theoretical efficiencies than similar SI engines. Since HCCI engines are designed to autoignite the fuel, higher compression ratios are desirable; a compression ratio of 12-15 in an SI engine would cause knock and engine damage.

The HCCI engine also has a number of critical disadvantages. First and foremost, the combustion phasing is very difficult to control. As a result, engine performance often degrades when a practical, existing engine is converted to HCCI operation. Manente converted a 4.1 cm<sup>3</sup> glow fuel engine to HCCI operation only to find that the overall efficiency dropped from 5-8% on glow fuel operation to 2-5% on HCCI operation [34]. Furthermore, thermal management is critical to managing the HCCI reaction and the heat transfer phenomena in HCCI engines is a rapidly developing field. In the case of HCCI, existing models are poorly posed not because of the size as is the case for the small SI engines considered in this work, but instead because of the different combustion physics. As an example, Chang *et al.* determined that the Woschni model, originally developed for CI engines, required modification through a restructuring of the characteristic velocity and length scale terms to improve the fit for an 0.5 L HCCI engine [35]. Thus, while HCCI holds promise for future applications, significant development is required before such an engine is even practical for a small aircraft application.

### **2.3. Fuel Delivery**

The method of fuel delivery and mixture preparation most appropriate for a given engine application depends on the fuel, ignition type, and engine size. This discussion will focus on the three most applicable technologies to small ICEs: air carburetors, throttle body/ port fuel injection, and direct fuel injection. The discussion will examine how these

technologies differ with respect to mixture preparation, reliable fuel metering, and mass as these are the aspects most applicable to the effort at hand.

### 2.3.1. Air Carburetor

The air carburetor is the earliest form of mixture preparation for ICEs and a schematic of a simple carburetor, reprinted from Heywood [21:283], is shown in Figure 4. An air carburetor works because of Bernoulli's principle. A venturi accelerates the flow of air into the engine causing a simultaneous pressure drop. The decreased pressure pulls fuel into the air flow from a tube connected to a reservoir. The reservoir level is maintained using a float to control flow from the main fuel tank, and the pressure is maintained using an equalization passage. Downstream of the venturi, a throttle plate meters the flow of air and fuel into the engine. Simple carburetors typically provide lean flow at low speeds (equivalence ratio of 0.8 to 0.9) and rich flow at high speeds (equivalence ratio of 1.1 to 1.2) [21:285]. The engine would prefer a constant mixture over the full operating range, except during starting when engine speed is low, where a rich mixture is beneficial. These requirements have led to the modern carburetor.

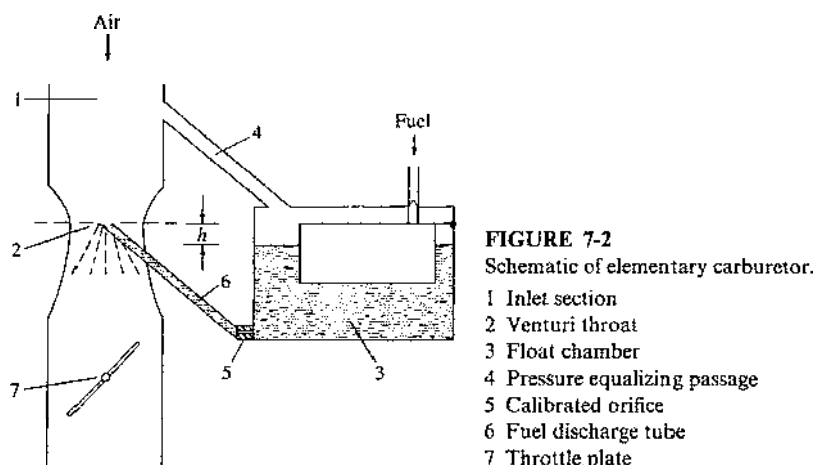


**Figure 4: Schematic of simple air carburetor, reprinted from Heywood [21:283] with permission from McGraw Hill Education.**

Modern carburetors offer a number of features to stabilize their performance over an engine's entire operating range. Frequently, a boost venturi (inside of the main venturi) is used to achieve higher flow rates and sufficient vaporization for operation near idle. Most modern carburetors also have a needle valve that allows the operator to adjust the metering of the fuel to the reservoir, in turn adjusting the amount of fuel introduced to the air flow for a given flow rate. The carburetors on the 10-100 cm<sup>3</sup> displacement ICEs considered herein usually have two such needles, one for low flow, low throttle operation and one for high flow, high throttle operation. A more complex schematic of a modern carburetor showing a boost venturi and an idle mixture adjustment screw is shown in Figure 5, reprinted from Heywood [21:288].

The primary benefit to air carburetors is their simplicity and in turn low cost and low weight. Even the most complex air carburetors are simply a series of near ambient flow passages. Most 10-100 cm<sup>3</sup> displacement COTS engines come stock configured with air carburetors. The devices typically have pressure compensation from the crankcase and two enrichment needles. Still, there are three significant performance drawbacks: variable

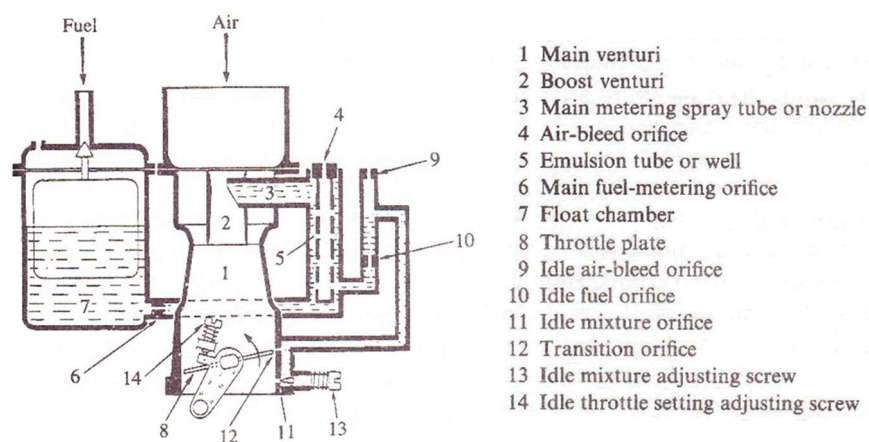


**Figure 5: Schematic of a Modern Carburetor, reprinted from Heywood [21:288] with permission from McGraw Hill Education.**

equivalence ratio over the engine operating range, poor altitude compensation, and an inability to deliver low volatility fuels.

Two enrichment needles permit the operator to tune the engine at dual operating conditions, specified by speed, ambient pressure, ambient temperature, and fuel. If the engine is tuned to the optimum power equivalence ratio of 1.05 to 1.1, then any deviation from the tuning conditions will cause off-design variance in equivalence ratio. The equivalence ratio results for a 55 cm<sup>3</sup>, spark-ignited two-stroke engine with a dual needle carburetor are shown in Figure 6, adapted from Ausserer *et al.* [10]. Over the entire speed range of the engine, the equivalence ratio varied as much as 0.4 at a given throttle setting, and by as much as 0.1 for a fixed speed over the throttle range. Attempts to improve the tuning and reduce the variation in equivalence ratio resulted in shifting the entire equivalence ratio curve richer or leaner and in some cases reducing the operational range

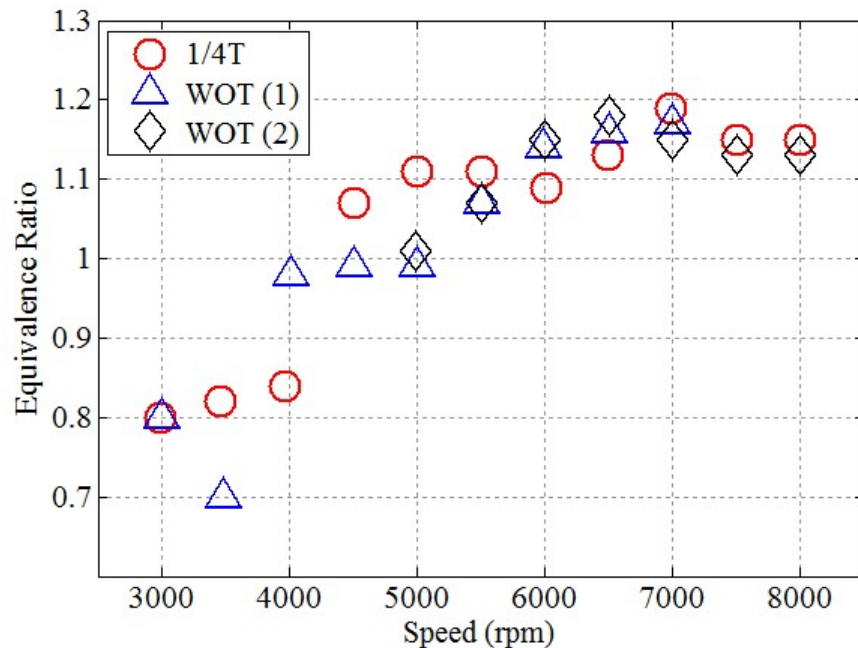


**Figure 6: Equivalence ratio for a 3W Modellmotoren 55i engine based on measured values of intake air and fuel flow rates, data from Ausserer *et al.* [10].**



of the engine. Other researchers have also noted that air carburetors are unreliable on ICE's less than 100 cm<sup>3</sup> displacement [15, 36-38], even at constant altitude.

For RPAs, altitude must also be considered, and the varying pressure and air density with altitude changes the flow characteristic through the venturi and in turn the mixture preparation. Carburetors on conventional aircraft engines employ a number of techniques to compensate for altitude, including bypass venturi, pressure controlled auxiliary fuel metering valves, and compensation bleed air [21]. However, these methods have not been effectively extended to ICEs appropriate for Group 1 or Group 2 RPAs. While running a 95 cm<sup>3</sup> engine in an altitude chamber, Crosbie concluded that at peak power and 10,000 feet the engine experienced a 40% power decrease compared to sea level conditions [39, 40]. Crosbie further concluded that the carburetor resulted in unpredictable and unstable high altitude operation, and that a fuel injection system improved the situation. At least one small RPA company, Currawong Engineering, has developed an aftermarket throttle body fuel injection system for a number of 10-100 cm<sup>3</sup> displacement ICEs to stabilize performance up to 20,000 feet [41].

Finally, carburetors depend on a highly volatile fuel so that the fuel vaporizes into the air stream instead of remaining a liquid and simply wetting the walls of the intake runner and crankcase. Virtually every attempt to convert a small glow fuel or gasoline engine to run on JP-8, JP-5, or diesel has encountered this issue. As Suhy *et al.* concluded during a 1991 conversion of a 388 cm<sup>3</sup> Mercury Marine engine to heavy fuel, "a cold spark-ignited engine with either a carburetor or fuel injection will not start on kerosene. Presumably insufficient vapor is available [42]." Solutions are varied, but typically involve the use of a fuel injection system. Wilson [43] and Groenewegen [44] opted for an air assisted direct

injection system, similar to that of Cathcart [15] and Orbital's FlexDI system [45]. Other groups have selected low pressure throttle body injection [41]. Duddy *et al.* attempted the conversion without a fuel injection system and as a result were forced to increase the thermal capacity of the cylinder head by adding a steel insert and to install preheaters in the crankcase to ensure the fuel was sufficiently vaporized to form a combustible mixture [38]. Both Tankaria and Ghosh [46] as well as Gupta and Ganesan [47] determined that significant richening was necessary during heavy fuel operation to match gasoline performance, most likely due to low atomization of the less volatile fuel.

### **2.3.2. Throttle Body / Port Fuel Injection (TBI & PFI)**

The main trouble with the air carburetor is that fuel metering is not directly tied to the engine's actual fuel requirement. Thus, it is logical to decouple the metering of the fuel from inlet air and engine conditions, and this is typically done through the use of a fuel injector. Historically, fuel rail pressure and injector timing were mechanically dependent on engine speed. Today, modern electrical injectors, engine control units, and fuel rails pressurized using auxiliary pumps allow fuel flow to be set by the operator or ECU, independent of ambient and engine operating conditions.

A generic cross section of a fuel injector is shown in Figure 7, from [48]. For TBI and PFI the fuel rail is pressurized to 3-4 bar, using an external pump [21:295, 41]. When the ECU sends a signal to the injector, the solenoid coil is energized, forming a magnetic field that compresses the spring and opens the valve, allowing fuel to flow from the pintel. In a PFI system the fuel is injected onto the back of the intake valve. The spray of fuel onto the hot valve cools the valve and vaporizes the fuel. Note that piston ported two-stroke engines do not possess valves and the fuel is often sprayed into the crankcase. In throttle body

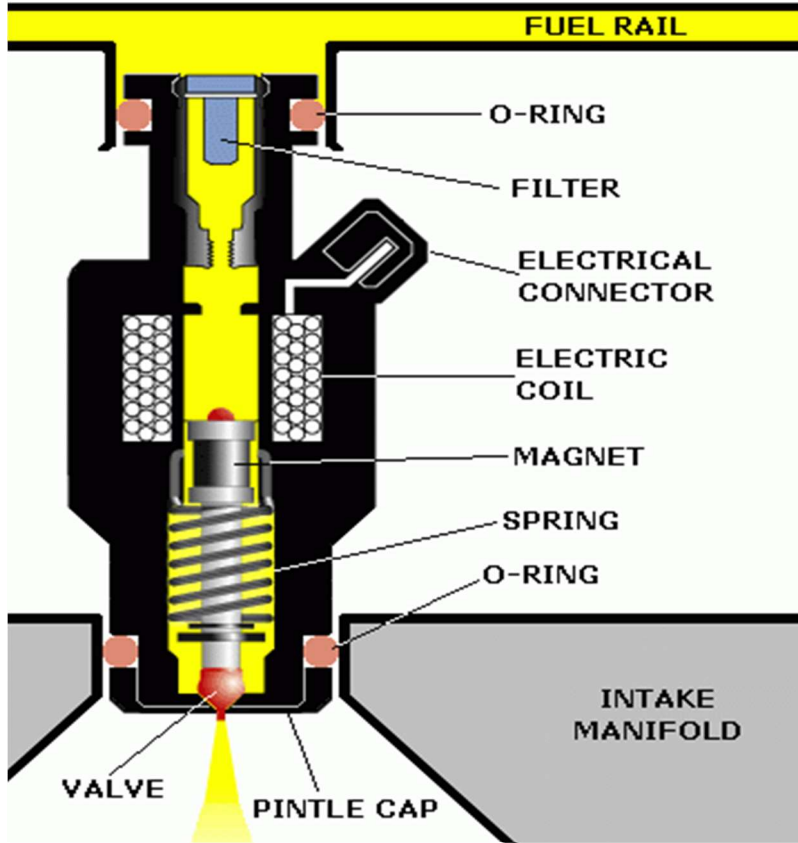


**Figure 7: Generic cross section of a modern fuel injector, reprinted from [48].**

injection, the fuel injector replaces the carburetor and sprays fuel into the intake flow upstream of the throttle plate and crankcase inlet valve. When the signal from the ECU terminates, the coil de-energizes, and the spring closes the valve, stopping the flow of fuel.

Equation (4) shows the mass flow rate of fuel through a nozzle, where the mass flow rate of fuel ( $\dot{m}_f$ ) is a function of the discharge coefficient ( $C_d$ ), the orifice area ( $A$ ), the density ( $\rho$ ), and the pressure drop ( $\Delta P$ ). From Equation (4), one can see that the fuel flow rate is a function of the area and discharge coefficient (design parameters), the fuel density, and the pressure drop across the injector (controlled by the intake manifold condition and the fuel pump). The amount of fuel dispensed is a function of the fuel flow rate and the open time of the injector. It should be clear that fuel flow is controllable entirely

independently of the engine operating condition, and the operator or ECU may compensate for changes in intake air and fuel density by adjusting the fuel rail pressure and/or duty cycle of the injector.

$$\dot{m}_f = C_d A \sqrt{2\rho\Delta P} \quad (4)$$

### 2.3.3. Direct Injection (DI)

Direct injection was originally developed for CI engines. There are three primary differences between DI and PFI/TBI. First, in DI the injection is straight into the cylinder. Second, in DI the injection event can directly control combustion phasing. Third, the pressures required for DI injectors are typically much higher (200 bar-1700 bar for DI versus less than 4 bar for PFI/TBI) since they must atomize the fuel by spraying it into the high pressure cylinder. The higher pressures require larger fuel injectors and larger fuel pumps. For small two-stroke engines, DI offers two key benefits. First, it provides atomization of the fuel directly into the combustion chamber, reducing the condensation of low volatility fuels onto the walls of the intake runner and crankcase [15]. Second, DI operation eliminates the short-circuiting of fresh fuel into the exhaust. Short-circuiting of fresh charge in carbureted and PFI/ TBI engines is a leading cause of UHC emissions. European engine manufacturers see DI as an enabling technology to meet new emissions requirements for handheld power tools [31, 49].

Trattner *et al.* [31] are associated with Stihl, a manufacturer of small, handheld power tools. In their paper reviewing current fuel injection technologies for small ICEs, they note several undesirable aspects of fuel injection for small engines (the same arguments also apply to RPAs). Fuel injection systems adapted from larger applications are heavy, and state of the art systems developed specifically for small ICEs are expensive. Meanwhile,

they also note a number of benefits, such as decreased emissions, easier starting, and better acceleration control [31]. Stihl has even introduced the first direct injection power tool, a 3.9 kW cutoff saw [49]. It is likely that continued research and development will combat weight and cost, securing fuel injection's place in future small ICEs. For this effort throttle body fuel injection was adopted as a research aid to improve repeatability and control beyond that of the stock air carburetor. It is important to realize, however, that fuel injection systems may one day become as common as air carburetors on small COTS ICEs, and that results obtained with fuel injection are relevant to practical, fielded systems.

#### **2.3.4. Control of Fuel Injector Flow Rate**

An advantage of PFI, TBI, and DI systems is that whether the application is fielded or research, the ECU has direct control over the flow rate of fuel. The control may be harnessed in several ways to control equivalence ratio over the entire engine operating range, something that is not possible with an air carburetor. For SI engines, there are three common ways to determine the required fuel flow rate. Most common for small ICEs is the use of a map of throttle position, engine speed, and manifold pressure to determine the duty cycle of the fuel injector for each expected operating point. This approach is used by the commercially available Ecotrons [50], MoTeC [51], and Haltech systems [52]. Currawong uses a similar approach that compensates for changes in altitude [41]. The disadvantage of this approach is that it requires a full map of the engine operating regime, and thus it may not work if the ambient conditions change significantly from those used to develop the map. Heywood calls this the “density-speed” approach and points out that the required sensors (engine speed, inlet pressure, and temperature) are simpler and lighter weight than the alternative methods.

A second method to set the fuel flow is to adjust the duty cycle of the injector based on the equivalence ratio as measured in exhaust. At stoichiometric and rich conditions, nearly all of the oxygen is consumed during combustion. Historically, narrow band oxygen sensors were used to determine if the engine was operating rich or lean of stoichiometric in a binary fashion [53]. As a result, engine operation typically oscillated around stoichiometric. In most modern engines, oxygen (lambda) sensors are constructed of three substrate layers of yttria ( $\text{Y}_2\text{O}_3$ ) stabilized zirconia ( $\text{ZrO}_2$ ), to form a Universal Exhaust Gas Oxygen (UEGO) sensor, originally developed by Bosch [54, 55]. When oxygen passes through the substrate, it generates a current proportional to the partial pressure of oxygen, or a current may be applied to force the movement of oxygen across the substrate. The substrates are used to create two separate channels: one exhaust and one reference (typically atmospheric gas) as shown in Figure 8, reprinted from Zhao and Ladommatos [56:48]. Oxygen is pumped from the surroundings into the exhaust gap in order to keep the relative oxygen concentration between the exhaust and reference (across the sensing gap) constant. The current required to pump or extract oxygen from the exhaust is measured to determine the equivalence ratio [56:46-48].

The signal from the oxygen sensor is supplied to the ECU, which adjusts the injector duty cycle to achieve the desired equivalence ratio. This technique is sufficiently accurate for a research setting and was employed by Baranski *et al.* as a feedback signal to help the operator set the fuel injector duty cycle on a Rotax 914 engine [13]. Unfortunately, this technique will not work on a two-stroke engine. The short-circuiting of fresh charge (see Section 5.3) adds oxygen and fresh fuel to the exhaust. Therefore, the UEGO sensor is not a valid method for this effort. (Note Zhao and Ladommatos discuss a number of other

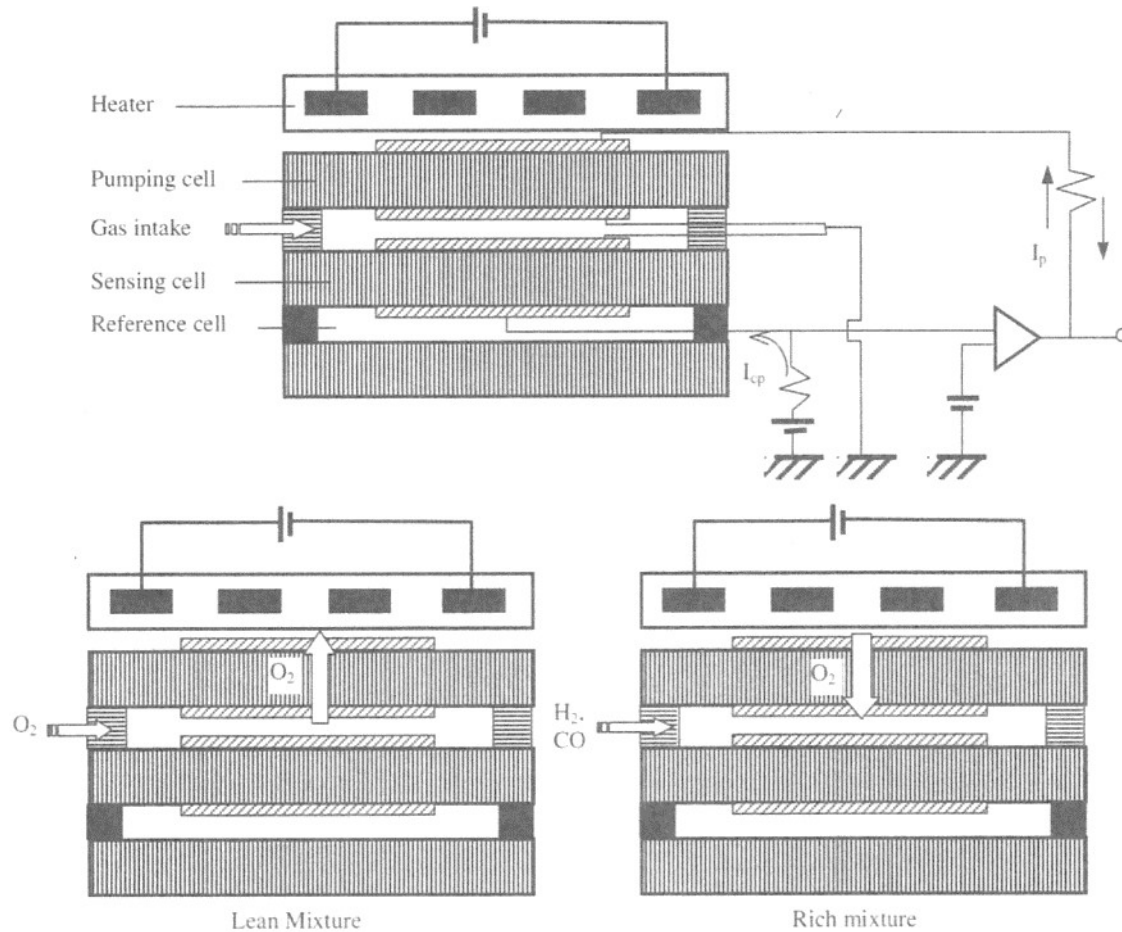


**Figure 8: Schematic of a UEGO sensor applied to determine the equivalence ratio of an engine by measuring oxygen concentration in the exhaust from Zhao and Ladommatos [56:48]. Reprinted with permission from SAE International.**

oxygen sensor technologies, although wide band UEGO sensors are the most commonly used [56:46-48]).

The third method to determine the fuel flow rate is to measure the air flow rate in the intake runner upstream of the throttle plate. The required quantity of fuel can be calculated using stoichiometry, and then the injector duty cycle may be set using the calibration curve of the injector (recall Equation (4)). This method offers a significant research advantage: it controls the equivalence ratio directly based on the amount of fresh air [21]. Thus, it

ensures the delivered equivalence ratio is a known, rather than an estimate based on exhaust measurements or interpolation of an engine map. Bosch has used air flow controlled systems since the late 1970s for closed loop control [57:630-31, 58]. However even one of the most advanced fuel injected small ICEs on the market, a 3.9 kW cutoff saw produced by Stihl, still uses operating maps and altitude compensation instead intake air flow measurements to meet weight, space, and complexity constraints [49]. Thus, it seems that air flow control for equivalence ratio has not yet reached the small ICE market outside of laboratory testing.

## **2.4. Cooling Types**

Without cooling, an ICE would overheat, melting the piston face, cylinder, head, and exhaust runners. The two practical methods of cooling ICEs are water cooling using a water or coolant jacket around the head and air cooling used forced convection and fins on the head. For RPA and handheld power tool applications, the coolant, pumps, and radiators for water cooling are impractically heavy. Thus small ICEs typically rely on forced convective air cooling. In handled power tools such as the Honda GX25 and GX35, a fan was built into the flywheel that forces air through the plastic case around the engine. On RPAs, cooling is typically performed by air flow from the propeller or free stream that is directed over the cooling fins of the engine. Many of the heat transfer correlations (discussed in Section 5.1) were developed for water cooled engines, yet another reason they may not directly translate to the small ICEs considered in this effort.

## **2.5. Gas Exchange and Scavenging**

The two-stroke engine compresses the four steps of a power cycle (intake, compression, combustion/expansion, and exhaust) into a single engine revolution. Figure 9, reprinted



from Heywood and Sher [22:3], shows a graphical representation of the gas exchange and phasing for a single cylinder of a two-stroke engine with crankcase compression. The inner ring represents the gas action in the crankcase, while the outer ring is the process in the cylinder.

### 2.5.1. The Gas Exchange Process

The combination of the intake and compression process and the combustion, expansion, and exhaust process into two-stroke engines creates overlap that complicates gas exchange compared to a four-stroke engine. In a four-stroke engine the intake and exhaust stroke of the piston and the timing of the intake and exhaust valves provide the driving force to expel the burnt gas and induct fresh charge from the intake runner. Two-stroke engines require an external means to pressurize the fresh charge and drive it into the cylinder while pushing

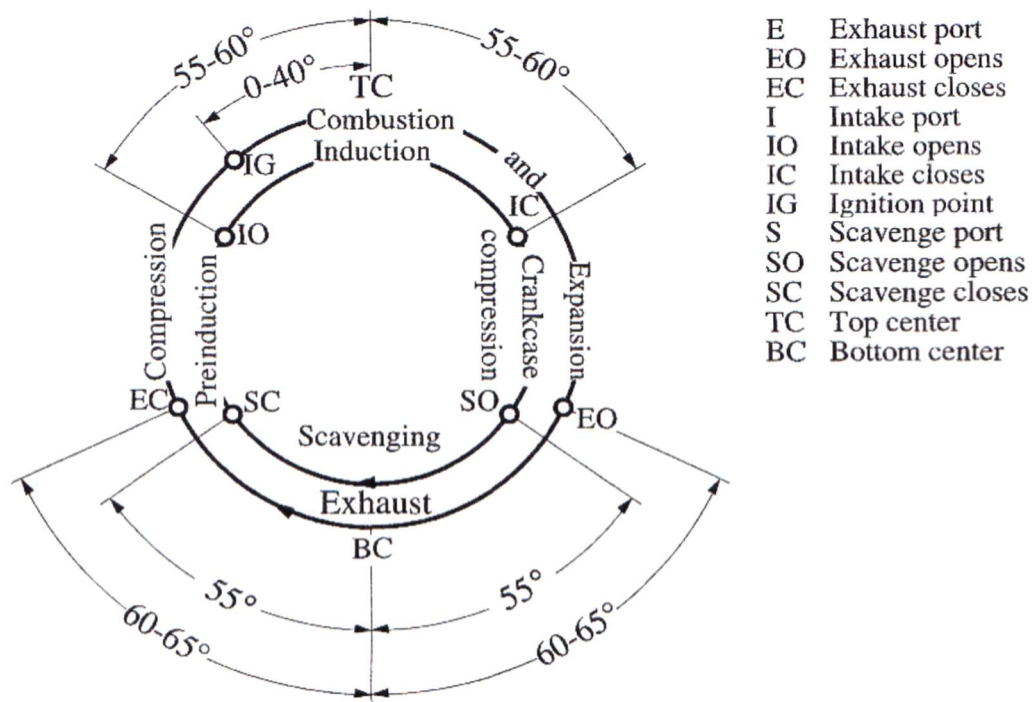


**Figure 9: Phasing of a two-stroke engine with crankcase compression, reprinted from Heywood and Sher [21:11] with permission from Taylor & Francis Ltd.**

out the combustion products. Large two-stroke engines, such as marine diesels, often employ pumps to provide the necessary driving force [22:47-71]. However, pumps are heavy, bulky, and have decreasing efficiency as the pump size and corrected mass flow decrease making them impractical for small engines.

Instead, most small two-stroke engines employ crankcase compression. In crankcase compression the downward motion of the piston during the expansion stroke is used to compress fresh charge in the crankcase driving it through the transfer ports into the cylinder. The upward motion of the piston during compression draws fresh charge from the intake runner into the crankcase. This complex balance of gas pressures requires careful attention to transfer port design and timing. The required pressure differences between the crankcase, cylinder, and exhaust for proper gas exchange also make it difficult to turbocharge or supercharge two-stroke engines [22:53-60].

Returning to Figure 9, consider the start of a cycle that begins when the exhaust port closes. The trapped charge is compressed (fresh charge is drawn into the crankcase) and combustion is initiated either using a spark or through autoignition. For maximum power in an SI engine, spark timing is typically 20 crank angle degrees (CAD) to 30 CAD before top dead center (bTDC) [21:828]. The timing achieves peak pressure near 16 CAD after top dead center (aTDC). Combustion proceeds until the exhaust port opens at about 120°aTDC. The exhaust port is typically timed to open slightly before the intake port, allowing the exhaust gas to begin exiting the cylinder and dropping the cylinder pressure to near ambient. This prevents the backflow of exhaust into the crankcase. About 5-10 CAD after the exhaust port opens, the transfer ports open, and the downward motion of the piston drives fresh charge into the cylinder. From this point until the exhaust port

closes, some fresh charge will mix with the exhaust and exit the cylinder. If the engine is not DI, then that fresh charge will contain raw fuel. After bottom dead center, the intake and exhaust ports close. Compression does not begin until the exhaust port closes (although there is some ram effect), and thus two different compression ratios may be defined for two-stroke engines. The geometric compression ratio is the same as the compression ratio for a four-stroke engine: the ratio of displaced volume to clearance volume. The trapped (or effective) compression ratio is ratio of the volume when the exhaust port closes to the clearance volume. The trapped compression ratio is more indicative of the thermodynamic characteristics of the cycle [9:216].

### **2.5.2. Ports and Valves**

Many small two-stroke engines are piston ported, meaning the exhaust and transfer ports are opened and closed as they are covered and uncovered by the piston. Thus the timing of the ports before and after bottom dead center is symmetrical. Often at low speeds the port open time becomes too long, leading to an excessive loss of fresh charge. At high speeds the open time is often too short, and the engine will struggle to expel the exhaust and induct sufficient fresh charge. Thus, a two-stroke engine will operate best near its design speed.

While the piston controls the transfer and exhaust ports, the intake to the crankcase also requires a valve to prevent the fresh charge from flowing back into the intake runner instead of into the cylinder. Originally, small ICEs employed clapper valves where a floating ball valve on a lapped seat prevented the back flow of charge out of the crankcase [59]. Eventually, clapper valves were replaced with reed valves made from beryllium copper, which had the correct stiffness to make an effective spring. Today plastic has replaced

beryllium copper [59]. Fleck *et al.* are credited with one of the more comprehensive investigations on reed valve design. Their 1987 paper presented comprehensive test data for a reed valve model incorporating valve material, geometry, and modal frequency. The model was based on fitting semi-empirical correlations with data collected by using a stroboscope on reed valves of different geometries installed on a 350 cm<sup>3</sup> engine [60]. High speed video remains a preferred method for evaluating reed valves, and one possible setup is described in Fleck *et al.* [61]. Both investigations indicate that reed valves do not eliminate directional flow oscillations in the intake runner, and damping of these oscillations is required if hot-wire type probes are used to measure the intake air flow rate.

An alternative to the reed valve is a rotary disk timed to the crankshaft. The disk rotates over the intake port, and slots in the disk control when the intake is open and closed. Unlike the reed valve, rotary disks provide controlled timing and do not flutter with flow oscillations. However, rotary disks increase the mechanical complexity of the engine and require large flat surfaces for installation [61]. Thus while early glow engines in the 1950s-1970s often used rotary disks and drums [59], many modern high performance two-stroke engines employ reed valves for their simplicity and small footprint [61].

### **2.5.3. Scavenging Methods**

Figure 10, reprinted from Heywood and Sher [22:47], shows a variety of scavenging methods for two-stroke engines. The fundamental goal of the scavenging process is to move fresh charge into the cylinder and remove the exhaust from the cylinder without expelling the fresh charge into the exhaust. Fresh charge escaping straight to the exhaust is called “short-circuiting”. The most basic scavenging design is cross scavenging, shown in Figure 10a. In cross scavenging, the flow enters at one side of the cylinder and exits on

the opposite side. Cross scavenged systems usually require a deflector on the piston to direct flow into the top of the cylinder so that fresh charge does not simply exit out the exhaust port without displacing the burnt charge. These deflectors can form hot spots in the engine, making it more prone to pre-ignition and knock. In loop scavenging, Figure 10b, the charge enters on the same side as the exhaust port and impinges on the opposite wall. In theory, the charge will then flow around the top of the cylinder before exiting out of the exhaust. Both cross flow and loop scavenging require high flow momentum. Taylor and Rogowski tested two engine heads that were identical except for the scavenging layouts to compare loop and cross flow scavenging [62]. They determined that with identical port areas the trapping efficiencies of the two systems were indistinguishable within the experimental error [62].

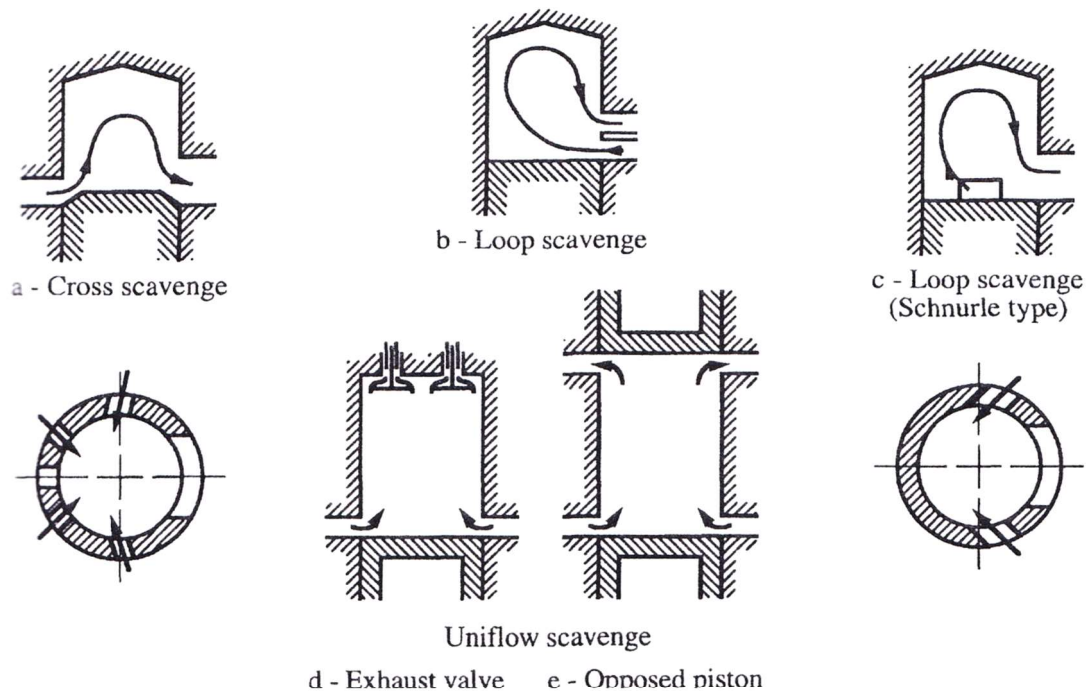


**Figure 10: Two-stroke scavenging methods, reprinted from Heywood and Sher [22:47] with permission from Taylor & Francis Ltd.**

As cylinder size increases, it becomes increasingly difficult to provide sufficiently energized flows for cross and loop scavenging. Since most large bore, two-stroke engines are DI CI engines, they employ (external) pump driven, uniflow blowdown systems. In a uniflow system, Figure 10d, valves are located on the head of the engine so that fresh air may displace the exhaust from the bottom to the top of the cylinder. In an opposed piston system, Figure 10e, two pistons are used; one controls the intake ports, and one controls the exhaust ports. When using DI, there are minimal issues from short-circuited fuel, and the fresh air flow rate may be increased to more completely clear the cylinder without risk of short-circuiting.

For small ICEs, a Schnürle, Figure 10c, scavenging system is most common. Although credited with the concept, it is likely Schnürle was not the first to propose such a system, and Blair [27:8] indicates a significant amount of patent litigation in Germany in the 1920s and 1930s over the subject. In a Schnürle type system, the transfer ports are on the side of the cylinder and angled toward the top of the cylinder to create the desired loop flow. Many modern designs also add a boost port opposite of the exhaust port. Schnürle scavenging is a very common scavenging design for small two-stroke ICEs. As Heywood and Sher indicate, modern performance of the Schnürle scavenged system usually exceeds the perfect mixing model (discussed in Section 5.3.1.1), now considered a worst case model for the scavenging process. However, the configuration is also sensitive to the ambient conditions, and thus Schnürle scavenged engines tend to have performance problems at altitude [22:47-60].

#### 2.5.4. Gas Exchange Terminology

The complex nature of scavenging has led to a set of metrics almost entirely unique from those used for gas exchange in four-stroke engines. The organization and terminology presented here are adapted from [22:43-47] and are consistent with the applicable SAE standard [63]. Other texts such as Heywood [21] and Blair [27] offer similar overviews. Gas exchange in a four-stroke engine is usually described using only the volumetric efficiency. As shown in Equation (5), the volumetric efficiency ( $\eta_v$ ) is the ratio of fresh charge delivered to the cylinder ( $V_{ch}$ ) to the displaced volume ( $V_d$ ).

$$\eta_v = \frac{V_{ch}}{V_d} \quad (5)$$

For two-stroke engines, the volumetric efficiency is called the delivery ratio ( $\Lambda$ ), and it is the ratio of fresh charge delivered to the engine ( $m_{ch}$ ) and the reference mass ( $m_0$ ). The reference mass is the amount of charge it would take to fill the cylinder at reference conditions, and the delivery ratio is shown in Equation (6).

$$\Lambda = \frac{m_{ch}}{m_0} \quad (6)$$

The delivery ratio does not describe how much of the fresh charge delivered to the engine actually remains in the engine once the transfer ports close. To describe the amount of fresh charge in the cylinder compared to how much charge the cylinder can hold, the charging efficiency is used. The charging efficiency ( $\eta_{ch}$ ), shown in Equation (7), gives the mass of fresh charge retained in the cylinder ( $m_{ret}$ ) as a fraction of the reference mass.

$$\eta_{ch} = \frac{m_{ret}}{m_0} \quad (7)$$

While the charging efficiency expresses how well the cylinder has been filled with fresh charge, it does not indicate how well the exhaust has been replaced. The burnt gas is likely warmer than the fresh charge, so the total mass of gas in the cylinder is less than the reference mass. The scavenging efficiency ( $\eta_{scv}$ ), shown in Equation (8), is the ratio of fresh charge to the mass of the cylinder contents ( $m_{cyl}$ ) at a given instant. It represents what fraction of the cylinder contents is fresh charge.

$$\eta_{scv} = \frac{m_{ret}}{m_{cyl}} \quad (8)$$

Finally, the retaining efficiency ( $\eta_{ret}$ ) and trapping efficiency ( $\eta_{tr}$ ) indicate how much of the delivered fresh charge remains in the cylinder. The retaining efficiency represents that ratio at each instant in time, while the trapping efficiency represents the ratio once the exhaust port closes and compression begins, as shown in Equation (9).

$$\eta_{ret} = \frac{m_{ret}}{m_{ch}} \quad (9)$$

$$\eta_{tr} = \left. \frac{m_{ret}}{m_{ch}} \right|_{\text{exhaust port close}}$$

All of these metrics are interconnected, and the delivery ratio, trapping efficiency, and charging efficiency may be related as in Equation (10).

$$\eta_{tr}\Lambda = \eta_{ch} \quad (10)$$

A final metric that is commonly used to compare how well a model matches experimental data from an engine is the exhaust gas purity. The exhaust gas purity,  $\beta$ , is a measure of how much fresh charge is in the exhaust gas at any given time, and is defined as the mass fraction of fresh charge in the emerging exhaust. Section 5 will further cover scavenging models and measurements methods considered for and relevant to the proposed effort.



## 2.6. Normal and Abnormal Combustion

Of the three obstacles to running an ICE on a low AKI fuel, the most challenging to overcome is abnormal combustion. Abnormal combustion is most easily discussed in the context of normal combustion, and thus an overview of the normal combustion process in an engine is the starting point of this section. Then, this section will cover in-cylinder pressure measurements as the most common means for tracking combustion in ICEs. With those two foundational pieces, the discussion will shift to abnormal combustion and knock. The discussion of knock will focus on three aspects: what it is, how it can be measured and quantified, and what methods can be used to mitigate it. Especially in the section on knock mitigation methods, the discussion will remain focused on techniques applicable to 10-100 cm<sup>3</sup> displacement engines.

### 2.6.1. Normal Combustion

Figure 11, reproduced from Baranski [53:8], shows the most important aspects of combustion using data collected on a Rotax 914 (SI) engine. In Figure 11, combustion is broken into three stages: flame development, sometimes called the ignition delay (ID), rapid burn, and combustion in the end gas. The progression of combustion through these events is measured by the mass fraction burned (MFB), shown with the solid green line. The calculation of mass fraction burned is directly enabled by in-cylinder pressure measurements using a zeroth order, single zone thermodynamics model. The first step is a model for the heat release, which is developed by solving conservation of energy with the cylinder as the control volume. The expansion and compression processes (when no combustion occurs) are assumed to be polytropic with a constant ratio of specific heats ( $\gamma \approx 1.3$ ). Heat transfer out of the cylinder is permitted, and the combustion gases are

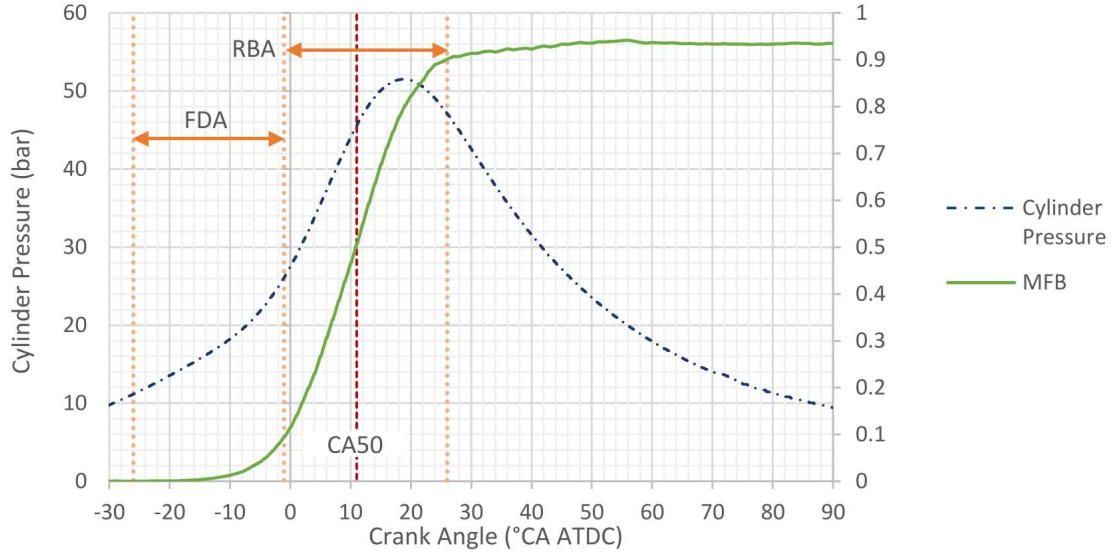


**Figure 11: Illustration of normal combustion process, reprinted with permission from Baranski [53:8].**

assumed to follow the ideal gas relationship. The result is the differential equation shown in Equation (11) [22:219, 64].

$$\frac{dQ_{cyl}}{dt} = \frac{1}{\gamma - 1} \left( \gamma p_{cyl} \frac{dV_{cyl}}{dt} + V_{cyl} \frac{dP_{cyl}}{dt} \right) + \frac{\delta Q_{cyl,loss}}{dt} \quad (11)$$

The time rate of heat release in the cylinder ( $\frac{dQ_{cyl}}{dt}$ ) is the sum of three terms. The first term ( $\frac{dV_{cyl}}{dt}$ ) is the rate at which the gases in the cylinder do work on the moving piston, and the differential volume may be calculated from engine geometry and speed. The second term ( $\frac{dP_{cyl}}{dt}$ ) represents the energy released by the combustion process that increases pressure in the cylinder. These first two terms, if taken in the absence of a loss term, are commonly called the Rassweiler and Withrow method after the researchers who developed the calculation in 1938 [65]. The third term ( $\frac{\delta Q_{cyl,loss}}{dt}$ ) in Equation (11) is the loss of energy through the cylinder walls as heat. Any of the instantaneous spatially averaged heat

transfer correlations presented in Section 5.1 would suffice for this term. Current efforts typically validate temporally resolved heat transfer models by computing the heat loss term and comparing the predicted pressure curve against the measured pressure [66-68]. Rassweiler and Withrow accounted for their lack of heat loss or release term by replacing the ratio of specific heats with a polytropic coefficient that differs from the ratio of specific heat by the amount necessary to adjust for thermal losses. Ball *et al.* [65] point out that the polytropic coefficient takes on substantially different values during expansion and compression (anywhere from about 1.2 to 1.35). To fix this problem Ball *et al.* suggest modifying Rassweiler and Withrow's equation to permit different polytropic coefficients during expansion and compression. This only changes the integrated form of the equation as the differential form in Equation (11) may be modified simply by changing the value of the ratio of specific heats at the appropriate step during numerical evaluation.

Recognizing that the heat released is a function of the amount of fuel in the cylinder, the heat release rate may be transformed into a differential equation for mass fraction burned using the air to fuel ratio ( $\frac{A}{F}$ ), the mass fraction of residual in the cylinder ( $x_r$ ), the total mass of cylinder gases ( $m_{cyl}$ ), and the heating value of the fuel ( $Q_{HV}$ ), as shown in Equation (12). Equation (12) may be discretized and integrated with pressure data to give a mass fraction burned profile as shown in Figure 11. Equation (12) does not account for dissociation of gases in the cylinder. Both Equations (11) and (12) may be expressed in crank angle space instead of time space; the conversion is simply the speed of the engine in degrees per second (assuming time is in seconds). Foster [20] compiles more complex models for the analysis of in-cylinder pressure data. Most of the models are based on an availability analysis using the second law of thermodynamics. While useful for

determining the interaction of thermal losses (for example the shifting of thermal loading from the exhaust gas to heat transfer through the cylinder), the model already presented is sufficient for tracking the MFB.

$$\frac{dx_b}{dt} = \left[ \frac{\frac{A}{F} + 1}{m_{cyl}(1 - x_r)Q_{HV}} \right] \frac{dQ_{cyl}}{dt} \quad (12)$$

The flame development angle (FDA) represents the amount of time it takes for the spark to ignite the fuel and for the flame front consume 10% of the fuel by mass. The crank angle where 10% of the fuel mass is consumed is called CA10. In a spark-ignition engine the FDA is typically about 25 CAD [53:8]. As engine speed increases the FDA usually increases since enhanced mixing accelerates combustion less quickly than faster rotational speeds shrink the time associated with a given crank angle space. The rapid burn angle (RBA) is the time for combustion to progress from CA10 to CA90, where 90% of the fuel mass is consumed. This process also takes about 25 CAD [53:8]. A common combustion metric is the timing of CA50, where 50% of the fuel mass is consumed. MBT timing typically occurs with a CA50 near 8°aTDC. Due to combustion inefficiency, quenching, and other effects, the MFB will not reach unity. Additionally, it should be noted that when MFB is evaluated numerically by the AVL Indisart that the MFB curve is normalized to unity, and thus MFB as reported herein represents the progression to completion of the combustion reaction. Therefore, a CA90 may be calculated even at rich equivalence ratios (example: 1.3) where less than 90% of the fuel will combust completely to H<sub>2</sub>O and CO<sub>2</sub> due to insufficient oxygen.

In many cases, it is easier to simply fit an empirical function to the MFB curve and use that fit as an input for further simulation of other operating parameters. In some cases, the

MFB profile is fit to a Wiebe function for further data reduction. The generic form is shown in Equation (13) where combustion proceeds in a sigmoid fashion based on the ratio of the crank angle from the start of combustion ( $\theta - \theta_0$ ) to the total crank angle for combustion ( $\Delta\theta$ ). Heywood suggests values of  $C_1 = 5$  and  $C_2 = 2$  [21:390].

$$x_b = 1 - \exp\left(-C_1 \left(\frac{\theta - \theta_0}{\Delta\theta}\right)^{C_2+1}\right) \quad (13)$$

The blue dash-dot trace in Figure 11 shows the in-cylinder pressure, an important parameter for modern SI combustion diagnostics that is invaluable for computing numerous performance parameters and detecting knock. One such parameter is the indicated mean effective pressure (IMEP). IMEP is one of three mean effective pressures (MEP) commonly used to quantify engine performance. Shown in Equation (14), IMEP is the effective pressure in the cylinder ( $p_{cyl}$ ) over the cycle. IMEP may also be expressed in terms of the indicated power ( $P_i$ ). Equation (14) uses a factor ( $n_r$ ) to adjust for four-stroke and two-stroke cycles:  $n_r = 2$  for four-stroke engines and  $n_r = 1$  for two-stroke engines. IMEP is a normalized quantity that represents how effectively an engine uses its displaced volume to create power. Since IMEP is measured in-cylinder, it does not include friction losses in the engine or the drivetrain.

$$IMEP = \frac{1}{2\pi} \int_0^{2\pi} p_{cyl} \left( \frac{dV_{cyl}(\theta)}{d\theta} \right) d\theta = \frac{P_i n_r}{\frac{N}{60} V_d} \quad (14)$$

When MEP is measured at the load (or brake), it becomes the brake mean effective pressure (BMEP). BMEP represents how well an engine uses its displaced volume to create useful work at the output shaft, called brake power ( $P_b$ ). For automotive scale SI engines, BMEP values range from 850 kPa to 1050 kPa, and for turbocharged engines

values may be as high as 1700 kPa [21:50-51]. The difference between BMEP and IMEP is friction mean effective pressure (FMEP), shown in Equation (15). Like IMEP and BMEP, FMEP is the friction power ( $P_f$ ) dissipated by the engine normalized by speed and displaced volume. FMEP values in spark-ignition engines are on the order of 50-200 kPa, depending on what accessories are attached [21:721], and IMEP values are correspondingly higher than BMEP values. IMEP is limited by the amount of fuel that can be combusted in the cylinder and the compression ratio of the engine. Turbocharging, supercharging, and raising the compression ratio are all viable methods for increasing IMEP and BMEP. Unlike BMEP, which can be affected by external losses, only combustion losses such as quenching and incomplete combustion affect IMEP. Sher *et al.* [33] and Menon and Cadou [16] indicate such losses become more severe in smaller engines, and thus one might expect IMEP to decrease with displaced volume. The mechanical efficiency of the engine ( $\eta_m$ ) may be calculated as the ratio of BMEP to IMEP as in Equation (16). MEP values are a common way to compare engines of different sizes, since MEP normalizes power production by the combustion volume, which directly influences the gross energy an engine can release from combustion during a single cycle.

$$IMEP = FMEP + BMEP \quad (15)$$

$$\eta_m = \frac{BMEP}{IMEP} \quad (16)$$

Cycle-to-cycle operation in an engine can vary significantly, especially in air carbureted two-stroke engines. The metric typically used to quantify this variation is the coefficient of variance (COV) of IMEP, often just called COV. The COV is the normalized standard deviation of IMEP. In an automobile, values less than 10% are considered “drivable” and values less than 5% are typical. Once values exceed 10%, the engine is

considered unstable and may experience damaging vibrations, misfires, mechanical damage, and may simply shutdown. During the course of this research effort, values as low as 1% were observed for small two-stroke engines running at full throttle in the design speed range and values over 25% were observed for low throttle, off design conditions.

Figure 11 also shows the peak pressure. The location of peak pressure is influenced by multiple factors including mixture preparation, fuel type, ignition timing, and flame speed. From an operational standpoint, the main control of peak pressure in an SI engine is spark timing. Usually, the spark is timed to give the maximum brake torque (MBT), which is also the maximum power at a given speed [21:374]. If the spark is too early (advanced), peak pressure will occur too early and work against the piston. If the spark is too late (retarded) combustion will progress into the expansion stroke, lowering the power output. Optimal spark timing for most conventional SI engines is 20-30°bTDC. This yields a peak pressure around 16°aTDC [21:374].

Normal combustion in an SI engine is most accurately described as a pre-mixed turbulent flame. Abraham *et al.* [69] are credited as the first to show how the flame regimes occurring in an SI engine may be mapped using the Damköhler number and the turbulent Reynolds number. Figure 12, reprinted from Menon and Cadou (who built on the work of Abraham *et al.* [69]), shows the flame regimes as a function of those non-dimensional parameters. The Damköhler number is the ratio of the chemical reaction time to the time required for mass transport in the system and describes how fast combustion will propagate relative to the rate that mass is transported through the system. The turbulent Reynolds number is an indicator of mixing intensity in the cylinder. Abraham *et al.* [69] indicate that conventional SI engines operate in the multiple reaction sheet regime, also called the

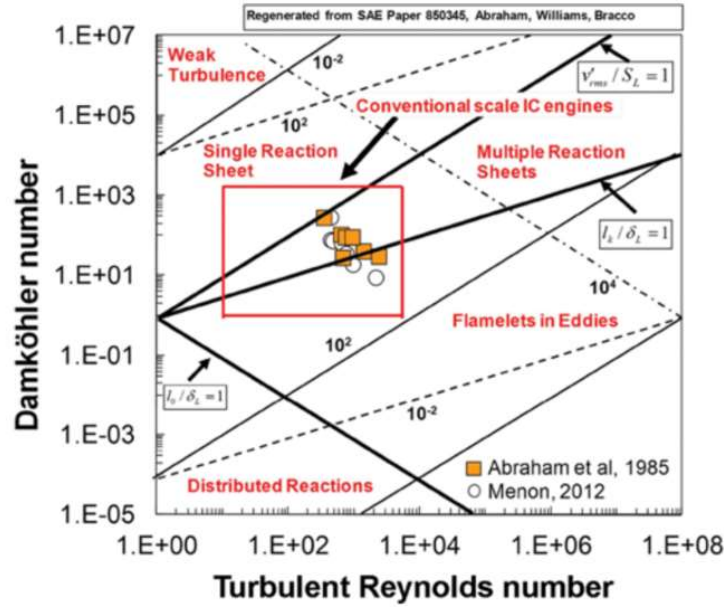


**Figure 12: Combustion regimes where automotive and larger scale ICEs as well as micro glow engines operate. Reprinted from Menon and Cadou [71] with permission from Taylor & Francis Ltd.**

wrinkled flame regime [70:460-461]. In this regime turbulence bends the laminar flame sheet, wrinkling it, but not breaking it into individual combustion eddies. Menon and Cadou [71] plotted data for nine micro glow fuel engines, comparing numerical results to observations through a quartz window in the top of the cylinder. Shown in Figure 12, Menon's results [2] indicate that some cycles do occur in the multiple reaction sheets regime. However, in some cycles combustion crosses over to the flamelets in eddies regime, where the turbulence breaks the flame sheet into combusting eddies. This can extinguish the flame prematurely, decreasing the combustion efficiency. Both Abraham *et al.* [69] as well as Menon and Cadou [71] acknowledge that for large, slow engines the combustion regime may also occur as a single reaction sheet. However, small engines generally do not run slowly enough to operate in this regime.



### **2.6.2. In-Cylinder Pressure Measurement Techniques**

The need for in-cylinder pressure measurements dates almost to James Watt's steam engine [72]. The earliest measurements were made using various mechanical methods, several of which are described by Rogers [73:2-19]. These mechanical methods often employed a mechanical diaphragm or spring to sense pressure and an angular encoder to track when the cylinder pressure reached the diaphragm or spring pressure. The trace was recorded by spark discharge or a writing instrument as in a seismograph. By the 1940's, these mechanical methods were too slow for state of the art engines.

In the 1950s, Kistler patented the first piezoelectric pressure transducer for in-cylinder pressure measurements in ICEs [73:38]. In a piezoelectric transducer the change in in-cylinder pressure deforms the crystal lattice in a quartz crystal in the sensor, generating a current. This phenomenon is the piezoelectric effect. The charge is gathered at a charge amplifier, which converts the charge to voltage. The voltage is then read by a high speed data acquisition system. In addition to piezoelectric devices, there are several modern devices available for in-cylinder pressure sensors, and all of them generate a variable resistance, charge, or voltage corresponding to cylinder pressure [73:14-15].

- Inductive transducer: measures the deflection of a diaphragm using a coil and magnet.
- Variable capacitance: the deflection of a diaphragm changes the capacitance and thus the voltage of a DC measurement circuit.
- Strain gauge: variable resistance with deflection, measured on a Wheatstone bridge.
- Optical: a fiber optic technique is used to detect the deflection of a diaphragm.
- Piezo electric: a quartz crystal procures a current proportional to the deformation of the crystal.

According to Rogers in the Society of Automotive Engineers' handbook on the subject, "this [piezoelectric] method has now been nearly universally adopted for in-cylinder pressure measurements," [73:14-15]. This universal adoption was enabled by two developments that modernized piezoelectric devices: the transistor and crystal cutting technology. First, the development of the transistor in the 1970s improved the quality of charge amplifiers, reducing drift and leakage around the gate resistor [28:119]. Second, companies developed polystable cuts of quartz crystal that increased the thermally stable range of the transducer up to 350°C [73:39], allowing the devices to be incorporated into uncooled flush mount transducers, spark plugs, and glow plugs. The most significant disadvantage of the modern piezoelectric transducer is that it only measures changes in pressure, and any absolute measurement must be accomplished by also measuring a reference signal in the data acquisition software [73:3].

Well established in industry, the largest challenge to employing a piezo electric transducer on a 10-100 cm<sup>3</sup> displacement engine is mounting the device. The two most practical options are small flush mount devices, typically 5 mm in diameter, and transducers incorporated directly into the spark plug. While flush mount transducers are seen as the reliable industry standard, they possess a distinct disadvantage: flush mount transducers require modification of the engine head. As Menon and Cadou note [71], modification of the head in a micro engine risks altering the combustion volume and compression ratio. Measuring spark plugs also have disadvantages. Roth *et al.* [74] investigated the differences between a piezoelectric flush mount and a measuring spark plug transducer in a DaimlerChrysler 4.7 L, V-8 engine. They determined that the flush mount and measuring spark plug transducers disagreed on the measured pressure by up to

8% (at peak pressure). Furthermore, Baranski [53] noticed performance differences of several percent between a stock spark plug and the spark plug in a measuring spark plug transducer. This quandary spurred the investigation of the differences between the two types of transducer on a 4.4 kW SI two-stroke engine. The entire paper [75] (presented at the SAE 2014 Small Engine Technology Conference) is included in Appendix D. The results indicate that as a spark plug, the measuring plug and stock plug are statistically indistinguishable. However, a 4.7% difference in IMEP at full throttle between the flush mount transducer and measuring spark plug transducer was observed, similar to the result from [74]. The results also indicate that modification of the engine head for the flush mount transducer caused up to a 4% difference in engine performance. From a measurement accuracy standpoint, the tradeoff between transducers is comparable, and either transducer could provide a reasonable source of pressure data for combustion analysis and knock detection.

### **2.6.3. Abnormal Combustion**

The SI engine depends on spark timing to control combustion phasing as well as a controlled fuel burn to limit the pressure rise rate and prevent thermal and mechanical damage to the engine. When combustion initiates without the spark or the burn rate progresses too rapidly, it is referred to as abnormal combustion or knock. The term knock refers to the pinging sound from pressure waves reflecting within the cylinder. Until 1945, there were two competing theories of knock. The first theory stipulated that hot spots in the combustion chamber and heat from the residual gas would ignite the fresh charge ahead of the spark event. The second theory stated that the flame front would heat and compress the unburnt charge (end-gas) causing it to autoignite. Proponents of this theory often

believed that the knock was a detonation, where the flame front accelerated to supersonic speeds. Modern evidence supports that for fast enough turbulent flame speeds, the flame front can exceed the Chapman-Jouguet speed and transition to a detonation [76]. Miller [77] unified these theories in 1945, stating that all knock is essentially a race between the desirable spark initiated combustion and the autoignition of the end gas. To describe the condition when knock will occur, Livengood and Wu [78] posed the now commonly used relation, shown in Equation (17), called the Livengood-Wu integral [79:58]. The characteristic ignition (delay) time of the fuel ( $\tau$ ) can be reduced by increasing temperature or pressure, or by decreasing the AKI quality of the fuel. Generally speaking, the AKI of the fuel describes its resistance to autoignition, and high AKI fuels tend to have longer ignition delays and lower laminar flames speeds than low AKI fuels [14, 23, 80]. When the conditions in the cylinder cause the integral to exceed unity, the end gas mixture autoignites ahead of the flame front. The delay time may be correlated to the Arrhenius rate equation, shown in Equation (18), where  $C_1$ ,  $C_2$ , and  $C_3$  are empirically fit parameters [79:58].

$$\int_0^t \frac{1}{\tau} dt = 1 \quad (17)$$

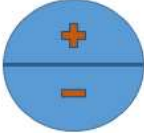
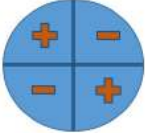


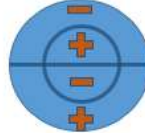
$$\tau = C_1 p_{cyl}^{-C_2} \exp \left[ \frac{C_3}{T_{cyl}} \right] \quad (18)$$

The knocking or pinging sound is the result of pressure waves reflecting off of the cylinder walls. Kalghatgi and Bradley [76] clarify that the pressure waves are the result of the accelerated flame front, and not vice versa. Heywood [21:451] poses one further stipulation: spark knock and surface ignition are separate phenomena. Spark knock may be controlled by retarding spark timing and lowering the pressure and/or temperature in the

cylinder, effectively increasing the characteristic delay time of the fuel. The hot spots in surface ignition generally cannot be mitigated using spark timing.

The easiest way to detect knock is by analyzing the in-cylinder pressure signal. Galloni [81] suggests that the fundamental frequency ( $f$ ) of each knock mode may be expressed as shown in Equation (19), where  $J_{m,n}$  is the zero of the derivative of the Bessel function of the first kind for the natural modes, ( $c$ ) is the speed of sound in the cylinder, and ( $B$ ) is the engine bore. Table 1, adapted from Baranski [53:14] and Galloni [81] shows the modes of knock and the appropriate Bessel function derivative zeroes. The 0,1 mode is the easiest to detect, but difficult to sense if the pressure sensing element is located in the center of the cylinder. Typically knock frequencies are 6-20 kHz [81].

**Table 1: Knock Modes and Corresponding Zeros of the Derivative of the Bessel Function of the First Kind, adapted from Baranski [53:14] and Galloni [81].**

m,n	1,0	2,0	0,1	3,0	1,1
Mode Shape					
$\rho_{m,n}$	1.841	3.054	3.852	4.201	5.332

$$f = J_{m,n} \frac{c}{\pi B} \quad (19)$$

There are many ways to quantify knock, but the maximum amplitude of pressure oscillations (MAPO) is the most common [82]. MAPO is the maximum amplitude of pressure oscillations relative to the pressure trace with the oscillations smoothed or removed with averaging or filtering. Figure 13, from Baranski [53:17] shows the three levels of knock on pressure traces for a Rotax 914 engine. The levels are light (MAPO up to 5 bar), medium (MAPO from 5 to 20 bar), and heavy (MAPO of 20 bar or more) [83,

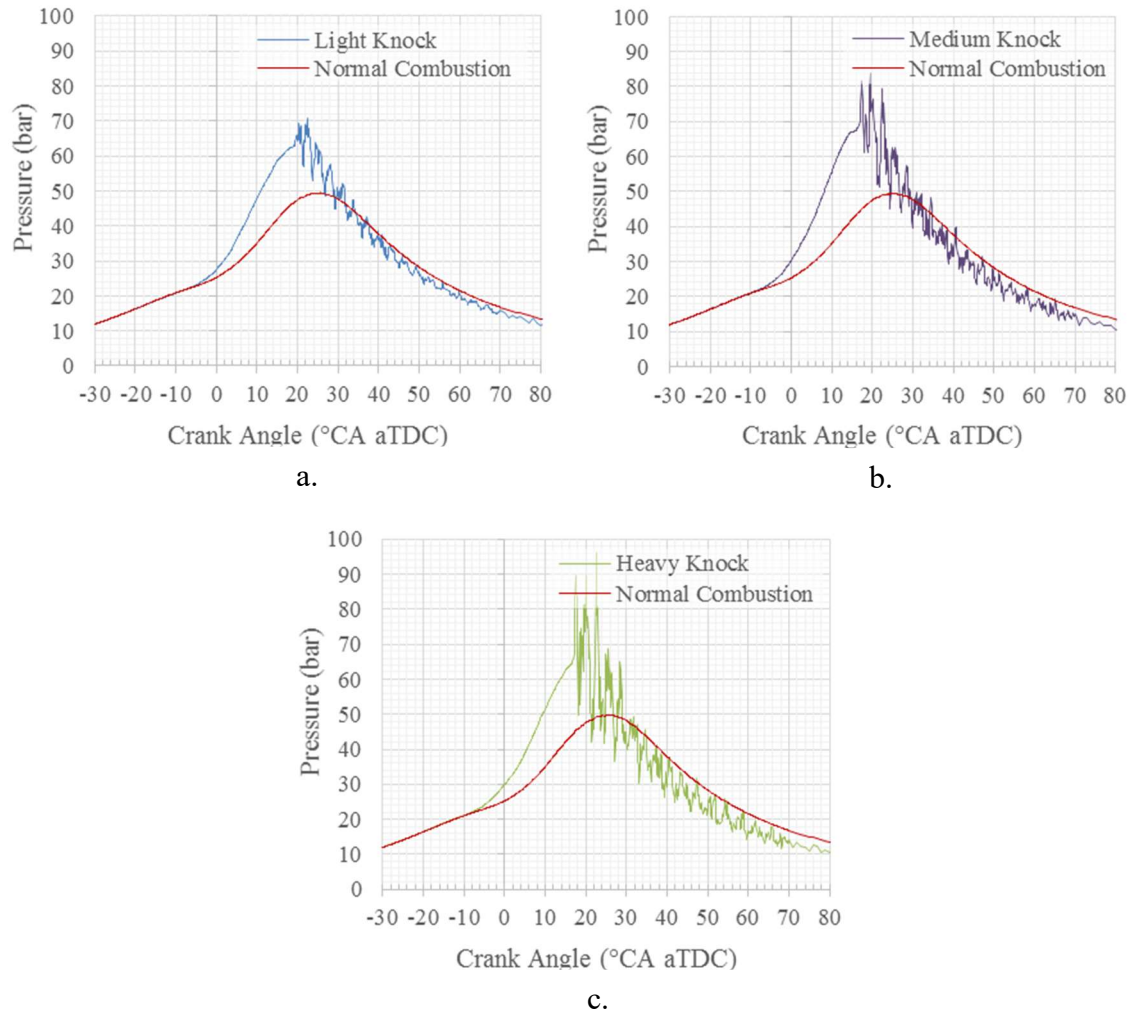


**Figure 13: Knocking cycle on a Rotax 914 engine showing (a) light, (b) medium, and (c) heavy knock. Reprinted with permission from Baranski [53:17].**

84]. When knock occurs, it is typically only in a fraction of engine cycles. Thus, it is necessary to specify how many consecutive cycles were evaluated for knock. Typical knock thresholds are 1 to 5 knocking cycles per hundred cycles. Even at 5% of cycles, light knock is unlikely to cause significant engine damage. However, the rapid pressure rise rates associated with heavy knock (10 bar/°CA [76]) can cause engine failure in just a few cycles, and the rapid heat release can melt holes in the piston and cylinder head. Since

damage associated with knock is often the result of the rapid pressure rise rates, peak pressure rise rate is another metric used to quantify knock.

There are numerous strategies to mitigate abnormal combustion and knock in an engine. Most of the strategies can be simplified to one of the following:

- 1) Use a more knock resistant fuel (longer ignition delay/ less prone to autoignition).
- 2) Lower the in-cylinder pressure or temperature to increase the induction time.
- 3) Increase the rate of combustion so the desirable combustion occurs before knock.

In the event one is converting an engine to run on a less knock resistant fuel, then approaches 2) and 3) must be pursued. Attard *et al.* compiled a comprehensive list of strategies and their estimated impact on a conventional SI engine. The table is reproduced here in Table 2 from Attard [85] and Baranski [53:25]. For each strategy the estimated change in ON requirement as a function of the change in the engine operating parameter is given. For the conversion of 10-100 cm<sup>3</sup> displacement ICEs to low AKI fuel, the most relevant factors are the fuel ON, equivalence ratio, combustion phasing (spark timing), and cooling of the cylinder (engine coolant). This assumes that altitude, humidity, and intake air temperature are dictated by the mission.

Fuel quality for engines is a complex topic. Edwards [86] provides a comprehensive overview of fuel development to meet anti-knock requirements over the last century, while Kalghatgi provides a concise overview of fuel manufacturing technology [87]. During World War I, knock-limited the performance of Allied aircraft depended on what depot supplied the aviation fuel. This led the Cooperative Fuel Research (CFR) committee in the United States to develop standards for rating the knock (or auto-ignition) resistance of various gasolines. Graham Edgar developed the modern octane number system where fuels

**Table 2: Knock Mitigation Strategies, Adapted from Attard [85] and Baranski [53:25]**

Parameter	Octane Number Requirement (ONR)	References	Range
Spark Advance	1 ONR $\uparrow$ / 1°C CA spark advance	[88], [89]	0-30°C CA bTDC
Intake Air Temperature	1 ONR $\downarrow$ / 7°C $\downarrow$	[88], [89]	20-90°C
Equivalence Ratio	2 ONR $\downarrow$ / 0.1 $\Phi$ ( $\Phi=1.05$ peak)	[89], [90], [91]	$\Phi=0.8-1.6$
Exhaust Gas Recycle	3-4 ONR $\downarrow$ / 10% $\uparrow$ cooled recycle	[92]	0-20% recycle
Manifold Pressure	3-4 ONR $\uparrow$ / 10 kPa $\uparrow$	[89], [91]	85-135 kPa
Compression Ratio	5 ONR $\uparrow$ / 1 CR $\uparrow$	[88], [89], [90], [93], [94]	CR = 5-12
Exhaust Pressure	1 ONR $\uparrow$ / 30 kPa $\uparrow$	[89]	0-65 kPa
Coolant Temperature (liquid coolant)	1 ONR $\uparrow$ / 10°C $\uparrow$	[89]	70-110°C
Altitude	1.4 ONR $\downarrow$ / 300 m $\uparrow$ 2.5 ONR $\downarrow$ / 300 m $\uparrow$	[88]	0-1800 m 1800-3600 m
Humidity	1 ONR $\downarrow$ / 10% $\uparrow$	[88]	40-50% at 30°C
Engine Deposits	6-9 ONR $\uparrow$	[88]	life of engine
Oil Consumption (wet sump only)	>12 ONR $\uparrow$	[88]	
Fuel Injection Type	4 ONR $\downarrow$ for DI over PFI	[95]	
Chamber Shaper	15 ONR $\downarrow$ for modern designs	[93]	
Hydrogen (gas) in Fuel	1 ONR $\downarrow$ / 1% H <sub>2</sub>	[91]	0-12% H <sub>2</sub>

are rated against a volumetric blend of two reference fuels. Iso-octane (2,2,4-trimethylpentane) is highly knock resistant and takes on a value of 100. N-heptane exhibits poor knock resistance and is assigned a value of 0. The actual fuel is compared to volumetric blends of the reference in two standardized tests to determine the Rated Octane Number (RON) [96] and the Motored Octane Number (MON) [97]. Both tests are performed on a standardized CFR engine and the ON is the volumetric blend of reference fuels that matches the knock limit of the actual fuel. The RON test is more demanding than the MON test, and the difference is called the sensitivity (typically about 10 points). By definition, a reference fuel blend has a sensitivity of 0. In the United States the AKI (reported at the pump) is the average of RON and MON.



Due to their molecular structures, some chemicals have an ON in excess of 100 or below 0. A comprehensive coverage of the fuel chemistry that drives ON is beyond the scope of this work, and Pulkrabeck [25:134-148] provides an excellent discussion on the matter. Early in the development of fuel for high performance engines, Thomas Midgely and Thomas Boyd of Kettering Labs tested over 30,000 different compounds and rated their potential to enhance ON. The most notable chemical was tetraethyl lead [86]. Edwards (among others) argues that the octane enhancements from tetraethyl lead may have allowed Allied aircraft to compete with German aircraft running superior engines [86], preventing a failure of the European air campaign in World War II. Tetraethyl lead was outlawed for ground vehicles in the United States in the 1970s for environmental reasons, although it is still used in some aircraft engines in a fuel called 100LL (which has an RON greater than 100). After lead was eliminated from automotive fuels, Methyl Tertiary Butyl Ether (MTBE) was used to improve the octane rating, although its use is decreasing in developed countries due to its toxic nature. Modern fuel in the United States relies primarily on improved refining methods (namely fluidized catalytic cracking and catalytic reforming) to meet AKI requirements through restructuring of the hydrocarbon blend during refining. This has led to a shift in the relevance of RON and MON for modern engines. Kalghatgi [87, 98] and Mittal and Heywood [99] note that for modern engines, RON is the more important parameter that dictates the knock-limited performance. Therefore, for two fuels with the same AKI, the one with the higher sensitivity will often yield better engine performance.

Objective 3 proposes that the increase in losses such as heat transfer may inherently decrease the AKI requirement of 10-100 cm<sup>3</sup> displacement ICEs, permitting the transition

from 98 AKI gasoline to ~20 AKI jet fuel (or diesel) with minimal modifications. The increase in heat transfer due to increasing surface area to volume ratio, which is essentially increasing engine cooling, is the primary mechanism of interest. In fact, Taylor [9:408-409] suggests that the increase in heat losses from increasing surface area to volume ratio alone may be enough to lower the AKI requirement. However, other parameters could also help to meet the ~20 AKI requirement. For example, spark timing is typically used to control knock in modern automotive engines. By retarding spark timing, efficiency and power can be traded for knock resistance at a rate of about 1 ON per degree of retardation. This technique has proven effective for heavy fuel conversions of larger engines [13, 15, 53]. Intake air temperature and altitude could also be investigated for their potential to aid in this conversion, although these parameters are more functions of the mission and ambient conditions.

## **2.7. Friction**

There are many sources of friction in ICEs, and engine friction and lubrication are extensively studied topics. This discussion will focus on the friction regimes and sources that are most applicable to small two-stroke engines. Figure 14 from Heywood and Sher [22:366] shows the three friction regimes commonly considered in ICEs as well as the Stribeck curve. The Stribeck curve describes the relationship between the friction coefficient ( $f$ ), which relates the normal force between the two surfaces to the tangential frictional force at the interface, and the duty parameter, which is also known as the Sommerfield number. The Sommerfield number is a non-dimensional parameter comparing the viscosity of the lubricant ( $\mu$ ) to the pressure loading on the contact surfaces ( $\sigma$ ) and the relative speed of the surfaces at the interface ( $N$ ).

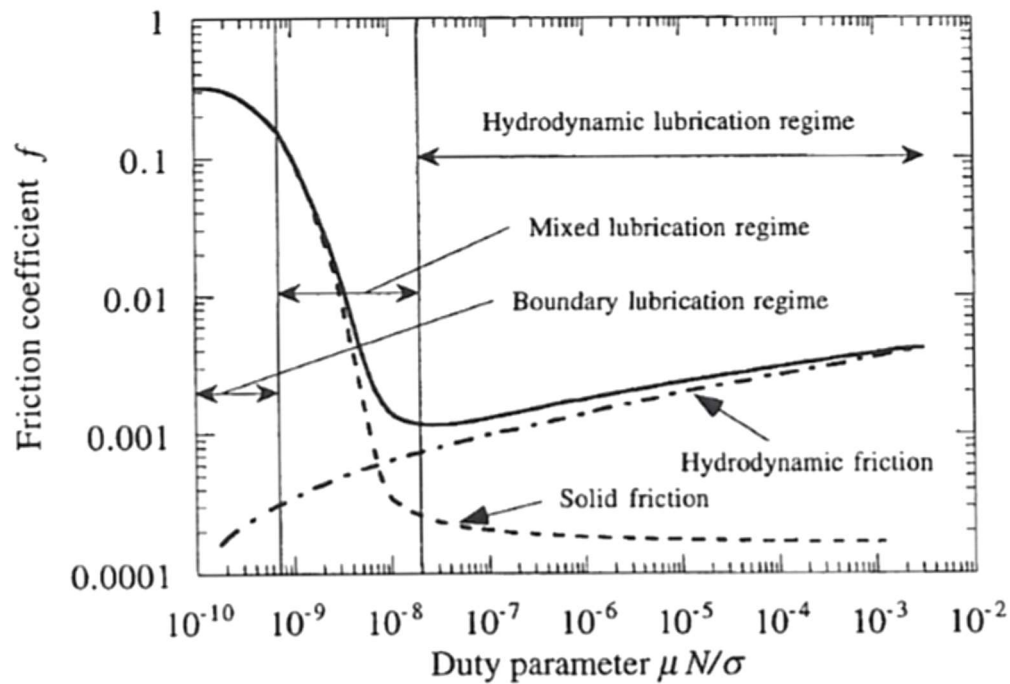


**Figure 14: Friction regimes and Stribeck curve as applicable to friction in an ICE, reprinted from Heywood and Sher [22:366] with permission from Taylor and Francis Ltd.**

In Figure 14 the boundary friction regime occurs when the normal force is sufficient to push the surfaces into metal-to-metal contact, causing rubbing, high friction, and mechanical wear. As the relative velocity between the components increases, the interface passes into the mixed lubrication regime, where portions of the surfaces are separated by the lubricating fluid and other portions are in direct contact. At high speeds and low normal forces, the interface will operate in the hydrodynamic lubrication regime, where the two surfaces are fully separated by lubricating fluid and the friction is the result of the viscous shear in the lubricant. This condition causes the least wear on engine components.

Small two-stroke engines contain components that operate in all three of these mechanical friction regimes. The journal bearings that support the main drive shaft and

the connecting rods function primarily in the hydrodynamic lubrication regime, and their contribution to friction increases with engine speed. The piston rings operate in the mixed regime during the faster part of their motion and in the boundary regime near TDC and BDC. Ball bearings and roller bearing operate in the boundary friction regime since their function depends on metal-to-metal contact between the rolling elements and the bearing race. In larger engines the valve train, accessories, and other components contribute additional mechanical friction losses, but the two-stroke engines considered here lack those components and thus those sources of friction.

Many small four-stroke engines are lubricated in a fashion similar to automobile engines using a wet sump. The crankcase contains an oil reservoir and the motion of the engine vibrates the oil onto and into the moving surfaces (automobiles typically use an oil pump to force the circulation of oil). Since small two-stroke engines often employ crankcase compression, they cannot use wet sump reservoirs in the crankcase. Instead, oil is added directly to the fuel. The low volatility of the oil relative to the fuel causes it to condense on the crankcase walls and components, lubricating the engine. Typically, small two-stroke engines use an oil that is premixed into the fuel at a fuel to oil ratio between 33:1 and 100:1 by volume.

Pumping losses are a non-mechanical friction loss, and they technically include the viscous losses during the gas exchange process as well as pumping losses incurred by any accessories, such as coolant pumps. As speed increases in large four-stroke engines, pumping losses increase with engine speed, typically driven by the accessories. Similarly, as the throttle valve is closed the pressure losses across the valve increase. In a two-stroke engine, slower engine speeds allow the crankcase and cylinder to fill more completely with

fresh charge, and thus, in a two-stroke engine the pumping losses actually increase with decreasing engine speed [22:360]. Unlike four-stroke engines, the pumping losses in a two-stroke engine often decrease as the engine is throttled. Since compression in the crankcase requires more pumping power than intake across the throttle plate, the decrease in pumping requirements at partial load often exceeds the increase in losses across the throttle plate, leading to lower pumping losses in a throttled two-stroke engine [22:360]. The result is that for two-stroke engines, mechanical efficiency often peaks at an engine speed in the middle of the operating range (as a tradeoff between pumping and mechanical friction) whereas mechanical efficiency decreases across the entire speed range of a four-stroke engine [22:362].

## 2.8. Other Engine Performance Metrics

There are several other engine performance metrics that are useful in discussing engine performance, such as the brake specific fuel consumption (BSFC). BSFC is the fuel consumption of the engine ( $\dot{m}_f$ ) normalized by brake power output ( $P_b$ ) as shown in Equation (20). Minimum BSFC values for conventional SI engines are about 270 g/kW-hr [21:52], while small SI engines may have SFC values two to four times greater [10, 39]. BSFC provides a normalized fuel consumption rate, useful for comparing the fuel consumption (and to some degree efficiency) of engines of dissimilar sizes. For non DI two-stroke engines, BSFC values are about 20% higher than a comparable four-stroke engines due to short-circuiting losses.

$$BSFC = \frac{\dot{m}_f}{P_b} \quad (20)$$

Another common parameter is the mean piston speed ( $\bar{S}_p$ ), calculated in Equation (21) using the engine speed ( $N$ ) and the connecting rod length ( $L$ ). The mean piston speed is a normalized engine speed comparing the true physical speed of engines. Since smaller engines have lower inertias, they can operate at higher rotational speeds than larger engines. Mean piston speed makes it possible to compare how fast two engines are running with regard to inertial loading. Typical values for conventional SI engines are 8-15 m/s [21:45]; small engines run anywhere from 3-10 m/s [5].

$$\bar{S}_p = 2NL \quad (21)$$

Finally, there are a number of efficiencies associated with engine performance. For this work, three different efficiencies will be considered: the combustion efficiency ( $\eta_c$ ), the thermal efficiency ( $\eta_{th}$ ), and the fuel conversion efficiency ( $\eta_{fc}$ ). The combustion efficiency is the ratio of the energy released during combustion, calculated using the enthalpy of the products ( $H_p$ ) and reactants ( $H_r$ ), to the total chemical energy contained in the fuel ( $m_f Q_{HV}$ ), as shown in Equation (22). It quantifies how well combustion releases the energy in the fuel. For lean combustion in conventional engines, combustion efficiency is usually 95%-98% [21:82]. For rich conditions, the efficiency drops essentially linearly with equivalence ratio until reaching the flammability limit. The thermal efficiency defines how well an engine converts the released heat into work ( $W$ ), as shown in Equation (23). The fuel conversion efficiency, sometimes called the overall efficiency, then describes the overall effectiveness of the engine at converting fuel into work as shown in Equation (24). The efficiencies may be related as shown in Equation (25). Figure 15 from Edwards *et al.* [100] shows representative fuel conversion efficiencies for various sizes of ICEs.

$$\eta_c = \frac{H_r - H_p}{m_f Q_{HV}} \quad (22)$$

$$\eta_{th} = \frac{W}{H_r - H_p} \quad (23)$$

$$\eta_{fc} = \frac{W}{m_f Q_{HV}} \quad (24)$$

$$\eta_c \eta_{th} = \eta_{fc} \quad (25)$$



**Figure 15: Typical fuel conversion efficiencies of various sizes of engines, reprinted with permission from Edwards *et al.* [100].**

## 2.9. Summary

Section 2 has provided an overview of two-stroke engines relevant to this effort. Section 2.1 provided context for the two-stroke engine within the broader class of internal combustion engines. Sections 2.2, 2.3, and 2.4 discussed ignition types, fuel delivery methods, and cooling methods, respectively. Section 2.5 provided background on the gas exchange process, which is necessary to understand the loss of fresh charge and thus fuel to the exhaust inherent to two-stroke engines. Section 2.6 explained combustion and knock, which directly affects the conversion to low AKI fuel. Section 2.7 gave an overview of friction sources in ICEs. Lastly, Section 2.8 covered a number of other metrics necessary to quantify, compare, and discuss engine performance.

### **3. Small Engine Literature and Testing**

Compared to conventional engines, the data available in literature for engines smaller than 100 cm<sup>3</sup> displacement is sparse. The information and data that is available is generally insufficient to satisfy the questions posed by the research objectives. This section reviews small engine testing literature for two purposes. The first purpose is to provide a sense of what data is available. The second purpose is to examine the issues inherent to testing small engines. This section begins with a short introduction to small engine testing (Section 3.1). The remaining sections are organized by time period (Sections 3.2 to 3.5) concluding with work done to inspire and support this effort (Section 3.6).

#### **3.1. Introduction to Small Engine Testing**

Until the last 20-30 years, most engines smaller than 100 cm<sup>3</sup> displacement were glow fuel engines for use in hobbyist aircraft. Compared to typical hydrocarbon fuels such as gasoline and JP-8, nitromethane has about ¼ of the heating value and about 2.5 times the air to fuel ratio [11]. The introduction of gasoline powered SI engines smaller than 100 cm<sup>3</sup> displacement improved the fuel consumption, reliability, and power output of small engines, widening their potential applications for hand held power tools and more recently commercial and military RPAs. Yet, the majority of small engine testing has been performed on either micro engines (less than 10 cm<sup>3</sup> displacement, 1 kW) or small motorcycle/scooter engines (greater than 100 cm<sup>3</sup> displacement, 7 kW), leaving a significant gap in the 10-100 cm<sup>3</sup> displacement range considered herein. The low cost of most small engines, driven in part by the low cost of their respective applications, has, historically, hindered research and in some cases limited measurements to those that are cost effective [101]. Indeed, it is difficult to justify spending over \$100,000 in equipment



for in-cylinder pressure measurements, exhaust gas analysis, and engine controls to quantify the performance of an \$800 engine used on a hobbyist aircraft. The expanded application market is changing this mentality. Emissions regulations in Europe are now affecting even small handheld power tools and companies such as Stihl have invested significant money into small two-stroke engine technology [49], although much of their data remains proprietary. The military RPA market has also driven research both at universities [15, 102] and in industry [41, 103]. A desire to improve the design and operation of Group 2 RPAs is ultimately the drive behind this effort.

### **3.2. 1950-1980 – Early Testing Efforts**

The most notable early small engine testing effort was performed in the 1950's at The Ohio State University [104]. The study surveyed a selection of 5-400 W engines for use in motor-generator sets. The researchers found that the engines had acceptable mechanical efficiencies above 60%, but poor overall fuel conversion efficiencies with a maximum of 7.5% to 9.0% for the two-stroke cycle engines tested. They also noted that when miniaturizing engines, fuel metering, ignition, and starting systems became more challenging to design and implement (although improvements in manufacturing in the last 60 years have solved a number of the observed issues). During testing, a number of reliability issues were observed, including crankcase failures due to vibrational loading and the light construction of the die cast aluminum engine bodies. Testing revealed that oscillatory airflow from two-stroke engines complicated intake air flow measurements. Taylor's solution was a large baffle between the engine and the air flow meter [24:610-611]). Even with careful control of operating conditions, erratic engine performance was

frequently observed. Ultimately, the effort concluded that small COTS ICEs did not yet possess the reliability and durability for military applications.

In 1973, Gierke published a series of three articles in a hobbyist magazine detailing his characterization of a number of small hobbyist glow engines. The testing was performed on a dynamometer constructed in his basement [105-107]. Gierke's extensive data included torque and power, measured using a pendulum on a reaction cradle attached to the engine, fuel flow measured using a graduated cylinder and a stop watch, and air flow measured with a homemade manometer. A schematic of Gierke's setup is shown in Figure 16 [106]. The engine load curve was varied by changing the propeller. For the average hobbyist, Gierke's data is surely adequate, if not excessive. For researchers

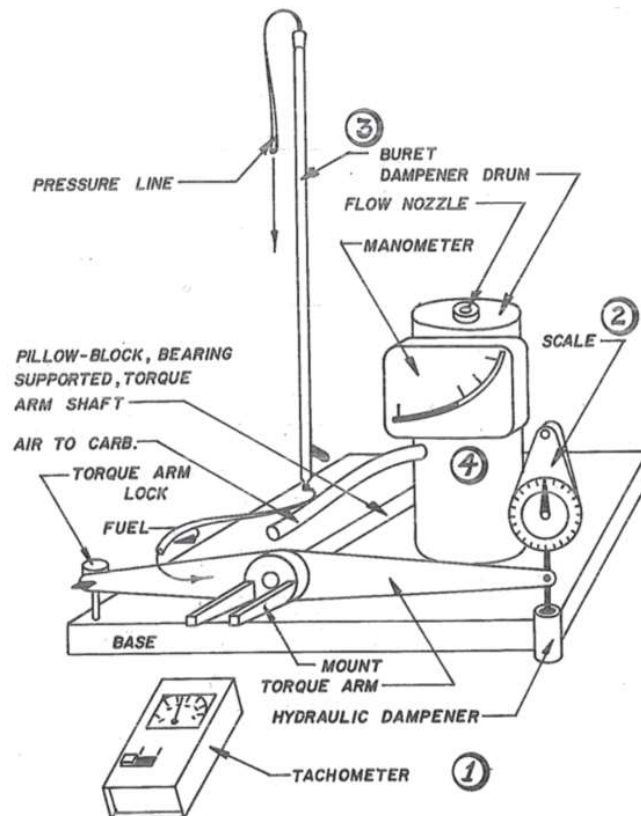


**Figure 16: Schematic of Homemade engine Test setup by Gierke [106].**

interested in developing scaling laws for individual losses in an engine, it is inadequate. Yet, until the work of Menon and Cadou [6, 16] (discussed in Section 3.3), it remained the most ‘complete’ set of micro engine data available.

### **3.3. Cadou, Menon, and Moulton: Micro Glow Fuel Engines: 2002-2013**

Cadou, Menon *et al.* provide the most comprehensive collection of data on modern glow fuel engines. Over the course of a decade, the research group developed a test bench and characterized nine glow fuel engines ranging from 8 to 650 W. Their earlier work [4, 7] details the development of a dynamometer rig to start and measure the power output and friction losses in micro glow fuel engines. Key difficulties with the bench development stemmed from the small engine size. The low power output of the engines required a dynamometer to be constructed from an electric motor and load cells since no appropriately sized commercial solution was available. The apparatus held the engine in a reaction cradle to measure power at the engine output shaft without drive train losses. A custom fuel flow scale was developed due to difficulty sourcing a low flow rate flow meter. Cadou *et al.* also noted significant performance variability in the engines between runs and resorted to controlling the fuel flow instead of air throttling. A paper published by Menon and Cadou in 2004 [36] documents their initial scaling analysis, which is discussed further in Section 4.2.

Menon and Cadou also published a paper on an attempt to model a micro glow fuel engine using numerical simulation [108]. The model used the friction model presented in Section 5.2.1 and the Annand model from Section 5.1.1 for heat transfer losses. The fit to actual engine data was poor, and the model failed to capture the observed decreases in efficiency from 5% to 3% from 8000 to 11,000 rpm, instead predicting essentially constant

efficiency over this range. Cadou and Menon conclude the discrepancies are the result of heat and friction models that were “developed for much larger engines and may not be at all appropriate for engines of this scale” [108]. The crude scavenging model that neglected the inertial aspect of gas flow during scavenging may also be partially at fault.

Menon wrote both his thesis [8] and dissertation [2] on data collected from the test setup, and both documents provide extensive information on testing techniques for micro engines, culminating in a scaling study of losses in micro engines less than 10 cm<sup>3</sup> displacement. This data is key because it provides contrast to data available from Taylor [9:401-417], Oak Ridge National Laboratories [100], and Heywood and Chon [109] for conventional engines, and indicates a change in the relative importance of loss pathways in the 10-100 cm<sup>3</sup> displacement engines considered in this effort. Menon’s key results were documented in two papers, the first [6] summarizing overall engine performance and the second [16] examining losses in the micro engines. In the case of loss pathways, Menon and Cadou only had data available for engines tested in their facility; manufacturer data was insufficient. However, for plotting gross power trends, they did compile manufacturer data from a variety of sources. The results highlight that information on 10-100 cm<sup>3</sup> displacement engines is particularly sparse. The losses and scaling aspects of their research are discussed more extensively in Section 4.2.

### **3.4. Small Engines from a Teaching Standpoint: Raine et al: 2002-2004**

Raine *et al.* [101] recognized the potential for using small ICEs as cost efficient hands-on examples to illustrate concepts for courses taught on automotive and larger scale engines. To that end, they developed a test stand for glow engines less than 4 kW. The stand measured torque using a pendulum reaction cradle, similar to Gierke’s setup. Fuel

flow was measured by introducing water droplets into the fuel line and tracking their linear velocity as they moved with the fuel. Exhaust gas measurements were made by collecting and cooling engine exhaust in 60 gallon trash bags. The bench was validated using a K&B Sportster 7.54 cm<sup>3</sup>, 7.6 compression ratio, two-stroke engine, which produced 650 W.

In 2004, Raine and Thorwarth used the bench to perform a parametric study on nitromethane concentration, glow plug type, and air to fuel ratio [110]. To measure indicated engine performance, they added a Kistler 601A pressure transducer and a Kistler 5011 charge amplifier. The engine was the same engine used to validate the bench, but a new head was machined to accommodate the pressure transducer. The study concluded that nitromethane aided in earlier ignition and more rapid combustion of the mixture, but 10% versus 20% of nitromethane in the fuel did not appear to have a large effect. The glow plug type did not appear to alter ignition timing. The engine exhibited COV of IMEP values of at least 7% and typically closer to 15%-20%. Raine and Thorwarth concluded that glow ignition is less consistent cycle-to-cycle than spark-ignition, leading to COV values that would be unacceptable in a typical spark-ignition engine.

### **3.5. Other Relevant Engine Testing (2000-Present)**

Manente [34] installed optical access in a 4.1 cm<sup>3</sup> displacement glow engine to study the differences between HCCI and glow plug initiated combustion. Combining optical access with measurements of cylinder pressure using a piezoelectric sensor, Manente managed to measure the flame speed for glow fuel in situ at 86 m/s with a 3-4 mm flame thickness. He then converted the engine from glow operation to HCCI, dropping the fuel conversion efficiency to 5%. The techniques indicate that even small engine heads may be modified with quartz optical windows to directly observe combustion.

Shin *et al.* [111] measured the friction in an Enya 25 cm<sup>3</sup> four-stroke model airplane engine. Unlike conventional engines, where the friction as a function of engine speed may be fit with the semi-empirical model presented in Section 5.2.1, Shin *et al.* found two distinct friction regimes, one below 7000 rpm and one above 8000 rpm. They concluded that at high engine speeds, lubrication was insufficient and the engine transitioned from hydrodynamic lubrication (surfaces separated by lubricant) to the mixed lubrication regime, where intermittent metal on metal contact occurs. The paper also provides a suggested fit to Equation (2) for small four-stroke engines, included in Section 5.2.1.

Papac and Dunn-Rankin [112, 113] provided insight into combustion modes and loss mechanisms in an O.S. FS-30-S 4.9 cm<sup>3</sup> engine. Using an optical pressure transducer, Papac and Dunn-Rankin measured the maximum power (80 W) and fuel conversion efficiency (9%) of the engine [113]. Initially, they speculated that the fuel combusts in two different zones, a rich mixture at the wall that burns like a CI engine and a more stoichiometric charge in the center of the cylinder that burns in HCCI type combustion [112]. Further analysis of the flame regime indicated a wrinkled laminar flame structure and incomplete combustion leading to significant losses through unburnt hydrocarbons in the exhaust. Ogawa and Kawaguchi [114] used the same engine in a parametric study of nitromethane concentration in glow fuel. Consistent with its volatility, nitromethane made the engine prone to earlier ignition and widened the flammability limits of the air fuel mixture.

Wiegand *et al.* [102] developed a micro engine test bench to investigate the practicality of converting an 11.5 cm<sup>3</sup>, two-stroke glow fuel engine to heavy fuel operation. Wiegand's [11] results indicate three primary obstacles to conversion: the poor lubricity of

JP-8 compared to glow fuel, poor vaporization of JP-8 compared to glow fuel, and pitting and thermal damage due to knock and abnormal combustion. Wiegand focused mostly on the first two issues. Lubrication in a typical glow fuel engine depends on castor oil, which makes up about 20% of the fuel by volume (the remainder being methanol and nitromethane). Wiegand determined that JP-8 required about 20% Techniplate oil (similar to castor oil) to match the performance of glow fuel based on testing following ASTM D6078 and ASTM D6079 standards. The results indicated that JP-8 has little inherent ability to lubricate a glow fuel or two-stroke engine [11]. To improve fuel vaporization during starting, Wiegand focused on retaining heat in the cylinder. Initially, ceramic cylinder coatings were tested and found to have little benefit. Directly heating the head caused warping of some components. Slowly heating of the head over 30 minutes required 68 MJ of energy (the amount of thermal energy in 1.75 kg of hydrocarbon fuel), which is impractical for such a small system. Intake air heating was found to decrease start time from 3-1/2 minutes to 2-1/2 minutes. Fuel heating attempts were unsuccessful. Wiegand did notice pitting and thermal damage on the piston crown [11], which could have been caused by knock during JP-8 operation. The heating strategies pursued to improve starting performance are also consistent with increased knock tendency.

Kass *et al.* [115] selected an OS-25-LA 4.0 cm<sup>3</sup> displacement glow fuel engine to study the feasibility of additive manufacturing techniques for small engines. They replaced the stock aluminum head of the engine with a laser sintered titanium head. Titanium was selected to demonstrate the feasibility of additive manufacturing for difficult to machine metals and because the higher thermal capacity relative to aluminum was expected to improve combustion efficiency in the engine. The additive manufacturing technique

proved mechanically suitable for ICE operation, but the replacement head proved troublesome. The location of the pressure sensor port on the titanium head altered the scavenging flow. The titanium head also retained more thermal energy leading to higher combustion temperatures. The higher temperatures increased the expansion of the piston resulting in higher friction between the piston and cylinder walls. (This engine was so small that it used a sliding fit between the piston and cylinder wall; there were no piston rings). The scavenging, thermal expansion, and increased friction lowered the power output of the engine by 20-30% at speeds above 4000 rpm compared to the stock aluminum head. Thus, while the additive manufacturing was a success, Kass *et al.* indicate that further studies of the exhaust gas composition would provide additional insight into how the titanium head affected scavenging and combustion efficiency.

### **3.6. Small Engines at AFRL (2010-2014)**

AFRL and the Air Force Institute of Technology (AFIT) have conducted significant research on a variety of small engines as part the Efficient Small Scale Propulsion program under the Aerospace Systems Directorate, Turbine Engine Division's Advanced Concepts Group. The small engine efforts have focused on altitude performance, fuel AKI reduction, alternative fuels, and engine scaling relationships. The second and final efforts were led by the author from 2012-2016.

#### **3.6.1. Engine Performance at Altitude**

It is an established fact that engine power output degrades with increasing altitude, primarily due to a decrease in ambient density [116:155]. Larger ICEs, such as the Rotax 914, a 1.2L four-cylinder, four-stroke engine used on the MQ-1b Predator, are turbocharged to meet performance requirements at altitude [13]. However, turbochargers and



superchargers are less practical for small two-stroke engines. Both turbochargers and superchargers are relatively heavy and bulky additions to a small aircraft [117], and the efficiency of turbomachinery decreases as corrected mass flow (and thus engine size) decreases. Turbochargers and superchargers pose an additional dilemma for two-stroke engines: they increase the pressure differential during blowdown and gas-exchange, potentially increasing short-circuiting losses [22:74-75].

AFRL and AFIT have attacked this problem using a two pronged approach. Crosbie [39] developed an altitude rig and characterized the impact of an aftermarket fuel injection system on the altitude performance of a 95 cm<sup>3</sup> Brison two-stroke engine. The fuel injection system stabilized mixture development, dropping brake specific fuel consumption from 850-2430 g/kW-hr with the stock carburetor to between 610-730 g/kW-hr with the fuel injection system. The fuel injection system also mitigated the power drop off with altitude (up to 40% at 10,000 ft) by up to 90% [39]. Husaboe furthered the effort, investigating how the power drop off at altitude compared to predictive models such as those shown in Equation (26) from Anderson [116:155], and Equation (27) from SAE J1349 [118]. In both cases the correction factor references the altitude power of the engine ( $P$ ) to the sea level power ( $P_{SL}$ ) using the temperature ( $T$ ), pressure ( $p$ ), density ( $\rho$ ), and/or humidity ( $w$ ).

$$CF = \frac{P}{P_{SL}} = 1.132 \frac{\rho}{\rho_{SL}} - 0.132 \quad (26)$$

$$CF = \frac{1-w}{1-w_{SL}} \left( \frac{p}{p_{SL}} \right)^{C_1} \left( \frac{T_{SL}}{T} \right)^{C_2} \quad (27)$$

While in previous literature the correction factors ( $C_1$ ,  $C_2$ ) in Equation (27) were constant with respect to engine speed, Husaboe's results indicate that the sensitive scavenging

nature of the two-stroke engine caused the power drop of to be a function of both altitude and engine speed. Therefore Husaboe *et al.* suggested that the exponents on the pressure and temperature terms be functions of speed [119]. The general forms of the speed corrected coefficients are shown in Equation (28) [119].

$$\begin{aligned} C_1 &= 9.01 \cdot 10^{-8} N^2 - 9.42 \cdot 10^{-4} N + 3.69 \\ C_2 &= 6.73 \cdot 10^{-8} N^2 - 8.07 \cdot 10^{-4} N + 3.01 \end{aligned} \quad (28)$$

The other prong of the AFRL approach was investigating new technologies for increasing intake pressure at altitude. To this end, Mataczynski *et al.* [117] simulated and tested a scaled version of the Compres wave rotor for the Brison 95 cm<sup>3</sup> displacement engine. The wave rotor used high pressure pulses from the exhaust to compress the inlet air, ideally without mixing the gases. Since the wave rotor was not a mechanical compressor and instead utilized a set of rotating channels, it had much lower parasitic losses [117].

### 3.6.2. Fuel AKI Reduction and Alternative Fuels

As the largest single consumer of transport fuel in the United States, the Air Force also has a vested interest in alternative fuels. Groenewegen *et al.* [120] investigated algae and Camelia biodiesels as well as JP-8 as alternative fuels for a Fuji IMVAC 34 cm<sup>3</sup>, four-stroke engine. Due to mixture preparation issues and the highly variable equivalence ratio delivered by the air carburetor, Groenewegen *et al.* modified the engine with an air-assisted PFI system. With the PFI system in place, they observed a 10-20% decrease in BSFC running JP-8 instead of 100LL Avgas [120]. At high speeds and loads, knock in the engine required the retardation of spark timing, and JP-8 exhibited higher BSFC than 100LL Avgas. JP-8 also decreased the maximum power of the engine. Groenewegen *et al.* [120]

did not have access to an in-cylinder pressure transducer, and thus detected knock audibly setting the knock threshold as an audible pinging detectable above the noise of the engine.

Wilson *et al.* [14] built on Groenewegen *et al.*'s [120] work and examined just the effects of octane requirement on the Fuji IMVAC engine. Using the same air-assisted PFI system, Wilson *et al.* mapped engine performance using primary reference fuel (PRF) blends of iso-octane and n-heptane from 100 ON to 0 ON. For the study Wilson [43:86] installed an OpRand in-cylinder pressure sensor to detect knock. The study concluded that n-heptane decreased fuel consumption by an average of 4.1% across the operating range of the engine. The more interesting results, however, were from the in-cylinder pressure transducer. The in-cylinder pressure trace indicated that n-heptane had a faster burn angle than iso-octane as the result of a shorter flame development time, as shown in the experimental data in Figure 17 from Wilson [43:49]. The decreased flame development

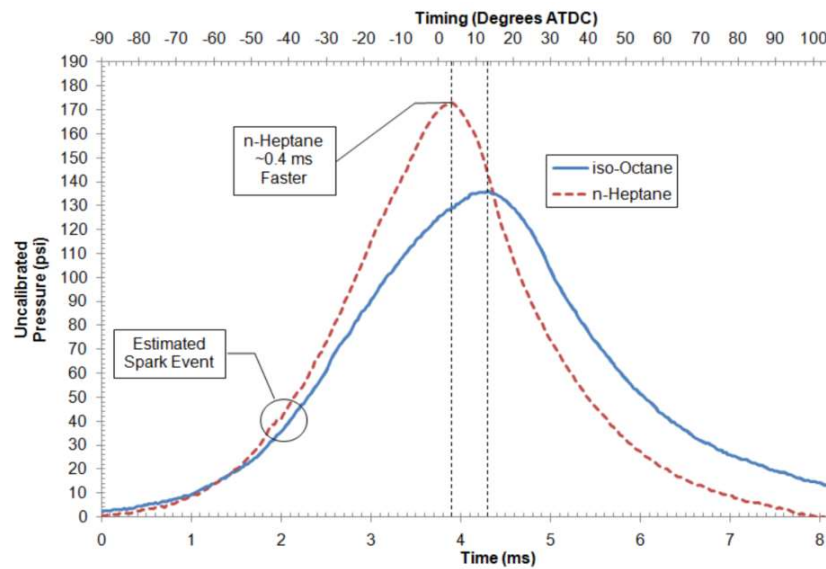


**Figure 17: In-cylinder pressure traces from a Fuji IMVAC 34-EI showing the faster, earlier, and shorter combustion phasing of n-heptane relative to iso-octane, reprinted from Wilson [43:49].**

time of n-heptane put combustion closer to TDC and constant volume combustion, improving the efficiency of the engine. The other notable result was the confirmation of knock when running n-heptane, as seen in the pressure traces in Figure 18 from Wilson's thesis [43:51]. Due to a lack of data and a reference transducer, MAPO levels to characterize the knock are not available. The noise in Figure 18 between 35°bTDC and 50°bTDC was caused by the spark event.

### 3.6.3. Engine Scaling Studies

The studies of Wilson *et al.* [14] and Groenewegen *et al.* [120] suggest 10%-20% improvements in fuel burn and aircraft endurance if the issues associated with heavy fuels, in this case knock, can be successfully mitigated. As displaced volume decreases, the surface area to volume ratio increases, and the losses driven by surface area increase relative to the power released during combustion (driven by volume). This drives down the fuel conversion efficiency of the engine. However, if these losses and their underlying

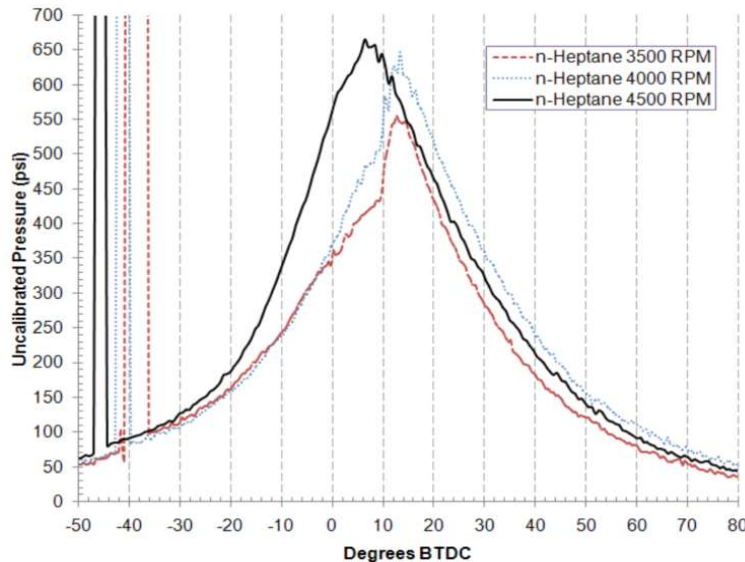


**Figure 18: In-cylinder pressure trace for n-heptane in a Fuji IMVAC engine at full throttle showing knock, reprinted from Wilson [43:51].**

mechanisms can be understood and leveraged to control knock, then the small engines may be converted to run on heavy fuel. This reasoning led the author, in collaboration with co-workers at AFRL and AFIT, to investigate how losses scale in small engines. Table 3 lists the papers detailing the author's efforts to set up and validate the Small Engine Research Bench (SERB), the starting point for this effort. All six papers are included as Appendices.

**Table 3: Preliminary AFRL and AFIT Papers on Engine Scaling**

<b>Location</b>	<b>Title</b>	<b>Description</b>	<b>Ref</b>
Appendix A	Development of Test Bench and Characterization of Performance in Small Internal Combustion Engines	Development and validation of the test set-up for characterizing performance of small 1-6 kW engines.	[10]
Appendix B	Preliminary Thermal Loss Measurements for a Small Internal Combustion Engine	Development and testing of methods to determine net heat losses from the engine cylinder.	[121]
Appendix C	Measuring Scaling Effects in Small Two-Stroke Internal Combustion Engines	Initial study of how heat transfer effects scale with engine size.	[5]
Appendix D	Comparison of In-Cylinder Pressure Measurement Methods in a Small Spark Ignition Engine	Investigation of in-cylinder pressure measurement techniques for small ICE's.	[75]
Appendix E	Dynamic Friction Measurements on a Small Engine Test Bench.	Characterization of drive train friction on the SERB.	[122]
Appendix F	Quantification of Short-Circuiting and Trapping Efficiency in a Small Internal Combustion Engine by GC-MS and GC-TCD	Development and validation of exhaust energy pathways measurements.	[123]

#### **4. Engine Scaling and Loss Pathways**

The hypothesis that decreasing the size of a COTS engine enhances its resistance to knock hinges on the concept that certain phenomena, such as heat transfer, scale with engine size. This work proposes that loss mechanisms in 10-100 cm<sup>3</sup> displacement engines cause at least the engines on the small end of the spectrum to possess an increased resistance to knock, intrinsically enabling operation on low AKI fuel. The first step to

leveraging these mechanisms is a quantification of how losses scale in geometrically similar COTS engines, which was the focus of Objective 1.

The remainder of this section is split into three parts to discuss scaling in ICEs. This first part (Section 4.1) discusses why one would expect engines to scale and presents empirical data showing why engines with displaced volumes between 10-100 cm<sup>3</sup> are a critical size class in the study of scaling. The second part (Section 4.2) reviews prior scaling studies from the standpoint of overall performance and losses. The third part (Section 4.3) summarizes the discussion and relates it back to Objective 1.

#### **4.1. Why Loss Pathways in ICEs Scale**

Recalling Figure 15, fuel conversion efficiency decreases with engine size. The fuel conversion efficiency is essentially a measure of losses relative to the amount of energy supplied to the engine as fuel. This scaling of efficiency is generally explained with two observations about losses and fuel energy. First, the amount of energy released during combustion is proportional to the volume of the combustion chamber. Second, the majority of losses are proportional to a surface area within the engine or are related to a volume that shrinks more slowly than the combustion volume.

This study considered five loss pathways: heat rejection from the cylinder, friction, short-circuiting of fresh charge, sensible enthalpy in the exhaust gases, and incomplete combustion. The first two, heat transfer and friction, are expected to scale with surface area. Short-circuiting is primarily controlled by port design [22:155-157] and must be accounted for in an energy balance on the engine. The final two mechanisms are sensible and chemical enthalpy in the exhaust. The chemical enthalpy from incomplete combustion is heavily influenced by mixture ratio and by quenching in crevices. Incomplete

combustion from quenching in crevices scales with the volume of the crevices, which is not necessarily a fixed percentage of the combustion volume. For example, if several differently sized engines used the same spark plug, the crevice volume associated with the spark plug will have a greater impact on the smaller engines, leading to higher losses from incomplete combustion.

The cylinder surface area ( $SA$ ) and the swept volume ( $V_d$ ) of an engine may be related to bore and stroke as shown in Equation (29) [5]. Accepting the premise that the energy released during combustion is proportional to the cylinder volume, the power output of the engine may be related to the cylinder volume using a power density ( $\rho_{pwr}$ ), as shown in Equation (30) [5]. For a square engine (bore=stroke), the relationships in Equations (29) and (30) may be simplified as in Equation (31), where the exponent should take on a value of  $n = 3$ .

$$\frac{SA}{V_d} = \frac{\pi BL + \pi \frac{B^2}{2}}{\pi \frac{B^2}{4} L} = \frac{4}{B} + \frac{2}{L} \quad (29)$$

$$P = \rho_{pwr} V_d = \rho_{pwr} \pi \frac{B^2}{4} L \quad (30)$$

$$P = \frac{\rho_{pwr} \pi}{4} \left( \frac{SA/V_d}{6} \right)^{-n} \quad (31)$$

If all losses were directly proportional to engine volume, then a single value of power density would suffice for all engine sizes. Figure 19, reprinted from Rowton *et al.* [5], plots the surface area to volume ratio and the manufacturer rated engine power for an assortment of COTS engines [124-134]. The model is a least squares regression fit of

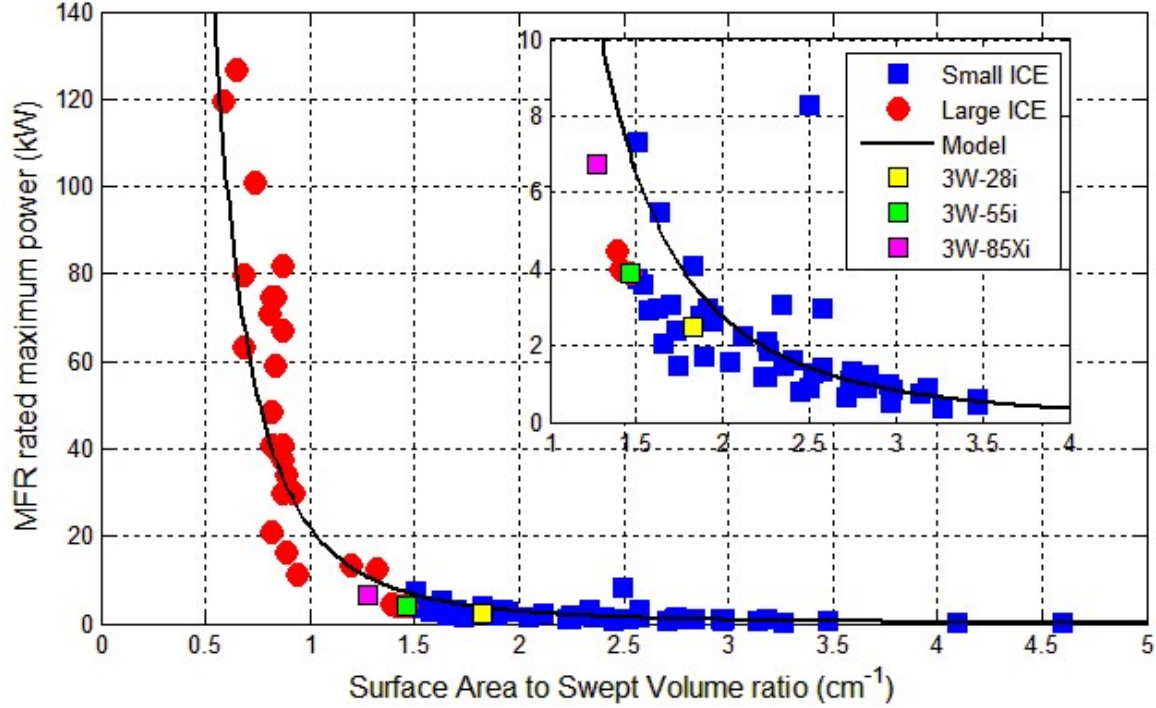


**Figure 19: Scaling of engine power with surface area to volume ratio, reprinted from Rowton *et al.* [5].**

Equation (31), shown in Equation (32). Note that  $n = 3.1$  is a result of most engines in the study being slightly off square.

$$P = 21.91 \left( \frac{SA}{V_d} \right)^{-3.1} \quad (32)$$

Working backwards to power density, the fit suggests  $106 \text{ W/cm}^3$  for the COTS ICEs. In his thesis [135], Rowton also performed the fit by assigning a dividing line between large and small engines at  $50 \text{ cm}^3$  of displaced volume. The author worked directly with Rowton to obtain the unpublished information on these fits. The fits suggest that the power density for the smaller engines (blue in Figure 19) is  $76 \text{ W/cm}^3$  while the power density for the larger engines (red in Figure 19) is  $165 \text{ W/cm}^3$ . The change in power density indicates that losses must play a more significant role as engine size decreases. During the revision of [5],



a number of the reviewers questioned whether the bore to stroke ratio, which alters the shape of the combustion volume, would have a significant impact on the relationship between the surface area to volume ratio and the displaced volume. Figure 20, reprinted from Rowton *et al.* [5], shows that practical variation of the bore to stroke ratio has little impact on the surface area to volume ratio over a wide range of displaced volumes.

Figure 19 also shows the three engines initially selected for this study. Based on the plot, 10-100 cm<sup>3</sup> displacement engines fall in the transition region between large engines and small engines where a change in the relative importance of loss pathways is expected to occur. Data from Menon and Cadou's scaling study [6], Heywood's discussion of energy pathways in engines [21:674], and a study released by Oak Ridge National Laboratory [100] support this conclusion. Thus, 10-100 cm<sup>3</sup> displacement engines are

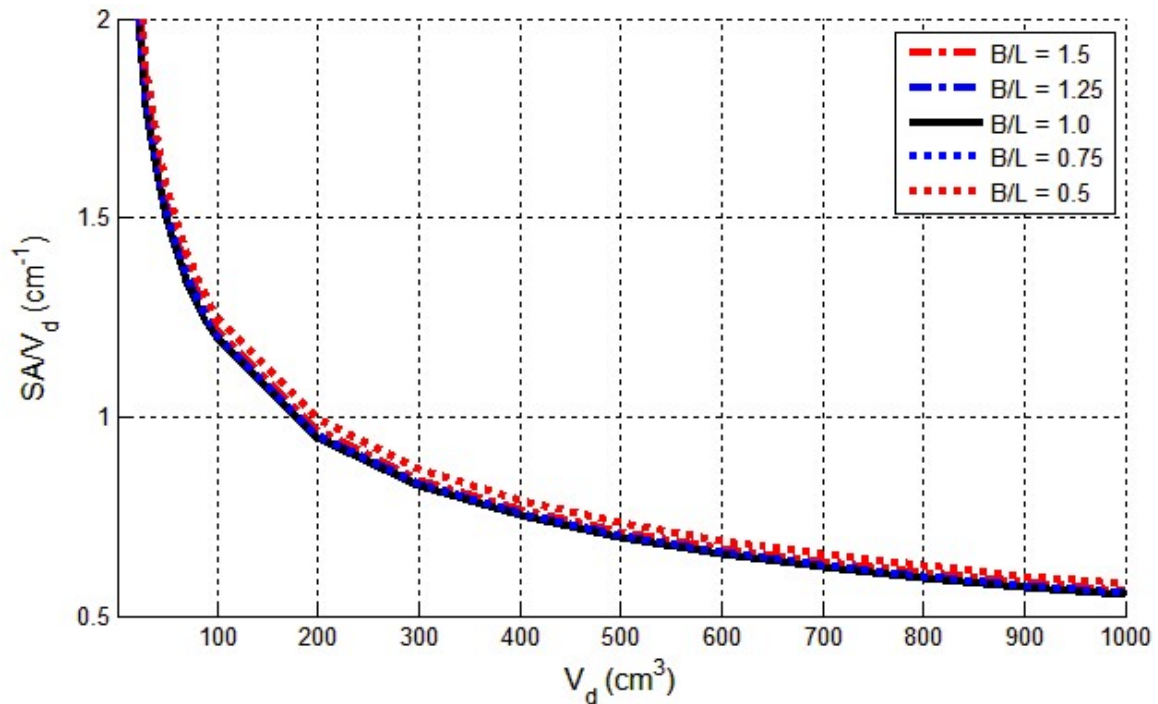


**Figure 20: Relationship between displaced volume, surface area to volume ratio, and bore to stroke ratio showing that bore to stroke ratio has a smaller impact on geometry than the surface area to volume ratio, reprinted from Rowton *et al.* [5].**

poised at a point where losses may be significant enough to permit relaxed fuel AKI requirements, but low enough to provide practical efficiencies compared to the less than 10% fuel conversion efficiencies observed in smaller glow engines.

#### **4.2. Scaling Studies on Losses in Internal Combustion Engines**

Literature indicates that Taylor and his students pioneered scaling studies in geometrically similar engines in the 1950's. Lacking access to geometrically similar commercial engines, Taylor and his students built three geometrically similar engines by using the same engine drawing constructed to three different scales [9:175-179].

**Table 4: MIT Similar Engine Geometry Information [9:178]**

<b>Engine</b>	<b>Bore (cm)</b>	<b>Stroke (cm)</b>	<b>Displacement (cm<sup>3</sup>)</b>
Small	6.35	7.62	241.3
Medium	10.16	12.19	988.3
Large	15.24	39.89	7277

The three engines were four-stroke engines with identical valve timing and the same materials of construction. The bore, length, and displaced volumes are listed in Table 4 [9:178]. Data taken on the engines appear throughout both volumes of Taylor's book [9, 24], but key results are summarized here.

- 1) Heat Rejection: Taylor notes that as engine bore increases, the engines become harder to cool since the surface area to volume ratio decreases [9:280-281]. Taylor's interest was primarily in engines much larger than those considered herein.
- 2) Manufacturer rated piston speeds and peak pressures decrease with engine size (bore) as more conservative ratings are used in place of results from destructive testing due to the expense of testing large engines to failure [9:406].

- 3) Efficiency is generally not a function of engine size (bore), except on scales much smaller than the size tested in Taylor's investigations [9:408].
- 4) For engine with bores greater than 6.0 cm, the fuel AKI requirement increases with bore (and thus engine size). The increase is due to an increase in surface temperatures due to the lower surface area to volume ratio. Also, flame speed remains relatively unchanged, and the large bore increases the time required for flame propagation to the end-gas [9:78-79].

Taylor points out in his discussion of small engines and efficiency that a more careful examination of very small engines (which he defines as anything less than 150 cm<sup>3</sup> displacement or about 10 kW) is warranted to separate poor performance due to immature technology from poor performance due to scale [9:408-409].

Much of the current research in engine scaling focuses on the minimum practical size of an engine. These studies are of interest because they indicate which loss mechanisms are ultimately responsible for preventing the function of an ICE. In 2005, E. Sher and D. Sher published a paper speculating that the HCCI engine could be extended to smaller sizes than the SI engine since autoignition of the fuel in an HCCI engine circumvents quenching of the flame front by conduction to the cylinder wall [136]. In 2009, Sher *et al.* [33] extended the hypothesis to state that if quenching, which limits the size of an SI engine, is not a factor, that friction and charge leakage through the piston gap must govern the minimum possible size of an HCCI engine. They examined the tradeoff between piston gap, friction, and charge leakage using a simulated engine model. The results indicated that as piston gap increases, friction decreases and loss of mass and pressure from the cylinder increases. As a result, the smallest practical HCCI engine was estimated at 0.3 cm<sup>3</sup>

displacement. A 2011 refinement of the model indicated that better manufacturing precision of the piston gap could reduce the minimum displaced volume by a factor of ten, but such manufacturing precision was not yet practical [137]. Menon and Cadou performed a similar analysis where they determined the minimum displaced volume by equating the rate of heat transfer from the combustion chamber to the rate of heat release by the combustion gases (thermal quenching) [6]. The result was 0.3-0.4 cm<sup>3</sup> as the minimum practical displacement [6].

Several studies have investigated incomplete combustion as a loss mechanism in small engines. As engine size decreases, increased rotational speeds help to compensate for increased thermal losses and charge leakage through the piston gap [33]. Faster rotational speeds shorten the residence time in the cylinder. Menon and Cadou [16] claim that upwards of 50%-60% of the fuel energy in glow engines less than 10 cm<sup>3</sup> displacement is lost to incomplete combustion. However, their technique calculated incomplete combustion indirectly as the total energy not accounted for by other pathways (power output, thermal exhaust enthalpy, and heat transfer), did not distinguish between short-circuiting and incomplete combustion, and heat transfer was measured using indirect methods. Attributing 50-60% of the engine's losses to incomplete combustion contradicts Cadou *et al's* earlier study that indicated combustion of hydrocarbons at standard conditions only takes about 1 ms and that that time is shorter at operational engine conditions [4]. Even at 16,000 rpm the residence time is still greater than 1.25 ms, which should allow more than enough time for complete combustion of the fuel. Papac and Dunn-Rankin characterized a similar 4.9 cm<sup>3</sup> OS-30X engine and determined that there was sufficient time for complete combustion of the fuel in the cylinder [112].

In 2000, Heywood and Chon [109] compiled a scaling study of engine data focusing on how engine performance has changed over the last 50 years. While the results focused on design parameters instead of performance and losses, some results are noted here.

- 1) Compression ratios for two-stroke and four-stroke SI engines are tightly grouped near 10 and are absolutely between 8 and 12, indicating the modern state of fuel AKI and knock mitigation technology.
- 2) Total power is best correlated to the displaced volume, and for automotive scale engines the relationship is linear within  $\pm 10\%$ . The power density is strongly dependent on the presence of turbo or super charging.
- 3) If the maximum power is normalized by mean piston speed, it may be correlated to total piston area. This is equivalent to suggesting that torque and piston area have a linear relationship.

At the time of writing, there is no comprehensive and readily available study on how loss pathways scale. Rather, there are a handful of studies showing how loss pathways relate for various sizes and types of engines. Typically, such studies are conducted by performing an energy balance on the engine. Then each energy pathway is determined through measurement, modeling, or as the amount of energy not accounted for by other pathways. This can make comparing different studies challenging. Figure 21 and Table 5 show one possible dissection of the energy pathways in an engine as presented by Heywood [21:674]. Any vertical line through the loss terms is a valid and complete energy accounting, and care is required to avoid double counting terms. For example, friction losses, which can be measured with a motoring dynamometer, are ultimately rejected from the engine as heat, which is a thermal loss split primarily between the coolant and

miscellaneous losses from the crankcase. This could lead to friction losses being double counted if care is not taken during the energy balance.

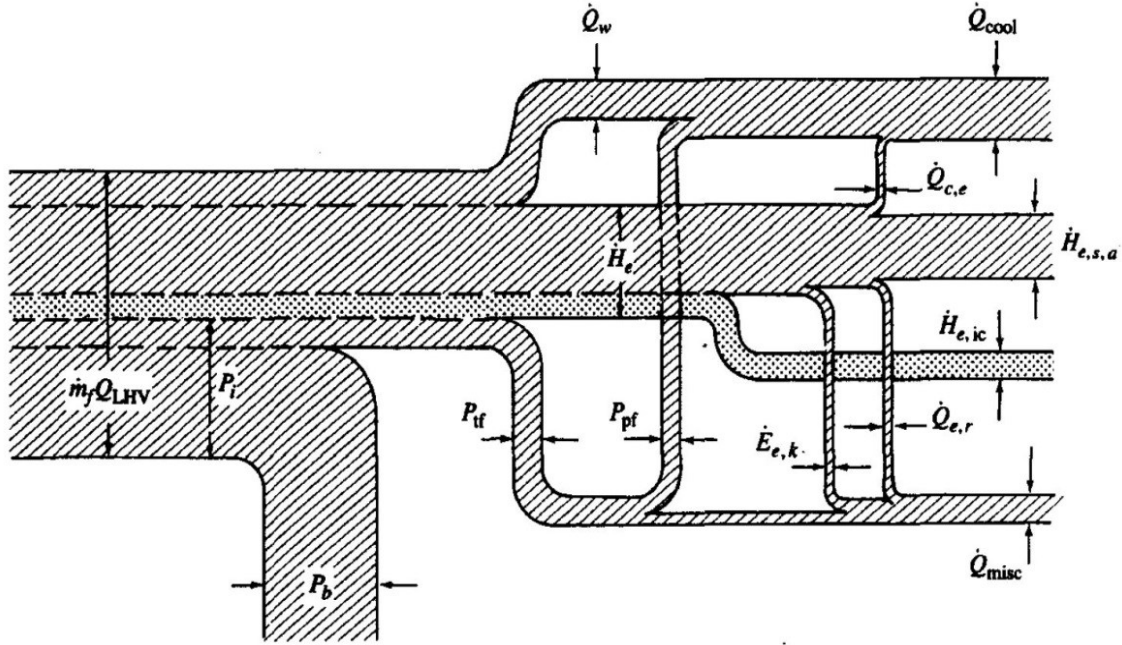


**Figure 21: ICE energy pathways from Heywood [21:674], reprinted with permission from McGraw Hill Education.**

**Table 5: ICE Energy Pathways [21:674].**

$\dot{m}_f$	fuel mass flow	$\dot{Q}_{cool}$	heat rejection rate to coolant
$Q_{LHV}$	fuel lower heating value	$\dot{Q}_{c,e}$	heat transfer rate to coolant from exhaust ports
$P_i$	indicated power	$\dot{H}_{e,s,a}$	exhaust sensible enthalpy flux entering atmosphere
$P_b$	brake power	$\dot{H}_{e,ic}$	exhaust enthalpy flux due to incomplete combustion
$\dot{Q}_w$	heat transfer rate to combustion chamber wall	$\dot{E}_{e,k}$	exhaust kinetic energy flux
$\dot{H}_e$	exhaust enthalpy flux	$\dot{Q}_{e,r}$	heat flux radiated from exhaust
$P_{tf}$	total friction power	$\dot{Q}_{misc}$	remaining energy fluxes and transfers
$P_{pf}$	piston friction power		

Figure 22 shows an energy accounting performed by Oak Ridge National Laboratories [100] on a 1.9 L light duty CI engine. For reference, the engine is an appropriate size for a large car or small truck. The study was performed in conjunction with the Department of Energy to determine the extent to which energy losses could be recovered to improve overall engine efficiency. The study identified that the largest sources of energy loss, especially at part load, were the “friction” losses used to drive engine accessories such as oil pumps, cooling fans, and in the case of a vehicle applications, the alternator, the air conditioner, and so forth. The study identified insulating the engine to lower thermal losses through the head as the best option for improving efficiency. While

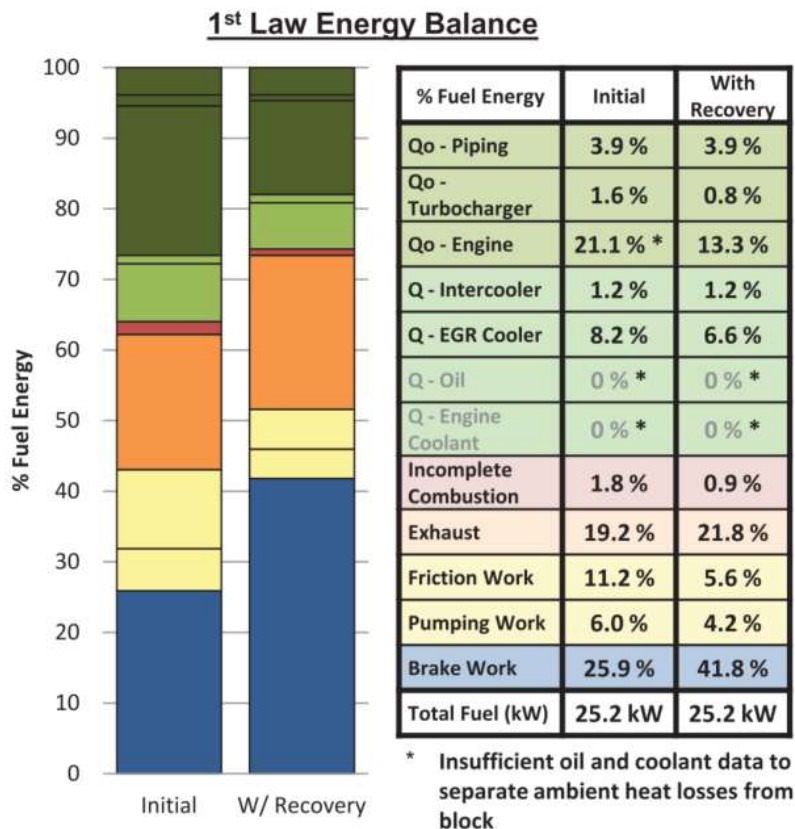


**Figure 22: Energy accounting on a General Motors 1.9 L Diesel engine at road load power and peak efficiency, with and without energy recovery options, reprinted with permission from Edwards *et al.* [100].**

insulating the head would inherently shift a significant portion of heat to the exhaust, the study proposed recovering the energy from the exhaust through the use of a supercharger. The total improvement in efficiency was projected at 15%, increasing overall engine efficiency from 25% to 40%, primarily through waste heat recovery using the supercharger.

Figure 23, reprinted from Menon and Cadou [16], shows a breakdown of the energy pathways for two glow fuel engines (as tested by Menon and Cadou) and generic automotive engines as compiled by Heywood [21:674]. The chart indicates that for small

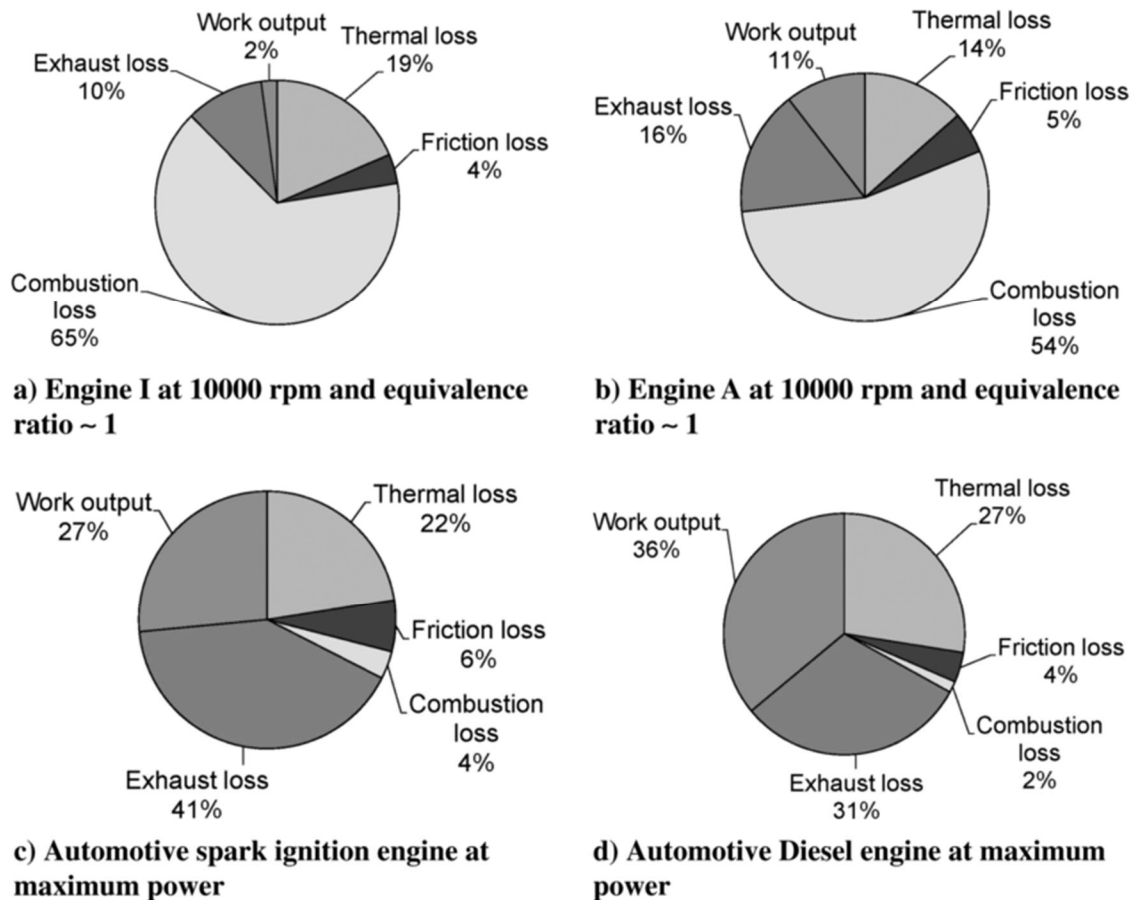


**Figure 23: Energy pathway breakdown for a) a 0.16 cm<sup>3</sup> Cox 010 glow fuel engine, b) a 7.54 cm<sup>3</sup> OS 46 FX engine, c) an automotive SI engine, and d) and automotive CI engine. The charts are reprinted with permission from Menon and Cadou [16] with data from Heywood for c) and d) [21:674].**



engines, combustion losses are the primary loss pathways, and for the large engines thermal losses and sensible enthalpy in the exhaust dominate. Note that short-circuiting (minimal in the four-stroke engines considered by Heywood) and incomplete combustion are considered part of the combustion loss category in Heywood's analysis. In Menon and Cadou's study, incomplete combustion losses were determined through indirect measurements as losses not accounted for by other mechanisms, and the study did not distinguish between incomplete combustion of the trapped charge and short-circuiting. Heat transfer losses were measured indirectly using Taylor and Toong's correlation [138] with coefficients that had not been validated for engines less than 100 cm<sup>3</sup> displacement. Thus, further research is warranted to measure each term in the energy balance, to verify those terms sum to 100% and that a key pathway was not omitted, misestimated, or incorrectly measured, and to verify that the correlations used to close the energy balance in previous studies were valid for this engine size and type.

The most relevant example of an energy accounting on 10-100 cm<sup>3</sup> displacement engines was performed by Rowton *et al.* [5], who attempted a preliminary energy accounting for the engines considered in this effort. Figure 24, from Rowton [135:116], shows the results of the analysis. Several issues with the analysis make it inconclusive concerning energy pathways and loss mechanisms and their scaling in 10-100 cm<sup>3</sup> displacement engines. First, both the exhaust chemical enthalpy and sensible (thermal) enthalpy were estimated using rough, simplistic correlations. Second, up to 33% of the energy was unaccounted for at some conditions. Third, friction that was dissipated as heat in the engine was double counted due to the technique used to measure the heat transfer losses. Finally, poor control of the equivalence ratio made it difficult to compare

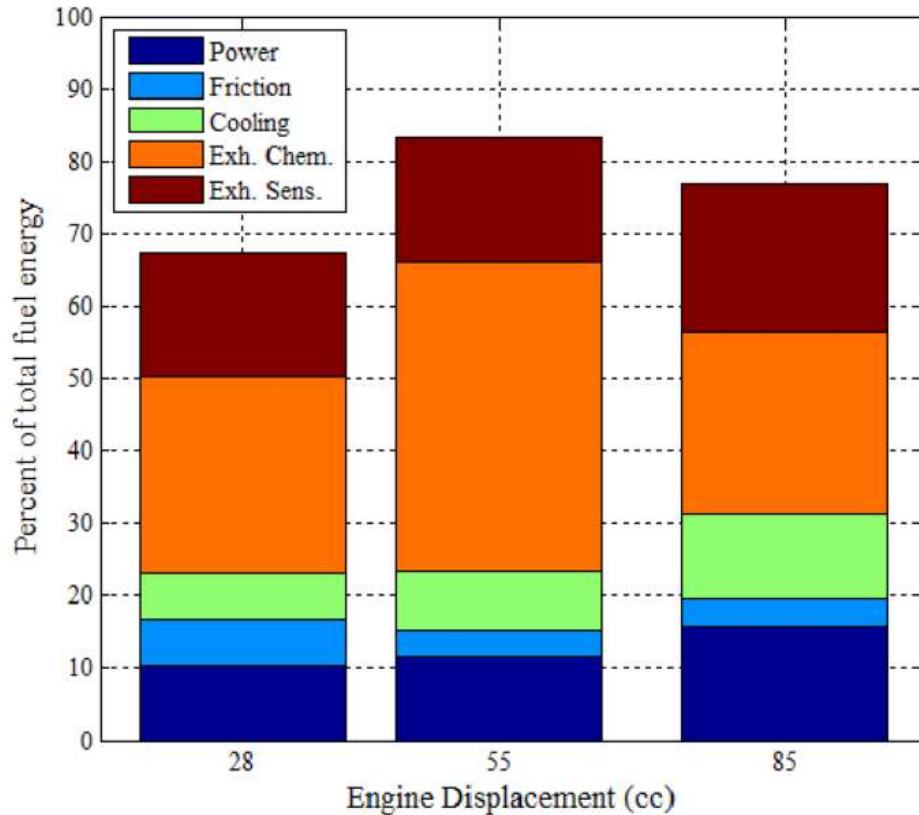


**Figure 24: Energy pathways in 3W Modellmotoren engines at wide open throttle and 6.5 m/s mean piston speed as determined by Rowton [135:116].**

performance differences without mixture as a confounding variable. Rowton [135:128-130] indicates in his recommendations for future work that a more complete accounting of the loss pathways should be performed, which is part of Objective 1 for this effort.

#### **4.3. Review of Objective 1: Engine Loss Scaling Study**

Objective 1 aimed to quantify five loss pathways: heat rejection from the cylinder, friction, short-circuiting of fresh charge, sensible enthalpy in the exhaust gases, and incomplete combustion, and to determine how those loss pathways scale with engine size. As discussed in Section 4.1, the increase in losses relative to energy released during combustion drives the decrease in fuel conversion efficiency observed in small and micro engines. As Section 4.2 explained, the relative contributions of these mechanisms change

between automotive scale engines and micro glow engines. To understand and manage these losses and their driving mechanisms as well as to provide improved models applicable to small engines, the losses must first be quantified, which was the goal of Objective 1.

## **5. Models and Measurements**

Models for losses for ICEs less than 100 cm<sup>3</sup> displacement are essentially non-existent in literature. In many cases [2, 11, 16, 108, 135] models for larger engines are simply applied without further validation. Yet, loss models are crucial for providing boundary conditions for numerical methods based engine models and for estimating engine performance for design calculations. This section provides background on available models and measurement methods for losses in support of Objective 2, which aimed to validate or modify existing models for heat transfer and friction losses for small engines using data available from Objective 1. Evaluating scavenging and gas exchange models for 10-100 cm<sup>3</sup> displacement engines was not included in Objective 2 as scavenging is more sensitive to port design than engine size. An investigation of the scaling of scavenging would have required a parametric investigation of port configuration for which the engines selected here were not suitable. However, an understanding of short-circuiting losses and how to measure them is necessary for Objective 1, which is why a discussion of relevant models for gas exchange and scavenging is included. Section 5.1 discusses heat transfer, Section 5.2 discusses friction, and Section 5.3 discusses scavenging.

### **5.1. Heat Transfer**

The thermal losses from the cylinder of an ICE directly impact engine efficiency, material requirements, and in the case of an application, cooling the integrated system.

However, the cyclic nature of the ICE makes modelling the heat transfer from the engine difficult. Most literature on engine heat losses focuses on either large engines, mainly for the purpose of cooling, or micro engines where losses limit the minimum possible size of the engine. A review of the literature yielded no heat transfer models that had been validated for engines between 10 cm<sup>3</sup> and 100 cm<sup>3</sup> displacement. The lack of literature for small engines should not be extrapolated to large engines, where papers detailing heat transfer models abound. This section reviews relevant research on heat transfer models to provide a basis for selecting, modifying, and validating a model useful for small ICEs. It is split into three parts. The first (Section 5.1.1) reviews models, and the second and third sections (Sections 5.1.2 and 5.1.3) discuss heat transfer and in-cylinder gas temperature measurement techniques, respectively.

#### **5.1.1. Heat Transfer Models**

Heat transfer is one of the primary loss pathways in ICEs, and the number of models proposed for ICEs in the literature is extensive. Many engine textbooks such as Heywood [22:668-703], Pulkrabeck [25:312-338], and Taylor [9:266-311] each include an entire chapter devoted to heat transfer losses, but only discuss one or two models. However, it is not difficult to find overview articles on the subject [19, 139, 140] that discuss about a dozen models each. Most are derivatives of 3 or 4 original models. This section highlights the key original models and the important derivatives thereof.

From an organization standpoint, models can be classified in a variety of ways. Franco and Martorano [140] provide one set of classifications. They group models into three categories: those that attempt to find the heat transfer coefficient using dimensionless parameters, those that solve the heat transfer network using Fourier analysis to define

boundary conditions, and those that use conservation of energy on the cylinder mass to determine thermal losses. Finol and Robinson [139] propose a different categorization. They also suggest three types of models, but those types are models that: solve for spatially and temporally averaged heat flux, solve for spatially averaged instantaneous heat flux, and solve instantaneous heat flux at specific locations in the engine. Finol and Robinson's approach better aligns with measurement techniques, and their categorization will be the organizational structure of this section. It should be noted that any of the approaches delineated by Franco and Martorano [140] could be categorized into the categories delineated by Finol and Robinson [139].

For overall heat losses from the engine, a spatially and temporally averaged model is certainly sufficient. However, the other two types of models can simply be averaged over their respective spatial and temporal domains to give an overall result. A desire to develop realistic boundary conditions for computational fluid dynamics has driven significant research in the spatially averaged, instantaneous models and to an extent the instantaneous spatially resolved models. Since all models can be adapted for the type of correlation or model desired as part of Objective 2, models of all three type will be presented. The remainder of this section is split into four parts. Section 5.1.1.1 provides background on the heat transfer network considered in many ICE models and the dimensionless groupings applicable to ICEs. Sections 5.1.1.2, 5.1.1.3, and 5.1.1.4 discuss temporally and spatially averaged models, instantaneous, spatially averaged models, and instantaneous, spatially resolved models, respectively.

#### 5.1.1.1. Heat Transfer Networks, Non-dimensional Groupings, & Nusselt Model

The loss of heat from the combustion chamber in an ICE occurs in three steps. First, heat is transferred by convection (and in CI engines, radiation) between the gases in the cylinder and the cylinder walls (to include the piston). Second, heat is conducted through the cylinder walls. Third, heat is transferred by convection between the exterior of the engine and the coolant and may be transferred by radiation to the surroundings. In the case of SI engines, the in-cylinder radiation term is often considered negligible since unlike DI CI engines, SI engines have a low tendency to produce soot, the primary radiative component in combustion gases [21:683]. Additionally, radiation to the coolant and surroundings is often cast in terms of a convection coefficient. The result is that the heat loss network for an ICE cylinder can be reduced to a series of three resistances using the electrical circuit analogy for heat transfer. The most commonly used network is shown in Figure 25 adapted from Franco and Martorano [140], and many analyses assume that the network satisfies instantaneous conservation of energy, such that heat transfer measured in one segment may be applied to another segment. If each of the parameters was known, then heat flux ( $\frac{\dot{Q}_{cyl,loss}}{A}$ ) could be calculated as shown in Equation (33).

$$\frac{\dot{Q}_{cyl,loss}}{A} = \frac{T_{g,cyl} - T_c}{\frac{1}{h_g} + \frac{t_{cyl}}{k} + \frac{1}{h_c}} \quad (33)$$

The coolant temperature ( $T_{cool}$ ) can be easily measured, cylinder wall thickness ( $t_{cyl}$ ) is a design variable, and the thermal conductivity of the cylinder ( $k$ ) is a material property. The temperature of the in-cylinder gas ( $T_{g,cyl}$ ) and the convection coefficients inside ( $h_g$ ) and outside ( $h_c$ ) the cylinder are more elusive. The exterior convection coefficient is

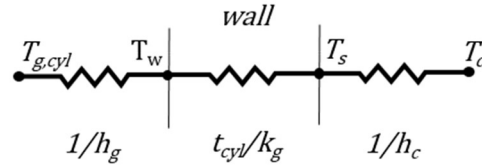


**Figure 25: Heat transfer network for an ICE cylinder with the cylinder gas on the left and the coolant on the right, adapted from Franco and Martorano [140].**

further complicated since it is typically used to capture the fin efficiency, which has an especially significant impact on air-cooled engines. The most common approach has been to correlate some combination of the heat transfer resistances, cast as a convection coefficient, to other operational parameters in the engine. Non-dimensional correlations are the most easily adapted to engines other than those for which they were developed, since their empirical coefficients are also non-dimensional. Annand's dimensional analysis of an ICE remains the most commonly considered set of non-dimensional terms, which are listed in Table 6, adapted from Annand [17].

Selecting the correct terms is only part of the battle. Once the terms are selected, choosing appropriate characteristic values is also a challenge. For example, either engine bore or stroke could be selected for the characteristic length. Another issue (in the case of instantaneous approaches) is whether to evaluate the properties instantaneously or to use a cycle average. Values such as cylinder pressure can be measured instantaneously. Some values, however, do not lend themselves to an instantaneous approach. Piston speed is often used as a characteristic velocity [69], but at TDC piston speed is zero, which in many correlations would erroneously imply that at TDC heat transfer is zero. Thus many correlations mix instantaneous and cycle averaged parameters. All of these considerations make developing a plausible model for an ICE difficult.

**Table 6: Non-dimensional Parameters for ICEs, Adapted from Annand [17]**

Name	Formula	Description
Nusselt number	$Nu = \frac{hD}{k_g}$	Non-dimensional form of the convection coefficient ( $h$ ) using the thermal conductivity of the gas ( $k_g$ ) and a characteristic length ( $D$ ).
Reynolds number	$Re = \frac{\rho VD}{\mu}$	Describes the relative importance of inertial and viscous effects in the flow, using a characteristic velocity ( $V$ ) and viscosity ( $\mu$ ).
Prandtl number	$Pr = \frac{C_p \mu}{k}$	The Prandtl number describes the relative importance of heat transfer due to convection and conduction using the heat capacity of the gas ( $C_p$ ).
“Mach” number	$\sqrt{\frac{V^2}{C_p T}}$	This coefficient has the form of the Mach number (a non-dimensional velocity referenced to fluid temperature ( $T$ )) (Annand used $C_p T/V^2$ ).
	$\frac{V}{ND}$	A residence time of sorts. Describes a characteristic velocity non-dimensionalized by engine speed ( $N$ ) and a characteristic length.
	$\frac{\dot{Q}_{comb}}{\rho C_p NT}$	Non-dimensional version of the heat release rate during combustion ( $\dot{Q}_{comb}$ ).
	$Y^*$	Non-dimensional length scale representing engine geometry.
	$V^*$	Non-dimensional velocity scale representing flow characteristics.

Nusselt was the first to attempt the problem in 1923 [18]. Nusselt modelled the chamber of an ICE as a constant volume sphere, using different coatings on the interior to separate the effects of radiation ( $h_r$ ) and convection ( $h_c$ ). The result was the correlation for the gas side heat transfer coefficient ( $h_g$ ) shown in Equations (34) to (36) [66], where ‘( $\theta$ )’ indicates that the variable is instantaneous (as is the case for the remainder of the section). For the remainder of the section, equations are presented in consistent SI base



units (Pa, K, m, s, kg and so forth) unless otherwise indicated. The most frequent deviation is pressure, which is in bar in many correlations.

$$h_g = h_r + h_c \quad (34)$$

$$h_c = C_1 \cdot (1 + 1.25\bar{S}_p) \left( p_{cyl}(\theta)^2 T_{g,cyl}(\theta) \right)^{1/3} [=] \frac{kW}{m^2K} \quad (35)$$

$$h_r = \frac{4.21 \times 10^{-4}}{\left( \frac{1}{\varepsilon_g} + \frac{1}{\varepsilon_w} - 1 \right)} \frac{\left( \frac{T_{g,cyl}(\theta)}{100} \right)^4 - \left( \frac{T_w}{100} \right)^4}{(T_{g,cyl}(\theta) - T_w)} [=] \frac{kW}{m^2K} \quad (36)$$

Using Equation (36), radiation effects are cast in terms of a convection coefficient to make them easier to combine into an overall convection coefficient. To simplify the problem, Nusselt only analyzed the heat transfer occurring from the cylinder gas to the cylinder wall, and thus he used the wall temperature ( $T_w$ ) and gas ( $\varepsilon_g$ ) and wall ( $\varepsilon_w$ ) emissivities.

There are many shortcomings of Nusselt's model. Most importantly, it was developed for a constant volume sphere, not an ICE geometry. The model was not developed using non-dimensional groupings causing the empirical constants to have dimensions that are difficult to scale compared to models with dimensionless constants. Additionally, the constant  $C_1$  must be empirically fit for each engine. When applied to an engine, the model tends to underestimate the peak heat flux and have late peak phasing. As indicated by the instantaneous terms in Equations (35) and (36), Nusselt's approach is an instantaneous, spatially averaged method. While inadequate for application to practical engines, Nusselt's work served as the basis for virtually all of the models developed thereafter; a selection of those models is presented in the next three sections.

#### 5.1.1.2. Temporally and Spatially Averaged Model: Taylor and Toong

In 1957, Taylor and Toong [138] published a paper detailing a temporally and spatially averaged model developed using dimensional analysis. The result was a correlation for the overall heat transfer coefficient for the entire heat transfer network ( $h_o$ ) as shown in Figure 25. Reproduced in Equations (37) to (40), the model uses bore ( $B$ ) as the characteristic length and the mass flow rate of the gas ( $\dot{m}_g$ ) divided by the piston face area ( $A_p$ ) as a combination of the gas density and characteristic velocity for the Reynolds number. Equation (37) shows how the overall heat transfer coefficient relates to the heat transfer network as shown in Figure 25. In Equation (38) the Nusselt number is related to the Reynolds number using dimensionless coefficients. Then the Nusselt number is related back to the heat transfer coefficient using characteristic geometry and gas properties. Equations (39) and (40) show the relationship between heat transfer from the cylinder and the Nusselt number as well as the calculation of the Reynolds number, respectively.

$$h_o = \frac{\dot{Q}_{cyl,loss}}{A_p(T_{g,cyl} - T_c)} = \left( \frac{1}{h_g} + \frac{t_{cyl}}{k} + \frac{1}{h_c} \right)^{-1} \quad (37)$$

$$Nu = C_1 Re^{C_2} = \frac{h_o B}{k_g} \quad (38)$$
$$C_1 = 10.6; C_2 = 0.75$$

$$Nu = \frac{\dot{Q}_{cyl,loss} B}{k_g A_p (T_{g,cyl} - T_c)} \quad (39)$$

$$Re = \frac{\dot{m}_g B}{\mu_g A_p} \quad (40)$$

Taylor and Toong [138] used data, shown in Figure 26, from water and air-cooled CI and water cooled SI engines to determine coefficients for Equation (38). The smallest engine

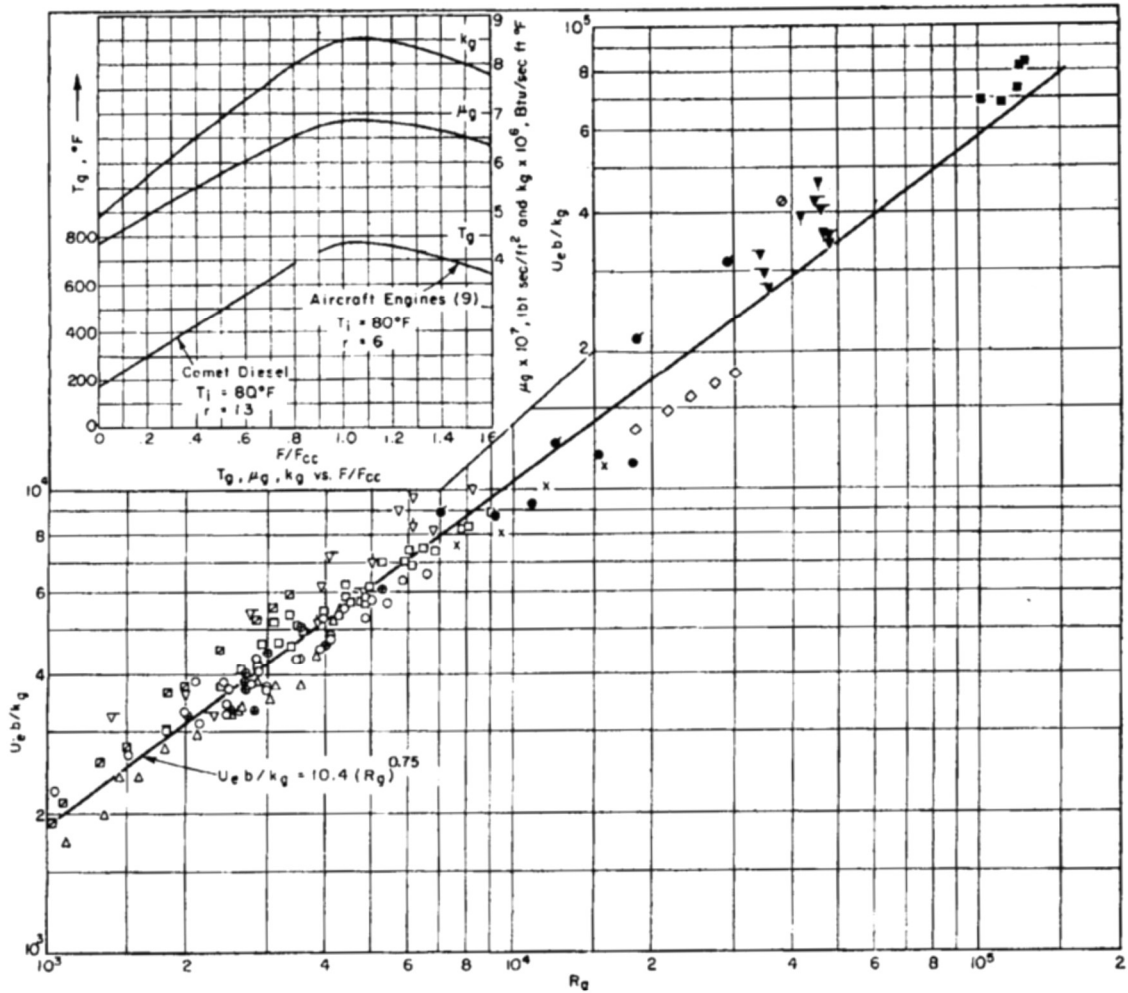


**Figure 26: Temporally and spatially averaged Reynolds and Nusselt number correlation, reprinted from Taylor and Toong [138] with permission from ASME.**

in the study was the 241 cm<sup>3</sup> displacement M.I.T. engine; the largest engine was the 3.3 L displacement M.I.T. engine.

Annand [17] reinterpreted Taylor's data, separating out the engines by type. His fit is shown in Figure 27. Annand found that  $C_2 = 0.70$  when the engines were divided by type. As written, Taylor and Toong's form suggests that the intensity of the convection and thus its magnitude is best described by the Reynolds number, an approach that was adapted from literature on turbulent flow over a flat plate. The relationship between flow speed

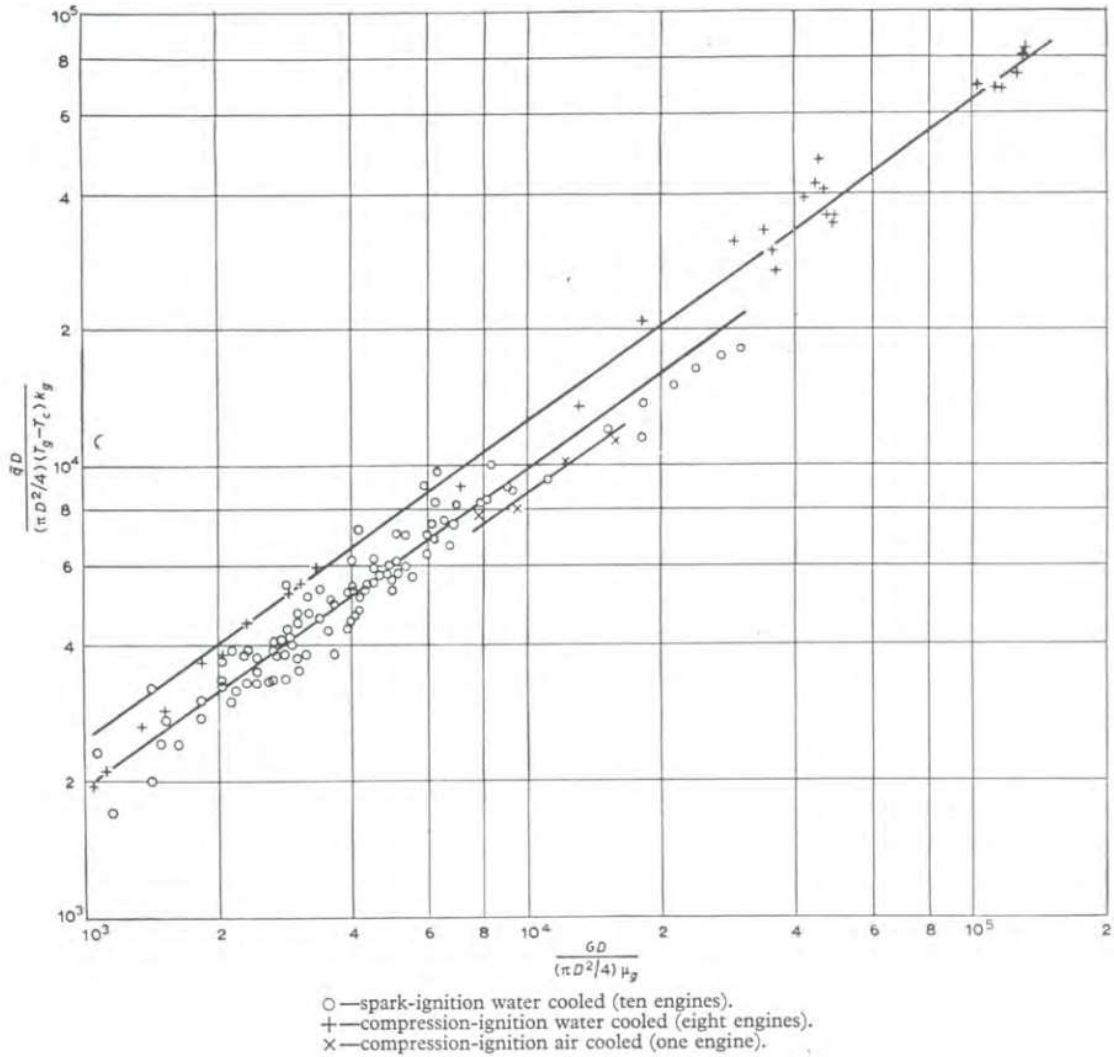


**Figure 27: Taylor's data [138] as reinterpreted by Annand [17], reprinted with permission from SAGE Publications.**

and convection is then described by the exponent ( $C_2$ ). Annand [17] determined that  $C_1$  was essentially a function of engine type, with values ranging from 7.7 to 10.6 for water cooled CI engines and up to 15.5 for water cooled SI engines. Taylor's model was not tested for engines smaller than 100 cm<sup>3</sup> displacement. Furthermore, the model does not consider non-dimensional terms outside of the Reynolds number and only captures scaling effects (engine size) through  $C_1$ . Finol and Robinson [139] also point out that Taylor and

Toong's correlation needs to be updated for modern engine technology. And, while Taylor and Toong's model may be sufficient for overall design calculations, it is not sufficient as a heat flux relation for calculating mass fraction burned or for use in CFD.

#### **5.1.1.3. Instantaneous, Spatially Averaged Models**

Instantaneous spatially averaged models attempt to predict the heat flux from the engine at each point in the cycle, but are averaged over the entire spatial domain of interest. They are appealing from a CFD standpoint as they provide a spatially uniform, temporally resolved boundary condition. Instantaneous, spatially averaged models can also be generalized to overall heat transfer from the engine by integrating over the cycle. Nusselt's model, presented earlier, is the earliest example of an instantaneous, spatially averaged model. This section will present several other important models that provide insight into what parameters and characteristic properties have proven effective in modelling engine heat transfer. In almost all of these cases, the model is actually a correlation to determine the heat transfer coefficient between the in-cylinder gases and the cylinder wall, under the assumption that heat transfer to the cylinder wall is then rejected in an instantaneous fashion to the coolant, and that the engine head itself is at a pseudo steady state condition.

##### **5.1.1.3.1. Eichelberg Model (1939)**

Eichelberg developed the first instantaneous spatially averaged model specific to ICEs for large scale two-stroke and four-stroke engines. The correlation is shown in Equation (41) [17]. It is suggested by Taylor and Toong [138] that  $C_1 \approx 2.43$ .

$$h_g = C_1 \cdot (\bar{S}_p)^{1/3} \cdot \left( (p_{cyl}(\theta)[bar]) \cdot T_{g,cyl}(\theta) \right)^{1/2} \quad (41)$$

According to Annand [17], Eichelberg was also the first to directly measure the heat flux through the use of thermocouples located on the engine head at locations where heat

transfer was assumed to be one dimensional. Eichelberg lumped radiative and convective effects into a single coefficient [139]. Compared to later models such as those of Woschni [141] and Annand [17] (presented in the following sections) that consider those terms separately, lumping radiation and convection together increases the exponent on temperature in Eichelberg's model. This artificial increase in the temperature exponent makes the model ill-equipped for SI engines, which compared to CI engines have low radiative transfer between the combustion gases and the cylinder walls. Compression ignition engines are assumed to have significant radiative heat transfer due to the formation of soot when fuel droplets are exposed to combustion temperatures. SI engines tend to have fully vaporized fuel prior to combustion, little soot formation, and short residence times at temperatures where radiative heat transfer is appreciable. Other shortcomings of the model include dimensional inconsistency and the assumption of free convection for heat transfer as opposed to forced convection, which is more appropriate for in-cylinder conditions. According to Annand [17], the model provides a reasonable fit for low speed CI engines (circa 1963), but diverges from test data as test conditions diverge from those used to develop the fit. As Stone and Ball [26] point out, to account for forced convection (a better choice inside the cylinder) the Nusselt number should be correlated to the Prandtl and Reynolds numbers, similar to Taylor and Toong's [138] approach. Thus, from a modern standpoint, this model is typically viewed as theoretically unsound [26].

#### ***5.1.1.3.2. Annand Model (1963)***

In addition to the issues discussed above with Eichelberg's model, Annand [17] noticed another issue common to other (now obsolete) models of the time: they failed to capture the phase lag between the temperature increase in the combustion gases and heat transfer

through the cylinder. Annand [17], like Taylor and Toong [138] considered applicable dimensional groupings and separated the convective and radiative terms. His selection of the Reynolds number exponent was based on his own analysis of Taylor and Toong's data [138]. The result was a correlation for the heat transfer coefficient for steady state turbulent combustion that is valid during compression, combustion, and expansion, but not during gas exchange. The model is shown in Equations (42) and (43), where the first term in Equation (42) handles convection and the second term handles radiation.

$$h_g = C_1 \cdot \frac{k}{B} \cdot Re^{0.7} + C_2 \cdot \frac{(T_{g,cyl}(\theta) - T_w)^4}{(T_{g,cyl}(\theta) - T_w)} [=] \frac{kW}{m^2K} \quad (42)$$

$$C_1 = 0.35 - 0.8$$

$$CI: C_2 = 4.3 \times 10^{-12} \frac{W}{m^2K^4}; \quad SI: C_2 = 5.64 \times 10^{-1} \frac{W}{m^2K^4}$$

$$Re = \frac{\rho \cdot \bar{S}_p \cdot B}{\mu} \quad (43)$$

Annand spent a great deal of time examining different values for the gas temperature and determined that the best fit was achieved by using the charge mass, pressure, and cylinder volume to determine the average gas temperature in the cylinder in lieu of direct measurement. He also estimated the transport properties of the combustion gases as nitrogen at that temperature. Similar to the model of Taylor and Toong,  $C_1$  is the scaling factor for engine geometry. Then,  $C_2$  controls the contribution from radiation. Watson and Janota [142:537] point out that  $C_2$  may be expressed as a fraction of the Stefan-Boltzmann ( $\sigma$ ) constant,  $0.57\sigma$  for SI engines and  $0.075\sigma$  for CI engines. Annand's fit is based on two engines: a two-stroke engine and four-stroke engine, both compression-ignition. The model fits data from Eichelberg better than Eichelberg's original model. The radiation term is neglected during intake, compression, and exhaust, when radiation effects are

negligible. Shortcomings of Annand's model include its inability to handle gas exchange, its under prediction of heat flux (by up to 40%), and its introduction of a phase lag (by up to 10° CA) [66].

#### 5.1.1.3.3. *Woschni Model (1967)*

Woschni [141] developed a model to capture the swirl and tumble introduced to the cylinder gases during scavenging, and the model is shown in Equation (44), where the subscript '*ref*' denotes values at the start of combustion [143].

$$h = C_3 B^{-0.2} (p_{cyl}(\theta) [\text{bar}])^{0.8} T_{g,cyl}(\theta)^{-0.53} \left[ C_1 S_p(\theta) + C_2 \frac{V_{cyl} T_{ref}}{p_{ref} V_{ref}} (p_{cyl}(\theta) - p_{mot}(\theta)) \right]$$

$$\begin{aligned} \text{Scavenging: } C_1 &= 6.18, C_2 = 0; \text{ Compression: } C_1 = 2.38, C_2 = 0 \\ \text{Combustion, Expansion: } C_1 &= 2.28, C_2 = 3.24 \times 10^{-3} \\ C_3 &= 110 \end{aligned} \quad (44)$$

Woschni's model captures gas motion in two terms. The term with the instantaneous piston speed ( $S_p(\theta)$ ) accounts for gas motion induced by the motion of the piston. The other term captures gas motion introduced by tumble and swirl in the intake. Note that the pressure from a motored pressure trace ( $p_{mot}$ ) is required in this instance. Pressure is measured in-cylinder and the temperature is determined from ideal gas law using the pressure [144]. The constant  $C_2$  has also been adapted for engines where the swirl/tumble are introduced intentionally by the design of the intake runner and inlet. The adapted values are given in in Equation (45) [139].

$$\begin{aligned} \text{Gas exchange: } C_2 &= 6.18 + 0.417 \frac{V_g}{S_p} \\ \text{Not Gas Exchange: } C_2 &= 2.28 + 0.308 \frac{V_g}{S_p} \\ \text{Scavenging: } V_g &= \frac{\pi B N_{an}}{60} \end{aligned} \quad (45)$$



In 1979 Sihling and Woschni applied this form to model a supercharged, water-cooled, four-stroke, single cylinder CI engine [143]. The performance of the model was poor during gas exchange and over predicted the peak heat transfer from the cylinder. Despite the adaptations, the model did not capture the turbulence and swirl/tumble during the gas exchange process [139]. The experiment also showed substantial variation in the local heat flux and heat transfer coefficient, which was missed by the spatially averaged model [139]. The model was fit to large CI engines, which operate significantly differently than the small SI engines considered here.

#### 5.1.1.3.4. *Annand and Ma (1970)*

In 1970 Annand and Ma [145] attempted to adapt Annand's [17] model to account for the spatial and temporal variation in heat flux observed while testing a naturally aspirated, DI, air-cooled, single cylinder CI engine. The first adjustment was the addition of a term proportional to the time rate of change of temperature ( $\frac{dT_g}{dt}$ ) to account for phase lag. The correlation is shown in Equation (46). In the correlation the mean piston speed is replaced with the energy mean velocity of the gas to calculate the Reynolds number. The energy mean velocity is the difference between the kinetic energy of the inflowing and outflowing gas, averaged over the mass of the gas. While the fit is good for the gas exchange portion of the cycle, it performs poorly during combustion. As in the previous correlations, Annand and Ma [145] chose to measure pressure in-cylinder and determine temperature from the ideal gas law [144].

$$h_g = \frac{k}{B} \cdot Re^{0.7} \left( C_1 - \frac{C_2}{\frac{2\pi N}{60}} \frac{dT_{g,cyl}(\theta)}{dt} \right) + C_3 \sigma \cdot \frac{(T_{g,cyl}(\theta) - T_w)^4}{(T_{g,cyl}(\theta) - T_w)} [=] \frac{kW}{m^2K} \quad (46)$$

$$C_1 = 0.12; C_2 = 0.20; C_3 = 1.50$$

#### 5.1.1.3.5. *Sitkei and Ramanaiah Model (1972)*

Sitkei and Ramanaiah's 1972 [146] model is a direct adaptation of Annand's model [17]. It was developed for four-stroke indirect injection CI engines [66]. The model selects the equivalent diameter ( $\frac{4V_{cyl}(\theta)}{A_p}$ ), which varies with crank angle, as a more appropriate characteristic length than the engine bore. The value of  $C_2$  depends on the turbulence level associated with the type of combustion chamber, as shown alongside the model in Equation (47).

$$h_g = C_1 \cdot (1 + C_2) \frac{(p_{cyl}(\theta)[bar])^{0.7} \cdot \bar{S}_p^{0.7}}{T_{g,cyl}(\theta)^{0.2} \left( \frac{4V_{cyl}(\theta)}{A_p} \right)^{0.3}} [=] \frac{kW}{m^2K}$$

$$C_1 = 0.046$$

$$\text{Direct combustion: } C_2 = 0 - 0.03;$$

$$\text{Piston chamber: } C_2 = 0.05 - 0.1;$$

$$\text{Swirl Combustion Chamber: } C_2 = 0.15 - 0.25;$$

$$\text{Precombustion chamber: } C_2 = 0.25 - 0.35$$
(47)

According to Wu and Chen [66], the Sitkei and Ramanaiah model is closer to the experimental heat flux curve measured on their engine than all models of this type discussed previously. Nevertheless, it introduces a phase lag and under predicts the peak heat flux. Still Sitkei and Ramanaiah's [146] work indicates that radiative heat losses due to soot in a CI engine can account for 20%-30% of heat transferred to the cylinder wall, making the consideration of a radiation term, at least for CI engines, critical.

#### 5.1.1.3.6. *Hohenberg Model (1979)*

In 1979, Hohenberg [147] tried to correct Woschni's [141] model, which under predicts the heat flux during gas exchange and over predicts heat flux during combustion. Hohenberg's [147] model improves those aspects of Woschni's model. The cylinder

volume term functions as a characteristic length. The model as presented by Finol and Robinson is shown in Equation (48).

$$h_g = C_1 \cdot V_{cyl}(\theta)^{-0.06} \cdot (p_{cyl}(\theta)[bar])^{0.8} \cdot T_{g,cyl}(\theta)^{-0.4} \cdot (\bar{S}_p + C_2)^{0.8} \quad (48)$$

$$C_1 = 120; C_2 = 1.4$$

Like Sitkei and Ramanaiah's [17] work, Hohenberg's [147] most important contribution was probably not the model. Rather, Hohenberg advanced the science of making temperature measurements for heat flux calculations by comparing insulated wall thermocouples with cylindrical heat flux gauges. His work compared heat fluxes measured by the two methods to heat fluxes in a motored engine cycle, which may be calculated with just the pressure trace in the absence of combustion. While both methods proved too locally sensitive to match the spatial average, it was the first time a cylindrical heat flux gauge (described in Section 5.1.2) was successfully insulated and sealed for use in a fired engine test [147].

#### **5.1.1.3.7. Han *et al.* Model (1997)**

The Han *et al.* [144] model is purely empirical and was developed for large, four-stroke SI engines [139]. The model predicts the instantaneous heat transfer coefficient using non-dimensional groupings. Like Woschni's model, Han tried to account for changes in gas velocity during combustion, where it was assumed the velocity increased as a result of heat release, even as instantaneous piston speed went to zero at TDC. The model is non-dimensional, and the terms in Equation (49) may be regrouped into a relation between the Nusselt number and the Reynolds and Prandtl numbers, where the exponent on the Reynolds number is 0.75 and consistent with the results of Taylor and Toong [138]. The model, shown in Equations (49) and (50) handles the non-combustion portion of the cycle

poorly (overestimating during compression and underestimating during expansion), and shows an increasing phase lag with decreasing engine speed [139].

$$h_g = C_1 p_{cyl}(\theta)^{0.75} V_g(\theta)^{0.75} B^{-0.25} T_{g,cyl}(\theta)^{-0.465} \quad (49)$$

$$C_1 = 687$$

$$V_g = C_2 S_p(\theta) + C_3 \left( \gamma \frac{p_{cyl}(\theta) dV}{d\theta} + \frac{V dp_{cyl}(\theta)}{d\theta} \right) \quad (50)$$

$$C_2 = 0.494; C_3 = 0.73; \gamma = 1.35$$

Reverting to methods where temperature is calculated and not measured directly, cylinder temperature was determined using the ideal gas equation and in-cylinder pressure measurements. Bore was used as the characteristic length since Han *et al.* [144] concluded literature provided no other well-studied options. Han *et al.* [144] also pointed out that the Reynolds number exponent is expected to be 0.7 to 0.8 for forced convection and turbulent flow on a flat plate and suggest that the smaller the engine, the less reasonable this assumption becomes. This could indicate that Taylor and Toong's [138] fit, upon which so many of these models based the Nusselt-Reynolds relation, will not work for small engines without some amount of adjustment.

#### 5.1.1.3.8. *Chang et al. Model (2004)*

Chang *et al.* [35] modified Woschni's model for use on HCCI engines. The spatially averaged nature of Woschni's model proved well suited for combustion in a 0.55 L displacement, single cylinder HCCI engine. The simultaneous autoignition of the entire charge in HCCI combustion significantly reduces the spatial variations compared to those observed in the cylinders of SI and CI engines. Chang *et al.* also noticed that the swirl and tumble term in the Woschni model [141] introduced substantial error into their fit, over predicting peak heat flux by almost 40% in some cases. Chang *et al.* [35] removed the

term and reduced the maximum heat flux error between the model and their spatially averaged measurement to 4.2% over the load range. They then replaced the engine bore with the instantaneous cylinder height ( $L(\theta)$ ), constrained to less than the bore. Further tweaks to exponents resulted in the model shown in Equation (51) [35]. Like the Woschni [141] model, the model of Chang *et al.* is not applicable during gas exchange.

$$h_g = C_3 L(\theta)^{-0.2} (p_{cyl}(\theta) [\text{bar}])^{0.8} T_{g,cyl}(\theta)^{-0.73} \left( C_1 S_p + \frac{C_2}{6} \frac{V_s T_{ref}}{p_{ref} V_{ref}} (p_{cyl}(\theta) - p_{mot}(\theta)) \right)^{0.80} \quad (51)$$

Scavenging:  $C_1 = 6.18, C_2 = 0$ ; Compression:  $C_1 = 2.38, C_2 = 0$   
Combustion, Expansion:  $C_1 = 2.28, C_2 = 3.24 \times 10^{-3}$   
 $C_3 = 3.4$

Chang *et al.* [35] measured heat flux using thermocouple pairs on the inside and outside of the cylinder, installed as a cylindrical heat flux probe. While the temperature outside of the cylinder ( $T_s$ ) (in the coolant) was essentially constant at steady state operation, the interior wall temperature ( $T_w$ ) fluctuated cyclically. Chang *et al.* fitted the interior temperature profile using a Fourier analysis, allowing them to solve for the heat flux using the unsteady heat conduction equation through the cylinder wall and finally overcoming the phase lag observed by Annand [17]. The Fourier form for the interior wall temperature is shown in Equation (52) and the unsteady conduction equation used to solve for heat flux is shown in Equation (53) [35].

$$T_w(t) = \bar{T}_w + \sum [A_n \sin n\omega t + B_n \cos n\omega t] \quad (52)$$

$$\dot{Q}_{cyl,loss} = \frac{k}{t_{cyl}} (\bar{T}_w - T_s) + k \sum_{n=1}^N \varphi_n [(A_n + B_n) \cos n\omega t - (A_n - B_n) \sin n\omega t] \quad (53)$$

#### 5.1.1.3.9. *Wu et al. Model (2006-2010)*

Wu *et al.* [66-68, 148] developed two models for HCCI engines based on an extensive review of many of the models already discussed. In 2006, Wu *et al.* [66] proposed a heat transfer model fit to data from a 125 cm<sup>3</sup> displacement four-stroke scooter engine. They determined that a new model for small engines of this size was necessary because small engines exhibit thermal losses of up to 50% of the fuel energy compared to larger engines where losses are 30% or less [66] and because none of the models reviewed provided acceptable results for instantaneous heat flux predictions. Figure 28 from Wu *et al.* [66] shows the discrepancies between five of the models and experimental data taken on the 125 cm<sup>3</sup> displacement scooter engine at 6000 rpm and 6 bar BMEP.

Some of the models decently predict the time averaged heat transfer, and Wu *et al.* [66] provide a comparison in their paper. The results are summarized in Table 7, which shows the correlation coefficient between the time averaged heat transfer predicted by the model and the experimental heat transfer from the engine. Wu *et al.* [66] collected their data on the engine operating between 1 bar and 7 bar BMEP (in 1 bar increments) and 3000 rpm and 6000 rpm (in 1000 rpm increments). From the results, the Annand model was the best of the historic models for time averaged data, while the Nusselt model had the poorest fit. The model developed by Wu *et al.* [66] and discussed next, shows an excellent fit, but its applicability beyond the studied engine has not been investigated, unlike many of the historical models which have proven useful for multiple engines of a given size and type.

The new model proposed by Wu *et al.* [66] was an exponential relationship between the mean piston speed and the Stanton number ( $St$ ), as shown in Equation (54). Unlike previous heat transfer models, the wall temperature is replaced with the spark plug

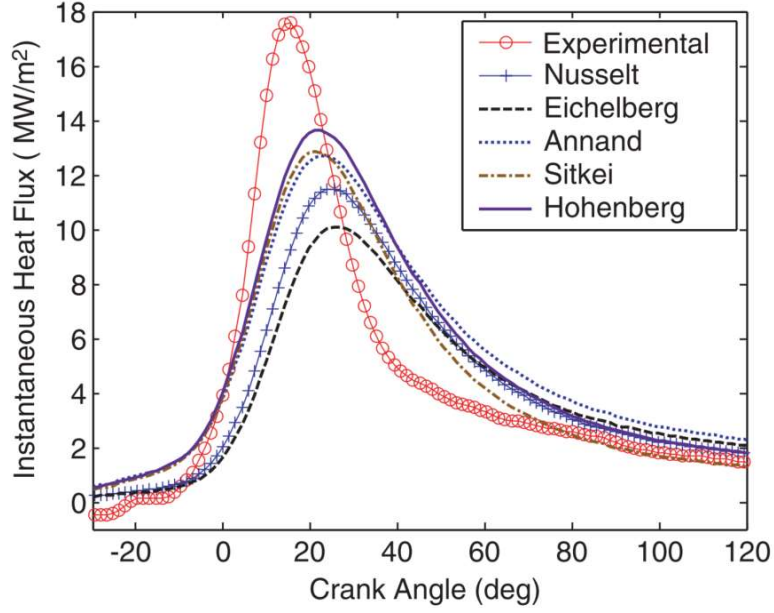


**Figure 28: Comparison of instantaneous, spatially averaged heat transfer models to 125 cm<sup>3</sup> displacement four-stroke engine data, reprinted with permission from Wu *et al.* [66].**

**Table 7: Models and the Correlation Coefficient for Time Averaged Heat Transfer from a 125 cm<sup>3</sup> displacement, Four-Stroke Engine at 1-7 bar BMEP and 3000 to 6000 rpm from Wu *et al.* [66]**

Model	Correlation coefficient for Time Averaged Heat Transfer
Nusselt	0.68
Eichelberg	0.72
Annand	0.94
Sitkei	0.77
Hohenburg	0.85
Wu <i>et al</i>	0.99

temperature to provide a defined, repeatable, location. The wall/spark plug temperature was fit to a second order polynomial in engine speed and intake manifold pressure ( $p_{im}(\theta)$ ) pressure, shown in Equation (55). The characteristic area is two times the piston area. The

remainder of the model is shown in Equations (56) to (59), where Equation (58) is the calculation of gas specific heat and Equation (59) is the polynomial fit for the ratio of specific heats. As in Chang *et al.* [35] the one dimensional conduction equation (with time dependence) was solved using the surface temperature on the inside of the cylinder, which was fit using a Fourier analysis, and the temperature on the outside of the cylinder, which was essentially constant. The proposed model is superior to Annand's model at most operating points, but still exhibits some amount of phase lag and under predicts the peak heat flux, as shown in Figure 29, reprinted from Wu *et al.* [66].

$$St \approx 0.718 \cdot \exp(-0.145 \cdot \bar{S}_p) \quad (54)$$

$$T_{sp}(\theta) = C_1 + C_2 \left( \frac{2\pi N}{60} \right) + C_3 \left( \frac{2\pi N}{60} \right)^2 + C_4 p_{im}(\theta) + C_5 p_{im}(\theta)^2 + C_6 \omega p_{im}(\theta) \quad (55)$$

$$\frac{dQ_{HT}}{dt} = h \cdot 2A_p (T_{g,cyl}(\theta) - T_{sp}(\theta)) \quad (56)$$

$$h = St \cdot \rho \cdot C_p \cdot 0.5 \bar{S}_p \quad (57)$$

$$C_p = \frac{R}{1 - \frac{1}{\gamma}} \quad (58)$$

$$\gamma \approx 1.338 - 6 \times 10^{-5} T_{g,cyl} + 10^{-8} T_{g,cyl}^2 \quad (59)$$

In 2008, Wu *et al.* [67, 68] attempted to improve the model by fitting data from a second 125 cm<sup>3</sup> displacement four-stroke scooter engine. The new data led Wu *et al.* to adjust the fit for spark plug temperature and the correlation for the Stanton number as shown in Equations (60) and (61), respectively, where *CR* is the compression ratio [67].

$$T_{sp}(\theta) \approx a_1 \left( \frac{2\pi N}{60} \right) + a_2 \omega \left( \frac{2\pi N}{60} \right)^2 + a_3 p_{im}(\theta) + a_4 p_{im}(\theta)^2 + a_5 \omega p_{im}(\theta) + a_6 CR \quad (60)$$



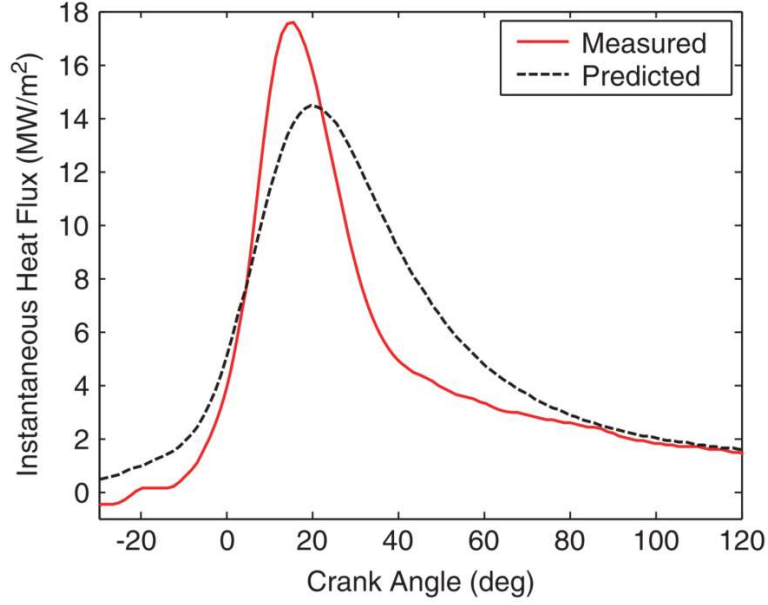


**Figure 29: Fit of Wu *et al.*'s heat transfer model to data from a 125 cm<sup>3</sup> displacement, four-stroke engine, reprinted with permission from Wu *et al.* [66].**

$$St = 5.91488CR \cdot S^2 \left[ 0.0089 \left( 10^5 V_{cyl}(\theta) \right)^2 + \exp(-0.0106 C_m^2) \right] \quad (61)$$

Compared to the experimental results, the model fit was good for the new engine, but did not work as well for the previously studied engine as the original model. Therefore, the model cannot yet be considered widely applicable to small engines, especially two-stroke engines and engines of sizes other than 125 cm<sup>3</sup> displacement.

#### 5.1.1.4. Instantaneous, Spatially Resolved Models

Unlike the homogenous autoignition in HCCI engines, the flame front in SI engines and the burning jet in DI CI engines results in a spatial distribution of heat flux throughout the cylinder. Instantaneous spatially resolved models build on instantaneous spatially averaged models to capture this spatial variance. Typically, the variance is related to a non-dimensionalized position such as the distance from cylinder center divided by the cylinder radius. This section presents three instantaneous such models as examples.

#### 5.1.1.4.1. *Alcock et al. (1975)*

One of the earliest examples of a spatially resolved model was that of Alcock *et al.* [149, 150]. Alcock *et al.* developed a purely empirical model [139] fit to data from over 200 large engines [149, 150], and the form requires *a priori* knowledge of similar engines to fit the coefficients. The model is shown in Equations (62) and (63) [139]. The leading constant ( $C_1$ ) is used to account for engine type, and that constant also contains information about chamber geometry and location within the chamber. The ‘*ambient*’ and ‘*boost*’ subscripts adjust between ambient and turbocharged or supercharged intake conditions. The model is only useful for engines similar to those already characterized due to the sensitive nature of the geometry factor.

$$\dot{Q}_{cyl,loss} = 10^{-6} C_1 \left( \frac{\dot{m}_f}{A_{p,tot}} \right)^{C_2} \left( \frac{p_{ambient}}{p_{boost}} \right)^{C_3} \left( \frac{T_{boost}}{T_{ambient}} \right) \quad (62)$$

$$Two - Stroke: C_2 = 0.6, C_3 = 0.3; Four - Stroke: C_2 = 0.75, C_3 = 0.3 \quad (63)$$

#### 5.1.1.4.2. *LeFeuvre et al. Model 1969*

LeFeuvre *et al.* [151] attempted to correlate the heat flux to radial distance from the bore axis ( $r$ ). As a result  $C_1$  is specifically a function of engine bore, as well as other geometry and engine design factors. The model is shown in Equation (64). Gas velocity is accounted for by the use of a swirl velocity ( $\omega_g$ ) in the Reynolds number term, as seen in Equation (65). The results of the model were compared against a supercharged CI engine with two thermocouples installed in the head. Only one of the thermocouples agreed with the model; thus it does not properly handle the high variation in gas velocity due to the induced swirl [139]. The use of bulk gas properties is also questionable [139].

$$\dot{Q}_{cyl,loss} = C_1 \frac{k_g}{r} Re^{0.8} Pr^{0.33} (T_{g,cyl}(\theta) - T_w(\theta)) \quad (64)$$

$$C_1 = 0.047$$

$$Re = \frac{r^2 \omega_g}{\nu} \quad (65)$$

#### 5.1.1.4.3. *Dent and Suliaman (1977)*

Dent and Suliaman [152] tried a variation on the model of LeFeuvre *et al.* [151]. First, they assumed a constant Prandtl number, absorbing it into the leading coefficient as shown in Equation (66). They then altered the characteristic length and swirl velocity. The characteristic velocity is the tangential velocity ( $\omega_g(r)$ ) at the radial position ( $r$ ) and the characteristic length is the circumference at that position. The model works well for unfired conditions, but fails to capture the increased temperature and swirl effects of fired conditions; increased deviations from experimental results are noted at 40% and 80% load [139]. Based on the three models presented for instantaneous, spatially resolved heat transfer, such models are overly complex (and would likely perform poorly) for the effort considered herein.

$$\dot{Q}_{cyl,loss} = C_1 \frac{k_g}{r} Re^{0.8} (T_{g,cyl}(\theta) - T_w(\theta)) \quad (66)$$

$$C_1 = 0.023$$

$$Re = \frac{2\pi r (\omega_g(r) [\frac{m}{s}])^2}{\nu} \quad (67)$$

#### 5.1.2. Heat Transfer Measurements

There are many different methods for making a heat transfer measurement on an ICE. This section briefly reviews several relevant methods. Net heat flux measurements (time and spatially averaged) are the simplest to make. In a water or liquid cooled engine, heat

rejection from the cylinder can simply be measured as the change in coolant temperature in the coolant circuit and multiplied by the coolant mass flow rate and heat capacity. Air-cooled engines, meanwhile, generally do not have closed cooling circuits. A straight forward solution is to contain the cooling circuit on the engine to measure the enthalpy change in the coolant. As an example, Rittenhouse *et al.* [121] developed an enclosure for measuring coolant enthalpy change for 10-100 cm<sup>3</sup> displacement engines by passing the cooling air flow through an insulated box and measuring temperature at the intake and outlet as well as flow rate through the enclosure. Figure 30 shows an engine installed in the insulated box and the insulated box as part of the engine cooling system, reprinted from Rowton *et al.* [5]. Challenges with determining the enthalpy increase in the cooling circuit included measuring a small temperature change in the fluid and an accurate measurement of the fluid velocity. In the case of Rittenhouse *et al.*'s [121] setup, temperature measurements were performed with calibrated Type J thermocouples and air flow velocity was measured with a hot-wire anemometer.

Another popular technique to measure heat flux is a heat flux gauge. Heat flux gauges come in a number of different styles, but all function in about the same fashion. Thermocouples or resistance temperature detectors (RTDs) are used to measure the temperature on opposite sides of a material with a well-defined thermal conductivity. The device is mounted in/on the engine so that the heat transfer is approximately unidirectional through the gauge. Then the heat flux may be calculated as shown in Equation (68). In this technique, the size of the thermocouple must be minimized to decrease its thermal capacity and response time, and vacuum deposition is commonly used for manufacturing thermocouples on the order of a micron thick [143].

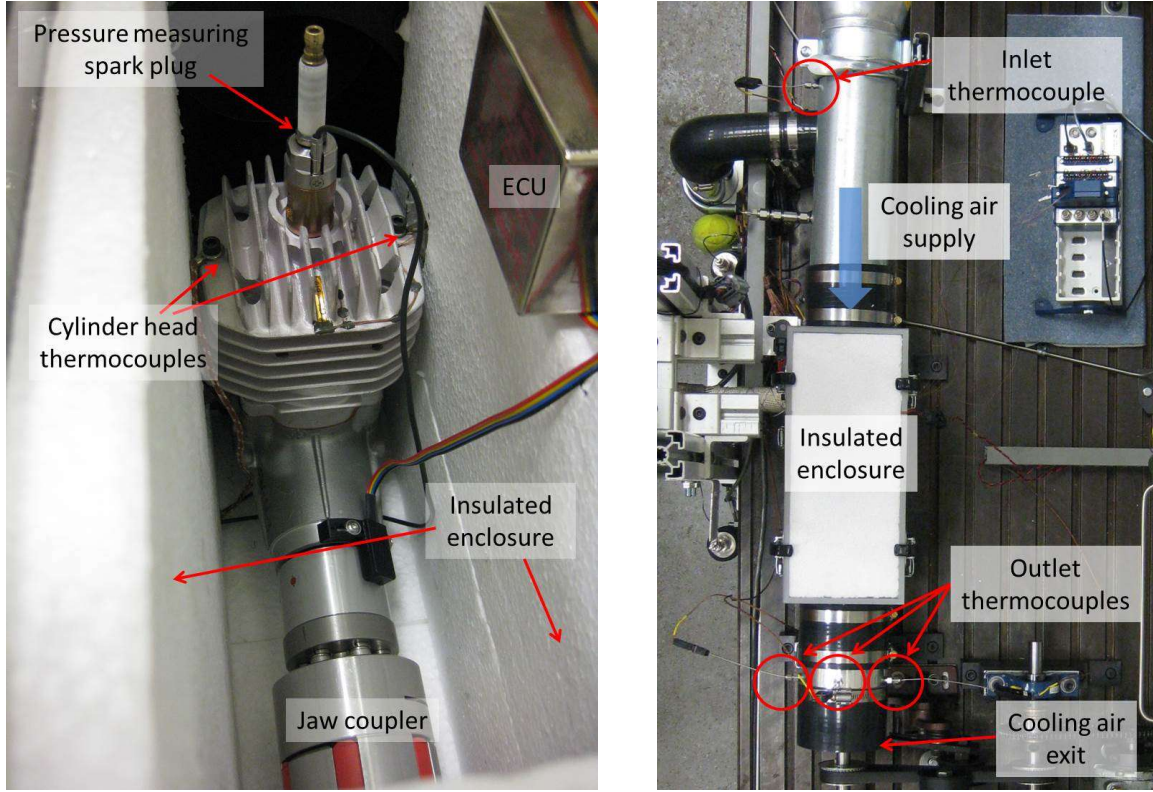


**Figure 30: Left: 3W-55i engine installed in insulated enclosure. Right: Insulated enclosure showing cooling air path. Figure reprinted from Rittenhouse *et al.* [121].**

$$\dot{Q}_{cyl,loss} = Ak\Delta T \quad (68)$$

Several researchers, Woschni and Sihling [143] and Wu *et al.* [66-68] for example, simply place thermocouples inside and outside of the cylinder, using the cylinder wall as the material of known thermal conductivity. Others, Chang *et al.* [35] and Hohenberg [147] for example, developed cylindrical inserts to minimize conduction along the thermocouple wires, creating sensors that are installed like flush mount pressure transducers. These cylindrical sensors typically reference the thermocouple junction inside the cylinder to ambient conditions in the coolant (air in the case of Chang *et al.* [35]), directly measuring the temperature drop across the cylinder wall. Figure 31 from Chang *et al.* [35] shows a

surface thermocouple where the two thermocouple materials are separated by an insulation material so temperature is measured only at the micron thick vacuum deposited couple in the cylinder. The response time of such a device is on the order of microseconds [35].

Rittenhouse *et al.* [121] used a thin film heat flux gauge, which can be attached to the surface of the engine. The gauge consisted of two RTDs with a piece of polyimide film, in their case Kapton®, between them. The gauges were then adhered to the engine. A picture of the heat flux gauges used by Rittenhouse *et al.* [121] is shown in Figure 32. Rittenhouse [153] found that the gauges were highly sensitive to installation location and required regular calibration of the zero voltages, which was complicated by the approximately 100°C difference in the Kapton® temperature between calibration and engine operation. Moreover, installing the gauges risks altering the heat transfer from the engine and the results were still temporally averaged.

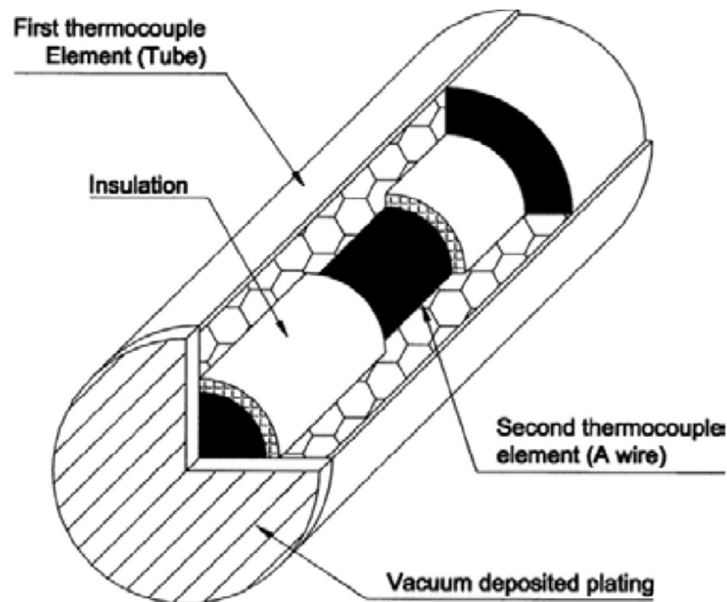


**Figure 31: Schematic of a heat flux gauge, reprinted from Chang *et al.* [35], reprinted with permission from SAE International.**

A variation on the thin film heat flux gauge uses a thermopile. A thermopile is a series of thermocouples in series with the hot junctions on one side of the conducting material and the reference junctions on the other side. As the thermocouples are in series, the output is amplified by the number of junction pairs, increasing the signal to noise ratio. Boyce *et al.* [154] applied a thermopile heat flux gauge to a 147 cm<sup>3</sup> displacement, four-stroke utility engine. The gauge allowed Boyce *et al.* to quantify the relation between spark timing, air fuel ratio, and heat flux. They found that as spark timing advanced both the phasing and magnitude of heat flux increased. Heat flux reached a peak near stoichiometric conditions.

Demuynck [155] applied heat flux gauges to a CFR engine in an attempt to derive a heat flux correlation not dependent on fuel type. The correlation took a similar form to many of those mentioned in the previous section, relating the Nusselt number to the Reynolds and Prandtl numbers. The measurement only included hydrogen, methanol, and methane and Demuynck concluded more data is needed on other fuels [155:161-162]. Spitsov [156] used thermopile type heat flux gauges to investigate thermal losses from a four-stroke Indenor Diesel engine.

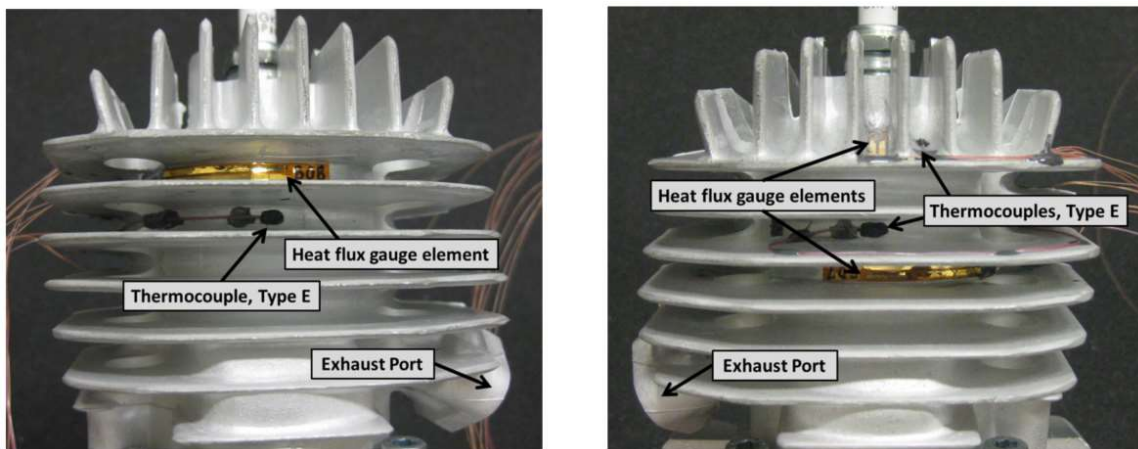


**Figure 32: Thin film heat flux gauges installed by Rittenhouse *et al.* on a Modellmotoren 3W-55i engine, reprinted from Rittenhouse *et al.* [121].**

As described, heat flux gauges only measure a localized flux, and instrumenting an entire engine is impractical both due to the impact on the engine's operation and space considerations. Rittenhouse *et al.* [121] imaged the head of a Modellmotoren 3W-55i engine using an infrared camera. The images provided an indication heat transfer intensity, but the technique was not sufficiently refined to provide useful quantitative results. Figure 33 shows an infrared image of the 3W-55i engine from Rittenhouse *et al.* [121].

If optical access is available on the engine, then infrared measurement could also be used to determine the in-cylinder gas temperature directly. Line emission spectra may also be used to measure in-cylinder temperature, although as Gegg *et al.* [157] indicate, the small size of a utility engine combustion chamber makes it difficult to get sufficient signal strength for the measurement. Additionally, optical access is expensive and time-intensive, so most studies resort to estimating gas temperature with a surface thermocouple similar to the devices used by Chang *et al.* [35] or estimating the temperature from in-cylinder pressure data and the ideal gas law.

### **5.1.3. In-Cylinder Temperature Measurements**

Essentially all of the heat transfer models discussed in Section 5.1.1 use in-cylinder gas temperature. Measurements of in-cylinder gas temperature may be divided into two categories: indirect and direct. Indirect methods extrapolate or calculate the gas temperature from other parameters. Direct methods measure the gas temperature directly using experimental techniques. Typically, indirect techniques are faster and less expensive than direct techniques which require specialized equipment and expertise. They are also less accurate. The following two subsections discuss indirect (Section 5.1.3.1) and direct (Section 5.1.3.2) measurement techniques for in-cylinder gas temperature.



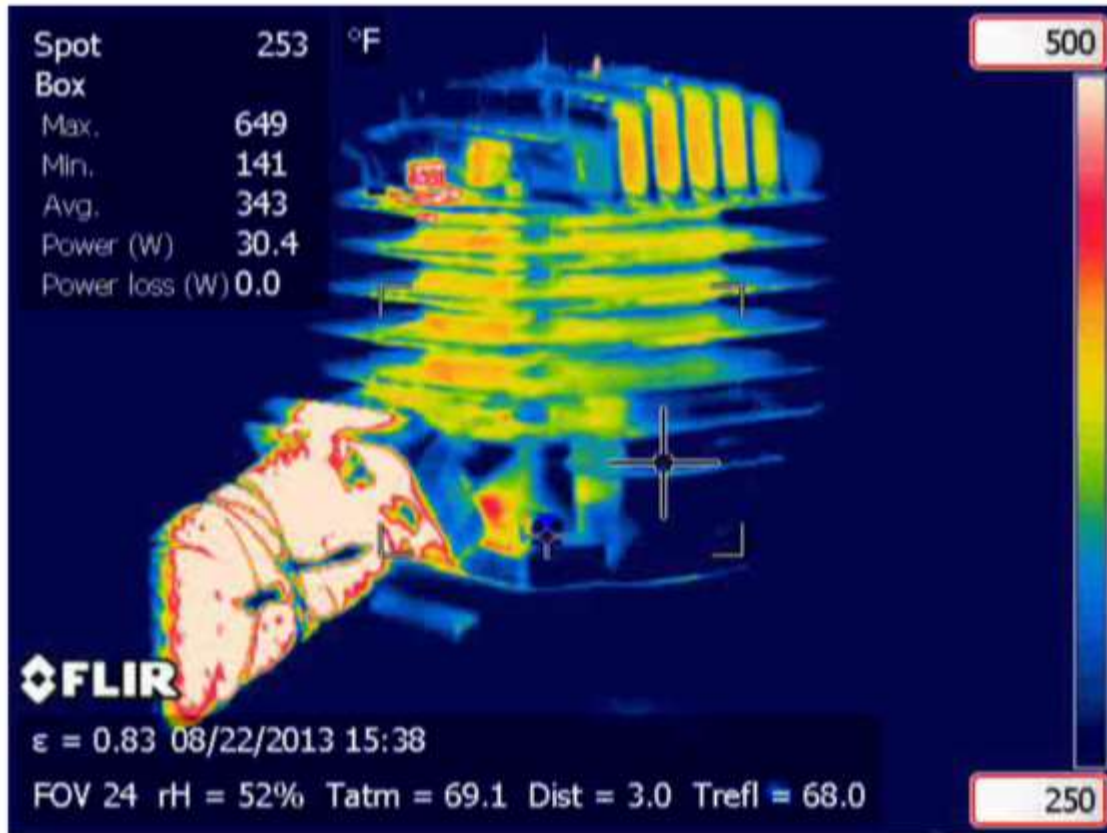


Figure 33: Sample infrared image of a Modellmotoren 3W-55i engine, reprinted from Rittenhouse *et al.* [121].

#### 5.1.3.1. Indirect Measurement Methods

There are three indirect methods commonly used to estimate in-cylinder gas temperature: calculation from the pressure curve, estimation from a surface thermocouple, and estimation from the adiabatic wall temperature. The most commonly approach is to estimate the in-cylinder gas temperature from the in-cylinder pressure trace, as shown in Equation (69). Equation (69) is based on the total derivative of the ideal gas law. In addition to the in-cylinder pressure trace, Equation (69) also requires an estimate of the in-cylinder gas composition, the trapped mass in the cylinder, and knowledge of the engine geometry. This method provides an average, crank angle resolved temperature in the

cylinder. However, temporally resolved models developed using this temperature often lag measured heat flux. Additionally, the model is highly sensitive to the initial mass in the cylinder, which is difficult to determine in a small two-stroke engine.

$$\frac{dT_{g,cyl}}{d\theta} = \left( \frac{1}{m_{cyl}R} \right) \left( V_{cyl} \frac{dp_{cyl}}{d\theta} + p_{cyl} \frac{dV_{cyl}}{d\theta} \right) \quad (69)$$

Another option for estimating the in-cylinder temperature is to use a small, fast response thermocouple on the inner surface of the cylinder [35]. Advantages of this approach include low cost and straightforward data acquisition. However, the measured temperature is not the true gas temperature due to convective lag as well as conduction and radiation effects. Rather, it serves as a characteristic temperature that captures at least some of the variation in the actual gas temperature with operating condition and provides an option when a gas temperature measurement cannot be made. Moreover, routing thermocouple wires out of the engine, especially a small two-stroke engine, is difficult while maintaining a sealed combustion chamber.

A third approach for determining in-cylinder temperature is to extrapolate the adiabatic wall temperature as done by Menon and Cadou [2, 16]. In this approach, cylinder surface temperature is plotted as a function of coolant temperature at a fixed coolant flow rate. The line is then extrapolated to the point where both temperatures are equal. This point is the adiabatic wall temperature and has been used as a characteristic temperature in place of the mean gas temperature [2, 16] in the correlations of Taylor and Toong [138] and Annand [17]. The technique depends on linearly extrapolating a distinctly non-linear system and is further complicated by shifting of the heat load between the cylinder and exhaust. The technique should be reserved for when no better measurement technique is available.

#### 5.1.3.2. Direct Measurement Methods

Direct methods typically require optical access to the combustion chamber. As Gegg *et al.* [157] state, the small size of a utility engine combustion chamber makes it difficult to get sufficient signal strength for optical measurements. Additionally, optical access is expensive and time-intensive. However, when optical access is available, there exist a wide variety of methods for measuring the in-cylinder gas temperature. Zhao and Ladommatos [56:575-644] provide a comprehensive overview of available optical measurement techniques. Those techniques are summarized (with some additions) in Table 8 [56:640]. Crank angle resolved measurements can resolve the temperature at discrete crank angles in a single cycle. Cycle average measurements average the results from many cycles to give a temperature profile for the average cycle.

The techniques may be divided into three categories: radiation thermometry, spectroscopic techniques, and laser diagnostic techniques. Radiation thermometry techniques measure the broadband thermal emission of gases in the cylinder over a specific band of wavelengths. Radiation thermometry methods usually only work at high temperatures with substantial thermal emissions, and issues may also arise from chemiluminescence during combustion. Spectroscopic techniques measure the absorption or emission of gas molecules at specific wavelengths in the cylinder. Spectroscopic techniques may be tuned for one or two specific features (narrow band, example: rotational transitions of the OH<sup>-</sup> radical) or for range of many wavelengths (broadband, example: FTIR). The applicable temperature ranges and concentrations depend on the wavelengths and species being measured. Laser diagnostic techniques are based on measurements of Rayleigh and/or Raman scattering which occur when a photon collides with a molecule. There also exist

absorption spectroscopy techniques that use lasers as a light source, such as Tunable Laser Absorption Spectroscopy.

**Table 8: In-Cylinder Gas Temperature Measurement Techniques, Adapted and Augmented from Zhao and Ladommatos [56:640].**

Method	Species*	Spatial Resolution	Temporal Resolution	Critical Disadvantages	Reference
<b>Radiation Thermometry</b>					
Chopped Method	CO <sub>2</sub> , H <sub>2</sub> O	line-of-sight	CA resolved	none	[158, 159]
Null Method	CO <sub>2</sub> , H <sub>2</sub> O	line-of-sight	cycle average	time intensive	[158]
Line Reversal	Sodium	line-of-sight	cycle average	particle seeding	[160]
Two Color Method	CO <sub>2</sub> , H <sub>2</sub>	line-of-sight	CA resolved	emissivity ratio	[161]
<b>Spectroscopic Techniques</b>					
Rotational Temperature	OH	line-of-sight	CA resolved	not valid at high temperature	[162]
Line Absorption	Iodine	line-of-sight	CA resolved	particle seeding	[163]
Tunable Laser Absorption Spectroscopy	H <sub>2</sub> O, CO <sub>2</sub> , CO, HCs	line-of-sight	CA resolved	extinction levels of CO and CO <sub>2</sub> in ICE applications	[164-166]
FTIR Spectroscopy	H <sub>2</sub> O, CO <sub>2</sub> , CO	line-of-sight	cycle average	time intensive	[167, 168]
<b>Laser Diagnostics</b>					
Ramen Thermometry	N <sub>2</sub>	single point	cycle average	weak signal	[169, 170]
Rayleigh Thermometry	gas mix, NO	two dimensional	cycle average	unsuitable for burnt gas	[171]
Coherent Anti-Stokes Ramen Thermometry	N <sub>2</sub>	single point	cycle average	complex equipment, single point	[172-174]
Monochromatic Fluorescence Thermometry	O <sub>2</sub>	two dimensional	cycle average	interference of fuel with beam	[175]
Two Line Fluorescence Thermometry	3-pentanone indium	two dimensional	cycle average	complex equipment	[176]

*\*Species are examples of historically measured species and not intended as an exhaustive list.*

Clearly, selecting and implementing a specific measurement technique is a substantial undertaking in itself, and the author does not claim to be an optical diagnostics expert. Therefore, the author consulted with the Advanced Combustion Diagnostics Group (within the Air Force Research Laboratory, Aerospace Systems Directorate, Turbine Engine Division, Combustion Branch), which specializes in optical and laser based diagnostics in

combustion environments. Specifically, Dr. Keith Rein (Spectral Energy) and Dr. Andrew Caswell (AFRL/RQTC) helped to select a measurement technique. Technique selection was based on two criteria: the technique had to be appropriate for the measurement environment, and the equipment and expertise had to be available in the Advanced Combustion Diagnostic Group. Ultimately, two measurement methods were pursued: Tunable Laser Absorption Spectroscopy (TLAS) (the primary method in this work) and FTIR (also implemented and used on the SERB). An overview of the theory behind those measurement methods is discussed next. A detailed discussion of the other methods is beyond the scope of this work and the interested reader is referred to the references in Table 8 or Chapter 11 in Zhao and Ladommatos [56:575-644].

One way that a molecule can change energy states is by the emission or absorption of a photon. The energy of that photon corresponds to the energy of the transition between the initial and final energy levels ( $\Delta E$ ), and that energy may be related to the photon's frequency ( $f$ ) or wavelength ( $\lambda$ ) using Planck's constant ( $h$ ) and the speed of light ( $c$ ) in the Planck-Einstein relation shown in Equation (70).

$$\Delta E = E_p = \frac{hc}{\lambda} = hf \quad (70)$$

Since energy levels of a specific molecule are discrete, so are the wavelengths that may be emitted or absorbed when a molecule transitions between energy levels. Both TLAS and FTIR spectroscopy measure the absorption of specific wavelengths of light (typically rotational and vibrational transitions in the infrared spectrum [56:604]) in order to determine the temperature and pressure (or concentration) of a gas. Both TLAS and FTIR spectroscopy are line-of-sight averaged measurements and as a result, number density

averages. In the presence of density gradients, both methods will be biased towards the more dense regions, typically the cooler, unburnt end gas in the case of ICEs.

#### 5.1.3.2.1. *Fourier Transform Infrared Spectroscopy*

FTIR spectroscopy is a well-studied measurement technique and entire reference volumes are available on the subject [177, 178]. This section provides an overview of the technique. Figure 34, reprinted from [167], shows a schematic of an FTIR spectrometer. In FTIR spectroscopy a coherent IR source is directed at a beam splitter. Half of the beam is directed to a fixed mirror while the remainder is modulated using a moving mirror, which together form a scanning (Michelson) interferometer [56:44]. The modulated light recombines with the coherent light reflected from the fixed mirror and is directed through the sample compartment. The attenuation of the modulated and recombined beam is measured on the opposite side of the sample compartment using an IR sensor and recorded

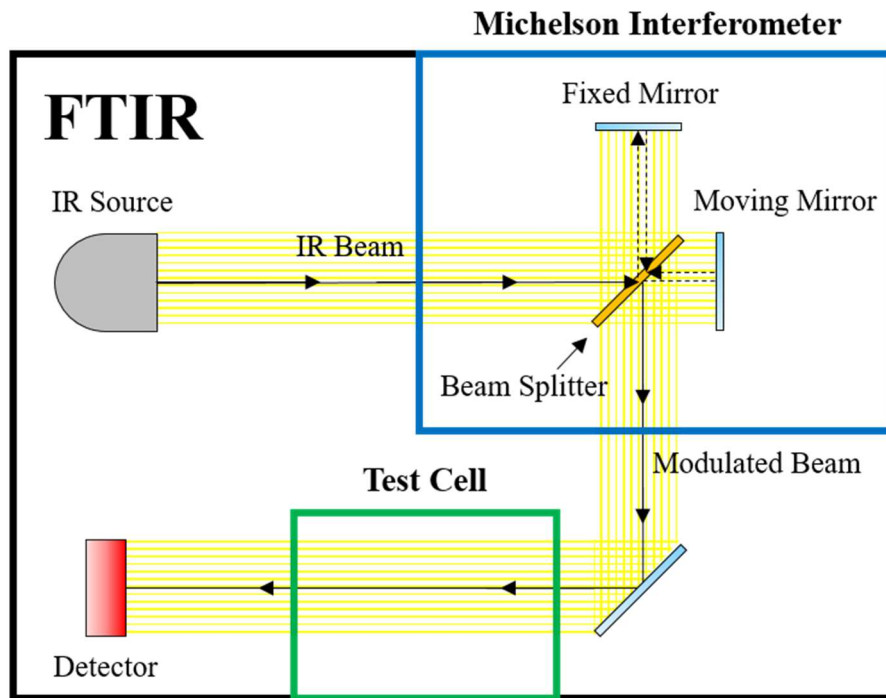


Figure 34: Schematic of a FTIR spectroscopy unit, reprinted from [167].

with respect to mirror position. At each mirror position the path length of the light from the fixed mirror and moving mirror differ forming an interference pattern, and thus each recorded data point contains information about the entire IR spectra. The data as a function of mirror position make up an interferogram. Typically mirror position is tracked using a helium neon laser and a detector that counts the fringes after the laser passes through the interferometer [179]. By taking the Fourier transform of the interferogram, the data is transformed into frequency space (wavenumber) giving a broadband IR spectra like that in Figure 35 [180]. The sampling rate of the detector determines the resolution, while the travel distance of the mirror determines the spectral range. The relationship between the absorption of the light (a function of species and temperature) and the molecular concentration is governed by the Beer-Lambert law [168], which relates absorbance ( $A$ ), absorptivity ( $\alpha$ ), path length ( $l$ ), and concentration ( $n$ ) as shown in Equation (71).

$$A = \alpha(T, p) \cdot l \cdot n \quad (71)$$

To determine the temperature, pressure, and species concentrations, the measured spectra are fit to simulated spectra using a technique such as the one developed by Kranendonk *et al.* [181]. A spectral database is used to generate simulated spectra at varying temperatures and pressures. Goodness of fit between measured and simulated spectra is evaluated using a least squares methodology yielding temperature and pressure. Concentration is then determined by scaling the measured spectrum to the reference spectrum (which was generated with a known species concentration).

Perhaps the most relevant examples of FTIR spectroscopy are the work of Rein [168], Deutsch [182], and Deutsch *et al.* [167]. Rein applied FTIR spectroscopy to measure gas composition in a 190 cm<sup>3</sup>, four-stroke gasoline spark-ignition engine. By tracking mirror

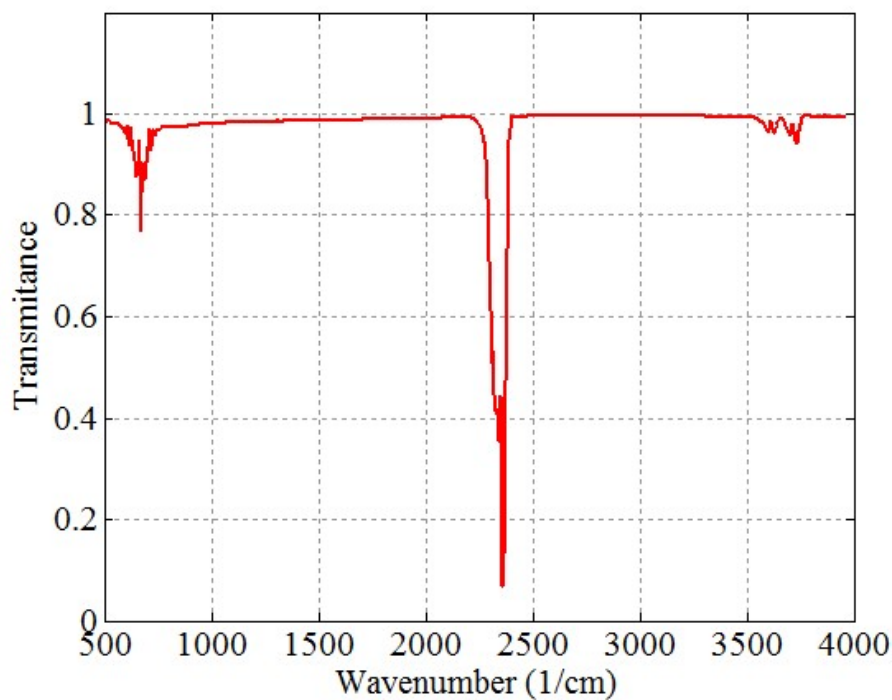


**Figure 35: Mid infrared spectrum for gaseous CO<sub>2</sub> collected by Dow Chemical Company, raw data obtained from NIST [180].**

position and crank angle, Rein was able to bin the absorption measurements by crank angle, reorder the bins using mirror position, and create IR spectra for each 4 CAD bin. The end result was 90 spectra showing how in-cylinder composition changed over the course of an average cycle. The resolution was sufficient to identify water and carbon dioxide as well as peaks caused by various combinations of hydrocarbons and aldehydes [168]. Deutsch adapted Rein's methodology to the 3W-55i engine used in this study [182]. Using FTIR spectroscopy, Deutsch was able to resolve broad trends in gas temperature and concentration of CO, CO<sub>2</sub>, and H<sub>2</sub>O. Engine and combustion variability during the approximately 20 minute sample time required to collect a single crank angle average spectrum caused the technique to miss finer details, such as the peak temperature. Signal to noise ratio also proved problematic as it was difficult to collimate the FTIR source into



a sufficiently narrow beam to fit through the 1.6 mm windows installed in the engine. As a result, creating a strong, narrow light source is one of the primary reasons a laser based temperature measurement technique was pursued for this work. In addition to the 3W-55i engine, Deutsch also developed optical access for the remaining engines used in this study, and that access was utilized for TLAS measurements in the fired engines. FTIR spectroscopy has also been used extensively in emissions measurements on ICEs and several examples are provided in Section 5.3.2.2.3.1.

#### ***5.1.3.2.2. Tunable Laser Absorption Spectroscopy***

While FTIR spectroscopy looks at a broad range of wavelengths, TLAS focuses on a narrower band (although not necessarily individual features). Generally, FTIR spectrometers have a spectral resolutions on the order of  $1\text{ cm}^{-1}$  while tunable lasers are capable of spectral resolutions on the order of  $10^{-5}\text{cm}^{-1}$  [165]. Therefore, TLAS can be used to create a high resolution broadband spectrum over a small wavenumber range or to resolve individual absorption lines of a specific molecule, avoiding interference from other molecules [165]. To achieve its higher resolution, TLAS replaces the broadband IR source of the FTIR spectrometer with a tunable laser. Instead of using a scanning interferometer, the tunable laser is rapidly swept over a range of wavelengths. The time for one scan in TLAS is based on the sweep speed of the laser (typically greater than 10 kHz) as opposed to the physical motion of the mirror (typically less than 1 Hz). Thus, the primary advantage of TLAS is speed and resolution over a small range of wavenumbers (typically less than  $100\text{ cm}^{-1}$ ), while FTIR spectroscopy provides a broader picture of the IR spectrum (typically more than  $1000\text{ cm}^{-1}$ ) [165]. For broadband spectra, the collected spectrum is then compared to simulated or reference spectra to determine temperature, pressure, and

concentration using techniques similar to FTIR spectroscopy. Extracting temperature and concentration from only one or two features is somewhat different, and Chen *et al.* [163] provide an example. Spectroscopy is called ‘broadband’ if the fit is performed using more than two or three lines and the spectral shape contributes to the fitting. Line absorption spectroscopy (‘narrowband’) typically fits only one or two line absorption features.

For indicating measurements in a small engine, TLAS offer several advantages over FTIR spectroscopy. First, TLAS is capable of much faster measurements than FTIR spectroscopy as it is not dependent on the physical motion of a mirror. For example, in Deutsch *et al.*, a single complete scan of the mid-IR range using FTIR spectroscopy required on the order of a second [167]. Therefore, for use on an ICE, the data had to be binned and reconstructed to resolve crank angle dependent features, requiring approximately 20 minutes of operation to provide a single average cycle. Even at only 10 kHz, TLAS is sufficiently fast to resolve the temperature profile in a single cycle to approximately 4 CAD. Second, since TLAS uses a laser as the source, the beam is much narrower (and stronger) than the coherent broadband light source used in FTIR spectroscopy. Therefore, in a small ICE (with a narrow optical path), TLAS has a stronger signal and better signal to noise ratio than FTIR spectroscopy. Third, FTIR spectroscopy requires knowledge of the species present in the sample in order to generate simulated spectra. This makes fitting FTIR spectra difficult in regimes with many molecules of overlapping absorption lines. For example, there are thousands of C-H lines between  $2840\text{ cm}^{-1}$  and  $3000\text{ cm}^{-1}$  making it nearly impossible to identify and quantify specific hydrocarbon species. In comparison, since TLAS looks at a narrower band for a specific molecule (or molecules), the exact specie(s) to simulate is known *a priori*.

A review ICE literature indicates that TLAS is primarily used to measure temperature and pollutant concentration in exhaust. Hill and Majkowski employed a TLAS system tuned to  $1250\text{ cm}^{-1}$  to  $1300\text{ cm}^{-1}$  to quantify methane and sulfuric acid in vehicle exhaust, improving response time for the measurement from 10 min with the original technique (filters) to 2.4 s [165]. Ma *et al.* used a similar system to quantify aldehydes in CI engine exhaust using a laser tuned to  $2940\text{ cm}^{-1}$  with  $10^{-4}\text{ cm}^{-1}$  spectral resolution [164]. Thiel *et al.* developed a fast response TLAS system to measure NO, CO, and CO<sub>2</sub> in engine exhaust with a response time of 5 ms in order to improve engine tuning to meet Low Emission Vehicle and Ultra Low Emissions Vehicle exhaust requirements [183]. More recent studies have used TLAS to study ammonia emissions [184, 185] and even developed systems sufficiently portable for use in road emissions testing [184].

#### **5.1.4. Summary: Heat Transfer**

The literature has a number of available models for heat transfer. From the perspective of small RPA design, a model for the overall heat transfer from the engine would allow design engineers to better incorporate cooling requirements and heat management into the airframe. From a heavy fuel conversion standpoint, such a model would provide a tool for studying how thermal management in a small ICE might be leveraged to relax the fuel AKI requirement. (Even measurements of in-cylinder temperature would expand the understanding of how engine control parameters influence knock in small engines.) Yet, all of the models discussed here remain un-validated for small ICEs (though some have been applied to small ICEs, for example Menon *et al.* [16]). Thus, the aim of the first part of Objective 2 was to investigate and validate or adapt historical models for heat transfer in a family of small, geometrically similar 10-100 cm<sup>3</sup> displacement COTS ICEs.

## 5.2. Friction

Friction, like heat transfer, is a significant loss mechanism in ICEs. Practically all engines have multiple sources and types of mechanical friction as well as pumping losses, as discussed briefly in Section 2.7. The study of these friction sources is a highly sophisticated field, however models and correlations for total friction in an engine are sparse in the literature. Furthermore, as Heywood and Sher [22:368] point out, “engine friction data for two-stroke engines are insufficient to validate these models for two-stroke engines”. This section will discuss friction loss models and measurement techniques in two parts. First, Section 5.2.1 will describe whole engine correlations and models for friction losses that are available in the literature. Second, Section 5.2.2 will briefly discuss three engine friction measurement techniques.

### 5.2.1. Engine Friction Loss Models

The literature does contain a handful of friction loss models developed for four-stroke engines [186-190]. Heywood and Sher indicate these models are not necessarily appropriate for two-stroke engines [22:368]. The most popular form for a total engine friction loss model is shown in Equation (72) and is the form used by Heywood [21:719], Heywood and Sher [22:367], and Menon and Cadou [16].

$$FMEP[kPa] = C_1 + C_2 \left( \frac{N}{1000} \right) + C_3 \left( \frac{N}{1000} \right)^2 \quad (72)$$

Each of the three terms is a different source of friction (recall Figure 14 from Section 2.7). The first term is a constant primarily due to boundary friction, specifically metal-to-metal contact. Since FMEP is non-dimensionalized by engine speed, the power dissipated by the boundary friction is proportional to engine speed. The correlation in Equation (72) is shown in a dimensional form in Equation (73) to illustrate this concept.

$$P_f[kW] = \left( C_1 + C_2 \left( \frac{N}{1000} \right) + C_3 \left( \frac{N}{1000} \right)^2 \right) \frac{N}{60} V_d \quad (73)$$

The second term is friction in the hydrodynamic regime generated by the shear of the lubricating fluid between the two sliding surfaces. The power dissipated by this term is proportional to the square of velocity. The third term encompasses the pumping losses, and the power dissipated by pumping is proportional to the cube of engine speed as a result of physics similar to those that cause power losses from drag to be proportional to vehicle speed squared. (Drag is proportional to speed squared, and power is force multiplied by velocity).

The value of the constant  $C_3$  is driven primarily by pumping work. The differences in pumping losses between two-stroke and four-stroke engines cause  $C_3$  to vary with engine type. Similarly, the values of the other two constants in Equations (72) and (73) depend on lubrication methodology and mechanical design, leading to variations in the values of those constants between engines. Furthermore, Equations (72) and (73) fail to capture any scaling of losses between engines of different sizes as they assume that the power to overcome friction losses is directly proportional to displaced volume, even though one would expect at least  $C_1$  and  $C_2$  to scale with surface area and increase with decreasing engine size. Still, a number of groups have compiled constants for use in Equations (72) and (73), and those constants are shown in Table 9. It is interesting to note that two of the fits have negative coefficients for the hydrodynamic regime term. Since neither  $C_1$  nor  $C_2$  capture the effects of the mixed lubrication regime, it is likely that these negative coefficients are the result of  $C_1$  and  $C_2$  attempting to capture all three mechanical friction

regimes in two terms. Note that from a physics standpoint,  $C_2$  should always be positive. Negative coefficients are a purely mathematical result.

**Table 9: Constants for Equations (72) and (73)**

Displacement	Engine Type	Cylinders	Load	$C_1$ (kPa)	$C_2$ (kPa)	$C_3$ (kPa)	Source
845 to 2000 cm <sup>3</sup>	Four-Stroke	4	WOT	97	15	5	[21:722]
4250 cm <sup>3</sup>	SI Engines	8	WOT	166	-2.5	3.5	[22:368]
350 cm <sup>3</sup>	Two-Stroke SI Engines	2	WOT	190	-20	3.6	[22:368]
		2	Idle	130	17	1.2	[22:368]
0.16 to 7.54 cm <sup>3</sup>	Two-Stroke Glow Fuel	1	WOT	224.4	0	0	[16]

Blair [27:378-380] proposes a different correlation for total friction losses, shown in Equation (74). In this form, friction losses are accounted for with just two terms. The first term represents friction sources in the boundary regime, such as metal-to-metal contact and  $C_1$  is zero for friction sources that operate in the hydrodynamic lubrication regime, such as journal bearings. The second term assumes that all other friction sources are proportional to the engine speed. Blair's proposed correlation assumes that pumping losses may be modeled as part of the hydrodynamic lubrication term.

$$FMEP = C_1 + C_2 \bar{S}_p \quad (74)$$

Table 10 shows constants for Equation (74) as compiled by Blair [27:379]. The text is non-specific on the engines used to create the correlation outside of the information already provided in Table 10. Blair [27:379] notes in his text that this correlation has not been validated for engines smaller than 100 cm<sup>3</sup> displacement stating, "from the experimental evidence, there appear to be somewhat proportionately higher friction characteristics for small industrial engines, i.e., of cylinder capacity less than 100 cm<sup>3</sup>." Finally, Heywood

[21:724] includes a compromise between Equations (72) and (74) for large CI engines, shown in Equation (75).

$$FMEP = C_1 + 48 \frac{N}{1000} + 0.4(\bar{S}_p)^2 \quad (75)$$

$C_1 = 75$  for DI engines

$C_1 = 100$  (144) for large (small) swirl chamber with IDI

**Table 10: Constants for Equation (74) as compiled by Blair [27:379]**

Displacement	Engine Type	Bearings	$C_1$ (kPa)	$C_2$ (kPa-s/m)
>100 cm <sup>3</sup>	SI: Vehicle	Roller	0	4.5
	SI: Industrial		0	3.15
	SI	Plain	25	3.75
	CI: Automobiles		34.4	5.25
	CI: Trucks		61	6.0

### 5.2.2. Engine Friction Measurement Techniques

There are a number of different techniques to determine the friction losses in an engine. The most precise method is to measure the IMEP using an in-cylinder pressure transducer and the BMEP at the dynamometer and to take the difference of the two values as FMEP. This method assumes that the friction losses in the drivetrain between the dynamometer and the engine are either negligible, or characterized. The later assumption is applied by the pillow blocks and belt drive on the test bench in this work, described in Horn *et al.* [122], included in Appendix E.

Another popular method is to motor the engine (unfired). In this technique, a motor in a reaction cradle, such as the one described in Cadou *et al.* [7], spins the engine. By measuring the power delivered by the motor to the drive train without the engine attached,

the power dissipated by the drive train may be determined. Then, by motoring the engine and the drive train, the engine friction losses may be determined by subtracting the drive train losses. The trouble with all motored testing is matching the motored engine conditions to firing operation as closely as possible. Firing an engine involves higher temperatures, pressures, and forces than motored operation. As a first pass, the engine should be sufficiently heated so that the viscosity of the oil is comparable to firing conditions [21:719-720].

Similar to the motored measurement described above is what Heywood describes a ‘grab’ [21:720] test. In a grab test the engine is allowed to reach a steady state firing condition. The ignition system is disabled and the engine is switched to motoring operation to make the friction measurement. While this method tests the engine closer to the operational temperature, there are still several differences between the motored ‘grab test’ friction losses and the fired friction losses [22:364-365]. In motored operation cylinder pressures are lower, decreasing the measured friction loss. Temperatures in the cylinder are also lower, increasing measured friction loss, and the blow-down and gas exchange processes are significantly altered, which especially affects two-stroke engines. Patton *et al.* [188] compared motored and firing test data and indicate that these differences offset one another and that grab tests are just as accurate as measurements of BMEP and IMEP.

Another type of test that begins with a firing engine is an inertial test, developed by Harari and Sher for two-stroke cycle engines [191]. In an inertial test, a large flywheel of known inertia is connected to the engine output shaft. The engine is fired and allowed to reach a steady state condition. The ignition is then disabled, and the angular deceleration



and inertia of the flywheel allow the calculation of the friction torque. Harari and Sher [191] indicate that inertial methods are within  $\pm 3\%$  of motored tests.

There are other testing methods that are even more indirect. One such method is the ‘Willans Line’ [22:720]. In the Willans Line method, the BMEP of the engine is plotted as a function of fuel flow. The data is then fit with a curve and extrapolated back to zero fuel flow, which is taken as the value of FMEP. Realistically, this method is difficult to implement as the BMEP to fuel flow relationship is non-linear and the extrapolation distance is about half of the range of the data [22:720]. Another indirect method, called the ‘Morse Test’, works only on multi cylinder engines [22:720]. In a Morse Test, BMEP is plotted as a function of the number of firing cylinders. The intercept of this line, where no cylinders are firing is the FMEP. In the Morse method, care must be taken to avoid altering the gas flow in the intake and exhaust runners when cylinders are not-firing. Generally speaking, the indirect methods leverage risky extrapolations and should only be used if none of the previously described techniques are practical.

### **5.2.3. Summary: Friction Loss Models**

An overall friction loss model, such as the form presented in Equation (72), would provide RPA designers and operators an understanding of the tradeoff between engine friction losses, engine size, and operational speed. Yet, validated models remain limited for small ICEs and practically non-existent for small SI two-stroke engines. Furthermore, none of the available models account for scaling with engine size as anticipated in the discussion in Section 4.1. The second part of Objective 2 aimed to fill this void by adapting and validating a friction loss model for two-stroke engines with displaced volumes between 10-100 cm<sup>3</sup>. Additionally, with the available data on friction in micro glow engines from

Menon *et al.* [16] and information on larger engines from sources such as Heywood and Sher [22:368], this investigation will fill in the missing size range providing a complete view of overall friction losses in COTS engines.

### **5.3. Gas Exchange: Scavenging and Short-Circuiting**

In this effort, there were two concerns associated with gas exchange. First, it was necessary to determine how much fresh charge was lost to short-circuiting to quantify that loss pathway and how it changes with engine size. Second, exhaust gas composition was a required quantity to determine the sensible and chemical enthalpy lost in the exhaust. When a two-stroke engine short-circuits fuel, chemical enthalpy is lost to the exhaust before combustion occurs. As a heuristic, Heywood estimates that 20% of fuel is lost directly to the exhaust [21:5-6]. This estimate is simplistic and neglects that the scavenging behavior of a two-stroke engine is a function of throttle, speed, and engine design. One method to determine the short-circuiting is through measurement. Characterizing the entire operational envelope of an engine is expensive if the engine is available, and impossible if the engine is not yet built. Models that can provide an indicator of scavenging performance are useful for engine design as well as performance simulation. According to Heywood and Sher [22:121-22], scavenging models may be grouped into three categories: single phase (one and two zone models), multizone models, and multidimensional computational fluid dynamics (CFD) models. The objective of each model is to provide a relationship between the scavenging efficiency, charging efficiency, and delivery ratio of the engine. This section is split into two parts, the first discussing scavenging models and the second addressing measurement techniques.

### 5.3.1. Scavenging Models

As model complexity increases, so does the number of empirical constants required to fit the model to experimental data. It is arguable that as the number of empirical constants increases, the universal applicability, and certainly the practicality, of the model decreases, since more experimentally obtained information must be provided to tune the model. The turbulence, combustion, and heat transfer processes make modelling the engine cycle and gas exchange through computational fluid dynamics (CFD) difficult. In many cases, CFD models are used to predict the impact of changes to an existing engine when the model has already been developed using boundary conditions and tuning parameters from experimental data. Galdo and Vidal [192] provide an overview of a CFD model for gas exchange in a two-stroke engine, and Cagin *et al.* [193] examine a comprehensive list of parameters for developing two-stroke CFD models. For investigating effects such as scaling, a simplified single or multi zone model is more appropriate [22:122, 194].

This section presents four relevant models: the perfect mixing model and the perfect displacement model (Section 5.3.1.1), the Maekawa three zone model (Section 5.3.1.2), and the S-curve model (Section 5.3.1.3). Blair [27:211] credits Hopkinson [195] with originally developing the concepts of perfect displacement and perfect mixing. Neither model realistically represents a modern two-stroke engine. However, the models are frequently considered bounding cases for scavenging performance. Given a lack of better information, the two models can be used in conjunction to bound the scavenging performance of an engine, as in Rowton *et al.* [5]. Numerous authors have proposed more complex models to better match the experimentally measured gas exchange process. The Maekawa model is presented here as a classic example of a more complex, three zone

model. The S-curve model, which is a mix of the perfect displacement model and the perfect mixing model, is presented as it is particularly effective.

### 5.3.1.1. The Perfect Displacement and Perfect Mixing Models

The perfect displacement and perfect mixing models presented here (and their derivations) are available from multiple sources [22:122-26, 194, 196]. Figure 36, reprinted from Heywood and Sher [22:123], shows a schematic of the perfect displacement and perfect mixing models. The perfect displacement model assumes that each unit of fresh charge ( $\dot{m}_i$ ) that enters the cylinder displaces an equal volume of burnt mixture, without mixing. Short-circuiting does not occur until all of the burnt charge has left the cylinder. As such, the perfect displacement model is the best case for scavenging. In other words, all real engines will short-circuit more fresh charge than this case. The perfect displacement model makes the following assumptions:

- 1) The cylinder walls are adiabatic.
- 2) There is no heat or mass exchange between the burnt and unburnt gas.

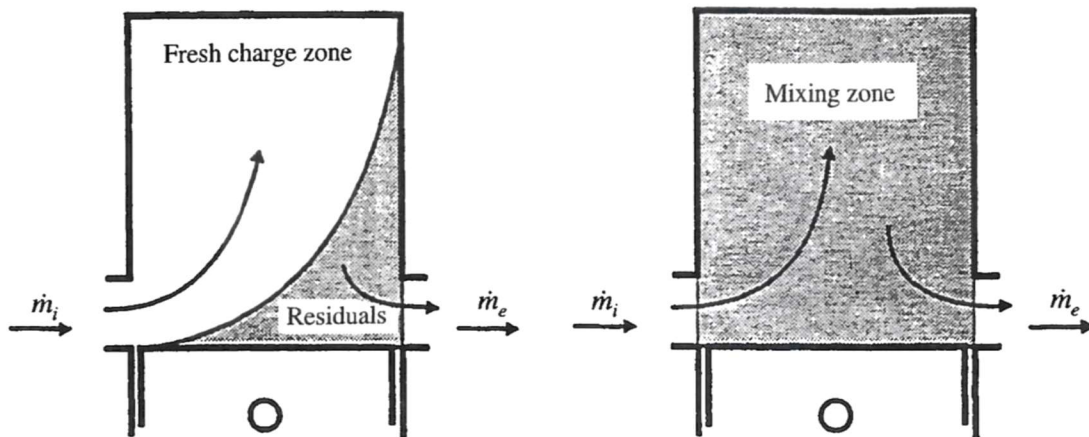


**Figure 36: Idealized scavenging models. Left: Perfect displacement model. Right: Perfect mixing model. Reprinted from Heywood and Sher [22:123] with permission from Taylor & Francis Ltd.**

- 3) Cylinder volume is constant. Since gas exchange occurs within about 80° CA of BC, this is an approximation.
- 4) Cylinder pressure is constant. With both ports open, this is a reasonable approximation.
- 5) The fresh charge (subscript 'i'), reference conditions (subscript 'o'), and burnt gas (subscript 'b') all have different compositions (and temperatures) and thus different densities ( $\rho$ ).

With these assumptions, the charging efficiency, scavenging efficiency, and exhaust gas purity are given by Equations (76), (77), and (78), respectively.

$$\eta_{ch} = \begin{cases} \Lambda & \text{for } \Lambda < \frac{\rho_i}{\rho_o} \\ \frac{\rho_i}{\rho_o} & \text{for } \Lambda \geq \frac{\rho_i}{\rho_o} \end{cases} \quad (76)$$

$$\eta_{sc} = \begin{cases} \left[ 1 + \frac{\rho_b}{\rho_i} \left( \frac{1}{\Lambda} \frac{\rho_i}{\rho_o} - 1 \right) \right]^{-1} & \text{for } \Lambda < \frac{\rho_i}{\rho_o} \\ 1.0 & \text{for } \Lambda \geq \frac{\rho_i}{\rho_o} \end{cases} \quad (77)$$

$$\beta = \begin{cases} 0 & \text{for } \Lambda < \frac{\rho_i}{\rho_o} \\ 1.0 & \text{for } \Lambda \geq \frac{\rho_i}{\rho_o} \end{cases} \quad (78)$$

As discussed previously, when the exhaust port closes, the charging efficiency and delivery ratio relate to the trapping efficiency as in Equation (10) (page 44). From a loss standpoint, the trapping efficiency is a critical metric, as it relates the amount of fresh charge in the cylinder during combustion to the total fresh charge delivered. Unity less the trapping efficiency represents the fraction of fresh charge that simply short-circuits to the exhaust.

The perfect mixing model assumes that each volume of fresh charge entering the cylinder mixes instantaneously and uniformly with the gas already in the cylinder, displacing an equal volume of uniformly mixed gas. The perfect mixing model is often considered a worst case model for scavenging and the loss of fresh charge. However, an engine where charge simply short-circuits through the cylinder without displacing or mixing with the burnt gas could have poorer scavenging and higher short-circuiting than the perfect mixing model. Thus the perfect mixing model is not a firm lower bound. However, modern engines typically outperform this model and, therefore, it is commonly suggested as a lower bound [22:124, 197]. The assumptions of the perfect mixing model are as follows:

- 1) The cylinder walls are adiabatic.
- 2) The fresh charge and burnt gas may be modelled as ideal gases and have identical molecular weights and specific heats.
- 3) Cylinder volume is constant. Since gas exchange occurs within about  $80^\circ$  CA of BC, this is an approximation.
- 4) Cylinder pressure is constant. With both ports open, this is a reasonable approximation.
- 5) The charge leaving the cylinder and the cylinder contents are instantaneously homogenous.
- 6) The fresh charge and the cylinder contents at the end of gas exchange (subscript '1') may have different compositions and temperatures ( $T$ ).

With these assumptions, the charging efficiency, scavenging efficiency, and exhaust gas purity are given by Equations (79), (80), and (81), respectively.

$$\eta_{ch} = \frac{T_i}{T_1} \eta_{sc} \quad (79)$$

$$\eta_{sc} = \frac{T_1}{T_i} [1 - \exp(-\Lambda)] \quad (80)$$

$$\beta = \eta_{sc} \quad (81)$$

Both the perfect displacement and perfect mixing models may be further simplified by assuming that they are isothermal. In this case, temperatures and densities are the same in the fresh charge and burnt gas, and the temperature and density ratios in Equations (76) to (80) reduce to unity. In both the form presented above and the isothermal form, the perfect displacement model is considered a two zone model, while the perfect mixing model is only a single zone model. Neither model contains an empirical parameter for tuning to actual engine performance. Early on, this was recognized as a shortcoming of the models, eventually relegating their use to bounding engine performance.

#### 5.3.1.2. Maekawa and Other Notable Models

By the late 1950s, the limitations of the perfect displacement and perfect mixing models spurred researchers to develop multizone models. Heywood and Sher [22] credit Maekawa [198] with the first multizone model. Like the perfect mixing model, Maekawa's model occurs at constant pressure and volume, where the burnt gas and the fresh charge have the same density and specific heat. However, Maekawa introduces three different zones into the cylinder as shown in Figure 37, reprinted from Heywood and Sher [22:127]. The fresh charge zone represents gas that enters and remains in the cylinder. The mixing zone represents the loss of fresh charge that mixes with the burnt gas and exits into the exhaust. A third fraction represents fresh charge that simply short-circuits. The model is adjusted to experimental data using two parameters: one that splits the fresh charge into

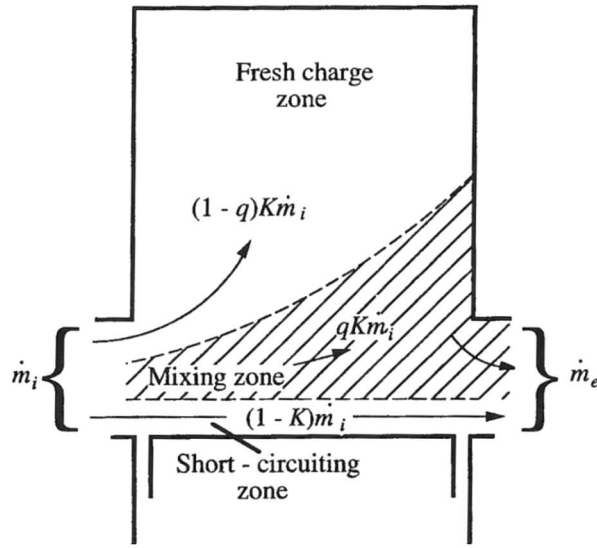


**Figure 37: The three zones of the Maekawa scavenging model, reprinted from Heywood and Sher [22:127] with permission from Taylor & Francis Ltd.**

pure and mixing zones ( $q$ ) and one that controls the amount of fuel that short-circuits ( $K$ ).

Mathematically, the model is shown in Equations (82) to (85) [22:128-29].

$$\eta_{ch} = \begin{cases} K(1-q)\Lambda + [1 - K(1-q)\Lambda]\eta_m & \text{for } \Lambda < [K(1-q)]^{-1} \\ 1.0 & \text{for } \Lambda \geq [K(1-q)]^{-1} \end{cases} \quad (82)$$

$$\eta_{sc} = \eta_{ch} \quad (83)$$

$$\beta = \begin{cases} (1-K) + K\eta_m & \text{for } \Lambda < [K(1-q)]^{-1} \\ 1.0 & \text{for } \Lambda \geq [K(1-q)]^{-1} \end{cases} \quad (84)$$

$$\eta_m = q \left\{ 1 - \exp \left( \frac{-K\Lambda}{1 - K(1-q)\Lambda} \right) \right\} \quad (85)$$

As suggested by the combination of fresh charge and mixing zones, Maekawa's model can predict scavenging and charging efficiencies between the perfect displacement and perfect mixing models. Additionally, the short-circuiting parameter can be used to predict higher losses than the perfect mixing model. The model often fails, however, to qualitatively capture the behavior of the exhaust purity [22:128-29]. Numerous other



researchers have developed variations on the model. Benson and Brandham developed a three zone model similar to that of Maekawa, replacing the fresh charge zone with a burnt gas zone [199]. The model was adapted for an opposed piston engine by Wallace and Cave [200]. Benson [201] also proposed a model where the gas exchange process occurs in three phases. The model requires a step-wise solution of four differential equations and up to five empirical constants, making it somewhat impractical.

### 5.3.1.3. S-curve and Crest Models

The S-curve model is a semi-empirical model developed by Sher [202] that is a compromise between the perfect displacement and perfect mixing models. Based on data, the model assumes that the exhaust gas purity may be approximated with a sigmoid curve using empirical factors ( $C_1, C_2$ ) to fit the curve to actual engine data. A parameter ( $\tau$ ) tracks the progress of the gas exchange process using the difference between crank angle ( $\theta$ ) and the scavenge port open ( $\theta_{so}$ ) and close ( $\theta_{sc}$ ) angles. The model is summarized in Equations (86) to (88).

$$\beta = 1 - \exp(-C_1 \Lambda \tau^{C_2}) \quad (86)$$

$$\text{where: } \tau = \frac{\theta - \theta_{so}}{\theta_{sc} - \theta_{so}}$$

$$\eta_{ch} = \Lambda - \int_0^\tau \frac{\beta \frac{d\Lambda}{d\tau}}{\beta + (1 - \beta) \left(\frac{T_b}{T_i}\right)} d\tau \quad (87)$$

$$\eta_{sc} = \left(\frac{T_1}{T_i}\right) \eta_{ch} \quad (88)$$

When  $C_1 = 0$ , the S-curve model reduces to the perfect displacement model. If  $C_1 = 1$  and  $C_2 = 0$ , then one may recover the perfect isothermal mixing model. In the limit

as  $C_1 \rightarrow \infty$ , pure short-circuiting occurs. For cross, loop, and uniflow scavenged two-stroke engines, Sher [202] suggests  $C_1 = 1.7$  and  $C_2 = 2.0$ . While the model is superior to prior models, it has a small defect as the exhaust gas profile approaches its maximum value. The S-curve model misses a crest in the purity profile a little over halfway through the scavenging process. This protrusion is the result of short-circuiting at BC followed by back flow from the exhaust into the engine. Sher and Harari [203] suggest a correction to the S-curve model, called the Crest model to correct the hump. The form of the correction presented by Sher and Harari [203] is shown in Equation (89) where  $C_1$  controls the strength of mixing and  $C_2$  controls the short-circuiting. The model was evaluated for a Schnürle scavenged engine; Sher and Harari [203] suggest  $C_1 = 0.57$  and  $C_3/C_{3,max} = 0.81$ . Experimental data is required to tune the model to the size and type of engine.

$$\beta = \eta_{sc}^{(1-C_1)/C_2}$$

$$\text{where: } C_2 = C_3 \tau' \frac{d\Lambda}{d\tau'} \quad (89)$$

$$\text{and: } \tau' = \frac{\theta_{sc} - \theta_{so}}{2\pi N}$$

### 5.3.2. Gas Exchange Measurements

There are multiple approaches to experimentally investigating the gas exchange process. The approach selected is a direct consequence of the challenge(s) the researcher is attempting to tackle. If the goal is to determine how changing the ports alters engine performance, than a method investigating flow in the transfer channels is most appropriate. For improving combustion in the cylinder, a method that images in-cylinder velocity makes the most sense. When the goal is to understand and quantify how much fresh charge is lost to short-circuiting as well as how much chemical enthalpy is in the exhaust due to

incomplete combustion, a direct measurement of the exhaust is most appropriate. This section reviews several methods applicable to motored and fired engines, focusing on the methods most applicable to the short-circuiting quantification in this effort.

#### **5.3.2.1. Measurement in Motored Engines**

There are two types of motored engine tests: static and dynamic. In a static test, the piston is fixed in place with the transfer and exhaust ports open, and air is blown through the engine. Jante [204] is credited with the first static test in which he removed the head of the engine, introduced fresh air to the engine using an external blower, and measured the velocity at the plane of the cylinder head using a rake of pitot probes. By moving the rake across the top of the cylinder, he generated a flow profile in the plane of the cylinder head. The presence of the cylinder head has a substantial impact on flow within the cylinder, and static tests may be performed even when the cylinder head remains in place. Fleck *et al.* [205] used static tests on a 125 cm<sup>3</sup> displacement engine to determine the effects of varying the port geometry. By blowing gas through the engine at a constant rate, they were able to quantify the discharge coefficients of the ports and losses in the transfer channels. Despite some utility, static tests completely ignore the cyclic, unsteady nature of the scavenging process as well as the effect of the combustion process on the temperatures and pressures in the cylinder and crankcase.

Dynamic motored tests introduce the cyclic nature of the flow. In a dynamic test the engine is driven with an external motor, permitting a dynamic measurement of the flow field. Still, the tests fail to match the exact conditions of a fired engine as there is no heat release or chemical reactions and the pressures and temperatures are well below those in a fired engine. Depending on the phenomena to be studied, researchers may attempt a level

of dynamic similarity by matching a combination of the Reynolds, Prandtl, Eckert, Schmidt, Euler [22:78-79], and Lewis numbers to a fired engine as well as other fluid and boundary conditions.

Dynamic test methods permit visualization techniques that would not be possible on a fired engine. One example is Particle Image Velocimetry (PIV). In PIV, the flow is seeded with particles. The particles in a single plane are illuminated using a pulsed laser. By comparing images from two closely spaced pulses, the velocity of each particle may be determined and developed into a flow field in the illuminated plane [56:299]. Ghandi and Martin [206] used PIV to map flow seeded with  $\text{TiO}_2$  in the clearance volume of a 309  $\text{cm}^3$  displacement Kohler K309-1T engine, as well as a Mercury Marine single cylinder research engine. Additional examples of the use of PIV for engines are discussed by Zhao and Ladommatos [56:298-332]. Seeding the flow in a fired engine as well as providing sufficient optical access is incredibly difficult, typically restricting the use of PIV to motored tests.

Another method to aid in visualizing the flow is the use of a liquid in lieu of a gas. Most liquids are about three orders of magnitude denser than air, allowing the engine speed to be slowed by a similar factor while maintaining Reynolds number similarity. As liquids may not be compressed as gases, the engine must be altered to expel the liquid during compression or the test must be run at constant volume. Running the liquid test at constant volume is consistent with the criteria for a static test, although Heywood and Sher [22:79-80] categorize it as a dynamic test. Liquid tests often employ dyes or PH indicators as a visualization aid. A good example of a liquid test was conducted by Sanborn *et al.* [207]. They compared liquid flow visualization to the Jante method as well as to data from the

fired engines. The results indicated that while the Jante and liquid similarity methods do not provide quantitative accuracy, the methods can differentiate between the flow patterns in well and poorly scavenged arrangements, allowing the qualitative prediction of fired performance from static and dynamic measurements.

A special type of dynamic gas test is the single cycle test. In a single cycle test, two different gases are utilized, one to represent the fresh charge and another to represent the burnt charge. Sweeny *et al.* [208] documented such an experiment, where CO<sub>2</sub> was used as the fresh charge and air was used as the burnt gas (providing a density ratio of 1.6, similar to a fired engine). Sweeny *et al.* noted that both their quiescent test and that of Sanborn *et al.* [207] failed to capture the turbulent effects induced by the high speed piston motion and gas exchange process in a fired engine. Thus, while motored tests can provide insight into engine function and allow for a parametric evaluation of certain design variables, a precise quantification of fresh charge losses to the exhaust necessitates a direct measurement of a fired engine.

#### **5.3.2.2. Measurement in Fired Engines**

There are two options for gas exchange measurements in fired engines: visualization through optical access and measurement of the cylinder gases. Depending on the methodology selected, the available options for measurement equipment will change. This section briefly mentions Laser Doppler Velocimetry (LDV), a possible visualization technique. It then explains how gas sampling may be used to determine gas composition and in turn scavenging. Finally, it discusses techniques for actually measuring the gas composition.

#### **5.3.2.2.1. *Fired Visualization Methods:***

If optical access is available, then gas exchange measurements may be taken using a technique such as LDV. In LDV the Doppler (frequency) shift caused when light emitted by a laser encounters a particle in a flow field is measured to determine the particle's velocity. LDV has two substantial drawbacks in a fired engine. First, it requires optical access to the cylinder. Secondly, it only maps one point at a time [56:268], which is insufficient for the complex three-dimensional nature of modern two-stroke engines.

#### **5.3.2.2.2. *Tracer Gas Methods***

A simpler approach is to measure the composition of the cylinder gases directly. Such a measurement can either be performed on a single cycle or on a time averaged basis. In either case, most researchers opt to use a form of a tracer gas method. A tracer gas must meet one of the following criteria:

- 1) It must be present in the fresh charge in a known quantity and completely destroyed (or in a known ratio) during the combustion process.

OR

It must be absent (or relatively negligible) in the fresh charge and created during combustion in a ratio proportional to the amount of fresh charge trapped in the cylinder.

- 2) The tracer must be stable outside of the combustion environment.

The simplest choice of tracer gas during rich combustion is oxygen. Present in the fresh charge in a known quantity ( $[O_2]_{fc}$ ) (roughly 21% for atmospheric conditions), in a rich mixture all of the oxygen trapped in the cylinder will be consumed during combustion. Then all oxygen in the exhaust will be from the short-circuited charge. Measuring the mole

fraction of oxygen in the exhaust ( $y_{O_2,ex}$ ) allows the calculation of trapping efficiency as in Equation (90), provided the molecular mass of the fresh charge ( $MW_{fc}$ ) and exhaust ( $MW_{ex}$ ) may be estimated or calculated.

$$\eta_{tr} = 1 - \frac{y_{O_2,ex} MW_{fc}}{y_{O_2,fc} MW_{ex}} \quad (90)$$

If the molecular weight of the fresh charge and exhaust gases are approximately equal then Equation (90) reduces to Equation (91), as described by Heywood and Sher [22:90].

$$\eta_{tr} = 1 - \frac{y_{O_2,ex}}{y_{O_2,fc}} \quad (91)$$

If the fuel and air flow rates as well as the engine speed are measured, then the delivery ratio may be calculated, and trapping efficiency and delivery ratio may be used to determine charging efficiency. However, knowledge of the burnt gas temperature when the exhaust port opens is required to obtain the scavenging efficiency [22:91] as shown in Equation (92). The trapping efficiency alone is sufficient to determine chemical enthalpy losses from short-circuiting, so the scavenging efficiency is not inherently necessary to quantify short-circuiting losses.

$$\eta_{sc} = \frac{\eta_{ch}}{c_r} = \frac{\Lambda \eta_{tr}}{c_r} \quad (92)$$

$$\text{where: } c_r = \frac{p_b}{p_0} \frac{V_b}{V_d} \frac{T_0}{T_b}$$

During lean combustion, oxygen will be present in the exhaust both from short-circuited charge, and from unconsumed oxygen. In lean cases, CO<sub>2</sub> may be used as a tracer if the mixture is sufficiently lean that incomplete combustion may be assumed. The analysis for scavenging efficiency from lean combustion is somewhat more complicated. As seen in Figure 38, reprinted from Heywood and Sher [22:93], knowledge of the unburnt

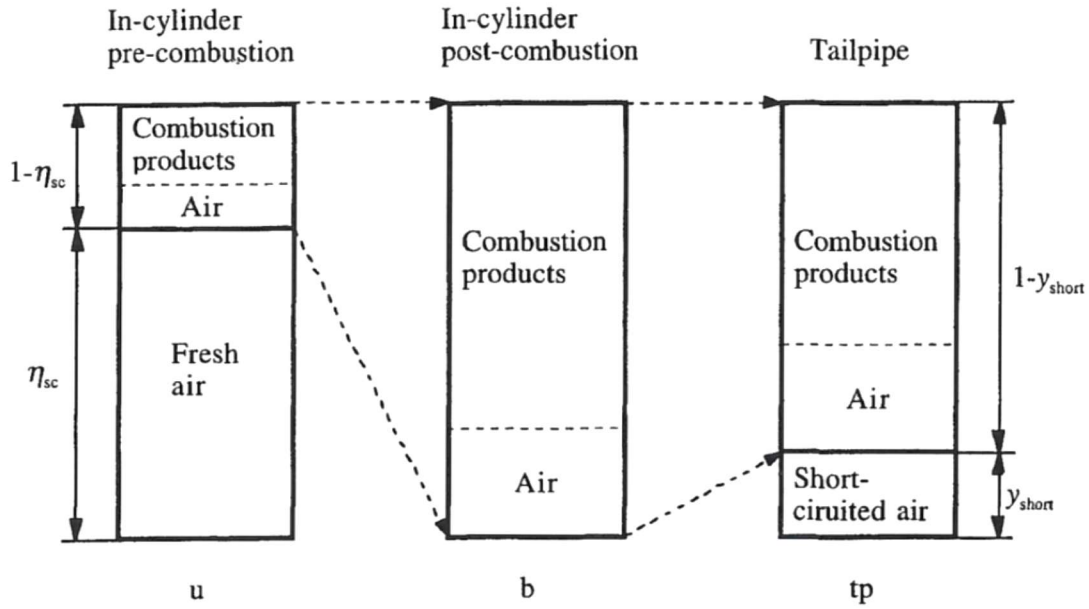


**Figure 38: Tracking of gases during scavenging. The dotted lines denote a control volume. Figure reprinted from Heywood and Sher [22:93] with permission from Taylor & Francis Ltd.**

gas composition (subscript ‘*u*’) when the exhaust port closes and opens (subscript ‘*b*’) is required in addition to knowledge of the fresh charge and the exhaust (subscript ‘*tp*’). In this case the scavenging efficiency may be calculated directly as shown in Equation (93), where subscript ‘*a*’ denotes ambient conditions [22:93]. Temperature and composition information are required in order to find the trapping efficiency as well as the actual chemical enthalpy losses from short-circuiting fresh fuel. Thus, a tracer method is generally faster for determining chemical losses in the exhaust.

$$\eta_{sc} = \frac{y_{CO_2,b} - y_{CO_2,u}}{y_{CO_2,b} - y_{CO_2,a}} \quad (93)$$

Researchers have tested a number of tracers and sampling techniques, and Table 11 adapted and augmented from Heywood and Sher [22:89-90] lists a number of them. In most cases, the easiest technique is to add a hydrocarbon, such as monomethylamine, to



the fresh charge or use oxygen under rich conditions. Equations (90) and (91) are valid for any tracer present in the fresh fuel but destroyed during combustion. To that end, some sources do not consider  $O_2$  a tracer gas, even though its categorization as such is mathematically consistent. In principle, even the raw fuel could be used as a tracer. However, hydrocarbon fuels are typically a mix of hundreds of different compounds, and the ratio of those compounds varies from refinery to refinery [87], making such an approach impractical. When a fuel consisting of only known chemicals, such as a PRF blend of iso-octane and n-heptane, is used, then the fuel may function as the tracer. (Even for rich mixtures, the iso-octane and n-heptane will partially combust to smaller hydrocarbons, essentially destroying the original fuel trapped in the cylinder during combustion.)

The method of sampling the exhaust gases depends on whether the scavenging measurements are to be resolved by cycle or as a multiple cycle average. The gas exchange process exhibits substantial cyclic variation that many investigators such as Foudray [197], Tobis *et al.* [209], and Gegg [210] sought to resolve. To resolve gas exchange on a cycle by cycle basis or to sample pre and post combustion gases in-cylinder, high speed electromagnetic [210, 211] or poppet [209] valves must be employed to extract the sample at the appropriate time. If an averaged performance result is acceptable, then the exhaust may be sampled downstream of the exhaust port where the mixture is homogenous. The tracer must be resistant to reaction at exhaust conditions [212], and to that end carbon monoxide is a poor choice as it continues to react in the exhaust. Interestingly Olsen *et al.* [212] also indicate that monomethylamine, while a historical tracer gas of choice, decomposes significantly at exhaust conditions and that  $N_2O$  may be a more stable tracer.

**Table 11: Tracer Gas Methods, Adapted and Augmented  
from Heywood and Sher [22:89-90]**

Investigators	Year	Citation	Tracer	Method
Schweitzer & De Luca	1942	[213]	CH <sub>3</sub> NH <sub>2</sub>	Sample the exhaust gas and measure the tracer concentration.
Taylor and Rogowski	1954	[214]	CH <sub>3</sub> NH <sub>2</sub>	Sample the exhaust gas and measure the tracer concentration.
Hori	1962/63	[215, 216]	n/a	Measure in-cylinder CO <sub>2</sub> before and after the scavenging process
Bazika & Rodig	1963	[217]	CO	Continuous measurement of tracer in exhaust gas
Miyabe & Shimomura	1963	[218]	O <sub>2</sub> /CO <sub>2</sub>	Sample the exhaust gases and measure unburnt O <sub>2</sub> for rich conditions and CO <sub>2</sub> for lean conditions.
Isigami et al	1962/69	[219, 220]	CH <sub>3</sub> NH <sub>2</sub>	Sample the exhaust gas and measure the tracer concentration.
Oggero	1968	[221]	CO <sub>2</sub>	Sample lean exhaust gas after exhaust port opens and measure CO <sub>2</sub>
Ohigashi & Hamamoto	1971	[222]	O <sub>2</sub>	Sample cylinder gases before and after exhaust port opens and closes and measure O <sub>2</sub> .
Huber	1971	[223]	C <sub>4</sub> H <sub>10</sub>	Continuous measurement of tracer in exhaust gas
			O <sub>2</sub>	Continuous measurement of tracer in exhaust gas
Wallace & Cave	1971	[200]	CO	Continuous measurement of tracer in exhaust gas
Blair et al	1976/80	[207, 224]	CO <sub>2</sub>	Sample lean exhaust gas after exhaust port opens and measure CO <sub>2</sub>
Hashimoto et al	1985	[225]	O <sub>2</sub> /CO <sub>2</sub>	Sample the exhaust gases and measure unburnt O <sub>2</sub> for rich conditions and CO <sub>2</sub> for lean conditions.
Nuti & Martorano	1985	[226]		Full analysis of exhaust gas contents
Sata et al	1992	[227]	O <sub>2</sub>	Continuous measurement of tracer in exhaust gas
Tobis et al	1994	[209]	CO <sub>2</sub>	Sample cylinder contents and measure CO <sub>2</sub>
Murayama et al	1996	[228]	UHC	Sample the exhaust gas and quantify hydrocarbons.
Foudray et al	2002	[197]	O <sub>2</sub> /CO <sub>2</sub>	High speed sampling of in-cylinder gases.
Olsen et al	2002	[212, 229]	N <sub>2</sub> O/ CH <sub>3</sub> NH <sub>2</sub>	Sample the exhaust for the tracer gases.

#### **5.3.2.2.3. *Measuring Exhaust Gas Composition***

The challenge of quantifying the exhaust gas composition of an engine is that no single technique is capable of measuring each of the components. Modern exhaust benches typically use a combination of three methods to measure exhaust gas composition: a Nondispersive Infrared (NDIR) sensor to measure CO and CO<sub>2</sub>, a chemiluminescence sensor to measure NO<sub>x</sub> and SO<sub>x</sub>, and a Flame Ionization Detector (FID) to measure the unburned hydrocarbons [197, 230, 231]. Other common techniques are Fourier Transform Infrared (FTIR) spectroscopy, gas chromatography (GC), and mass spectrometry (MS).

The combination of techniques selected depends heavily on what compounds are to be identified and quantified. For example, when measuring CO and CO<sub>2</sub> emissions, an NDIR sensor will identify the compounds more easily than GC will separate them from air. If the goal is to quantify an unburnt fuel consisting of two similar hydrocarbons such as iso-octane and n-heptane, GC can separate and distinguish between the compounds, whereas a flame ionization detector (FID) cannot. Many emissions standards, such as those enforced by the California Air Resource Board [232] and the Federal Clean Air Act [233] are focused on limiting the total NO<sub>x</sub>, SO<sub>x</sub>, and UHC emissions (to include CO). This explains why many exhaust test facilities are equipped with NDIR sensors, FID, and electrochemical sensors as described above. In the case where specific compounds in the fuel are of interest, for example to make a scavenging measurement, a more targeted approach such as GC-MS may be warranted. This section will cover the most common options for exhaust composition sensing including NDIR sensors, electrochemical sensors, FID, and GC-MS. FTIR spectroscopy was covered in Section 5.1.3.2.1.

#### 5.3.2.2.3.1. *Infrared Spectroscopy Methods (NDIR and FTIR Spectroscopy)*

Both NDIR sensors and FTIR spectroscopy are absorption spectroscopy techniques. Absorption spectroscopy (specifically FTIR spectroscopy) was already discussed in Section 5.1.3.2 in the context of in-cylinder temperature measurements. To briefly review, absorption spectroscopy operates on the principle that a given molecule will absorb certain frequencies of light based on its molecular structure and temperature, and that absorption can be used identify and quantify the species. There are also emission spectroscopy techniques where the line emissions of the molecules, which are well-defined functions of temperature and molecular structure, may be used to identify and quantify gas composition. ICE exhaust temperatures are often too low for emissive spectroscopy to be feasible, and absorption methods are more appropriate.

In NDIR sensors, the exhaust gas flows through a cuvette with an IR emitter on one end and a detector on the opposite end. The IR source is tuned for a specific molecule or chemical bond. The attenuation of the IR signal is measured by a detector and used to calculate the concentration of the molecule. Again, the relationship between the attenuation of the light and the molecular concentration is governed by the Beer-Lambert law [168]. One common tuning molecule for NDIR sensors is  $C_3H_8$ . In the case of propane, the measurement focuses on the carbon hydrogen bond and is useful for quantifying unburned hydrocarbons [234]. NDIR sensors may also be tuned to measure CO and  $CO_2$  [230, 231]. Figure 35 [180] shows the infrared absorption band of  $CO_2$ . The IR light for measuring  $CO_2$  absorption might be tuned to  $4,200\ \mu m$  to coincide with the peak at  $2400\ cm^{-1}$  wavenumber. In infrared spectroscopy, the wavenumber is simply the inverse of the wavelength. NDIR sensors often employ both a sample chamber and a

reference chamber, and modern setups use a beam splitter or deflector to use the same light source for the sample and reference cells [56:40].

NDIR sensors cannot distinguish between two molecules with overlapping absorption bands, such as CO and CO<sub>2</sub>, unless an optical filter is used [56:40]. When two compounds overlap in the targeted band, the absorption, and thus concentration measurement represents the total concentration for both molecules. That measurement will be in error if the sensor was tuned using only one of the molecules or if it was tuned for a different concentration of the pairing. For example, the NDIR sensors used by ENERAC are tuned to propane for hydrocarbon detection [234]. However, other hydrocarbons such as methane, ethane, butane, and so forth will interfere with the propane band. Thus the concentration of UHCs is reported as a concentration of UHCs “as propane”. While an NDIR sensor is an industry standard for UHC measurement in vehicle emissions [235], it cannot provide the necessary exhaust measurements to quantify scavenging.

Where NDIR sensors only target specific portions of the mid-infrared spectrum, FTIR spectroscopy can capture the entire mid-infrared spectrum. (For a more extensive description, the reader is referred back to Section 5.1.3.2.1). Compared to NDIR sensors, which must split the light using a grating or a prism to resolve multiple wavelengths, FTIR spectroscopy is faster for sampling multiple wavelengths and higher spectral resolutions [236]. As discussed previously, the length of the wavenumber domain is controlled by the distance the mirror traverses, and the resolution is controlled by the number of samples taken to construct the interferogram.

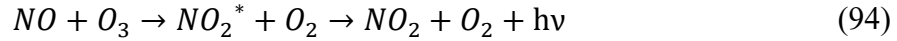
FTIR spectroscopy is commonly used for online measurements of vehicle emissions and catalytic converter catalyst performance. An early example is the work of Lowry *et*

*al.* [237], who determined that FTIR spectroscopy meets the requirements for measuring exhaust emissions during vehicle driving tests, and that the instrument was relatively immune to noise and vibration from test cell conditions. Shore and deVries [179] used FTIR spectroscopy to measure ethene, propene, ethyne, and formaldehyde in the exhaust of a 2.3 L displacement engine. The relatively fast sampling rate of the FTIR spectrometer (about a second per spectra), allowed Shore and deVries to track the 93 second warm up of the catalyst to operating conditions and the effect of the warmup period on conversion of UHCs in the exhaust. Daham *et al.* [238] took the concept of online measurement a step further and installed an FTIR spectrometer in a vehicle to measure actual road emissions performance. They found that the FTIR spectroscopy measurements collected in the vehicle were within 10% of the laboratory setup under steady state conditions. Despite these successes, some chemicals, especially trace pollutants such as NO<sub>x</sub>, are easier to quantify using chemical type detectors, such as chemiluminescence detectors.

#### 5.3.2.2.3.2. *Chemiluminescence Detector*

Both NO<sub>x</sub> and SO<sub>x</sub> are usually quantified using chemical detectors. SO<sub>x</sub> is primarily a concern in diesel fuel due to the refining process, and thus its emissions are difficult to control using the engine. NO<sub>x</sub> meanwhile is formed during combustion, especially in slightly lean environments where high temperatures and excess oxygen create favorable conditions for the Zeldovich (thermal) mechanism [70:168-171]. The formation of NO<sub>x</sub> is an issue in ICEs regardless of fuel (unless fuel causes excessively low combustion temperatures). NO<sub>x</sub> detectors make use of two chemical reactions. To detect NO, the device bombards the molecule with ozone to form NO<sub>2</sub>\*. When the NO<sub>2</sub>\* returns to its ground state, it emits a photon. The entire reaction chain is shown in Equation (94). At a

constant temperature, the emitted light is a linear function of NO concentration [56:40]. N<sub>2</sub>O in the exhaust is measured by converting it to NO with a catalyst and then applying the aforementioned technique.



#### 5.3.2.2.3.3. *Flame Ionization Detector*

An FID is a simple way to determine the hydrocarbon content of an exhaust gas and is a common component of many exhaust test benches [230, 231]. In simple terms, an FID functions as a carbon atom counter. The exhaust gas is combusted in a hydrogen air diffusion flame, as shown in Figure 39, reprinted from Zhao and Ladommatos [56:114]. As the result, the fuel is split into positively and negative charged ions [56:114], which are collected at the cathode and anode of the detector, respectively. The ions generate a voltage at the detector ( $V$ ), which is proportional to the number of hydrocarbon molecules ( $[HC]$ ),

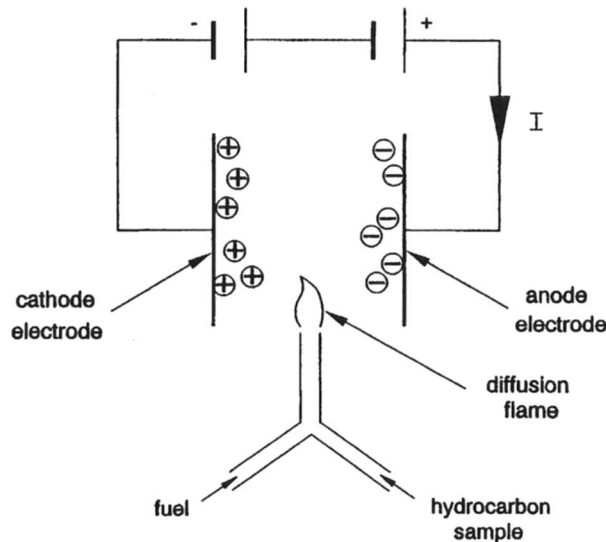


**Figure 39: Operation schematic of an FID, from Zhao and Ladommatos [56:114], reprinted with permission from SAE International.**

the number of carbon atoms in the molecule ( $C_{\#}$ ), and most critically, the sensitivity of the type of hydrocarbon ( $N_{HC}$ ), as in Equation (95).

$$I\alpha[HC]C_{\#}N_{HC} \quad (95)$$

Generally speaking, the response of a given hydrocarbon is proportional to the number of carbon atoms. For example, if methane has  $N = 1$ , propane would have  $N = 3$ . It seems it would then be simple to calibrate such a detector. However, the voltage response is a function of the molecular structure, and two molecules with the same number of carbon atoms could have different responses. Consider propane, propene, and propyne, all of which have three carbon atoms. Alkenes have about 0.95 the response of alkanes [56:118], so propene would have an  $N = 2.85$  instead of 3. Alkynes, meanwhile, have a response 1.3 times that of alkanes [56:118], giving propyne  $N = 3.9$ . For known mixtures or a standard, an FID may be calibrated with samples of known composition. Often they are calibrated to either ppm methane or ppm propane. Thus, FID, like FTIR and NDIR spectroscopy will struggle to separate different types of hydrocarbons.

#### 5.3.2.2.3.4. *Gas Chromatography (and Mass Spectrometry, FID, and TCD)*

So far all methods discussed (FID, FTIR spectroscopy, NDIR sensors) are detection methods. They take the sample and determine, to the best of the method's ability to resolve different compounds, how much of what is present. Gas chromatography (of which GC-MS is one type) offers a solution to the problem of compounds that yield similar signals. Figure 40, from the University of Colorado - Boulder [239], shows the basic layout of a GC-MS unit. GC-MS operates in two steps. First, the sample is injected into the column of the gas chromatograph using a sampling valve or a needle and septum. The sample travels through the column (usually about 30 meters long and 250-320  $\mu\text{m}$  in diameter).



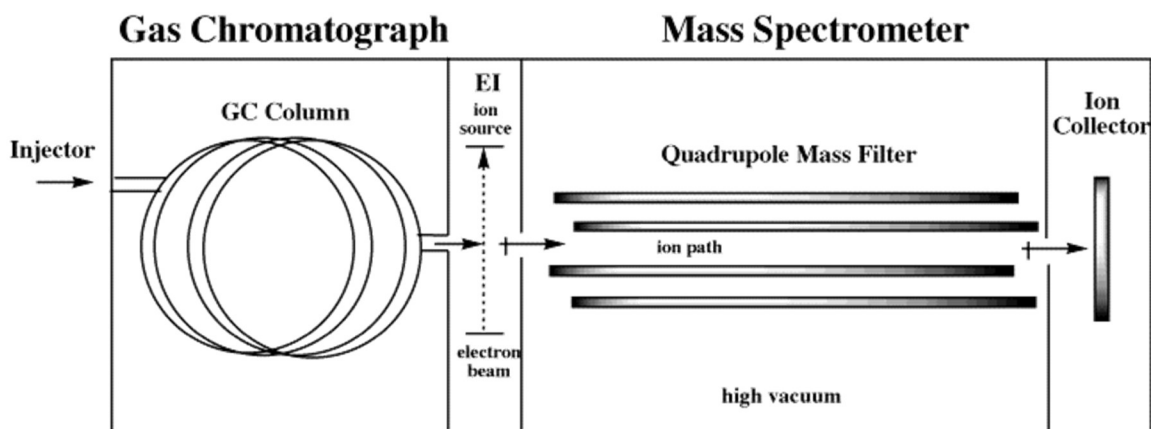


**Figure 40: Schematic of a GC-MSD system for emissions measurements, reprinted with permission from the University of Colorado - Boulder [239].**

The sample is carried by a carrier gas, typically helium, argon, nitrogen, or in newer models, hydrogen. The column interior is coated with a substrate, forming a distillation column. Thus the column separates the molecules by size and affinity for the column. The column is contained in an oven, and temperature adjustment as well as carrier gas flow rate determine the separation between similar compounds. The compounds elute from the GC, separated by size and affinity.

Separating and resolving the compounds of interest is a function of the column type. Agilent's HP-5MS thin film column is a non-polar column made with (5%-phenyl)-methylpolysiloxane that excels at separating compounds heavier than C<sub>6</sub>. Meanwhile the Molsieve column excels at separating permanent gases, specifically Ar, O<sub>2</sub>, CO, NO, H<sub>2</sub> and N<sub>2</sub> [240]. Even with the right column, some separations will remain difficult. For example, isomers are difficult to separate in GC. Figure 41 shows a sample gas chromatogram of ICE exhaust gas produced using the Agilent 7890 GC chromatograph at AFRL on an HP-5MS column. The first peak contains O<sub>2</sub>, H<sub>2</sub>O, Ar, CO, and CO<sub>2</sub>, showing how the column fails to resolve permanent gases. The other two peaks are iso-octane

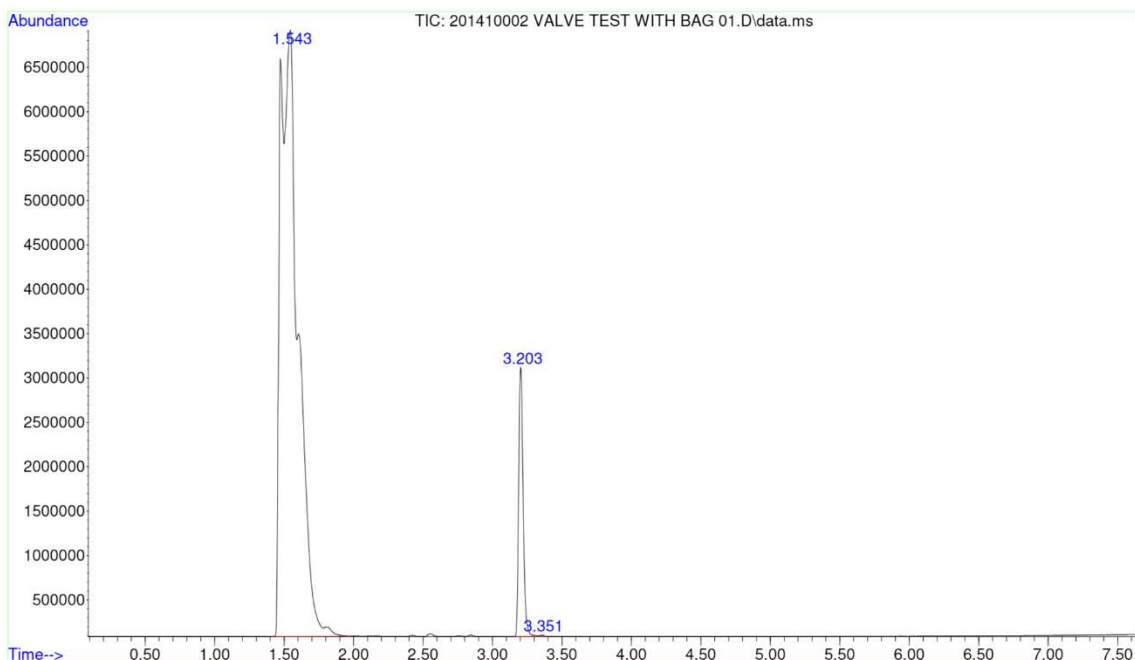


**Figure 41: Raw gas chromatogram using HP-5ms column to separate exhaust gas from a small two-stroke, gasoline engine. Time is in minutes and abundance is molecular counts at the mass selective detector.**

(3.202 minutes) and n-heptane (3.351 minutes) from the raw fuel, showing that the column can separate these similarly sized compounds. Peak identification was carried out using MS, which will be discussed shortly. The critical metric for GC is called the Trenn Zahl number, shown in Equation (96) [241]. The Trenn Zahl number is the ratio of the difference in retention times of two sequentially eluting compounds to the difference in the peak half widths. Qualitatively, it represents how well the peaks are separated. The larger the TZ number, the better the separation.

$$TZ = \frac{t_{n+1} - t_n}{W_{n+1} - W_1} - 1 \quad (96)$$

Gas chromatography is, by itself, only a separation method. It still requires a device to identify and quantify the compounds. Any of the detectors (except Chemiluminescence) mentioned previously would suffice although coupling NDIR and FTIR spectroscopy to

GC systems is uncommon in ICE literature. FID, meanwhile, is a common choice. Since elution time from the column may be used to identify a compound (assuming the column has been run against a standard), FID can then be used to determine the amount of each compound in the sample. As early as 1958, Hurn *et al.* [242] published a report to the Society of Automotive Engineers detailing the high potential for GC techniques to improve vehicle emissions measurements. In 1967, Papa [243] had applied GC-FID to measure hydrocarbon emissions as low as parts per billion. The total run times were about 30 minutes, long compared to sampling rates on the order of one second for FTIR spectroscopy and NDIR spectroscopy. The run time is driven by the travel time of the heaviest compounds through the GC column.

The reduction of run time and maximization of the number of quantified species is a primary challenge. Rudlein *et al.* [244] utilized cryogenic traps, column switching, and two different parallel columns to separate C<sub>2</sub>-C<sub>12</sub> compounds in ICE exhaust in less than 35 minutes. Otsuki *et al.* [241] took this one step further using four parallel columns and ovens to separate and identify C<sub>2</sub>-C<sub>12</sub> compounds in about five minutes. Each column and oven targeted a specific range of compounds: C<sub>2</sub>-C<sub>5</sub>, C<sub>5</sub>-C<sub>7</sub>, C<sub>7</sub>-C<sub>8</sub>, and C<sub>8</sub>-C<sub>12</sub>. Compounds lighter than the column target eluted in a single, early peak. Heavier compounds were back flushed from the column. Landen and Perez [245] utilized GC-FID for a CI engine to quantify the reactivity of the exhaust gases by burning the gases in an FID. The FID response provided an indication of the chemical enthalpy lost to the exhaust. The information was ultimately used for pollution control since reactive hydrocarbons form air pollutants when emitted to the atmosphere. Arning *et al.* [246] applied both GC-FID and fast acting sampling valves to track cylinder gas composition in an HCCI engine. By

analyzing light (C4 and smaller) and heavy (C5 and larger) hydrocarbons they determined that combustion phasing is heavily dependent on the pilot fuel volume, which in turn controls exothermic combustion propagation reactions.

Similar to an FID, GC units may also be coupled to a thermal conductivity detector (TCD) or a Helium Ionization Detector (HID). A TCD works similar to a hot wire anemometer. The device compares the rate of heat loss of the carrier gas (reference) to the sample [226]. The difference in the rate of heat loss (thermal conductivity) can be correlated to the concentration of a known sample during calibration. An HID works by using a low voltage arc to ionize helium atoms, typically from the carrier gas. When the helium atoms return to the ground state they emit a photon with sufficient energy to ionize any molecule with an ionization potential below 17.7 eV [247]. This photon ionizes the molecules in the sample, and the ionized molecules are electrically attracted to a detector. Thus, like the FID, the TCD and HID offer no ability to identify the sample. Identification must be performed by calibration of GC elution time with known gases.

Mass spectrometry offers a solution for positively identifying compounds. When combined with a GC, MS is typically called a mass selective detector (MSD). Returning to Figure 40, the compounds flow from the GC to the MSD in the order of elution. The MSD uses a high voltage electric field to create a beam of electrons at the source. The electrons fragment the molecules into ions of varying mass. The ions are then trapped by the quadrapole. The quadrapole is a three axis rotating magnetic field that traps the ions based on their cyclotron frequency, which is linearly related to mass to charge ratio. By varying the field, the quadrapole releases ions based on mass/charge ratio to the detector, where they are quantified. By scanning over a range from about 10 to 500 AMU/e<sup>-</sup>, the

detector quantifies all of the molecular fragments. Each scan takes about 0.5 seconds. A scatter pattern for iso-octane is shown in Figure 42, using data from NIST [248]. The scatter pattern for each peak in the chromatogram in Figure 42 may be compared to a library to identify the compound. As in FTIR spectroscopy, it can be difficult to distinguish similar molecules such as isomers. The fraction of a compound is directly related to the peak area on the chromatogram, and that relation may be determined by calibrating the device with samples of known composition.

Despite the expense and system size, GC-MSD is gaining popularity in ICE emissions testing because of its ability to identify unknown compounds. Elghawi *et al.* [249] applied GC-MSD to the exhaust of both an SI and an HCCI engine. They found that HCCI combustion did not produce 1,3-butadiene, a carcinogenic compound found in SI engine exhaust. They also found that C6-C12 compounds (unburnt fuel) contributed about 19%

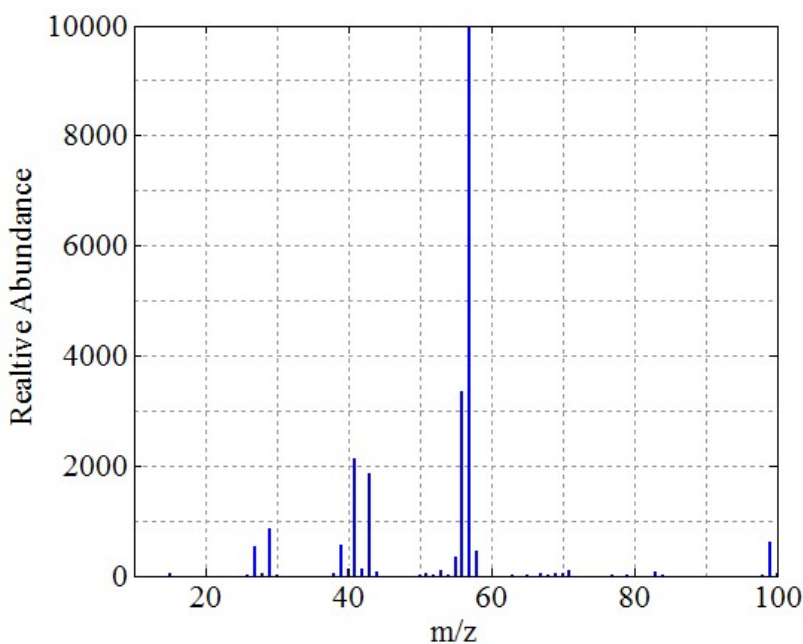


**Figure 42: Electron ionization mass spectrum of iso-octane (2,2,4 tri methyl pentane), data from the National Institute of Standards and Technology [248].**

more to UHCs in HCCI combustion than in SI combustion. Farrguia and Olson [250] demonstrated that a ‘fast’ GC method using multiple columns agrees within 10% of a standard single column method. Olson *et al.* [251] then applied the ‘fast’ GC technique to CI engine exhaust to identify 160 organic, ozone forming compounds in the exhaust of an automotive ICE. The technique provides a faster avenue to determine if a vehicle meets ever more stringent emission regulations.

### **5.3.3. Summary of Gas Exchange**

From the standpoint of this effort, there are three concerns associated with gas exchange. First, it is necessary to determine how much fresh charge is lost to short-circuiting to quantify that loss pathway and to disentangle its effects from the scaling of other losses. Second, exhaust gas composition is a required quantity to determine the sensible and chemical enthalpy lost to the exhaust, separate from the raw fuel. Third, identifying an appropriate gas exchange model for small ICEs could aid in the development of future propulsion systems.

## **5.4. Review of Objective 2: Models for Small Engines**

Validated correlations and models for heat transfer and friction losses in small ICEs were sparse to non-existent in the literature. Instead, most studies of small ICEs to date had adapted and applied correlations developed for larger engines, often without validation [2, 11, 16, 108, 135]. Objective 2 aimed to develop and validate models for overall heat transfer and friction losses for small COTS two-stroke spark-ignition engines using the data collected as part of the loss scaling study in Objective 1. Section 5 has reviewed models and measurements techniques for heat losses (Section 5.1) and friction losses (Section 5.2). As mentioned in the introduction of Section 5, a scaling study on scavenging

models would require a parametric investigation of engine port design, which is beyond the scope of this work. However, an understanding of scavenging and short-circuiting losses is necessary to disentangle those pathways from the other losses, to quantify those losses, and to complete Objective 1. Furthermore, exhaust measurements are necessary to quantify the sensible and chemical enthalpy in the exhaust gases, also considered as part of Objective 1. Therefore, Section 5.3 provided an overview of scavenging models and measurement techniques. Ultimately, the heat transfer and friction models provide mathematical insight into how those losses scale with engine size and valuable tools for designing RPA propulsion systems.

## **6. Operation on Heavy Fuel**

As mentioned in Chapter I, Section 1.3 and Chapter II, Section 3.6.2 there are both benefits and obstacles to running a small engine on a low AKI (heavy) fuel. The goal of Objective 3 was to determine if the mechanisms driving the losses in Objective 1 inherently reduce (or may be leveraged to reduce) the fuel AKI requirement in small engines. Furthermore, this objective sought to quantify if an improvement in performance is possible, specifically a reduction in fuel consumption, when switching from manufacturer recommended 98 ON fuel to heavy (20 ON) fuel such as JP-8 or diesel. This section is split into five parts. The first (Section 6.1) reviews the benefits and obstacles to heavy fuel conversion of a small SI engine. The next three subsections (Sections 6.2, 6.3, and 6.4) summarize heavy fuel conversions documented in the literature that address one or more of the obstacles and/or benefits. Those subsections are ordered chronologically. The efforts performed at AFRL and described in Section 3.6.2 will not be rehashed in this section. The final subsection (Section 6.5) provides a review of the goals of Objective 3.

## 6.1. Heavy Fuel Conversion: Benefits and Obstacles

There are two benefits to converting small COTS engines to run on heavy fuel, one known and one theoretical. The definitive benefit is allowing small RPAs to operate on a standard battlefield fuel as specified in DoD Directive 4140.25 [12]. The theoretical benefit is that a lower AKI fuel may also reduce fuel consumption and improve efficiency. Wilson *et al.* [14] concluded that n-heptane (a low AKI fuel) decreased fuel consumption by an average of 4.1% across the operating range of a 34 cm<sup>3</sup> Fuji engine. This benefit is theoretical because there is conflicting research. For example, Cathcart *et al.* [15] observed a 5-50% increase (depending on operating condition) in fuel consumption running JP-5 (heavy fuel) in a 50 cm<sup>3</sup> two-stroke engine.

Based on Wilson *et al.*'s [14] results a performance benefit may be realized and is worth pursuing for the following reasons. First, Wilson [43:49] demonstrated that the low AKI nature of the fuel reduced the flame development time (CA0-CA10 burn angle). This reduction resulted in a narrower and higher pressure peak. Variable spark timing could then permit this peak pressure to be positioned near 16°aTDC to maximize engine power. In Cathcart *et al.* [15] spark timing was retarded away from this optimum to combat abnormal combustion, dropping peak power by 5%-15% across the wide open throttle (WOT) speed range. The losses already inherent to small engines should help to combat knock, relaxing the engine's AKI requirement and realizing higher power output from reducing the CA0-CA10 burn angle in combination with advanced spark timing.

There are several challenges to operating an engine on a low AKI fuel and they may be grouped into three categories. The first is creating a vaporized fuel and a well-mixed air fuel mixture. Creating a viable mixture, especially during starting is difficult due to the



low volatility of heavy fuels such as JP-8, diesel, and kerosene, relative to regular gasoline. This challenge is almost universally attacked using a fuel injection system [14, 15, 38, 41, 43, 103, 252]. The second issue is that the lubricity of JP-8 differs from both gasoline and from glow fuel [11:64]. For two-stroke engines with pre-mix oil, this challenge may be solved by adjusting the amount of oil added to the fuel. The third challenge and the focus of this work is abnormal combustion due to the low AKI nature of heavy fuels. How engine losses affect the AKI requirement and the potential for conversion was the focus of Objective 3.

## **6.2. Early Efforts (1970-2000)**

Studies of kerosene in SI engines date back to at least the 1970s. In 1974 Tankaria and Ghosh [46] reported that peak power from kerosene was lower than gasoline when used in air carbureted engines. They also concluded that an air carbureted system may not provide sufficient atomization to mix kerosene sufficiently for efficient combustion. In 1984 Gupta and Ganesan [47] published a paper detailing similar results.

As early as 1990 there was DoD interest in heavy fuel conversions for small military aircraft. Lawton [253] authored a proposal for the U.S. Navy to develop a 37.5-56.25 kW heavy fuel engine for use on naval RPAs. Three contracts were awarded: two for rotary engines and one for a two-stroke engine. It is unclear if any of the engines were tested. However, the proposal does highlight the need for DoD driven technology development of small ICEs when COTS parts cannot fulfill mission requirements.

In 1991, Suhy *et al.* [42] investigated the feasibility of converting a 390 cm<sup>3</sup> displacement Mercury Marine two-stroke engine to run on heavy fuel. Similar to the engines considered in this effort, the engine had a trapped compression ratio of 7.57, reed

valve induction, and Schnürle loop scavenging. Suhy *et al.* [42] addressed poor vaporization of the heavy fuel in the carburetor by equipping the engine with a vortex atomizer. Preheating was required to start the engine and Suhy *et al.* [42] state, “a cold spark ignited engine with either a carburetor or fuel injection [system] will not start on kerosene. Presumably insufficient vapor is available.” The engine was run at 9 different operating conditions and knock was evident at medium throttle and WOT settings. However, the data show that kerosene produced higher IMEP than gasoline and reduced the burn time by 8° CA at low throttle and about 30° CA at medium throttle when the atomizer was used (under non-knocking conditions). Using the carburetor, gasoline and kerosene exhibited comparable burn times for a given throttle setting, indicating that mixing and fuel preparation was critical for heavy fuel operation. At WOT kerosene showed 60%-80% higher SFC because of the retardation of spark timing required to combat knock. For conditions where the kerosene spark timing could be maintained, the specific fuel consumption of gasoline and kerosene were comparable. Suhy *et al.* [42] concluded the major challenges to heavy fuel conversion were knock limitations and preheat requirements.

### **6.3. Turn of the Millennium (2000-2010)**

By 2005, Orbital Engineering [45] had developed an air assisted direct injection system, called the FlexDI® system. The system used high pressure air to inject fuel directly into the cylinder of a two-stroke engine. Orbital Engineering [45] claimed that the use of air in the injection process improved the atomization of the fuel, increasing the number of droplets by a factor of 50 and the droplet surface area by a factor of 3.5. Cathcart *et al.* [15] investigated the use of Orbital Engineering’s FlexDI® system on three two-

stroke engines with 50 cm<sup>3</sup>, 625 cm<sup>3</sup>, and 700 cm<sup>3</sup> displaced volumes to enable the use of heavy fuel in aircraft spark-ignition engines. Orbital's FlexDI® system attempted to enable heavy fuel operation through better mixture and phasing control coupled with variable spark timing. The air-injection system excelled at creating a combustible mixture even with low volatility JP-5. In fact, the atomization was too effective, and it actually increased the tendency for the engine to knock. To compensate, Cathcart *et al.* [15] retarded spark timing. As a result, JP-5 delivered 5-15% lower output torque across the WOT operating range. The lower power output caused gasoline to outperform JP-5 and kerosene from a fuel consumption standpoint. As shown in Figure 43, reprinted from Cathcart *et al.* [15], the DI system outperformed the stock carburetor at almost all speeds. However, gasoline in the FlexDI® system outperformed both JP-8 and kerosene at essentially all operating conditions, supporting the conclusion that the improvement in fuel consumption is related more to the use of a DI system than to the type of fuel, at least in this instance.

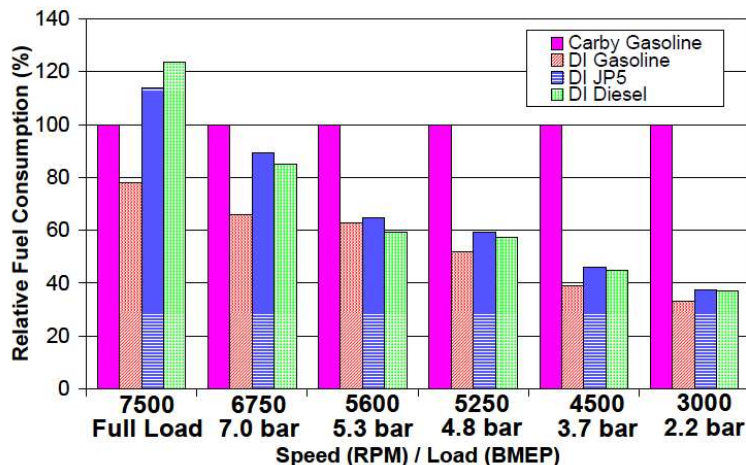


**Figure 43: Fuel consumption for the FlexDI® system compared to the stock carburetor on a 50 cm<sup>3</sup> two-stroke engine, reprinted from Cathcart *et al.* [15] with permission from SAE International.**

Cathcart *et al.* [15] observed a number of other problems during the conversions. First, the heavy fuel engine variants ran hotter. In a duration test they observed piston seizure in less than 10 hours of operation. The seizure was the result of the low volatility of the JP-5 and kerosene with air assisted direct injection, the combination of which resulted in inadequate deposition of two-stroke oil in the engine. Cathcart *et al.* [15] also noticed significant spark plug fouling from rich operation. It is likely that the carbon build up causing the fouling was partially due to the injector's orientation relative to the spark plug (fuel droplets on the spark plug). In spite of these limitations, Orbital Engineering's website [45] claims there is at least one military RPA powered by their system. The RPA is a modified Aerosonde vehicle, produced by Textron. It runs a 3 kW heavy fuel engine with Orbital Engineering's FlexDI® system and produces 300 W of power for payloads [254].

The U.S. Army also has an interest in heavy fuel powered engines for portable generator sets. The benefits of a converted SI engine as opposed to a CI engine for a generator set are similar to an aircraft; compression-ignition engines that use heavy fuel have historically been unappealing due to low power to weight ratios, trouble with cold start, noise, vibration, and incompatibility with gasoline [15]. To that end, in 2006 Cordon *et al.* [255] studied the use of catalytic plasma torch ignition to convert a Honda EU1000i generator to run on JP-8. The stock generator contains a 50 cm<sup>3</sup> displacements four-stroke SI engine and produces 0.9 kW continuous power and 1 kW of surge power [256]. The catalytic plasma torch ignition system was similar to a glow-plug. The torch could be electrically heated to help start the engine and the surface was plated with a noble metal to catalyze combustion even when the plug was not powered during operation. The torch also

contained a small volume filled during the gas exchange process. When this small volume of mixture ignited, its expansion projected it into the cylinder at high velocity, similar to the turbulent jet igniter described in Attard *et al.* [257].

Before conversion the Honda generator was about 17.8% efficient at its full power of 900 W and 7.6% efficient at 1/4 power, based on manufacturer data [256]. After conversion to JP-8, the generator only produced 500 W without constant electrical heating of the torch and 700 W if the torch was continuously powered. The converted system's efficiency ranged from 3%-14% depending on load. Performance on JP-8 degraded significantly with fuel temperature and by -10°C, performance was unreliable. Atomization and mixture preparation provided by the stock carburetor proved highly sensitive to needle setting. As a result of the previous observations, Cordon *et al.* [255] recommended preheating the fuel and better mixture preparation through a fuel injection system in future iterations.

#### **6.4. Expanding Interest in Heavy Fuel Conversion (2011-Present)**

While the previous efforts have begun with gasoline engines, in 2011 Wiegand [11] attempted the conversion of an 11.5 cm<sup>3</sup> displacement glow fuel engine to JP-8. Glow fuel engines already operate on compression-ignition but receive significant lubrication and cooling from components in the fuel (castor oil for lubrication and nitro methanol for evaporative cooling). Controlling combustion phasing to create a reliable system was the biggest hurdle. According to the Wiegand [11:5], "The ignition process in a micro engine can be initiated by heat from the compression process, the heat supplied by a filament style glow plug, or a catalytic reaction of methanol with the platinum coating applied to the glow

plug. None of these processes can be intelligently controlled.” Arguably this hurdle was not overcome as COV values upwards of 40% were observed at some conditions [11:60].

Lubricating the glow fuel engine running on JP-8 also proved difficult. Glow fuel typically contains 20% castor oil, so Wiegand attempted to match the lubricity of glow fuel by adding oil to JP-8. Since there were no published lubricity standards for glow fuel, Wiegand [11:64-66] used comparative testing as outlined in ASTM D6078 [258] and ASTM D6079 [259]. The testing demonstrated that 20% by volume of Techniplate oil (a JP-8 compatible oil) was required to match the lubricity of glow fuel [11:64-66].

Heating was required to start the modified engine and Wiegand [11:64-82] compared a number of different methods including heating the crankcase, warming the external fuel and air charge, ceramic coatings inside the cylinder, and heaters on the cylinder head. Direct heating of the head caused warping of some components [11:67] and ceramic coatings seemed to have little effect on starting times [11:69]. Heating the intake air successfully decreased the starting time by a minute to two and a half minutes [11:69]. Crankcase heating was also attempted but found to be energy intensive, requiring 68 MJ of energy over a 30 minute period [11:81]. There were also issues with unreliable mixture preparation in the stock carburetor and overheating the engine while running on JP-8. Pitting and high temperature thermal damage were observed on the piston crown, an indication that knock was occurring at some operating conditions [11:67-68]. From analysis of in-cylinder data, JP-8 was slower to ignite in the engine resulting in longer burn angles, later combustion phasing, and lower energy density than glow fuel [11:106-108].

In a manner similar to Cathcart *et al.*'s [15] test of the FlexDI® system, in 2011 Duddy *et al.* [38] tested a system manufactured by SONEX [103] to convert 15-30 kW SI engines

to JP-8 for use on unmanned platforms. The SONEX system managed heat losses from the engine, increasing the thermal mass of the engine head to provide additional energy to vaporize incoming fuel. The SONEX system replaced the stock aluminum cylinder head with the SONEX combustion system, which was a machined cylinder head with a steel insert. The steel insert held more heat than the aluminum head and thus helped to rapidly vaporize the heavy fuel [103]. The head was shaped to induce swirl when used in conjunction with a fuel injection system. The modified head also included a glow plug to preheat the head before starting the engine.

Duddy *et al.* [38] claimed that IMEP was unchanged between the stock and modified engines and that cylinder head temperature actually decreased when operating on JP-8. However, plots included in the paper [38] indicate that the 30 kW engine only developed 70% of rated power when operating on JP-8. Duddy *et al.* [38] also claimed that knock did not occur in the engine, although there was no explanation of the procedure implemented to detect knock. In a related effort, Lee *et al.* [260] investigated the lubrication issues raised by converting the engine to run on JP-8. They determined that for an SI gasoline two-stroke engine using premixed oil, about 2% two-stroke oil by volume was required to provide sufficient lubricity when running on JP-8 [260]. That amount of oil was comparable to the amount required when running on gasoline.

As of December 2014, SONEX had a website [103] documenting their 2004-2008 combustion system development, including design and testing notes. According to SONEX, the system used the engine's stock carburetor or fuel injectors, intake and exhaust system, spark system, and compression ratio. The system was capable of reducing fuel consumption by 18%-28% at cruise conditions, but one should bear in mind that this was

relative to an air carbureted setup. Thus much of the improvement may actually have been through the use of DI. The system was tested by Insitu on the Scan Eagle, which was powered by a 3W-28i engine, and in January 2007 the plane completed a world record 28 hour, 44 minute endurance flight burning 28% less fuel than the stock configuration. Despite this success, as of December 2014 the Scan Eagle was not currently using the SONEX system on the deployed platform.

In addition to SONEX and Orbital Engineering, as of the writing of this document there were at least three companies working on heavy fuel capable engines. Currawong Engineering [41] (Power4Flight [261] in the United States) manufactured equipment for heavy fuel conversions in small RPA engines. Their approach focused on custom fuel injectors designed for the low flow rate of small engines as well as small, lightweight fuel pumps (as well as custom ECU solutions). Their injectors were modified Siemens Deka 60LB 630 cm<sup>3</sup> High Impedance Fuel Injectors (48 mm) with flow plates adapted for the lower fuel flow rates required small engines less than ~85 cm<sup>3</sup> displacement. For reference, the smallest commercially mass produced injectors at the time were designed for 125 cm<sup>3</sup> to 250 cm<sup>3</sup> displacement scooter engines. The system also included a 3 bar (4 bar for heavy fuel) fuel pump, an ECU, and a custom ignition system. While running heavy fuel, fuel consumption was reduced by 5-10% on the 3W-28i engine. Power4Flight has also developed a 29 cm<sup>3</sup> displacement two-stroke engine based on the 3W-28i engine, and converted the engine to run on heavy fuel by installing throttle body fuel injection and a custom ECU. Their power and specific fuel consumption results are comparable to those presented in Chapter VI.



Hirth Motoren, a manufacturer of 30-300 cm<sup>3</sup> displacement two-stroke aircraft engines (their primary market was engines larger than 100 cm<sup>3</sup> total displacement or 18 kW-75 kW), debuted their heavy fuel system in 2014 [262]. Hirth approached heavy fuel conversion by redesigning the entire fuel delivery system. The new system, called iPower, uses a resonance tube to extract hot gases from the cylinder. Fuel is then injected into the resonance tube, and the gases are passed back into the cylinder after the ports close. Hirth claims the system leads to upwards of 40% fuel savings [263], mostly by reducing short-circuiting losses. Due to its design, the system has a high degree of exhaust gas recycle, which could negatively impact combustion efficiency and BMEP. However, the use of hot combustion gasses in the resonance tube improves vaporization of low volatility heavy fuels. The system requires substantial modification/ redesign of the engine and, as of the time of writing, was only available for Hirth Motoren engines.

3W Modellmotoren, the manufacturer of the family of engines proposed for this effort, opened a heavy fuel engine arm in 2013 [252], although internal efforts began at least in 2009. The engines were converted versions of their standard engines. The conversion added a second spark plug and a heater on the fuel system. The second spark plug added additional weight to the system as it required a second ignition module. The technical data showing the impact on engine performance was limited, and is shown in Figure 44 and Figure 45 [252]. This data is used in a comparison to manufacturer performance as part of Chapter IV, Section 2.2. As indicated in Figure 44, fuel consumption appears to be lower for the heavy fuel variant, but it was reported as fuel flow rate and not specific fuel consumption. No information on produced power was provided. Figure 45 does provide information on specific fuel consumption, and it appears the heavy fuel variant consumed

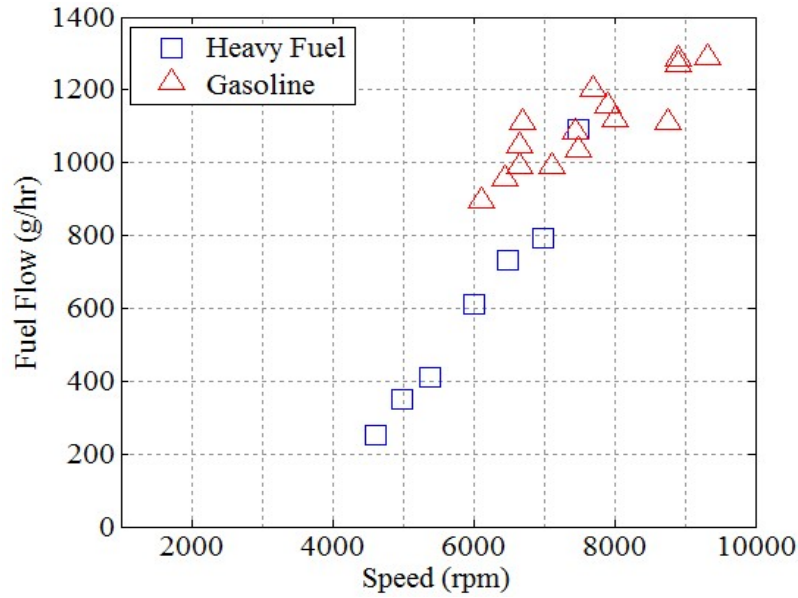


**Figure 44: Fuel consumption of a 3W-28i two-stroke engine converted from gasoline to heavy fuel, data from the 3W International website [252].**

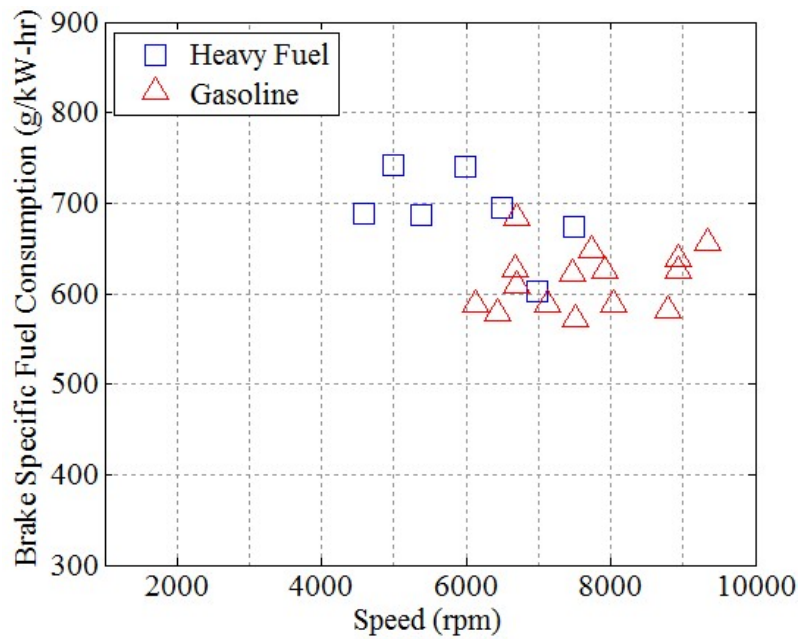


**Figure 45: Specific fuel consumption of a 3W-28i two-stroke engine converted from gasoline to heavy fuel, data from the 3W International website [252].**

an additional 50-100 g/kW-hr. In combination with Figure 44, this indicates the heavy fuel variant took an extreme power penalty, possibly to prevent knock.

### **6.5. Review of Objective 3: Relaxation of AKI Requirement with Engine Size**

The literature documented several attempts at heavy fuel conversion, but it lacked a systematic effort to examine how the losses and the underlying mechanisms in small engines affect their ability to run on heavy fuel and to determine if the increase in losses with decreasing engine size correlate to an inherent knock resistance. Furthermore, there was no conclusive study to indicate whether or not the conversion will actually decrease the fuel consumption of the engine and if so, how that will alter the power output. Objective 3 aimed to resolve these shortcomings by systematically investigating the fuel AKI requirements of the small engines studied in Objective 1.

### III Methodology

#### 1. Chapter Overview

As delineated in Chapter I, the research effort was split into three objectives. Objective 1 focused on the experimental evaluation of loss pathways and understanding how those losses and their driving mechanisms scale in practical 10-100 cm<sup>3</sup> displacement, COTS engines. Objective 2 was an evaluation of models and correlations for the heat transfer and friction loss pathways, informed using data collected during Objective 1. Objective 3 was an investigation into the AKI requirements in 10-100 cm<sup>3</sup> displacement engines. Completion of these objectives required a mixture of experiments and modelling. This chapter explains the methodology for those tasks.

The remainder of this chapter is broken into four sections. Section 2 describes the Small Engine Research Bench (SERB), at the AFRL's SERL. Constructed under the direction of the author, the SERB provided the capabilities necessary to control small engines and quantify their performance. The subsequent sections focus on each of the research objectives. Section 3 specifically describes the instrumentation necessary to make loss measurements to accomplish Objective 1. Section 4 discusses additional measurements and the models used as starting points for the study of heat transfer and friction losses. Section 5 explains how the fuel AKI requirement was determined in each engine to discern if there was an inherent relaxation in the fuel AKI requirement with decreasing engine size for Objective 3. Many aspects of the methodology have been documented in published papers (especially the instrumentation in Sections 2 and 3); an overview of those capabilities is provided here. The reader is then referred to the appropriate papers, included as Appendices, for additional details.

## 2. Facility: Small Engine Research Bench

This section describes the instrumentation and control systems of the SERB required for engine testing, but not installed specifically to support loss mechanism quantification, modelling, or heavy fuel operation. This includes the equipment to measure power, speed, fuel consumption, air consumption, and engine temperature as well as to control the engine fuel system, intake air system, and spark timing. The discussion is organized by subsystem; these subsystems are the drivetrain and dynamometer (Section 2.1), intake air system (Section 2.2), combustion analysis system (Section 2.3), engine control system (Section 2.4), and computer control and instrumentation systems (Section 2.5). Figure 46 shows the layout of the SERB. The layout of the SERB changed over the course of the

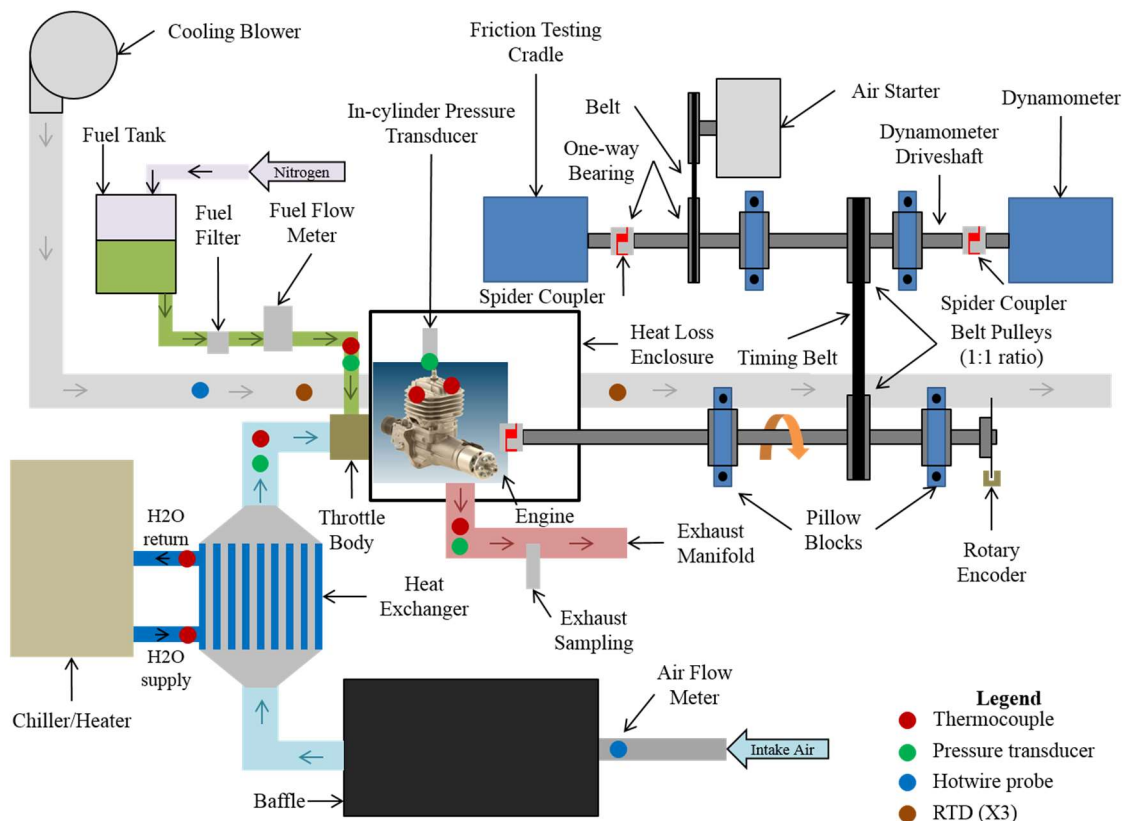


**Figure 46: Layout of Small Engine Research Bench as of April 2016 during data collection for Objectives 1, 2, & 3.**

research. The layout presented here is the most representative of data collection for Objectives 1, 2, and 3. In addition to the systems discussed in this section, Figure 46 also notes the location of the three systems that were used for loss measurements in Objective 1: the thermal loss enclosure (Section 3.2), the friction testing cradle (Section 3.3), and the exhaust sampling port (Section 3.4).

## 2.1. Drivetrain and Dynamometer System

The drivetrain and dynamometer system provided an adjustable load for the engine. The engine was coupled to the dynamometer by a drive train, which also linked the engine to a rotary encoder for precise crank angle position sensing, an air motor for starting, and a friction testing cradle. A photograph of the drive train is shown in Figure 47 and a simplified version of Figure 46 showing only the drive train components is shown in Figure 48. The dynamometer was a Magtrol brand, 2-WB-65 eddy current, water cooled dynamometer. It provided a continuous load of up to 12 kW and ran at speeds up to

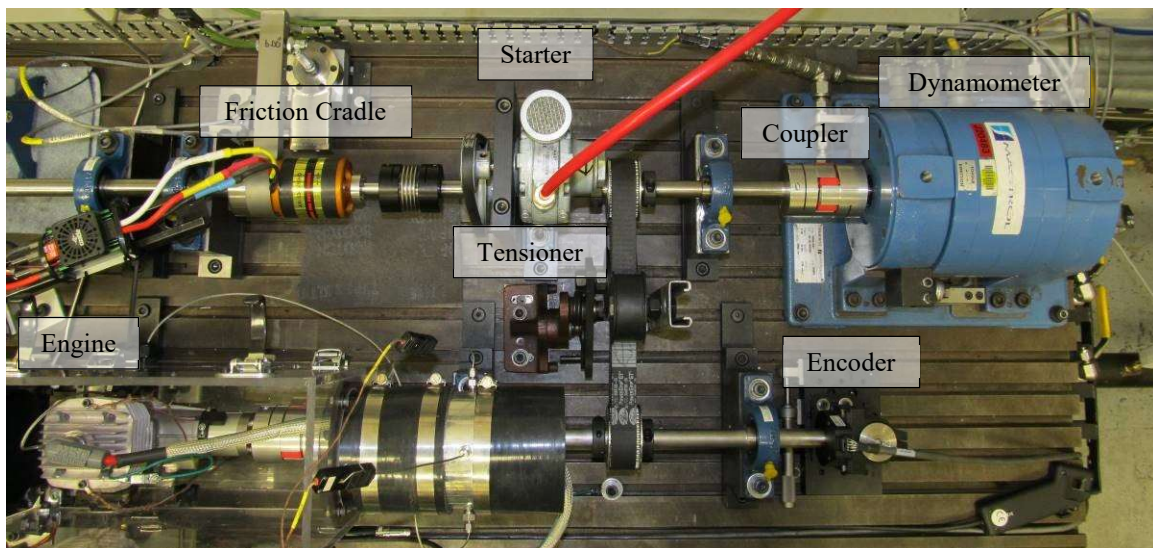


**Figure 47: Photograph of SERB drivetrain as of July 2015. The optics tower is not installed in this view.**

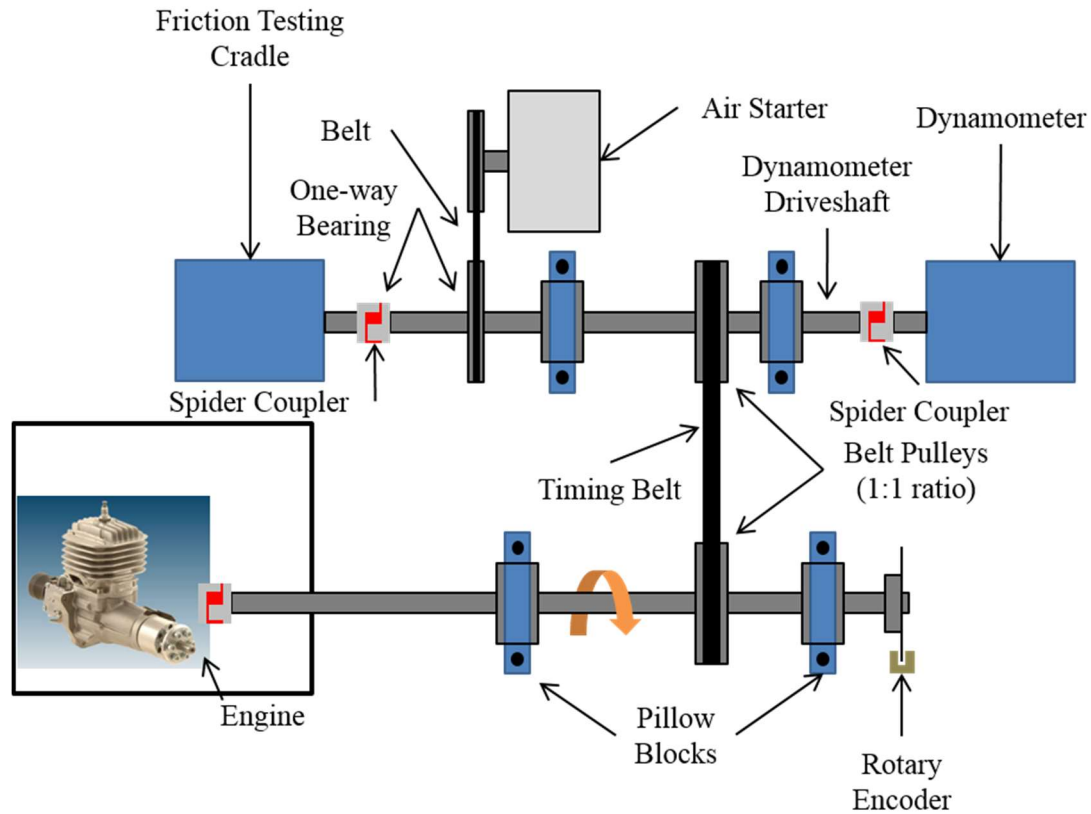


**Figure 48: Schematic of SERB drivetrain components.**

10,000 rpm, about 2,000 rpm above the manufacturer rated speed of the engines considered in this effort. The maximum torque rating of the dynamometer was 20 N-m, and the measurement accuracy on both speed and torque was  $\pm 0.5\%$  of full scale. The dynamometer was controlled using a Magtrol DSP6001 dynamometer controller with an inline TSC 401 torque and speed conditioner. The DSP6001 controller was linked directly to the data acquisition and control computer using a National Instruments (NI) General Purpose Interface Bus (GPIB). There were three data acquisition and control programs used on the SERB (described in Section 2.5); the program that controlled the dynamometer was the “low speed data acquisition and control” program (referred to as the “LSDAQ” in the remainder of the document). The LSDAQ allowed the user to set torque and speed set

points and to monitor and record torque and speed readings from the dynamometer. Figure 49 [264] depicts the connections between the dynamometer, dynamometer controller, signal conditioner, and LSDAQ.

The dynamometer and engine were connected to separate shafts to speed the alignment process when changing engines. Each shaft was supported by two ABEC-1 class bearings, press fit into pillow-blocks. The drive shafts were  $\frac{3}{4}$ " diameter, precision ground stainless steel and keyed to the power transmission pulleys with standard ANSI keys. The shafts were connected using a Power Grip G2 toothed belt, designed for high speed power transmission applications. The belt rode on two taper lock pulleys and was configured for 1:1 gearing between the engine and dynamometer. The belt was tensioned using a spring loaded tensioner on the return side of the belt and an idler pulley on the tension side of the belt. The engine was started using a GAST 2AM-NCW-7B lubricated air motor, which was connected to the drive train by a v-belt. The sprocket on the dynamometer shaft

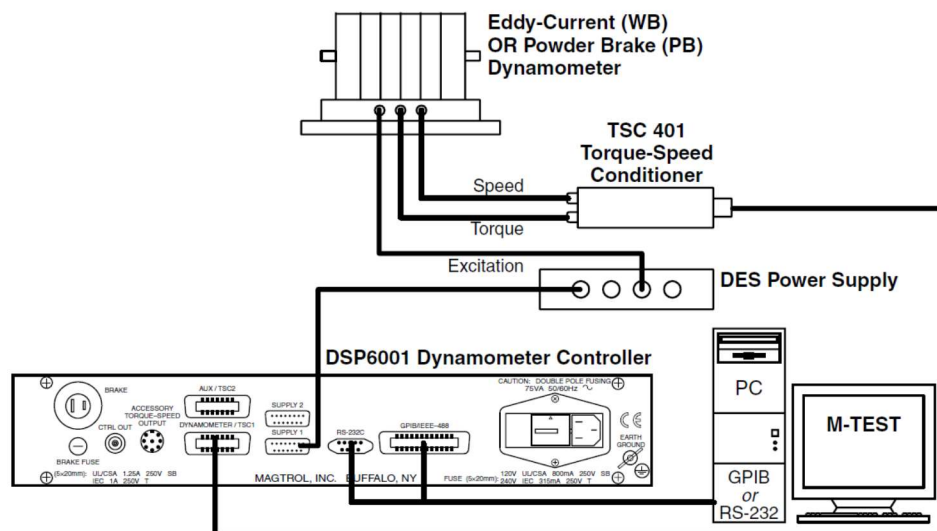


**Figure 49: Connection diagram for Magtrol Dynamometer system consisting of a 2 WB 65 Eddy Current Dynamometer, a DES 311 Power supply, a TSC401 Signal Conditioning Unit, and a DSP6001 High-Speed Dynamometer Controller [264].**



contained a clutch bearing, automatically disengaging the starter motor once the engine started. The shafts were connected to the engine and dynamometer using Ruland Jaw couplers and 98 Shore hardness polyurethane spiders.

During the testing in Horn *et al.* [122], the friction in the drivetrain was determined to be 78.8 W/krpm. Testing the configuration used in this effort yielded  $69.2 \pm 8.0$  W/krpm (discussed later in Section 3.3). This friction was added back to the power measured at the dynamometer to provide a more accurate value of the engine power produced at the output shaft. Additional information on the drivetrain components is available in Ausserer *et al.* [75], in Appendix D. Note that early versions of the drivetrain used Ruland bellows style couplers between the engine, dynamometer, and the drive train as well as a chain linkage between the starter motor and the drive train. These aspects were changed to improve reliability and performance; the older designs are only mentioned here for clarity when comparing the setup to previous versions. All data presented in this document including the friction results reported above are for the drive train as described in this section and in Ausserer *et al.* [75] in Appendix D.

## **2.2. Intake Air System**

The intake air system controlled the intake air temperature and measured flow rate, temperature, and pressure. A schematic of the system is shown in Figure 50 and a photograph of several of the key components is shown in Figure 51. Two different air flow measurement setups were used during testing. In the first setup, fresh air entered the system through a 2 in diameter pipe. Inside the pipe was an Omega Engineering FMA 902A-V1-S hot-wire mass velocity transmitter, capable of measuring 0-5.08 m/s of air flow and transmitting the measurement as 0-5 VDC analog signal. The transmitter had an accuracy

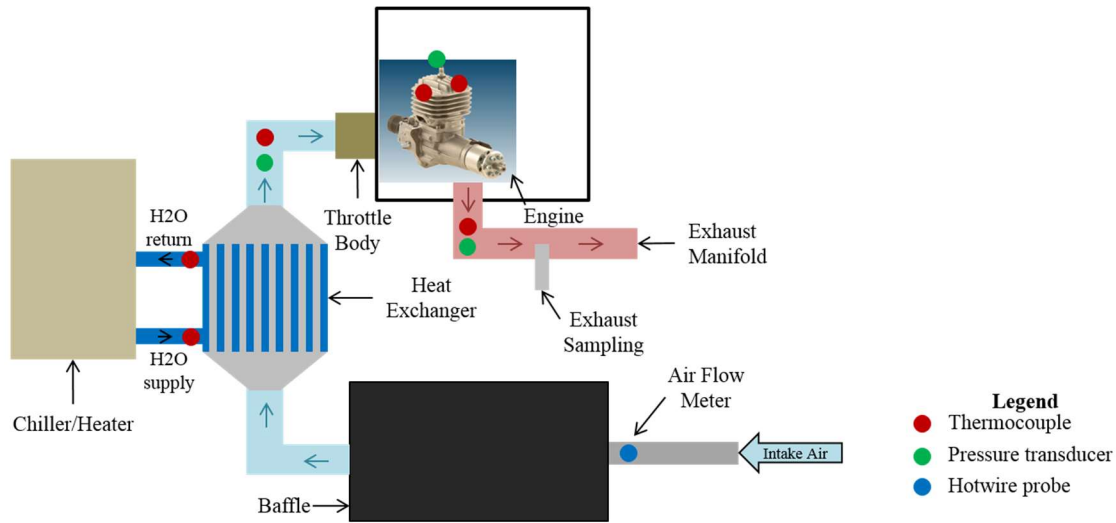


**Figure 50: Schematic of SERB intake air system components.**

of  $\pm 1.5\%$  of full scale plus  $\pm 0.5\%$  of the reading. The design of the transmitter automatically corrected the velocity measurement to reference conditions with a density of  $1.184 \text{ kg/m}^3$ . The transmitter was mounted along the centerline of the duct. The Reynolds number in the duct was  $O(10^4)$  indicating a turbulent flow. The volumetric flow rate through the duct was calculated by assuming a power law velocity profile [265:338-340] as shown in Equation (97). Integrating across the duct yields Equation (98). Çengel and Cimbala [265:340] indicate a power law exponent of  $n \approx 7 - 9$  is appropriate for most flows of air. A factor of  $n = 8$  was selected for this effort with an error of  $\pm 1\%$  in the volumetric flow rate measurement for values from 7-9. The air flow measurement was also verified using sonic nozzles. The second setup used three TSI 40211 High Performance Linear Mass Flow Meters in parallel, capable of measuring flow rates up to 300 SLPM (each) with an accuracy of  $\pm 2\%$  of the reading. The calibrations on these sensors were also verified using a sonic nozzle.

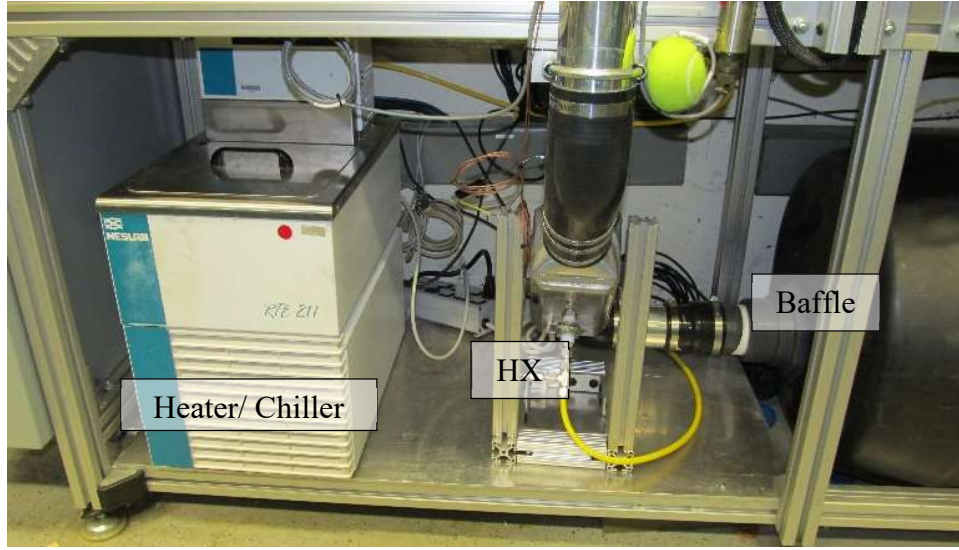


**Figure 51: Photograph of SERB showing the intake air system.**

$$\bar{V} = V_{max} \left( \frac{y}{R} \right)^{\frac{1}{n}} \quad (97)$$

$$\dot{V} = \frac{2\pi R^2}{2 + \frac{1}{n}} V_{max} \quad (98)$$

The air then entered a 55 gallon baffle, installed to damp flow oscillations propagating from the engine and to prevent them from reaching the mass velocity transmitters. The baffle was sized according to heuristics in Taylor [24:611]. The air then entered a heat exchanger. The water side of the heat exchanger was controlled using a Thermo Neslab RTE-211 recirculating water bath chiller. The chiller could heat up to 0.8 kW or cool up to 0.5 kW and was capable of holding intake air temperature to  $\pm 2^\circ\text{C}$ . After it exited the heat exchanger the temperature and pressure of the intake air were measured before entering the throttle body.

Unless otherwise noted, all thermocouples were Class 1, Type J, accurate to  $\pm 1.5^\circ\text{C}$  from  $-40$  to  $375^\circ\text{C}$  plus  $\pm 0.004^\circ\text{C}$  per degree over  $375^\circ\text{C}$ . All RTDs were Omega brand,

platinum class A RTDs accurate to  $\pm 0.15^{\circ}\text{C}$  plus  $\pm 0.002^{\circ}\text{C}$  per degree from  $-100^{\circ}\text{C}$ - $400^{\circ}\text{C}$ . All low speed pressure transducers were low bandwidth (maximum frequency of 2000 Hz) Honeywell TJE pressure transducers with an accuracy of  $\pm 0.1\%$  of their full range. These transducers were used to monitor constant and slowly changing pressures in the intake, exhaust, fuel lines, and ambient conditions. High speed pressure transducers are listed as part of the combustion analysis system in Section 2.3. A listing of the temperature measurement devices and low speed pressure transducers on the SERB (both expanded from Ausserer *et al.* [10], Appendix A) can be found in Table 12 and Table 13, respectively.

**Table 12: Listing of Temperature Measurement Names and Locations**

Name	Location
<b>Class I, Type J Thermocouples</b>	
Intake air	Upstream of carburetor, downstream of intake air heat exchanger
Exhaust gas	Exhaust pipe, 30 cm downstream of exhaust port
Cylinder Head	Top fin of engine head, one over exhaust port, one opposite exhaust port
Ambient	Beneath bed plate, left hand side facing bench
Intake baffle	In intake baffle
Intake heat exchanger water inlet	In water bath line, upstream of intake air heat exchanger
Intake heat exchanger water outlet	In water bath line, downstream of intake air heat exchanger
Fuel	Fuel line downstream of fuel flow meter
Dyno cooling water inlet	Inlet of dynamometer cooling water line
Dyno cooling water outlet	Outlet of dynamometer cooling water line
<b>Class A, Platinum RTDs</b>	
Cooling Air Inlet	Upstream of “heat loss enclosure”
Cooling Air Outlet	Downstream of “heat loss enclosure”

Exhaust gases were routed out of the engine to the laboratory exhaust system. Since the exhaust manifold exited the heat loss enclosure, exhaust thermal losses were accounted for separately from the thermal losses measured by the enclosure. Designed to match the

stock exhaust pipe sold with the engine, the exhaust manifold was not tuned. Based on data in Heywood and Sher [22:91], a gas sampling port was located approximately 0.5 m downstream of the engine, where the exhaust and short-circuited charge were spatially and temporally well mixed. The use of the port for sampling exhaust gases is described in Section 3.4. The exhaust manifold was indirectly coupled to the laboratory exhaust system, preventing the laboratory exhaust fan from pulling a vacuum on the exhaust port of the engine. The engine exhaust manifold had a 2 in diameter, the laboratory exhaust system had a 6 in diameter, and the gap between the two systems pulled air from the laboratory instead of pulling a vacuum on the engine (see Ausserer *et al.* [75] in Appendix D).

**Table 13: Pressure Measurements Installed on the SETB**

Name	Location	Range (kPa)
SEB01	Exhaust pipe 12 in downstream of exhaust port. Remotely mounted.	0-344.7
SEB02	Fuel line, downstream of flow meter.	0-344.7
SEB03	Ambient, mounted under bed plate.	0-103.4
SEB04	Intake manifold, tap upstream of throttle body. Remotely mounted.	0-103.4

### 2.3. Combustion Analysis System

The combustion analysis system facilitated the determination of IMEP, the detection of knock, and the calculation of combustion parameters such as MFB. The SERB operated using both flush mount and measuring spark plug transducers. The latter were preferable since measuring spark plugs did not require engine modifications. A more complete investigation of the tradeoffs between the two transducer types is available in Ausserer *et al.* [75], included in Appendix D. The measuring spark plug used for the SERB was a Kistler Type 6113B, which has a linearity of  $\pm 0.5\%$  of full scale and a sensitivity of  $\pm 1\%$

at  $200 \pm 50^\circ\text{C}$ . The flush mount transducer, which required an M5 port to be added to the engine, was a Kistler model 6052C high temperature pressure sensor with a linearity of  $\pm 0.3\%$  of full scale and a sensitivity of  $\pm 0.5\%$  at  $200 \pm 50^\circ\text{C}$ . The transducers as well as a stock spark plug are shown in Figure 52. Both in-cylinder pressure transducers were piezoelectric type devices, producing a charge proportional to the change in pressure. This charge signal was converted into an analog voltage signal using a Kistler SCP 2852A12 signal conditioning chassis fitted with a 5064C charge amplifier. The 5064C charge amplifier could process two signals concurrently, and thus both a flush mount and measuring spark plug could be run simultaneously.

To calculate parameters such as IMEP and MFB, the in-cylinder pressure signal was referenced to the crank angle position of the engine. A US Digital E6 style optical encoder was used to provide an 1800 counts per revolution signal, corresponding to  $0.2^\circ\text{CA}$  of

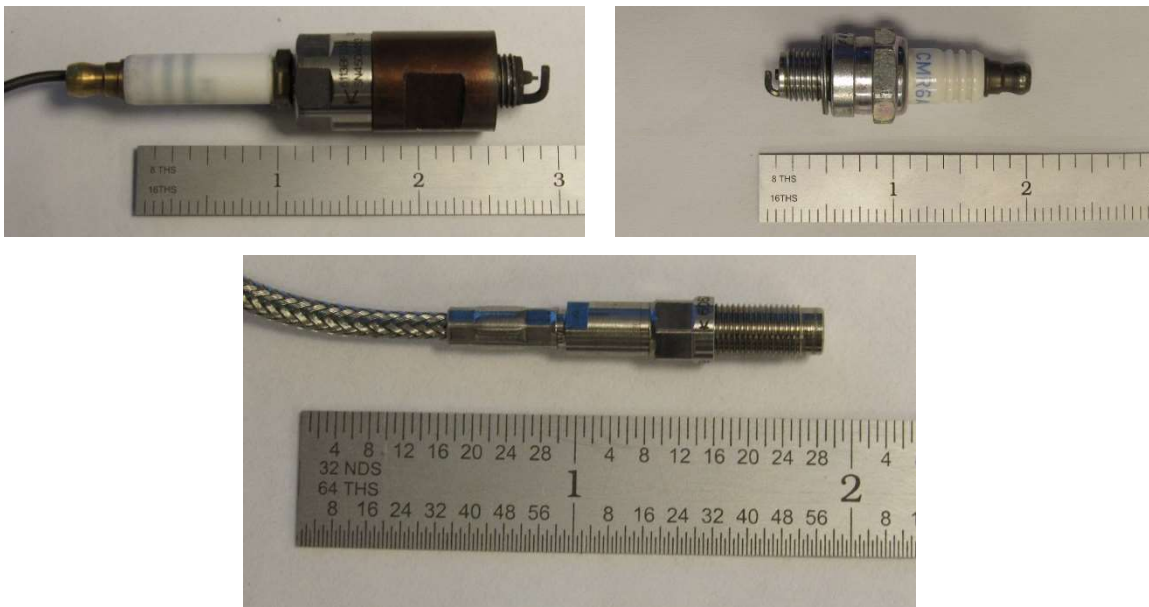


**Figure 52: Top Left: Custom Kistler Measuring spark plug with copper spacer washer installed. Top Right: Stock CM-6 spark plug. Bottom: Kistler Flush Mount Pressure Transducer.**

resolution. The encoder also provided a once per revolution index signal. Since the encoder was not keyed to the engine, the offset between the encoder index signal and the TDC position of the engine had to be determined each time the engine or encoder were adjusted on the drive shaft. There are multiple methods available to determine the offset. The simplest is to motor the engine and record in-cylinder pressure. The location of peak pressure less the thermodynamic loss angle, which is typically about  $1^\circ\text{CA}$  [73:188], is taken as TDC. However, typical values for thermodynamic loss angle are not readily available for 10-100  $\text{cm}^3$  displacement engines. There are other methods to determine the TDC offset that do not require an estimate of thermodynamic loss angle, such as replacing the spark plug with an inductive proximity sensor or motoring the engine in both directions and finding the midpoint of the forward and backwards motored pressure. Coupled with the record of in-cylinder pressure, these methods can also be used to determine the loss angle. In this work, all three methods were used to determine the TDC offset and the loss angle on each engine, and the results are discussed in Chapter IV, Section 3.5.

The voltage pressure signals and encoder signals were recorded by an AVL Indismart Combustion Analyzer, which processed the high speed signals and relayed them to a personal computer. The combustion analyzer could monitor up to eight high speed analog signals such as in-cylinder pressure, spark timing, injection timing, and reference pressure, and report those signals in crank angle space for each cycle. The AVL system was configured to monitor in-cylinder pressure from a measuring spark plug and/or a flush mount transducer, the spark timing and injection signals from the ECU, and the actual spark event using an inductive current clamp. The AVL combustion analysis program is described in additional detail in Section 2.5.

Piezoelectric pressure transducers only create a signal in response to a change in pressure. As a result of integration error, these signals can drift over time. Historically, the primary source of integration error was leakage around the gate resistor in the charge amplifier, a problem solved with the introduction of modern film resistors. Still, AVL recommended that the in-cylinder pressure transducer be referenced to an absolute pressure transducer every cycle. In the SERB the transducers were referenced to the intake manifold pressure (not the crankcase) near BDC of every cycle.

In summary, the combustion analysis system provided the necessary data to determine the indicated (in-cylinder pressure based metrics) performance of the engine and to monitor engine combustion in real time. The system also allowed the operator to monitor and record control signals provided to the engine through the engine control unit (ECU), such as the spark and injection timing. More information on the setup of the in-cylinder pressure measurement system and the tradeoff between flush mount pressure transducers and measuring spark plugs is available in Ausserer *et al.* [75], included in Appendix D.

## **2.4. Engine Control System**

The engine control system set the throttle and spark timing, and when applicable, signaled the fuel injector. It also included the fuel supply and pressurization system. The central component of the system was the JABTronic ECU. The ECU was a custom hardware and software solution developed by Baranski at AFRL [53]. The engine control software was built onto an XMOS integrated circuit board running a custom engine control program called JABTronic. The JABTronic program communicated through an NI LabVIEW program via RS232 communications protocol, allowing the user to set spark timing, injection timing and duration, and to control the throttle servo on the engine. The



spark timing signal was used to drive an AEM Performance Electronics High Output Smart Coil (P/N: 30-2853). The inductive ignition coil charged starting on the rising edge of the signal and fired on the falling edge. Likewise, the injector opened on the rising edge of the injection signal; the injector closed on the falling edge. The injector logic signal was amplified using a transistor to provide sufficient current to drive the coil. The fuel injector was a Siemens Deka 60LB 630 cm<sup>3</sup> High Impedance Fuel Injector with a modified flow plate to reduce the fuel flow rates to those required by the engine. All timing signals were accurate to  $\pm 0.1^\circ$  CA, the same accuracy as the optical encoder used to time the ECU. It should be noted that the ECU required the same TDC to encoder index tick offset as the AVL combustion analyzer.

The fuel system is shown as a schematic in Figure 53. Once mixed, the fuel was stored in a bladder accumulator. During operation, the dry side of the accumulator was filled with nitrogen, pressurizing the fuel up to 5 bar. The nitrogen pressure was set by a high precision regulator (less than  $\pm 0.04$  bar). When using an air carburetor, the fuel line pressure should be sufficient to overcome losses in the fuel line such as the flow meter, the filters, and the pressure and temperature taps and to reach the carburetor near ambient pressure to simulate operation from a fuel tank. This required a nitrogen pressure at the accumulator of  $\sim 0.2$  bar for the SERB running an air carburetor. The fuel pressure for a fuel injector is usually based on the manufacturer recommended pressure, typically 3-4 bar for TBI. In the case of the injectors used for the SERB, the manufacturer recommended 3 bar for volatile fuels (gasoline, PRF blends), and 4 bar for heavy fuels (kerosene, JP-8). From the bladder the fuel passed through a 40  $\mu$ m filter followed by a 7  $\mu$ m filter and then into a piston flow meter. The fuel flow meter was a Max Machinery 213 positive

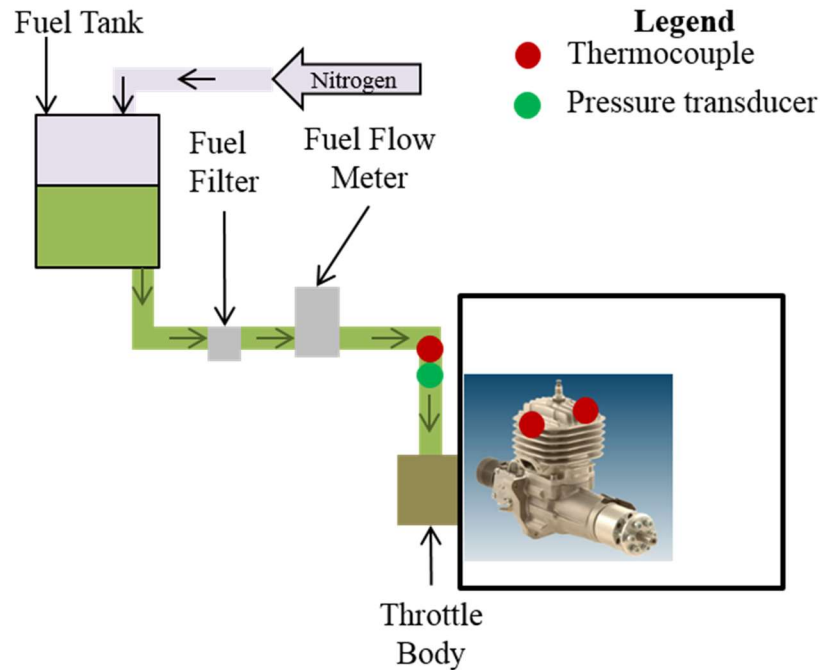


**Figure 53: Schematic of SERB fuel system components.**

displacement analog flow meter capable of measuring  $0.5\text{-}1800\text{ cm}^3/\text{min}$  with an accuracy of  $\pm 0.2\%$  of the reading or  $0.027\text{ cm}^3/\text{min}$ , whichever was larger. The flow meter provided a  $0\text{-}10\text{ VDC}$  analog signal. Downstream of the flow meter the temperature and pressure of the fuel was measured. The temperature was used to determine the fuel density (a function built into the LSDAQ). The fuel then entered either the air carburetor or a fuel injector. With the exception of the fuel injector, the remainder of the fuel system was monitored through the LSDAQ; the nitrogen pressure on the accumulator was controlled manually.

## 2.5. Computer Control and Instrumentation Systems

The computer control and instrumentation system provided an interface between the user and the SERB as well as a platform for collecting and recording data. It consisted of three separate programs: the LSDAQ, the JABTronic control program, and the AVL program. The JABTronic and LSDAQ programs were eventually consolidated into a single

user interface. First, the LSDAQ was a low speed data acquisition and control system. Its primary hardware consisted of two NI Compact Field Point backplanes, each holding up to eight signal processing cards. These cards were used for a mix of data acquisition and control. For data acquisition there were six thermocouple cards (TC-120) and three analog input cards (two AI-100 and one AI-118). These cards were used to monitor the temperatures listed in Table 12, the pressures listed in Table 13, the load cell on the friction cradle, the intake and cooling air hot-wire probes, the intake mass flow meters, the fuel flow meter, and back-up analog speed and torque signals from the dynamometer. For control purposes, an analog output card (AO-210) and a relay card (RLY-425) were used. The analog output card controlled the starter motor and the engine cooling blower. The relay card provided safety interlocks on throttle servo power and the air starter. Previous versions of the SERB used additional channels for engine controls (throttle) and safety interlocks (ECU). These functions were later off loaded to the laboratory safety system and the JABTronic ECU.

In addition to the Field Point modules that the LSDAQ connected to over Ethernet, the LSDAQ also controlled several other pieces of test bench equipment. Its primary responsibility was the dynamometer, which it communicated with over an NI General Purpose Input Bus (GPIB). The LSDAQ allowed the user to set torque and speed set points, read torque, speed, and power in real time, and monitor the dynamometer cooling circuit. The LSDAQ also controlled the heater/chiller used to maintain intake air temperature. The heater/chiller used an RS232 based communication protocol, and the LSDAQ provided a user-friendly front end, allowing the operator to control water bath temperature and monitor the water bath cooling circuit temperatures. All values monitored by the LSDAQ

could be recorded at up to 10 Hz, which is low speed compared to the 800 kHz sampling frequency (per channel) of the AVL and the 1 GHz frequency of the JABTronic ECU.

The second program was the JABTronic 3.0 control program. JABTronic 3.0 was the LabVIEW based user interface that accompanied the JABTronic ECU. Like the LSDAQ for the heater/chiller, the JABTronic provided a front end for the RS232 communications protocol connecting the JABTronic ECU to the control computer. The program allowed the operator to set spark timing, coil charge duration, fuel injection angle and duration, and control two servos via a PWM signal. For additional information on the JABTronic ECU including hardware and software specifications, the reader is referred to Baranski [53].

The third program was the AVL program that provided a user interface for the AVL Indismart Combustion Analyzer. On the SERB, the AVL program's primary function was to monitor the in-cylinder pressure sensors, the spark timing signal, and the fuel injection signal. It displayed these signals to the user in real time (down sampled on the display to one of every ten cycles). It also calculated and displayed moving averages of IMEP and (CA10-CA90) burn angle. Based on user selected criteria such as MAPO level, the AVL program also monitored for knock in real time and notified the user if knock occurred and the percentage of cycles in which it occurred. For collecting data, the user could either manually trigger or use an event trigger (such as the detection of a knocking cycle) to instruct the program to collect and store data for 400 consecutive cycles. The data could then be exported and synced to the LSDAQ data using Microsoft Excel and MATLAB.

## **2.6. Summary: Facility**

This section has described the aspects of the SERB necessary for the operation and testing of small ICEs but not installed specifically to accomplish one of the three proposed

research objectives. These systems include the drivetrain and dynamometer (Section 2.1), intake air system (Section 2.2), combustion analysis system (Section 2.3), engine control system (Section 2.4), and computer control and instrumentation systems (Section 2.5). Each of the remaining sections of the chapter addresses the methodology to accomplish one of the three objectives proposed for this research effort.

### **3. Objective 1: The Scaling of Loss Pathways and Engine Performance**

The goal of Objective 1 was to quantify the dominant loss pathways in a family of 10-100 cm<sup>3</sup> displacement, COTS engines that were as geometrically similar as possible and then to identify how the importance of those losses scales with engine size and surface area to volume ratio. Additionally, the impact of each of the five primary engine control parameters (speed, equivalence ratio, combustion phasing, head temperature, and throttle) on the loss pathways was investigated and quantified to provide insight into the mechanisms driving the loss pathways. The selected engines were SI two-stroke engines and thus the following energy pathways were considered:

- 1) Brake power (Section 2.1)
- 2) Heat rejection through the cylinder walls and head (Section 3.2)
- 3) Friction within the engine (Section 3.3)
- 4) Short-circuiting of fresh charge to the exhaust (Section 3.4)
- 5) Sensible enthalpy in the exhaust gases (Section 3.4)
- 6) Incomplete combustion (Section 3.4)




To examine how these losses scale, they were normalized by engine power in terms of an MEP or a percentage of fuel energy supplied to the engine as in Rowton *et al.* [5] (Appendix C), for example. This normalization required measurements of engine speed,

torque, and power as well as the ability to control engine operating parameters. The necessary equipment to make those measurements and achieve that control was described in Section 2. The remainder of the section is split into four subsections to describe the remaining equipment and instrumentation required for Objective 1. The first section (Section 3.1) describes the engines selected for the study. Then, Sections 3.2, 3.3, and 3.4 describe the methodology for measuring the thermal losses from the engine, the friction losses in the engine, and the sensible and chemical energy losses (incomplete combustion and short-circuiting) in the exhaust, respectively.

### **3.1. Engine Selection**

As outlined in Chapter II, Section 4, engines with displaced volumes between  $10\text{ cm}^3$  and  $100\text{ cm}^3$  fall in a region of shifting importance of the primary loss pathways where efficiency begins to decrease rapidly with displacement. To study that trend in practical engines, a series of geometrically similar (as commercially possible) engines were selected, with surface area to volume ratios ranging from 1.3 to 1.8. To reduce confounding variables, all engines were spark-ignited, naturally aspirated, two-stroke engines with the same materials of construction (mostly aluminum) and the same geometric compression ratio. The port timings were close, but not identical, and thus an understanding of the scavenging process (especially trapping efficiency) was necessary to disentangle the impact of scavenging from the influence of engine size (an analysis not reported in other small engine scaling work such as Menon *et al.* [6, 16]). The important engine characteristics are summarized in Table 14. The following three sections address the equipment to measure the following loss pathways: thermal losses (Section 3.2), friction losses (Section 3.3), and sensible and chemical energy losses in the exhaust (Section 3.4).

**Table 14: Design Characteristics of 3W Modellmotoren Engines Selected for Loss Study to Complete Objective 1**

Engine	3W-28i	3W-55i	3W-85Xi
Displacement (cm <sup>3</sup> )	28	55	85
Power (kW)	2.5	3.82	6.76
Mass (kg)	1.21	1.94	2.39
Specific Power (kW/kg)	2.07	1.97	2.83
Bore (cm)	3.61	4.50	5.08
Stroke (cm)	2.84	3.51	4.09
Compression Ratio	10:1	10:1	10:1
Cylinder Surface Area to Volume Ratio (1/cm)	1.81	1.46	1.28
Trapped compression ratio	7.2:1	7.1:1	6.3:1
Surface area to swept volume ratio (cm <sup>-1</sup> )	1.83	1.46	1.27
Exhaust port open (°aTDC)	106	103	104
Scavenge port open (°aTDC)	125	118	124
Boost port open (°aTDC)	122	110	118
Aux. ex. port open (°aTDC)	n/a	n/a	97
Exhaust port area (cm <sup>2</sup> )	1.9	2.1	2.8
Scavenge port area (cm <sup>2</sup> )	1.8	2.4	3.7
Boost port area (cm <sup>2</sup> )	1.3	1.1	1.0
Aux. exhaust port area (cm <sup>2</sup> )	n/a	n/a	0.7
Engine Photograph [252]			

Note: the stock performance of the selected engines using an air carburetor was characterized by Rowton, Rittenhouse, and the author. That characterization is documented in Rowton et al. [5], included in Appendix C. While that characterization successfully measured thermal losses from the engines and estimated friction losses, sensible and chemical enthalpy were not addressed. Moreover, the use of the stock carburetor led to variations in equivalence ratio of up to 0.4 across the operational range of

each engine, confounding the results. As described in Section 2.4, a fuel injection system was installed to reduce the variability from the stock carburetor.

### 3.2. Thermal Loss Measurements

The thermal loss measurement technique for this work was installed on the SERB by Rittenhouse, Rowton, and the author and is documented in Rittenhouse *et al.* [121] (Appendix B). Shown as a schematic in Figure 54, the system consisted of a cooling blower ducted to a sealed enclosure around the engine. Mass flow was measured using an Omega Engineering FMA 905A-V1 hot-wire anemometer, capable of measuring 0-50.8 m/s of flow at an accuracy of  $\pm 1.5\%$  of full scale plus  $\pm 0.5\%$  of the reading. Before and after the enclosure the temperature of the air was measured using Class A, platinum RTDs. It was assumed that any air leaking around the seal of the box was approximately the same temperature as the main flow of air leaving the box through the cooling air exhaust duct (which is distinct from the engine exhaust duct). The overall thermal losses from the engine were then calculated using the mass flow rate of air (density determined from ambient pressure and inlet temperature), the specific heat of the cooling air, and the temperature rise across the enclosure).



**Figure 54: Schematic of SERB cooling air system components.**



### 3.3. Engine Friction Measurements

The friction testing setup was installed to measure the power losses in the drivetrain, which should be included in the engine's power output. Shown as a schematic in Figure 55, the system consisted of a motor, supports, a reaction arm, and a load cell. The torque applied to the drive train by the motor was measured at the reaction arm. Because the motor's axial rotation was constrained only by the reaction arm, the power into the drive train was measured before any losses in the bearings and belts. The difference between the power measured at the dynamometer and the power delivered by the electric motor was the friction dissipated by the drive train and any connected components. The load cell was a Honeywell Model 41 low profile load cell with a range of 0-44.5 N (0-10 lbf) and an accuracy of  $\pm 1\%$  of full scale. The reaction arm was 12.7 cm (5 in) long. The electric

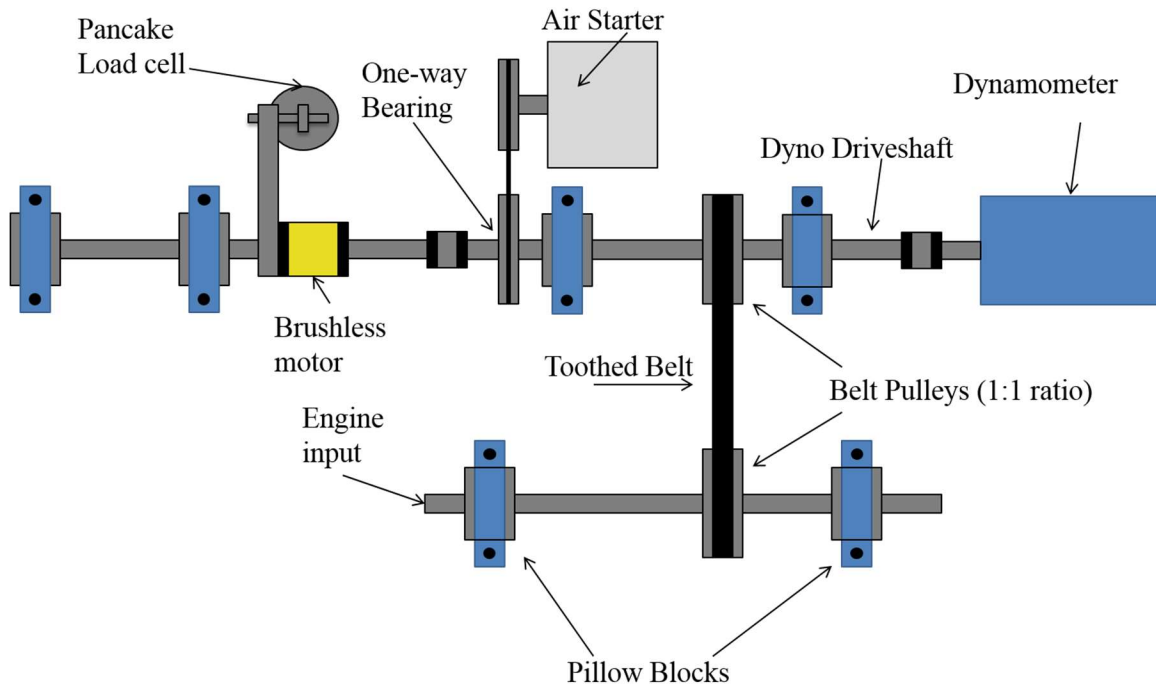


**Figure 55: Schematic of SERB friction testing setup and drivetrain.**

motor was an AXI 5330-18 brushless motor controlled using a Castle Edge HV160F brushless motor controller.

The test setup was used to determine the friction losses in the drive train in order to correct engine power measured at the dynamometer. First, the engine was disconnected from the drivetrain at the spider coupler. All other components including the belt drive, pillow blocks, rotary encoder, and air starter motor remained connected. The electric motor was then connected and used to spin the drivetrain at thirteen different test speeds between 1500 rpm and 7500 rpm. The speed was controlled using the dynamometer. The torque at the load cell, the drive train speed, and the power at the dynamometer were collected for 30 seconds on the LSDAQ and averaged. Each operating point was tested at least three times. The friction loss in the drivetrain was calculated as the difference between the power delivered by the electric motor and the power absorbed by the dynamometer, and the friction was averaged at each test speed. To account for small changes in couplers (the specific coupler not the type), other components, and the alignment of the drive train, friction testing was accomplished three different times throughout testing the engines, and the average of those tests was used to establish the baseline friction loss of the drivetrain. Results from all three friction testing trials along with the final friction correction and its 95% confidence interval are shown in Figure 56. The friction loss in the drive train was determined to be  $69.2 \pm 8.0$  W/krpm. Additional details on the friction test setup may be found in Horn *et al.* [122], included in Appendix E.

The friction testing setup also provided several different capabilities necessary to fulfill Objectives 1 and 2. First, the power dissipated in the drivetrain could be added to the power measured at the dynamometer during engine operation. This provided the true brake

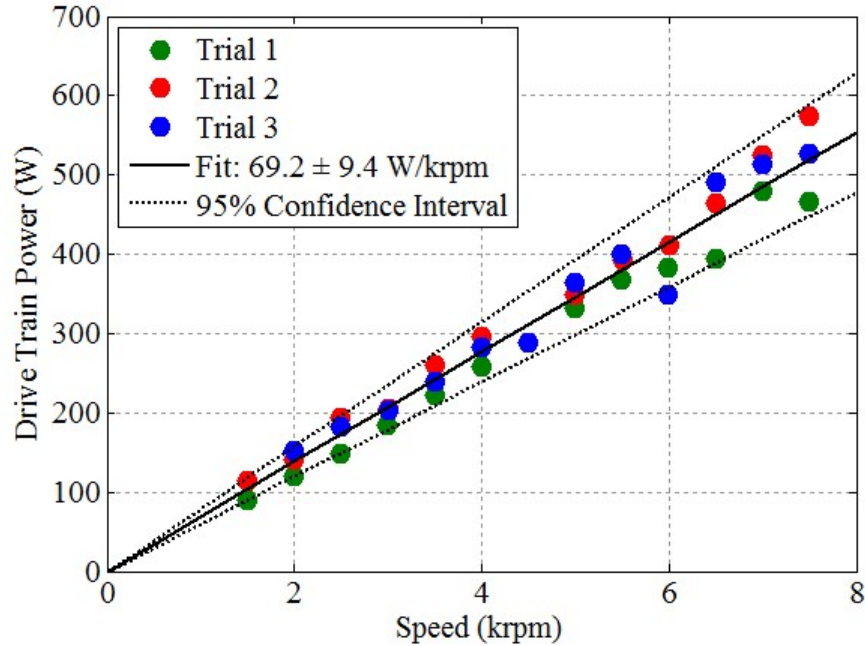


**Figure 56: Power dissipation by SETB drivetrain measured as the difference between power delivered at the electric motor cradle and power dissipated at the dynamometer. For the fit,  $R^2=0.96$ .**

power of the engine, where all remaining mechanical losses were internal to the engine. The difference between indicated power measured using the in-cylinder pressure transducer and the brake power then gave the losses due to friction. The friction cradle could also be used to spin (motor) the engine, allowing both cold testing as well as testing where the engine was brought to temperature, the ignition was switched off, and the engine was motored at operational temperature (see Chapter II, Section 5.2.2 for more details on these methods and their advantages).

### 3.4. Short-Circuiting and Exhaust Enthalpy Measurements

There are three losses that were measured in the exhaust: short-circuiting of fresh charge (and thus chemical energy in the fuel), sensible enthalpy losses (heat), and incomplete combustion of the fuel (chemical energy not released during combustion). The following incomplete combustion products were considered: hydrogen, carbon monoxide,

and unburned hydrocarbons. All of the measurements were accomplished using a combination of gas chromatography for separation coupled with an MSD, a TCD, or an FID for identification and quantification. The time required to analyze one sample using the methods ranged from 3-20 minutes. Therefore, exhaust samples were collected in exhaust sampling bags and analyzed after each engine test. The next four subsections describe the system to extract exhaust samples (Section 3.4.1), and the GC-MS (Section 3.4.2), the GC-TCD (Section 3.4.3), and the GC-FID (Section 3.4.4) methods for analyzing the samples. Section 3.4.5 discusses the calculation of sensible exhaust enthalpy. Section 3.4.6 discusses the validation of the exhaust sampling system and is followed by a review and summary of the section (Section 3.4.7).

#### **3.4.1. Exhaust Sampling System**

Figure 57 shows a schematic of the exhaust system on the SERB. The system consisted of three separate pieces. The first piece was an adapter that joined the engine to the exhaust sampling runner. The adapter was a 10.2 cm long section of 2.5 cm diameter tube. Each engine run on the SERB used its own adapter (of equal length) allowing the remainder of the exhaust system to remain consistent for all engines tested. The exhaust system was not tuned, and instead emulated a straight pipe configuration. It is acknowledged that tuning of the exhaust runner for a specific speed (and thus a specific application) will decrease short-circuiting and increase engine power. However, since there is no specific platform identified in this work, all engines were operated in an un-tuned configuration with the understanding they could later be tuned for use on a specific platform.

The exhaust sampling runner consisted of a 30.4 cm length of 2.5 cm diameter tube welded to a 45.7 cm section of 5.1 cm diameter tube, with eight sampling ports. The

spacing of those ports is shown in Figure 57. A 2 m section of flexible steel tube connected the exhaust sampling runner to the laboratory exhaust system. The annulus between the laboratory exhaust system and the flexible portion of the exhaust runner was open to the atmosphere. This indirect coupling prevented the laboratory exhaust fans from pulling a vacuum on the engine exhaust port. The setup also kept the back pressure on the engine at the end of the runner consistent across all engines tested. All exhaust gas sampling locations were located at least 0.5 m from the outlet of the exhaust runner to the laboratory exhaust system, consistent with best practices described in SAE Standard J254 [235] for preventing unintended dilution of exhaust gas samples with ambient air. Pressure and

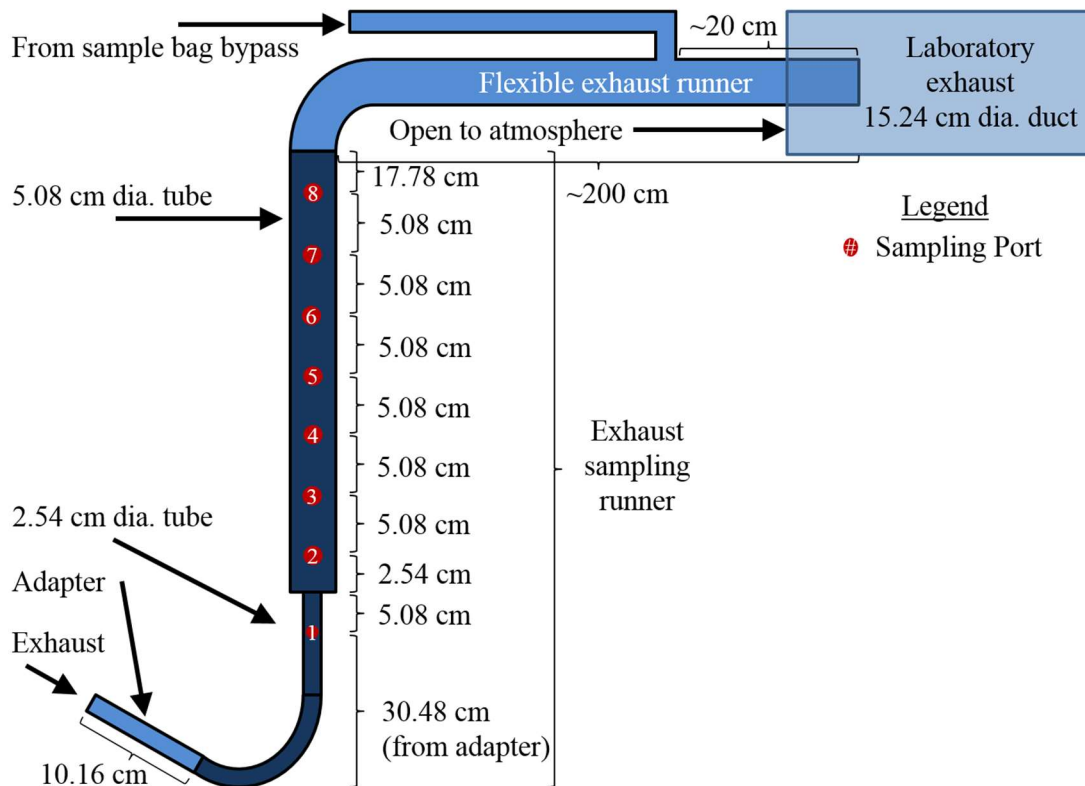


**Figure 57: SERB exhaust system schematic showing sampling port locations. Diagram is not drawn to scale.**

temperature taps were located opposite of Port 1 for the 3W-28i and 3W-55i engines and in Port 6 for the 3W-85Xi engine.

The exhaust was sampled by inserting a probe into one of the sampling ports while leaving the other ports sealed. The selection of exhaust sampling port is discussed in Chapter III, Section 3.4.6. The sampling probe was built from 6 mm (0.25 in) stainless steel tube, consistent with the best practices recommended in the SAE J254 [235]. A photograph of the probe is shown in Figure 58. The tapered end of the probe was oriented such that the opening was pointed downstream in the flow, again, consistent with recommended practices documented in SAE J254 [235].

A schematic of the sampling system is shown in Figure 59. The exhaust sample was drawn from the runner by a Dia-Vac inert sampling pump, model R254-AT-AA1. Before reaching the sampling pump, the sample passed through a cold trap that was chilled in an ice water bath to remove unburnt two-stroke oil and water. Valves between the cold trap and sampling pump allowed the operator to pull fresh air from the laboratory through the

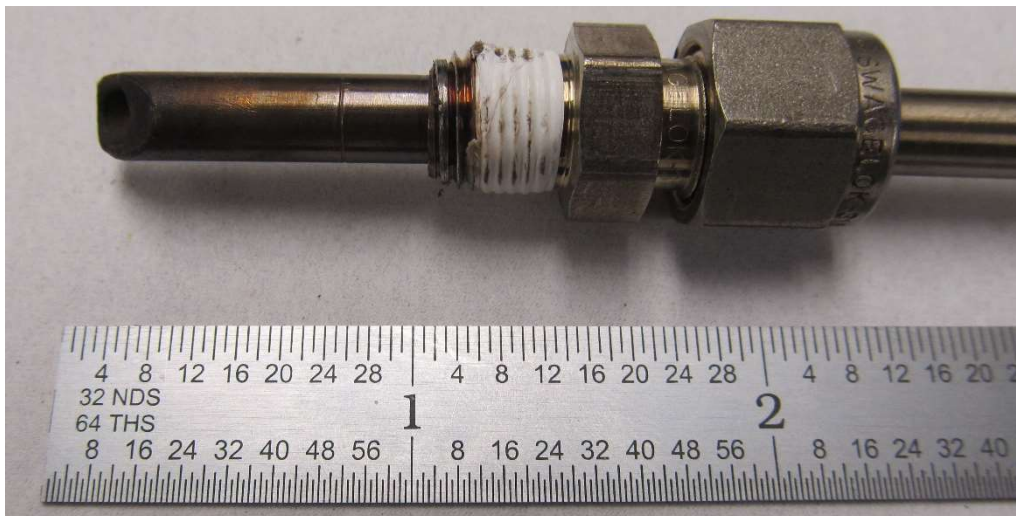


**Figure 58: Exhaust sampling probe for the Small Engine Research Bench.**

pump when it was not collecting samples. After the exhaust sample passed through the pump, it was pushed into a 2 L Supel-Inert Foil Gas Sampling Bag. A regulator between the pump and sample bag split the flow between the bag and a return line that returned the extra exhaust flow to the flexible exhaust runner approximately 20 cm from the coupling to laboratory exhaust system as shown in Figure 57. The sampling bag fill rate was approximately 2 L/min and the bypass rate was approximately 12 L/min.

To collect an exhaust sample, the engine was brought to the prescribed operating condition. A stable operating condition was reached when the engine operating parameters listed in Table 15 remained within the listed limits for at least 2 minutes. Then, the valve allowing the sampling pump to pull engine exhaust (Figure 59, valve 1) was opened and the atmospheric bypass valve (Figure 59, valve 2) was closed. The exhaust system was allowed to purge for 90 seconds. As previously stated, the flow rate through the sampling system was approximately 12 L/min compared to the approximately 0.2 L volume of the system itself. Therefore, 90 seconds was deemed sufficient to completely purge the system and fill it with exhaust representative of the engine's operating condition. While the system

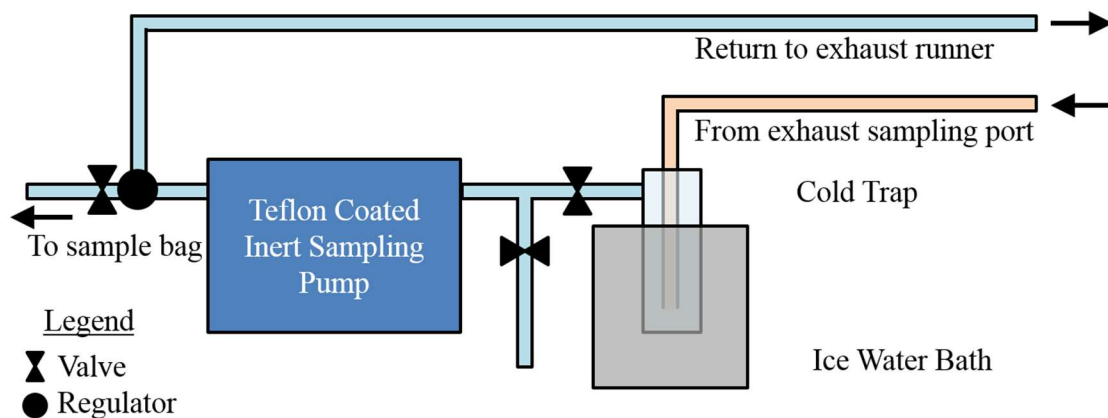


**Figure 59: Schematic of the SERB exhaust sampling system.**

was purging, the engine operating parameters listed in Table 15 were monitored for changes induced by engaging the exhaust sampling system. Following the addition of the sampling pump bypass, which returned most of the flow to the exhaust runner, there were no observable changes in engine performance induced by engaging the sampling system. The exhaust sample was then analyzed using three different techniques, described in the following subsections. Each of the techniques used a separate sample (or samples) extracted from the exhaust sample bag.

**Table 15: Engine Control Limits For a Stable Operating Condition.**

Parameter	Typical Values	Control Limits
IMEP (400 cycle moving average)	4-6 bar at WOT	$\pm 0.2$ bar
CA50 (400 cycle moving average)	8° ATDC	$\pm 0.5^\circ$
Equivalence Ratio (10 second running average)	1.05-1.10	$\pm 0.02$
Engine Head Temperature	130°C	$\pm 2^\circ\text{C}$
Exhaust Temperature (Opposite port 1)	360°C-490°C	$\pm 5^\circ\text{C}$

### 3.4.2. GC-MS: Lean Short-Circuiting (Iso-octane & Ar)

Gas chromatography with a mass selective detector (mass spectrometer) was the first of two methods used to measure short-circuiting. The method used the iso-octane in the PRF blend as an analyte and argon as an internal standard. It was assumed that at the right combustion conditions (equivalence ratio less than 1.3) the iso-octane was broken down into smaller hydrocarbons, even if combustion was globally incomplete. Adapting Equation (90) (Chapter II, Section 5.3.2.2.2) for these choices yields Equation (99).



$$\eta_{tr} = 1 - \frac{\left(\frac{y_{iso-octane,ex}}{y_{Ar,ex}}\right)}{\left(\frac{y_{iso-octane,fc}}{y_{Ar,fc}}\right)} \quad (99)$$

As described previously, the fuel volumetric flow rate was measured using a piston type flow meter and converted to a mass flow rate using the fuel temperature, pressure and tabulated properties for iso-octane [266] and n-heptane [267] (Section 2.4). The intake air flow rate was measured using a hotwire and the volumetric flow rate was then calculated using the 1/7<sup>th</sup> power law velocity profile for turbulent flow [265:340] or using mass velocity transmitters as discussed in Section 2.2. The mass flow rates of fuel and air were used to determine the iso-octane to air ratio delivered to the engine, which is the denominator in Equation (99).

The collected exhaust was analyzed using an Agilent 7890 GC and an Agilent 5975 EI MSD with a triple axis detector. The GC was operated with a split inlet set at a 100:1 split ratio. For the separation, an HP5-MS (5%-phenyl)-polysiloxane column was used. Additional details about the column and temperature profiles are listed in Table 16. While the HP5-MS column excelled at separating hydrocarbons by size, permanent gases eluted in a single peak. Therefore, the MSD was operated in SIM/Scan mode. Selective Ion Mode (SIM) permitted the quantification of specific ions of interest, while Scan mode provided a coarse spectra for the purpose of identifying compounds. SIM mode was used to detect the 40 AMU/e<sup>-</sup> peak from argon (distinct from all other permanent gases) and the 99 AMU/e<sup>-</sup> peak from iso-octane. The full spectra was used to confirm the identity of the iso-octane peak.

The GC-MS was calibrated using samples of air with a known concentration of the same iso-octane that was used to create the PRF fuel blend. To create each sample, 1 L of

**Table 16: GC-MS Parameters for Iso-Octane and Argon Separation and Quantification**

Carrier Gas	Helium
<b>Oven:</b>	
Initial Temperature	40°C
Ramp Speed	15°C/min
Ramp Start Time	2 min
Final Oven Temperature	120°C
<b>Column (Agilent):</b>	PN: 19091S-433 25 m x 250µm
Flow Rate	1 mL/min
<b>Inlet:</b>	
Split Ratio	100:1
Purge Flow	4 mL/min
Temperature	120°C

air was added to a clean exhaust sampling bag using a gas syringe accurate to  $\pm 10$  mL ( $\pm 1\%$ ). Then iso-octane was added to the bag using a 50  $\mu\text{L}$  gas tight syringe accurate to  $\pm 0.25$   $\mu\text{L}$ . Six bags were created using volumes of iso-octane ranging from 0  $\mu\text{L}$  to 80  $\mu\text{L}$  in 20  $\mu\text{L}$  increments. The sample bags were sealed and then heated to  $57.5 \pm 2.5^\circ\text{C}$ . For each calibration point, 10  $\mu\text{L}$  of sample was withdrawn from the bag using a 50  $\mu\text{L}$  gas tight syringe accurate to  $\pm 0.25$   $\mu\text{L}$  which was heated in the oven along with the bags. The sample was then injected into the GC. Each calibration sample was injected six times; the resulting calibration curve is shown in Figure 60. The resulting linear fit is shown in Equation (100) with uncertainty values for a 95% confidence interval. Exhaust samples were processed in the same fashion as the calibration samples, but injected three times instead of six. The iso-octane/argon ratio from the SIM response was used to calculate the molar iso-octane to argon ratio in the exhaust using the calibration curve in Equation (100).

The result was divided by the molar ratio calculated from the intake to yield the trapping efficiency as shown previously in Equation (99).

$$\left(\frac{A_{iso-octane}}{A_{Ar}}\right)_{SIM} = (0.652 \pm 0.041) \left(\frac{y_{iso-octane}}{y_{Ar}}\right)_{mol} - (0.001 \pm 0.03) \quad (100)$$

During validation of the experimental setup, the iso-octane method was compared to the Watson method, discussed in the next section. The detailed results of the comparison are available in Ausserer *et al.* [123] included in Appendix F. The results showed that iso-octane is sufficiently immune to decomposition in the exhaust to function as an analyte, and the short-circuiting results determined using the iso-octane method overlapped those from the Watson method within a 95% confidence interval. The primary advantage of the iso-octane method was that it works at lean combustion conditions where the Watson method does not. The disadvantage of the method is its large experimental uncertainty

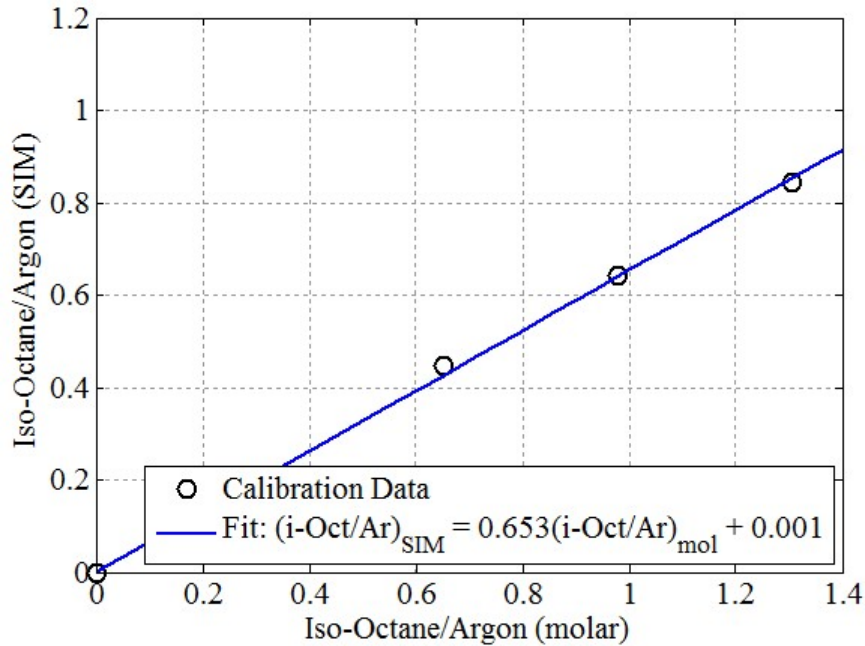


**Figure 60: Calibration curve for the GC-MS. SIM mode was used to quantify the argon 40 AMU/e<sup>-</sup> ion and the iso-octane 99 AMU/e<sup>-</sup> ion.**

(10-15%) that resulted from a combination of the calibration of the instrument and the measurements of intake air and fuel flow rates.

### 3.4.3. GC-TCD: Rich Short-Circuiting (O<sub>2</sub> & N<sub>2</sub>), Incomplete Combustion (H<sub>2</sub> & CO)

Initially, the Watson method was pursued to validate the short-circuiting measurements made using the iso-octane method. The use of GC-TCD was later expanded to measurements of hydrogen and carbon monoxide to calculate their contribution to the incomplete combustion energy pathway. The primary concerns with the iso-octane method were precipitation of iso-octane in the sampling lines as well as the possibility that iso-octane in the fresh charge could decompose in the high temperature exhaust. Developed by Watson in 1908, the method uses oxygen as an analyte at a rich combustion condition. In this effort, nitrogen served as an internal standard. Mathematically, the calculation of trapping efficiency using the Watson method is shown in Equation (101).

$$\eta_{tr} = 1 - \frac{\left(\frac{y_{O_2,ex}}{y_{N_2,ex}}\right)}{\left(\frac{y_{O_2,fc}}{y_{N_2,fc}}\right)} \quad (101)$$

The GC-MS used for the iso-octane method could not separate nitrogen and carbon monoxide so an HP 6890 GC with an Agilent brand HP-MOLSIV column was used. The column outlet was connected to a thermal conductivity detector, and relevant method parameters are listed in Table 17.

Recognizing that the instrument could also provide information on carbon monoxide and hydrogen, two of the three primary sources of incomplete combustion energy, the responses to those compounds were also calibrated. The oxygen, nitrogen, and hydrogen responses of the detector were calibrated using 100 µL samples made from mixtures of air

**Table 17: GC-TCD Parameters for Oxygen and Nitrogen Separation and Quantification**

Carrier Gas	Argon
<b>Oven:</b>	
Temperature	35°C
<b>Column (Agilent):</b>	PN: 19095P-MSOE 30 m x 530 µm Film: 50 µm
Flow Rate	7.5 mL/min
<b>Inlet:</b>	
Split Ratio	Splitless
Purge Flow	4 mL/min
Temperature	150°C
<b>TCD:</b>	
Temperature	150°C
Reference Flow	20 mL/min (Ar)
Makeup Flow	3 mL/min (N <sub>2</sub> )

and hydrogen. The calibration samples ranged from 0%-100% air in 10% increments. The calibrations for oxygen, nitrogen, and hydrogen are shown in Figure 61, Figure 62, and Figure 63, respectively. The calibration curves with an uncertainty of one standard deviation are shown in Equations (102), (103), and (104).

$$(A_{O_2})_{TCD} = (64.9 \pm 2.5)(\%O_2)_{molar} + (33.4 \pm 29.9) \quad (102)$$

$$(A_{N_2})_{TCD} = (52.5 \pm 1.8)(\%N_2)_{molar} - (94.5 \pm 86.0) \quad (103)$$

$$(A_{H_2})_{TCD} = (544.6 \pm 4.2)(\%H_2)_{molar} \quad (104)$$

$$(A_{CO})_{TCD} = (50.9 \pm 5.3)(\%CO)_{molar} - (0.6 \pm 15.2) \quad (105)$$

Due to the low concentration of hydrogen in the exhaust relative to the calibration samples, the calibration was forced through zero to determine the detector's response factor (slope). The hydrogen response of a background of air was subtracted from the hydrogen

response of each exhaust sample. The detector response of carbon monoxide was calibrated using an 8.6% carbon monoxide calibration gas standard, diluted using nitrogen. As with the other TCD calibrations, 100  $\mu\text{L}$  samples were used. The carbon monoxide calibration is shown in Figure 64 and the calibration curve is shown in Equation (105).

To analyze the exhaust a 100  $\mu\text{L}$  sample was injected onto the column. The calibration curves were used to determine the percentages (and thus mole fractions) of oxygen, nitrogen, hydrogen, and carbon monoxide. For short-circuiting the oxygen and nitrogen results were used to calculate the numerator of Equation (101). Fresh charge composition was calculated using the standard dry atmospheric composition adjusted for ambient humidity and was then combined with the exhaust measurement to determine the short-circuiting as shown in Equation (101).

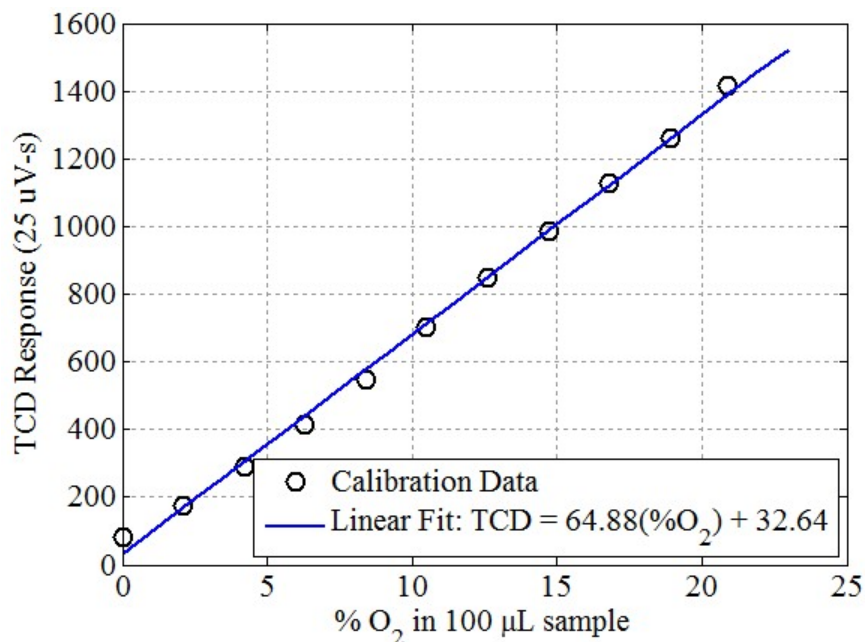


**Figure 61: Calibration of TCD O<sub>2</sub> response for a 100  $\mu\text{L}$  sample of air and hydrogen.**

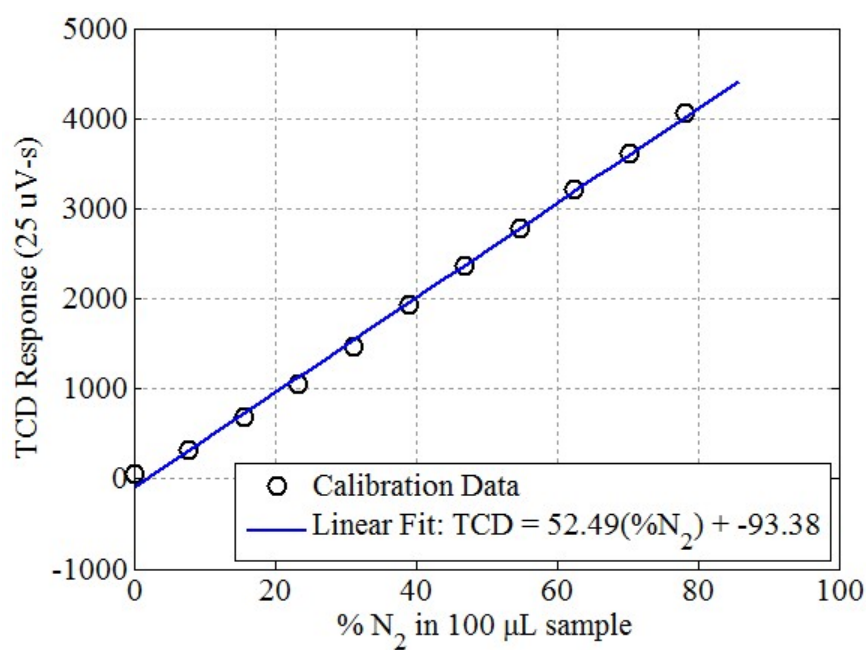


**Figure 62: Calibration of TCD  $N_2$  response for a  $100 \mu L$  sample of air and hydrogen.**

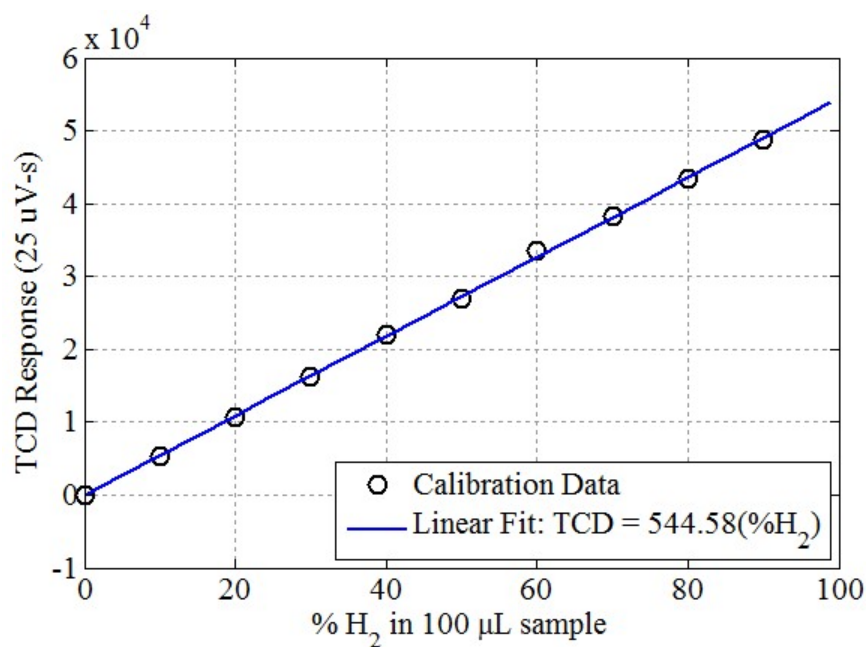


**Figure 63: Calibration of TCD  $H_2$  response for a  $100 \mu L$  sample of air and hydrogen.**

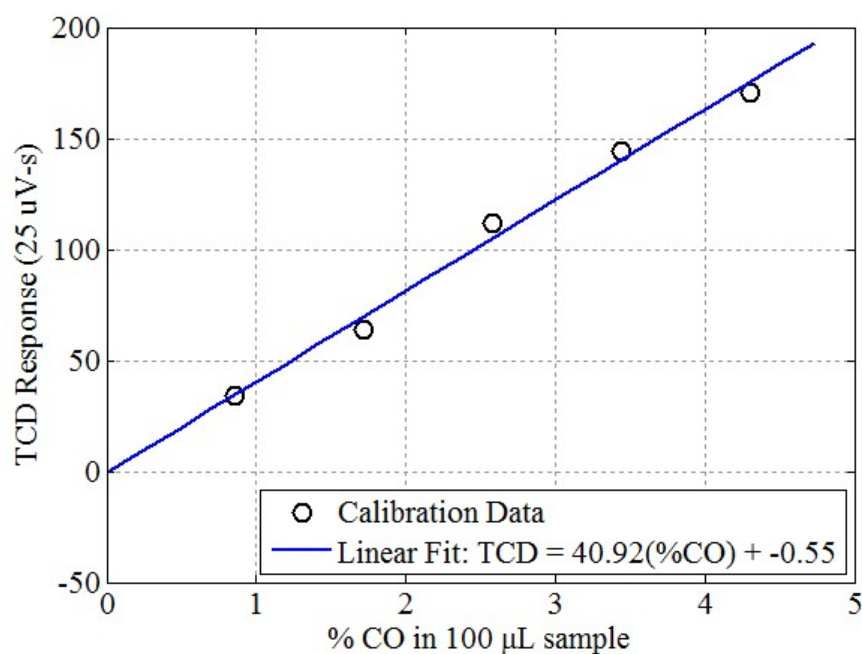


**Figure 64: Calibration of TCD CO response for a 100  $\mu$ L sample of carbon monoxide and nitrogen.**

For short-circuiting measurements, the primary advantage of Watson's method was that it had much lower experimental uncertainty and variability (3%-5%) compared to the iso-octane method. Part of the reduction in variability came from better repeatability on the instrument, and part came from the method's lack of dependence on air and fuel flow rate measurements. Thus Watson's method offers a distinct advantage on small engines where measuring flow rates of fuel and air is difficult. The primary disadvantage of the method is its restriction to globally rich combustion conditions.

The carbon monoxide and hydrogen in the exhaust were two of the three incomplete combustion pathways considered. Similar to the methodology used for oxygen, nitrogen was used as an internal standard to determine the flow rates of carbon monoxide and



hydrogen in the exhaust, as shown in Equations (106) and (107). The mass flow rates were then converted to energy flow rates using the enthalpy of combustion for each species.

$$\dot{m}_{H_2} = \left( \frac{\%H_2}{\%N_2} \right) \frac{(\dot{m}_{air})(x_{N_2})}{MW_{N_2}} MW_{H_2} \quad (106)$$

$$\dot{m}_{CO} = \left( \frac{\%CO}{\%N_2} \right) \frac{(\dot{m}_{air})(x_{N_2})}{MW_{N_2}} MW_{CO} \quad (107)$$

#### 3.4.4. GC-FID: Incomplete Combustion (UHCs)

The third incomplete combustion pathway consisted of chemical energy in UHCs, which result from incomplete combustion in the trapped charge and are distinct from the short-circuited fuel. The primary UHCs in the exhaust samples were identified using the scan data collected using the GC-MS by matching a mass spectra for each UHC to the NIST database. To quantify the UHCs, GC-FID was used. Similar to the GC-TCD method for short-circuiting, an HP 6890C GC was employed, this time a J&W Scientific 113-4332 GasPro column installed in the GC with helium as the carrier gas. The relevant method parameters are listed in Table 18. The elution order was verified with a C1-C6 alkane standard.

Equation (108) proposes that the area response of the FID ( $A_i$ ) is a function of the number of carbon atoms in the molecule ( $C_i$ ), the concentration of the component ( $[i]$ ), and a sensitivity factor ( $\zeta$ ) that accounts for difference in the FID response to alkanes, alkenes, alkynes, and aromatics. Equation (108) may also be expressed in terms of mole fraction since iso-octane acts as an internal standard for the other hydrocarbons, and that expression is shown in Equation (109). The sensitivity factors were approximated from data compiled by Zhao and Ladommatos [56:118] and are shown in Table 19. The mole fraction of each

**Table 18: GC-FID Parameters for Iso-Octane and Argon Separation and Quantification**

Carrier Gas	Helium
<b>Oven:</b>	
Temperature	90°C
Ramp Speed	10°C/min
Initial Ramp Time	4 min
Final Temperature	260°C
Final Hold Time	4 min
<b>Column (J&amp;W Scientific):</b>	PN: 115-3532 30 m x 320 µm
Flow Rate	3.0 mL/min
<b>Inlet:</b>	
Split Ratio	20:1
Purge Flow	2.5 mL/min
Temperature	200C
<b>FID:</b>	
Temperature	250°C
Hydrogen Flow	40 mL/min
Air Flow	450 mL/min
Makeup Flow	6 mL/min (He)

UHC was then used to estimate the quantity of that hydrocarbon in the exhaust based on the quantification of iso-octane. The iso-octane flow rate in the exhaust was calculated as the product of short-circuiting, the flow rate of fuel delivered to the engine, and the percent of iso-octane in the fuel. That flow was then used to determine the flow rate of each of the UHCs as shown in Equation (110). The mass flow rate was then converted to an energy flow rate using the standard heat of combustion for each of the hydrocarbons.

$$[i] = [i - octane] \left( \frac{A_i}{A_{iso-octane}} \right) \left( \frac{C_{iso-octane}}{C_i} \right) \zeta \quad (108)$$

$$y_{i,ex} = y_{iso-octane,ex} \left( \frac{A_i}{A_{iso-octane}} \right) \left( \frac{C_{iso-octane}}{C_i} \right) \zeta \quad (109)$$

$$\dot{m}_i = \left( \frac{y_{i,ex}}{y_{iso-octane,ex}} \right) \frac{(\dot{m}_{fuel})(x_{iso-octane,fuel})}{MW_{iso-octane}} MW_i \quad (110)$$

**Table 19: FID Sensitivity Relative to Hydrocarbon Family as Compiled by Zhao and Ladommatos [56:118].**

Hydrocarbon Family	Response Relative to Alkanes
Alkane	1.00
Alkenes	0.95
Alkynes	1.30
Aromatics	1.00

### 3.4.5. Sensible Exhaust Enthalpy

The third loss pathway measured in the exhaust was the sensible exhaust enthalpy. To measure the sensible exhaust enthalpy, a Class 1, Type K thermocouple was installed in the exhaust runner (see Section 3.4.1). The exhaust runner was insulated between the engine and the sampling port. Since water was removed from the exhaust gas prior to analysis for short-circuiting and carbon monoxide, hydrogen, and UHCs, an estimate of the exhaust composition was used. The exhaust composition was approximated as the perfect incomplete combustion products of the trapped charge to form CO, CO<sub>2</sub>, and H<sub>2</sub>O and by assuming the short-circuited charge was unreacted. The composition was used to calculate the enthalpy available from cooling the exhaust from the exhaust temperature to the fresh charge temperature.

### 3.4.6. Validation of Exhaust Sampling System

The exhaust sampling system required several validation experiments to address concerns over the precipitation of hydrocarbons in the sampling system and bias introduced by the sampling location. The first concern was loss of hydrocarbons in the cold trap. To

test if the cold trap was condensing UHCs or short-circuited fuel, samples taken using the routing depicted in Figure 62 were compared to samples collected using a warm sample line and no bubbler. The iso-octane (the heaviest hydrocarbon observed in the exhaust excluding engine oil) contents of the samples from the two systems were statistically indistinguishable, and thus the cold trap was used to prevent engine oil and water from accumulating in the sampling pumps, bags, and instruments.

The second issue was possible bias introduced by the location of the sampling probe. As discussed by Heywood and Sher [22:91], locating the sampling port too close to the engine can result in an axial spatial dependence of exhaust composition on the probe's location. Therefore, the exhaust sampling location must be far enough downstream from the engine to provide a sufficiently large mixing volume so that the time stratification and in turn the spatial stratification of the exhaust is eliminated. One may empirically determine the point at which the exhaust becomes well mixed by measuring the change in oxygen concentration axially along the runner to observe where it stabilizes. For the engines used in the work, the exhaust was sampled at each of the seven sampling ports in Figure 57 at a WOT point representative of the highest mass flow rate through the engine. As an example, the 55 cm<sup>3</sup> engine was run at 6000 rpm and WOT. Figure 65 shows a plot of oxygen concentration as a function of exhaust sampling port for the three engines. On the 3W-55i engine, the samples taken at Ports 3-6 showed no statistically significant difference in oxygen concentration. Therefore Port 6 was used for the 3W-55i engine in this work. Similar tests were performed on the 3W-28i and 3W-85Xi engines, validating the use of Port 6 for both engines (although the 3W-85Xi engine was sampled using Port 7).

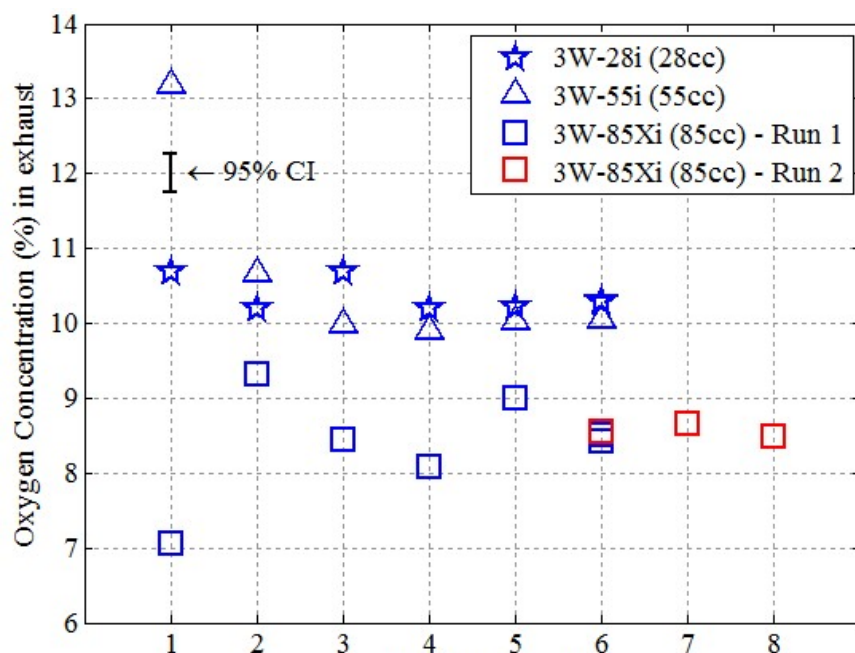


**Figure 65: Oxygen in Exhaust Sample as a function of sampling port. For exhaust geometry and sampling port location see Figure 57.**

Two runs are shown for the 3W-85Xi engine since additional sampling ports (7 & 8) were added after reviewing the Port 1-6 data.

### 3.4.7. Summary: Short-Circuiting and Exhaust Measurements

This section has described the measurement techniques for the three loss pathways that were measured in the exhaust: short-circuiting of fresh charge (and thus chemical energy in the fuel), sensible enthalpy losses (heat), and incomplete combustion of the fuel (chemical energy not released during combustion). Incomplete combustion products included hydrogen, carbon monoxide, and unburned hydrocarbons. Short-circuiting measurements were accomplished using two methods: GC-MS (Section 3.4.2) and GC-TCD (Section 3.4.3). The GC-MS based iso-octane method was used for lean combustion conditions where the GC-TCD based Watson method would not work. The GC-TCD based Watson method was used for rich operating conditions due to its lower

experimental variability, and rich operation accounted for the majority of tested conditions. Carbon monoxide and hydrogen levels in the exhaust were measured using GC-TCD (Section 3.4.3) and the levels were used to calculate the energy losses from incomplete combustion of those species. UHCs were measured using GC-FID (Section 3.4.4) as the third portion of the incomplete combustion pathway. Sensible exhaust enthalpy (Section 3.4.5) was measured using a thermocouple in the exhaust and an estimate of exhaust composition. Finally, Section 3.4.6 discussed several issues regarding the validation of the exhaust sampling system.

### **3.5. Summary: Objective 1**

Objective 1 was to study the scaling of loss pathways in a family of geometrically similar small engines. Additionally, the impact of each of the five primary engine control parameters (equivalence ratio, combustion phasing, head temperature, speed, and throttle) on the loss pathways was investigated and quantified. This section described the methodology for measuring the loss pathways. First, Section 3 described the engines (Section 3.1) selected for the scaling study. The remaining sections described the measurement techniques for measuring loss pathways (thermal losses – Section 3.2, friction – Section 3.3, and short-circuiting, incomplete combustion, and sensible exhaust enthalpy – Section 3.4) on the SERB as well as in Objective 1. The results for Objective 1 are discussed in Chapter IV.

## **4. Objective 2: Heat Transfer, Friction, and Gas Exchange Modelling**

Objective 2 was to evaluate and validate or adapt models/correlations for heat transfer and friction for small ICEs and to determine if the scaling of surface area to volume played a quantifiable role in those losses. The goal of this section is to set up the results and

discussion in Chapter V by explaining the relevant methodology. It is split into three subsections, each discussing one of the three losses. Section 4.1 discusses heat transfer, Section 4.2 discusses friction, and Section 4.3 discusses gas exchange and scavenging. Chapter II, Section 5, provided a comprehensive review of available models and commonly used terms. The subsections that follow serve two purposes. The first purpose is to describe additional measurements used over the course of the modelling effort. The second purpose is a brief review the models chosen as starting points for this work.

#### **4.1. Heat Transfer**

Based on Table 6 (page 100), there are eight different possible non-dimensional groupings for heat transfer, and some of those groupings can be evaluated using multiple sets of characteristic values. It became readily apparent that an evaluation of every possible characteristic value was not feasible in the allotted time frame. To focus the investigation, Table 6 was used to determine a minimum set of parameters required to evaluate historical models. The characteristic values in Table 6 were reorganized into Table 20 to evaluate what measurements were required in addition to those already available from Objective 1. Then, the feasibility of each the required measurements was evaluated, and a subset of those measurements was implemented based on time, cost, and utility. As a result, some aspects of the models presented in Chapter II, Section 5.1 cannot be evaluated with the data collected herein. The remainder of this section is split into three subsections. The first subsection (Section 4.1.1) discusses additional measurements considered for the heat transfer modelling effort and the implications of the chosen subset. The second subsection (Section 4.1.2) discusses the implementation of those measurements. The third subsection (Section 4.1.3) reviews the model chosen as a starting point for this effort.

**Table 20: Evaluation of Measurement Availability for Heat Transfer Modelling**

Parameter		Typical Values	Technique	Issues
$\dot{Q}_{cool}$	heat flux	n/a	thermal enclosure	not time resolved
$T_{g,cyl}$	cylinder gas temperature	n/a	Tunable Laser Absorption Spectroscopy	Added for Objective 2
$T_w$	interior wall temperature	cylinder	no available technique	not installed
$T_s$	exterior wall temperature	cylinder	thermocouple	not time resolved
$P$	pressure	fresh charge, exhaust, cylinder	pressure transducer (high speed for in-cylinder)	none
$\rho$	density	fresh charge, exhaust, cylinder	Property based on pressure, temperature, composition	none
$k$	thermal conductivity			
$\mu$	viscosity			
$C_p$	heat capacity			
$D$	characteristic length	bore, stroke, clearance height	measurement of engine	none
$V$	characteristic gas velocity	intake air, in-cylinder	Estimated: mean piston speed, intake air velocity, exhaust gas velocity	none
$S_p$	piston speed	n/a	optical encoder, geometry	none
$N$	engine speed	n/a	optical encoder, dyno	none
$\theta$	engine crank angle	n/a	optical encoder	none
$A$	characteristic area	Piston, cylinder head	measurement of engine	none
$Y^*$	non-dimensional length scale	bore to stroke ratio, compression ratio	measurement of engine	none
$V^*$	non-dimensional length scale	normalized engine speed	optical encoder	none

#### 4.1.1. Potential Additional Measurements

Table 20 is divided into two sections using thick borders. The top section contains measurement capabilities that were either insufficient or non-existent but were necessary to evaluate the time resolved, spatially averaged, and time and spatially averaged models outlined in Chapter II, Section 5.1. The parameters on the bottom section were available



as part of the basic SERB, engine geometry, or Objective 1. The four parameters listed in the top section of Table 20 are each discussed in their own subsection.

#### **4.1.1.1. Heat Flux**

The heat transfer modelling portion of Objective 2 was designed to address the following engineering problem: estimating the required thermal rejection for an engine installed on an operational platform without testing the engine *a priori*. A valid temporally and spatially averaged correlation (in the form of Taylor and Toong presented in Chapter II, Section 5.1.1.2) would be sufficient to address this problem. Such a model only requires a temporally averaged heat flux measurement, and temporally averaged heat flux measurements were available as part of Objective 1.

Most modern models go one step further, temporally resolving the heat flux. To work with these models there are two options: install some sort of temporally resolved heat flux sensor or time average the models and fit them to time averaged data. Clearly, the first option would be preferable, since it allows a comparison of the predicated time resolved heat flux to the measured time resolved heat flux. Therefore, a market survey of heat flux gauges was conducted. The smallest gauge available at the time was a custom built M10 sized gauge from Vatel Corporation. The gauge required an install space comparable to the spark plug used on the engines. Due to the small size of the head and combustion chamber, such an install was simply not feasible. Therefore, at the time, there was no commercially available solution for a time resolved heat flux measurement on this scale, and a second path was pursued. As a consequence, temporally resolved models may be evaluated for how well they predict the time average heat transfer, but a direct comparison of measured and predicted time resolved heat fluxes was not possible.

#### **4.1.1.2. Cylinder Gas Temperature**

In-cylinder gas temperature appears in virtually every model as the driving force for heat transfer. In most models the gas temperature is actually estimated from the in-cylinder pressure trace and the ideal gas model as described in Chapter II, Section 5.1.3.1. For consistency when comparing these results to historical models, such an approach was also used herein. Additionally, an actual in-cylinder temperature measurement was pursued to evaluate the use of in-cylinder pressure and the ideal gas model as a proxy for as actual measured temperature. Furthermore, in-cylinder temperature measurements provided insight on combustion conditions in the engines and allowed for the impact of the engine control variables on in-cylinder temperature to be directly evaluated. Therefore, when time, space, and cost constraints limited the number of measurements that could be added for the heat transfer study, the in-cylinder gas temperature was prioritized over a localized heat flux measurement and the interior wall temperature. Two different in-cylinder temperature measurement techniques were installed: FTIR spectroscopy and TLAS, with the latter being the primary method for this work. The installation of TLAS is described in Section 4.1.2.2. Since FTIR spectroscopy measurements were not used in this work, the reader is referred to [167, 182] for details on the FTIR spectrometer.

#### **4.1.1.3. Interior Wall Temperature**

Many of the correlations also use an interior wall temperature in order to isolate the heat transfer network to convection (and radiation) between the gas and cylinder wall. Similar to heat flux gauges, COTS instrumentation that could be adapted to a small engine was difficult to find. A number of flush mount pressure transducers with a fifth wire broken out as a thermocouple were investigated, but none were suitable for installation in the

engines without significant modifications to the head. Of the potential transducers, the Kulite Semiconductor Product Inc. XTEH-10L-190M-70BARA was the most promising. It had a diameter of 5 mm, but the probe length was longer than the depth of the threads in the engine head. Thus mounting the probe would have required a prohibitively wide diameter sleeve or welding a bung to the engine head, potentially changing the heat transfer characteristic. Additionally, there was not enough space to install the probe in the engine head once optical access for in-cylinder temperature measurements was installed. Therefore, an actual measurement was abandoned in favor of a mathematical solution.

Many of the heat transfer models discussed model the gas side heat transfer to the cylinder wall. However, if the heat transfer network is extended to include transfer through the wall to the surface, which was measured using a thermocouple, the heat transfer network can then be written using the resistance analogy as shown in Equation (111). For comparison to historical models, a representative wall thickness (taken at the spark plug) and the conductivity of the cylinder material (tabulated for aluminum) can be used to back out  $h_g$ . Such a treatment offers another practical advantage: it eliminates an estimate of interior wall temperature for using any developed model or correlation in the future. An in-cylinder temperature would still be required, but it may be determined using in-cylinder pressure (measuring spark plug) or correlated to other engine operating/control parameters.

$$\frac{\dot{Q}_{cyl,loss}}{A} = \frac{T_{g,cyl} - T_s}{\frac{1}{h_g} + \frac{t_{cyl}}{k}} \quad (111)$$

#### 4.1.1.4. Exterior Wall Temperature

The fourth and final measurement considered for adjustment in the heat transfer study was the exterior wall temperature of the engine. For Objective 1, the exterior head

temperature was measured using thermocouples bolted to fins above the boost and exhaust ports. The thermocouple signals were recorded using the LSDAQ at a frequency of 4 Hz, far too slow to resolve anything but a time averaged measurement. Modifying the system to provide crank angle resolved temperature measurements of the cylinder exterior was considered. However, a review of the correlations and models available in the literature indicated that due to the thermal capacity of the cylinder head, variations in the external head temperature with crank angle are relatively small and typically the external cylinder surface temperature is assumed to be constant. Therefore, the external head temperature measurement remained in the same configuration as Objective 1.

#### **4.1.2. In-cylinder Temperature Measurement Methodology**

The primary addition to the SERB for the heat transfer modelling study was optical access to the engine so that TLAS measurements could be made in-cylinder. Many of the optical components were shared with the FTIR system installed by Deutsch [182]. Only the components used for the TLAS measurement are reviewed here. This section is further organized into two subsections describing the modifications. Section 4.1.2.1 describes how optical access was implemented and section 4.1.2.2 describes the TLAS system.

##### **4.1.2.1. Optical Access**

The first optical access challenge was creating an optical path through the head, without substantial modifications. First, optical probes were created using 1.6 mm diameter sapphire rods and 12 mm long M3x0.5 stainless steel machine screws. The center of each screw was removed and a sapphire window was glued into the screw using a standard two-part epoxy. Later versions of the probe had a 1.5 mm diameter opening (instead of 1.6 mm) at the head of the screw to prevent the sapphire from ejecting into the optical components

if the epoxy failed during engine operation. Copper spacers were machined to provide a seal between the bolt and the engine and to keep the bolt from protruding into the combustion chamber. Figure 66 shows a schematic of the optical probe [167] as well as a photograph of the M3x0.5 bolt and a sapphire rod.

Two probes were installed in the head of each modified engine to create an optical path through the combustion dome as shown in Figure 67. The optical path was selected based on three criteria. First, it had to be high enough in the cylinder that it was not broken by the motion of the piston and preferably high enough to be above the squish region. Second, it had to be low enough to avoid the spark plug electrode. Third, there had to be sufficient material to engage at least three threads on the optical probe after a flat was machined to provide a sealing surface for the copper spacing washer. Even with those criteria, there was a component of chance in the modification due to variations between the cast heads and the drawings obtained from the manufacturer. The location of the optical path is described using two parameters: the optical path length (the importance of which should

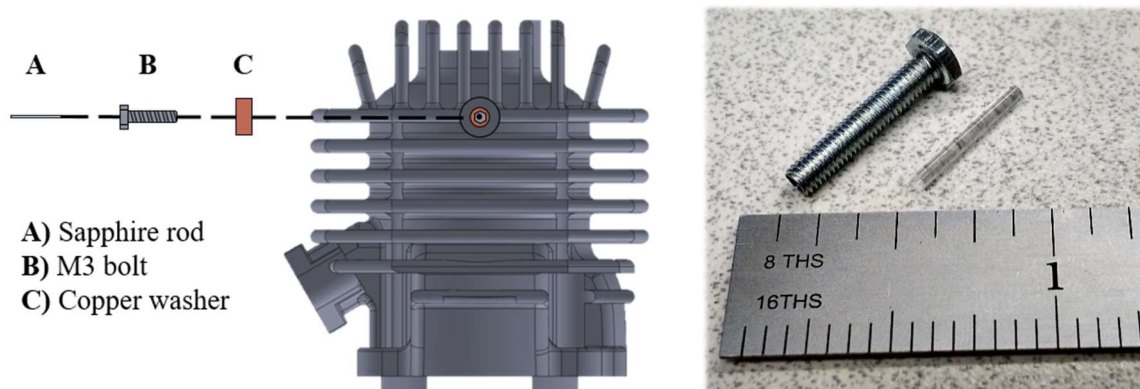


**Figure 66: Left: Schematic of optical probe assembly and installation [167]. Right: Photograph of optical probe and sapphire rod.**

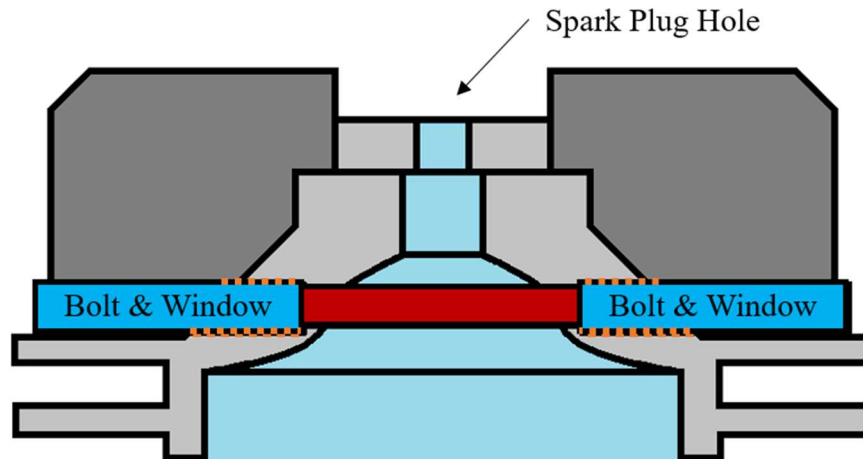


**Figure 67: Schematic of optical path in 3W-XXi engines.**

be evident from the Beer-Lambert Law) and the distance from the spark plug electrode to the middle of the optical path. Those two characteristics are reported in Table 21.

**Table 21: Optical Path Characteristics**

Engine	Optical Path Length	Spark Plug to Optical Path Centerline
3W-28i	20.55 mm	2.06 mm
3W-55i	26.50 mm	4.87 mm
3W-85Xi	18.72 mm	1.95 mm

The second challenge was getting optical access to and from the engine during operation. An optical tower was constructed around the cooling box as shown in Figure 68. The tower held an optical breadboard, and adjustment stages and optical posts were mounted to the breadboard. The platform holding the breadboard was attached to a winch so the optical stages could be raised for alignment and to work on the engine and then lowered into place to take measurements. The ends of the optical posts could be equipped with either a collimator or a detector. Figure 68 shows two collimators, which was the

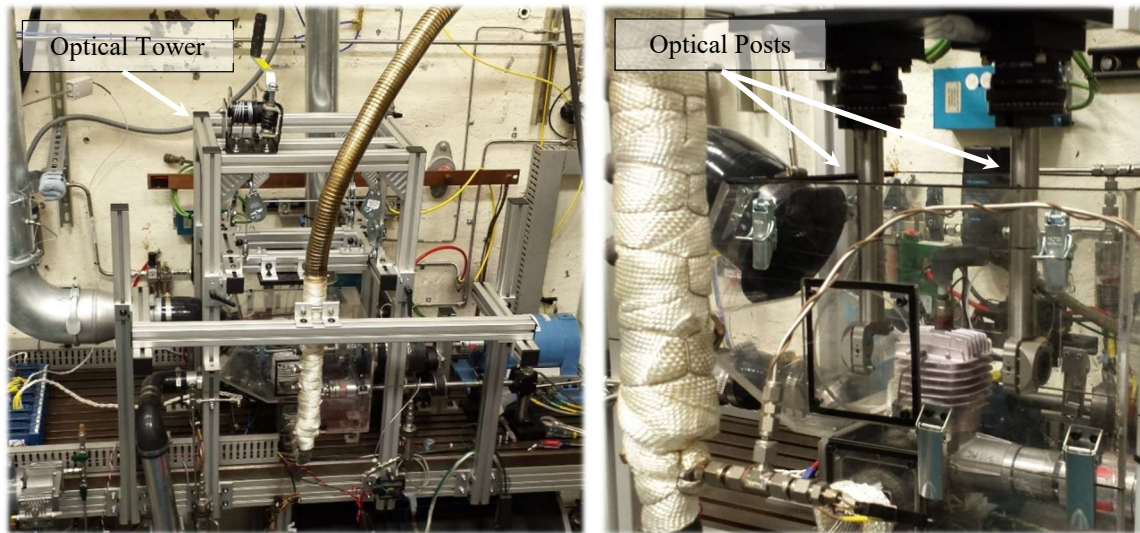


**Figure 68: Optical access for the SERB.**

configuration used with the FTIR spectrometer. During TLAS, the collimator upstream of the engine (left side of right image in Figure 68) was replaced with the detector.

#### **4.1.2.2. TLAS System**

The TLAS system was borrowed from the Advanced Combustion Diagnostics Group and operated by Dr. Keith Rein. This section provides a brief description of the system, and a more complete description may be found in Rein *et al.* [268]. Figure 69 shows a schematic of the measurement setup. The light source was a microelectromechanical system (MEMS) vertical-cavity surface-emitting laser (VCSEL) (Thorlabs part number SL1310V1-SP4) with a 30 nm bandwidth centered at 1345 nm. The output was amplified to 22 mW using a booster optical amplifier (BOA) (Thorlabs part number BOA1036S). The beam was then split into four equal beams using three 50:50 beam splitters. The first beam was directly coupled to an InGaAs photodiode (GPD Optoelectronics GAP544) to create a reference signal. Three identical photodiodes were used as detectors for the remaining beams. The second beam was directed through a 3 mm thick solid-plane CaF<sub>2</sub>

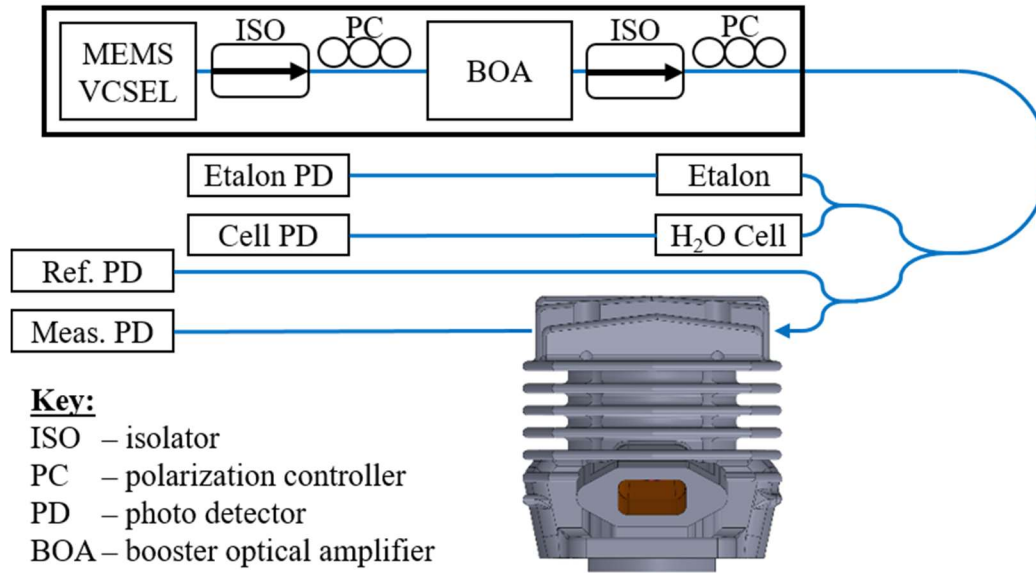


**Figure 69: Schematic of TLAS setup used on the SERB.**

etalon to measure the relative wavelength axis. The third beam was directed through a 15 Torr H<sub>2</sub>O gas cell to create an absolute wavelength reference. The fourth and final beam was directed via single mode fiber into an optical collimator and then into the optical access port of the engine. The optical pathway between the collimator and the engine head as well as between the engine head and the detector were covered using optical tubes, purged with nitrogen during operation. The laser was run at a scan repetition rate of 10 kHz and a 70% duty cycle.

Extraction of temperature from the measured spectra was performed by Dr. Keith Rein using data analysis software developed in-house. A brief description of the process is provided here, and the reader is referred to Rein *et al.* [268] for additional details. The fitting process was based on the methodology of Kranendonk *et al.* [181]. First, the signals were corrected for relative delays caused by time of travel and for voltage offsets caused by thermal emission in the test section as well as bias from the photodiodes, preamplifiers,



and data acquisition system electronics. Base absorbance was calculated using the Beer-Lambert law. As collected, the spectra were functions of time. The etalon signal was used to convert the spectra to a relative wavenumber basis. The spectra were then shifted to an absolute wavenumber basis by matching the peaks from the H<sub>2</sub>O reference cell to peaks predicted using a HITRAN [269] simulation. Finally, a beam steering correction was applied based on the algorithm described in Schulze *et al.* [270]. Simulated spectra (300-3000 K, 0.1-1 cm<sup>-1</sup>) were calculated using the Voight [271] line shape profile calculated in HITEMP [272]. The simulated spectra were subjected to the same corrections for instrument broadening and baseline removal as the measured data. A least squares matching technique was used to fit the temperature and H<sub>2</sub>O concentration of each spectra.

#### 4.1.3. Models

The modeling effort began by testing the performance of historical models on data collected from the selected engines. Originally, two models were chosen as starting points. Taylor and Toong's [138] (Chapter II, Section 5.1.1.2) model was a logical starting point for a time averaged correlation and is reproduced below in Equations (112) to (115).

$$Nu = C_1 Re^{C_2} = \frac{h_o B}{k_g} \quad (112)$$

$$h_o = \frac{\dot{Q}_{cyl,loss}}{A_p(T_{g,cyl} - T_c)} = \left( \frac{1}{h_g} + \frac{t_{cyl}}{k} + \frac{1}{h_c} \right)^{-1} \quad (113)$$

$$Nu = \frac{QB}{k_g A_p (T_{g,cyl} - T_c)} \quad (114)$$

$$Re = \frac{\dot{m}_g B}{\mu_g A_p} \quad (115)$$

The utility and validity of Taylor and Toong's model is explored in Chapter V, Section 2. Initially, the research plan also involved evaluating temporally resolved models, starting

from the work of Annand [17] (Chapter II, Section 5.1.1.3.2), whose model is reproduced in Equations (116) and (117). While all instantaneous spatially averaged models have issues with phase lag and peak values compared to experimental results, the Annand model has a clear delineation of the convective and radiation effects and is dimensionally consistent. During the execution of Objective 2, measuring and modelling the in-cylinder temperature was more involved than initially anticipated, which precluded the exploration of temporally resolved models in this work. However, sufficient data is available from the presented work that temporally resolved models could be pursued in a later effort.

$$h_g = C_1 \cdot \frac{k}{B} \cdot Re^{0.7} + C_2 \cdot \frac{(T_{g,cyl}(\theta) - T_w)^4}{(T_{g,cyl}(\theta) - T_w)} [=] \frac{kW}{m^2K} \quad (116)$$

$$Re = \frac{\rho \cdot \bar{S}_p \cdot B}{\mu} \quad (117)$$

## 4.2. Friction

The approach for friction modeling was similar to the approach for heat transfer modeling. However, there were fewer relevant characteristic values for engine friction losses. In fact, most literature only considers a characteristic speed. Typically, the characteristic speed is either the mean piston speed or the engine rotational speed. These two parameters are related by the stroke, which is a function of the engine geometry.

Initially, friction losses were measured by subtracting BMEP from IMEP during fired operation. BMEP and IMEP had uncertainties of about 6% and 5%, respectively. As a consequence, the resultant of the difference, FMEP, had uncertainties upwards of 100%, too high for a useful measurement. Therefore, the motored friction method (see Section 3.3) was used. Of the five engine control variables used during Objective 1, only two could be evaluated for their impact on engine friction losses using the motoring

method: speed and throttle. However, since virtually all literature models are based solely on speed (or a proxy for speed), this restriction was deemed acceptable. As in heat transfer models, fits to historical correlations were pursued first. The correlation shown in Equation (118) (Chapter II, Section 5.2.1) was selected as a starting point since it is the most common in the literature, and the correlation includes terms that account for all three types of friction losses: boundary, hydrodynamic, and viscous flow losses. In addition to a fit based on speed in Equation (118), the impact of delivery ratio was also evaluated.

$$FMEP = C_1 + C_2N + C_3N^2 \quad (118)$$

### 4.3. Gas Exchange and Scavenging

Examining the scaling of gas exchange through a parametric study of port design was beyond the scope of the proposed effort. Still, there was sufficient data available from Objective 1 to evaluate engine performance in terms of several models and to draw several conclusions regarding gas exchange and scavenging. As discussed in Chapter II, Section 5.3.1, scavenging models come in both temporally averaged (typically capturing conditions as the exhaust port closes) and temporally resolved (typically measuring purity in the exhaust) varieties.

Initially, Horn [273] proposed using FTIR in the exhaust to measure temporally resolved exhaust gas purity, which could have then been fit to a temporally resolved model such as the S-Curve or Crest model (Chapter II, Section 5.3.1.3). However, Horn's measurement methodology never came to fruition, at least not to the extent required for gas exchange modelling. Therefore, comparisons in this work were restricted to the temporally averaged models: specifically, the perfect isothermal displacement model, shown in Equations (119) to (121) and the perfect isothermal mixing model, shown in

Equations (122) to (124). Since these models are considered bounds of the best and worst cases, respectively, they were used to evaluate current COTS engine performance in the context of potential performance through investment in gas exchange technology.

$$\eta_{ch} = \begin{cases} \Lambda & \text{for } \Lambda < 1 \\ 1 & \text{for } \Lambda \geq 1 \end{cases} \quad (119)$$

$$\eta_{sc} = \begin{cases} \left[ 1 + \left( \frac{1}{\Lambda} - 1 \right) \right]^{-1} & \text{for } \Lambda < 1 \\ 1.0 & \text{for } \Lambda \geq 1 \end{cases} \quad (120)$$

$$\beta = \begin{cases} 0 & \text{for } \Lambda < 1 \\ 1.0 & \text{for } \Lambda \geq 1 \end{cases} \quad (121)$$

$$\eta_{ch} = 1\eta_{sc} \quad (122)$$

$$\eta_{sc} = 1[1 - \exp(-\Lambda)] \quad (123)$$

$$\beta = \eta_{sc} \quad (124)$$

#### 4.4. Summary: Objective 2

Objective 2 was to evaluate and validate or adapt models/correlations for heat transfer and friction losses for small ICEs and to determine if the scaling of surface area to volume played a quantifiable role in those losses. For heat transfer, the Nusselt number in the Taylor and Toong model includes a grouping that reduces to  $4/\pi B$ , which tracks with the surface area to volume ratio for engines with similar bore to stroke ratios. Other models included similar groupings, although they typically are not explicitly called out as a surface area to volume ratio. Chapter V will discuss the validity and applicability of the Taylor and Toong model for the studied engines. Scheduling (specifically of the TLAS system) did not permit further investigation of an explicit surface area to volume term for heat transfer losses, although the presented data could be used to make such an evaluation in a future effort. The surface area to volume ratio was not explicitly included in any of the

historical models for friction losses presented as starting points in this section. The analysis in Chapter V will suggest how the surface area to volume ratio might be used to improve the prediction of friction in small, two-stroke SI, engines.

The goal of this section was to set up the results and discussion in Chapter V. It was split into three subsections, each discussing one of the three losses. Section 4.1 discussed heat transfer, Section 4.2 discussed friction, and Section 4.3 discussed gas exchange and scavenging. The work of Taylor and Toong [138] as well as that of Annand [17] provided a starting point for heat transfer modelling. For friction modelling, the three term speed based model in Equation (118) provided a starting point. Finally, the perfect isothermal mixing and perfect isothermal displacement models were suggested to evaluate the gas exchange process.

## **5. Objective 3: Fuel AKI Relaxation**

The goals of Objective 3 were to identify relationships between the fuel AKI requirement, loss mechanisms, and engine size, to quantify the performance impacts of switching from 98 ON fuel (manufacturer recommended) to 20 ON fuel (JP-8 and diesel), and to determine which engine control parameters were most effective at controlling knock in 10-100 cm<sup>3</sup> displacement engines. The investigation was accomplished in two steps. First, the knock limit of each engine was mapped using PRF blends ranging from 0 ON to 98 ON. Then, the impact of each engine control parameter on the knock limit was investigated in a parametric study. The results of this parametric study were linked to the parametric study performed as part of Objective 1 to draw conclusions about the influence of loss pathways on the knock limit. The remainder of this section is split into three subsections. The first explains the knock limits and detection methodology. The second

section describes mapping the fuel AKI requirement; the third section describes the procedure for the parametric study.

### **5.1. Defining and Detecting Knock**

The knock limit defines the boundary between acceptable and unacceptable abnormal combustion. In this work two knock limits were established, one based on typical practice for automotive scale engines and a second limit intended to prevent damage to the engines. The first limit was 5 bar MAPO for 1% of 400 consecutive cycles. This limit is the boundary between light and medium knock and commonly used in engine research [53, 76, 83, 84]. Pressure oscillations caused by end gas knock have a number of oscillatory modes (see Chapter II, Section 2.6.3). Of these modes, the strongest and most commonly detected in a MAPO type knock analysis is the 1,0 circumferential mode (see Table 1, page 57) [53:14, 81]. However, detecting the 1,0 mode requires the pressure transducer to be off center [73:238]. On the SERB, the pressure transducer was integrated into the centrally located spark plug reducing the detected intensity of the 1,0 circumferential mode.

Therefore, a second knock limit was established to supplement the MAPO limit and to prevent damage to the engine. Typically, damage from knock can be traced to one of two sources: mechanical damage from rapid pressure rise and thermal damage from hot spots (which form due to rapid combustion which is in turn tied to rapid pressure rise). In spark-ignition engines, pressure rise rates are typically less than 2.5 bar/CAD [83]. Values of 10 bar/CAD and higher are associated with heavy knock and can lead to rapid engine failure in SI engines [76]. HCCI engines typically operate with peak pressure rise rates from 3 bar/CAD to 5 bar/CAD, on the high end of the typical limit for SI engines [53:36]. For the engines and rotational speeds in this work, peak pressure rise rates were typically

less than 2.5 bar/CAD when operating free of abnormal combustion. Therefore, 5 bar/CAD for 1% of cycles was selected as the second knock limit. The engine was considered knock-limited once the peak pressure rise rate exceed 5 bar/CAD or MAPO exceeded 5 bar for more than 1% of 400 consecutive cycles.

Knock was detected using the in-cylinder pressure transducer and the AVL Indismart Combustion Analyzer (see Chapter III, Section 2.3). The AVL Indismart was equipped with knock detection protocol and formulae, which were adapted for this study to measure peak pressure rise rate and MAPO and to report the percentage of cycles exceeding the predefined limits. Both the calculation of peak pressure rise rate and MAPO required filtering the raw pressure signal to eliminate noise and to isolate oscillations caused by knock, respectively. Filter frequency selection was based on the sampling rate of the pressure signal and the fundamental knock frequency of the engine. The fundamental knock frequency of each engine was initially estimated using Equation (125) [73:224] and later verified using pressure traces from knocking cycles.

$$f_p[Hz] = \frac{570}{B[m]} \quad (125)$$

Table 22 shows the engine operational and pressure sampling frequency ranges as well as the fundamental knock frequency for each engine. To create a smoothed pressure trace for calculating MAPO, the raw pressure signal was filtered using a low pass infinite impulse response filter with a cutoff frequency of 10 kHz. The result was subtracted from the raw pressure signal to isolate oscillations caused by knock. The maximum amplitude of the resultant gave the MAPO for each cycle. Peak pressure rise rate was calculated by taking the derivative of the pressure signal. Before taking the numerical derivative, a low pass infinite impulse response filter with a cutoff frequency of 60 kHz was applied to the raw

pressure signal to prevent electrical noise from causing artificially large derivative values. Threshold counters were used to determine the percentage of 400 running cycles exceeding the predefined MAPO and peak pressure rise rate limits.

**Table 22: Knock Frequency Characteristics of 3W Modellmotoren Engines**

	<b>3W-28i</b>	<b>3W-55i</b>	<b>3W-85Xi</b>
First Fundamental Knock Frequency (kHz)	15.8	12.7	11.2
Engine Operational Frequency (kHz)	66-133		
Pressure Sampling Frequency (kHz)	24-48		

## 5.2. Determination of Fuel AKI Requirement

In this work, the knock limit of an engine was defined as the maximum throttle setting the engine could operate at for a given operating condition without exceeding the knock limits established in the preceding section. During knock free operation, this corresponded to WOT. For points where knock was encountered, the engine was throttled until the knock was back under the established limits. During mapping, each engine was run across its operational speed range, 4000 rpm to 7900 rpm, in 500 rpm increments on PRF blends ranging from 0 ON to 98 ON in 10 ON increments. For the initial mapping, the primary engine controls (combustion phasing, equivalence ratio, and engine head temperature) were held constant, and the target values and control limits for each are shown in Table 23, indicated by ‘engine control’ in the middle column.

In addition to the engine control variables, Table 2 listed a number of parameters that influence the propensity of an engine to knock. Clearly, these variables could confound the results if not appropriately controlled [53:25, 85]. Table 23 also lists these variables along with their control or correction strategy as implemented on the SERB. ‘Controlled’



indicates that the variable was actively controlled, ‘constant’ indicates that the variable was held constant (for example altitude), and ‘N/A’ indicates that the parameter was not applicable to the testing. The effect of each of the remaining variables is discussed next.

**Table 23: Control of Knock Influence Parameters on the SERB**

Parameter	Controlled or Constant?	Value
Spark Advance/ Combustion Phasing	Engine Control	CA50 = $8 \pm 0.5^\circ$ aTDC
Equivalence Ratio	Engine Control	$1.05 \pm 0.02$
Engine Head Temperature	Engine Control	$130 \pm 1^\circ\text{C}$
Intake Air Temperature	Controlled	$25^\circ \pm 2.5^\circ\text{C}$
Manifold Pressure	No, but relatively constant compared to 1 ON/30 kPa	Atmospheric
Exhaust Pressure	No, but relatively constant compared to 1 ON/30 kPa	Atmospheric
Humidity	No, correctable at 1 ON/ 10%	Atmospheric
Engine Deposits	No, monitored/negligible.	N/A
Fuel Temperature	No, minor impact over observed range.	$20^\circ\text{C}$
Compression Ratio	Constant	10:1
Altitude	Constant	~820 ft ASL
Fuel Injection Type	Constant	TBI, 3-4 bar
Chamber Shape	Constant	Dome
Oil Consumption	Constant	2% of fuel
Exhaust Gas Recycle	N/A	N/A
Hydrogen (gas) in Fuel	N/A	N/A

- 1) *Manifold Pressure:* The intake manifold pressure depended primarily on the daily atmospheric pressure. Atmospheric variations in pressure were less than 6,000 kPa, which corresponds to less than 0.2 ON based on 1 ON/30kPa as documented in Attard *et al.* [85]. Thus atmospheric variation was ignored.
- 2) *Exhaust pressure:* Like manifold pressure variation, exhaust pressure variation was largely a function of atmospheric conditions and was negligible for similar reasons.
- 3) *Humidity:* Humidity was not controlled on the SERB. For a given engine, most fuel AKI testing occurred on consecutive days with little variation in relative humidity. The

variations that did occur were negligible within the experimental noise. Had large swings in humidity occurred, the data could have been corrected using 1 ON↓/10%↑ relative humidity as documented in Attard *et al.* [85].

- 4) *Engine Deposits*: Engine deposits are a concern over the lifetime of a commercial vehicle engine, corresponding to thousands of hours. In most of the testing in this work, short run times and lean fuel:oil mixtures (100:2) led to few deposits. Deposit build up was observed while testing one of the 3W-55i engines. Removal of the deposits did not measurably change the knock limit of the engine on 20 ON PRF blend. Therefore, it was assumed that deposits did not play an appreciable role in the knock limit.
- 5) *Fuel temperature*: Fuel temperature on the SERB was not controlled and varied with lab temperature. Observed swings in the fuel temperature amounted to approximately  $\pm 5^{\circ}\text{C}$ . The main concern with varying fuel temperature was a change in the cooling effect of the fresh charge. Given isooctane and assuming an air to fuel ratio of 15.05 (stoichiometric), a  $\pm 5^{\circ}\text{C}$  swing in fuel temperature resulted in a  $\pm 1.5^{\circ}\text{C}$  change in intake air temperature. This variation was within the control limits on intake air temperature. Furthermore, the swings in laboratory and fuel temperature were more seasonal than day to day, and thus had relatively little impact on tests for any single engine taken on consecutive days.

### **5.3. Parametric Study of Engine Controls**

During Objective 1 the influence of engine control parameters on the energy pathways in each engine was quantified. After mapping the knock limit on each engine, another parametric study was performed to quantify the influence of each engine control parameter on the knock limit of the engine and in turn identify connections between loss pathways

and the knock limit in small engines. As previously noted, in Objective 1 there were five engine control variables: equivalence ratio, combustion phasing, engine temperature, speed, and throttle. During the octane study, the throttle was used to control knock and was no longer an independent variable. Furthermore, knock propensity was strongly tied to engine speed, leaving only three truly independent variables. Therefore, the remaining three parameters were swept on 20 ON PRF (selected as approximately the same ON as diesel and JP-8) at three different speeds.

The speeds were chosen based on knock intensity. One speed (the slowest) was selected such that engine operation was severely knock-limited. This served to quantify how much each engine control could increase (or decrease) knock-limited IMEP (KLIMEP) when varied from its baseline setting, listed in Table 23. The knock-limited IMEP is the maximum power an engine can produce at a given condition without exceeding the established knock limit. The second speed was selected at the border of knock-limited performance. At the baseline of this condition, abnormal combustion was observed but was not severe enough to warrant throttling the engine to mitigate knock. This speed tested the stability of a borderline knock condition by determining what variations in each control could push the engine into a knocking condition. The third and final speed was chosen at a condition free from any abnormal combustion at the baseline. Similar to the second speed, the third speed tested what change (if any) in the engine controls could cause abnormal combustion.

#### **5.4. Summary: Objective 3**

The goals of Objective 3 were to identify relationships between the fuel AKI requirement, loss mechanisms, and engine size, to quantify the performance impacts of

switching from 98 ON fuel (manufacturer recommended) to 20 ON fuel (JP-8 and diesel), and to determine which engine control parameters were most effective at controlling knock in 10-100 cm<sup>3</sup> displacement engines. Accomplishing this objective required establishing knock limits and implementing a detection methodology, which were described in the first subsection (Section 5.1). Then, the KLIMEP was mapped across the operational speed range of each engine on PRF blends from 0 ON to 98 ON, as described in the second subsection (Section 5.2). Lastly, the influence of each engine control parameter on the knock limit was quantified as described in the third and final subsection (Section 5.3). The results for Objective 3 are discussed in Chapter VI.

## **IV Objective I: The Scaling of Loss Pathways and Engine Performance**

### **1. Chapter Overview**

The goal Objective 1 was to quantify the interaction between loss pathways, performance, and efficiency in 10-100 cm<sup>3</sup> displacement engines. As detailed in Chapter III, Section 3.1, the engines studied herein were selected specifically because they fell between automotive scale engines and micro glow fuel engines. Thus, they were sized appropriately to understand what mechanism(s) drove the observed decrease in efficiency across the aforementioned size range. The loss pathways in each engine were measured at a variety of operating conditions using the experimental apparatus described in Chapter III, Sections 2 & 3. This chapter explores the impact of those losses on engine performance and efficiency and compares the results to larger and smaller engines.

To that end, the remainder of this chapter is split into two sections. The first section (Section 2) presents energy balances for each of the studied engines and the scaling study that was the primary focus of Objective 1. The balances demonstrate a full accounting of the energy delivered to each engine. The discussion focusses on the relationship between the shifting dominance of the loss pathways and the decrease in fuel conversion efficiency with engine size. The second section (Section 3) presents a number of parametric studies describing the interactions between engine operating parameters, engine performance metrics, and the loss pathways. These studies are intended to provide practical, quantitative insight that is directly applicable to the integration of similar engines onto fielded RPAs.

## **2. Energy Balances and Scaling Trends**

### **2.1. Introduction**

The first half of this chapter explores the scaling of loss pathways as engine displacement decreases from greater than 100 cm<sup>3</sup> to less than 10 cm<sup>3</sup>. As described in Chapter III, Sections 2 & 3, five energy pathways were measured: brake power, cooling load, exhaust enthalpy, incomplete combustion, and short-circuiting. Due the chosen control volume, friction losses are grouped with the cooling load and sensible exhaust enthalpy. Results from the motored friction testing are deferred to Chapter V, Section 3. First, Section 2.2 compares engine performance on the SERB to manufacturer engine data, providing validation of the engine testing configuration. In Section 2.3 the energy balances on the 3W Modellmotoren engines tested as part of the effort are presented along with a discussion of the dominant loss pathways. In Section 2.4 the studied engines are discussed in the context of larger automotive and smaller micro glow fuel engines to examine how dominant loss pathways shift with displaced volume (and surface area to volume ratio). Lastly, Section 2.5 summarizes the conclusions of the scaling study portion of Objective 1.

### **2.2. Comparison to Manufacturer Data (COTS Configuration)**

All of the studied engines exhibited a high degree of short-circuiting, upwards of 40%-60% at WOT. Given the availability of techniques to reduce short-circuiting and the potential impact of the laboratory intake air and exhaust systems on the engines, it is reasonable to ask if the performance of the engines was comparable to that expected from the engines by the manufacturer. After all, the goal of this study was to provide insight into COTS engines that could be purchased off the shelf and then integrated onto an RPA with minimal modifications. As previously noted, manufacturer data sets on the hobbyist

variants of the 3W Modellmotoren engines were sparse. However, 3W International (the “military grade” arm of 3W Modellmotoren) began selling a variant of the 3W-28i engine (in 2014) and provided performance data on BSFC and fuel flow [274], which in turn allowed the calculation of brake power. The data were collected using gasoline (presumably 92-98 ON), which has a similar specific energy to the 98 ON PRF blend used for Objective 1. The primary selling point of 3W International’s engine variants was operation on heavy fuel. As such, the engines were retrofitted with low pressure fuel injection and also included a banana style muffler that wraps around the engine (to save space on the aircraft). This engine configuration was unavailable when the engines for this project were acquired and was not tested as part of this effort.

Figure 70 compares the brake power derived from the manufacturer data for a 3W-28i engine with banana muffler and heavy fuel injection system (representing a COTS configuration) to the 3W-28i engine tested on the SERB. Two data sets are included for the 3W-28i engine tested in-house: one when the engine was practically new (less than 10 hours) and one after the engine had operated for approximately 50 hours. Prior to the second data set, the reed and reed carrier were replaced in response to several failures on the 3W-55i engine. It is important to note that the replacement reed shipped from the distributor was a different type of plastic than the original reed, but was less prone to chipping at the tips.

The most glaring discrepancy between the manufacturer data and the data collected on the SERB is the speed range over which the engines were operated. The engines purchased for this study had a red line of 8500 rpm based on the documentation that shipped with engines, and the stock ECU was speed limited to 8000 rpm. Attempting to run faster than

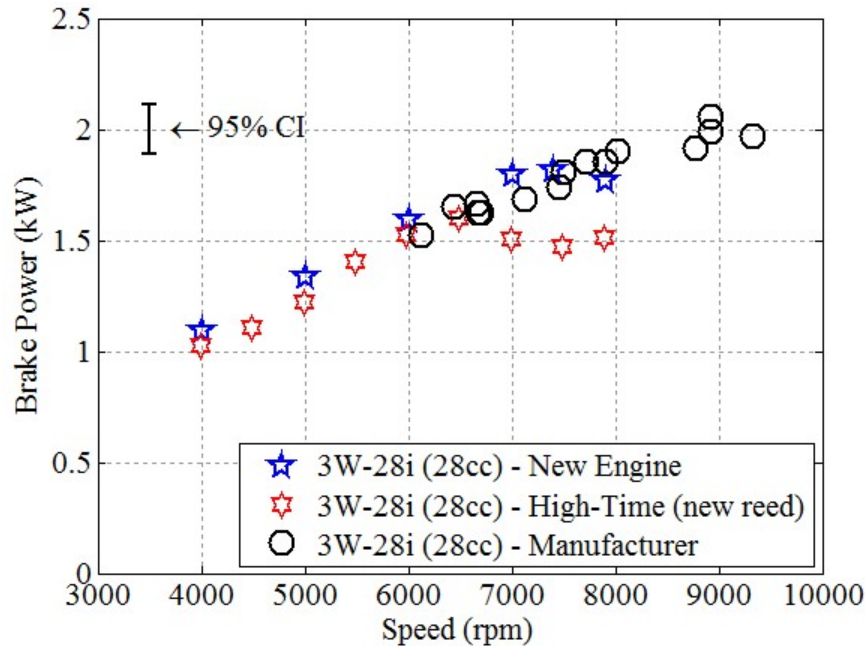


**Figure 70: Comparison of brake power produced by a 3W-28i with heavy fuel injection system and banana muffler to a 3W-28i engine as tested on the SERB.**

8000 rpm on the stock ECU caused it to disable the spark for cycles over 8000 rpm. Below 7000 rpm, the differences in the brake power delivered by the manufacturer engine and the engine tested herein were indistinguishable at the 95% confidence level. At and above 7000 rpm, the results were less clear. When originally tested, the 3W-28i engine matched the manufacturer results within a 95% confidence interval. However, decreasing delivery ratios above 7000 rpm indicated the engine was becoming air limited and if run to higher speeds would fall short of the manufacturer test above 8500 rpm, ECU limitations aside. Meanwhile the (same) engine (high-time) with a new reed and reed carrier exhibited a drop in power at and above 7000 rpm. The decrease in power corresponded to lower air flow than observed in the previous testing, despite no changes in the intake and exhaust systems, except for the replacement of the reed and reed carrier. A number of variables were tested in an attempt to reproduce the high end power with the high-time engine, including the



intake runner pressure drop, the exhaust runner pressure drop, and the head temperature, all of which had minimal impact. Replacing the head and piston ring increased power by about 7%-8%. While this indicates the power drop may have resulted from wear of the piston ring and cylinder liner, there were no visual indications that the liner or ring were excessively worn. Without a dynamometer or indicating pressure equipment (i.e. installed on an aircraft), the loss in power due primarily to reed configuration would have been very difficult to detect. Interestingly, the manufacturer literature rates the 3W-28i engine for a peak power of 2.5 kW even though it only developed a peak power of 2.1 kW at 500 rpm above the red line during the manufacturer's own testing.

The comparison of power developed on the SERB to manufacturer data led to the following conclusions. First, the SERB did not change the power output of the tested engines relative to the manufacturer tests. However, subtle changes during engine aging and reed/ reed carrier condition did impact high speed engine performance by up to 10%. Since the source of the power discrepancy was the engine and not the test setup, it was concluded that power production measured on the SERB was representative of the COTS engine configuration.

However, simply because the two engines produced the same amount of power does not mean they produced it with equal fuel efficiency. In fact, the high short-circuiting observed in the engines was the primary reason to vet engine performance on the SERB against a manufacturer data set. To that end, Figure 71 compares the BSFC of the same two engines, again showing the in-house engine as both a newer engine and after running approximately 50 hours of additional tests. Based on the figure, the engines as tested by the manufacturer had up to 50-125 g/kW-hr greater specific fuel consumption than the

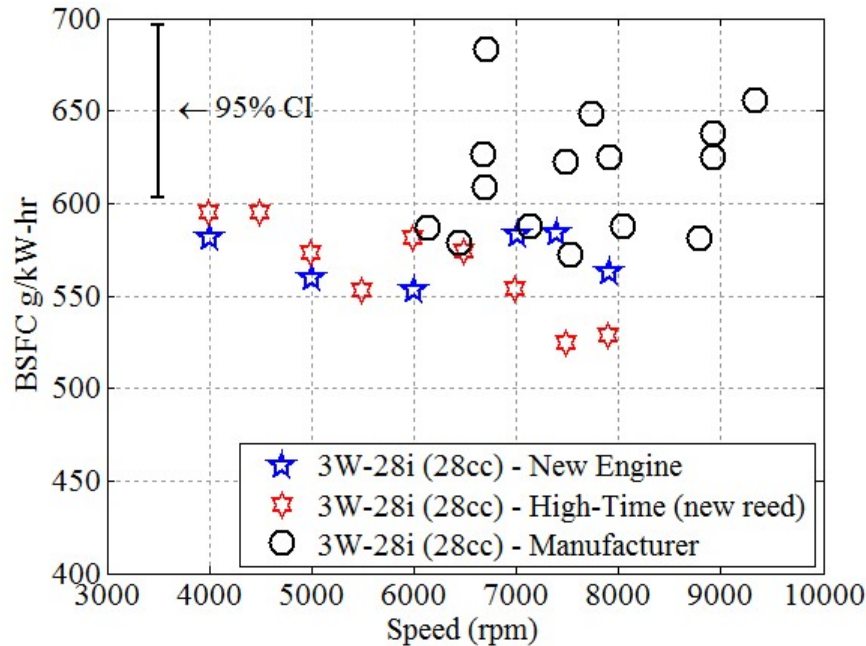


**Figure 71: Comparison of brake specific fuel consumption on a 3W-28i with heavy fuel injection system and banana muffler to a 3W-28i engine as tested on the SERB.**

engine tested on the SERB (in the speed range where the tests overlapped). This means the engines as tested in this study had slightly higher fuel conversion efficiencies than manufacturer tests. Quantifying the exact margin would require more precise information on the fuel used in manufacturer testing; the analysis assumes that the 98 ON PRF blend had approximately the same specific energy as the gasoline used by the manufacturer.

Above 7000 rpm, the high time engine actually has the best BSFC of any of the tests. As will be discussed later in this chapter, throttling these small engines tends to reduce short-circuiting. The reduced airflow observed in the high time engine at and above 7000 rpm effectively acted like throttling the engine, leading to a reduction in short-circuiting and explaining the corresponding improvement in BSFC. Combined, Figure 70 and Figure 71 show that installation and testing on the SERB did not increase the losses

(most importantly short-circuiting) relative to manufacturer expectations, and that results obtained from the SERB were reasonably representative of COTS system performance.

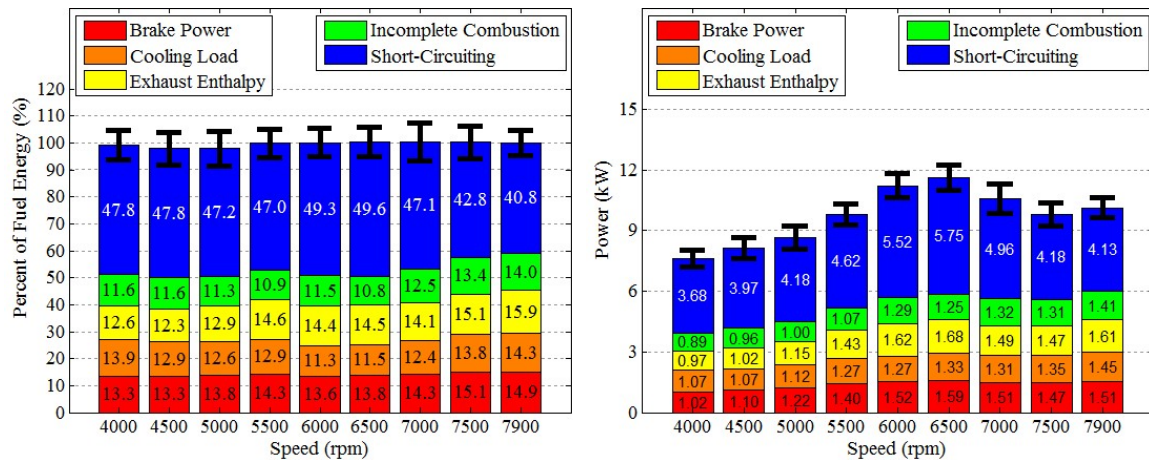
Regardless of the OEM's expectations, there still seemed to be a discrepancy between the performance of these COTS hobbyist engines and similarly sized engines produced for commercial applications such as scooters and small power equipment. In the United States, such engines, unlike hobbyist engines, are governed by the EPA Tier 4 regulations. Meanwhile, the 3W engines herein had emission levels consistent with engines commercially available under EPA Tier 1 (hydrocarbon) and EPA Tier 2 (CO) emissions standards (based on comparison to market survey data [231]). Therefore, it seems that engines designed for specific commercial applications such as power equipment and scooters have lower short-circuiting out of a necessity to meet emissions regulations (not required for hobbyist engines) and that manufacturers are able to meet those goals through fuel-to-tailpipe design of the power train and load as well as by diffusing the research and development cost over thousands (if not millions) of units. In fact, the relatively small production runs of small RPAs (TVS sold 60,000 scooter engines a month in 2015 [275] compared to the Boeing/Insitu Scan Eagle (3W-28i engine) which sold 50 aircraft per month at peak production [276]) are the entire reason COTS hobbyists engines are appealing for military RPAs; they are a means of reducing development cost. Short-circuiting mitigation techniques, discussed in the next section, range from relatively inexpensive (exhaust tuning, lean operation) to time and cost intensive (port redesign, LPDI). Future RPA programs should weigh the cost of short-circuiting mitigation options against the benefits to the operational concept envisioned for the platform.

### 2.3. Energy Balances on 3W Modellmotoren Engines & Speed Parametric Study

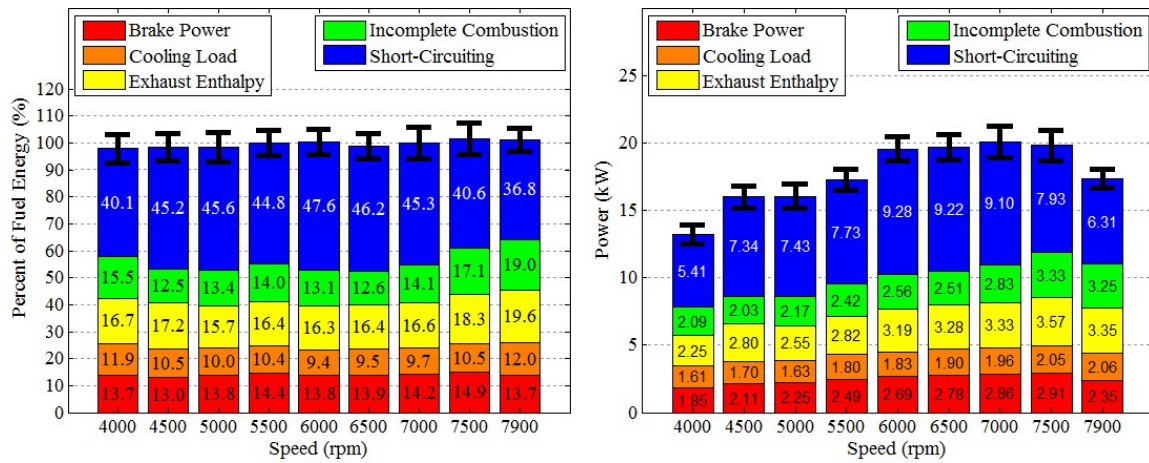
Figure 72 shows the energy balances on all three engines across their operational speed range at WOT with a CA50 of  $8 \pm 0.5^\circ \text{aTDC}$  (nominally MBT timing), an equivalence ratio of  $1.06 \pm 0.02$  (nominally peak power), and a head temperature of  $130 \pm 2^\circ \text{C}$ . As discussed in the preceding section, the results show that short-circuiting was the dominant loss mechanism in all three engines accounting for 40%-60% of the total fuel energy at WOT. In small two-stroke engines, especially those that are air carbureted, short-circuiting compounds with typically rich operation to doubly penalize fuel conversion efficiency.

First consider an engine operating near stoichiometric, with approximately 50% short-circuiting (as was typical of the 3W Modellmotoren engines in this study). For this condition, assume a reasonable combustion efficiency of 95% [21:82]. Now consider increasing the equivalence ratio of the engine to 1.2. Despite insufficient oxygen to completely combust all of the fuel, the trapped charge will still partially combust, releasing some of the chemical energy. Assuming perfect incomplete combustion to water, carbon dioxide, and carbon monoxide, the combustion efficiency for the trapped charge would be 83%, resulting in a 4.6% increase in released energy for 20% additional (trapped) fuel. Therefore, an increase in equivalence ratio from unity to 1.2 (20% increase in fuel consumption) will increase released energy by about 4.6% in an engine with negligible short-circuiting. An engine with 50% short-circuiting would still gain a 4.6% increase in released power, but the fuel cost would double. The extra fuel in the short-circuited charge is entirely wasted compared to the extra trapped fuel which is at least partially combusted. This example illustrates why engines with high short-circuiting, such as the two-stroke engines considered here, pay a larger penalty for rich operation.

### Modellmotoren 3W-28i Engine (SA/V=1.81 cm<sup>-1</sup>)



### Modellmotoren 3W-55i Engine (SA/V=1.46 cm<sup>-1</sup>)



### Modellmotoren 3W-85Xi Engine (SA/V=1.27 cm<sup>-1</sup>)

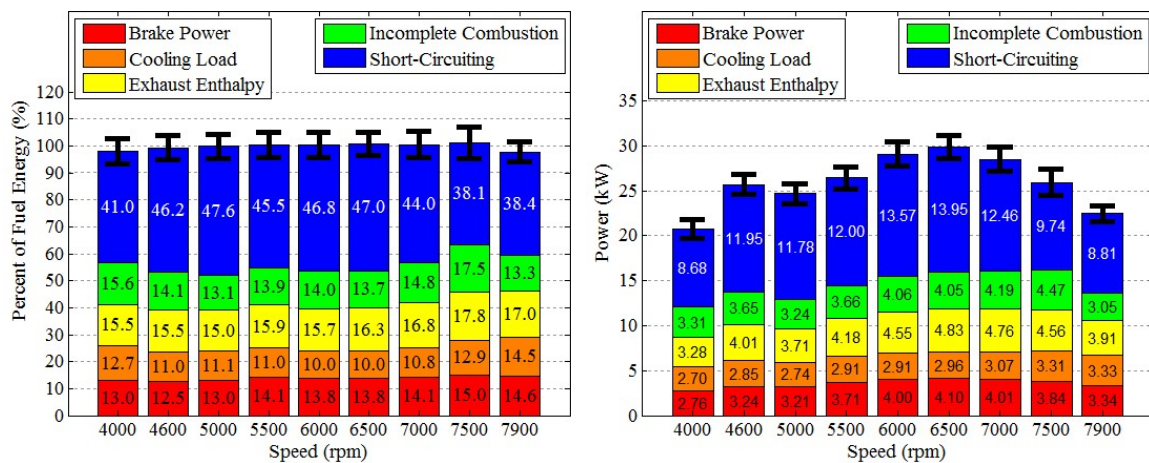


**Figure 72: Energy balances at WOT,  $\phi=1.06\pm0.02$ , CA50=8 $\pm$ 0.5°aTDC, & CHT=130 $\pm$ 2°C for the 3W-28i, 3W-55i, and 3W-85Xi engines. Uncertainty bars are for a 95% confidence interval.**

There are three primary avenues to mitigate short-circuiting: tuning, some form of direct injection, and as noted in the preceding discussion, lean operation. Tuning of two-stroke engines is a well-documented field of study. The basic premise is to design the exhaust so that the pressure wave that exits the engine when the exhaust port opens reflects off of the far wall of the exhaust runner and returns to the port as it is closing. The wave returns the last charge exiting the cylinder (typically rich in fresh charge) to the cylinder, reducing short-circuiting losses. Calculating the appropriate exhaust geometry is then a function of engine speed, exhaust temperature, and exhaust composition. It follows that engine tuning must target the operational speeds of the specific application. Indeed, tuning for a given speed will detune the engine at other speeds (the pressure wave has reflected and is leaving the exhaust port upon closure) increasing short-circuiting during off condition operation.

When complete redesign of the cylinder is an option, the port geometries may be optimized to mitigate short-circuiting. For example, Garg *et al.* used CFD to model the gas exchange in a 70 cm<sup>3</sup> displacement single cylinder moped engine [275]. The model was used to adjust the port angles and areas to reduce short-circuiting by 30%, leading to a 10% reduction in fuel consumption. While such a redesign was costly, the company sold approximately 60,000 units/month in 2015, offsetting the development and tooling costs.

Direct injection and/ or charge stratification are other alternatives to reduce short-circuiting. Direct injection involves injecting the fuel directly into the cylinder after the ports have closed. While conceptually simple, direct injection on a small engine is practically difficult due to the short time between port closing and the spark to inject the fuel and form a well-mixed combustible charge. As a result, direct injection systems for

10-100 cm<sup>3</sup> displacement engines are relatively uncommon, although emissions requirements have created renewed interest in the subject and a number of companies are investigating LPDI for small motorcycle engines [277, 278]. For example, Winkler *et al.* developed an LPDI system for a 300 cm<sup>3</sup> displacement single cylinder motorcycle engine using commercially available throttle body fuel injectors adapted into a custom designed cylinder head with ports optimized using 3D CFD [278]. The results showed a significant reduction in fuel consumption from 450 to 500 g/kW-hr down to 250 to 300 g/kW-hr. Implementation of the system necessitated a complete redesign of the engine head and the addition of an oiling circuit to the crankcase. Thus, like port redesign, addition of an LPDI system to a COTS engine is a costly endeavor for limited production runs.

Charge stratification and lean operation are two other alternatives. In charge stratification, the injection of fuel into the crankcase or intake runners is timed such that the first charge entering the cylinder is very lean (since it is more likely to short-circuit) while the tail portion of the fresh charge is rich. Charge stratification does not eliminate short-circuiting, and its effectiveness varies from engine to engine. Lean operation does not reduce short-circuiting, but it does reduce the fuel lost to short-circuiting. During the discussion of parametric study of equivalence ratio, the tradeoff between power, equivalence ratio, and efficiency will be examined in greater detail. While implementing strategies to reduce the short-circuiting in the studied engines is outside the scope of this work, the high short-circuiting underlines the necessity and value of mitigation strategies appropriate to the specific application and platform.

The high short-circuiting values obscured trends in the other loss pathways. Figure 73 shows the same energy balances as Figure 72 with the short-circuiting removed. This

demonstrates how the engines expended the trapped fuel that was available for combustion. Thus the energy balances in Figure 73 are indicative of engine performance if a direct injection strategy were implemented and the remaining operating parameters remained relatively constant. With short-circuiting removed, the fuel conversion efficiencies of the engines jumped to 21%-28%, with peak efficiencies for each engine of about 26%-28%. It should be noted that this is an optimistic assumption as no short-circuiting management technique is 100% effective. For example, LPDI typically leads to inhomogeneity in the charge increasing incomplete combustion products. Tuning would reduce (but not eliminate) short-circuited charge, but it would also reduce the charge cooling effect from the short-circuiting, increasing in-cylinder temperatures and thermal losses to the cooling flow while reducing charging efficiency.

Figure 73 provides insight into the combustion efficiency of these small engines. Combustion efficiency is the fraction of trapped fuel energy that is released during the combustion process. For automotive scale SI ICEs, combustion efficiency is typically 92%-98% for equivalence ratios between unity and about 1.10 [21:82]. In the studied engines, combustion efficiencies were approximately 72%-78% at an equivalence ratio of  $1.06 \pm 0.02$  across the operational speed range. The difference in incomplete combustion can be linked to a combination of wall effects (quenching) and mixture inhomogeneity. Quenching can be tied back to changes in the surface area to volume ratio, while the mixture issues were primarily the result of the scavenging process. The ability of TBI and crankcase scavenging to create a homogenous fresh charge is well documented [279]. It was hypothesized at the onset of this effort that increasing cylinder surface area to volume ratio would contribute to increasing incomplete combustion losses.



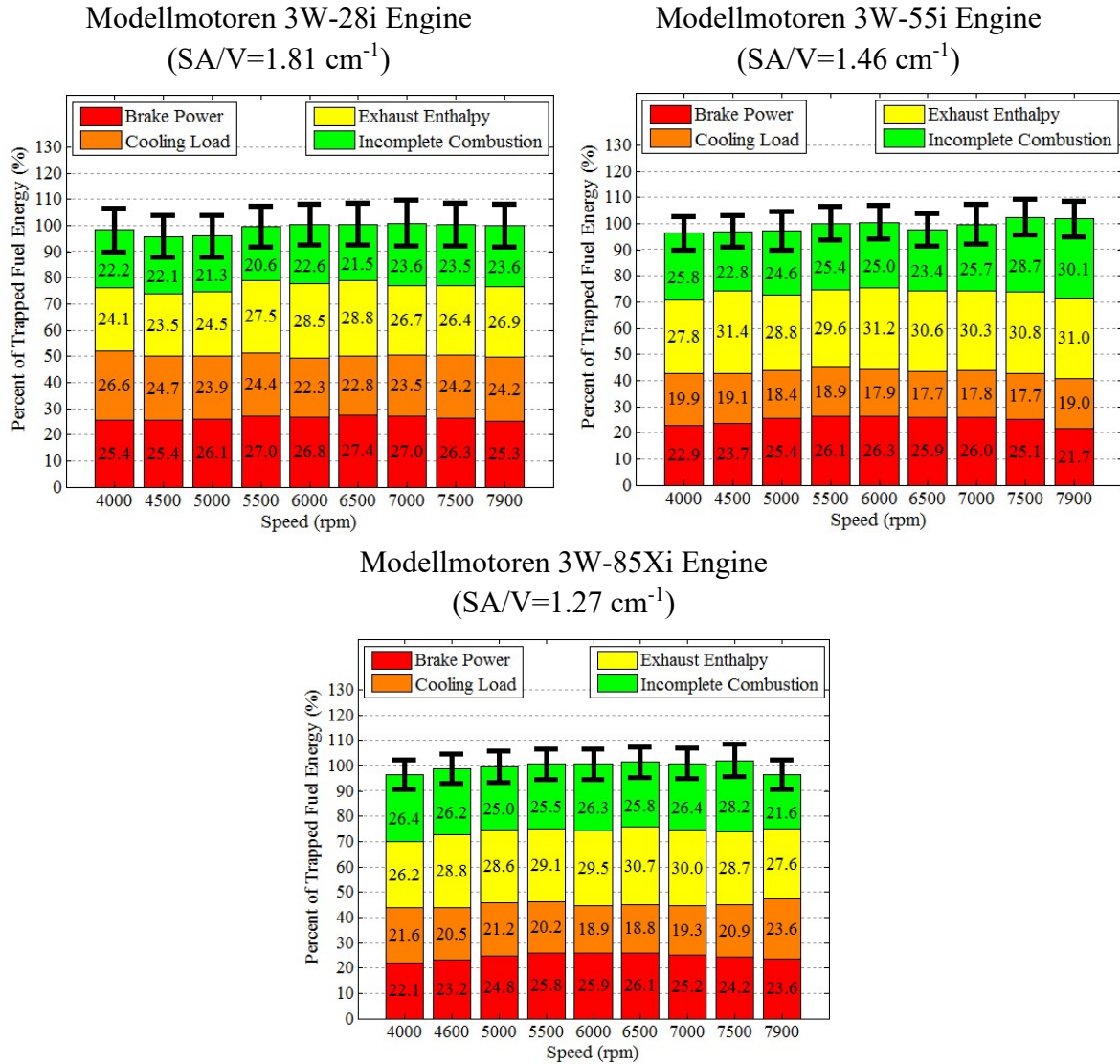


**Figure 73: Trapped energy balances at WOT,  $\phi=1.06\pm0.02$ , CA50=8 $\pm0.5^\circ$ aTDC, & CHT=130 $\pm2^\circ$ C for the 3W-28i, 3W-55i, and 3W-85Xi engines. Uncertainty bars are for a 95% confidence interval.**

One hypothesis going into this effort was that decreasing engine size would lead to increasing thermal losses, again due to increasing the surface area to volume ratio. Figure 73 shows that across the operational speed range, the WOT cooling load increases by 4-7% from the 3W-85Xi and 3W-55i engines to the 3W-28i engine. However, the increase in cooling load was almost completely offset by a corresponding decrease in

sensible exhaust enthalpy. Thus, in the range of surface area to volume ratios studied here, the primary effect of increasing the surface area to volume ratio was shifting thermal loading from the exhaust to the cylinder head. While this shift had little impact on fuel conversion efficiency, shifting thermal loading from the exhaust gases to the cylinder reduced energy transfer from the exhaust gas to the fresh charge. In the case of the studied engines, this transfer contributed to an increase in knock resistance with decreasing engine size as will be discussed in Chapter VI, Section 2. As will be discussed in the following section, heat transfer losses do not appear to increase drastically until the bottom end of the 10-100 cm<sup>3</sup> displacement range, and in that context the similarity of the 3W-55i and 3W-85Xi heat losses is somewhat unsurprising.

While the energy balances presented here show a full accounting of the fuel energy for the tested engines and provide insight into the dominant loss pathways, they are by themselves insufficient to answer the overarching question posed by Objective 1: what makes 10-100 cm<sup>3</sup> displacement engines less efficient than larger engines and more efficient than smaller engines as observed in Figure 74? Despite efforts to select geometrically similar engines, design variations between the engines dominated the differences between the studied engines. Therefore, to draw conclusions about the losses driving the observed drop in efficiency (Figure 74) as engine displacement decreases from larger than 100 cm<sup>3</sup> to less than 10 cm<sup>3</sup>, the energy balances for the tested engines should be examined in the context of both larger and smaller engines whose energy balances are available from the literature.

## 2.4. Scaling of Loss Pathways

More insight into the scaling of loss pathways may be gained by examining these engines in the context of both larger and smaller engines. At the heart of Objective 1 was the following question: what loss pathways drive the decrease in efficiency and the knee in the efficiency curve as engine displacement decreases from 100-1000 cm<sup>3</sup> (motorcycle, scooter engines, and small automotive engines) to 0.1-10 cm<sup>3</sup> (glow fuel engines). Figure 74 shows the studied engines plotted against engine data aggregated by Menon and Cadou [6]. The individual points plotted by Menon and Cadou have been replaced with ranges representative of engine type. The highway and large transport engine data was collected primarily from engine manufacturers. The micro engine (glow fuel) data was collected by Menon and Cadou, who also created the fits shown in the Figure 74 [6]. The original plot contained sparse engine information for engines with displaced volumes between 10 cm<sup>3</sup> and 100 cm<sup>3</sup>, which is the appropriate displacement for Group 2 RPAs and the size that is the focus of this study. It should be noted that the manufacturer data used to create the small vehicle SI range consisted primarily of two-stroke engines that all fell below the fit suggested by Menon and Cadou [6]. Meanwhile, the Group 2 RPA range was an estimate based on three four-stroke engines, manufactured by Honda Motor Company.

Figure 74 clearly shows decreasing efficiency with displaced volume, with a more rapid decrease beginning in the Group 2 RPA size range. That decrease in efficiency is driven by different phenomena in different size ranges. For example, large ship and train engines tend to be blower scavenged, turbo charged, direct injection, CI two-stroke engines, which have fundamentally higher theoretical efficiencies (due to higher compression ratios) than four-stroke spark-ignition highway engines.

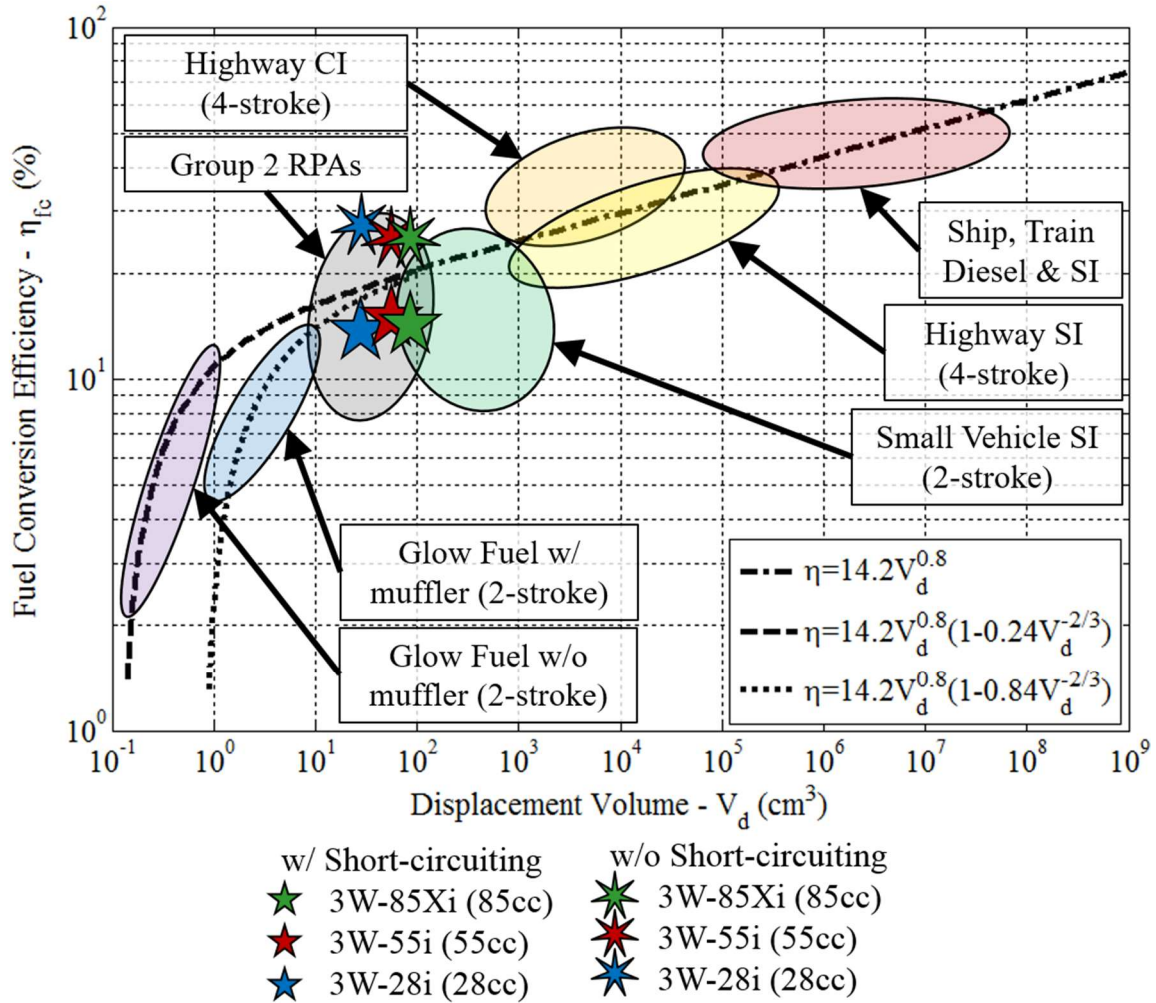


**Figure 74: Relationship between fuel conversion efficiency and engine displacement grouped by type of engine. Adapted (including fit) with permission from a similar plot by Menon and Cadou [6]. Data for glow fuel engines collected by Menon and Cadou [6]. Data for small vehicle, highway, and large diesel engines based on manufacturer specifications compiled by Menon and Cadou [6].**

Before considering the energy balances and loss pathways, it was necessary to verify that the efficiencies of the engines selected for this study were consistent with the observed trends and thus representative of 10-100  $\text{cm}^3$  displacement engines. Two sets of data are included in the plot. The first data set shows the fuel conversion efficiency for the studied engines with short-circuiting included. When short-circuiting is included, the engines in this study fell slightly below the efficiency fit shown in Figure 74. The second data set

shows the fuel conversion efficiency if short-circuiting were eliminated, which is above the line. Applying short-circuiting mitigation strategies for a specific application would fall somewhere between the two cases. Furthermore, all manufacturer data for two-stroke small vehicle SI engines also fell below the fit shown in Figure 74. Therefore, the engines considered were consistent with expectations of engine performance for two-strokes in the Group 2 RPA size range. This is critical because it means the chosen engines were representative of the performance expected from 10-100 cm<sup>3</sup> displacement engines and could be used to draw conclusions about what loss pathways drive the efficiency decrease across the aforementioned regime.

The three engines studied herein also demonstrate the difficulties of confounding variables when discussing “engine size”. To this point in the document, “engine size” has typically implied “displaced volume”. However, there are other variables that change implicitly with engine size. For example, while all engines studied herein had geometric compression ratios of 10:1, each engine had different port timings and therefore different trapped compression ratios (see Table 14, page 203). Trapped compression ratio is a better indicator of thermodynamic performance as it is more representative of the compression that actually occurs in the trapped gas. In Figure 74 it appears that for the engines tested herein that the fuel conversion efficiency actually decreased from the 3W-55i engine to 3W-85Xi engine. However, the trapped compression ratio also decreased from 7.2:1 for the 3W-28i engine to 7.1:1 for the 3W-55i engine and 6.3:1 for the 3W-85Xi engine. For an ideal Otto cycle a decrease in compression ratio from 7.2:1 to 6.3:1 results in a 2.4% decrease (from 54.6% to 52.1%) in theoretical thermal efficiency. Thus, confounding variables make it difficult to identify scaling trends over small engine size ranges,

especially when limiting the scope to COTS engines. However, since the engines in this study were representative of the 10-100 cm<sup>3</sup> displacement range, the collected data does provide insight into trends in how loss pathways scale from displacements larger than 100 cm<sup>3</sup> to those smaller than 10 cm<sup>3</sup>.

Figure 75 shows the energy balances at peak power for the three 3W Modellmotoren engines studied in this effort. It also includes representative energy balances for larger automotive scale CI and SI engines compiled from Heywood [21:674], and smaller glow fuel engines compiled from Menon and Cadou [6, 16]. It should be noted that data for the small glow fuel engines did not distinguish between short-circuiting and incomplete combustion losses. Instead the exhaust losses were calculated as the total energy delivered to the engine less the other pathways. The engines that Heywood considered in the representative automotive energy balances were four stroke and/or configured for direct injection, explaining the lack of a short-circuiting term for the automotive scale energy balances. Additionally, the cooling load on the 3W engines includes the friction losses, which are broken out separately on the automotive and glow fuel engines.

As observed in Figure 72 and Figure 73, short-circuiting dominated the loss pathways for the 3W Modellmotoren engines. In terms of chemical energy in the exhaust, short-circuiting was approximately four times incomplete combustion at WOT. The available micro glow fuel engine data indicates that the combination of short-circuiting and incomplete combustion played a dominant role in the losses from the micro glow engines as well, although the study did not distinguish between the two pathways. Based on this data, it is reasonable to hypothesize that a significant portion of the exhaust losses observed in the micro glow engines was the result of short-circuiting. Therefore, short-circuiting

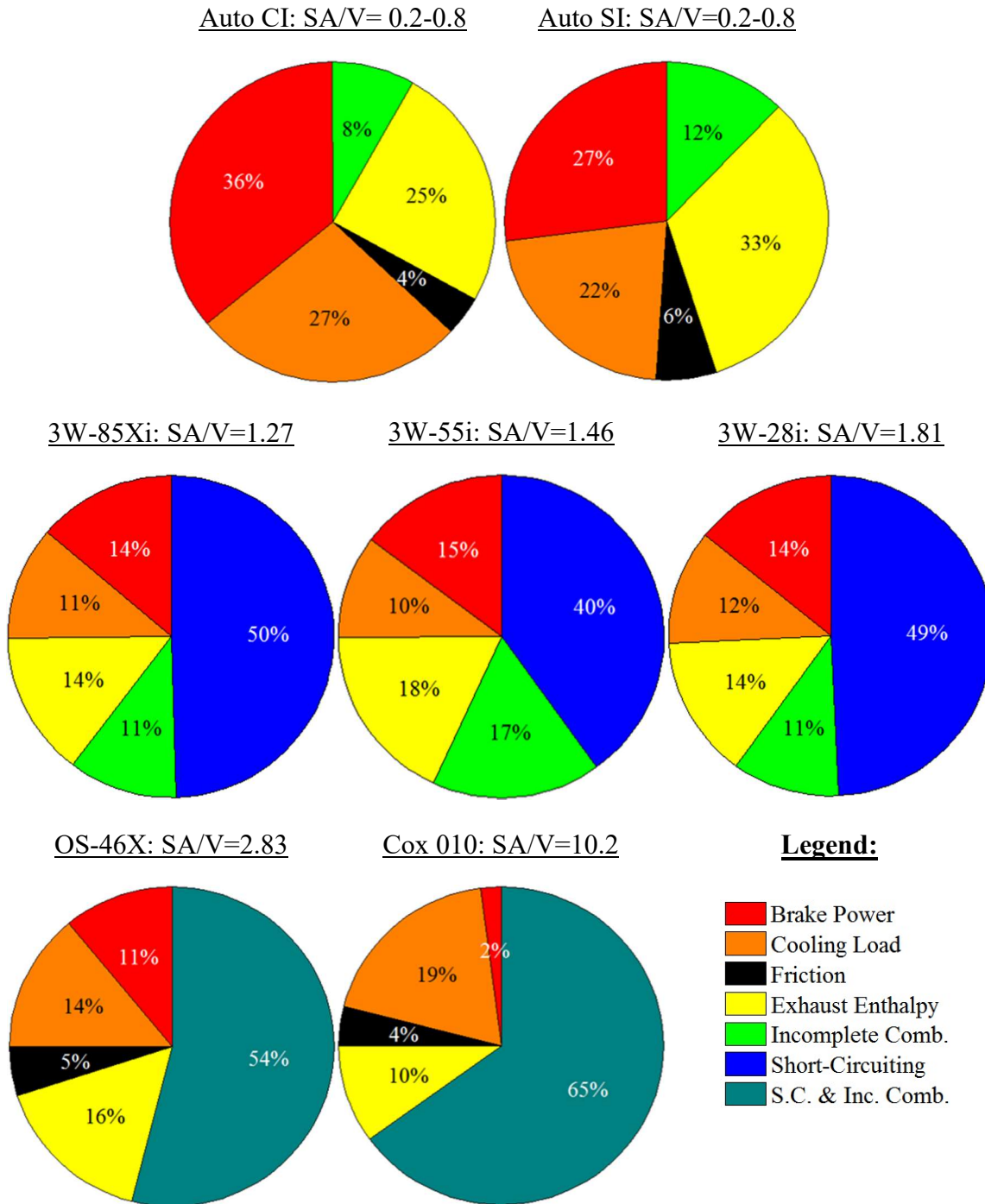


**Figure 75: Complete energy balances for seven engines. Data for automotive engines was compiled from Heywood [21:674]. Data for the micro glow fuel engines was collected by Menon and Cadou [16]. Friction losses from the 3W engines are part of the cooling load and sensible exhaust enthalpy. Deviations in chart totals from 100% are due to rounding errors during normalization of the data.**

plays a dominant role in decreasing fuel conversion efficiency as engine displacement decreases from the automotive scale to less than  $100 \text{ cm}^3$ , at least in two-stroke engines.

The majority of engines developed for small aircraft (typically hobbyist) and small handheld power equipment are two-stroke engines, primarily because they have higher specific power than comparable four-stroke engines. Four-stroke engines have a fundamentally different gas exchange process than two-stroke engines and as a result, typically have much lower short-circuiting. However, since they only produce power every other revolution, they have higher thermal losses from the engine head, cooler head temperatures, and on the small scale are more prone to quenching at the walls (which leads to increased incomplete combustion). Since increased thermal losses would partially offset the gains from decreased short-circuiting (and that offset would increase in micro engines), it is difficult to tell where small four-stroke engines ultimately fall with respect to two-stroke engines. Thus there exists an opportunity for future research to examine how losses differ between two-stroke and four-stroke engines smaller than  $100 \text{ cm}^3$  displacement.

As the discussion proceeds, it will be helpful to think of each loss in terms of an efficiency, where the overall fuel conversion efficiency ( $\eta_{fc}$ ) is the product of each of the component efficiencies (see Chapter II, Sections 2.5.4 & 2.8). The complementary efficiency to short-circuiting is the trapping efficiency ( $\eta_{tr}$ ), which describes how well the engine retains delivered fuel. Mathematically, the trapping efficiency is unity less the short-circuiting. The energy lost to short-circuiting is a facet of the gas exchange design of the engine and as already discussed, can be managed through a variety of methods. While clearly detrimental to overall efficiency, the short-circuiting has little impact on the actual thermodynamic performance of the engine as far as releasing heat from the trapped



fuel and converting the released heat into useful work. Rather, the thermodynamic performance of the engine is described by the remaining pathways which detail how an engine expends the fuel trapped in the cylinder that is available for combustion.

Figure 76 shows the same energy balances (peak power) as Figure 75 with the short-circuiting removed. The energy balances on the micro glow engines were omitted due to insufficient data to disentangle incomplete combustion from short-circuiting. With short-

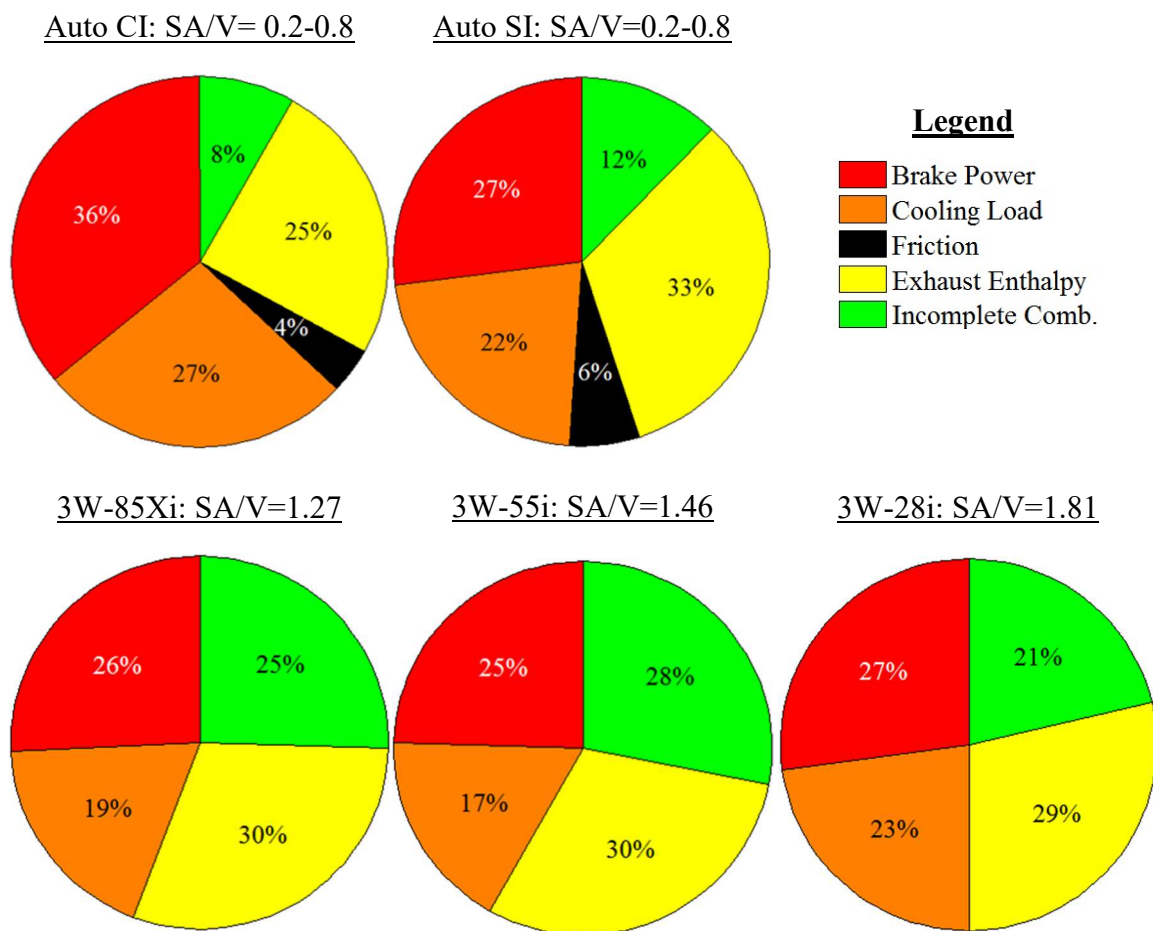


**Figure 76: Energy balances on trapped fuel energy for five engines showing trends in loss pathways with surface area to volume ratio. Friction losses from the 3W engines are part of the cooling load and sensible exhaust enthalpy. The data for automotive engines was compiled from Heywood [21:674]. Deviations in chart totals from 100% are due to rounding errors during normalization of the data.**

circuiting removed, incomplete combustion became the dominant loss mechanism in the studied engines. Here, the relevant efficiency is the combustion efficiency ( $\eta_c$ ), which describes how well an engine releases the energy contained in the fuel during combustion. Mathematically, the combustion efficiency is unity less the fraction of trapped fuel energy lost to incomplete combustion (or in the case of Figure 76, the sum of all pathways except incomplete combustion).

Incomplete combustion can be caused by both the gas exchange process and quenching at the cylinder wall (and excess fuel during rich operation). As part of the gas exchange process, fresh air and fuel must mix in the intake runner, crankcase, and cylinder to form a combustible mixture while expelling the combustion products. Poor mixing and high residuals negatively impact combustion efficiency. For example, during throttled operation (see Section 3.4) of the 3W-28i engine at 6000 rpm, incomplete combustion more than tripled from 11% of total fuel energy at a delivery ratio of 1.1 (WOT) to 36% of the total fuel energy at a delivery ratio of 0.3 (1/4 throttle). Quenching of the trapped charge at the cylinder wall is caused by loss of heat from the hot combustion gases to the wall faster than heat is released by combustion, which in turn can be caused by decreasing wall temperature, increasing the wall surface area relative to the combustion volume, and/or decreasing the amount of heat released during combustion.

Incomplete combustion losses as a fraction of trapped fuel energy were 10% to 20% (absolute) lower in large CI and SI engines than in the studied 3W engines. CI engines generally operate significantly lean of stoichiometric, so the automotive SI energy balance offers a better benchmark for comparing the 3W Modellmotoren engines to larger engines. Compared to larger SI engines, the studied engines lost 2-2.5 times more of the energy in

the trapped fuel to incomplete combustion. As stated in the preceding paragraph, some of this loss was due to poor mixture formation and gas exchange with the remainder resulting from an increasing ratio between the cylinder surface area and the combustion volume.

Just as short-circuiting losses could be removed to look at how an engine expends trapped fuel, incomplete combustion losses may also be removed to examine how an engine uses the energy actually released during combustion and converts it into useful work. Figure 77 shows all seven energy balances reduced to only the released energy terms. Again, the friction in the 3W engines is included in the cooling load and exhaust enthalpy losses. The relevant efficiency is the thermal efficiency ( $\eta_{th}$ ), which represents how well an engine converts the released energy into useful work. In the strictest sense, that useful work is the work at the piston face, which will be further reduced by friction losses in the engine and in the drive train (or as is common in aircraft, the gearbox). These friction losses are typically described using a mechanical efficiency ( $\eta_m$ ), which is the fraction of brake power divided by the sum of brake power and friction. The thermal efficiency may then be calculated as the sum of the brake power and friction terms divided by the total released heat.

A common heuristic for conventional engines is that 1/3 of the released energy is lost to heat from the head, 1/3 is lost as heat through the exhaust, and 1/3 is converted into work (some of which is then lost to friction). As seen in Figure 77, the automotive and transport vehicle scale CI and SI engines roughly follow that heuristic. One of the hypotheses going into Objective 1 was that thermal losses from the cylinder would be the dominant factor in decreasing fuel conversion efficiency in the 10-100 cm<sup>3</sup> displacement range. Based on Figure 77, this was not the case. While the 3W Modellmotoren engines exhibited a

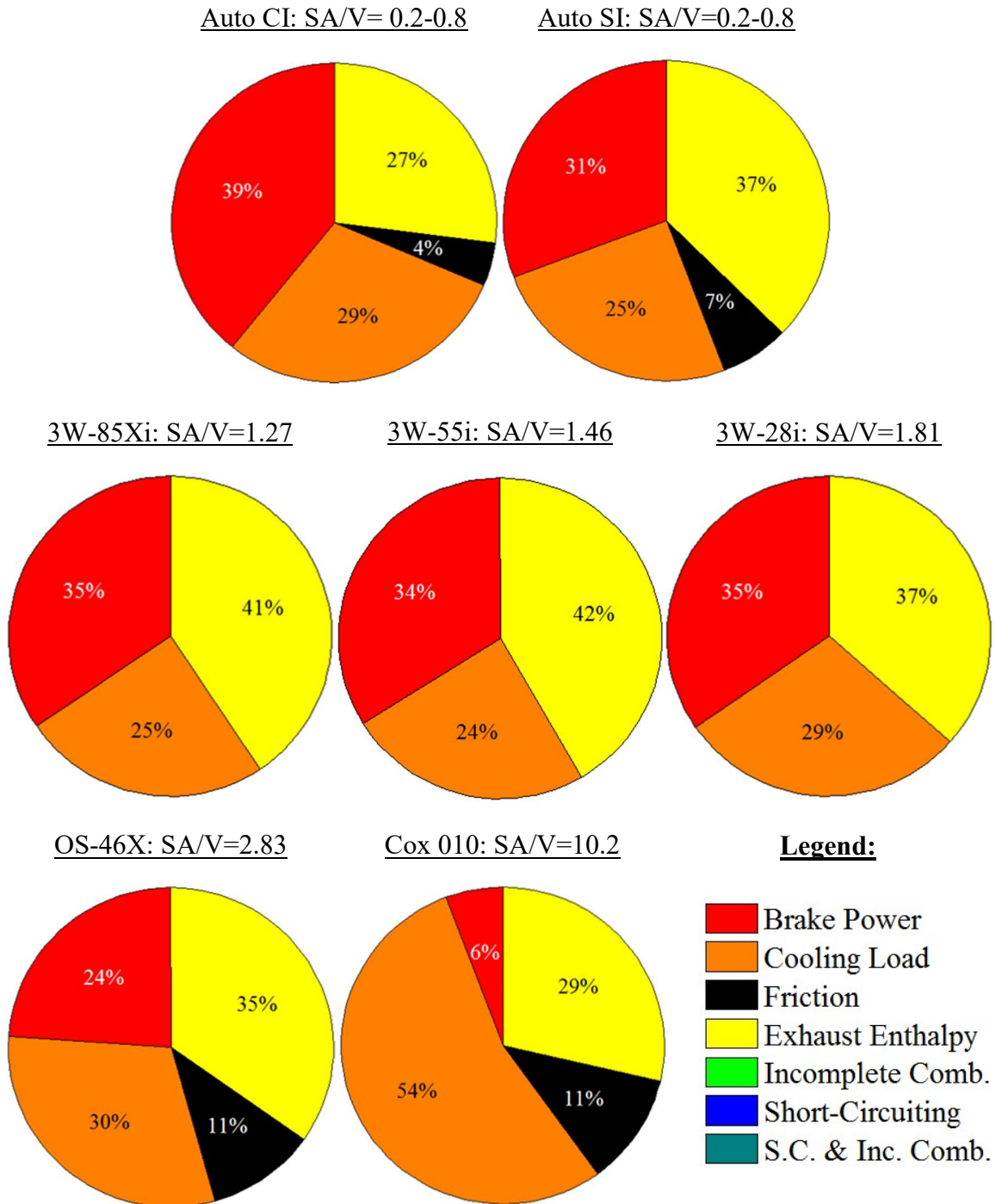


**Figure 77: Energy balances on released fuel energy for seven engines, showing trends in loss mechanisms with surface area to volume ratio. Friction losses from the 3W engines, rejected as heat, are part of the cooling load and sensible exhaust enthalpy. The data for automotive engines was compiled from Heywood [21:674]. Data for the micro glow fuel engines was collected by Menon and Cadou [16]. Deviations in chart totals from 100% are due to rounding errors during normalization of the data.**

tendency to shift thermal loading from cooling through the head to the exhaust, their thermal efficiencies were comparable to automotive scale engines. Therefore, it can be concluded that the efficiency drop observed as engine displacement decreases from larger than 100 cm<sup>3</sup> displacement to the 10-100 cm<sup>3</sup> displacement range was caused by short-circuiting and incomplete combustion losses, not heat transfer losses.

Next consider the micro glow engines. As the displacement decreased below 10 cm<sup>3</sup>, thermal losses from the engines played an increased role in dissipating the released chemical energy. Over 50% of the energy released in the Cox 010 engine was rejected as heat, cutting into the thermal efficiency and in turn brake power of the engine. Therefore, for engines smaller than 10 cm<sup>3</sup> displacement increasing thermal losses due to increasing surface area to volume ratio play an increasingly important role. Combined with high exhaust chemical energy losses (short-circuiting and incomplete combustion), the increasing dominance of heat transfer causes the rapid drop in efficiency observed in Figure 74 as engine displacement falls below 10 cm<sup>3</sup>.

So far the examined losses have described how efficiently the engines used the delivered fuel, a discussion which only implicitly considers total power. Brake mean effective pressure describes how effectively an engine uses its displaced volume to produce power. Lower BMEP values mean that less power is produced per physical unit of engine, and for obvious reasons, higher BMEP's are advantageous, especially for an aircraft application. Similar to Figure 74, Figure 78 is a plot showing how BMEP relates to displaced volume for several types of engine. As was the case with efficiency, the effect of engine design (scavenging, compression ratio, etc.) on BMEP made it difficult to draw conclusions about BMEP scaling without the context of data from larger and smaller

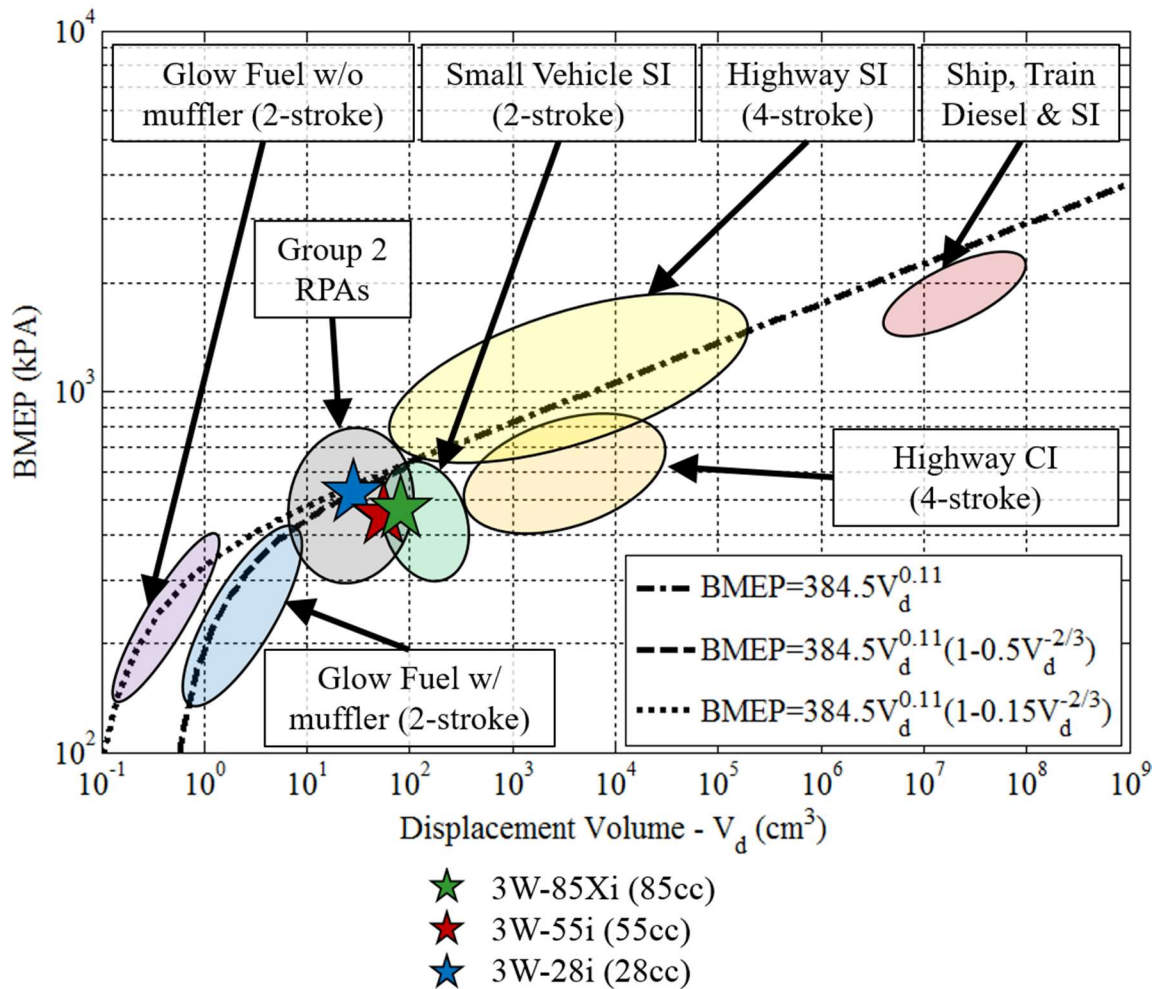


**Figure 78: Relationship between internal combustion engine BMEP and engine displacement grouped by type of engine. Adapted (including fit) with permission from a similar plot by Menon and Cadou [6]. Data for glow fuel engines collected by Menon and Cadou [6]. Data for small vehicle, highway, and large diesel engines based on manufacturer specifications compiled by Menon and Cadou [6].**

engines. As with fuel conversion efficiency, the decrease in BMEP with displaced volume is driven by different phenomena at different sizes. Compression ignition engines typically run at lean equivalence ratios compared to SI engines, leading to lower BMEP values and explaining the difference between highway SI and CI engines. Thus while CI engines are more efficient than SI engines, they are heavier, a significant disadvantage for an aircraft. (Also note that their higher compression ratios that develop higher theoretical efficiency

bring an additional weight penalty in terms of engine structure). Very large engines are typically turbocharged or supercharged, also increasing their BMEP.

The three engines studied in this effort showed no clear trend in BMEP at peak power with increasing engine size. As previously mentioned, BMEP describes how effectively an engine uses its displaced volume to create power. Therefore, BMEP is directly proportional to how efficiently fresh charge is trapped and subsequently converted into power. Thus BMEP is influenced by the trapped compression ratio, friction, incomplete combustion, and thermal losses, but not short-circuiting (outside of its relationship with trapping efficiency). Discussed next, the trapped compression ratio and charging efficiency were the dominant factors driving the observed difference in peak power IMEP.

Equation (126) [21:171] for the ideal air standard Otto cycle [21:163] provides a means for estimating the impact of trapped compression ratio and charging efficiency on IMEP (and by proxy, BMEP), using conditions at the start of compression ( $p_1, T_1$ ), the ratio of specific heats ( $\gamma$ ), the compression ratio ( $CR$ ), the gas constant ( $R$ ), and the energy released during combustion per unit of working fluid ( $Q^*$ ). While, the effect of compression ratio is clear in Equation (126), the effect of the charging efficiency is more subtle. Charging efficiency is implicitly included in working fluid energy released term ( $Q^*$ ). As charging efficiency decreases, the specific chemical energy in the working fluid that may be released by combustion decreases proportionally. In other words, a 10% change in charging efficiency would cause an approximately 10% change in  $Q^*$ .

$$IMEP = p_1 \left( \frac{Q^*}{RT_1} \right) \left( \frac{CR}{CR - 1} \right) \left( 1 - \frac{1}{CR^{\gamma-1}} \right) \quad (126)$$

In two-stroke engines, the trapped compression ratio is controlled by the port timing. Raising the port timing reduces the amount of charge that can be trapped in the cylinder relative to the total displaced volume. Referring to Table 22, trapped compression ratios for the studied engines ranged from 7.2 for the 3W-28i engine and 7.1 for the 3W-55i engine to 6.3 for the 3W-85Xi engine. Based on Equation (126), reducing the trapped compression ratio from 7.2 to 6.3 results in a 2% reduction in IMEP. The change between 7.2 and 7.1 is negligible.

Decreasing charging efficiency, discussed in more detail later in this section, also decreased BMEP. Despite similar trapped compression ratios on the 3W-55i and 3W-28i engines, the charging efficiency at peak power was lower for the 3W-55i engine (47% at 7500 rpm) than for the 3W-28i (54% at 6500 rpm) and 3W-85Xi (50% at 6500 rpm) engines. Based on Equation (126), the lower charging efficiency of the 3W-55i engine would reduce IMEP by 13% compared to the 3W-28i engine and by 5% compared to the 3W-85Xi engine. Combining both the changes in trapped compression ratio and charging efficiency, Equation (126) predicts that IMEP in the 3W-55i engine would be 13% lower than the 3W-28i engine and 3% lower than the 3W-85Xi engine. Differences in BMEP should be similar, but slightly higher since IMEP includes friction, which will be discussed in Chapter V, Section 3. Indeed, the measured differences in BMEP at peak power between the 3W-55i engine and the 3W-28i and 3W-85Xi engines were 15% and 4%, respectively, indicating that variations in charging efficiency and trapped compression ratio dominated the BMEP behavior in the studied engines.

As in the case of fuel conversion efficiency, to draw conclusions about overall scaling of BMEP, the tested engines had to be examined in the context of larger and smaller



engines. The energy balances above explain what happens as engine size decreases through the 10-100 cm<sup>3</sup> displacement range (Group 2 RPAs). Compared to engines larger than 100 cm<sup>3</sup> displacement, the increase in incomplete combustion (or decrease in combustion efficiency) as well as residuals from incomplete scavenging result in less efficient use of the cylinder volume for 10-100 cm<sup>3</sup> SI two-strokes. Numerically, the result is similar to lean operation. Despite operating near stoichiometric, the 3W Modellmotoren engines exhibited BMEP values comparable to highway CI engines and consistent with larger small vehicle SI two-stroke engines. Unlike highway CI engines where the drop in BMEP relative to highway SI engines is driven by lean operation, the drop in BMEP observed in the studied small, two-stroke engines was driven by an increase in losses, specifically incomplete combustion. (Remember, short-circuiting, while also higher than highway SI engines, does not directly impact BMEP). As engine displacement continues to decrease below 10 cm<sup>3</sup>, increasing thermal losses compound with incomplete combustion losses creating the rapid drop off in BMEP.

While short-circuiting negatively impacts the overall fuel conversion efficiency, its impact on BMEP is indirect and limited to its impact on the gas exchange process. The gas exchange process determines the amount of trapped (fresh) charge in the cylinder (trapping efficiency) and the efficiency with which fresh charge replaces burnt charge (charging efficiency). Figure 79 shows the effect of engine speed on charging efficiency at WOT, and Figure 80 shows impact of engine speed on BMEP. In the tested engines, charging efficiency drops about 4%/krpm and the BMEP in Figure 80 tracks the trends in charging efficiency. Figure 80 also shows the impact of trapped compression ratio, since the 3W-8X5i engine had BMEP values lower than the 3W-28i engine even at points where

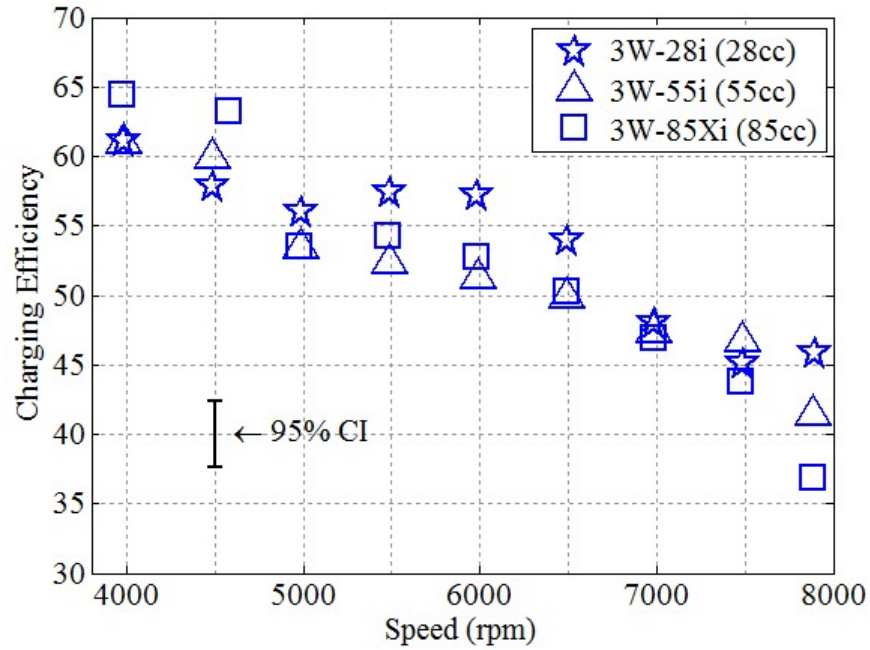


Figure 79: Charging efficiency at WOT,  $\phi=1.06\pm0.02$ ,  $CA_{50}=8\pm0.5^\circ\text{aTDC}$ , &  $CHT=130\pm2^\circ\text{C}$  for the 3W-28i, 3W-55i, and 3W-85Xi engines.

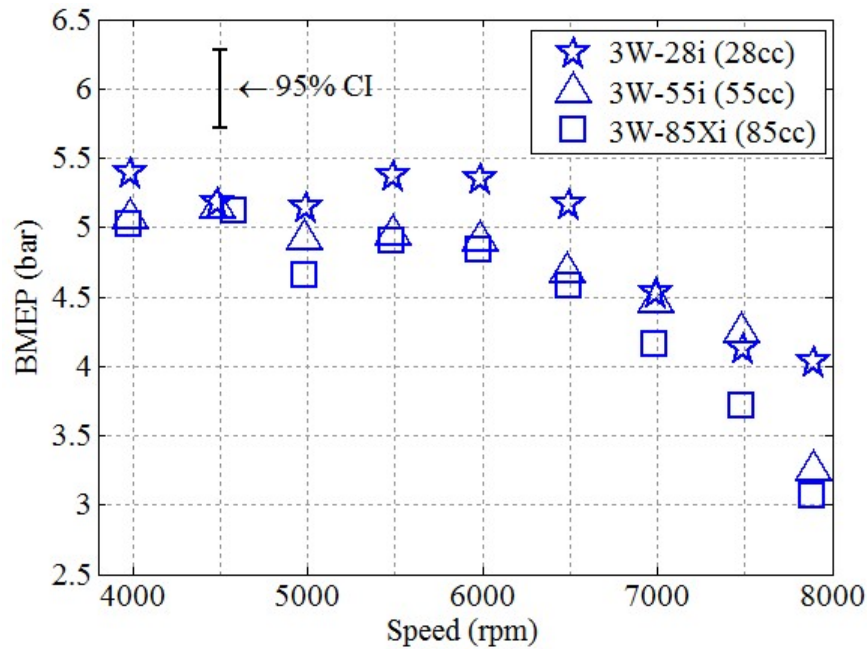
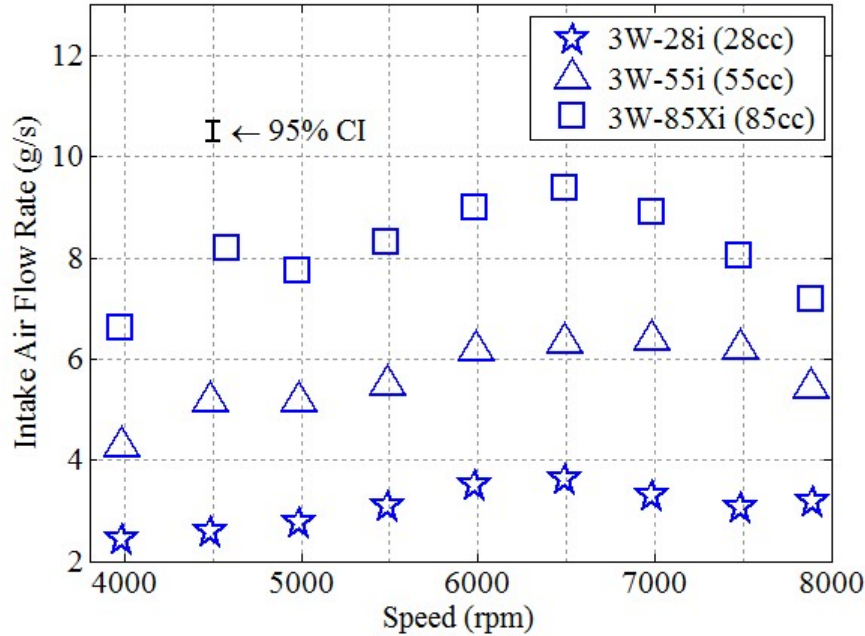


Figure 80: BMEP at WOT,  $\phi=1.06\pm0.02$ ,  $CA_{50}=8\pm0.5^\circ\text{aTDC}$ , &  $CHT=130\pm2^\circ\text{C}$  for the 3W-28i, 3W-55i, and 3W-85Xi engines.

its charging efficiency is greater. As is clear from the figures, the drop in BMEP (brake power normalized by engine speed and displaced volume) with engine speed was directly tied to a decrease in charging performance. A more detailed examination of the gas exchange performance will be presented in Chapter V, Section 4. At this point, it suffices to say that all three of the studied engines became breathing limited at high speeds. If the breathing performance (and thus IMEP/BMEP) at 6000 rpm of the engines extended more uniformly to the red line of 8500 rpm, then the engines would also be substantially closer to developing full manufacturer rated power.

The intake air system on the SERB was investigated and ruled out as the cause of poor breathing at high speed. Indeed, for each engine the total air flow rate peaked between 6000-7000 rpm as seen in Figure 81; if the test setup were limiting air flow into the system, then one would expect the air flow rate to rise and then plateau at high speeds, not to peak and fall off. At approximately 6500 rpm and below, the IMEP/BMEP values of the tested engines were consistent with expectations for small vehicle SI two-stroke engines. There is no reason to believe that with proper attention to the design components controlling the gas exchange process (in this case the throttle body, intake, and reeds) that the IMEP/BMEP observed at 6000-6500 rpm could not be extended to higher speeds, yielding increased engine power. (If IMEP/BMEP remains constant, then power increases directly with engine speed for a fixed displacement.)

From an aircraft standpoint, BMEP dictates how large of an engine is required to meet mission requirements, while short-circuiting factors into overall efficiency and in turn how



**Figure 81: Intake air flow at WOT,  $\phi=1.06\pm0.02$ ,  $CA_{50}=8\pm0.5^\circ$ aTDC, &  $CHT=130\pm2^\circ\text{C}$  for the 3W-28i, 3W-55i, and 3W-85Xi engines.**

much fuel the aircraft must carry. There are numerous sources (example [4, 7]) that discuss the minimum required efficiency to make a hydrocarbon based propulsion system preferable to an electric system. Often those analyses assume comparable electric motor and engine weights, implying at a minimum consistent power densities as each type of power plant is scaled down. Based on a review of manufacturer data [280] this is generally true for 60 W to 6 kW motors. Of the 46 motors surveyed, the average specific power was  $4.15\pm1.3$  kW/kg with essentially no correlation ( $R^2 = 0.09$ ) between mass and specific power. As is clear in Figure 78, this is not the case for internal combustion engines where there exists a clear economy of scale.

At some point short-circuiting, incomplete combustion, and heat transfer make the combustion based power plant uneconomical. Additionally, short-circuiting mitigation techniques, especially direct injection, carry a weight penalty due to the associated

hardware (mufflers, injectors, fuel pumps). Therefore, not only does ICE fuel conversion efficiency scale unfavorably with engine size [36], so too does the power density. Thus there exist two size limits on small internal combustion engines. The smaller of the two limits, discussed in Chapter II, Section 4.2 is the current practical limit (displacement of about  $0.3 \text{ cm}^3$  [33]), below which an engine is too small to sustain combustion. (This could be extended with better manufacturing tolerances to about  $0.03 \text{ cm}^3$  [137]). The larger of the two limits is the size below which ICEs become inefficient relative to other propulsion options such as electric power. Depending on the mission, that limit is around 1 kW (or about  $10 \text{ cm}^3$  displacement), at the lower end of Group 2 RPA propulsive requirements. Managing the loss pathways explored here could extend that limit as well as improve the performance of engines in the  $10\text{-}100 \text{ cm}^3$  displacement range where they are already superior to electric options.

## **2.5. Section Summary and Conclusions**

The first half of this chapter (Section 2) examined how loss pathways scale as engine displacement decreases through the  $10\text{-}100 \text{ cm}^3$  range, driving a decrease in fuel conversion efficiency. Based on fuel conversion efficiency and BMEP, the engines tested herein were representative of  $10\text{-}100 \text{ cm}^3$  displacement engines, applicable to Group 2 RPAs. A comparison of the energy balances for those engines to balances for automotive and transport vehicle scale CI and SI engines revealed that short-circuiting and incomplete combustion losses drive the decrease in efficiency as engine displacement decreases below  $100 \text{ cm}^3$ . Available short-circuiting mitigation options range from inexpensive (exhaust tuning, lean operation) to cost and time intensive (port redesign, LPDI) and future RPA programs should carefully weigh the trade space between the cost to reduce short-circuiting

and the benefits afforded to the operational concept of the platform. When only the energy released during combustion is considered (thermal efficiency), the 10-100 cm<sup>3</sup> displacement engines had thermal efficiencies comparable to automotive scale engines and followed the heuristic that released energy is split about evenly between thermal losses from the engine, sensible enthalpy in the exhaust, and brake power. Considering data for micro glow engines smaller than 10 cm<sup>3</sup> displacement, as engine displacement further decreases below 10 cm<sup>3</sup>, heat transfer becomes increasingly important, driving down thermal efficiency. Since exhaust losses (incomplete combustion and short-circuiting) remained on the order of 60%, the net result is an increasingly steep drop off in efficiency with decreasing engine displacement below 10 cm<sup>3</sup>. The next section will take the energy balances and engine performance metrics and provide insight into practical issues for employing 10-100 cm<sup>3</sup> displacement engines for small aircraft propulsion.

### **3. Parametric Engine Studies**

The first half of this chapter provided insight into how the loss pathways in commercially available 10-100 cm<sup>3</sup> displacement, two-stroke engines change in magnitude and relative importance with engine size. The second half of this chapter examines engine performance from a more practical standpoint. It presents four parametric studies exploring the interactions between engine control parameters, loss pathways and the underlying mechanisms, and performance. It also discusses the implications of the trade space for integrating small engines onto operational aircraft. The following subsections each cover one of the engine control parameters: equivalence ratio (Section 3.1), combustion phasing (Section 3.2), engine temperature (Section 3.3), and throttle (Section 3.4). Results for the fifth engine control parameter, speed, were shown in the

previous section. The fifth and final subsection (Section 3.5) discusses the thermodynamic loss angle determined during motored testing. Each parametric sweep was performed by varying the applicable control parameter from the base case condition. The base case for each sweep is listed in Table 24.

**Table 24: Base Case for Parametric Engine Studies**

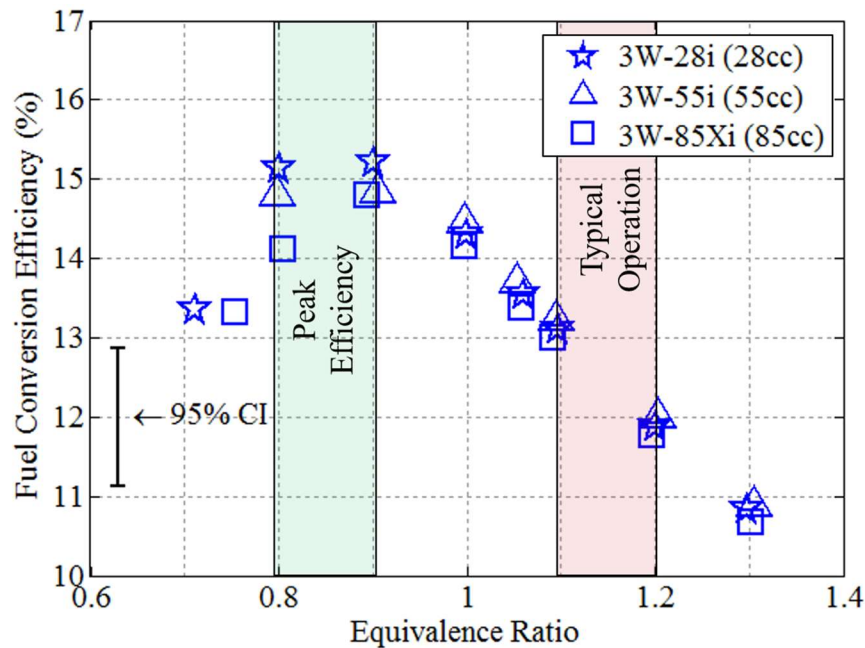
Parameter	Values
Equivalence Ratio (10 second average)	1.06
CA50 (400 cycle moving average)	8°ATDC
Engine Head Temperature	130°C
Intake Air Temperature	28°C
Speed	6000 rpm
Throttle	WOT

Table 15 (page 212) listed the control limits defining a steady state for an engine operating condition. Due to run-to-run variation in engine performance, there is some variation in absolute values between the sweeps. For example, IMEP at the baseline condition on the equivalence ratio sweeps may vary by about 5% from IMEP at the same baseline condition during the speed sweeps presented previously. Since each sweep was collected as consecutive points during a single run, the parametric sweeps capture the trends in engine performance from varying operating parameters that would otherwise be obscured by the run-to-run variation. Based on repeat testing, these trends relative to the baseline condition are consistent, despite the run-to-run variation in the baseline condition.

### 3.1. Equivalence Ratio

For engines with adjustable fuel delivery systems such as throttle body injection, equivalence ratio is the largest control available to the engine operator. Where equivalence ratio is concerned, there are two questions worth asking: where is the peak efficiency and where is the peak power? Figure 82 shows the impact of varying equivalence ratio on the fuel conversion efficiency of the engines in this study. Operation of the 3W-55i engine lean of an equivalence ratio of 0.80 was too variable/ unstable due to a high misfire rate to take a data point. Peak efficiency occurred lean of stoichiometric at an equivalence ratio between 0.8 and 0.9. This is somewhat leaner than typical automotive engines (usually just lean of stoichiometric) due to the high degree of short-circuiting.

Figure 82 also shows the typical operational equivalence ratio for small air carbureted engines. Small engines are usually operated rich as a cooling measure and to provide a



**Figure 82: Effect of equivalence ratio on fuel conversion efficiency. The engines were operated at 6000 rpm, WOT, CA50=8±0.5°aTDC, & CHT=130±2°C.**



margin against the wide swings in equivalence ratio typical in simple carburetors over the operating range of such engines. For example, during carbureted operation, the 3W-55i engine was tuned to an equivalence ratio of 1.1 at 6000 rpm, which resulted in equivalence ratios varying from 0.8 to 1.2 over the entire operational speed range of the engine. Therefore, installation of a fuel injection system not only improved the repeatability (and decreased the variability) of the fuel metering, the improved control also enabled stable operation at lean equivalence ratios, offering an approximately 33% improvement in fuel conversion efficiency at some points.

In addition to efficiency, it is also important to consider the impact of equivalence ratio on power as shown in Figure 83. Peak power for each of the engines was slightly rich of stoichiometric. This is comparable to larger engines where peak power typically occurs at an equivalence ratio near 1.05. While the peak power and peak efficiency zones do not

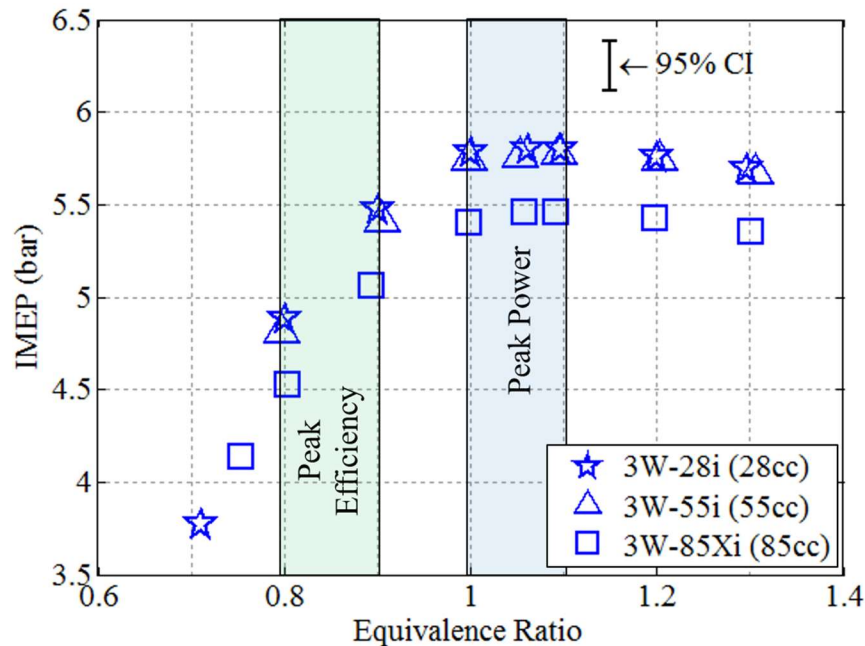


**Figure 83: Effect of equivalence ratio on engine power, normalized as MEP. The engines were operated at 6000 rpm, WOT, CA50=8±0.5°aTDC, & CHT=130±2°C.**

overlap, both are leaner than the typical air carbureted operation range. Shifting from the peak power regime to the peak efficiency regime reduced power output by approximately 10%. Additionally, actions taken to mitigate short-circuiting will tend to shift the peak fuel conversion efficiency towards an equivalence ratio of one, closing the gap between peak power and peak efficiency. Thus, operation near stoichiometric offers both power and efficiency benefits compared to the rich operation typical of small air carbureted engines.

Figure 84 shows the COV of IMEP, which is a measure of the cycle-to-cycle variation in indicated pressure and an indicator of combustion stability (see Chapter II, Section 2.6). For automotive engines, COV of IMEP is typically 1% to 3%, while values above 11% are generally considered un-drivable. During carbureted operation of the engines, COV of IMEP exceeded 30% at some WOT operating conditions, particularly at the extremes of the operational speed range. This was primarily due to exceedingly rich and lean (less than

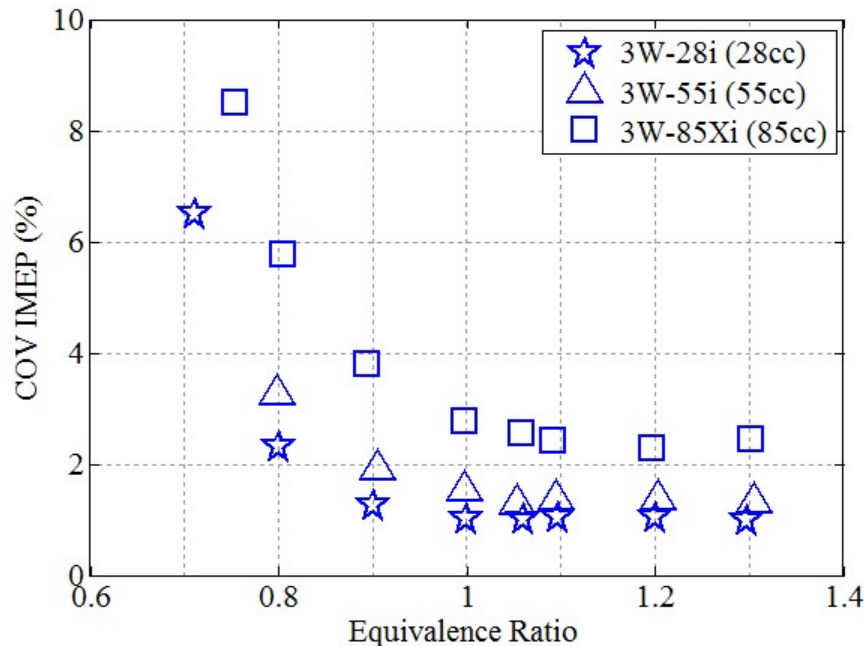
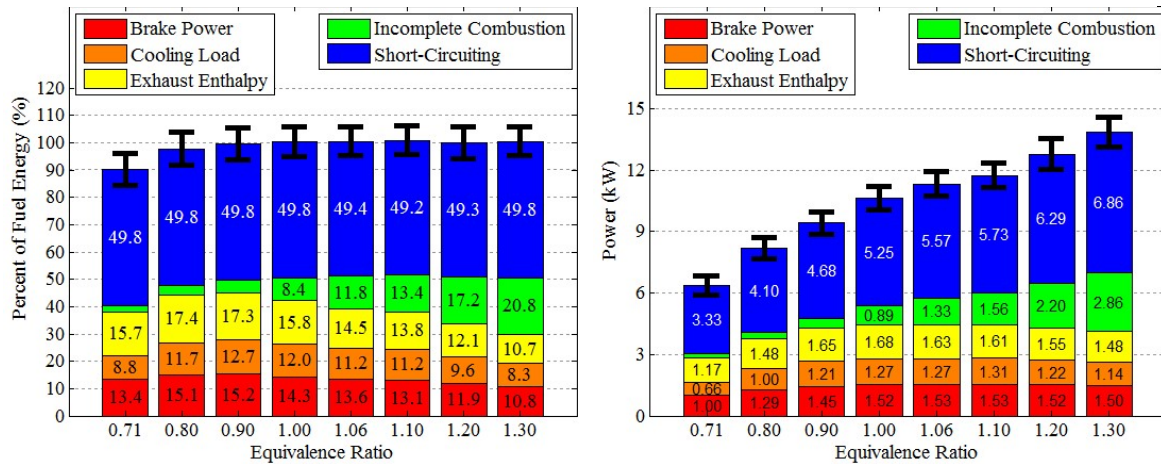


**Figure 84: Effect of equivalence ratio on COV of IMEP. The engines were operated at 6000 rpm, WOT, CA50=8±0.5°aTDC, & CHT=130±2°C.**

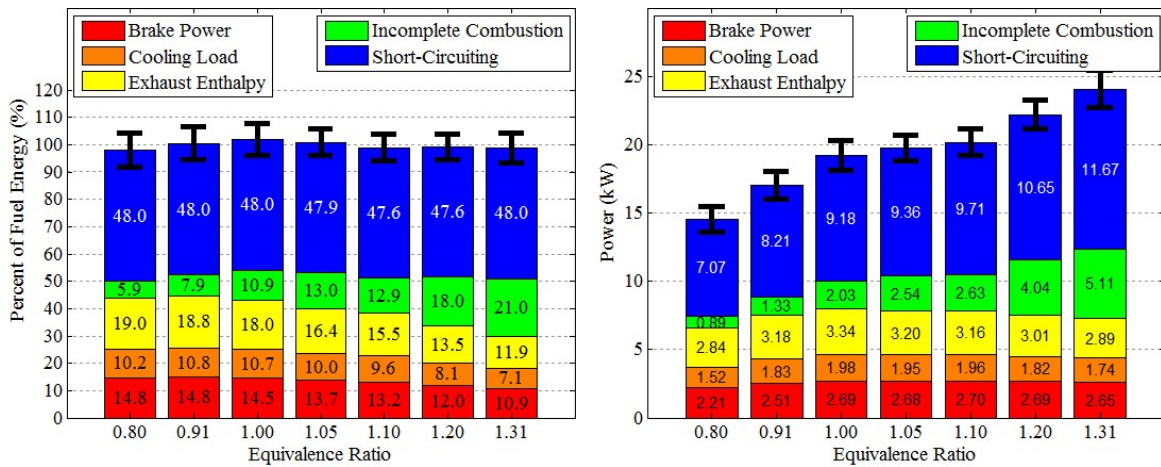
0.8 or greater than 1.2) equivalence ratios where fuel delivery was presumably inconsistent cycle-to-cycle. Installation of the fuel injection system dramatically improved the situation. As seen in Figure 84, COV of IMEP was less than 4% for all points richer than an equivalence ratio of 0.9. The results at equivalence ratios leaner than 0.9 varied from engine to engine. For the 3W-28i engine, stable operation as lean as an equivalence ratio of 0.7 was possible, with a COV of IMEP between 6% and 7%. Meanwhile operation of the 3W-55i engine leaner than an equivalence ratio of 0.8 was unreliable; on the day the parametric sweep was performed, the misfire rate was over 2% of cycles, making it too unstable to take a useful data point. The 3W-85Xi was in between, with a stable operational limit near an equivalence ratio of 0.75. Generally speaking, operation of each engine at its peak efficiency equivalence ratio was possible while maintaining COV of IMEP less than 5%, sufficiently stable for vehicle or aircraft operation.

Figure 85 shows the effect of the equivalence ratio on the engine energy balances. Under reporting of the 3W-28i and 3W-85Xi energy balances at lean equivalence ratios (less than 0.8) was the result of unstable operation. As equivalence ratio richened beyond stoichiometric the most pronounced impacts were on short-circuiting losses (discussed in Chapter IV, Section 2) and incomplete combustion (caused by excess fuel). While the percentage of short-circuited charge remained relatively constant, the absolute magnitude of fuel lost to short-circuiting increased lock-step with increasing equivalence ratio. The excess of fuel trapped in the cylinder caused both incomplete combustion to increase both relative to the other pathways and in absolute magnitude. Less pronounced were the impacts on cooling load, brake power, and exhaust enthalpy. Exhaust enthalpy peaked near stoichiometric, while cooling load peaked slightly rich of stoichiometric. Excess fuel

### Modellmotoren 3W-28i Engine (SA/V=1.81 cm<sup>-1</sup>)



### Modellmotoren 3W-55i Engine (SA/V=1.46 cm<sup>-1</sup>)



### Modellmotoren 3W-85Xi Engine (SA/V=1.27 cm<sup>-1</sup>)

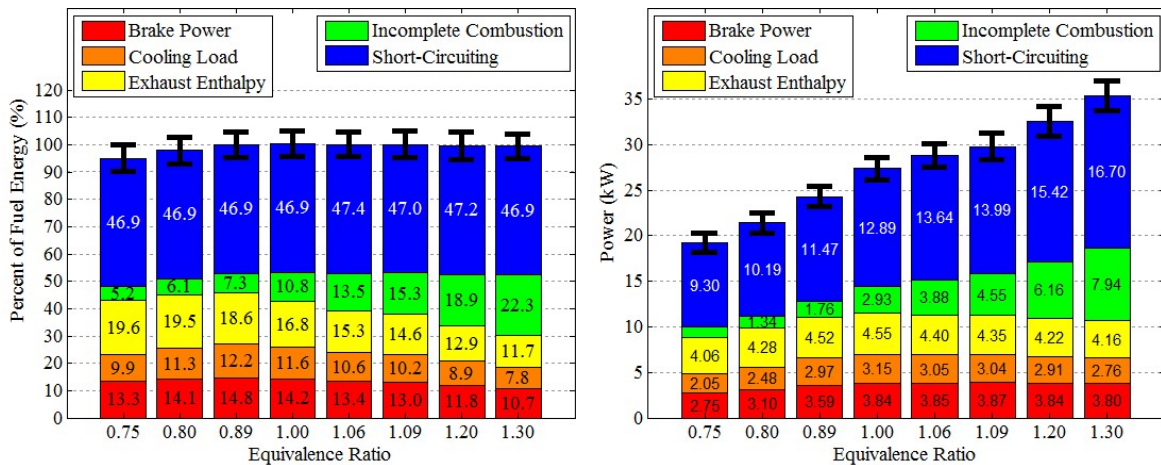


**Figure 85: Effect of equivalence ratio on energy pathways & balances. The engines were operated at 6000 rpm, WOT, CA50=8±0.5°aTDC, & CHT=130±2°C. Uncertainty bars are for a 95% confidence interval.**

for rich mixtures acted as charge cooling, driving down the in-cylinder temperatures. The decrease in temperature decreased the combustion efficiency (beyond the impact from simply a lack of oxygen) cutting into the released heat. As a result, the brake power, cooling load, and exhaust enthalpy all showed slight decreases with increasing equivalence ratio. Thus the charge cooling (useful for knock mitigation) from rich operation comes at high price in terms of fuel consumption and efficiency.

### **3.2. Combustion Phasing**

One of the primary advantages of SI engines over CI and HCCI engines is the control of combustion phasing through adjustable spark timing. Recalling the discussion in Chapter II, Section 2.6, optimal combustion phasing places the peak pressure about 16°aTDC as a balance between early combustion working against the rising piston and late combustion losing its effectiveness due to the expansion stroke. The spark timing to achieve optimal timing varies from engine to engine (and spark plug to spark plug), so combustion phasing is often discussed in terms of CA50, or the crank angle at which the combustion reaction is 50% complete (which may be less than 50% of the fuel consumed for rich operating conditions). The calculation of MFB was shown in Equation (11) (page 46). The calculation of CA50 was carried out in real time by the AVL Indismart, which used a version of Equation (11) adapted to the methodology of Ball *et al.* [65]. Ball *et al.* incorporated the heat transfer term into the pressure and temperature terms by using polytropic coefficients in place of the ratio of specific heats. Like Ball *et al.* suggest, different polytropic coefficients were used for compression (1.33) and expansion (1.27). The values were chosen based on the values suggested by the AVL Indismart manual.

Figure 86 and Figure 87 show the impact of combustion phasing on fuel conversion efficiency and indicated engine power (normalized as IMEP). As is typical for larger engines, the optimal combustion phasing was CA50 between 5°aTDC and 10°aTDC. For combustion phasing earlier than optimal, too much of the burn occurs prior to TDC and works against the upward motion of the piston. While early phasing increases the burn rate and peak pressure, the work performed against the piston causes a decrease in both IMEP and efficiency as timing is advanced beyond MBT timing. Advancing the timing also increases the propensity of the engine to knock by increasing the peak temperature and pressure in the cylinder, although that was not an issue in this study since a 98 ON PRF blend was used. Late combustion phasing causes the majority of the burn to occur while the piston is on its downward stroke, leading to reduced peak pressure and temperature as well as poor combustion.

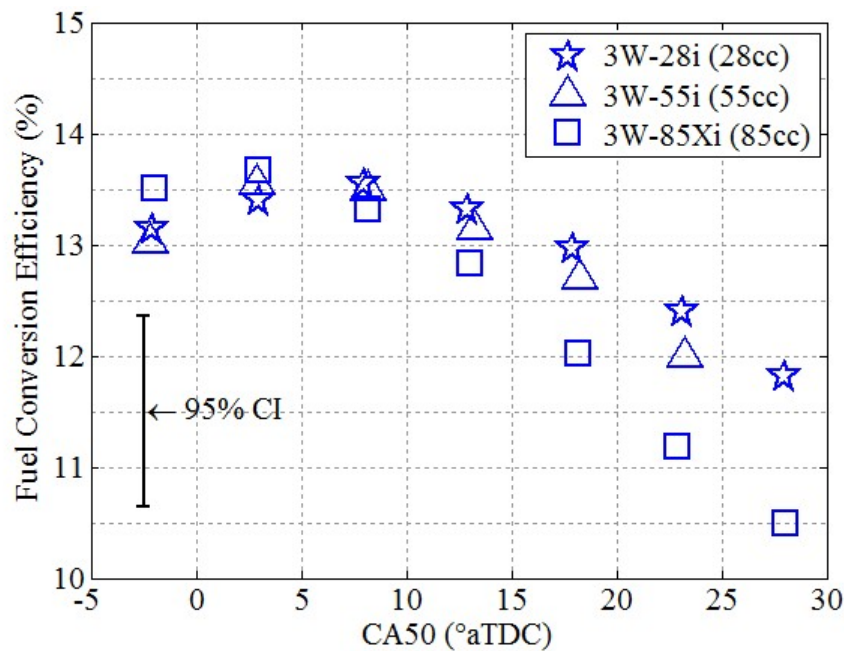


**Figure 86: Effect of combustion phasing on fuel conversion efficiency. The engines were operated at 6000 rpm, WOT,  $\phi=1.06\pm0.02$ , & CHT=130±2°C.**

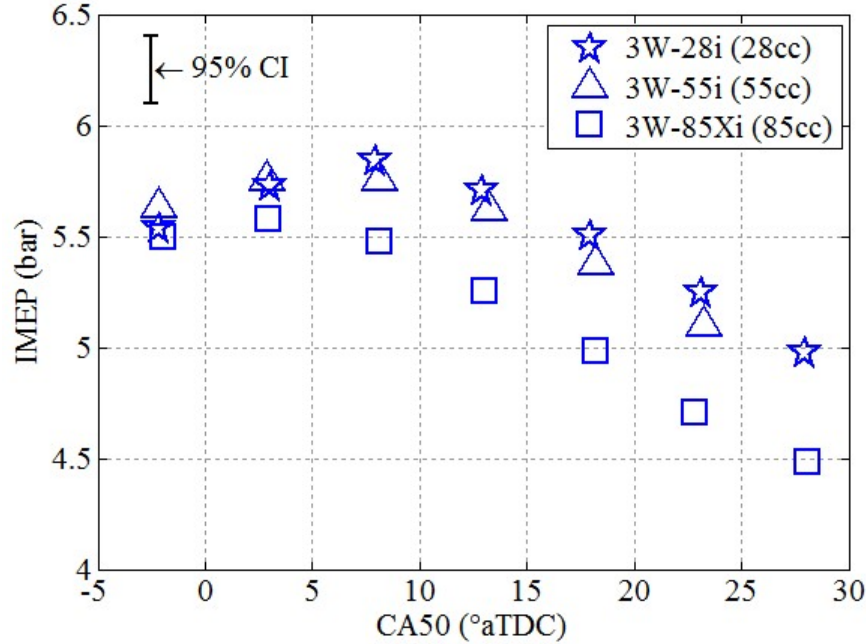


**Figure 87: Impact of combustion phasing on IMEP. The engines were operated at 6000 rpm, WOT,  $\phi=1.06\pm0.02$ , &  $CHT=130\pm2^{\circ}\text{C}$ .**

Both the fuel conversion efficiency and IMEP (power) show an increasing penalty with increasing engine size for retarding timing from MBT timing. For example, the fuel conversion efficiency of the 3W-28i engine dropped approximately 0.4%/5 CAD of retard, while the 3W-85Xi engine dropped almost 0.9%/5 CAD of retard. The 3W-55i was in-between and similar trends occurred in IMEP. This drop can be tied back to the changes in port timing discussed in Section 2.4. Higher port timings (the 3W-85Xi engine) result in lower trapped compression ratios as well as earlier opening of the exhaust port. Earlier opening of the exhaust port cuts into the expansion stroke of the engine, and the penalty paid for shortening the exhaust stroke increases as burn angle is retarded and the bulk of the burn is pushed later into the cycle.

Figure 88 shows the impact on burn stability caused by retarding the combustion phasing from MBT. As the combustion phasing was retarded, the COV of IMEP



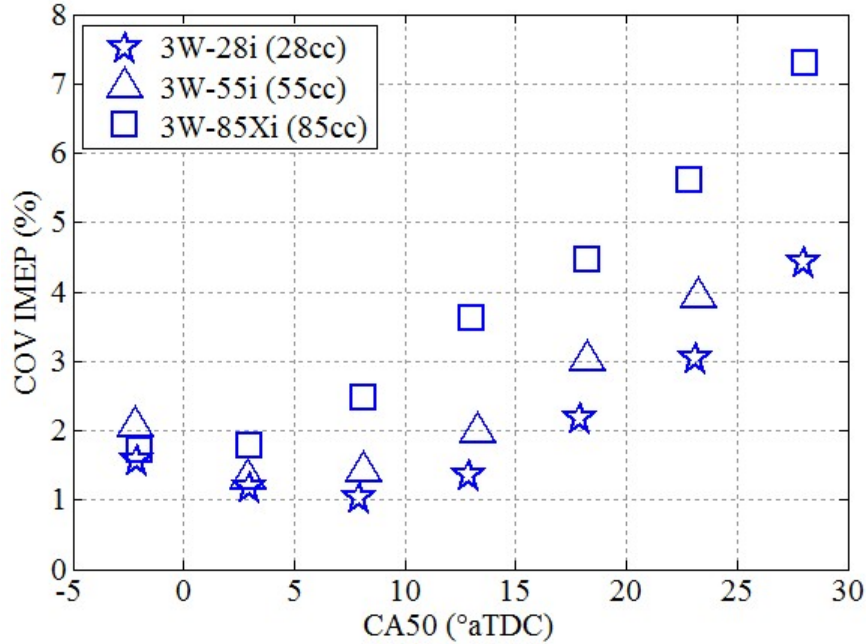


**Figure 88: Effect of combustion phasing on IMEP. The engines were operated at 6000 rpm, WOT,  $\phi=1.06\pm0.02$ , &  $CHT=130\pm2^{\circ}C$ .**

(represented by the error bars) increased from 1% to 1.5% at MBT timing (near 8°aTDC) to over 4% for the most retarded combustion phasing. In automotive applications, vehicle drivability is compromised as COV of IMEP exceeds 10% to 11%. Controlling combustion phasing to within 5 CAD of MBT timing, COV of IMEP remained below 5% and power was within 5% of peak power for all three engines.

For this effort, the combustion phasing was controlled in real time by adjusting the spark timing through the ECU. Most small COTS engines ship with more rudimentary (and arguably rugged) ECUs. While the laboratory ECU could be adjusted based on engine operating conditions such as varying speed, equivalence ratio, and throttle, stock ECUs usually determine the spark timing using a linear speed map. Figure 89 compares the timing map of the stock ECU to the MBT timing using the laboratory ECU. For most conditions above 4000 rpm, the stock ECU was within 5 CAD of the MBT timing. Thus,



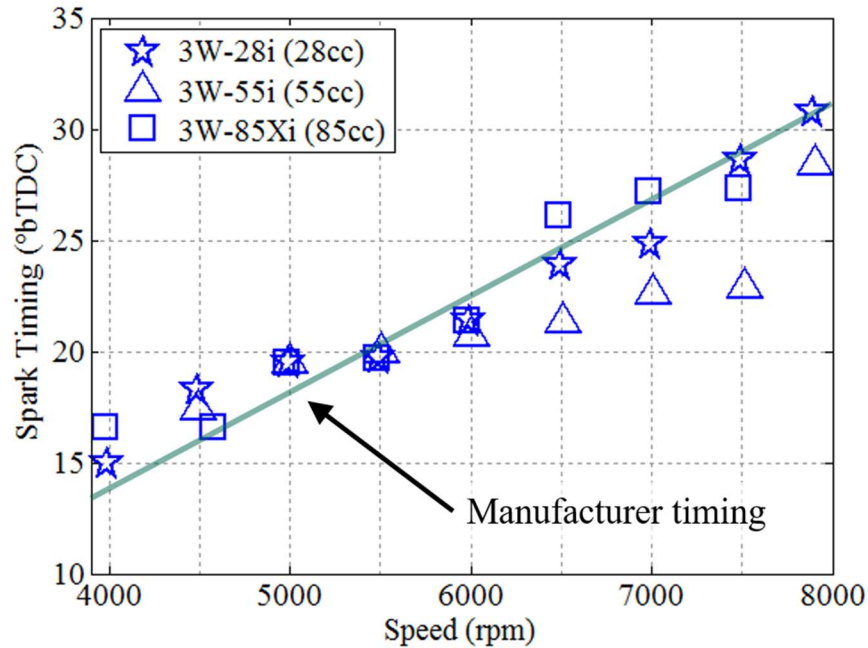


**Figure 89: Comparison of manufacturer timing curve and MBT timing curve. The engines were operated at 6000 rpm, WOT,  $\phi=1.06\pm0.02$ , & CHT=130 $\pm$ 2°C.**

under most circumstances, the average user would be unaware of the less than 5% impact in efficiency (relative) and power. Based on testing these engines, engine to engine variation itself was on the order of 5%. Rather, the primary issue with the stock ECU arose when attempting to start the engine. When starting an engine on the SERB, the engine would be motored at 1000-2000 rpm, similar to using a hand held motor applied to the propeller shroud on a small RPA. At those speeds, the stock ECU spark timing was between 5°bTDC and TDC, which provided unreliable starting and often required motoring the engine for a minute or more. Setting the laboratory ECU to approximately 20°bTDC decreased engine start time to under 15 seconds of motoring. For a ground start, especially hobbyist application, the starting characteristics of the stock ECU are a minor inconvenience. For starting the engine in a contested environment or in midair (hybrid configuration), there is a clear advantage for using a non-linear timing map.

While combustion phasing's impact on efficiency could be traced primarily to the shifting of peak pressure relative to TDC, that shift also had consequences for incomplete combustion as well as the balance of cooling load, brake power, and sensible exhaust enthalpy. Figure 90 shows the energy pathways for a combustion phasing sweep of the three engines in this study. The energy balances tended to over report for retarded combustion phasing (especially the points taken at  $CA_{50} \approx 28^\circ \text{aTDC}$ ). The over reporting was tied to the measurement of incomplete combustion, which will be discussed first along with short-circuiting. A discussion of the trade space between the remaining three pathways will then follow.

Since shifting the combustion phasing had little impact on engine airflow and equivalence ratio was controlled, the short-circuiting as well as the total amount of energy delivered to each engine remained relatively constant over the combustion phasing sweep as seen in Figure 91. Yet, the energy balances in Figure 90 show an overall increase in the amount of energy found in the remaining pathways, leading to increasing over reporting of the total energy balances (i.e. balances in excess of 100%) for increasingly retarded combustion phasing. The over-reporting was correlated to an increase in incomplete combustion with retarded combustion phasing, suggesting that the methodology used to measure incomplete combustion may have caused the issue.

Figure 92 shows the primary incomplete combustion pathways expressed in terms of emissions as a function of combustion phasing. Hydrogen and CO showed slight increases at retarded combustion phasing, which would be expected as temperatures and pressures decrease as the combustion event is pushed away from TDC into the expansion stroke. Meanwhile, UHCs increased much more rapidly than CO and  $H_2$ , and the increase

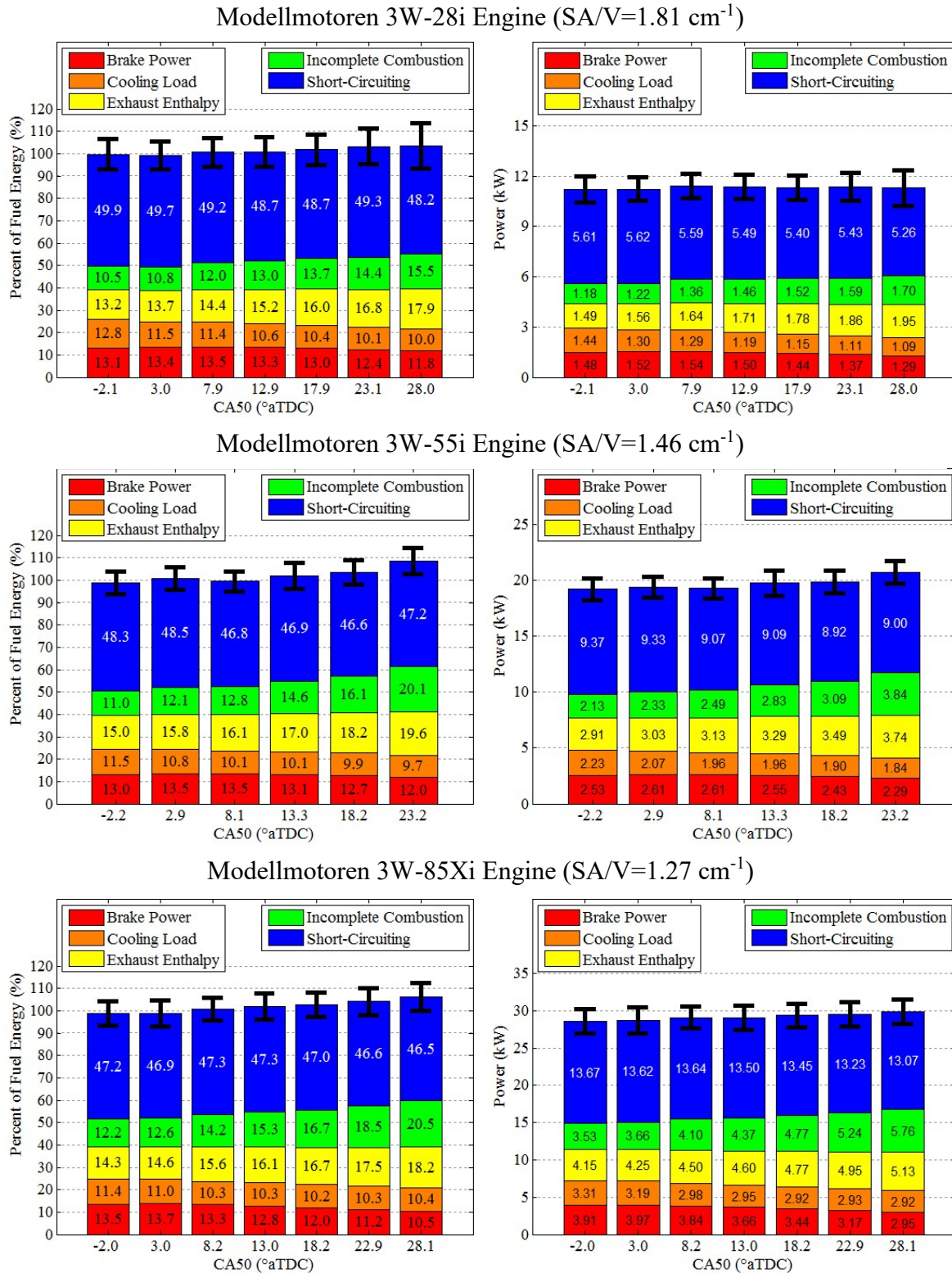


**Figure 90: Effect of combustion phasing on energy pathways & balances. The engines were operated at 6000 rpm, WOT,  $\phi=1.06\pm0.02$ , & CHT=130 $\pm$ 2°C. Uncertainty bars are for a 95% confidence interval.**

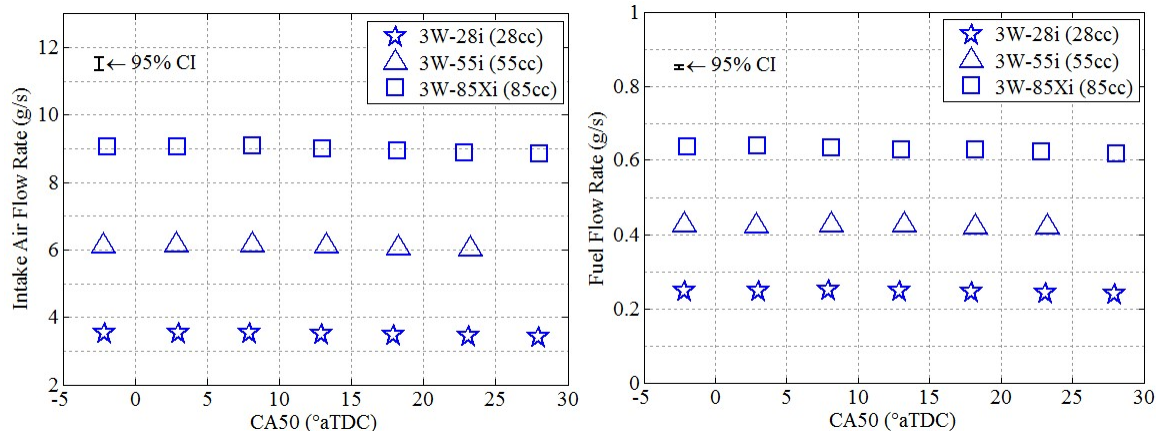


**Figure 91: Effect of combustion phasing on intake air and fuel flow rate. The engines were operated at 6000 rpm, WOT,  $\phi=1.06\pm0.02$ , & CHT=130 $\pm$ 2°C.**

accelerated beyond CA50 $\approx$ 15°aTDC, especially in the 3W-55i and 3W-85Xi engines, the points where the most dramatic over reporting of energy occurred. Examining specific UHC species revealed that the majority of the UHC products (and those that increased most rapidly) were 1,3-butadiene, acetylene, and other similar alkenes and alkynes. According to Davidson *et al.* [281], these species are common by-products formed during the thermal decomposition (pyrolysis as opposed to oxidation) of iso-octane and n-heptane.

Figure 93 shows the impact of retarding the combustion phasing on the exhaust gas temperatures. The exhaust gas temperature (EGT) is representative of the short-circuited charge and the burnt gas from inside the cylinder. Therefore, the actual gas temperatures in the cylinder as fresh charge entered were hotter than the reported EGT values. As combustion phasing was retarded, EGTs increased, increasing the potential for thermal decomposition of some of the fuel in the short-circuited charge.

The methodology used to calculate incomplete combustion energy and short-circuiting over counts thermally decomposed fuel from the fresh charge. The methodology assumed (see Chapter III, Sections 3.4.2 & 3.4.4) that the iso-octane in the fresh charge was resistant

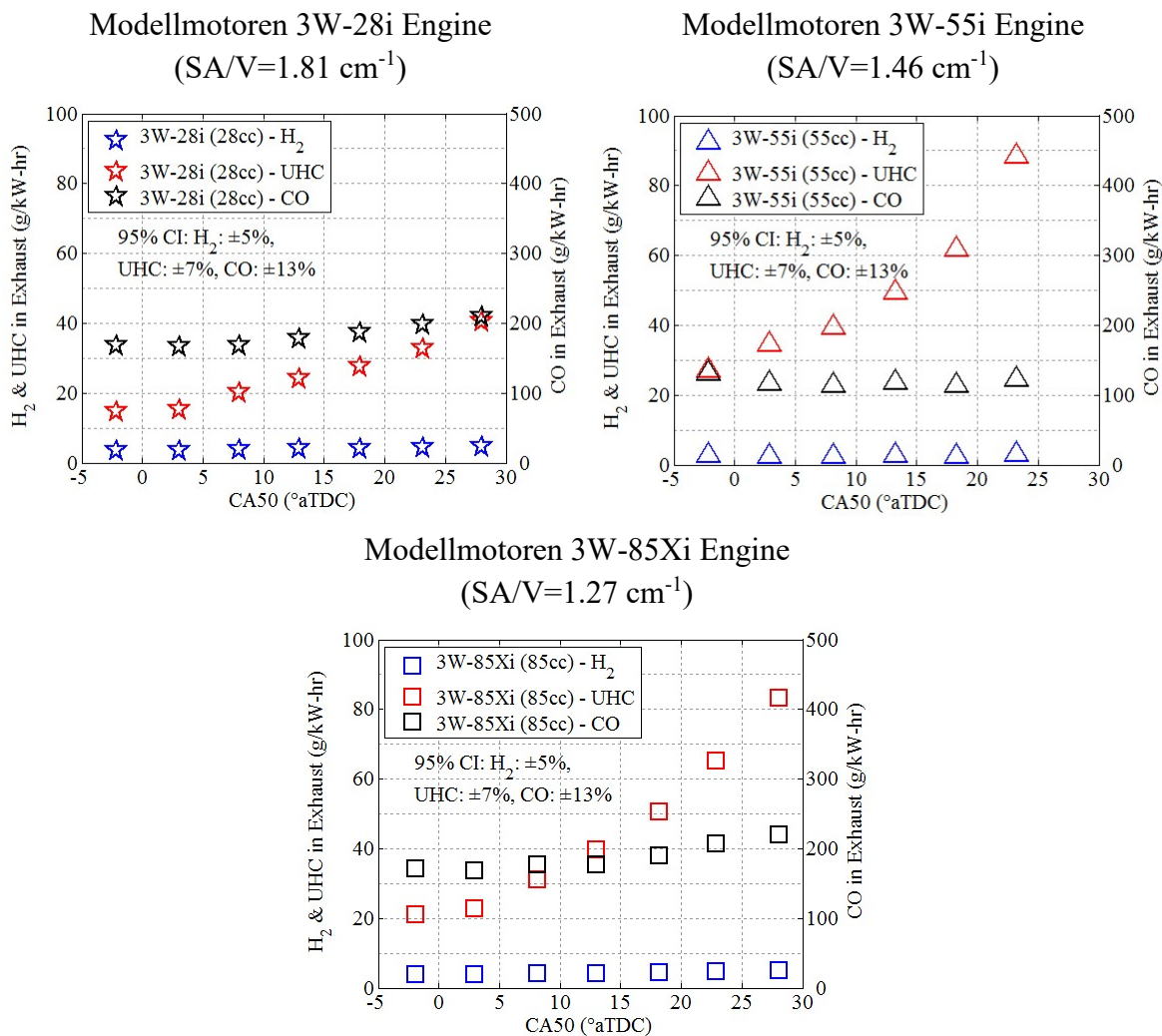


**Figure 92: Effect of combustion phasing on measured emissions. The engines were operated at 6000 rpm, WOT,  $\phi=1.06\pm0.02$ , & CHT=130±2°C.**

to thermal decomposition and could be used as a standard (once short-circuiting was calculated) to quantify the remaining hydrocarbons in the exhaust gas samples. Thermal decomposition caused the iso-octane measurement used as the standard to under report. Meanwhile the decomposed fuel was identified as incomplete combustion products and double counted; it was also included in short-circuiting since short-circuiting was calculated via the modified Watson method, which measured oxygen. As a result, thermal decomposition resulted in a slightly more than double counting of any fuel that

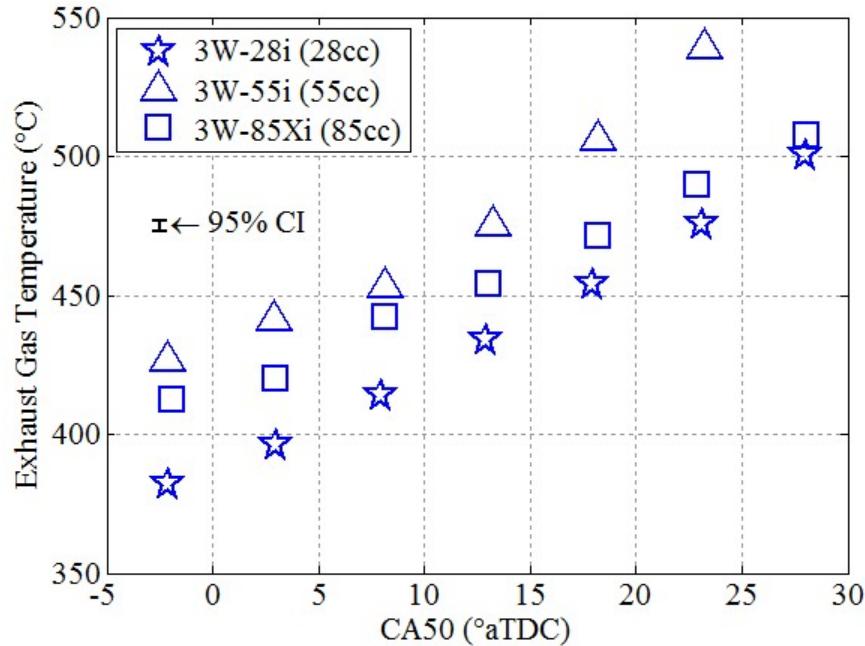


**Figure 93: Effect of combustion phasing on EGT. The engines were operated at 6000 rpm, WOT,  $\phi=1.06\pm0.02$ , & CHT= $130\pm2^\circ\text{C}$ .**

decomposed during contact with the burnt charge and subsequently short-circuited. Coupled with higher temperatures caused by retarded phasing, the measurement methodology broke down for CA50 greater than  $20^\circ\text{aTDC}$ , especially for lower port timings such as the 3W-85Xi engine. In practice such timings are uncommon and inefficient except when avoiding heavy knock, and the methodology presented here was functional for operating conditions near MBT timing. In spite of these issues, examining CO indicates that incomplete combustion also increased slightly with retarded combustion phasing, cutting into released heat and combustion efficiency.

Retarding the timing also caused a noticeable shift in the thermal pathways: cooling load, brake power, and sensible exhaust enthalpy. The negative impact on brake power from releasing energy too late in the cycle has already been discussed. In addition to the impact on brake power, shifting of the heat release later into the cycle caused a noticeable



shift in energy (up to 30%) from cooling load to exhaust enthalpy. This shift was caused by two factors. First, more advanced combustion phasing created higher pressures and temperatures in the cylinder, leading to a higher driving force for heat transfer from the cylinder. Second, advancing the combustion phasing caused the peak pressures and temperatures to happen earlier in the cycle, leaving more time for heat transfer to occur before the exhaust port opened. Therefore, as combustion phasing was retarded, the thermal load shifted from losses through the cylinder head to losses in the exhaust. Lower temperatures and pressure as well as the extension of combustion later into the cycle decreased the combustion efficiency and increased the quantity of incomplete combustion products. As an engine control, the primary reason to retard combustion phasing from MBT timing is to prevent knock via lower cylinder temperatures and pressures. The shift in in-cylinder temperature and pressures will be shown explicitly in Chapter V, Section 2. For these engines, retarding the combustion phasing reduced the fuel conversion efficiency by about 0.4-0.9% per 5 CAD that CA50 was retarded from MBT timing, depending on the engine.

### **3.3. Engine Cooling and Head Temperature**

Typically, engines on hobbyist aircraft are cooled by a combination of flow from the free stream and prop wash (for aircraft in a tractor configuration). When the cylinder head is internal to the airframe, cooling is often accomplished via an external air scoop and ram effect to push air through the compartment containing the cylinder head. In either case cooling is primarily dependent on aircraft velocity and operators tend to err on the side of over cooling. On the SERB, the cooling flow was controlled using a blower controlled with a VFD. This permitted an investigation of the impact of cooling flow on engine

performance to examine what penalties (if any) arise from the err-on-the-side-of-over-cooling approach. When integrating a small ICE onto a platform, airspeeds are typically a design variable for the aircraft. Therefore, the air velocity where the cooling duct enters the thermal enclosure was used to compare cooling speeds. Due to a variety of geometric factors, the characteristic air speed reported here will not be an exact match (except perhaps by coincidence) to any installed configuration, but it should give a reasonable idea of the trends and effects of varying the engine cooling.

Figure 94 shows the relationship between engine head temperature and the approximate equivalent air speed incident on the engine. Equivalent air speed is defined as the air speed that would match the dynamic pressure on the engine at sea level standard conditions, as per the definition typically used for aircraft avionics. Due to material limitations, the manufacturer recommends limiting head temperature to 149°C (300°F). Exceeding this

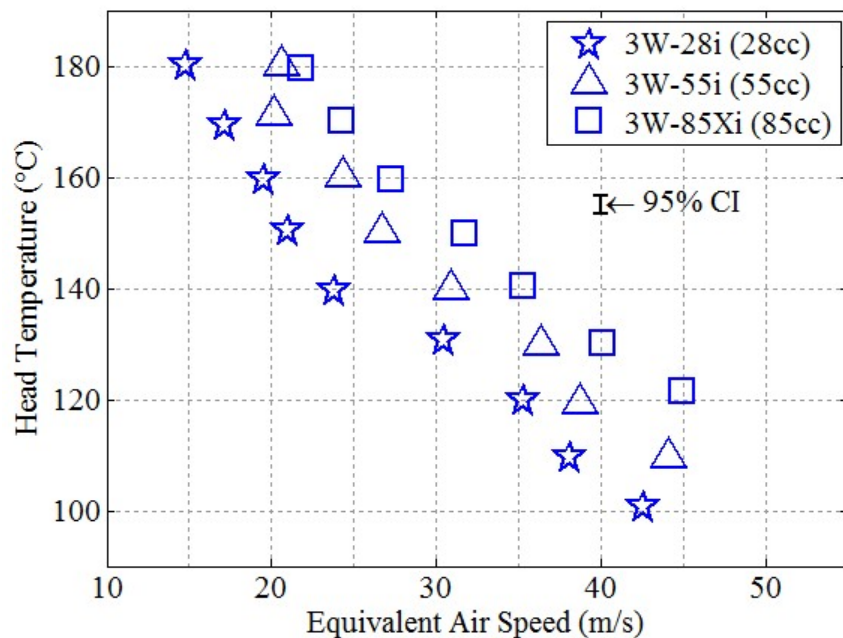


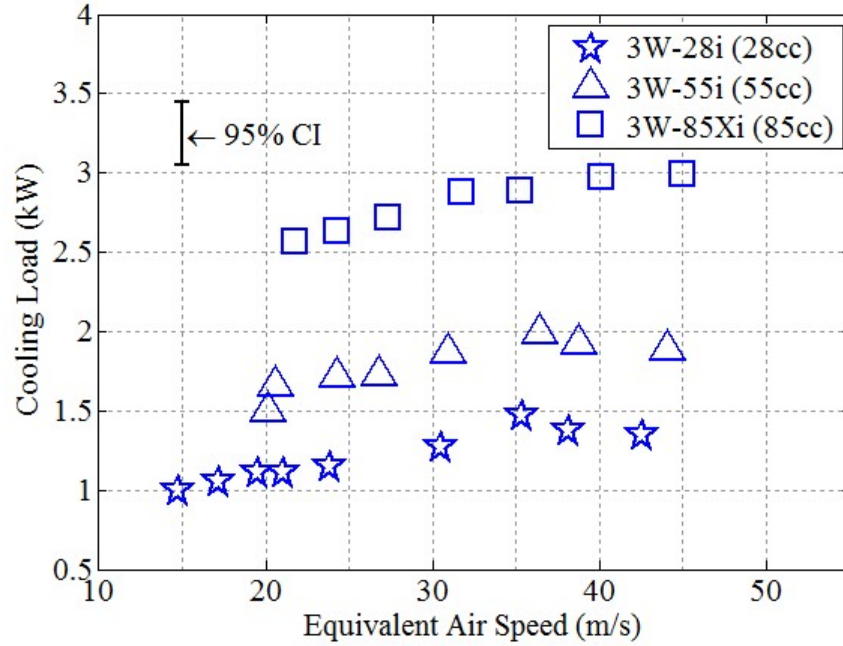
**Figure 94: Effect of cooling air speed on engine head temperature. The engines were operated at 6000 rpm, WOT,  $\phi=1.06\pm0.02$ , & CA50=8°aTDC.**



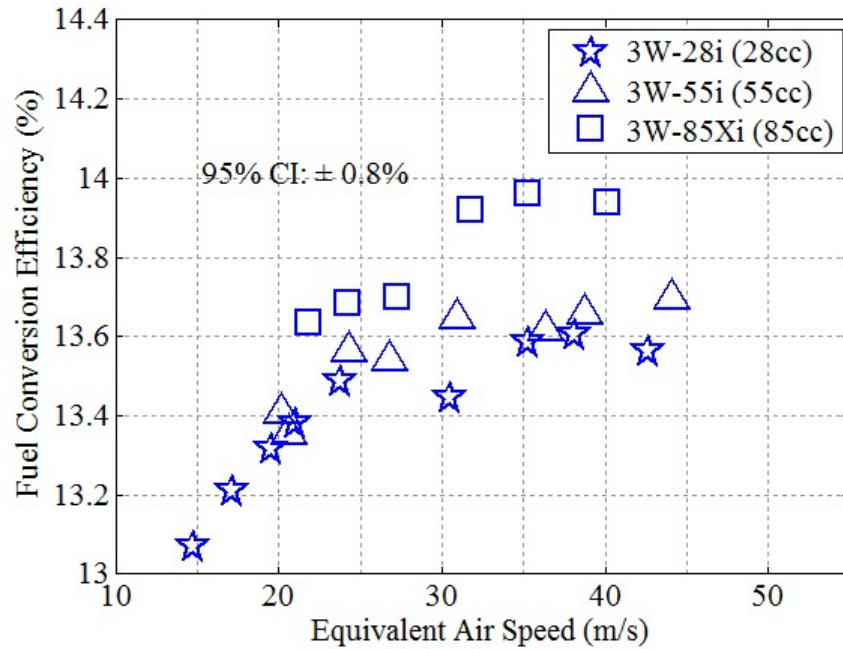
temperature can cause a variety of failures including failure of the spark plug threads, warping of the head, melting of the piston face and coking of oil on the piston ring leading to abrasion and destruction of the piston ring and cylinder liner. During testing, the most frequently observed issue was failure of the spark plug threads. At WOT, about 20 m/s to 35 m/s incident airspeed (depending on the engine) was required to maintain the head temperature below the manufacturer limit. For reference, 30 m/s is approximately 58 knots, which is well within reason for a Group 2 RPA at WOT, especially if the engine is mounted in the prop wash. For pusher configuration aircraft where the engine is only exposed to the free stream, WOT cooling could be a challenge, and the engine manufacturer notes as much in their documentation.

Figure 95 shows the influence of the air speed on the amount of heat rejected from the cylinder. Over the range of air speeds achievable on the SERB (without overheating and damaging the engine), the cooling load increased by about 30%. This corresponded to a change in cylinder head temperature of 60°C. When examined only in the context of cooling load, the 30% seems large. In the context of the total amount of fuel energy however, it is only a change of a few percent. Therefore, the real issue is the impact that cooling had on the engine power, efficiency, and the other energy pathways.

Figure 96 shows the impact of engine cooling on the fuel conversion efficiency. The changes in fuel conversion efficiency are small, and initially appear to be within the confidence interval. While the uncertainty does, in fact, represent the uncertainty on any individual point, the trend shown in the figure is both repeatable and real. Based on the discussion on flame quenching in Heywood [21:599-604], increasing cylinder temperatures should improve combustion efficiency by reducing quenching losses at the



**Figure 95: Effect of cooling air speed on engine cooling load. The engines were operated at 6000 rpm, WOT,  $\phi=1.06\pm0.02$ , & CA50=8°aTDC.**



**Figure 96: Effect of cooling air speed on fuel conversion efficiency. The engines were operated at 6000 rpm, WOT,  $\phi=1.06\pm0.02$ , & CA50=8°aTDC.**

walls (which are a significant source of incomplete combustion). However, in the case of the engines studied here, fuel conversion efficiency actually improved with lower engine temperature. Figure 97 shows that engine power also increased with decreasing cylinder head temperature, helping to explain the increase in fuel conversion efficiency. The increase in power was the result of less heat transfer to the fresh charge, leading to higher charge density and in turn improved charging efficiency as shown in Figure 98. The increase in trapped charge resulted in more energy released during combustion and an increase in IMEP. However, the increase in fresh charge density also increased the density of the short-circuited charge, which offset some of the efficiency gains from improved power production at lower temperatures. Therefore, the increase in engine power (5% to 10%) in Figure 97 is larger than the increase in fuel conversion efficiency (3% to 4%, relative) seen in Figure 96.

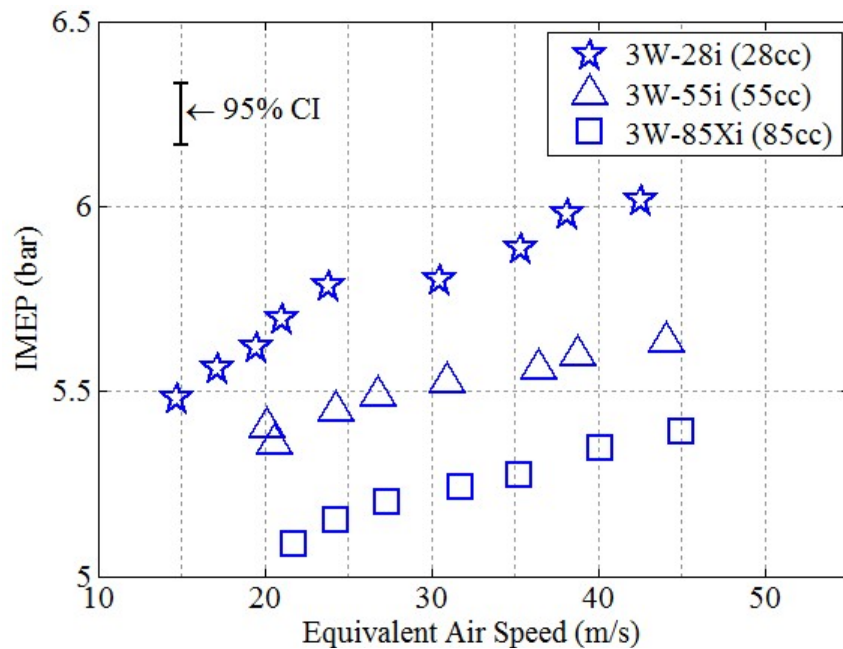


**Figure 97: Effect of cooling air speed on IMEP. The engines were operated at 6000 rpm, WOT,  $\phi=1.06\pm0.02$ , & CA50=8°aTDC.**

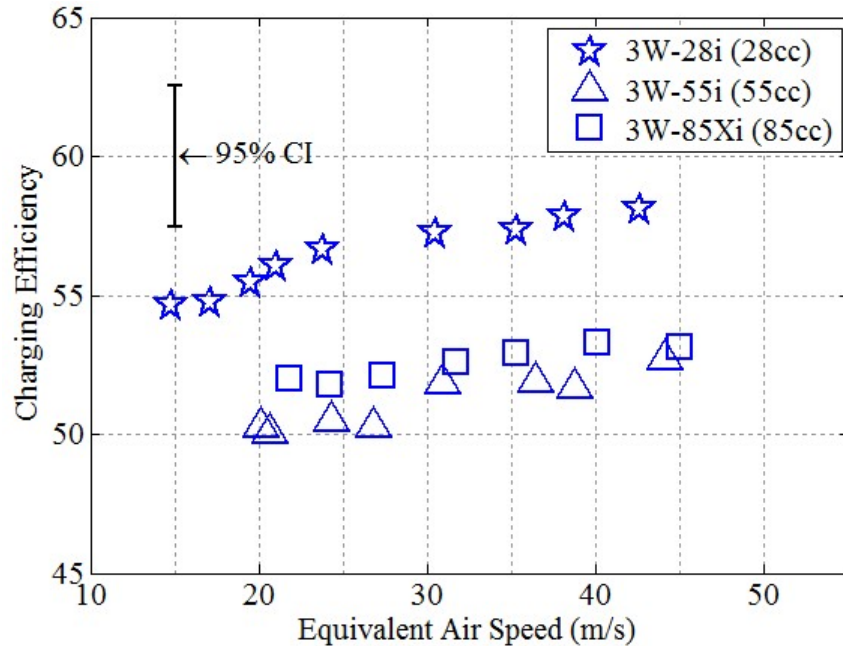
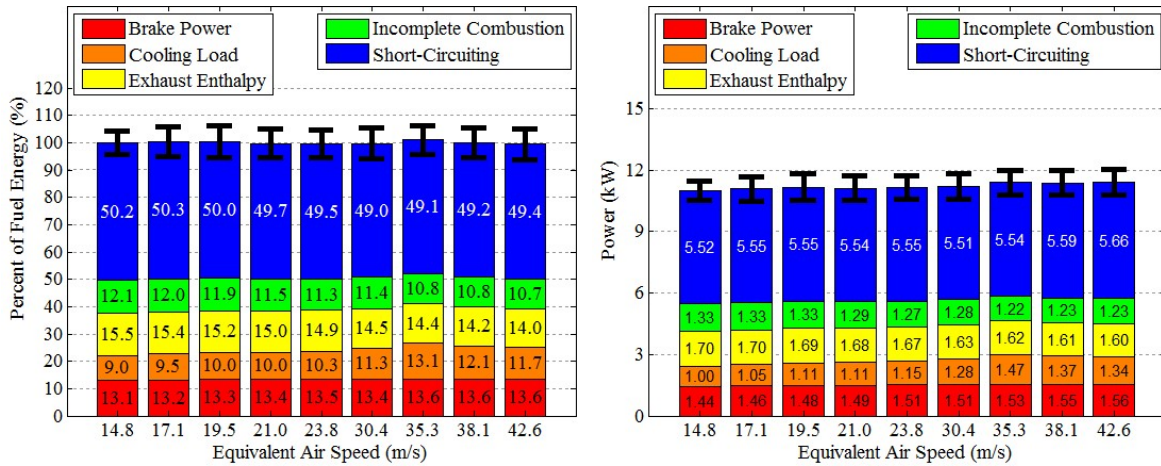


**Figure 98: Effect of cooling air speed on charging efficiency. The engines were operated at 6000 rpm, WOT,  $\phi=1.06\pm0.02$ , & CA50=8°aTDC.**

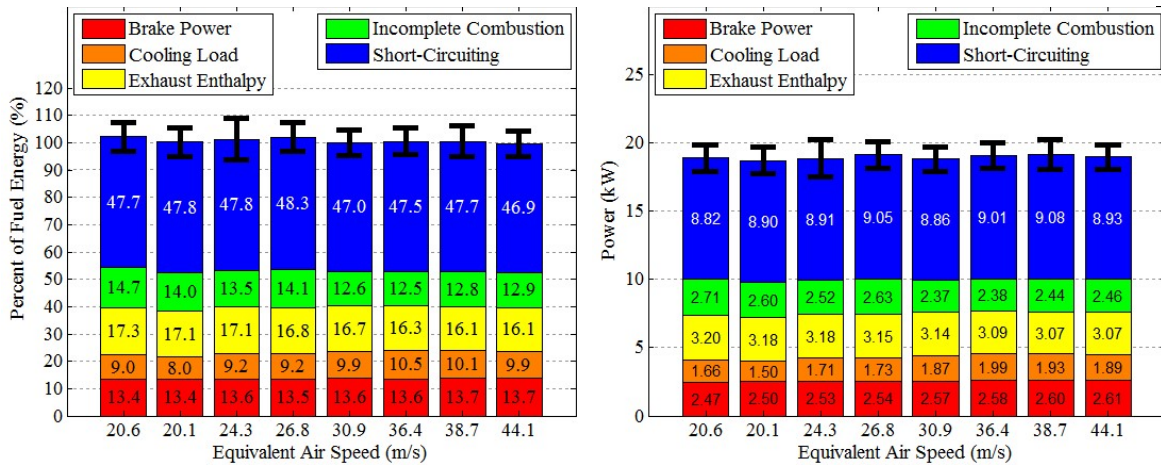
Figure 99 shows the impact of varying the engine cooling on the energy pathways. Of all of the controls investigated so far, cooling had the smallest impact. As cooling air speed was varied from 15 m/s to 45 m/s, short-circuiting remained virtually unchanged. Incomplete combustion decreased by about 10%, likely the result of better scavenging of residuals from the cylinder. Improved scavenging at cooler head temperatures also led to a small (less than 5%, relative) increase in brake power that was already discussed. Finally, a small trade (about 5-15%, relative) between the cooling load and exhaust sensible enthalpy was observed, as lower cooling air flow rates reduced the driving force for heat transfer from the cylinder head.

Ultimately, varying the cooling over the practical range for these engines had little impact on the efficiency and power. The impacts that were observed were traced to variation in the fresh charge density, which explains the improvement in both fuel

### Modellmotoren 3W-28i Engine ( $SA/V=1.81 \text{ cm}^{-1}$ )



### Modellmotoren 3W-55i Engine ( $SA/V=1.46 \text{ cm}^{-1}$ )



### Modellmotoren 3W-85Xi Engine ( $SA/V=1.27 \text{ cm}^{-1}$ )

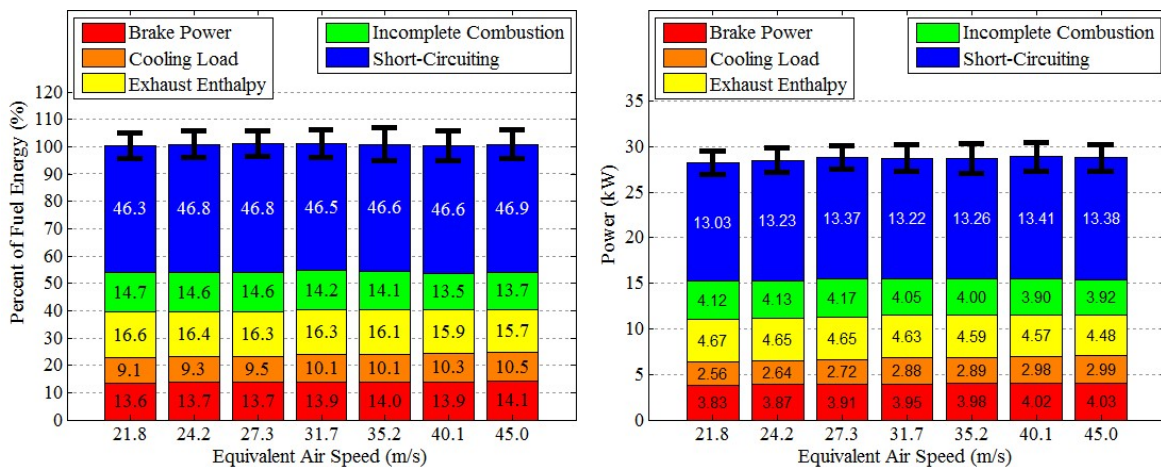


**Figure 99: Effect of cooling air speed on energy pathways & balances. The engines were operated at 6000 rpm, WOT,  $\phi=1.06\pm0.02$ , &  $CA50=8^\circ\text{aTDC}$ . Uncertainty bars are for a 95% confidence interval.**

conversion efficiency (3% to 4%, relative) and power (5% to 10%) as engine temperature was reduced. This supports the err-on-the-side-of-over-cooling approach. Finally, it is important to note that while air speed had little impact on the energy pathways, it had a dramatic effect on head temperature. This is critical since head temperature has a direct impact on an engine's knock resistance (at least for conventional engines). Engine head temperature will be revisited as a control variable as part of Objective 3 in Chapter VI.

### 3.4. Throttle

In a two-stroke engine, the throttle is primarily a control of the delivery ratio (see Chapter II, Section 2.5.4). On the SERB the throttle setting was converted to a pulse width signal used to control the throttle servo, so its physical meaning was obscured. Therefore, for this discussion throttle will be discussed in terms of delivery ratio, which has direct physical meaning for engine operation. The primary reason to throttle an engine is to

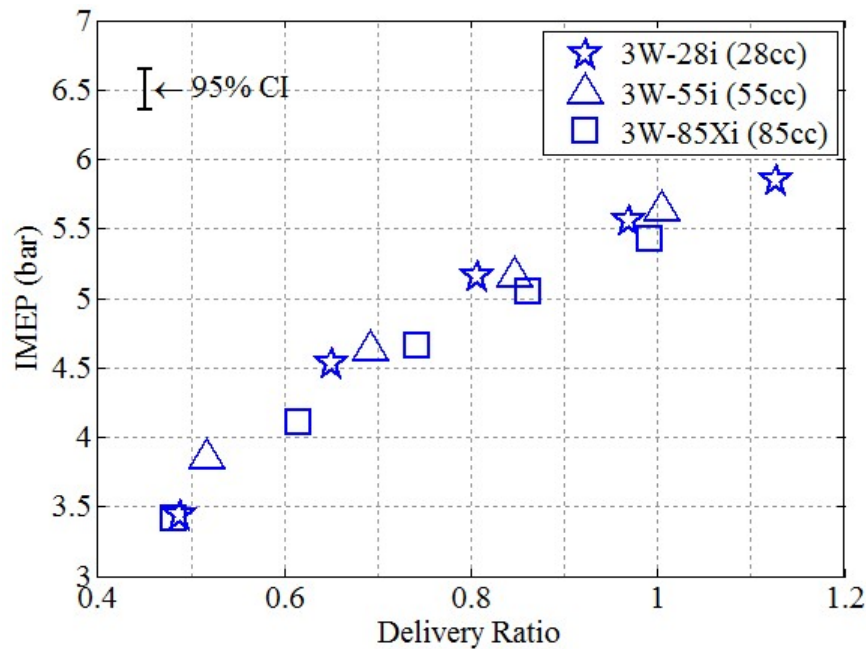


**Figure 100: Effect of delivery ratio (throttle) on IMEP. The engines were operated at 6000 rpm,  $\phi=1.06\pm0.02$ , CA50=8°aTDC, & CHT=130±2°C.**



reduce the power output to the required level at a given engine speed. Figure 100 shows the impact of throttle on engine power. Throttle conditions were established as fractions of WOT airflow. For example, if the WOT delivery ratio was 1.2, then half throttle would correspond to a delivery ratio of 0.6. As observed in Figure 100, reducing the delivery ratio by 50% to half throttle only resulted in a 30% reduction in engine power. Since the delivered equivalence ratio was maintained to 1.05 to 1.10 at all operating points, this discrepancy was not a function of mixture. Rather, the discrepancy indicates an improvement in trapping (reduction in short-circuiting) that had significant, positive impact on fuel conversion efficiency.

Figure 101 shows the energy pathways and balances for the engines at several throttle settings. Note that reducing the total measured energy at partial throttle magnifies errors in the energy balances, explaining the deviation from 100% at the lowest throttle setting on the 3W-28i engine. The largest pathway shift was the reduction in short-circuiting, which fell from upwards of 50% at WOT to 15% to 20% at approximately half throttle. For conditions where the delivery ratio exceeded unity, short-circuiting of the delivered charge in excess of a delivery ratio of unity was guaranteed because there simply was not enough space in the engine to hold all of the delivered charge. This assumption is based on the perfect isothermal displacement model (see Chapter II, Section 5.3.1.1).

Throttling the engines also increased the pressure drop across the throttle plate in turn lowering the amount of charge that could be inducted through the reed valve into the crankcase. In the case of these engines, WOT to 50% throttle resulted in a 60% reduction in short-circuiting losses for a 50% decrease in engine airflow and a 30% decrease in engine power. Some of the gains of trapping efficiency were offset by increases in incomplete

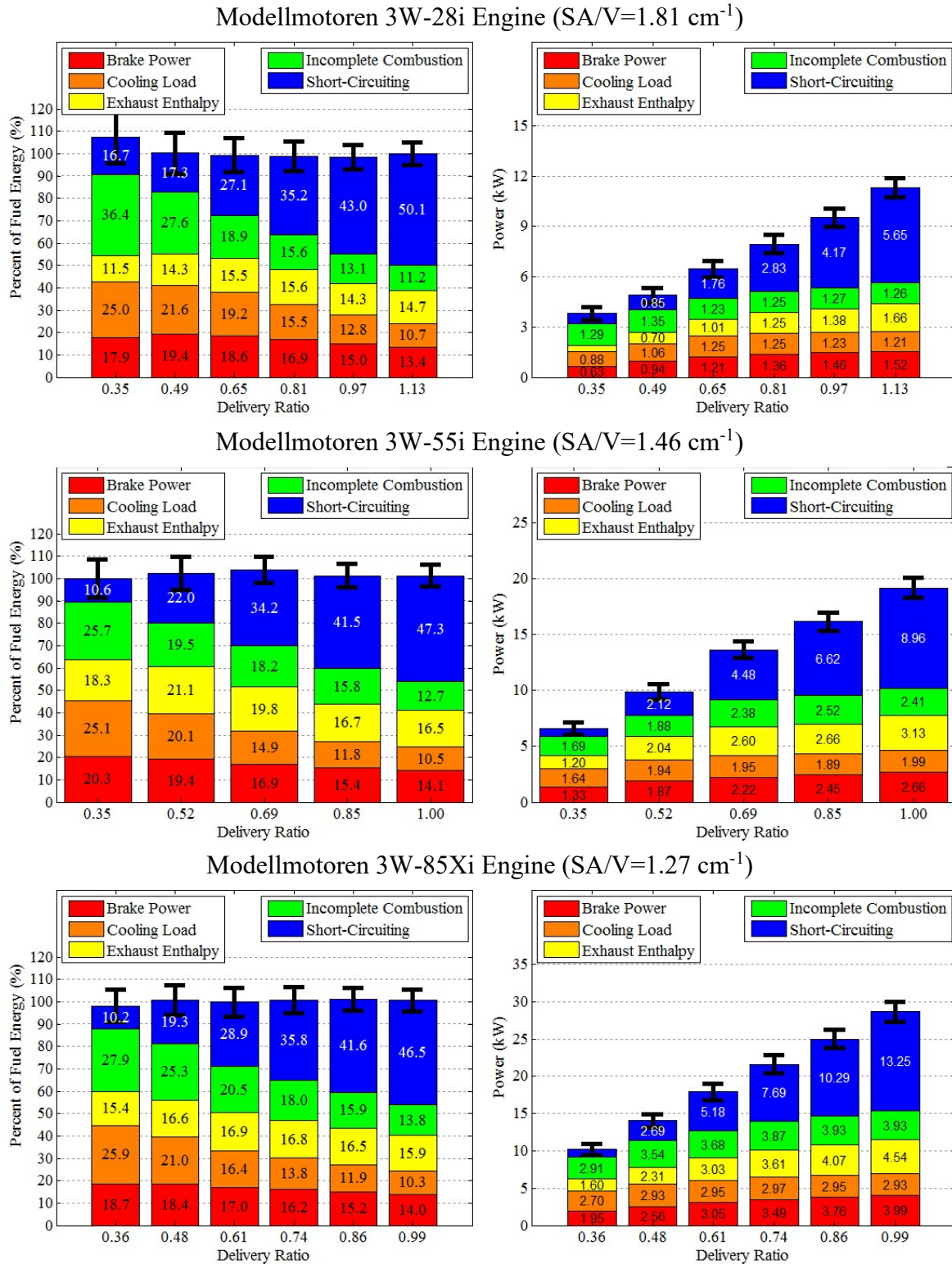


**Figure 101: Effect of delivery ratio (throttle) on energy pathways & balances. The engines were operated at 6000 rpm,  $\phi=1.06\pm0.02$ , CA50=8°aTDC, & CHT=130±2°C. Uncertainty bars are for a 95% confidence interval.**



combustion with decreasing throttle. While a larger percentage of the fresh charge was trapped, the charging efficiencies of the engines still decreased when throttled as shown in Figure 102. Decreasing charging efficiency led to an increase in residuals in the trapped charge, which in turn led to a decrease in combustion efficiency and an increase in incomplete combustion products.

Typically, throttling an automotive scale SI engine at a given speed leads to decreased efficiency as friction and heat transfer become larger portions of the released energy, and combustion efficiency decreases due to increased residuals. Indeed, in Figure 101 the percentage of total energy lost to the cooling load and incomplete combustion increases as throttle decreases, just not as quickly as short-circuiting decreases. To clarify the situation, the energy balances are shown again in Figure 103 with short-circuiting removed.

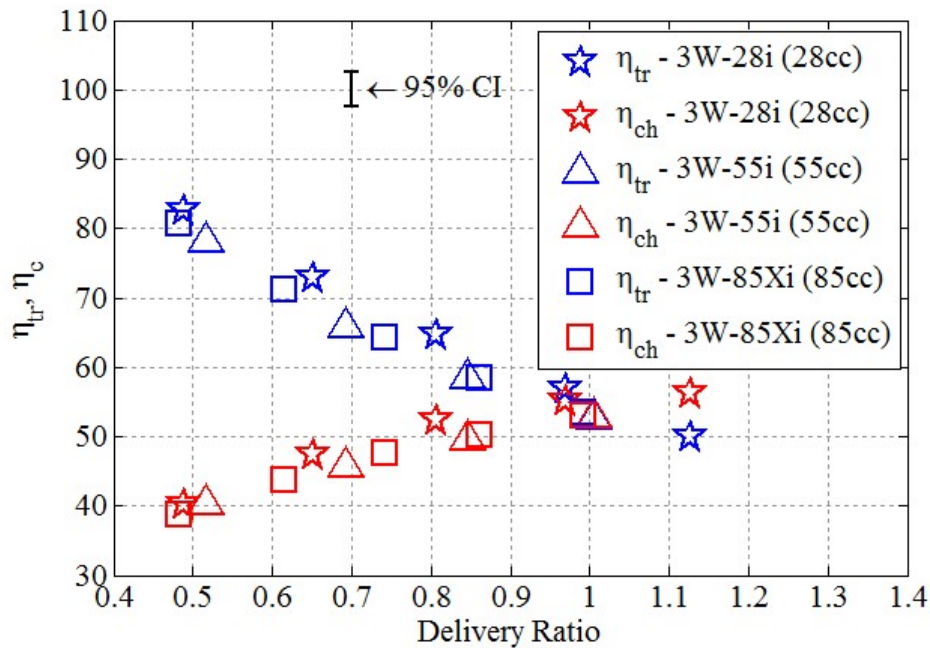


**Figure 102: Effect of delivery ratio (throttle) on charging and trapping efficiencies.**  
The engines were operated at 6000 rpm,  $\phi=1.06\pm0.02$ , CA50=8°aTDC, & CHT=130±2°C.

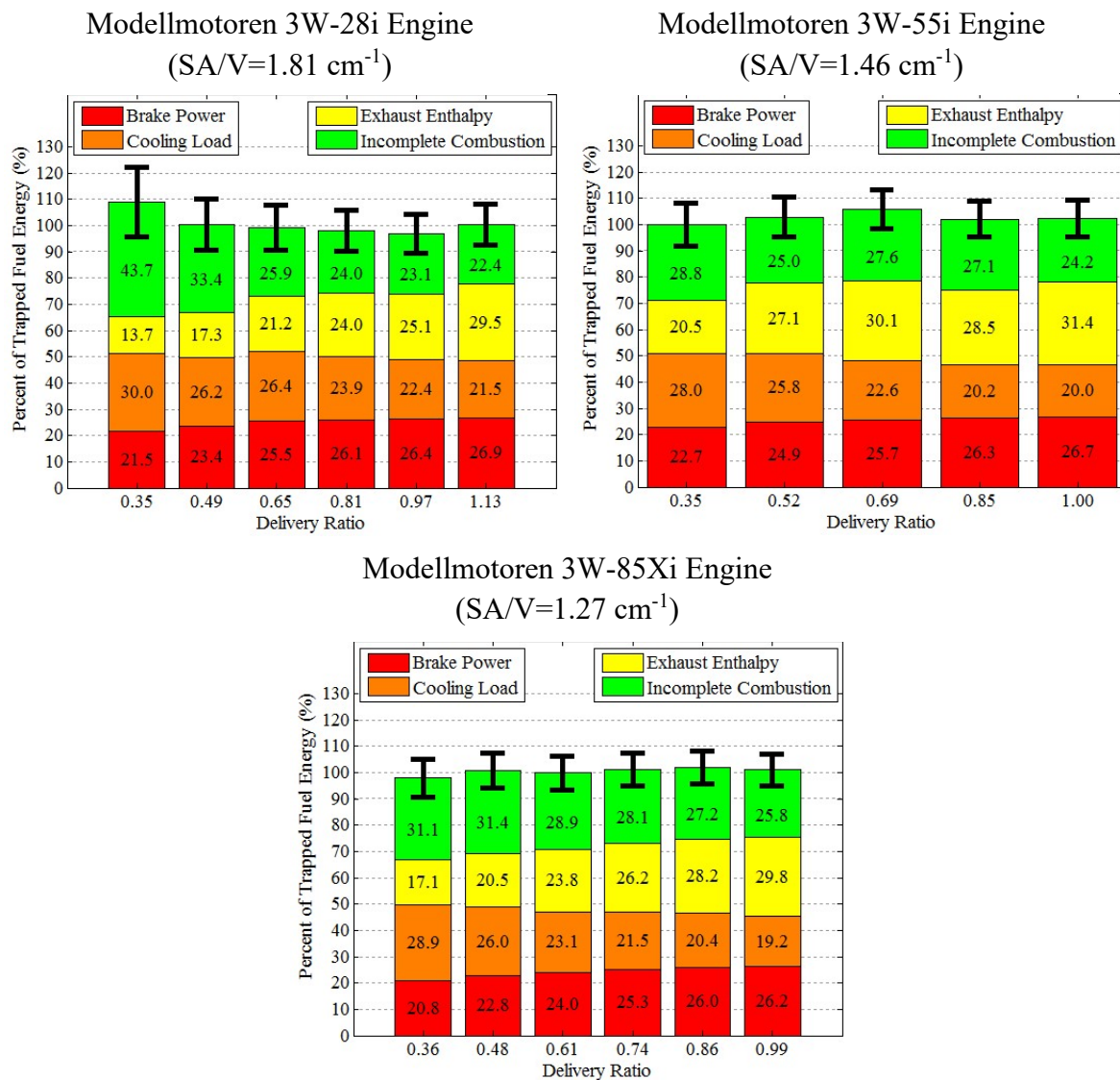


**Figure 103: Effect of delivery ratio (throttle) on trapped energy pathways & balances. The engines were operated at 6000 rpm,  $\phi=1.06\pm0.02$ , & CA50=8°aTDC, & CHT=130±2°C. Uncertainty bars are for a 95% confidence interval.**

Removing the short-circuiting amplifies errors in the energy balances, explaining the increase in deviations from 100% for some of the points. When just considering the expenditure of trapped fuel energy, fuel conversion efficiency generally decreased with throttle by 4% to 6% (absolute) between WOT and 1/2T. While the reduction in total trapped fuel energy reduced the thermal loading of the exhaust, increasing cooling loads

and incomplete combustion losses offset those changes. Decreasing delivery ratios and charging efficiencies allowed greater volumes of warm burnt gas to remain in the cylinder instead of being expelled to the exhaust, heating the fresh charge and shifting thermal loading from the exhaust to the cylinder head.

Ultimately, the consequences of throttled operation of a small COTS two-stroke engine are best summarized by Figure 104; despite increases in the relative magnitudes of incomplete combustion and heat transfer, the improvement in short-circuiting as the engines were throttled led to a 4%-6% (absolute) improvement in fuel conversion efficiency between WOT and half throttle. The impact on a small RPA depends on the configuration of the propulsion system. For an aircraft powered only by an engine sized for takeoff and high power maneuvers, the engine will be throttled during cruise, offering

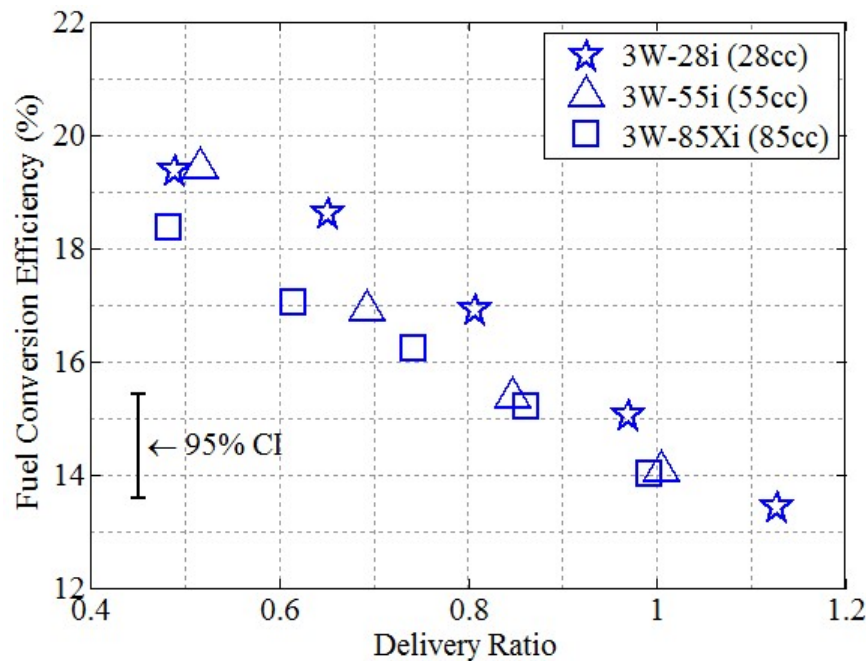


**Figure 104: Effect of delivery ratio (throttle) on fuel conversion efficiency. The engines were operated at 6000 rpm,  $\phi=1.06\pm0.02$ , & CA50=8°aTDC, & CHT=130±2°C.**

a significant efficiency benefit. However, some configurations such as catapult launched or hybrid systems are designed such that the engine (when engaged) always operates at WOT. The idea is to reduce system weight by using the smallest engine possible. However, for situations in which short-circuiting mitigation is not feasible, it may be beneficial to use a larger engine operated at partial throttle, compensating for the increased engine weight with decreased fuel weight enabled by higher fuel conversion efficiency.

To illustrate this concept, consider the 3W-28i engine and the 3W-55i engine both operating at the same power output at 6000 rpm, with the 3W-28i engine at WOT and the 3W-55i engine just under 1/2T. Both engines develop 1.52 kW of power, but the 3W-28i has a fuel conversion efficiency of 13.4% while the 3W-55i has a fuel conversion efficiency of about 20%. As a result, the fuel burn rate of the 3W-28i is 15.2 g/min while the 3W-55i only consumes 10.2 g/min. The 3W-55i engine is 730 g heavier than the 3W-28i engine. Therefore, beyond 145 min (about 2.5 hours) running the 3W-55i engine at partial throttle would actual yield an overall weight savings compared to the 3W-28i at WOT (at a rate of 5 g/min). For a fielded application, the exact break-even point is a function of many factors including mission duration, weight, and cost of short-circuiting mitigation strategies, and in the case of a hybrid configuration, engine duty cycle. Generally speaking, longer missions stand to benefit more from throttled engine operation in cruise as a short-circuiting mitigation strategy.

### **3.5. Thermodynamic Loss Angle**

During motored engine operation, blow-by and heat transfer cause the peak pressure in the cylinder to occur before the physical top dead center. (If the engine were externally heated during motoring, the peak pressure could occur after TDC, but such a situation is

atypical.) The difference between the TDC location of the piston and the peak pressure is referred to as the thermodynamic loss angle. When TDC is determined using an in-cylinder pressure sensor an adjustment should be made to account for the loss angle. Approximations for automotive and transport scale engines are tabulated by engine type and can be found in sources such as Rogers [73:188]. Small engines like those studied here have fewer piston rings (typically one or two instead of three or four) and higher surface area to volume ratios than automotive and larger scale engines. As a result, it was unclear if loss angles tabulated for those engines would be reasonable for small engines.

Loss angles in the studied engines were determined using two different methods: bisection of the forward and backward motored pressure traces, and the difference between a capacitive TDC sensor and the forward and backward motored pressure traces. Figure 105 shows the results from both methods. Note that subtraction of the forward and backwards pressure traces from the capacitive sensor actually yielded two different values. The two methods agreed within  $\pm 0.25$  CAD, which is well within the 95% confidence interval. At high speeds, the thermodynamic loss angle on the 3W-85Xi engine was negative at several points. Since the engine was not heated during testing, the loss angle should not have been negative. Rather the negative points were the result of variations induced by vibrations in the capacitive TDC sensor at high speed as well as sensor adjustments made as a consequence of the vibrations. The 3W-85Xi engine exhibited much stronger vibrations than the other two engines, which made it difficult to maintain the spacing between the piston and capacitive probe at high speeds. Thus, the spacing between the probe and piston had to be increased, lowering the signal strength and creating

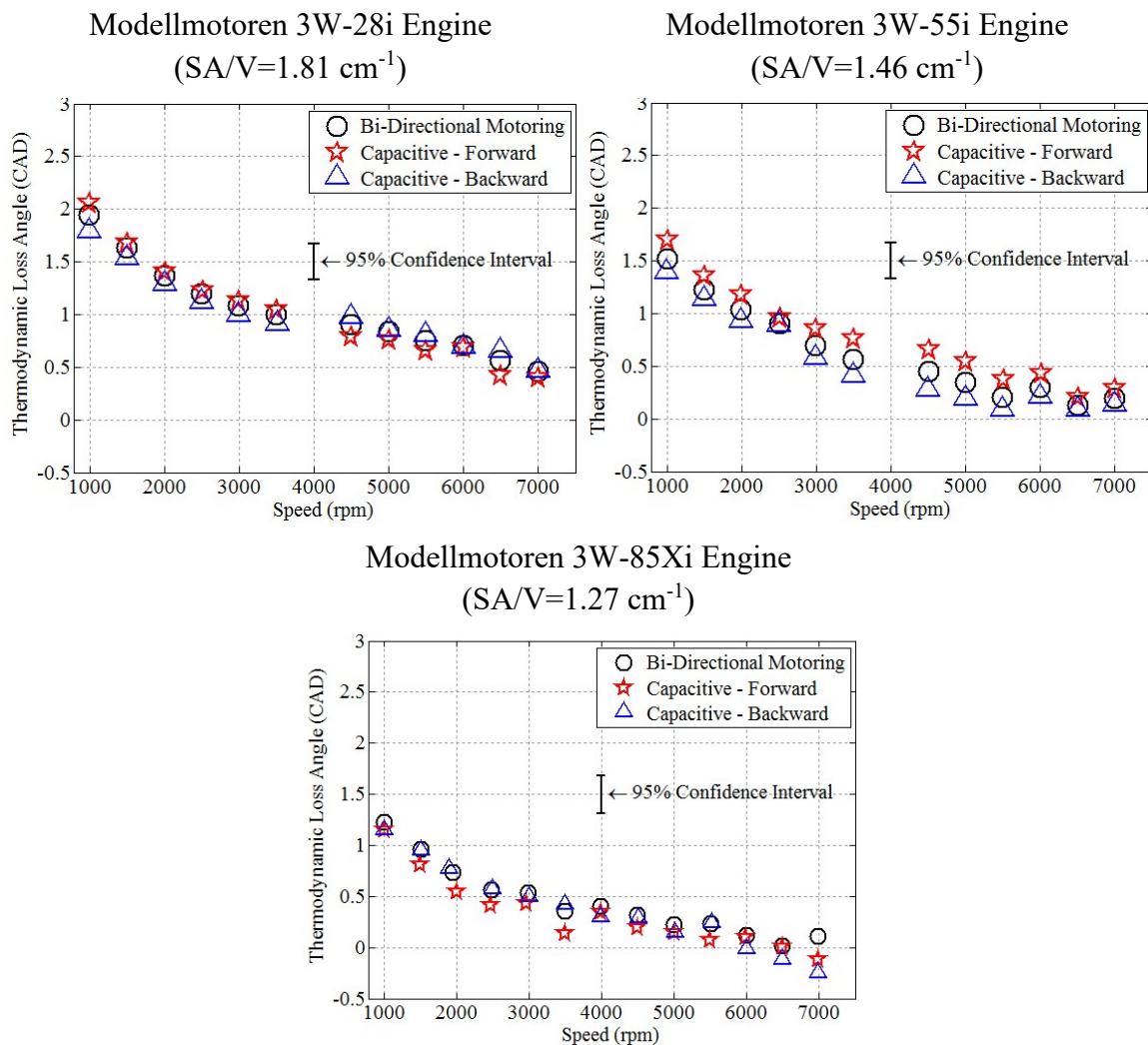


**Figure 105: Thermodynamic loss angles under motored conditions determined using two methodologies.**

additional variability/ uncertainty in the results. Therefore the 3W-85Xi data at and above 6000 rpm should be interpreted as a loss angle that is near zero, not a loss angle that is negative. Such a finding is consistent with the reported confidence interval.

Figure 106 shows the average thermodynamic loss angle each speed for the three engines in this study. The thermodynamic loss angle increased with decreasing engine size, and there were at least four contributing factors. First, as discussed earlier in this

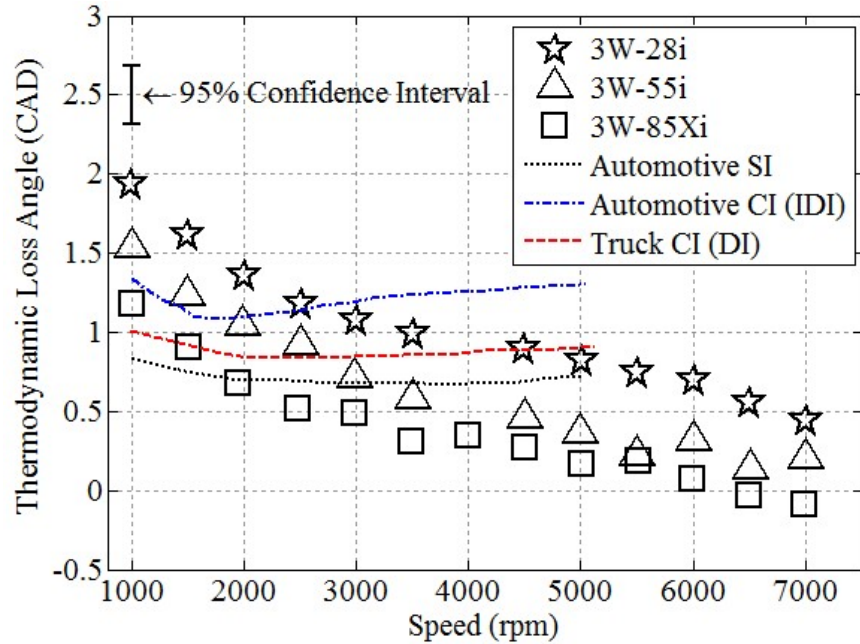


**Figure 106: Thermodynamic loss angle on 3W Modellmotoren engine compared to tabulated loss angles for conventional engines documented in [73:188].**

chapter, trapped compression ratio also increased with decreasing displacement. Increasing the trapped compression ratio increases the peak pressure and temperature, increasing the driving forces for blow-by and thermal losses. Second, as engine displacement decreases the relative piston ring area (and the piston ring gap area) increases, which allows for increased blow-by losses relative to the cylinder volume. Third, a similar argument may be made about thermal losses increasing relative to displaced volume as displacement decreases. Finally, the 3W-85Xi engine had a second piston ring (compared to the 3W-28i and the 3W-55i which only had one). Increasing the number of piston rings increases friction, but reduces blow-by losses.

Figure 106 also compares the loss angles for the engines in this study to loss angles on automotive and transport scale engines tabulated in Rogers [73:188]. The small engines in this study show three to four times greater variation in loss angle between 1000 rpm and

3000 rpm than larger engines. They deviated from the conventional engine curves by up to a degree at some speeds. A degree of error in the TDC location of the piston results in a 2% to 4% error in IMEP, depending on the engine operating condition. Therefore, when accurate, absolute measurements of IMEP are required, automotive and transport scale engine data should not be used to estimate loss angles for 10-100 cm<sup>3</sup> displacement, two-stroke engines. Instead, estimates could either be made based on the data presented in Figure 106, or one of the methods employed to collect this data could be used.

### **3.6. Section Summary and Conclusions**

The parametric study offered insight into the interaction of engine control parameters and energy pathways, providing practical insight for integration of small ICEs onto fielded platforms. Four control parameters were investigated: equivalence ratio, engine head temperature, combustion phasing, and throttle. The key results for each are summarized here. Typically, small ICEs are air carbureted in their COTS configuration, operating at equivalence ratios of 1.1 to 1.2. The parametric study showed that lean operation using a throttle body fuel injection system lowered short-circuiting and incomplete combustion losses. Shifting from typical operation at an equivalence ratio of 1.1 to 1.2 to lean operation at an equivalence ratio of 0.8 to 0.9 resulted in a 4% (absolute) increase in fuel conversion efficiency at the expense of a 10% decrease in power. Based on the parametric study, 5 CAD of deviation from MBT timing caused a 0.5% (absolute) decrease in fuel conversion efficiency, and further deviations caused larger decreases in efficiency and potentially unstable engine operation. For simplicity, most COTS engines use linear timing maps to set spark timing based on engine speed. The stock, linear timing maps were excessively retarded below 3000 rpm, making starting the engine difficult. Engines on small RPAs are



usually cooled either by exposing the head to the free stream or through forced cooling using a scoop. Due to the impact on trapped charge density, decreasing head temperature from 180°C to 120°C led to a 5-10% increase in power, and a 0.5% (absolute) increase in fuel conversion efficiency, which would correspond to a 4% increase in endurance. Finally, at cruise conditions engines typically operate at part throttle, unless takeoff and climb power margins are met through other means. Unlike conventional size engines, fuel conversion efficiency of small two-stroke ICEs improved at throttled conditions by 4%-6% (absolute) due primarily to decreased short-circuiting. When no additional short-circuiting mitigation techniques are employed, running a larger engine at partial throttle may lead to an overall weight savings on longer missions. At 6000 rpm, the 3W-55i engine at partial throttle would yield an overall weight saving compared to the 3W-28i engine at WOT for missions exceeding 2.5 hours (at a savings of about 5 g/min).

#### **4. Summary: Objective 1**

The goal Objective 1 was to understand the interaction between loss/energy pathways (brake power, cooling load, exhaust enthalpy (sensible), short-circuiting, and incomplete combustion) in 10-100 cm<sup>3</sup> displacement engines and overall performance and efficiency. The chapter was split into two sections. The first section (Section 2) presented energy balances for each of the studied engines and the scaling study that was the focus of Objective 1. These balances demonstrated a full accounting of the energy delivered to each engine. Comparison to manufacturer data showed that performance of the tested engines was comparable to manufacturer expectations of these specific engines as well as performance of typical 10-100 cm<sup>3</sup> displacement engines.

Despite the tested engines varying in displacement from 28 cm<sup>3</sup> to 85 cm<sup>3</sup>, their fuel conversion efficiencies (13%-15%) and peak normalized power outputs (IMEP of 5.5-6.0 bar) were roughly similar. In fact, fuel conversion efficiency at peak power decreased slightly with increasing displacement in the tested engines. Therefore the trends in fuel conversion efficiency and BMEP were more the result of design decisions, specifically the increase in port timing (decrease in trapped compression ratio) with increasing displacement in this particular family of engines. When the studied engines were compared to larger SI and CI engines and smaller glow fuel engines, a clear trend in loss pathways emerged explaining the drop in power and efficiency observed as engine displacement decreases from larger than 100 cm<sup>3</sup> to smaller than 10 cm<sup>3</sup>. As engine displacement decreases below 100 cm<sup>3</sup>, short-circuiting and incomplete combustion losses drive the observed decrease in efficiency. When these losses are removed and only the energy released during combustion is considered (thermal efficiency), the studied engines had thermal efficiencies comparable to automotive scale engines. Based on data for micro glow engines smaller than 10 cm<sup>3</sup> displacement, as engine displacement further decreases below 10 cm<sup>3</sup>, heat transfer becomes increasingly important, driving down thermal efficiency more rapidly. Combined with exhaust losses (incomplete combustion and short-circuiting) that remained on the order of 60%, the net result is an increasingly steep drop off in efficiency with decreasing engine displacement below 10 cm<sup>3</sup>. Thus, the primary obstacle to improving performance in 10-100 cm<sup>3</sup> displacement COTS two-stroke engines is addressing short-circuiting, not heat transfer as was hypothesized at the beginning of this effort. Short-circuiting can be mitigated through intake and exhaust tuning, direct

injection, and lean operation with varying degrees of cost and difficulty, and the trade space between those approaches was discussed.

The second section (Section 3) presented a number of parametric studies describing the interactions between engine operating parameters (equivalence ratio, combustion phasing, head temperature, and throttle), engine performance metrics, and the loss pathways. The study identified ways to improve engine performance over the COTS configurations. Replacing the stock carburetor with throttle body injection significantly increased control over fuel delivery, enabling reliable lean operation. Lean operation at equivalence ratios between 0.8 and 0.9 increased fuel conversion efficiency up to 4% (absolute) from typical operation at an equivalence ratio between 1.1 and 1.2 with a power penalty of about 10%. The linear timing maps in the custom ECU were replaced with optimized spark timing. The stock maps were typically within  $\pm 5^\circ\text{CA}$  of the optimal timing (MBT) at WOT and 4000 rpm to 8000 rpm; significant deviations at low speed and/or low throttle led to difficulties starting the engines and running at low power. Decreasing head temperature from  $180^\circ\text{C}$  to  $120^\circ\text{C}$  lead to a 5%-10% increase in power and a 0.5% (absolute) increase in fuel conversion efficiency, indicating that generally more cooling is preferable. Improvements in engine performance due to cooling were primarily the result of improved charging efficiency due to higher density of trapped charge. Finally, fuel conversion efficiency improved at throttled conditions by 4% to 6% (absolute) due primarily to decreased short-circuiting. When no additional short-circuiting mitigation techniques are employed, running a larger engine at partial throttle may lead to an overall weight savings on longer missions. For example, at 6000 rpm, the 3W-55i engine yielded a fuel savings of 5 g/min beyond 2.5 hours compared to the 3W-28i engine.

## **V Objective 2: Heat Transfer, Friction Loss, and Gas Exchange Modelling**

### **1. Chapter Overview**

The goal of Objective 2 was to investigate models for heat transfer and friction losses in small, 10-100 cm<sup>3</sup> displacement ICEs. While the objective did not include modelling gas exchange, it did include comparing the observed gas exchange to simple models to provide insight into how much improvement might be made in the scavenging process. The remainder of this chapter is divided into three sections. The first section (Section 2) addresses heat transfer modelling. The second section (Section 3) investigates friction modelling. The third section (Section 4) compares gas exchange to historical models and discusses gas exchange performance observed in these engines compared to expectations for larger two-stroke engines.

### **2. Heat Transfer Modeling**

The first goal of Objective 2 was to investigate heat transfer models for 10-100 cm<sup>3</sup> displacement, SI two-stroke engines that would be useful for engine designers seeking to estimate the cooling load of an engine for integration into an aircraft. One input common across many historical models is the in-cylinder gas temperature, which is frequently estimated using the ideal gas law via the in-cylinder pressure and the trapped mass in the cylinder. Compared to temperature, pressure is much easier to measure in-cylinder. A single pressure transducer measures pressure in the entire cylinder except during knocking conditions and in-cylinder pressure transducers (both stand alone and integrated into the spark plug) are readily available from a number of manufacturers. To satisfy the interests of an aircraft designer seeking to model an engine, the temperature profiles computed using

the ideal gas model were used to evaluate the validity of historical models. Two different variants of the ideal gas model will be discussed: a variable mass model and an average mass model. In the variable mass model, the trapped mass used in the model varied with operating condition based on the temperature and pressure at port closure. In the average mass model, an average mass (at port closure) from the sweep was used. The average mass model is more representative of an instance where nothing is known about the engine's trapping performance as a function of operating condition *a priori*, where the variable mass model suggests *a priori* knowledge of how trapping varies with operating condition.

In light of the model options, there remained a question as to how well the temperature calculated from the in-cylinder pressure (which is subject to a variety of sensitivities that will be discussed in the next section) captured trends in in-cylinder temperature caused by sweeping the engine control variables. As discussed in Chapter III, Section 4.1.2, TLAS was used to measure the in-cylinder gas temperature across a line-of-sight several millimeters below the spark plug electrode. Those results were compared to the model results to ascertain if the trends predicted by the model tracked the trends observed in the measured temperature.

Collecting the TLAS temperature data and comparing it to the ideal gas model predictions was more time intensive than initially anticipated and to an extent redirected the focus of this portion Objective 2 away from heat transfer modelling toward an evaluation of the use of the ideal gas law as a proxy for the measurement of in-cylinder temperature. The first subsection, Section 2.1, is dedicated to this subject. The following subsection, Section 2.2 discusses the modelling results for heat transfer, specifically, the evaluation of the Taylor and Toong model for small, two-stroke, SI engines. Due to

equipment constraints (namely availability of the TLAS system), heat transfer modelling data was not available for the 3W-85Xi engine at the time of writing; only results from the 3W-28i and 3W-55i engines will be presented.

## 2.1. In-cylinder Temperature Results

This section compares the in-cylinder temperature results from TLAS to the ideal gas law based model commonly used in the literature. Similar to the parametric study discussion in the previous chapter, this section will be divided into five subsections, one for each parametric sweep of an engine control variable. Speed will be discussed first and that section will also present additional notes on the data reduction and analysis. Following the discussion of speed, results for equivalence ratio, combustion phasing, head temperature, and throttle will be presented.

Most of the heat transfer models discussed in Chapter II, Section 5.1.1 do not make a direct measurement of in-cylinder gas temperature. Instead, the models estimate the in-cylinder gas temperature using the ideal gas law as shown in Equation (127). While the numerator of the equation may be determined from the engine geometry and the in-cylinder pressure trace; the denominator is more complicated. In this effort, the mass of the cylinder contents was estimated using the temperature provided by TLAS and the in-cylinder pressure at the instant the exhaust port closed. The gas constant was calculated based on cylinder contents that were approximated using the mass fraction burned profile derived from the in-cylinder pressure as well as the assumptions of perfect complete or incomplete combustion depending on equivalence ratio.

$$T_{g,cyl} = \frac{p_{cyl} V_{cyl}}{m_{cyl} R} \quad (127)$$

### 2.1.1. Speed

Figure 107 shows the in-cylinder temperature and pressure for the sweeps of engine rotational speed. Due to vibration in the system and signal degradation caused by window fouling, the TLAS data could not be post-processed into a temperature profile at some operating conditions. Additionally, some points were sufficiently poor in real time that they were not attempted. Therefore, the points collected for the in-cylinder temperature study will not perfectly match the parametric study presented in Objective 1, and for some

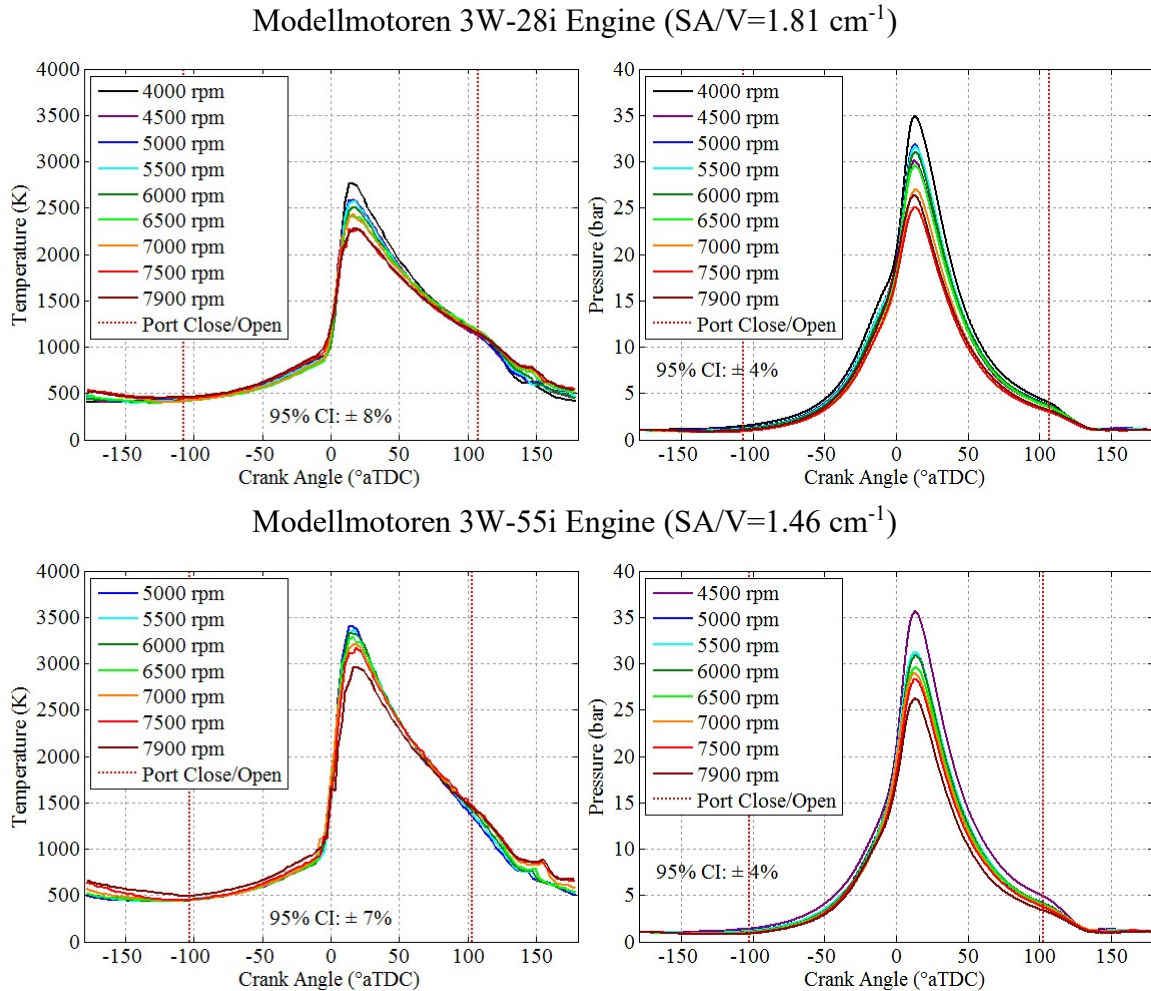


**Figure 107: Impact of speed on in-cylinder temperature (TLAS) and pressure. The engines were operated at WOT,  $\phi=1.06\pm0.02$ ,  $CA_{50}=8\pm0.5^\circ\text{aTDC}$ , &  $CHT=130\pm2^\circ\text{C}$ . Pressure is a 400 cycle average, temperature is a 500 ms average.**

points, pressure and temperature model data will be presented where there is no corresponding TLAS data.

Figure 107 shows the peak cylinder pressures decreasing with operational speed, which was expected since IMEP also dropped off with speed as observed in Objective 1 (see Chapter IV, Section 2.3). The peak temperature followed a similar trend. The drop in IMEP indicates a less effective use of the cylinder volume due to decreased delivery ratio and charging efficiency (see Chapter IV, Section 2.4). The result of decreasing charging efficiency was less fuel consumed per cycle and in turn lower in-cylinder temperatures. Therefore, while the in-cylinder temperatures were admittedly for a specific line-of-sight that was influenced by the traverse of the flame front, the measurements were qualitatively consistent with other measured quantities.

Figure 108 compares 500 ms of pressure and temperature data (approximately 50 cycles) to the average traces. The data was collected using the 3W-55i engine operating at the baseline condition. The average temperature trace was calculated by binning the TLAS

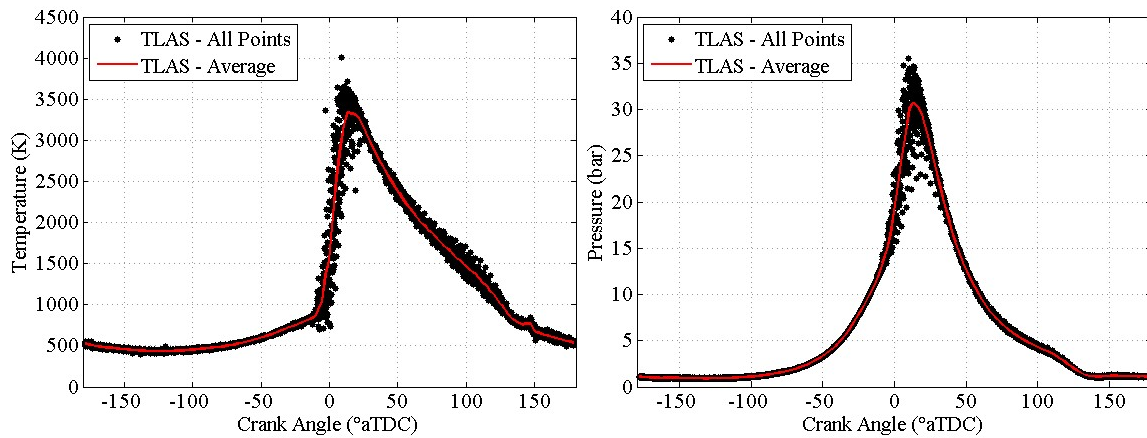


**Figure 108: Comparison of 50 cycles of pressure and temperature data to the average pressure and temperature trace. Data collected on the 3W-55i engine at 6000 rpm, WOT,  $\phi=1.06\pm0.02$ , CA50= $8\pm0.5^\circ\text{aTDC}$ , & CHT= $130\pm2^\circ\text{C}$ .**



data into bins 2.67 CAD wide and averaging the contents of each bin. Then each bin was assigned a crank angle location corresponding to the average crank angle of its constituent points. Several options were available for the averaged pressure trace. The AVL Indismart Combustion Analyzer natively provided a 400 cycle average pressure trace. However, since the TLAS system and AVL Indismart were synchronized manually, the cycles sampled by the AVL were not the exact same cycles sampled by the TLAS system.

To evaluate the impact on the average pressure trace, the pressure transducer signal was also recorded using the TLAS system and averaged using the same procedure as temperature. The average pressure from the TLAS system for the 3W-55i engine operating at the baseline condition is compared to the corresponding average trace from AVL in Figure 109. Visually, the two traces are on top of one another, so the residual between the two traces was calculated as both an absolute pressure and as a percentage (and the results are shown in Figure 109). Based on Figure 109, the average pressure trace from the AVL IndiSmart and TLAS system may be used interchangeably with less than 2% error at most points throughout the cycle. Other operating conditions were spot checked and showed similar results. Unless otherwise specified, the pressure data for the remainder of this section was taken from the AVL Indismart.

Before proceeding to the first of the temperature models, it is useful to discuss the uncertainties of the measured temperature and pressure. Both quantities have two sources of uncertainty: measurement and cycle-to-cycle. The measurement uncertainty originated from the instrumentation and measurement technique while the cycle-to-cycle uncertainty was the result of averaging a number of cycles to create the traces. The TLAS system had a measurement uncertainty of  $\pm 50^{\circ}\text{C}$  while the in-cylinder pressure measurement was

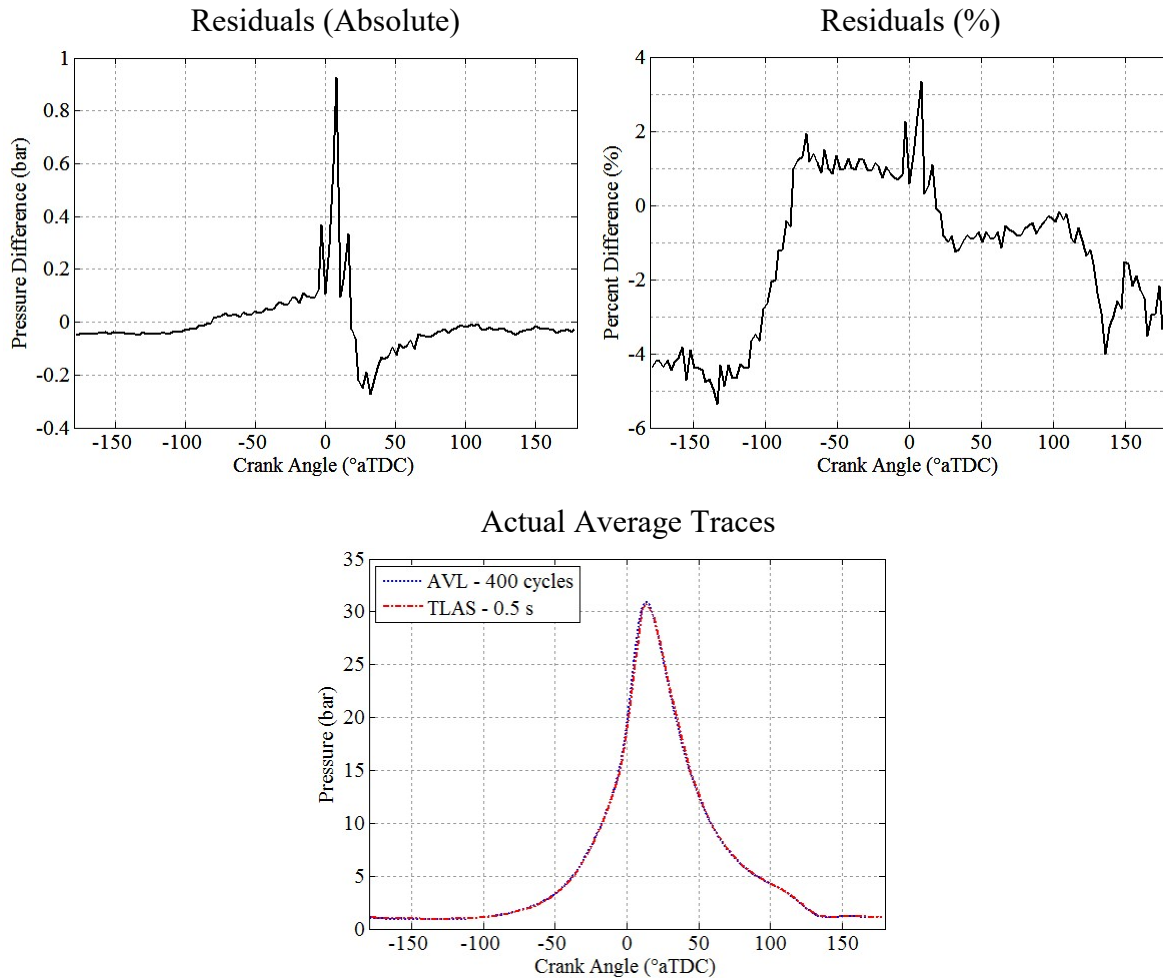
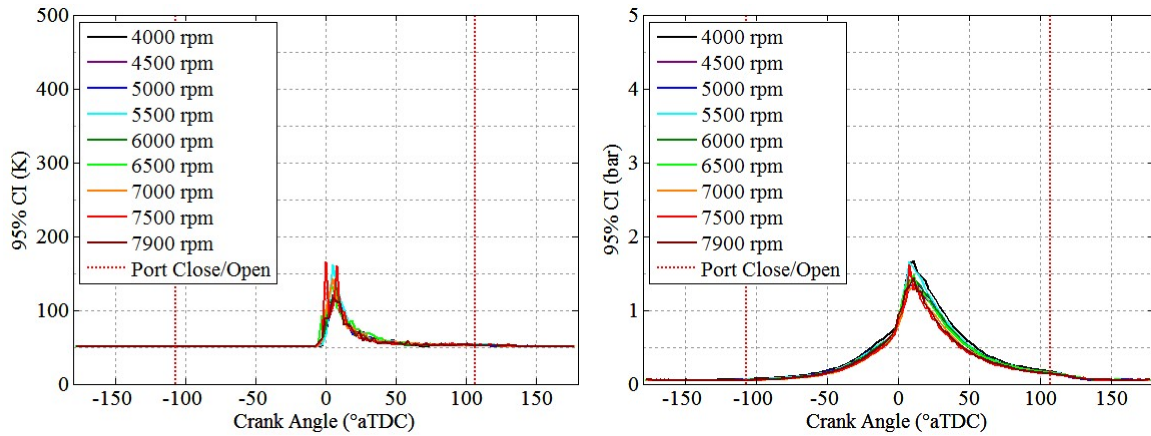


**Figure 109: Comparison of the average in-cylinder pressure trace as measured by the AVL Indismart to the trace measured by the TLAS system. Data collected on the 3W-55i engine at 6000 rpm, WOT,  $\phi=1.06\pm0.02$ ,  $CA_{50}=8\pm0.5^{\circ}aTDC$ , &  $CHT=130\pm2^{\circ}C$ .**

accurate to  $\pm 4\%$ . The cycle-to-cycle uncertainty was the result of averaging many cycles to create averaged traces. The uncertainty of the measurement technique ( $\pm 50$  K for TLAS and  $\pm 4\%$  for pressure) tended to dominate outside of the combustion event, especially at low temperature and pressure. Meanwhile the cycle-to-cycle variation tended to dominate during the combustion event (since cycle-to-cycle variations in pressure and temperature were primarily driven by variation in the combustion event). Cycle-to-cycle uncertainty

for the pressure trace was derived from TLAS data as a worst case scenario. The two uncertainties were combined using standard statistical methods. The cycle-to-cycle variation was reduced to a standard deviation of the mean of each bin, which was combined with the measurement uncertainty using a root sum squares approach. The final uncertainties are reported in Figure 110 as absolute values, and again in Figure 111 as a percentage of the average signal. Uncertainty values peak right after TDC, driven by cycle-to-cycle variation in the combustion phasing. Based on Figure 111, the average uncertainty in measured pressure was 4%-5% of the measured values. The average uncertainty on

#### Modellmotoren 3W-28i Engine (SA/V=1.81 cm<sup>-1</sup>)



#### Modellmotoren 3W-55i Engine (SA/V=1.46 cm<sup>-1</sup>)

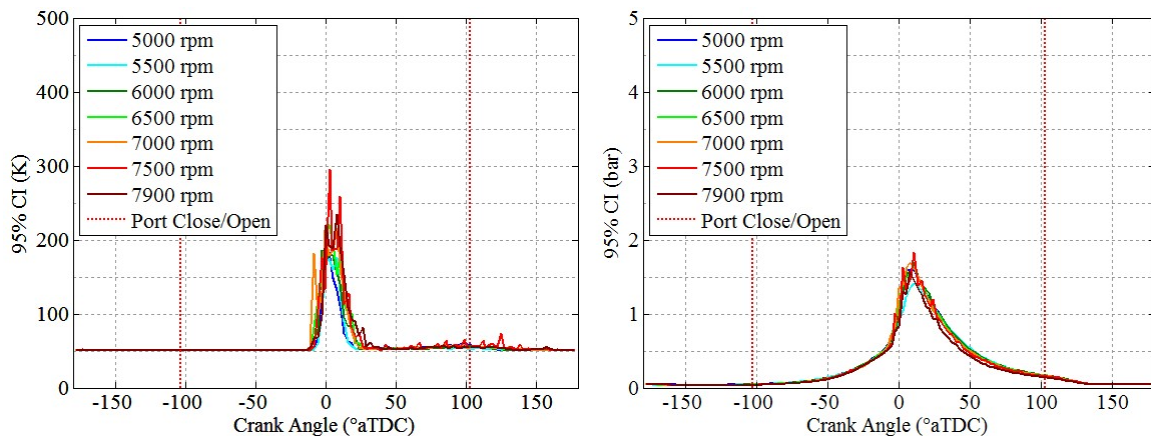
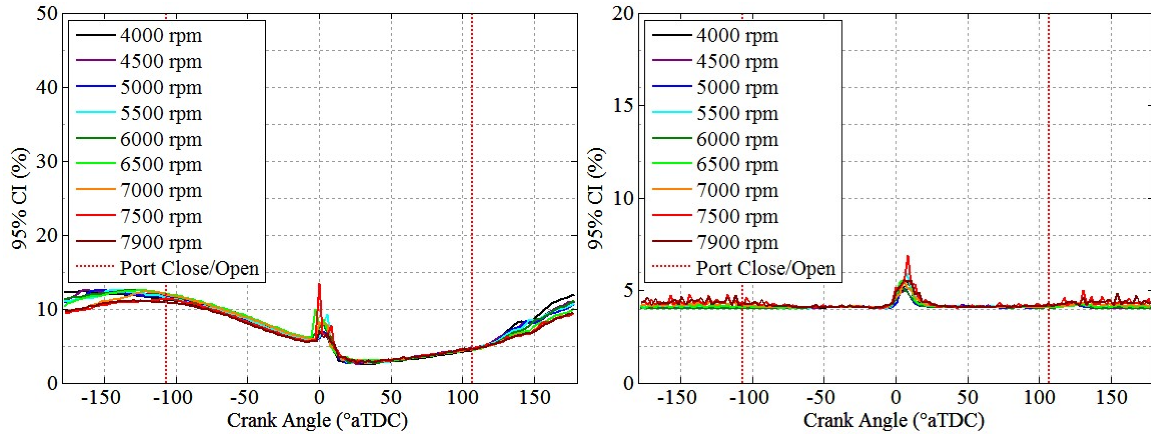


**Figure 110: 95% confidence interval on measured temperature and pressure expressed in absolute units for the speed sweep results in Figure 107.**

### Modellmotoren 3W-28i Engine ( $SA/V=1.81 \text{ cm}^{-1}$ )



### Modellmotoren 3W-55i Engine ( $SA/V=1.46 \text{ cm}^{-1}$ )

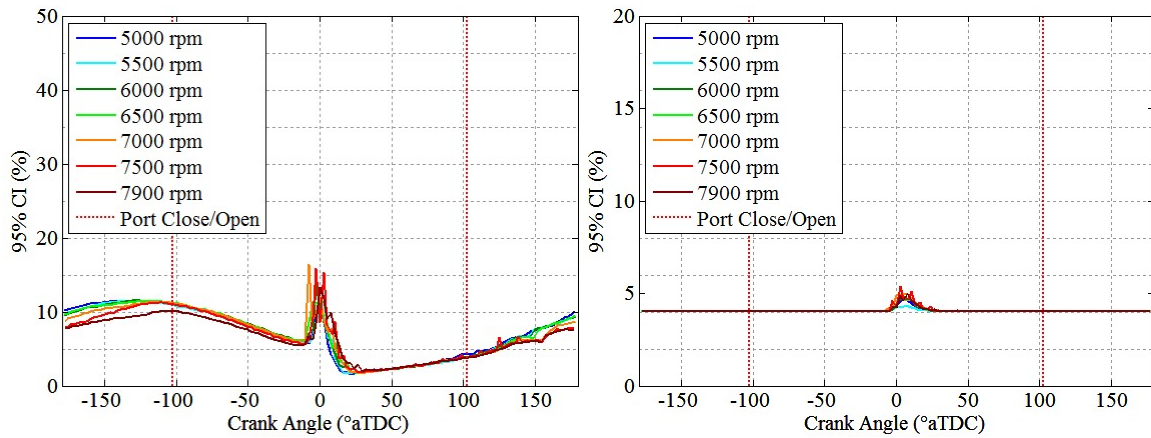


**Figure 111: 95% confidence interval on measured temperature and pressure expressed as a percentage for the speed sweep results in Figure 107.**

measured temperature was about 10% of the measured value. Uncertainty plots for the remaining sweeps were similar. In the interest of maintaining focus while still providing a complete documentation of the results, the uncertainty plots for those sweeps are included in Appendix G.

An attempt was made to model the in-cylinder temperature using Equation (127) as described in the introduction to Section 2.1. The results are shown in Figure 112. Since mass was not constant during the gas exchange process, the model in Figure 112 could not

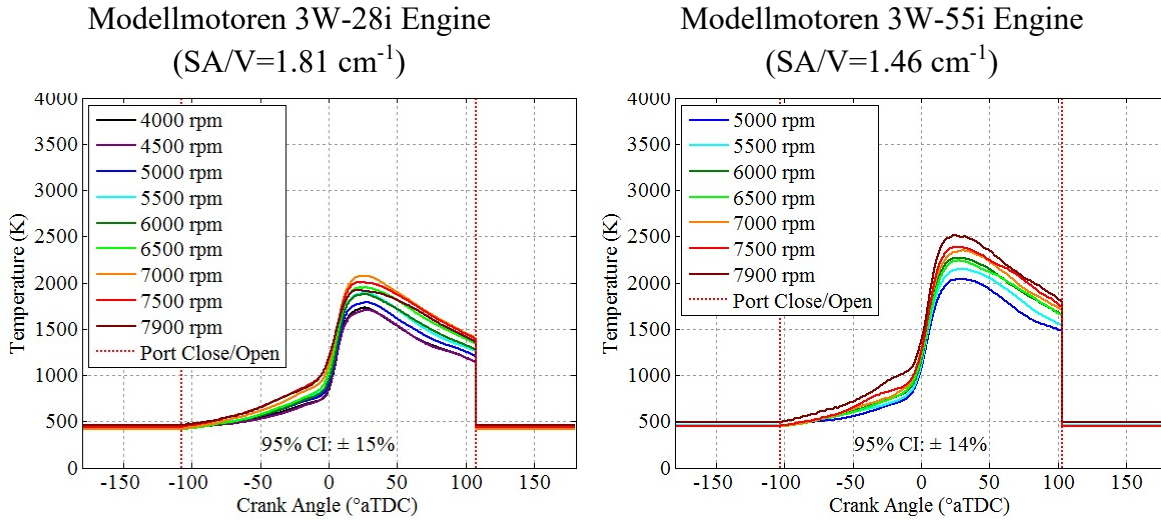


**Figure 112: In-cylinder temperature calculated using the variable mass model for the speed sweep. Trapped mass was calculated using cylinder temperature and pressure at exhaust port close. Gas exchange temperature was set equal to TLAS temperature at port close.**

be used when the ports were open. Therefore, during gas exchange the model temperature was set equal to the temperature when the exhaust port was closed, which in this case was the same as the temperature used to calculate the trapped mass. Most temporally resolved models struggle with gas exchange since they lack a way to predict the temperature from easily measured quantities. For temporally resolved models, an estimated temperature may be used for both the time during gas exchange and for calculating the trapped mass. Such an estimate could be made based on knowledge of the fresh charge temperature, exhaust temperature, delivery ratio, and charging/trapping efficiency. In this case the estimate was made based on a measured gas temperature.

Comparing Figure 107 and Figure 112, two differences between the modelled temperature and the measured temperature are readily apparent. The first is a difference between the peak values of the model and the measurement, where the model temperature is 500 K to 1000 K lower than the temperatures measured using TLAS. This difference is

readily explained by the fact that TLAS is a line-of-sight measurement across the combustion dome while the model represents an aggregate temperature for the entire cylinder contents. The traverse of the flame front increased the temperature as measured by TLAS compared to the cylinder contents as a whole. After the flame front passed, it is likely that the combustion dome cooled more quickly than the rest of the cylinder due to a higher surface area to volume ratio as well as due to the large, thermally conductive washer setting the spacing for the measuring spark plug.

The second difference is the discrepancy in the order of the peak temperatures with engine speed, which was essentially reversed from the trend observed in both the measured temperature and pressure. The reason for this reversal is somewhat complicated, and identifying it required further investigation into the calculation of the trapped mass. Theoretically, the mass of the cylinder contents may be calculated at any point during the cycle given an appropriate aggregate temperature, pressure, and cylinder volume. For consistent inputs, the calculated mass would be constant from the closing to the opening of the exhaust port(s), with small decreases possible due to blow-by. Note: reverse blow-by is possible for engines with multiple piston rings.

Such a calculation was carried out and the results are shown in Figure 113. Since changes in pressure propagate nearly instantaneously throughout the cylinder and volume may be calculated from crank angle and engine geometry, many of the deviations of the calculated cylinder mass from a constant value stemmed from the assumption that the temperature in the TLAS line-of-sight was representative of the temperature of the cylinder contents as a whole. Starting from the closure of the exhaust port, except at low speeds, the calculated cylinder mass was relatively constant ( $\pm 15\%$ ) until the flame front reached

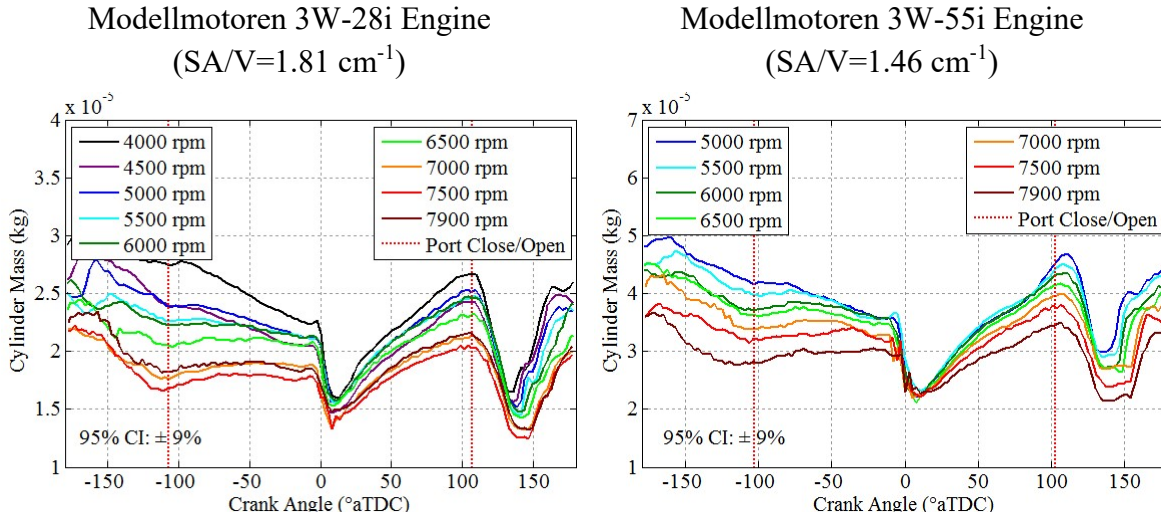


**Figure 113: Mass of cylinder contents calculated using the ideal gas law and the in-cylinder pressure and temperature for the speed sweep. The engines were operated at WOT,  $\phi=1.06\pm0.02$ , CA50=8 $\pm0.5^\circ$ aTDC, & CHT=130 $\pm2^\circ$ C.**

the field of view (near TDC). During this window, some decrease in the trapped mass could physically occur due to blow-by. The relative effect of blow-by would be expected to increase with decreasing engine speed since the time for a fixed crank angle window decreases with increasing engine speed. The flame front reached the line-of-sight relatively early in the combustion process (near CA10) before combustion had a significant impact on pressure and aggregate temperature outside of the flame kernel. Once the flame front reached the line-of-sight, the line-of-sight was hotter than the aggregate cylinder temperature causing the calculated mass to decrease rapidly. As the flame front passed beyond the line-of-sight into the remainder of the cylinder a combination of combustion in the rest of the cylinder and localized cooling in the combustion dome caused the calculated mass to rebound and over report compared to the value between port closing and the arrival of the flame front at the line-of-sight. Once the exhaust port opened, cylinder mass first decreased as burnt charge was expelled and then varied as the scavenging and boost ports



opened to deliver fresh charge. The qualitative behavior in Figure 113 is consistent with the expected physics and demonstrates that the trapped mass may only be calculated from the in-cylinder pressure and the TLAS measured temperature during a narrow window between port closure and the initiation of combustion (assuming blow-by is negligible). For this work, the closure of the exhaust port was used.

Quantitatively, the results of Figure 113 are less consistent. The results imply that the trapped mass changed by 50% to 100% (depending on the engine) between high speed operation at 7900 rpm and low speed operation below 4000 rpm. The difference was driven almost entirely by the in-cylinder pressure which exhibited variations of a similar magnitude (whereas the measured temperature traces remained within about  $\pm 50$  K of one another for the first 50 CAD after the ports closed). As identified and discussed in Chapter IV, of the studied engine control variables engine speed had the second-largest impact on the scavenging process, and some variation in the mass of the trapped contents with changing operational speed was expected. The variation of 50% to 100%, however, seemed large based on the measured IMEP and BMEP values.

At BDC of every cycle, the in-cylinder pressure transducer was pegged to a low speed pressure transducer in the intake runner, which introduced (a difficult to quantify) error into the absolute pressure measured in the cylinder. Normally, this error was assumed to be small in the context of peak pressure and also to be a constant that drops out in the calculation of IMEP. However, near port closing the in-cylinder pressure was near ambient. Piezoelectric pressure transducers are not particularly adept at measuring small variations in near constant pressures (such as what occurs between pegging at TDC and port closure). Moreover, changing engine speed directly affects the pressure waves that



set up in the intake runner and the crankcase that in turn impact the pegging of the piezoelectric transducer. Neither of these effects were captured by the reported confidence interval. Thus, changes in engine operational speed impacted the trapped mass calculation beyond the actual change in the physically trapped mass between operating points. For the remaining sweeps where the engine speed was held constant, the pegging behavior was more consistent between points in the sweeps, and the peak temperature trends from the variable mass model were more consistent with the trends observed in the measured peak temperatures.

Another possible source of unquantified error was the use of the TLAS temperature as a proxy for the aggregate in-cylinder temperature at and following the closure of the ports. However, the relatively constant mass between port closure and CA10 for most operating conditions indicates that the impact of inhomogeneity in the temperature of the cylinder contents was small compared to the aforementioned challenge of measuring the pressure near port closing. Inhomogeneity in the in-cylinder temperature would have caused swings in the calculated mass similar to those observed during and after combustion, and such swings were generally not observed prior to the combustion event.

The variable mass calculation used for the model in Figure 112 is at one bound for the calculation of trapped mass: it assumes that all of the variations in the measured temperature and pressure were actually representative of changes in the trapped mass. To bound the problem on the other side, the model was recalculated assuming an average initial mass for each of the points in the sweep. Using an average mass proposes that all of the variations in the temperature and pressure at the conclusion of gas exchange were artifacts of the measurement technique. The resulting model using an average mass for

each engine is shown in Figure 114. Except for 4000 rpm on the 3W-28i engine, the use of an average mass collapsed the variation in the models immediately preceding and during the peak temperature rise, much like the behavior observed in the TLAS data. The peak height remained comparable to the variable mass model, however, the order of the peaks reversed, again matching the trends observed in the TLAS data. This result was anticipated since once the trapped mass is fixed, the modelled temperature almost directly follows the in-cylinder pressure, which trended similar to the TLAS results.

The average mass model also had its short-comings. First, it did not capture any variations in the scavenging process caused by changing engine speed. Second, as a result of the constant mass assumption the initial temperatures varied significantly between the points, and some points such as 4000 rpm on the 3W-28i engine had unrealistically high temperatures at port closure. The variability in the calculated trapped mass between points

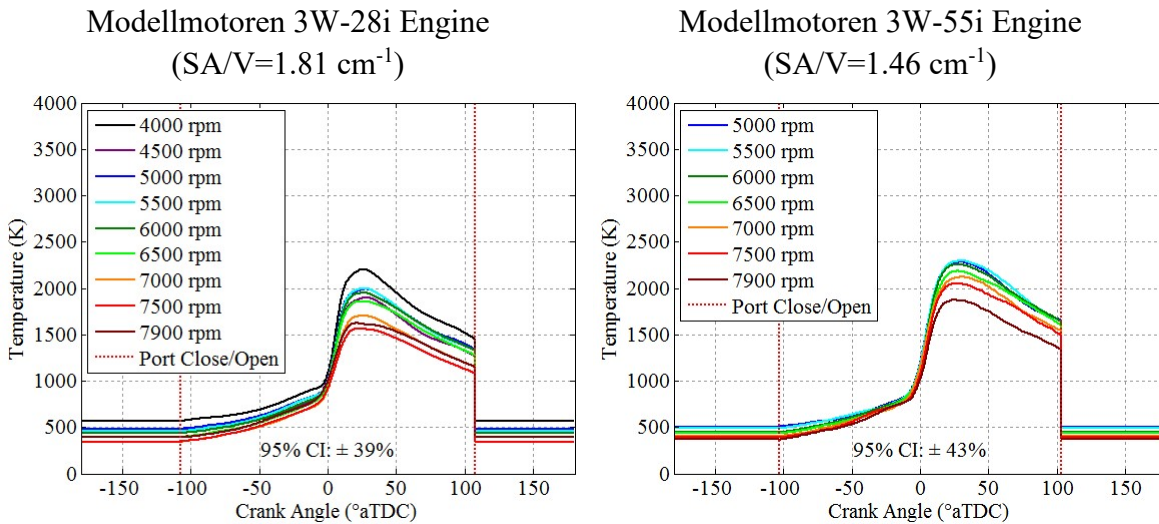


**Figure 114: In-cylinder temperature calculated using the average mass model for the speed sweep. Trapped mass was calculated as the average trapped mass for all points, calculated using cylinder temperature and pressure at exhaust port close. Gas exchange temperature was set equal to the calculated temperature at port close.**

also led to large uncertainty in the model results. Essentially, the average mass technique trades capturing real effects to better reproduce the trends seen in the measured temperature and pressure. In conclusion the trapped mass and resulting temperature models were highly sensitive to the initial temperature and pressure. In turn the initial pressure was highly sensitive to the engine speed.

The heat transfer modelling in Section 2.2 required an average in-cylinder gas temperature, and three different temperature profiles were available: the measured TLAS profile, the modelled profile using a variable mass, and the modelled profile using a constant (average) mass. The averages for all three profiles were computed and the impact on the model from the three different profiles was evaluated. A summary of the average temperatures for the speed sweep is shown in Figure 115. A summary of the peak temperatures and average pressures for the speed sweep is shown in Figure 116.

Two sets of averages were computed for each profile: an average based on the entire cycle and an average based only on the portion of the cycle when the ports were closed. The average based on the portion of the cycle when the ports were closed offered a simpler comparison to the TLAS data since the influence of the constant temperature assumed in the models during gas exchange was eliminated. In other words, the trapped averages only compare the portions of the cycle that were actually modelled. The second set of averages is for the entire cycle. The total cycle averages showed the same trend as the partial cycle averages, with an offset driven by the relatively constant measured and assumed temperatures during gas exchange. From a trend standpoint, the total cycle average and the trapped average were comparable. From a modelling standpoint, the appropriate temperature is dictated by the model. Heat transfer is a time-based phenomenon that occurs

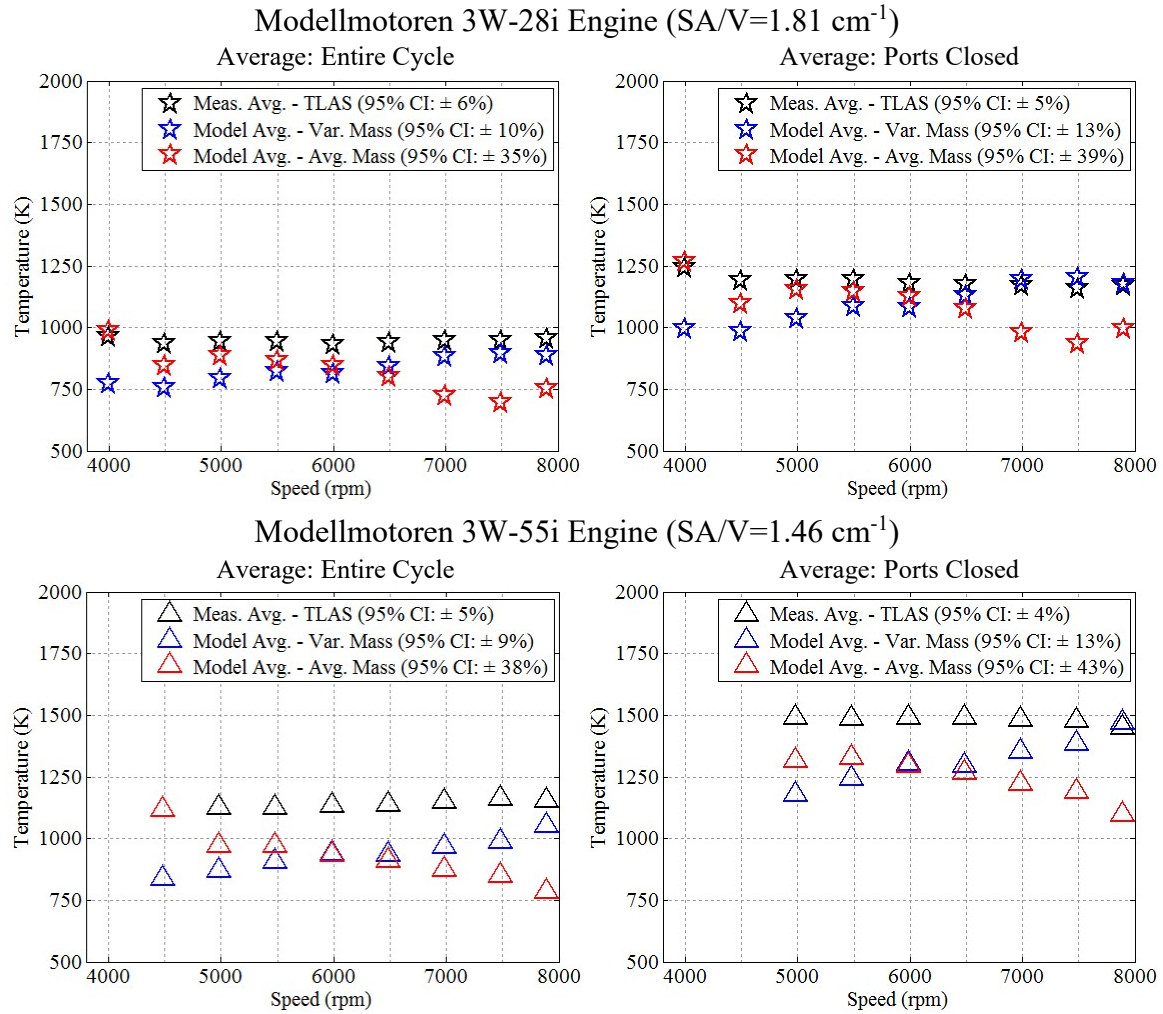
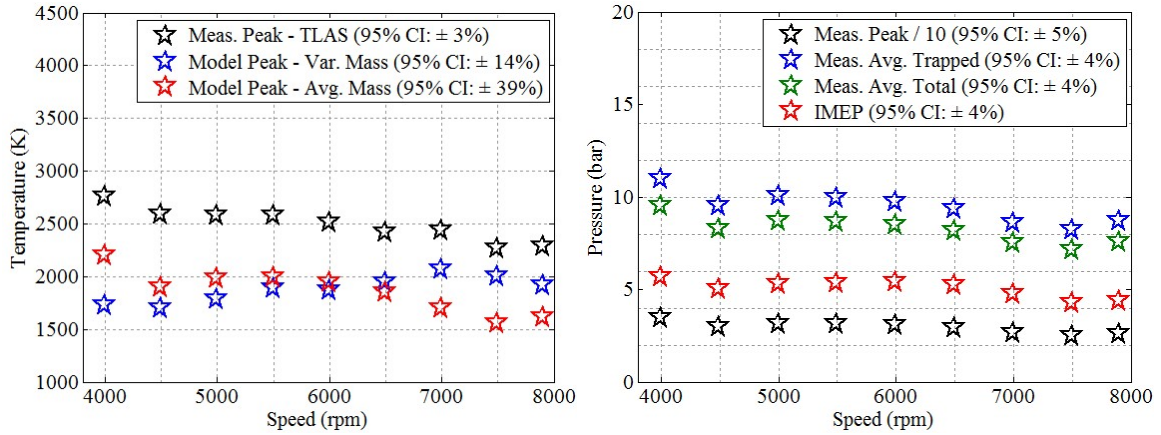


**Figure 115: Average temperature summary statistics for the speed sweep. The engines were operated at WOT,  $\phi=1.06\pm0.02$ ,  $CA50=8\pm0.5^\circ\text{aTDC}$ , &  $CHT=130\pm2^\circ\text{C}$ .**

over the entire cycle, so temporally and spatially averaged models require the total cycle average. Many of the temporally resolved models break down during gas exchange and therefore only model the portion of the cycle where the ports are closed.

The trends of both the variable mass and average mass models deviate from the measured averages reported in Figure 115. The measured averages are relatively constant with speed, while the average temperature from the average mass model tends to decrease with speed and the average temperature from the variable mass model tends to increase

### Modellmotoren 3W-28i Engine ( $SA/V=1.81 \text{ cm}^{-1}$ )



### Modellmotoren 3W-55i Engine ( $SA/V=1.46 \text{ cm}^{-1}$ )

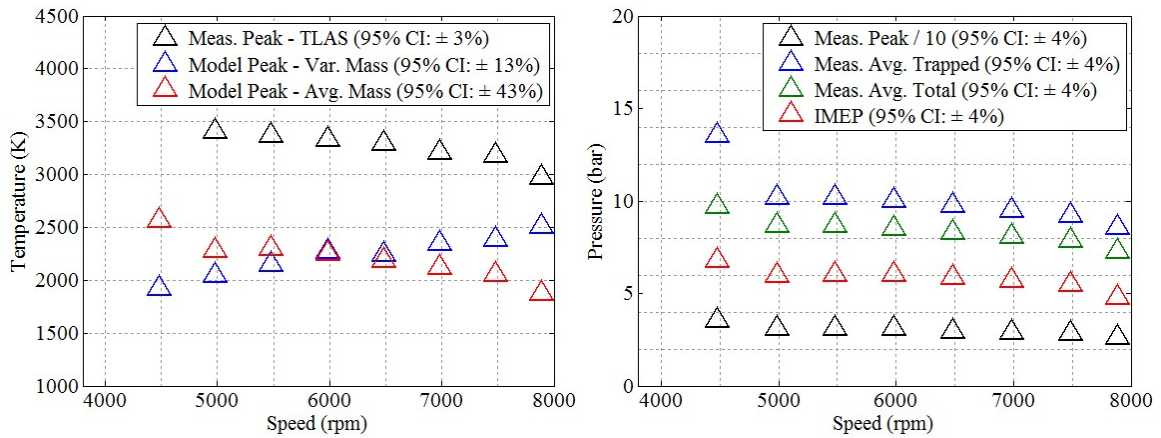


**Figure 116: Pressure and peak temperature summary statistics for the speed sweep. The engines were operated at WOT,  $\phi=1.06\pm0.02$ ,  $CA_{50}=8\pm0.5^\circ\text{aTDC}$ , &  $CHT=130\pm2^\circ\text{C}$ .**

with speed. As with peak temperature, the average mass model tracked pressure, while the variable mass model was more influenced by variations in the calculated trapped mass.

The remaining subsections in this section present data for the other four engine control variables, along with comments highlighting differences between those sweeps and the speed sweep. Results and analysis will be presented for the raw temperature data, temperature models, calculated trapped mass, and temperature and pressure summary

statistics. Plots showing the uncertainty on the measured pressure and temperature are included in Appendix G.

### 2.1.2. Equivalence Ratio

Figure 117 shows the impact of sweeping equivalence ratio on the in-cylinder temperature and pressure measurements. Due to an issue with the TLAS data collection, only limited data was available for the 3W-55i engine. As indicated by the power and IMEP discussion in Chapter IV, Section 3.1, the temperatures and pressure peaks were the

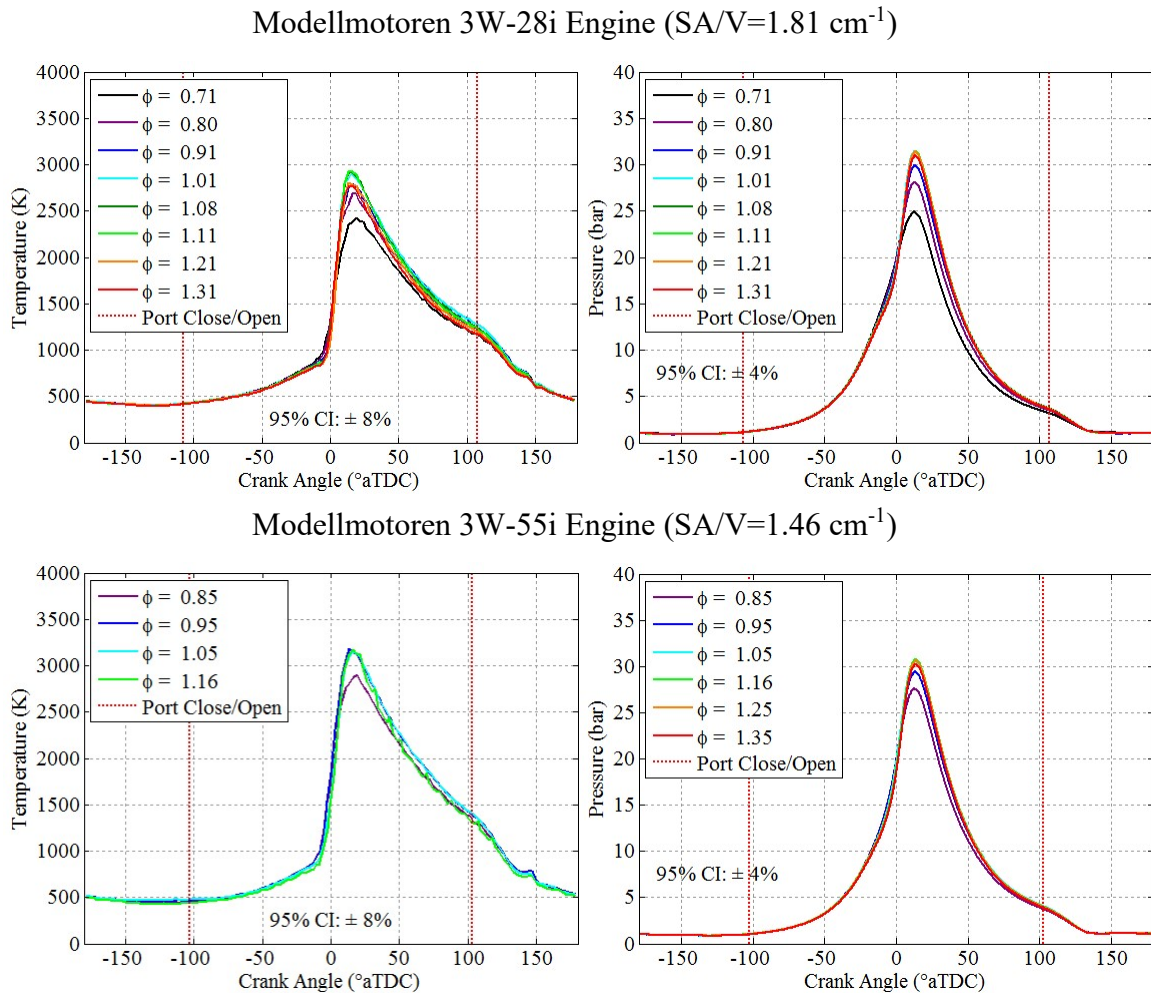


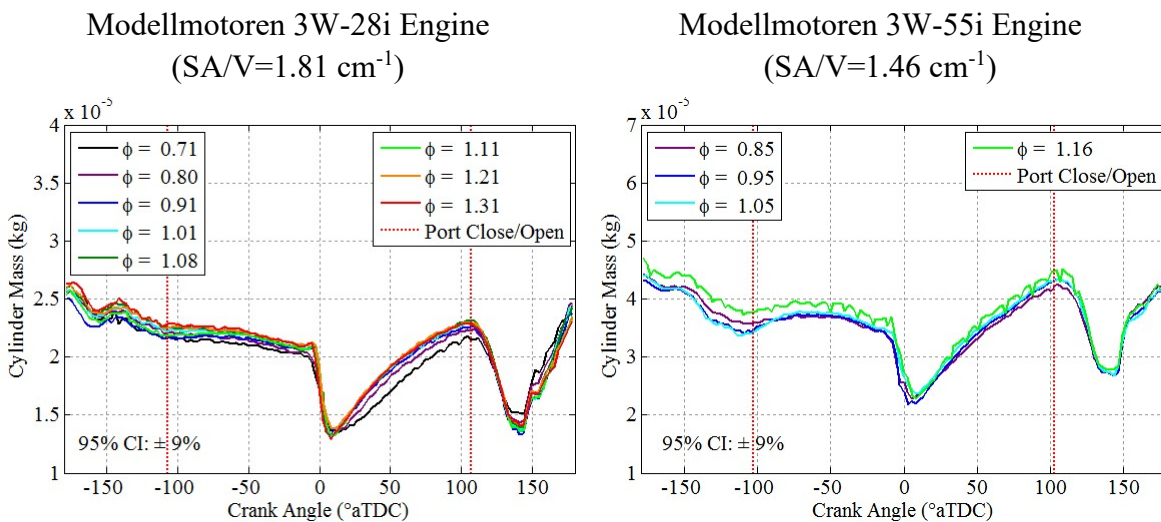
**Figure 117: Impact of equivalence ratio on in-cylinder temperature (TLAS) and pressure. The engines were operated at 6000 rpm, WOT,  $CA_{50}=8\pm0.5^{\circ}$ aTDC, &  $CHT=130\pm2^{\circ}\text{C}$ . Pressure is a 400 cycle average, temperature is a 500 ms average.**



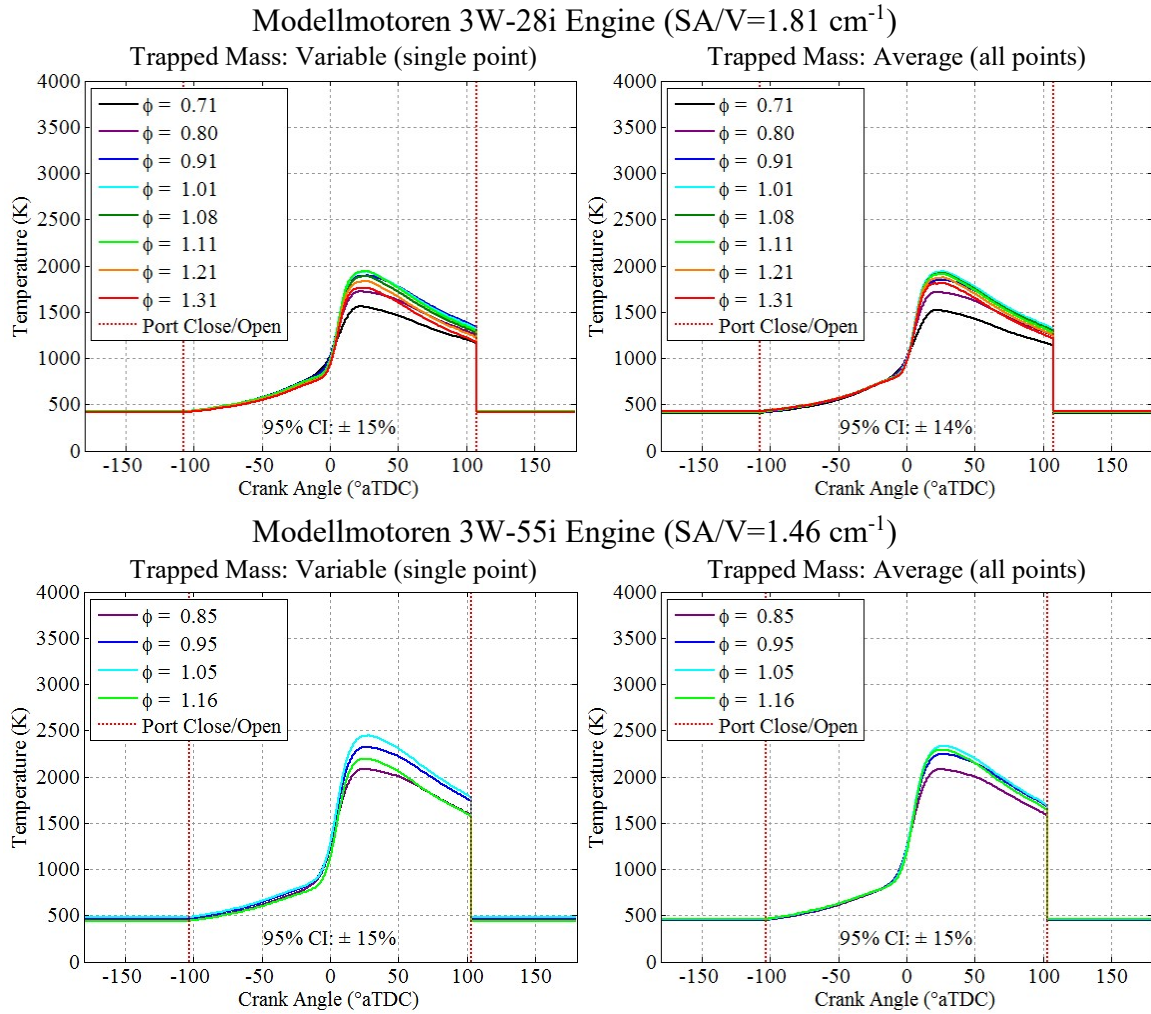
highest near an equivalence ratio of 1.05, falling as the mixture richened due to charge cooling and limited oxygen and dropping more rapidly as the mixture was leaned due to less energy available/released per unit cylinder volume.

Figure 118 shows the calculated trapped mass for the same operating conditions as in Figure 117. Compared to the speed sweep results, the initial masses at port closure were very consistent (within  $\pm 5\%$ ). This indicates that the neither the trapped mass nor the measurement of in-cylinder pressure around port closure were particularly sensitive to the equivalence ratio. Therefore, both the variable mass and average mass models in Figure 119 exhibited similar behavior, and both models captured the trend in the peak temperatures. However, as in the speed sweeps, the model peaks were lower, flatter, and fell off less rapidly than the temperature in the TLAS measurement.

A summary of the average temperatures is shown in Figure 120. A summary of the peak temperatures and pressures is shown in Figure 121. As expected based on the models



**Figure 118: Mass of cylinder contents calculated using the ideal gas law and the in-cylinder pressure and temperature for the equivalence ratio sweep. The engines were operated at 6000 rpm, WOT, CA50=8 $\pm$ 0.5 $^{\circ}$ aTDC, & CHT=130 $\pm$ 2 $^{\circ}$ C.**



**Figure 119: In-cylinder temperature calculated using the variable and average mass models for the equivalence ratio sweep. Trapped mass was calculated at exhaust port close. Gas exchange temperature was set equal to model temperature at port close.**

in Figure 119, the average and peak temperatures calculated from the models are nearly identical. Despite an offset due to the lower aggregate cylinder temperature predicted by the model relative to the temperature measured at the TLAS line-of-sight, the models' averages reproduced the trend in measured temperature nearly exactly. Therefore, the results indicate that the model in Equation (127) effectively captures variation in in-cylinder temperature with equivalence ratio. Plots showing the 95% confidence intervals



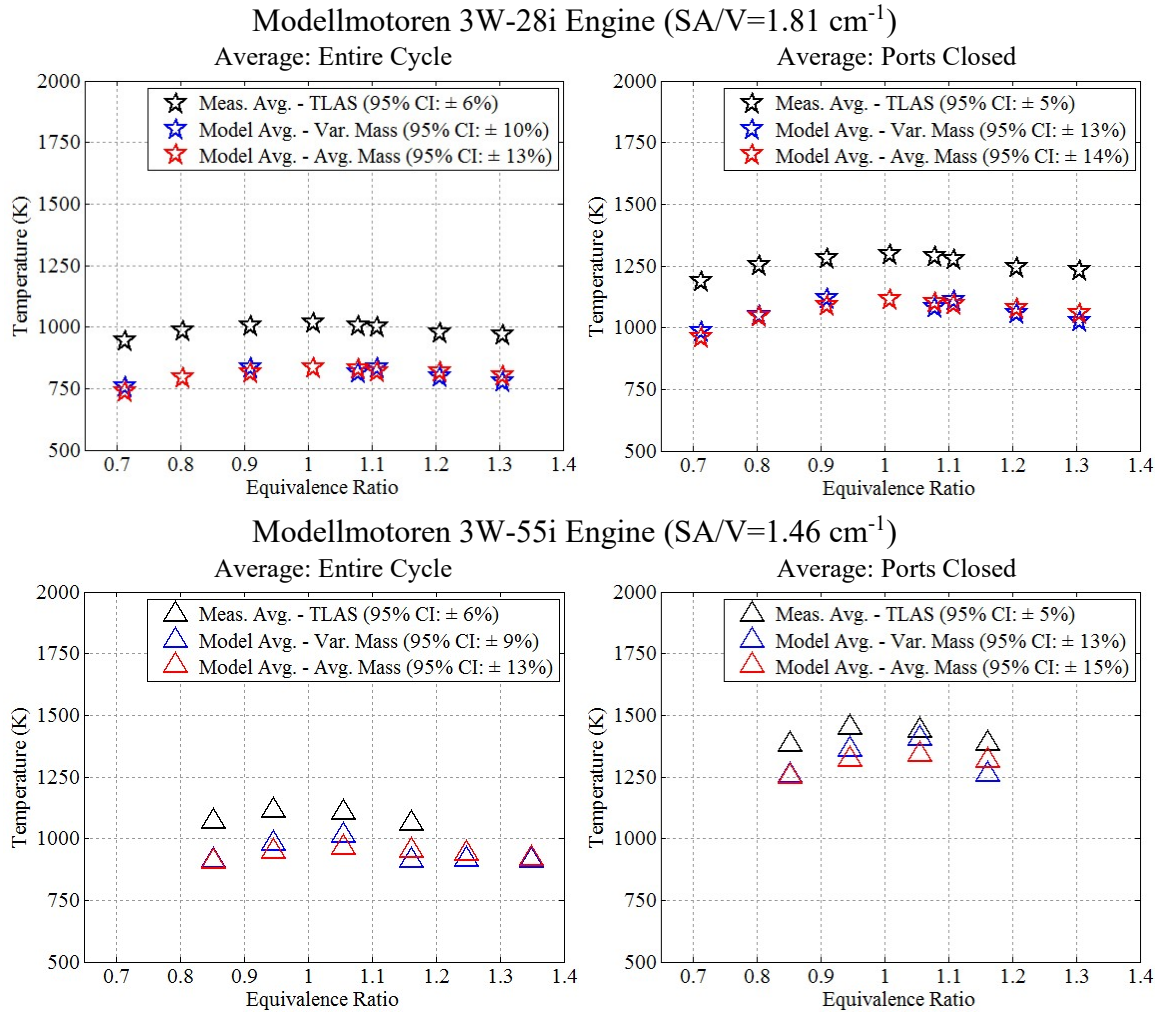


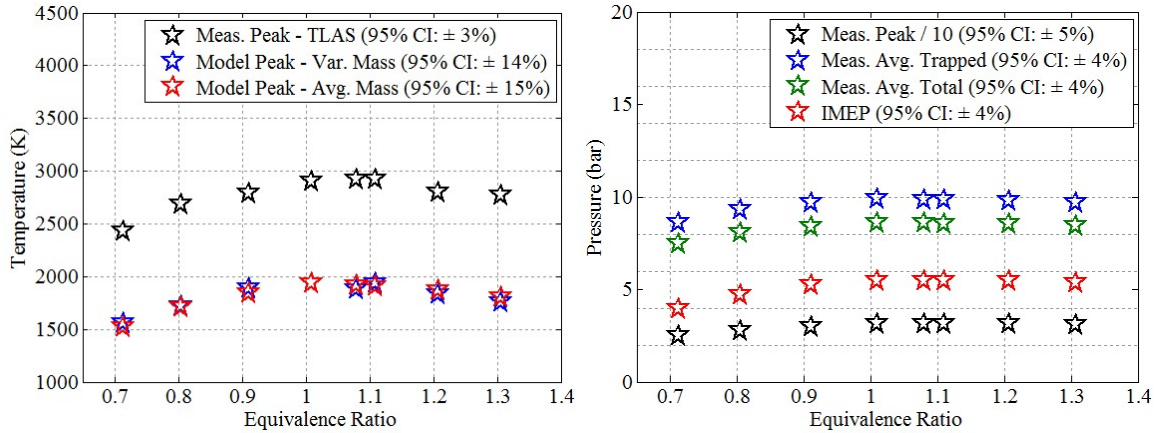
**Figure 120: Average temperature summary statistics for the equivalence ratio sweep. The engines were operated at 6000 rpm, WOT, CA50=8±0.5°aTDC, & CHT=130±2°C.**

on the measured temperatures and pressures for the equivalence ratio sweep are included in Appendix G, as Figure 177 and Figure 178.

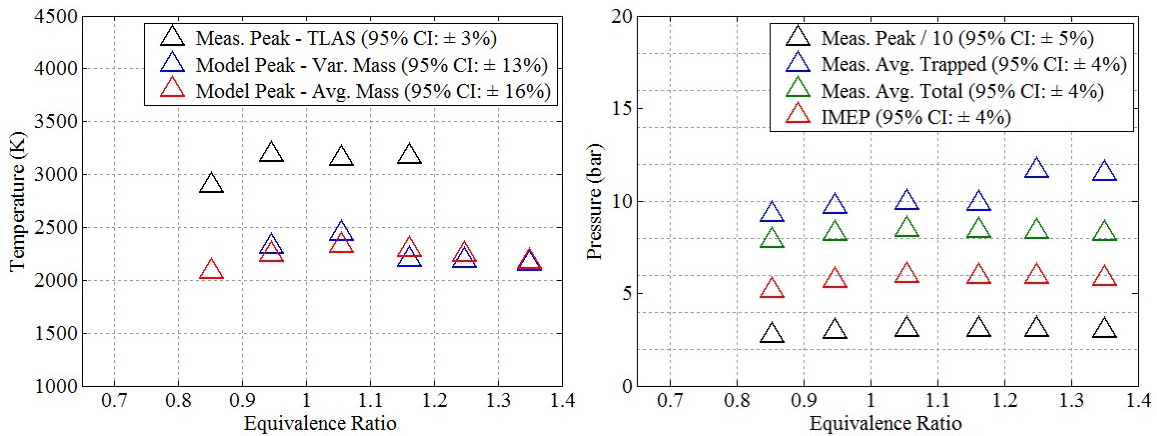
### 2.1.3. Combustion Phasing

Figure 122 shows the impact of sweeping the combustion phasing on the in-cylinder temperature and pressure measurements. As the combustion phasing was retarded, the measured temperature showed a lockstep retardation in phasing as well as a decrease in the

### Modellmotoren 3W-28i Engine (SA/V=1.81 cm<sup>-1</sup>)



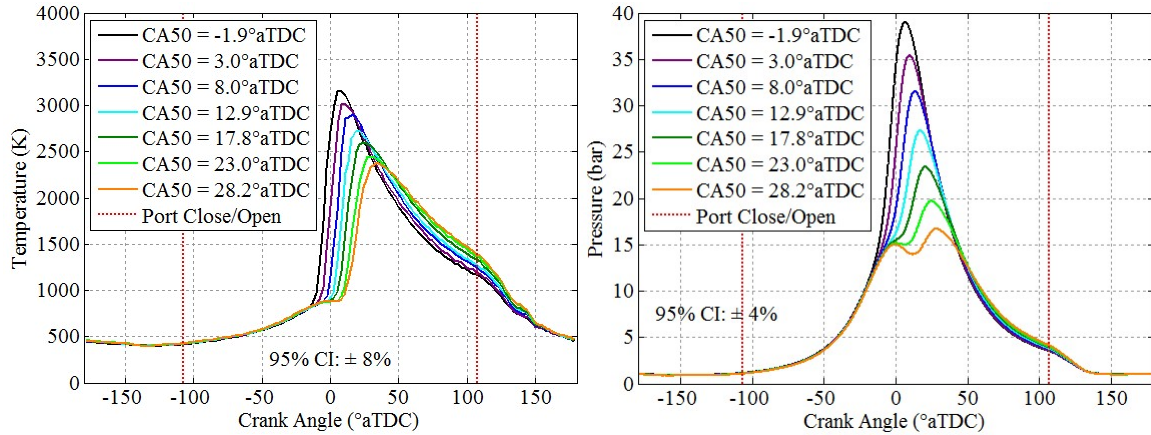
### Modellmotoren 3W-55i Engine (SA/V=1.46 cm<sup>-1</sup>)



**Figure 121: Pressure and peak temperature summary statistics for the equivalence ratio sweep. The engines were operated at 6000 rpm, WOT, CA50=8±0.5°aTDC, & CHT=130±2°C.**

peak temperature. The decrease in the peak temperature corresponded to an increase in the temperature in the latter portion of the expansion stroke (40°aTDC to port open). Since the equivalence ratio was held constant, the amount of heat released remained about the same (see the right hand side of Figure 90, page 295). However, by retarding the combustion phasing the heat was released later and later in the cycle and consequently, into a larger volume. Therefore, the peak pressure and temperatures decreased as did the driving force for heat transfer from the cylinder, and less work was extracted from the

### Modellmotoren 3W-28i Engine (SA/V=1.81 cm<sup>-1</sup>)



### Modellmotoren 3W-55i Engine (SA/V=1.46 cm<sup>-1</sup>)

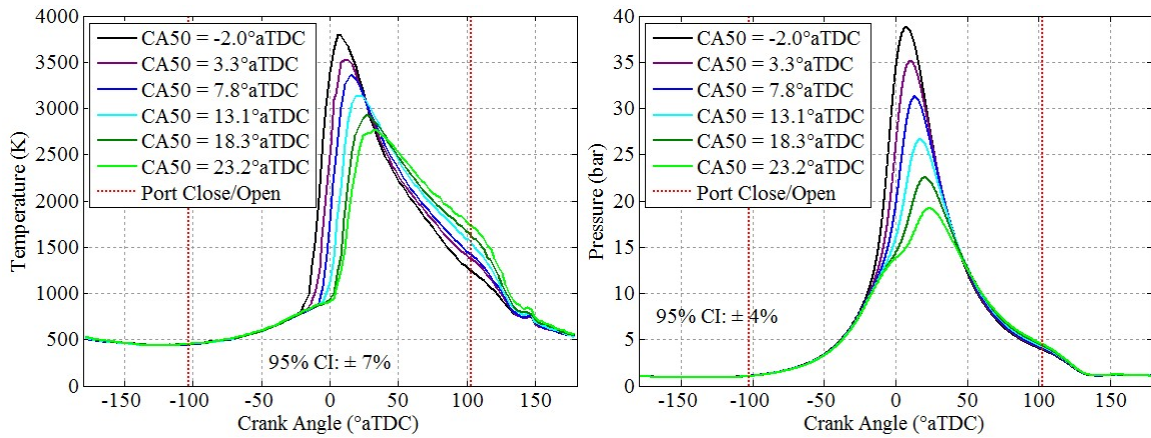


**Figure 122: Impact of combustion phasing on in-cylinder temperature (TLAS) and pressure. The engines were operated at 6000 rpm, WOT,  $\phi=1.06\pm0.02$ , & CHT=130±2°C. Pressure is a 400 cycle average, temperature is a 500 ms average.**

combustion gases, leaving more thermal energy in the cylinder later into the cycle. This shifted thermal losses from the cylinder head to the exhaust as seen in Chapter IV, Section 3.2 and increased the average temperatures later in the cycle. Thus, the temperature results confirm the explanation offered in that section.

Figure 123 shows the calculated mass. Similar to the equivalence ratio sweep, the combustion phasing sweep was conducted at a constant speed, and the pressure at port closure showed much less variation than in the speed sweep. The variation in the trapped

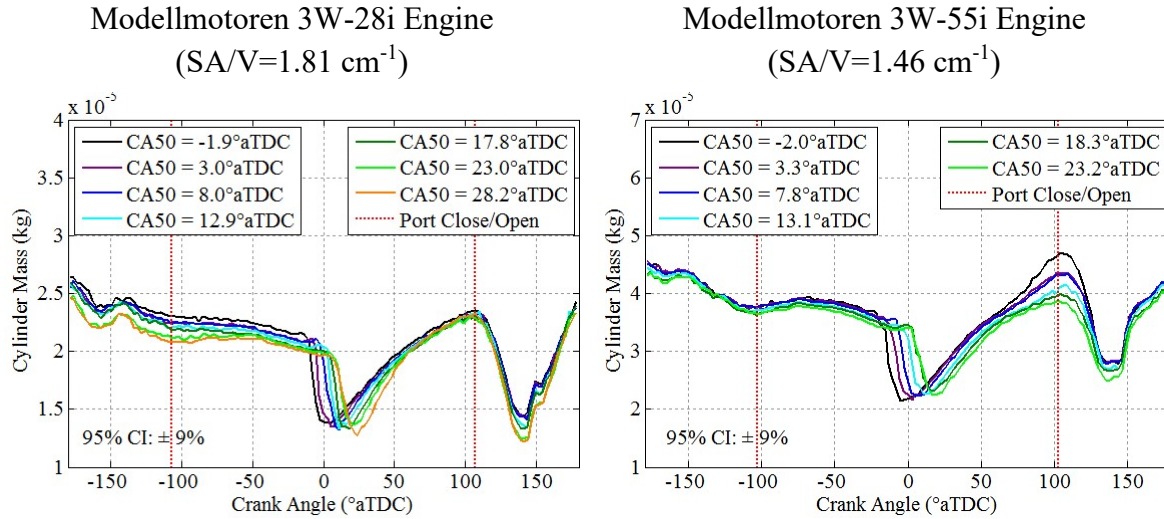


**Figure 123: Mass of cylinder contents calculated using the ideal gas law and the in-cylinder pressure and temperature for the combustion phasing sweep. The engines were operated at 6000 rpm, WOT,  $\phi=1.06\pm0.02$ , & CHT=130 $\pm$ 2°C.**

mass that did exist was traced to changes in the measured in-cylinder temperature. Since more thermal energy was available in the cylinder when the ports opened, heat transfer to the fresh charge increased with retarded combustion phasing, driving down the trapped charge density at port closure. This behavior is reflected in Figure 123, most clearly for the 3W-28i engine.

Figure 124 shows the variable mass and average mass models for the combustion phasing sweep. Generally, the models captured the aforementioned trends. The peak temperature followed combustion phasing and decreased as CA50 was retarded, except in the variable mass model for the 3W-28i engine where the two points with the latest timing show a slight increase in peak temperature. Generally, both models produced similar results. In all cases, increasingly retarded combustion phasing led to higher temperatures following the peak temperature.



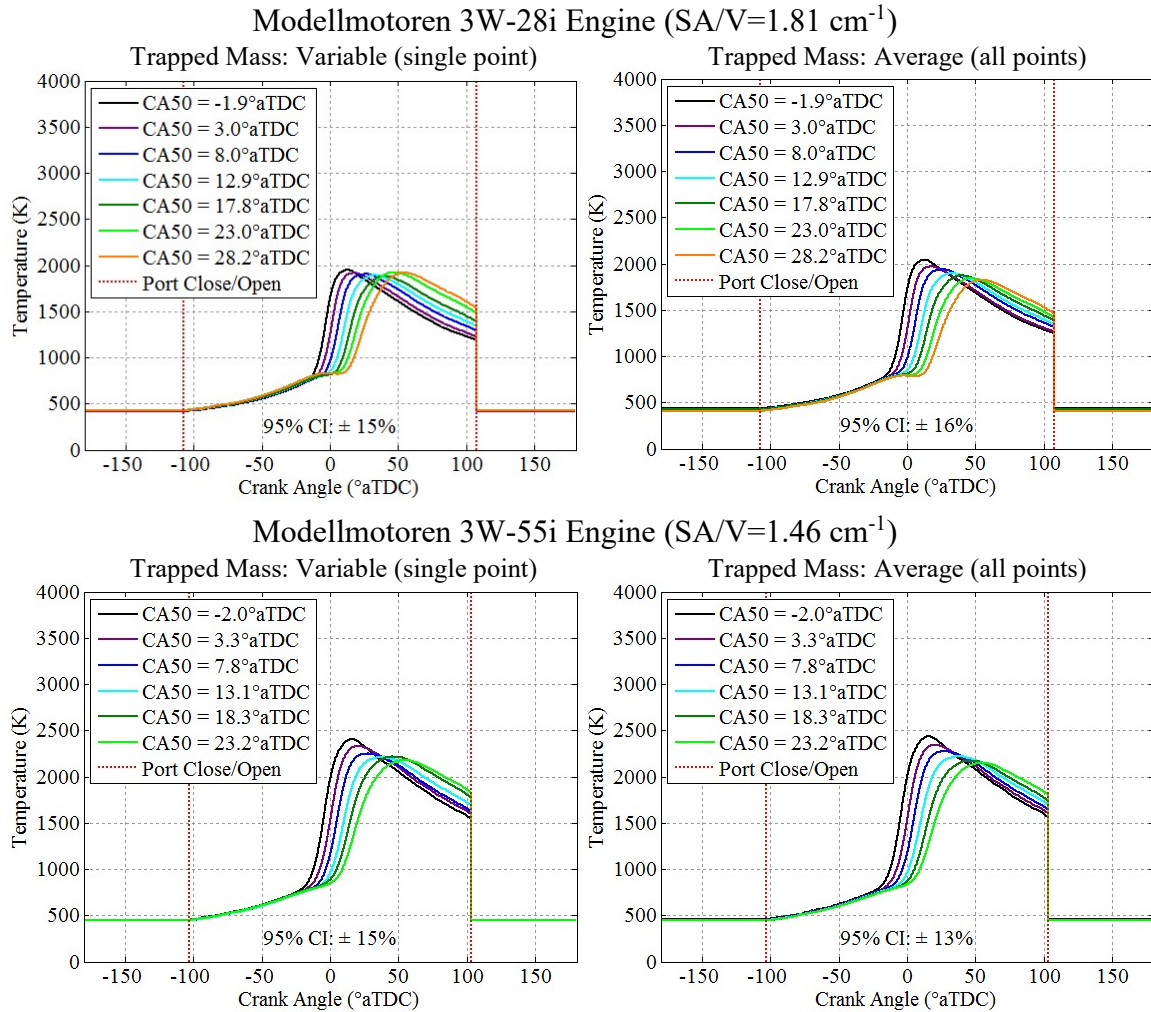


**Figure 124: In-cylinder temperature calculated using the trapped and average mass models for the combustion phasing sweep. Trapped mass was calculated at exhaust port close. Gas exchange temperature was set equal to model temperature at port close.**

The changes in the aggregate peak temperature from the models were less pronounced than those in the TLAS line-of-sight. As previously established, the peak temperature in the TLAS measurement was during the traverse of the flame front. Decreasing the pressure at which that traverse occurred directly decreased the observed temperature of that flame. The aggregate peak temperature was shifted later in the cycle by retarded combustion phasing, but the increasingly retarded phasing also corresponded to an increase in energy

retained in the cylinder (shifting of thermal loading to the exhaust and reduction in brake power). This energy partially offset the decrease in cylinder pressure during the flame's traverse of the line-of-sight. Furthermore, it was already established that the aggregate temperatures from the models were lower than those measured at the line-of-sight, causing a corresponding decrease in the relative magnitude of any change caused by the operating condition. This explains why the peak temperatures from the models were less variable across the range of combustion phasing than the peak temperatures from the measurement.

Figure 125 and Figure 126 show the summary of the peak and average temperatures and pressures. The average measured temperature decreased slightly with increasingly retarded combustion phasing. The peak temperatures also decreased with increasingly retarded combustion phasing. However, temperature later in the cycle increased as spark timing was retarded. The two phenomena offset one another leading to the relatively flat average temperature profiles. The variable mass model and average mass model yielded comparable results and because the average temperature profiles, especially for the total cycle, were relatively constant, the two models were practically interchangeable from heat transfer modelling standpoint. Except in the case of the 3W-28i engine at the most advanced and most retarded combustion phasing, the two models tracked the observed combustion phasing trends with an offset driven by aggregate cylinder temperatures lower than the temperature measured at the TLAS line-of-sight. Even for the 3W-28i engine at those points, it was difficult to discern if the difference in trends between the variable mass model and the measured temperature is significant given the stated uncertainty. Plots showing the 95% confidence intervals for the measured temperatures and pressures for the combustion phasing sweep are included in Appendix G, as Figure 179 and Figure 180.

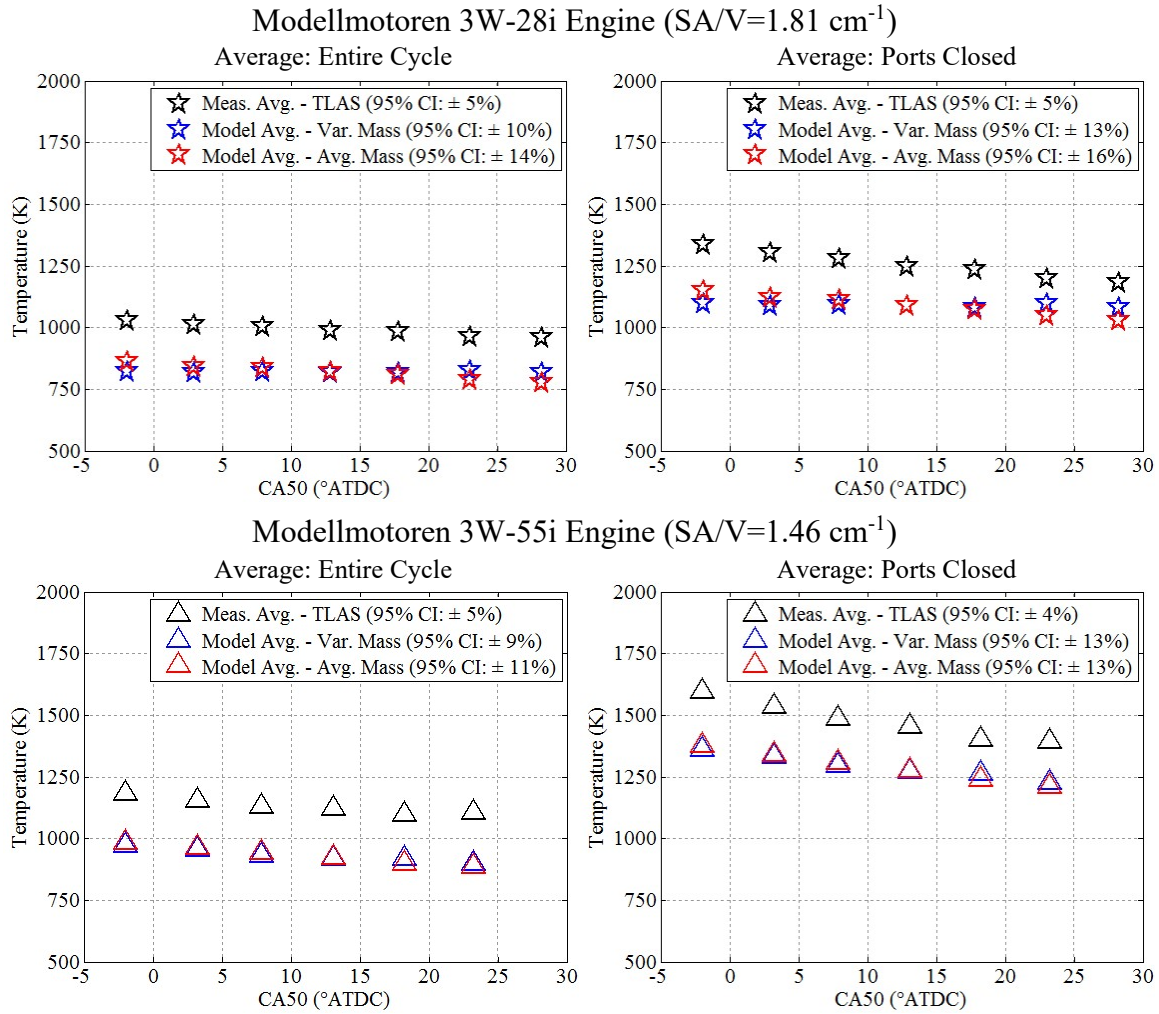


**Figure 125: Average temperature summary statistics for the combustion phasing sweep. The engines were operated at 6000 rpm, WOT,  $\phi=1.06\pm0.02$ , & CHT=130 $\pm$ 2°C.**

#### 2.1.4. Engine Cooling & Head Temperature

Figure 127 shows the impact of sweeping engine cooling on the in-cylinder temperature and pressure measurements. Due to concerns about over heating the (expensive and only) optical head for the 3W-55i engine, it was tested over a limited range of engine head temperatures (less the 150°C). Experience and testing of engines after the optical measurement on the 3W-55i engine alleviated these concerns allowing the 3W-28i engine to be tested over a wider range of temperatures (up to 180°C) and cooling flow rates.

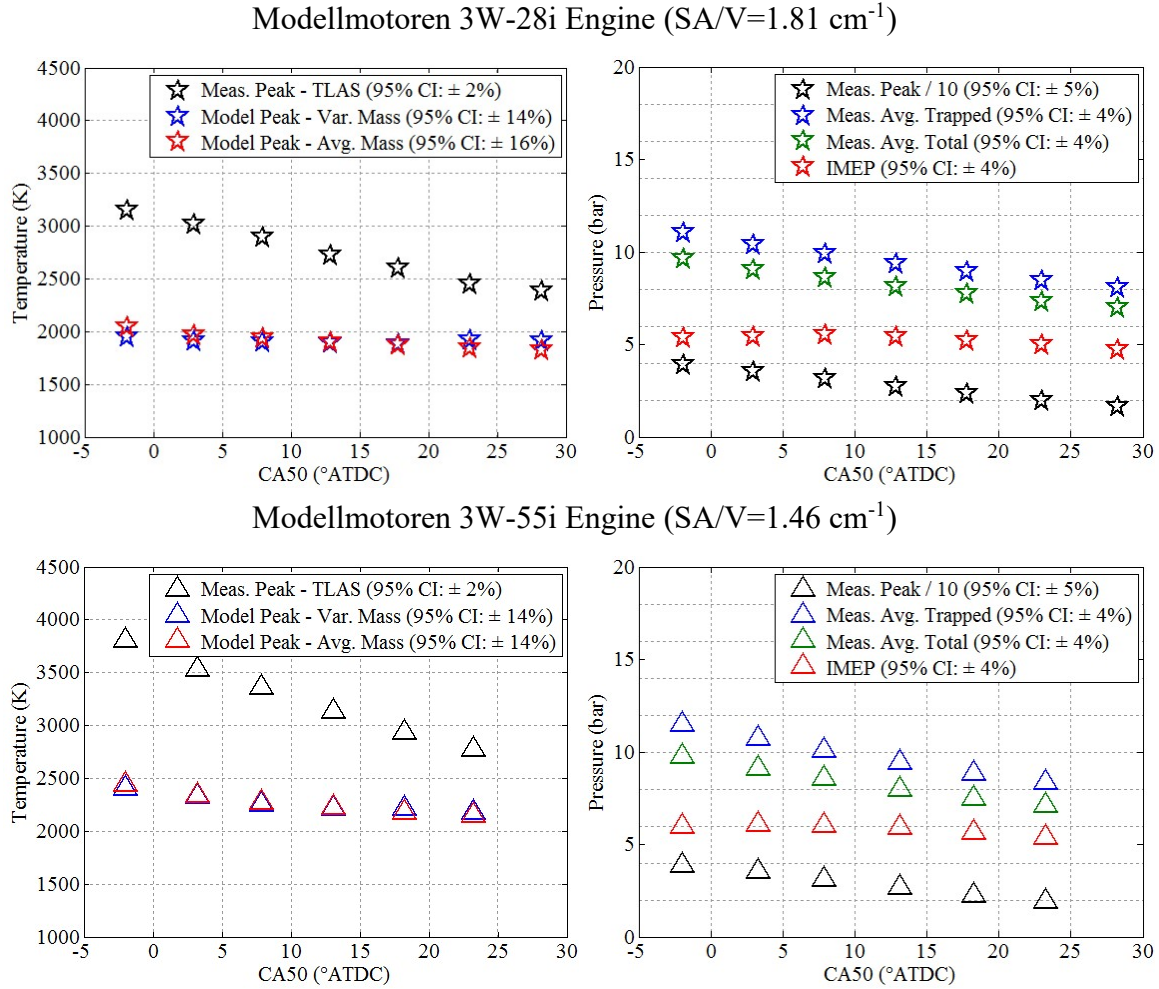
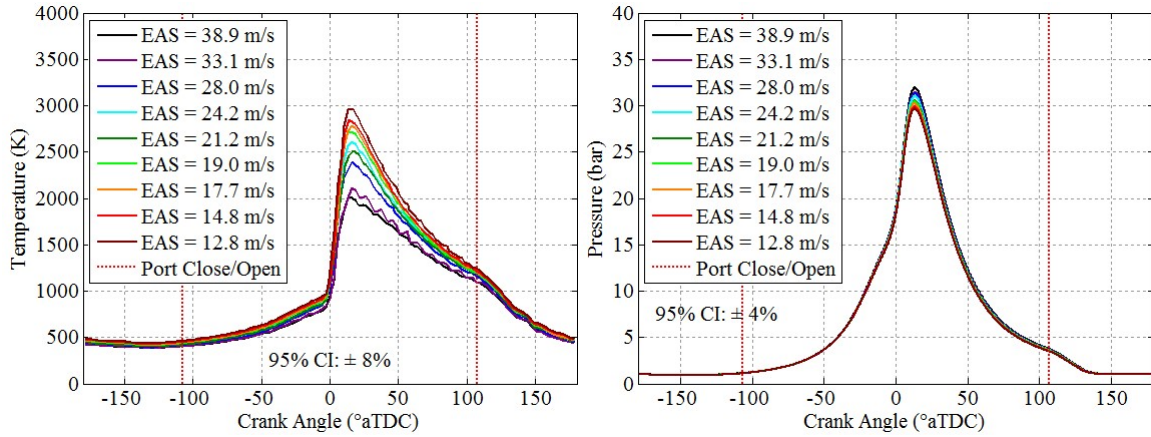


**Figure 126: Pressure and peak temperature summary statistics for the combustion phasing sweep. The engines were operated at 6000 rpm, WOT,  $\phi=1.06\pm0.02$ , &  $CHT=130\pm2^{\circ}\text{C}$ .**

Based on the discussion in Chapter IV, Section 3.3, the cooling flow rate was expected to have minimal impact on the engine performance. This observation was reflected very clearly in the pressure and temperature traces with the exception of the temperature trace on the 3W-28i engine. The temperature measurement in the 3W-28i engine was strongly influenced by the cooling flow rate (and head temperature), more so than the other engine and more so than the cylinder pressure suggests that it should have been. One possible explanation was an effect of the cooling flow rate on the measured temperature that did not



### Modellmotoren 3W-28i Engine ( $SA/V=1.81 \text{ cm}^{-1}$ )



### Modellmotoren 3W-55i Engine ( $SA/V=1.46 \text{ cm}^{-1}$ )

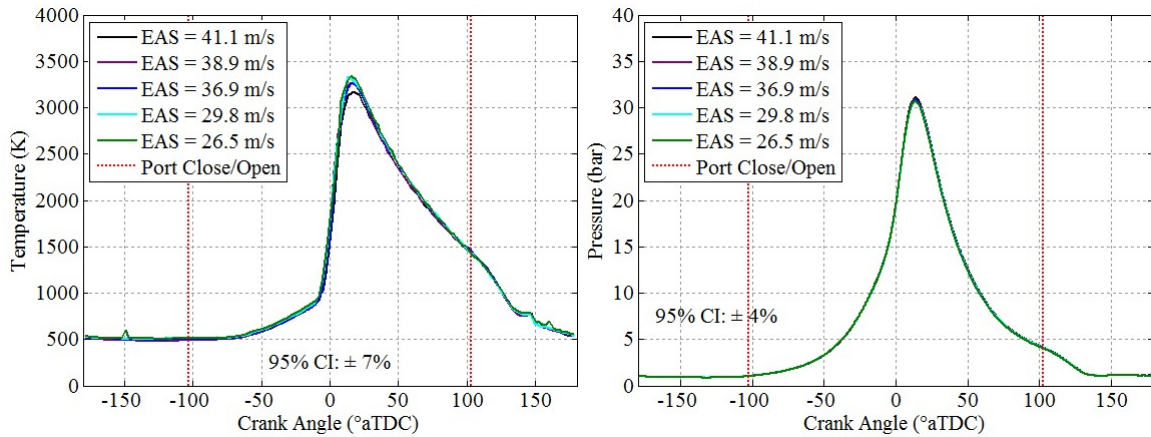


**Figure 127: Impact of engine cooling on in-cylinder temperature (TLAS) and pressure.**  
**The engines were operated at 6000 rpm, WOT,  $\phi=1.06\pm0.02$ , &  $CA_{50}=8\pm0.5^{\circ}$ aTDC.**  
**Pressure is a 400 cycle average, temperature is a 500 ms average.**

propagate proportionally to the remainder of the cylinder. As described in Chapter III, Section 4.1.1.2, the pitch collimator and the detector were both directly in the cooling air stream. While changing the cooling air flow rate did lead to some vibrational issues (loss of alignment) there was no indication that the cooling air otherwise impacted the technique itself. The optical path between the collimator and the engine as well as between the engine and the detector was covered using an optical tube and purged with dry nitrogen.

Therefore, it seems that the trend in the temperature measurement on the 3W-28i engine was real. It was established back in the discussion of the speed sweep (Section 2.1.1) that the TLAS measurement was influenced by localized cooling in the combustion dome, especially following the traverse of the flame front. It seems that this localized cooling played a significant role in the 3W-28i engine as the cooling air flow rate was adjusted.

As described in Chapter III, Section 4.1.1.2 the primary effect of varying the cooling air flow rate was an alteration of the trapped charge density at port closure. This trend can be seen clearly in Figure 128, which shows the trapped mass calculated at port closure decreasing with decreasing coolant flow rate and increasing head temperature. The large impact of localized cooling observed in the 3W-28i engine suggests that the variation in intake mass on the 3W-28i engine may be overstated based on reasoning similar to the issues observed with the in-cylinder pressure and varying the engine speed. In this case, instead of the pressure measurement being sensitive to the pegging of the in-cylinder

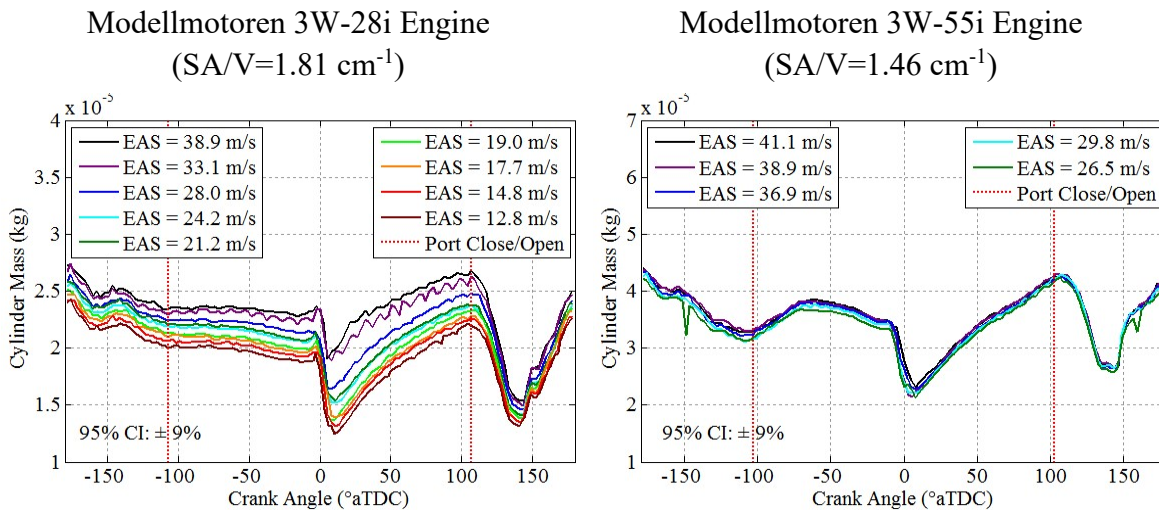


**Figure 128: Mass of cylinder contents calculated using the ideal gas law and the in-cylinder pressure and temperature for the cooling sweep. The engines were operated at 6000 rpm, WOT, CA50=8±0.5°aTDC, &  $\phi=1.06\pm0.02$ .**

pressure transducer with changing speed, the temperature measurement was sensitive to varying the cooling flow rate.

Figure 129 compares the variable mass and average mass models for the cooling air sweep. For the 3W-28i engine, the variable mass model did a better job of capturing the trend observed in the peak temperature, although with much less variation. This observation supports the previous comments on the raw temperature trace regarding the influence of localized cooling on the measured temperature. The models based on the in-

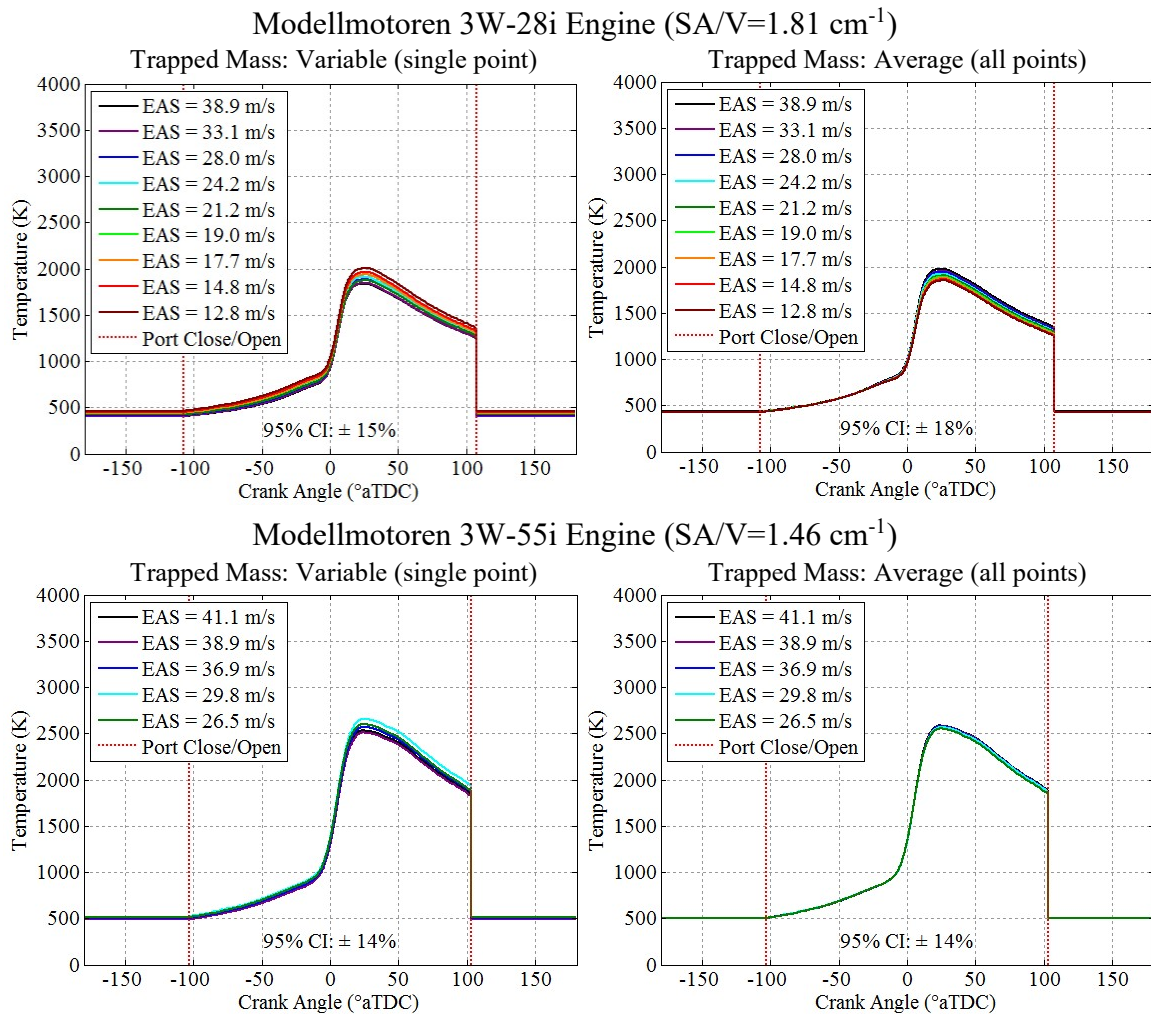


**Figure 129: In-cylinder temperature calculated using the trapped and average mass models for the cooling sweep. Trapped mass was calculated at exhaust port close. Gas exchange temperature was set equal to model temperature at port close.**

cylinder pressure suggest cooling had much less of an impact on the aggregate temperature, consistent with the observations made regarding engine cooling in Chapter IV, Section 3.3. In the 3W-55i engine the change in modelled in-cylinder temperature was less pronounced with cooling flow, suggesting that engines were less prone to localized cooling of the measurement pathway. The variable mass model more closely captured the peak temperature trend, suggesting the variation in the calculated trapped mass was real and not an artifact of the measurement technique. This observation agrees with the comments in Chapter IV, Section 3.3 regarding the increase in trapped charge density with increasing the cooling air flow rate, which was the primary driver of changes in engine performance with cooling air speed.

Figure 130 shows the average temperatures for the measurement and models and Figure 131 summarizes peak temperatures and peak and average pressures. For the 3W-28i engine, neither of the models reproduced the slope seen in the average measured temperature. This is because the models, based on pressure, did not capture the cooling driving down the temperature measured across the line-of-sight. However, since the measured temperature was more heavily influenced by localized cooling than the aggregate temperature (based on pressure), perhaps in this instance the model was definitively a better representation of the behavior in the cylinder than the measured temperature. For the 3W-55i engine the models were essentially interchangeable and matched the trends observed in the measured temperature.

There was one peculiar aspect of the 3W-55i models that has not been conclusively explained. Unlike the other sweeps, the model averages for the 3W-55i engine matched the magnitude of the average measured temperature for this sweep. If one looks carefully

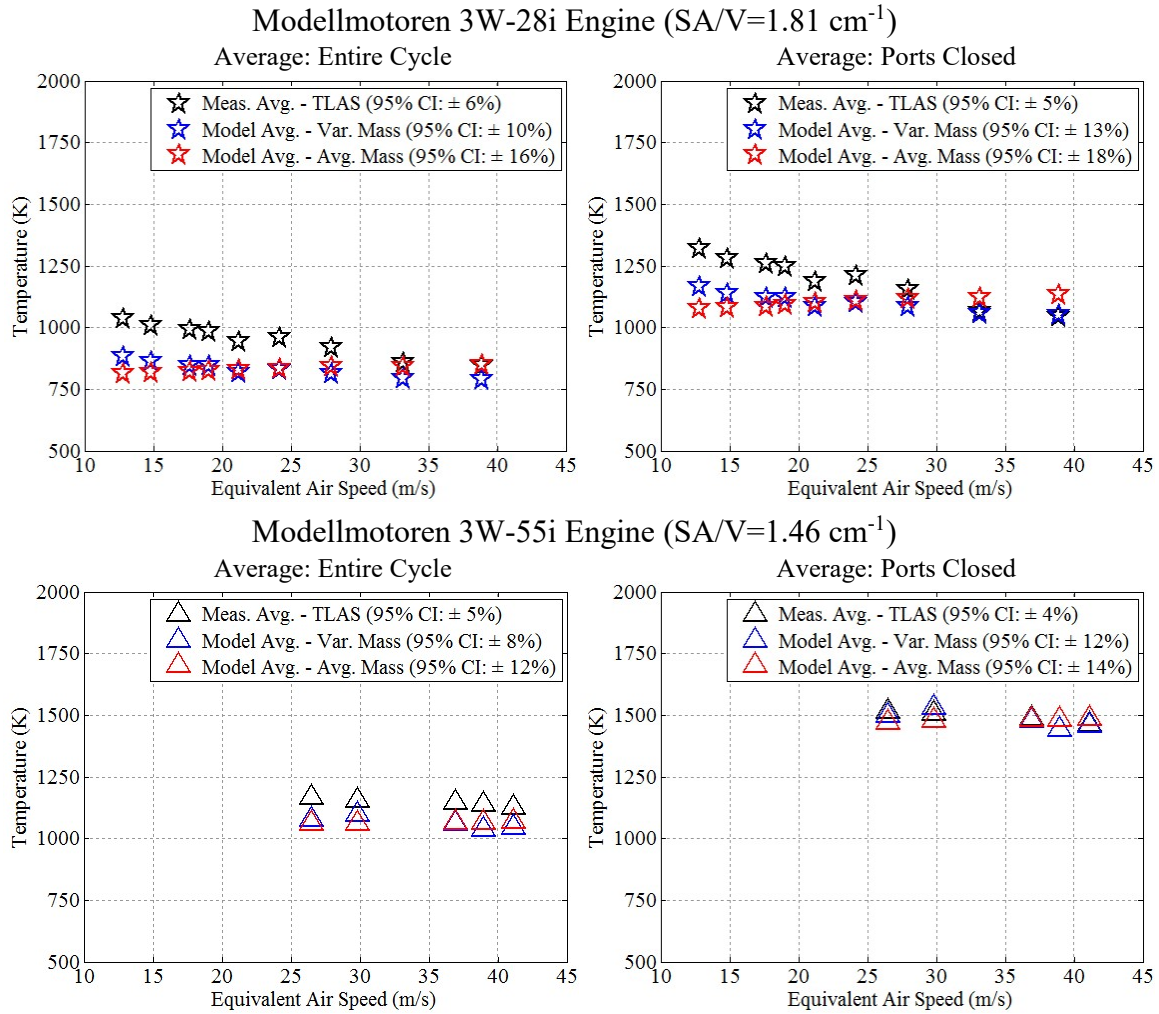


**Figure 130: Average temperature summary statistics for the cooling sweep. The engines were operated at 6000 rpm, WOT, CA50=8±0.5°aTDC, &  $\phi=1.06\pm0.02$ .**

at the modelled temperatures in Figure 129, the concavity of the modelled pressure traces on the 3W-55i engine following the peak are opposite of the concavity of the modelled temperature traces for all other engines and conditions. This slight change in concavity had a sufficient impact on the average temperature to cause the behavior observed in Figure 130. The change in concavity suggests an issue with the in-cylinder pressure measurement; a review of the test logs indicated no issues with the in-cylinder pressure transducer before, during, or after the test in question. Plots showing the 95% confidence



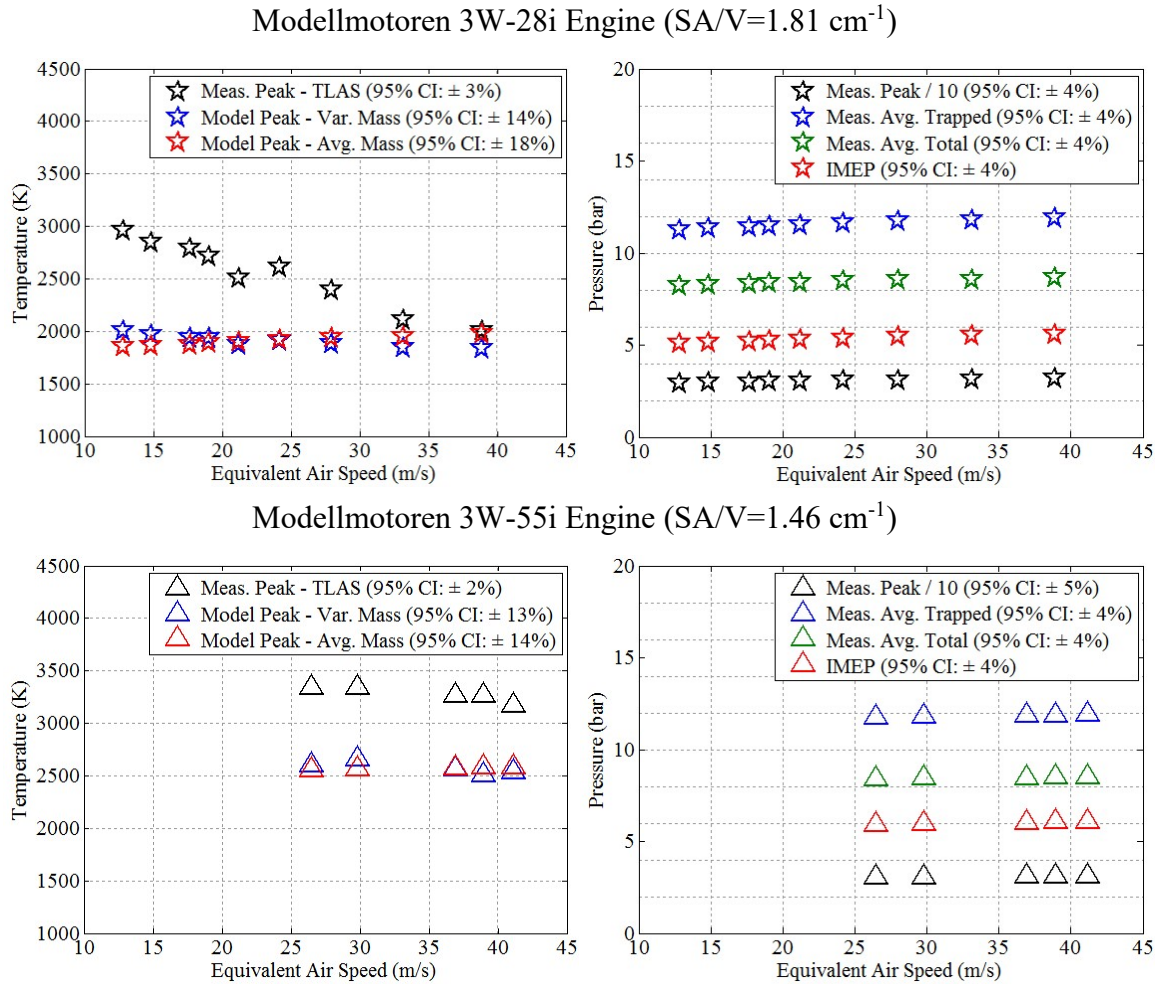


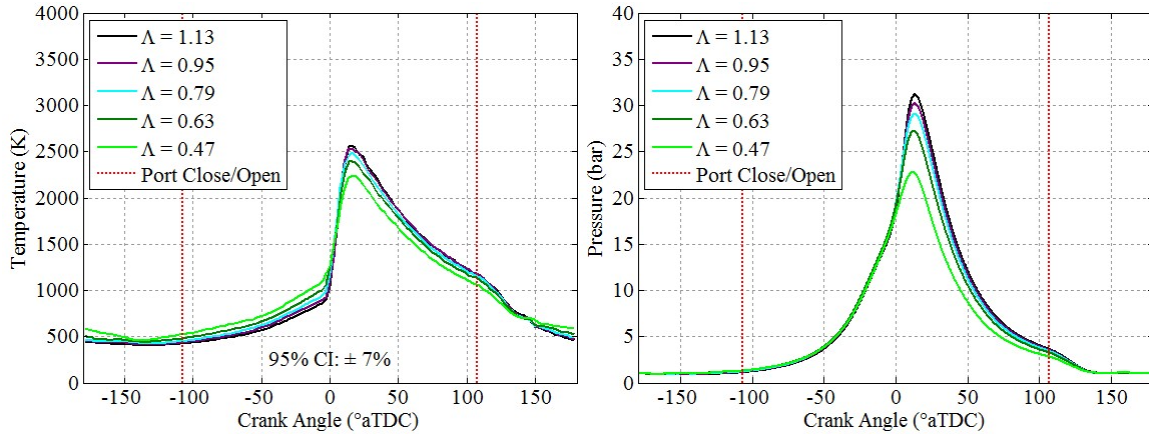
**Figure 131: Pressure and peak temperature summary statistics for the cooling sweep. The engines were operated at 6000 rpm, WOT,  $CA_{50}=8\pm0.5^\circ$  aTDC, &  $\phi=1.06\pm0.02$ .**

intervals for the measured temperatures and pressures for the cooling sweep are included in Appendix G, as Figure 181 and Figure 182.

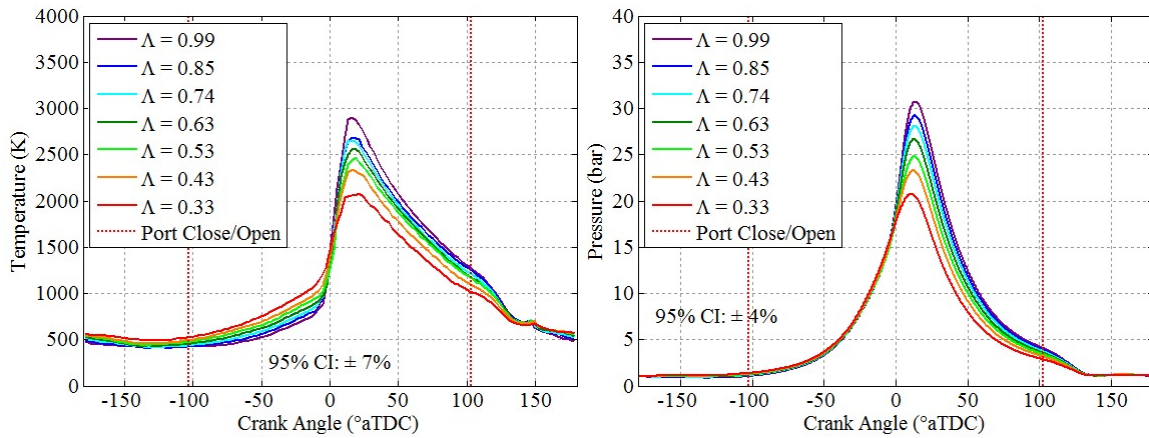
### 2.1.5. Throttle

Figure 132 shows the in-cylinder pressure and temperature measurements for the throttle sweep. Throttling the engines reduced the amount of fuel available for combustion, explaining the decrease in the peak temperature and pressure with decreasing delivery ratio. Throttling also increased the ratio of residuals to fresh charged in the cylinder. The impact

### Modellmotoren 3W-28i Engine ( $SA/V=1.81 \text{ cm}^{-1}$ )



### Modellmotoren 3W-55i Engine ( $SA/V=1.46 \text{ cm}^{-1}$ )



**Figure 132: Impact of throttle (normalized as delivery ratio) on in-cylinder temperature (TLAS) and pressure. The engines were operated at 6000 rpm,  $\phi=1.06\pm0.02$ ,  $CA_{50}=8\pm0.5^\circ\text{aTDC}$ , &  $CHT=130\pm2^\circ\text{C}$ .**

of the shift is apparent looking at the temperature during gas exchange. During gas exchange, the temperature order of the sweeps reversed, with the lowest throttle points corresponding to the highest temperatures during gas exchange due to reduced delivery ratio and reduced cooling of the cylinder contents with fresh charge.

Figure 133 shows the calculated mass profile based on the in-cylinder temperature and pressure. The calculated trapped mass was relatively constant at port closing, followed by a drop that increased with decreasing throttle. The drop was the result of increased

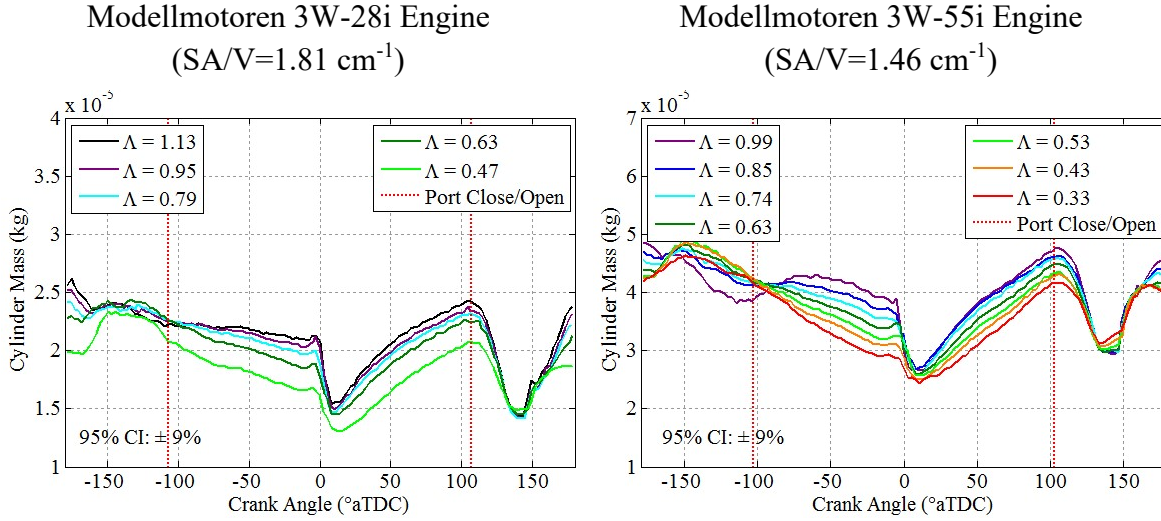


**Figure 133: Mass of cylinder contents calculated using the ideal gas law, in-cylinder pressure and temperature for the throttle sweep. The engines were operated at 6000 rpm,  $\phi=1.06\pm0.02$ , CA50=8±0.5°aTDC, & CHT=130±2°C.**

temperatures between port closure and combustion as seen in the traces in Figure 132. There are two possible explanations: heat transfer from the residual gasses to the fresh charge and heat transfer from the cylinder walls back to the trapped charge. Realistically, there was probably a combination of the two phenomenon, especially for lower throttle settings. This means that, like in the speed sweep, identifying an appropriate trapped mass was a nebulous problem. The trapped mass would be expected to change with throttle. However, decreasing the throttle negatively impacted mixing in the cylinder potentially creating inhomogeneity sufficiently significant to cause the TLAS temperature at port closure to not be representative of the cylinder contents as a whole. Calculating the trapped mass later in the cycle risks the influence of uneven heat transfer to the trapped gases.

Therefore, as in the speed sweep, the variable mass model and the average mass model were used bound the problem. Those models are shown in Figure 134. Since the trapped mass when the ports closed was relatively constant, the two models provided comparable,



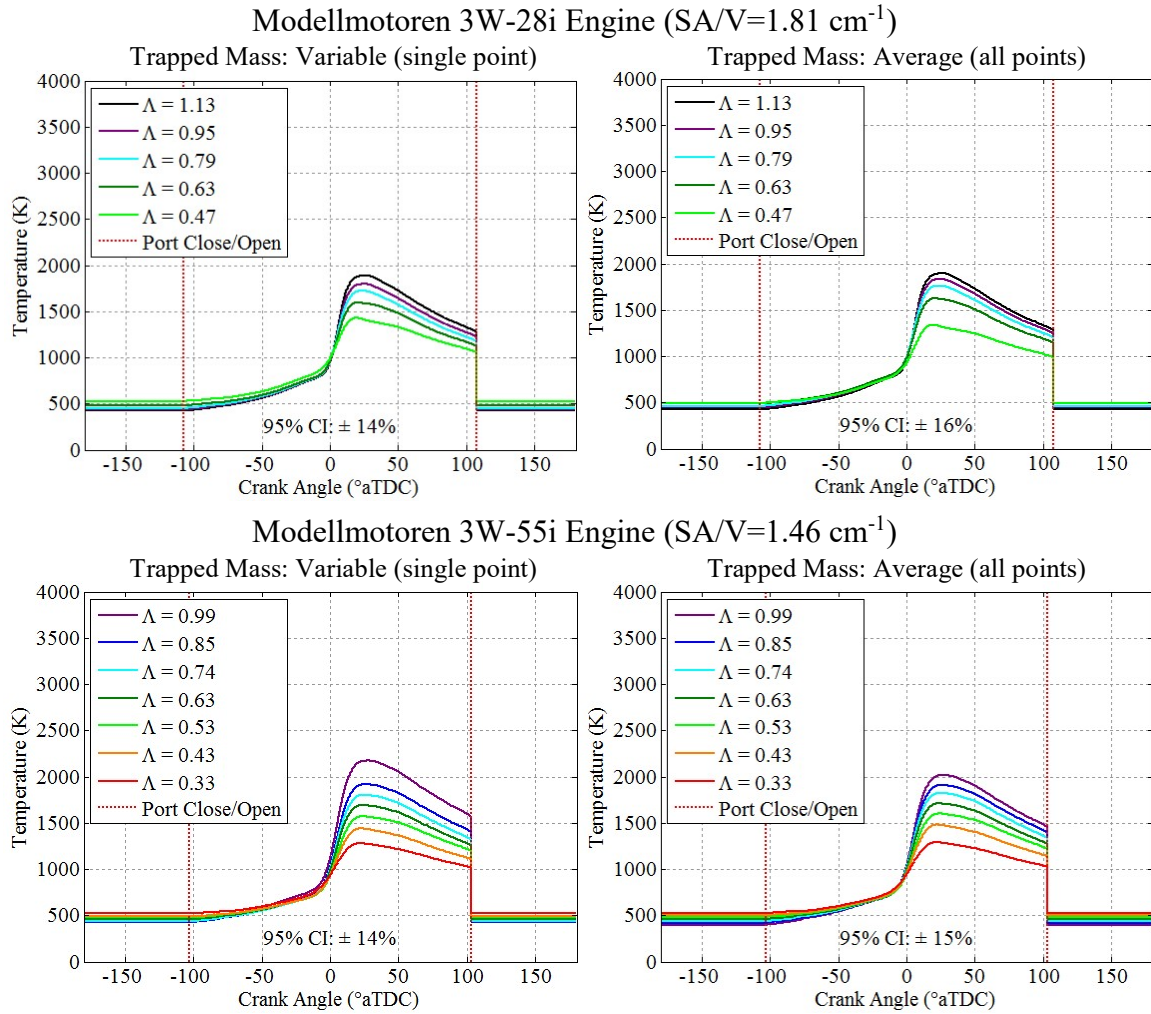


**Figure 134: In-cylinder temperature calculated using the trapped and average mass models for the throttle sweep. Trapped mass was calculated at exhaust port close. Gas exchange temperature was set equal to model temperature at port close.**

essentially interchangeable, results, reproducing the peak temperature trends observed in the measured traces. Unfortunately, neither of the models provides a solution for inhomogeneity in the trapped charge, which became worse with decreasing throttle. One possible solution for a future effort would be a second (and maybe even third) line-of-sight lower in the cylinder to quantify the temperature distribution within the trapped gas, specifically between port closure and combustion.

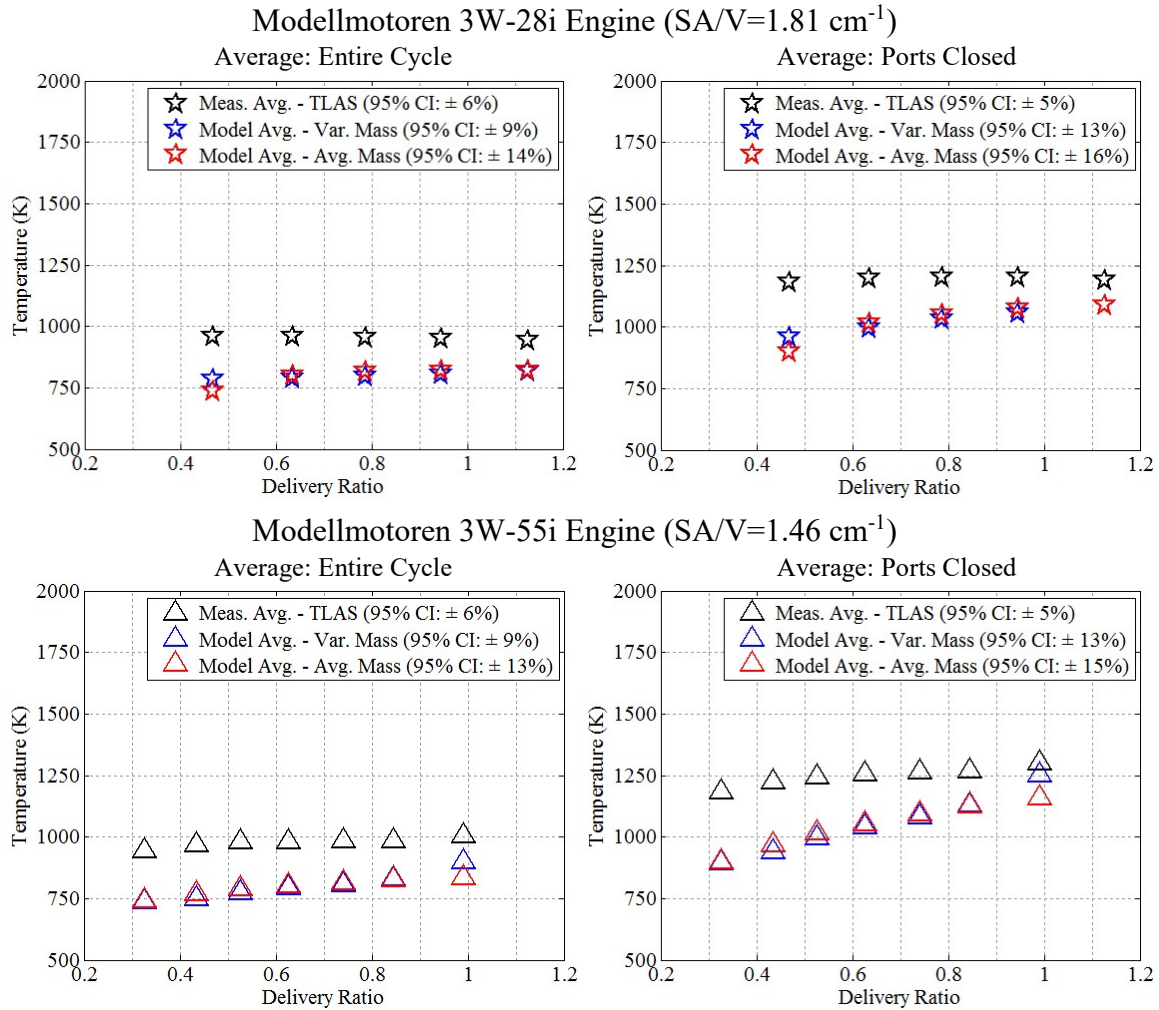


**Figure 135: Average temperature summary statistics for the throttle sweep. The engines were operated at 6000 rpm,  $\phi=1.06\pm0.02$ , CA50=8 $\pm$ 0.5 $^\circ$ aTDC, & CHT=130 $\pm$ 2 $^\circ$ C.**

Figure 135 shows the average temperature summary and Figure 136 shows the summary for the peak temperatures as well as the peak and average pressure. The two models were practically interchangeable. It is difficult to determine how well the models captured the trends observed in the average measured temperature. While performance on the 3W-55i engine was reasonable, capturing the trend in average temperature (especially for the total cycle) even with the offset expected from comparing a cylinder average to a

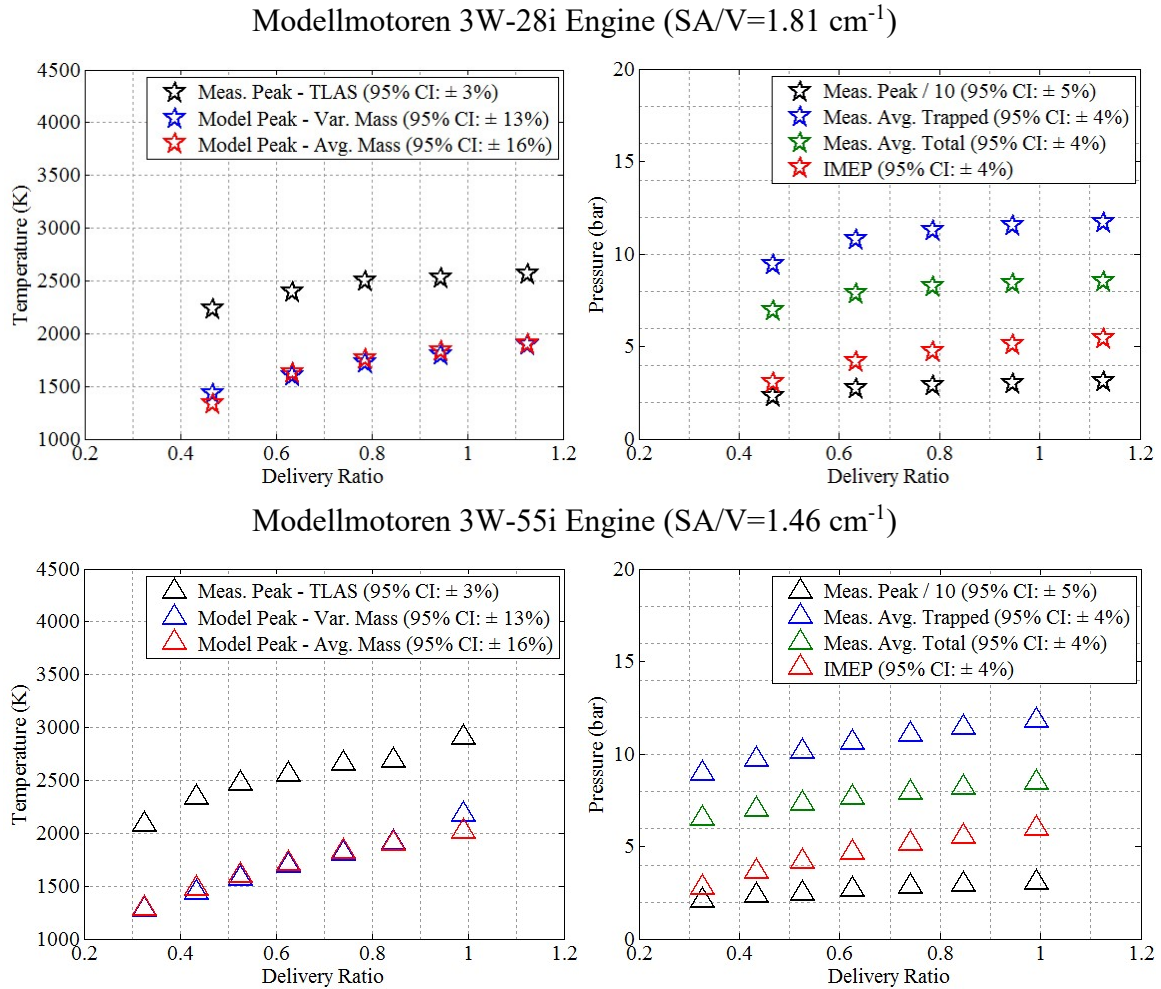


**Figure 136: Pressure and peak temperature summary statistics for the throttle sweep. The engines were operated at 6000 rpm,  $\phi=1.06\pm0.02$ ,  $CA_{50}=8\pm0.5^\circ\text{aTDC}$ , &  $CHT=130\pm2^\circ\text{C}$ .**

line-of-sight, the performance on the 3W-28i engine was unclear. The average temperature measured in the 3W-28i engine was relatively constant. Visually, the slight trends in the measured average and modelled average appear opposed, but the changes are sufficiently small that they may not be significant. Plots showing the 95% confidence intervals for the measured temperatures and pressures for the throttle sweep are included in Appendix G, as Figure 183 and Figure 184.

### 2.1.6. In-Cylinder Temperature Summary

As mentioned in the introduction of this section, many literature models use the temperature as estimated from the ideal gas law in lieu of a measured temperature. The primary benefit to doing so is that the model can then be applied to an engine without instrumenting it to measure in-cylinder temperature, using in-cylinder pressure instead. In-cylinder pressure is easier to measure than temperature since the measurement may be accomplished using a COTS measuring spark plug. In such cases, the trapped mass would be estimated based on an estimated temperature and the measured cylinder pressure and volume at port closure. This section evaluated how modelling in-cylinder temperature compared to a line-of-sight temperature measurement through the combustion dome. The results of that comparison are summarized in Table 25.

The biggest challenge was obtaining an estimate of the trapped mass in the cylinder. Pressure near port closing was shown to be highly sensitive to engine speed due to the methodology used to peg the in-cylinder pressure transducer. Using a variable mass overestimated the change in trapped mass with operating condition, especially during the speed sweep, due to variability in the pressure near port closure due to variations in pressure not caused by changes in trapped mass such as pegging the pressure transducer. Temperature near port closure was sensitive to mixing and heat transfer in the cylinder during gas exchange and in turn to changes in the throttle. Using an average trapped mass (similar to estimating a mass as is typically done in the literature) more consistently captured the trends observed in peak measured temperature at the expense of not capturing changes in trapping with operating condition.

**Table 25: Comparison of In-Cylinder Temperature Modelling Results to TLAS Measurement in the Combustion Dome**

Sweep	Criteria	Variable Trapped Mass	Average Trapped Mass
Speed	Captured peak trend?	No	Yes
	Capture total cycle average trend?	Yes, but steeper slope.	No
	Known issues?	Highly sensitive to pressure at port closure, measurement of pressure sensitive speed.	Assumes that trapped mass does not change with engine speed.
Equivalence Ratio	Captured peak trend?	Yes	Yes
	Capture total cycle average trend?	Yes	Yes
	Known issues?	No	No
Combustion Phasing	Captured peak trend?	Some, much shallower slope.	Some, much shallower slope.
	Capture total cycle average trend?	Mostly, hard to tell for 3W-28i engine.	Yes
	Known issues?	Measurement more strongly influenced by combustion phasing than the aggregate temperature due to measuring the flame front at varied pressure.	Measurement more strongly influenced by combustion phasing than the aggregate temperature due to measuring the flame front at varied pressure.
Engine Head Temperature & Cooling	Captured peak trend?	Yes, except 3W-28i engine.	Yes, except 3W-28i engine.
	Capture total cycle average trend?	Yes, slope steeper than measured temperature for 3W-28i engine.	Yes, except for 3W-28i engine.
	Known issues?	Measured temperature during and after combustion heavily influenced by localized cooling in 3W-28i engine.	Measured temperature during and after combustion heavily influenced by localized cooling in 3W-28i engine.
Throttle	Captured peak trend?	Yes	Yes
	Capture total cycle average trend?	Mostly, hard to tell for 3W-28i engine.	Yes
	Known issues?	Trapped mass calculation may have been influenced by poor mixing in the cylinder during low throttle gas exchange.	Trapped mass calculation may have been influenced by poor mixing in the cylinder during low throttle gas exchange.

Total cycle averages, which are the most appropriate for a temporally averaged correlation showed reasonable agreement in the trends between the measured and modelled temperatures. Typically, model averages were approximately 250 K cooler than measured temperatures since the line-of-sight was influenced by the traverse of the flame front whereas the model calculated an aggregate temperature of the cylinder contents. The flame reached the TLAS line-of-sight early in the measurement near CA10 explaining why the measured temperature peaked prior to the cylinder average. The TLAS measurement was also subjected to localized cooling after the flame front passed the line-of-sight. The impact of the two different temperature models (average mass and variable mass) and the TLAS measurement on the heat transfer model will be examined in the next section.

## **2.2. Heat Transfer Modelling Results**

As mentioned in the introduction to Section 2.2, collecting and analyzing the in-cylinder temperature measurements redirected the focus of the heat transfer modelling portion of Objective 2. This section presents a first attempt at modelling heat transfer by examining the validity of Taylor and Toong's model, originally developed for automotive and larger scale engines, for small, two-stroke, SI engines. Due to scheduling constraints with the TLAS system, data for the 3W-85Xi engine was not available until after the writing of this document, leaving no opportunity for an analysis of scaling influences. Furthermore, as will be seen in this section, the Taylor and Toong model was a poor predictor of heat transfer for the tested engines. Therefore, there remains a significant opportunity for future efforts to use the data collected herein to develop a more functional model for overall heat transfer.

The Taylor and Toong model [138] proposes that the Nusselt number may be calculated from the Reynolds number using a form similar to that for flow over a flat plate. The model is reproduced in Equations (128) to (131) for reference. Figure 137 shows the Nusselt and Reynolds numbers calculated using the characteristic quantities proposed by Taylor and Toong [138] as well as Annand [17]. Gas properties were approximated as nitrogen at the in-cylinder gas temperature [17]. Plots are shown for the modelled temperature profiles calculated using the average and variable masses discussed in the previous section as well as the temperature profile measured using TLAS. As observed during that discussion, the average temperatures computed from the ideal gas model tended to be approximately 250 K lower than temperatures measured using TLAS. Thus, the Nusselt numbers calculated using the measured temperature were smaller than those from the modelled temperature.

$$Nu = C_1 Re^{C_2} = \frac{h_o B}{k_g} \quad (128)$$

$$h_o = \frac{\dot{Q}_{cyl,loss}}{A_p(T_{g,cyl} - T_c)} \quad (129)$$

$$Nu = \frac{QB}{k_g A_p(T_{g,cyl} - T_c)} \quad (130)$$

$$Re = \frac{\dot{m}_g B}{\mu_g A_p} \quad (131)$$

With the exception of throttle, the scatter of points from the variable mass model was comparable to the scatter observed from the measured temperature. The average mass model's total neglect of variation in the trapped mass with operating condition shifted the scatter of the speed points, although in the other sweeps the average mass model behaved similar to the variable mass model and measured temperature. From a modelling standpoint, if the impact of operating condition on the trapped mass were known or could

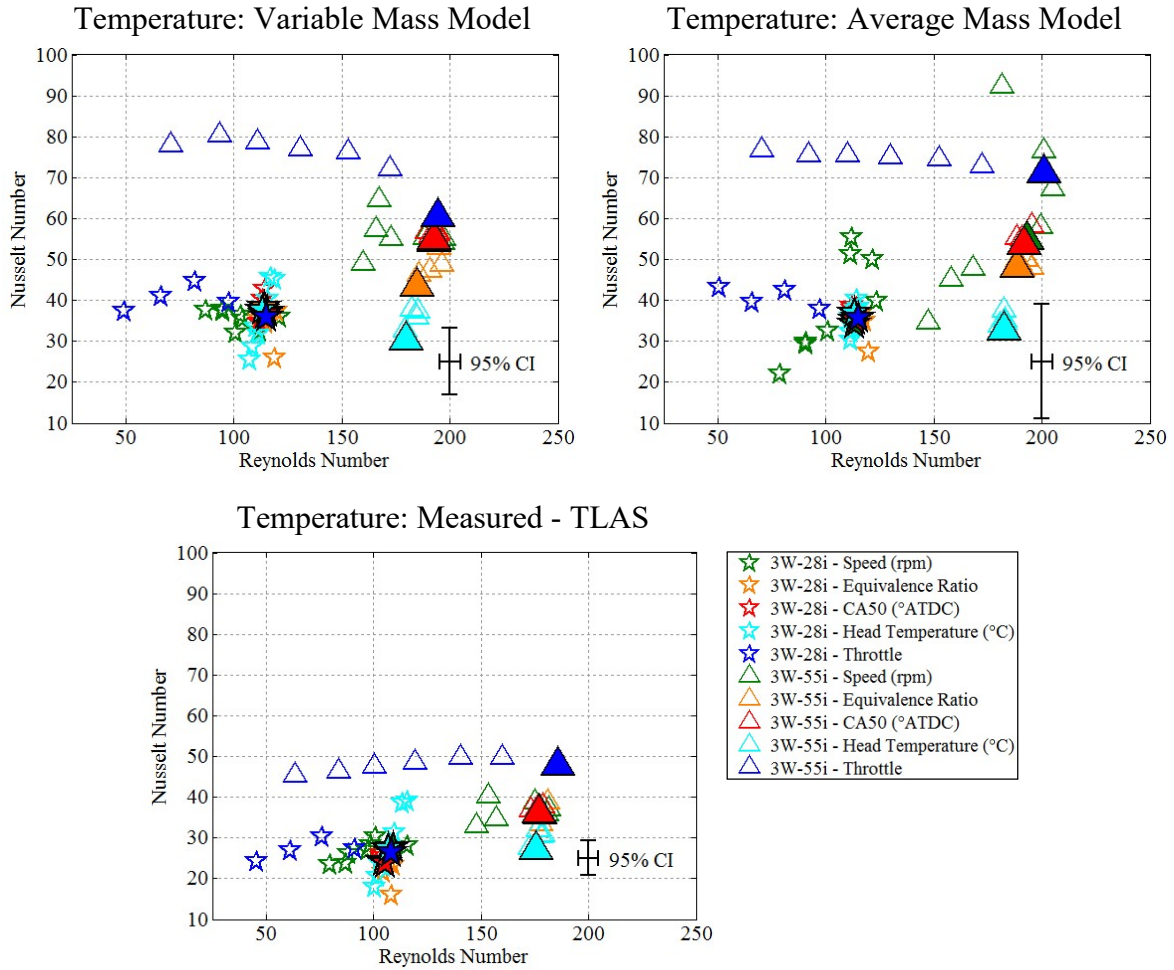


**Figure 137: Nusselt and Reynolds numbers calculated for the Taylor and Toong model. Large, filled points represent the baseline condition of 6000 rpm, WOT,  $\phi=1.06\pm0.02$ , CA50=8 $\pm$ 0.5°ATDC, & CHT=130 $\pm$ 2°C.**

be estimated, then the data suggests that using a variable mass estimate would be preferable to using a single fixed mass. Variation in the plots was driven by two sources: scatter in the baseline condition and variation due to intentional manipulation of the engine controls as part of each sweep. The sources will be discussed in that order. Each sweep began at the baseline operating condition and the symbols for those points are enlarged and filled in Figure 137 (and subsequent figures). Despite attempting to repeat the same condition, there was substantial variation between the baseline conditions, particularly in the Nusselt



number on the 3W-55i engine. Plots of the characteristic values used to calculate the Nusselt and Reynolds numbers were created to identify the source(s) of the variation.

Figure 138 shows the intake mass flow rate, average coolant temperature, and cooling load for the conditions plotted in Figure 137 with the symbols for the baseline conditions enlarged and filled. For the baseline conditions, intake mass flow rate was essentially constant for each engine. Even within the sweeps only the throttle and speed sweeps showed any appreciable variation in the intake mass flow rate, consistent with the results

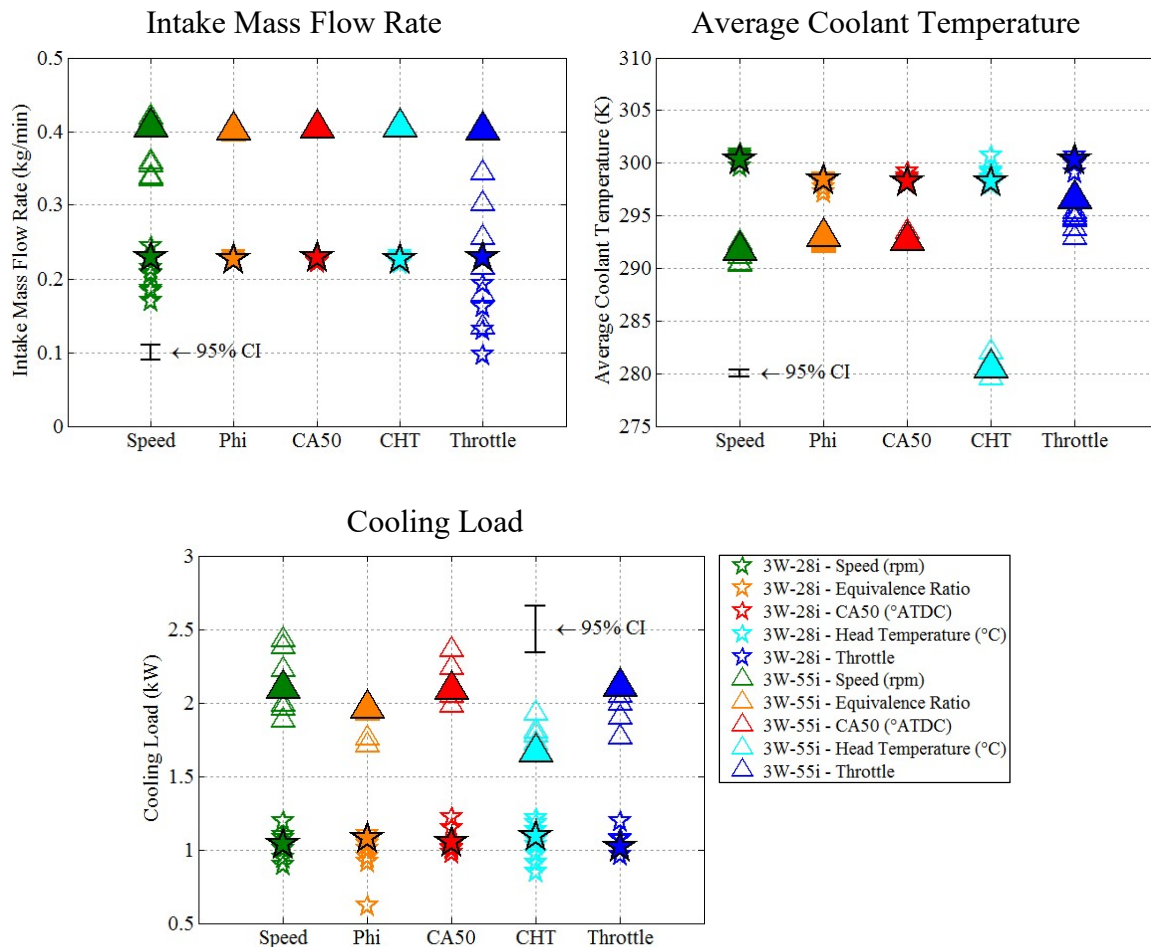


**Figure 138: Inputs to the Nusselt and Reynolds numbers for the Taylor and Toong model collected on the LSDAQ. Large, filled points represent the baseline condition of 6000 rpm, WOT,  $\phi=1.06\pm0.02$ , CA50=8 $\pm0.5^\circ$ aTDC, & CHT=130 $\pm2^\circ$ C.**

in Chapter IV. Average coolant temperature reflected ambient conditions in the laboratory during the tests. Since the laboratory was not climate controlled, the  $\pm 5^{\circ}\text{C}$  variations in coolant temperature on each engine were normal. The only outlier was the temperature for the cooling sweep of the 3W-55i engine. Testing on the 3W-55i engine was conducted in winter, and the four of the five sweeps were conducted with the exterior laboratory doors closed and the heaters running. To obtain additional cooling authority for the cooling sweep, the laboratory doors were opened and the heaters turned off, dropping the coolant temperature by approximately  $20^{\circ}\text{C}$ . Even so, the variations in coolant temperature were small compared to the temperature delta used to calculate the Nusselt number in the model (less than 5%). The cooling load baseline shows less than  $\pm 5\%$  variation with the exception of the cooling sweep on the 3W-55i engine, where colder cooling air shifted the baseline point by lowering the coolant velocity required to maintain the prescribed, external head temperature. In hindsight, the test would have been better served with a narrower sweep range and coolant temperatures more consistent with the other tests. With the exception of the cooling sweep on the 3W-55i engine, the results indicate the baseline scatter was not the result of variability in engine operating parameters measured on the LSDAQ.

Figure 139 shows the temperatures used to calculate the Nusselt numbers in Figure 137. Of the three temperatures, the measured temperature was the most consistent at the baseline conditions across all of the sweeps. Only the throttle sweep baseline point on the 3W-55i engine exhibited substantial variation, and that variation was directly traceable to the raw TLAS data, which showed lower temperatures during that sweep (see Section 2.1 for the temperature data). There is nothing in the data or run log as to why this occurred. Both of the models show  $\pm 10\%$  variation in the baseline conditions, and the variation tracks the

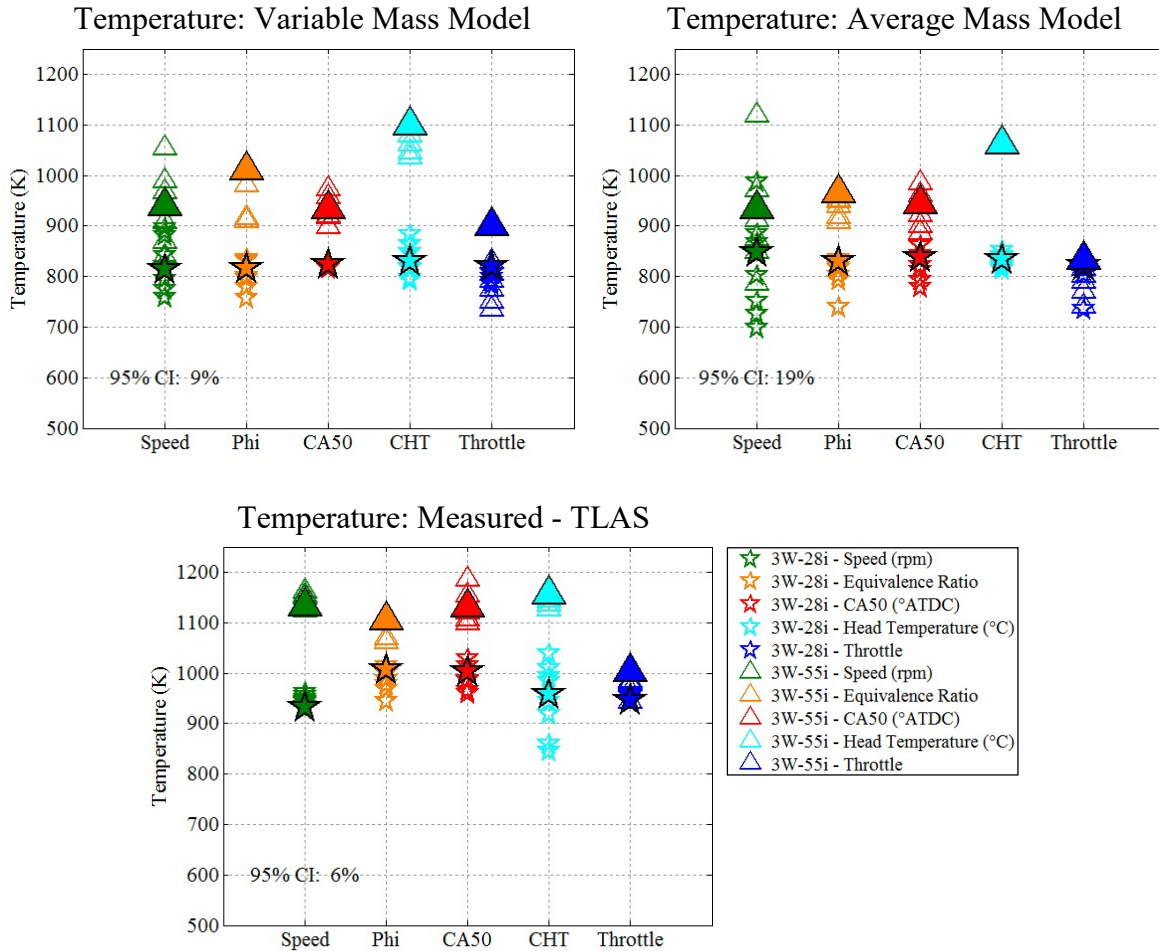


**Figure 139: Gas temperature used to calculate the Nusselt number for the Taylor and Toong model. Large, filled points represent the baseline condition of 6000 rpm, WOT,  $\phi=1.06\pm0.02$ , CA50= $8\pm0.5^\circ\text{aTDC}$ , & CHT= $130\pm2^\circ\text{C}$ .**

variation observed in the Nusselt numbers in Figure 137, just at a lesser magnitude. To understand why the  $\pm 10\%$  absolute temperature variation drove  $\pm 40\%$  to  $\pm 50\%$  variation in the Nusselt number requires revisiting the calculation shown in Equation (130). During the calculation of the Nusselt number, the average coolant temperature was subtracted from the gas temperature. Since average coolant temperature was approximately constant, differencing the two numbers amplified the variations in the in-cylinder gas temperature. Then the in-cylinder gas temperature was used to calculate the thermal conductivity and

dynamic viscosity (used in the Reynolds number). The results of those calculations are shown in Figure 140 for the thermal conductivity and Figure 141 for the dynamic viscosity. The relative variation in temperature was amplified in the calculation of thermal conductivity, which in turn further amplified the effect of temperature on the Nusselt number. Interestingly, dynamic viscosity was less sensitive to temperature, damping the variations at the baseline condition and explaining why the variation in Reynolds number between the baseline points was small relative to the variation in Nusselt number. This

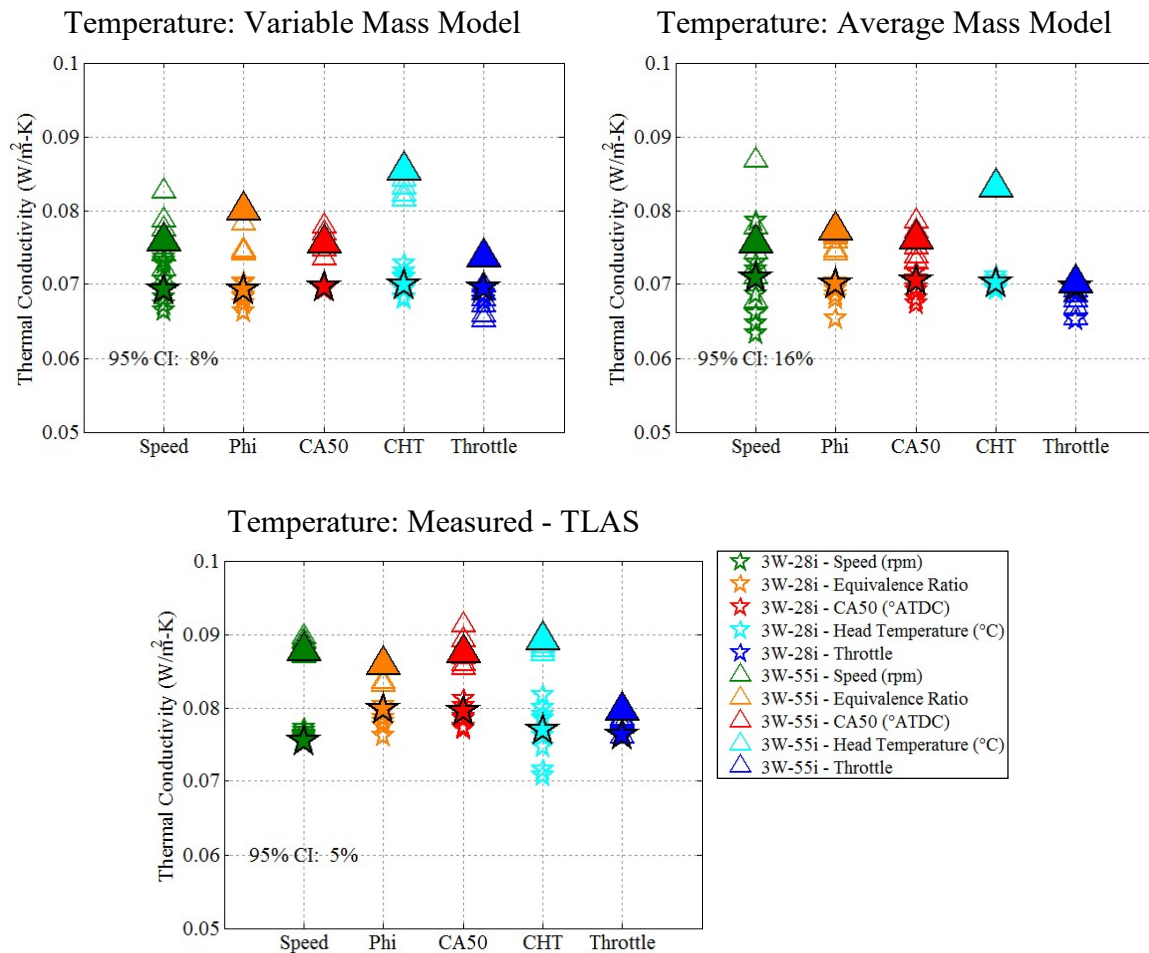


**Figure 140: Thermal conductivity used to calculate the Nusselt number for the Taylor and Toong model. Large, filled points represent the baseline condition of 6000 rpm, WOT,  $\phi=1.06\pm0.02$ , CA50=8 $\pm0.5^\circ$ aTDC, & CHT=130 $\pm2^\circ$ C.**

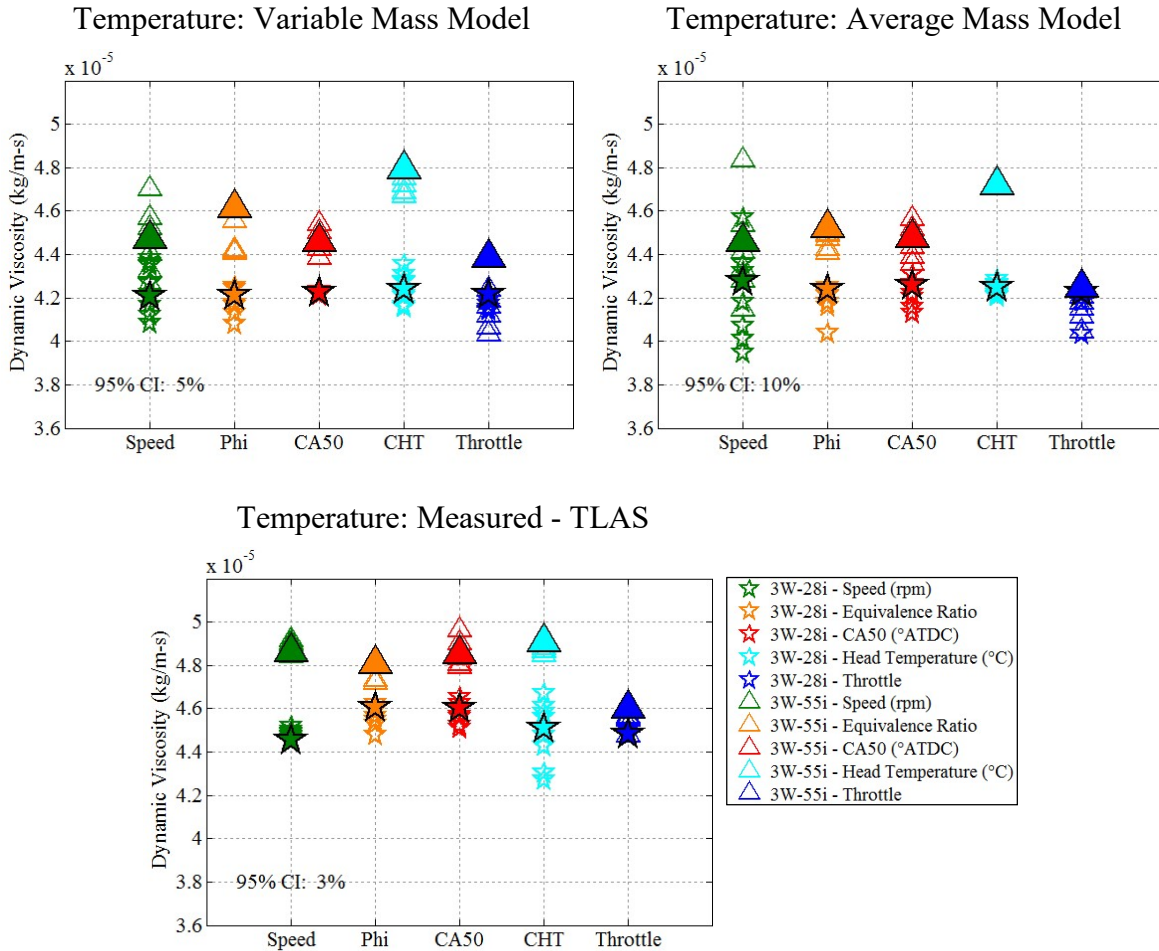


**Figure 141: Dynamic viscosity used to calculate the Nusselt number for the Taylor and Toong model. Large, filled points represent the baseline condition of 6000 rpm, WOT,  $\phi=1.06\pm0.02$ , CA50= $8\pm0.5^{\circ}$ aTDC, & CHT= $130\pm2^{\circ}$ C.**

demonstrates that the Taylor and Toong form for the Nusselt number is highly sensitive to the characteristic gas temperature, which itself was difficult to model (and in some cases difficult to measure consistently even across the baseline conditions).

The other variation observed in Figure 137 was caused by intentional changes to the operating condition during the sweeps. The trends created by sweeping some of the engine control variables indicates control parameters that the terms in Taylor and Toong's model were not formulated to handle. Discussing those specific conditions is easier in the context

of a fit to the data using the proposed form in Equation (128), and fits of Taylor and Toong's model to the data are shown in Figure 142. The fits are summarized numerically in Table 26. Ultimately, all of the fits were poor with small correlation coefficients less than 0.2, suggesting very weak correlation. The best fit was for the measured temperature profiles. However, Taylor and Toong's model executed with the measured temperature still seems particularly ill equipped to capture changes in throttle as well as variation in engine coolant flow rate. Throttling caused a lock step reduction in the mass flow rate

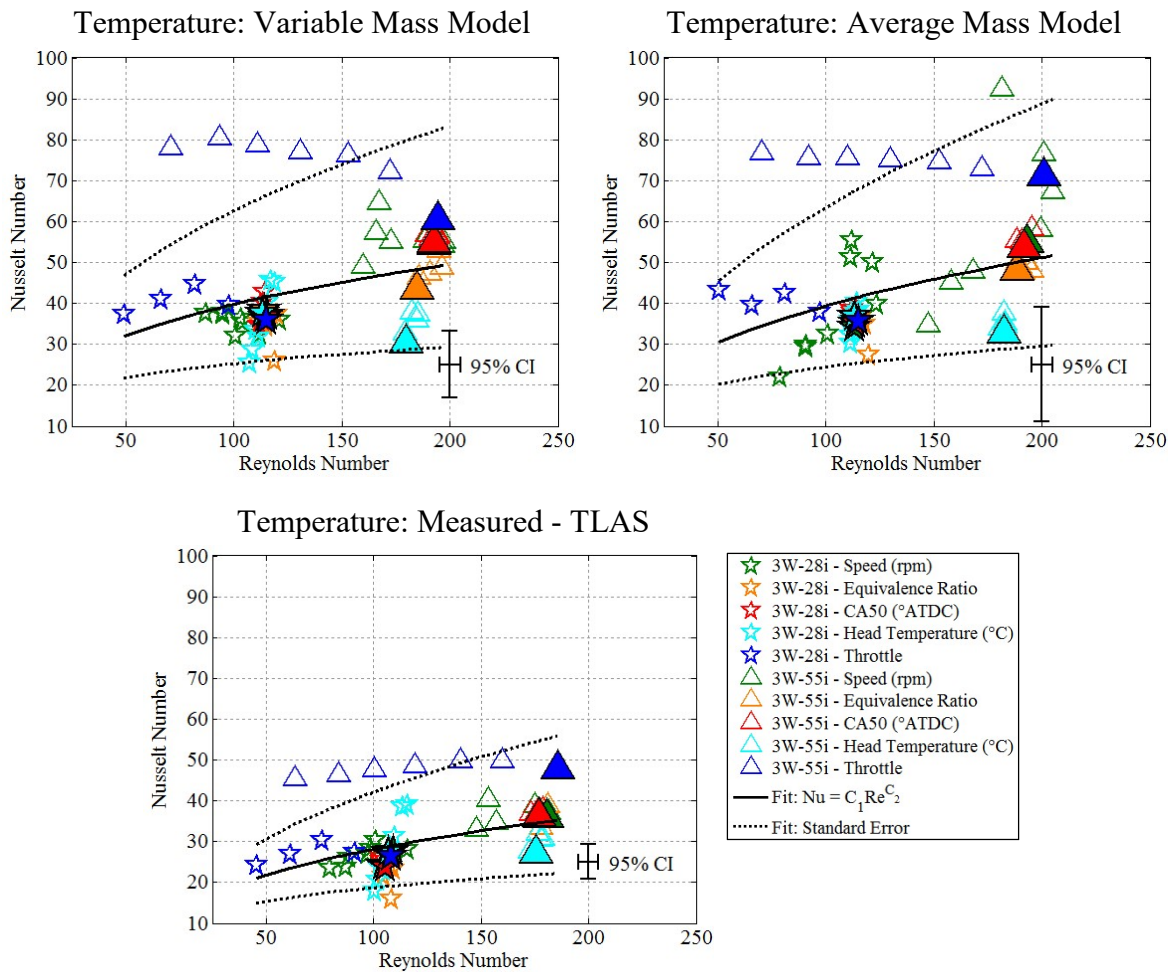


**Figure 142: Fits of Taylor and Toong's model to data collected on the 3W-28i and 3W-55i engines. Large, filled points represent the baseline condition of 6000 rpm, WOT,  $\phi=1.06\pm0.02$ , CA50=8 $\pm$ 0.5°aTDC, & CHT=130 $\pm$ 2°C.**

through the engines and in turn Reynolds number. However, the cooling load (for a constant head temperature) did not drop off as rapidly. Thus, the Reynolds number based on the mass flow rate through the engine used in Taylor and Toong's model did not fully describe the heat transfer behavior of the system. Additionally, changing the coolant flow rate changed the heat transfer and Nusselt number despite minimal changes in the Reynolds number. The characteristic velocity in the Reynolds number of Taylor and Toong's model suggests that the heat transfer network was dominated by convective transport in the cylinder. Since the Reynolds number only describes flow through the cylinder and not the cooling external to the cylinder, it is not surprising that the model does not capture behavior driven by changing the coolant flow rate and convection from the cylinder exterior.

**Table 26: Best Fit Coefficients for Equation (128), Nusselt Number as a Function of Reynolds Number for Characteristic Values Suggested by Taylor and Toong**

<b>Temperature Profile</b>	<b><math>C_1</math></b>	<b><math>C_2</math></b>	<b><math>R^2</math></b>
Variable Mass Model	9.4±5.8	0.31±0.10	0.10
Average Mass Model	6.9±5.3	0.38±0.10	0.14
Measured Temperature	5.2±2.7	0.37±0.09	0.18

With a correction for throttle and external cooling, the Taylor and Toong model might be usable with measured temperature data. However, collecting in-cylinder temperature data negates the utility of a simple model, and ultimately a modelled temperature as opposed to a measured temperature is desirable. Due to the issues discussed with modelling the temperature, neither the average mass nor the variable mass model provided Nusselt numbers that were well-described by Taylor and Toong's proposed form. In

addition to the throttle and cooling issues observed using the measured temperature data, the modelled temperatures also exhibited uncaptured variation in the speed sweep data.

Taylor and Toong's model offers at best an order-of-magnitude estimate of cooling requirements for small, two-stroke, SI engines, and clearly there is substantial room for improvement. Based on the results, there are several recommendations for future efforts to adapt the model. First, before even considering the heat transfer model, a more reliable temperature model must be established. Accomplishing that task relies on improving the calculation of the trapped mass. The trapped mass calculation might be better approached by measuring or estimating the trapping and charging efficiency. Second, for air-cooled engines the characteristic velocities for the coolant should be incorporated, based on the issues observed with the cooling sweep data. Third, the characteristic velocity (and/or flow) used in the Reynolds number should be reevaluated since it fails to capture the throttle behavior; in the case of throttling, the intake mass flow rate changed more rapidly than the heat transfer. Alternatively, a term reducing the impact of changing the throttle on the Reynolds number could be added.

Despite their weak correlation, the fits offered in Table 26 still described the approximate shape (slope) of the data. Table 27 lists fits suggested by Taylor and Toong [138] and Annand [17] to data for larger (greater than 241 cm<sup>3</sup> displacement) engines. The data used to construct the literature fits had Reynolds numbers from 10<sup>3</sup> to 10<sup>5</sup> and Nusselt numbers with a similar range of values. At their minimum, the literature data are an order-of-magnitude higher than the Reynolds and Nusselt numbers for the studied engines. Annand [17] suggested that the exponent on the Reynolds number should be relatively constant as it serves to capture the interaction of inertial and viscous forces and convective



thermal transport. The relationship also supposes that convective heat transfer inside the cylinder dominates the heat transfer network. Annand [17] further suggested that the constant in front of the Reynolds number is driven by engine type, presumably shifting the curve vertically on the graph depending on the characteristic temperatures.

**Table 27: Literature Coefficients for Equation (128), Nusselt Number as a Function of Reynolds Number for Characteristic Values Suggested by Taylor and Toong**

Engine	$C_1$	$C_2$	Source
Water cooled SI, CI, & air-cooled CI engines larger than 241 cm <sup>3</sup>	10.6	0.75	[138]
Water cooled CI larger than 241 cm <sup>3</sup>	7.7-10.6	0.70	[17]
Water cooled SI larger than 241 cm <sup>3</sup>	15.5	0.70	[17]

Figure 143 shows the literature fits in Table 27 plotted alongside the three fits created from the 3W engines. While the leading constants ( $C_1$ ) are similar, the exponents are substantially different. The engines tested in this effort had exponents from 0.3 to 0.4 (depending on how the temperature profile was obtained) compared to 0.7 to 0.75 for the literature data. Therefore, the fits to Taylor and Toong's model offered in literature are not appropriate even to make an order-of-magnitude estimate for spatially and temporally averaged heat transfer from small, two-stroke, SI engines. The literature fits overstate the impact of the Reynolds number (inertial and viscous forces, turbulence) on the Nusselt number (normalized convective heat transfer). Therefore, the Taylor and Toong model struggles to capture variation in small two-stroke engine operation, and the available fits in the literature are not appropriate even for order-of-magnitude estimates. As already suggested, further study is necessary to develop a useful model for spatially and temporally averaged heat transfer in 10 cm<sup>3</sup> to 100 cm<sup>3</sup> displacement, two-stroke, SI engines.

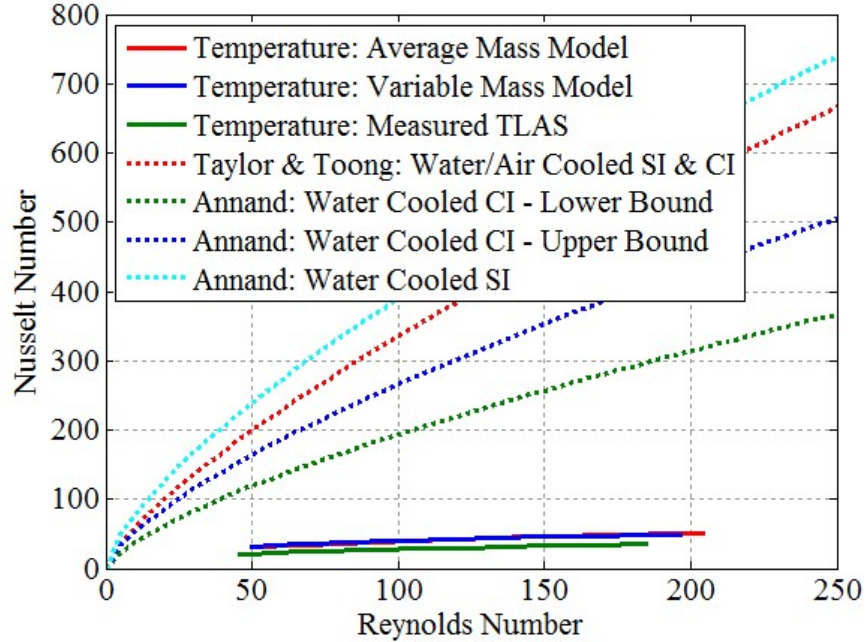


**Figure 143: Comparison of fits to Taylor and Toong model for the studied 3W engines to literature models from Taylor and Toong [138] and Annand [17] for automotive and larger scale engines.**

### 2.3. Heat Transfer Modelling Summary

The first goal of Objective 2 was to investigate heat transfer models for 10-100 cm<sup>3</sup> displacement, SI two-stroke engines that would be useful for engine designers seeking to estimate the cooling load of an engine for integration into an aircraft. One input common to many models is the in-cylinder temperature, typically estimated from in-cylinder pressure data and an estimate of the trapped mass. Two models, one based on a trapped mass that varied with the engine operating condition and one that used an average trapped mass that did not change with the operating condition were compared to temperature results from a line-of-sight measurement (several millimeters below the spark plug) made using TLAS. Compared to the models, the temperature measured using TLAS exhibited an earlier, sharper, and higher peak caused by the flame front traversing the line-of-sight,

followed by a more rapid drop due to localized cooling. In most cases, the modelled temperatures captured the qualitative behavior of the measured temperature as engine controls were swept over their operational range. Key exceptions were the speed and throttle sweeps, where the pressure and temperature measurements exhibited variation with changes in the operating condition that were not caused solely by variation in the trapped mass. The results demonstrated that it was difficult to calculate a consistent trapped mass as speed, temperature, and cooling all affected the in-cylinder temperature and pressure measurements used in the estimate. As long as the effect of changing operating conditions on the trapped mass could be estimated, the variable mass model was more appropriate.

Working with the modelled temperatures as well as delayed availability of the TLAS system cut into the time and resources for heat transfer modelling. A first attempt was made at applying the Taylor and Toong model, originally developed for automotive and larger scale engines, to data collected on the 3W-28i and 3W-55i engines. Of the two temperature models, the variable mass model provided a visually better fit, shown in Equation (132). However, the correlation was relatively weak. Small variations in the modelled temperature, which was difficult to model to begin with, were amplified during the calculation of the Nusselt number. Moreover, the Taylor and Toong model was not formulated to handle variations in throttle, speed, and cooling flow rate. Overall, the model offered at best an order-of-magnitude estimate of the cooling requirements for small, two-stroke, SI engines. Additionally, coefficients provided in the literature for larger engines were not appropriate for the engines studied herein.

$$Nu = (9.4 \pm 5.8)Re^{(0.31 \pm 0.1)} \quad (132)$$

Several steps should be pursued to improve and adapt the model. First, a more reliable temperature model must be established by improving the calculation of the trapped mass. The trapped mass calculation could be approached by measuring or estimating the trapping and charging efficiency. Second, for air-cooled engines the characteristic velocity of the coolant should be incorporated. Third, the characteristic velocity (and/or flow) used in the Reynolds number should be reevaluated since it failed capture the throttling behavior.

### **3. Friction Loss Modelling**

For the purposes of Objective 1, friction losses in the engine were within the control volume of the cooling enclosure and thus measured as heat rejection to the coolant (and possibly the exhaust gases). Note that “friction losses” as used in the proceeding discussion encompasses both mechanical friction sources as well as viscous dissipation during the movement of fresh charge through the intake, crankcase, and cylinder. As discussed in Chapter II, Section 5.2 the literature is sparse on models for friction losses in small engines. Therefore, engine friction losses were measured using a motored engine test as described in Chapter III, Section 3.3. Prior to each test, the engine was heated to  $130 \pm 2^\circ\text{C}$  via fired operation. Once the engine reached steady state, the spark and cooling fan were turned off and the engine was motored using the friction testing cradle. Fuel remained at the fired setting to ensure the engine remained lubricated throughout the test.

Since a motored engine friction test was used, of the five engine control variables only speed and throttle could be evaluated for their impact on friction losses (and only speed is commonly used for models in the literature). The remainder of this section is divided into three subsections. The first, Section 3.1 explores the impact of engine speed on friction losses in 10-100 cm<sup>3</sup> displacement, two-stroke engines and compares the results to data for

larger and smaller engines available from the literature. Section 3.2 discusses the impact of throttle on friction losses and Section 3.3 summarizes the key friction loss results.

### 3.1. Speed Results

As described in Chapter III, Section 4.2, the three term speed model was chosen as the starting point for friction loss modelling. Equation (133) shows the three term model rearranged with the power dissipated by friction normalized by displaced volume. As will be shown, FMEP was almost constant for the studied engines, and thus it was easier to judge goodness of fit by fitting Equation (133) rather than by fitting directly to Equation (134). The comparison to literature data will be made both in terms of friction power density and FMEP. Three different fits were performed: a cubic fit (all terms), a quadratic fit ( $C_1$  and  $C_2$ ), and a linear fit (only  $C_1$ ). A linear least squares regression was used; the results are shown numerically in Table 28 and graphically in Figure 144. The linear term corresponds to sliding mechanical friction. The quadratic and cubic terms correspond to hydrodynamic regime friction and pumping losses, respectively.

**Table 28: Best Fit Coefficients for Equations (133) and (134), Friction Losses as Linear, Quadratic, and Cubic Functions of Engine Rotational Speed**

Engine	Cubic				Quadratic			Linear	
	$C_1$ (kPa)	$C_2$ (kPa)	$C_3$ (kPa)	$R^2$	$C_1$ (kPa)	$C_2$ (kPa)	$R^2$	$C_1$ (kPa)	$R^2$
<b>3W-28i</b>	96.1 ±30.5	-3.82 ±12.31	0.91 ±1.17	0.948	74.3 ±12.0	5.57 ±1.97	0.951	107.2 ±3.7	0.926
<b>3W-55i</b>	52.7 ±12.6	4.22 ±5.05	-0.26 ±0.48	0.975	59.0 ±4.9	1.53 ±0.79	0.977	68.0 ±1.3	0.973
<b>3W-85Xi</b>	92.8 ±16.4	-5.45 ±6.41	0.46 ±0.60	0.959	81.0 ±5.6	-0.61 ±0.93	0.962	77.4 ±1.4	0.964

*\*Uncertainty bands are the standard error of the regression.*

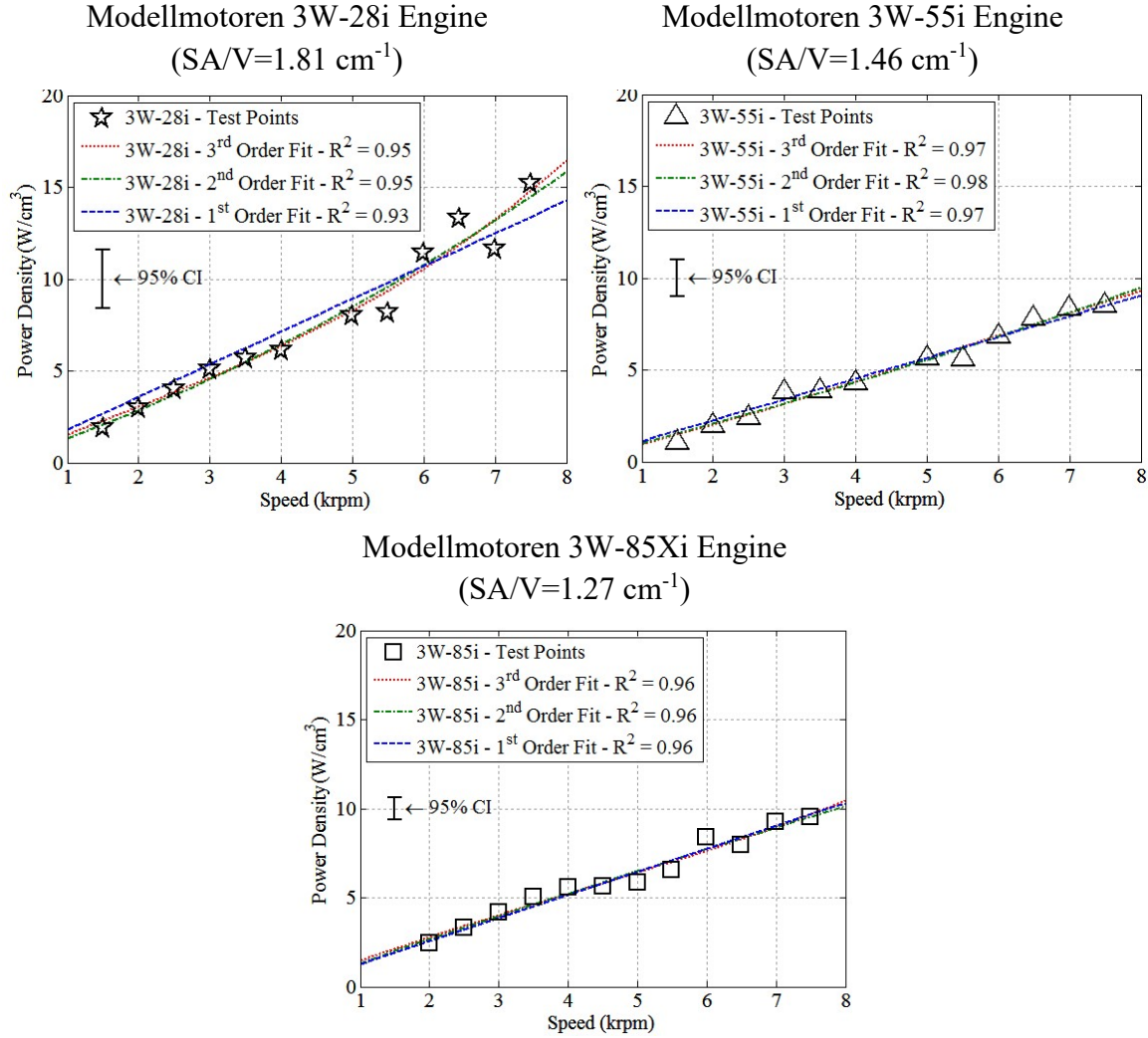


**Figure 144: Engine friction loss testing results as a function of speed. Fits created using linear least squares regression to the (linearized) three term model.**

$$\frac{P_f}{V_d} [kW/cm^3] = \left( C_1 + C_2 \left( \frac{N}{1000} \right) + C_3 \left( \frac{N}{1000} \right)^2 \right) \frac{N}{60} \quad (133)$$

$$FMEP = C_1 + C_2 N + C_3 N^2 \quad (134)$$

Overall, normalized friction losses as a function of engine speed were strongly linear, especially for the 3W-55i and 3W-85Xi engines. The 3W-28i engine showed a slight higher order tendency, although the scatter driving the higher order fit could be in part caused by larger variations/ uncertainty in the 3W-28i compared to the other engines. With

the exception of the quadratic fit for the 3W-28i engine, the quadratic and cubic fits offered no appreciable advantage over the linear fit. Furthermore, most of the cubic and quadratic fits for the studied engines contained negative coefficients for at least one of the higher order terms (this is not uncommon in literature, see Table 9, page 138). These terms may be negative only mathematically, they cannot be physically negative. The small impact of the cubic and quadratic terms suggests that the majority of the friction losses stemmed from mechanical sliding contact and that hydrodynamic regime friction (quadratic) and pumping losses (cubic) were small and/or reasonably captured as a linear function of speed. In this sense, small, two-stroke, SI engines behave more closely to the micro glow fuel engines studied by Menon and Cadou [16] than larger engines [21:722, 22:368]. Menon and Cadou [16] concluded that a linear fit to speed was sufficient to predict WOT friction loss behavior; the same holds true here.

Figure 145 compares the linear fits for the studied engines to the proposed fits from literature in Table 29, and Figure 146 makes the same comparison for the cubic fits. The

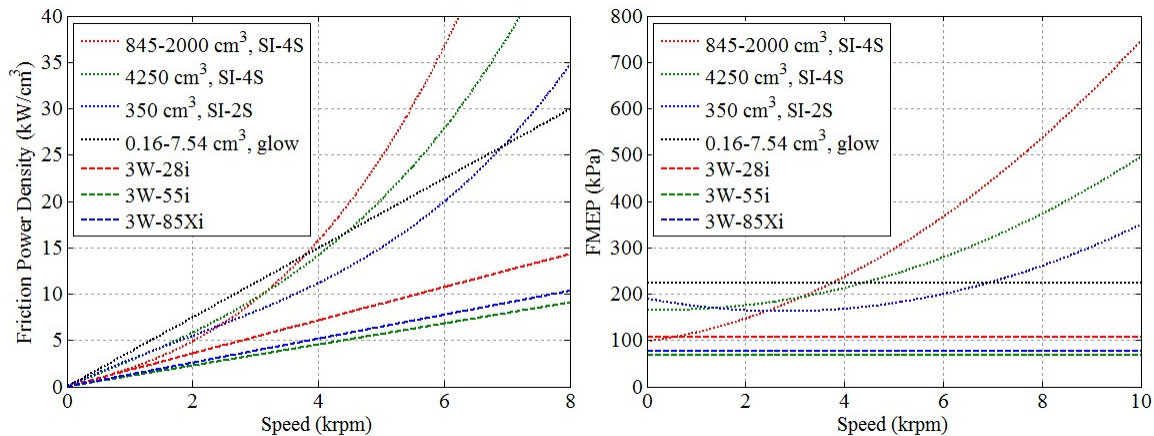


**Figure 145: Comparison of linear friction loss model fits for 3W engines to literature models for automotive and larger scale engines and micro glow fuel engines in terms of power density and FMEP. Literature data collected from Heywood [21:722], Heywood and Sher [22:368], and Menon and Cadou [16].**

engines tested herein were different from larger engines in two regards: First, the normalized friction losses were lower, and second, the impact of the quadratic and cubic terms (in power) were less pronounced (i.e.  $C_2$  and  $C_3$  had less of an impact), indicating lower hydrodynamic and pumping losses. Compared to micro glow fuel engines, the studied engines had lower friction losses; the micro glow engines also had negligible quadratic and cubic terms. Normalized friction losses lower than larger engines was not the expected outcome. Rather, it was expected that normalized friction losses would fall between automotive and larger scale engines and micro glow engines since many sources of friction scale roughly with the surface area to volume ratio, and the scaling of friction sources with surface area to volume ratio is discussed later in this section. However, this hypothesis did not take into account the number of friction sources present in the engines. In both Heywood [22:722] as well as Heywood and Sher [22:368], FMEP includes both friction sources in the engine (such as piston rings, journal bearings, and support bearings), as well as friction sources external to the engine such as coolant pumps and accessories.

**Table 29: Constants for Equations (133) and (134)**

Displacement	Engine Type	Cylinders	$C_1$ (kPa)	$C_2$ (kPa)	$C_3$ (kPa)	Source
845 to 2000 cm <sup>3</sup>	Four-Stroke	4	97	15	5	[21:722]
4250 cm <sup>3</sup>	SI Engines	8	166	-2.5	3.5	[22:368]
350 cm <sup>3</sup>	Two-Stroke SI Engines	2	190	-20	3.6	[22:368]
0.16 to 7.54 cm <sup>3</sup>	Two-Stroke Glow Fuel	1	224.4	0	0	[16]

*\*Uncertainty bands are the standard error of the regression.*



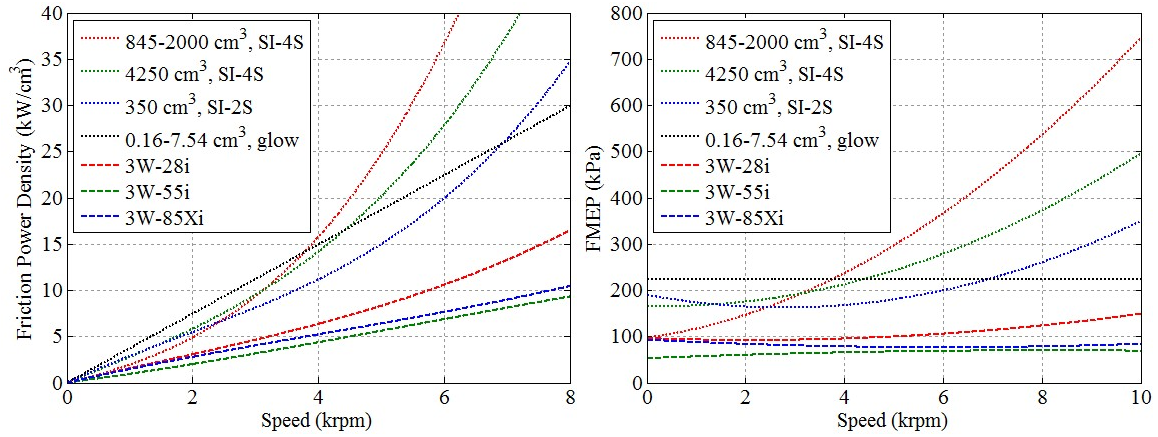


**Figure 146: Comparison of cubic friction loss model fits for 3W engines to literature models for automotive and larger scale engines and micro glow fuel engines in terms of power density and FMEP. Literature data collected from Heywood [21:722], Heywood and Sher [22:368], and Menon and Cadou [16].**

Additionally, two of the three fits provided in Table 29 are for four-stroke engines. Unlike two-stroke engines, four-stroke engines have a number of friction sources associated with the valve train. Meanwhile, the 3W engines studied herein (as well as most similar COTS two-stroke engines) were about as simple as one can make an engine in terms of friction sources. There was a single sliding contact between the piston ring and cylinder liner, two journal bearings (one on each side of the connecting rod), two roller bearings to support the driveshaft, and viscous losses from moving charge through the engine. The sheer simplicity results in lower normalized friction losses than automotive and larger scale engines. It is therefore debatable whether or not the comparison to conventional engines is a fair one. After all, it is not an apples-to-apples comparison since larger conventional engines have friction sources that 10-100 cm<sup>3</sup> displacement, two-stroke engines do not. However, those friction sources are usually required to run the engine. For example, a liquid cooled four-stroke engine cannot run without the coolant pump. Thus, the data suggests that the comparison is reasonable in the context of engines in an application. For

a small unmanned aircraft application, engine cooling is typically accomplished using the free stream air and any penalty paid would be included in the aircraft's drag.

The above comparison of conventional engines to 10-100 cm<sup>3</sup> displacement, two-stroke engines also offers some insight into why the friction curves take on different shapes than conventional engines. The cubic term ( $C_3$ ) accounts for viscous and pumping type losses and Menon and Cadou point out that in conventional engines this term is often driven by coolant and/or lubricant pumping systems [16], both of which are absent in small two-stroke engines, explaining the negligible contribution of  $C_3$ . It is interesting to note that Blair [27:379-380] proposes that the pumping losses from the induction and exhaust of fresh charge are better described by the quadratic term. The other texts consulted said nothing on the subject for two-stroke engines. The quadratic term ( $C_2$ ) accounts for hydrodynamic friction, or friction occurring between two solid surfaces separated with a liquid lubricant film. The linear term ( $C_1$ ) accounts for mixed and boundary friction that involve a degree of metal-to-metal contact. The dominance of ( $C_1$ ) compared to ( $C_2$ ) implies that boundary type friction (presumably the sliding fit between the piston and the cylinder) dominated the hydrodynamic sources (roller and journal bearings). As previously stated, the results show that 10-100 cm<sup>3</sup> SI, two-stroke engines behave more like micro glow fuel engines than conventional engines where friction losses are concerned. The micro glow fuel engines and the friction loss results will be revisited in additional detail following the discussion of Blair's proposed friction loss model.

Blair [27:379] proposed the model for two-stroke engines shown in Equations (135) and (136). Noting that mean piston speed is directly proportional to rotational speed, the model is somewhat similar to the quadratic variant of the three term model presented above.

However, plotting against mean piston speed normalizes by engine size. The maximum rotational speed of an engine is usually driven by inertial loading on the components (and balance/ vibration). Thus as engine size (and stroke) increases, rotational speeds decrease. Therefore mean piston speed offers a characteristic speed useful for comparing inertial loading and component speeds in engines of different sizes.

$$P_f[kW] = (C_1 + C_2 \bar{S}_p) \frac{N}{60} V_d \quad (135)$$

$$FMEP = C_1 + C_2 \bar{S}_p \quad (136)$$

Figure 147 shows the friction data from the 3W engines and the fits to Blair's model. The fits are summarized numerically in Table 30. As expected the fits are comparable to the quadratic fit from the three term model; in fact the  $C_1$  terms are exactly the same. The  $C_2$  terms only differ by the factor relating mean piston speed to rotational speed (which includes the stroke length). As in the three term model results, the linear term dominates. Similar to the preceding discussion, Blair describes the linear term as a friction from non-hydrodynamic sources. While Blair's proposed model is less universally applicable than the three term model (due to the lack of a third order term) it provides an equally good fit for the studied engines, largely due to the dominance of the first order term.

**Table 30: Best Fit Coefficients for Equations (135) and (136),  
Friction Losses as a Function of Mean Piston Speed**

Engine	$C_1$ (kPa)	$C_2$ (kPa)	$R^2$
<b>3W-28i</b>	74.3±12.0	4.77±1.68	0.951
<b>3W-55i</b>	59.0±4.9	1.31±0.68	0.977
<b>3W-85Xi</b>	81.0±5.6	-0.45±0.69	0.962

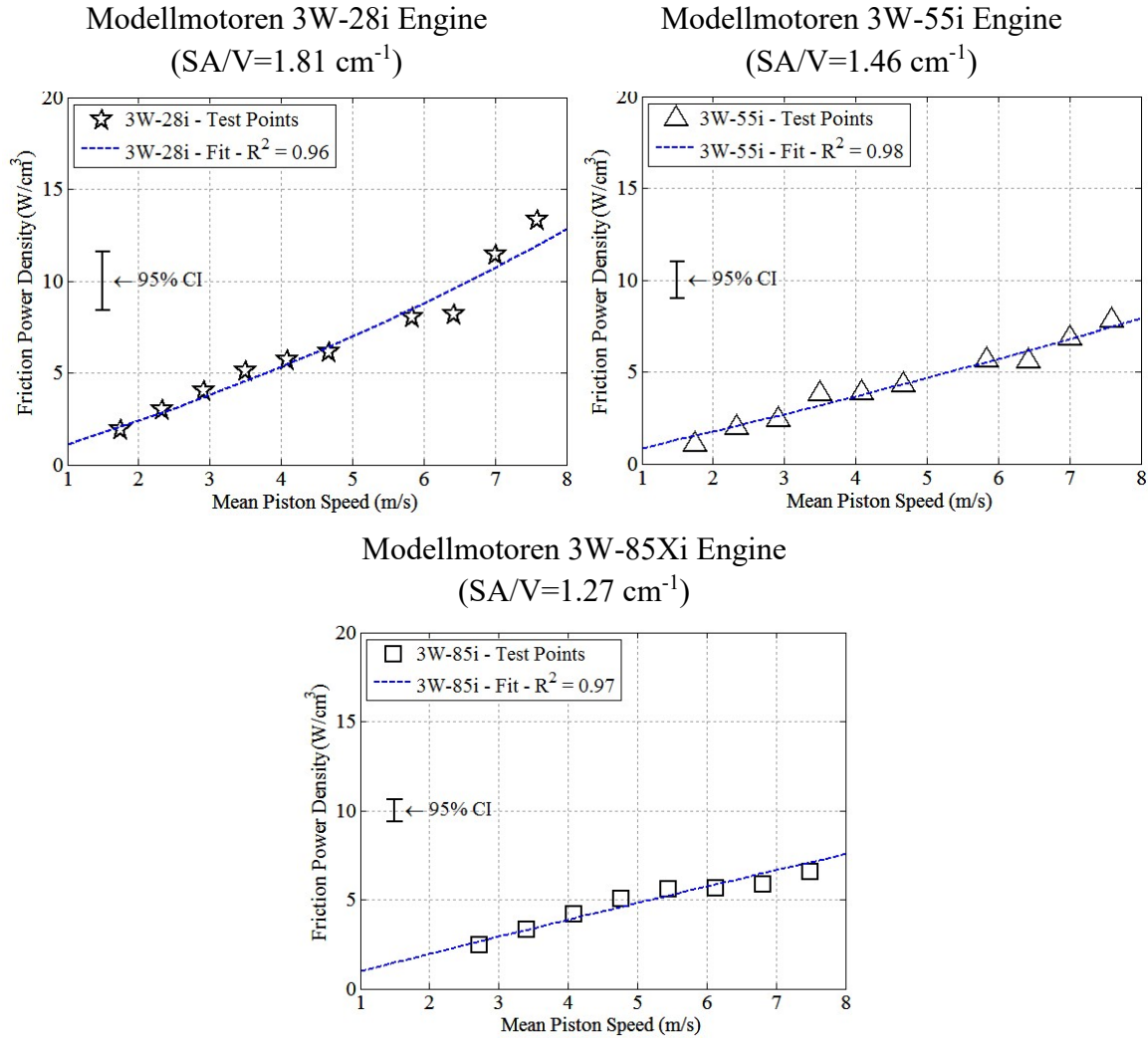


**Figure 147: Engine friction loss testing results as a function of mean piston speed. Fits created using linear least squares regression to Blair's model [27:379].**

Table 31 shows the proposed literature coefficients for Blair's model, which are plotted against the fits for the studied engines in Figure 148. Unlike the fits proposed for the three term model, the fits proposed by Blair indicate normalized friction losses lower than those observed in the 3W engines. This suggests that not only are the normalized friction losses higher in the tested engines than in the engines reported by Blair, but also that the engines

used to develop Blair's correlations had substantially lower friction losses than those reported by Heywood [22:722], Heywood and Sher [22:368], and Menon and Cadou [16].

**Table 31: Constants for Equations (135) and (136) Compiled by Blair [27:379]**

Displacement	Engine Type	Bearings	$C_1$ (kPa)	$C_2$ (kPa-s/m)
>100 cm <sup>3</sup>	SI: Vehicle	Roller	0	4.5
	SI: Industrial		0	3.15
	SI	Plain	6	3.75
	CI: Automobiles		34.4	5.25
	CI: Trucks		61	6.0

Heywood [22:722] as well as Heywood and Sher [22:368] reported the original sources for their compiled data and Menon and Cadou reported their raw friction data. Blair [27:379] reported neither making it difficult to identify the reason for the discrepancy. A reasonable theory is that the disparity originates in the definition of engine friction losses. Blair notes in his text that he had not resolved which accessories (specifically cooling fans), if any, were included in the reported friction loss estimates [27:379]. Therefore, it seems likely that the fits reported by Blair do not include friction sources outside of the cylinder and crankcase, in which case the friction sources would once again be comparable to the 3W engines. This in turn suggests that normalized friction losses do in fact scale with the surface area to volume ratio, since the largest engines (industrial) in Figure 148 have the lowest normalized friction, followed by automotive engines (CI is higher than SI due to increased temperatures and pressures), and finally by the studied engines.

While both the three term model and Blair's model may be fit to 10-100 cm<sup>3</sup> displacement, two-stroke engines, none of the coefficient sets available from literature

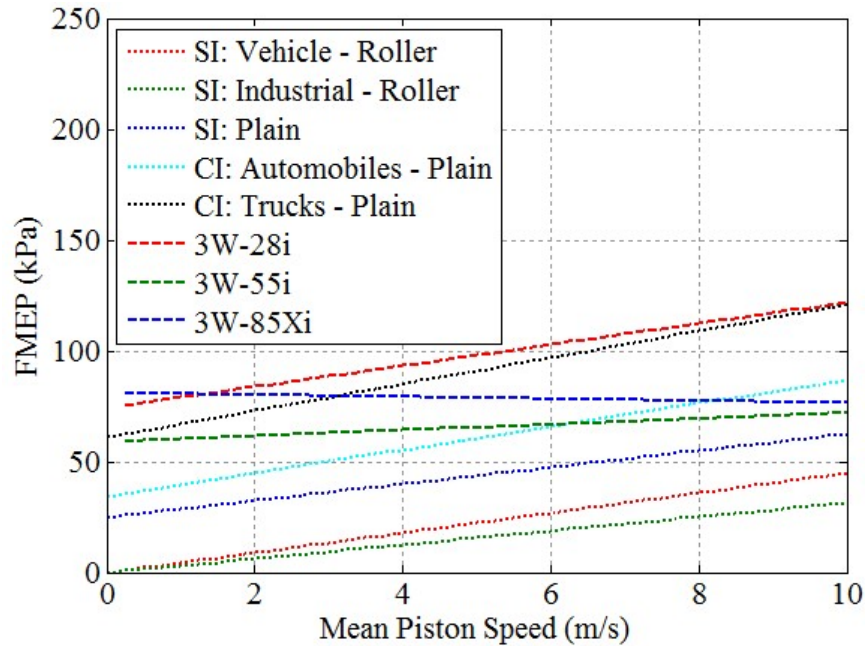


**Figure 148: Comparison of friction loss model fits for 3W engines to literature models for conventional two-stroke engines in terms FMEP. Literature data collected from Blair [27:379].**

were reasonable. The studied engines had nearly constant FMEP values lower than automotive and larger scale engines due to the lack of accessories (and valve trains) but higher than the large two-strokes reported by Blair. The fits provided in Table 28 and Table 30 provide a range of reasonable coefficients for 10-100 cm<sup>3</sup> displacement, two-stroke engines with the simple single term model (linear with power) being sufficient. While these results address the concerns of an aircraft designer desiring an *a priori* estimate of friction losses, they do not clearly address how much friction losses actually scale with the surface area to volume ratio outside of the generic observation that yes, indeed, normalized friction losses appear to increase for two-stroke engines (glow fuel and SI) less than 100 cm<sup>3</sup> displacement as displaced volume decreases.

To test the surface area to volume hypothesis, data from Menon and Cadou [16] was combined with the data from this study since both sets of engines were small two-stroke engines with roughly the same friction sources. Building on the observation that FMEP was essentially constant for all 12 engines, FMEP was plotted as a function of surface area to volume ratio as shown in Figure 149. The figure also shows a linear and a quadratic fit to the data. The form of those fits is given in Equations (137) and (138) and they are summarized mathematically in Table 32.

$$FMEP[kPa] = C_1 + C_2 \frac{SA}{V_d} [cm^{-1}]; R^2 = 0.92 \quad (137)$$

$$FMEP[kPa] = C_1 + C_2 \frac{SA}{V_d} [cm^{-1}] + C_3 \left( \frac{SA}{V_d} \right)^2 [cm^{-2}]; R^2 = 0.95 \quad (138)$$

**Table 32: Best Fit Coefficients for Equation (138), Friction Losses as a Function of Surface Area to Volume Ratio**

	$C_1$ (kPa)	$C_2$ (kPa/cm)	$C_3$ (kPa/cm <sup>2</sup> )	$R^2$
<b>Eqn. (137)</b>	44.2±12.5	36.2±2.9	n/a	0.918
<b>Eqn. (138)</b>	-0.5±17.8	62.5±9.2	-3.02±1.02	0.948

The reasoning behind the hypothesis that friction losses would scale with surface area to volume ratio suggests a linear relationship. Such a relationship is expected since friction sources would be expected to scale with surface area whereas FMEP is normalized by volume. As can be seen in Figure 149, the linear fit is reasonable with an  $R^2$  value of 0.92. However, the quadratic fit is slightly better with an  $R^2$  value of 0.95. The second order behavior indicates that some of the drivers of friction losses do not scale directly with cylinder surface area. Rather, the friction losses increase somewhat less rapidly than the

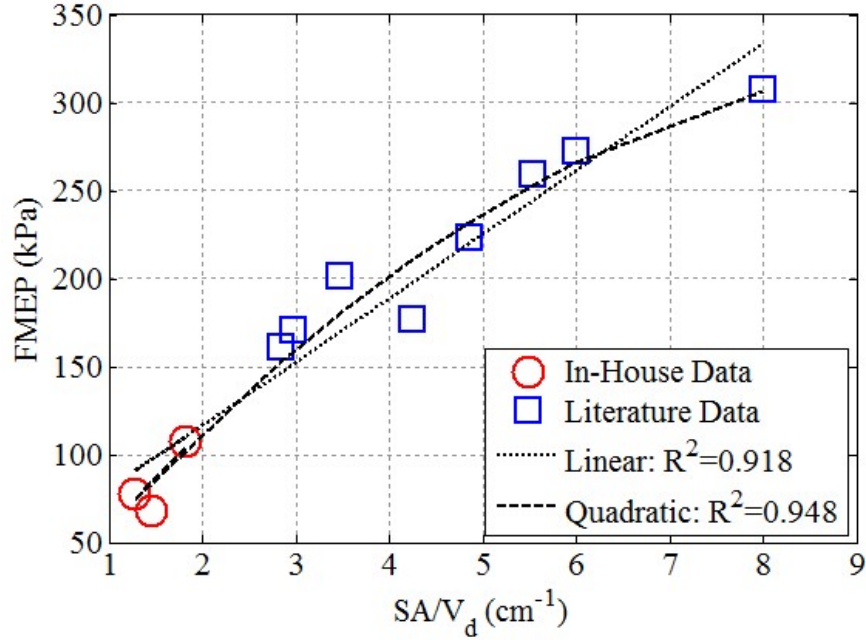


**Figure 149: Scaling of FMEP (normalized friction losses) with surface area to volume ratio at WOT for small two-stroke engines less than 100 cm<sup>3</sup> displacement. Literature data based on friction testing results reported by Menon and Cadou [16].**

surface area to volume ratio. In turn it is likely that the effective surface area of friction contacts increases less rapidly than the cylinder surface area as engine displacement decreases. For example, roller bearing contact area probably does not directly map to cylinder surface area and is probably heavily influenced by commercially available bearing sizes. Therefore, the cylinder surface area to volume ratio captures much of the scaling of friction, but not all of it. Thus, for predictive and design purposes, the quadratic fit offers a better prediction, although both fits would be acceptable. In either case, the fits presented here should not be extrapolated outside of small two-stroke engines, since the friction sources and relatively constant nature of FMEP necessary to construct the presented fits were specific to two-stroke engines less than 100 cm<sup>3</sup> displacement.



### 3.2. Throttle Results

The throttling results typically reported in the literature are driven by pumping losses for four-stroke engines, which almost universally include engine cooling accessories not present on the two-stroke engines tested herein. Throttled friction loss results for small two-stroke engines were, generally, not available. Figure 150 shows the impact of throttle, normalized as delivery ratio, on engine friction losses for the 3W-28i, 3W-55i, and 3W-85Xi engines at 6000 rpm. The presented confidence intervals increase with decreasing engine size due to the decrease in total power dissipated by friction (or in other words the decreasing magnitude of the difference between the dynamometer and drivetrain measurements). As was the case in the parametric studies, the observed trends were repeatable and real even though they were within the 95% confidence interval for any given point. In part, this is because the confidence interval included uncertainty sources (biases) that would shift the entire curve for a given engine.

Figure 150 also includes linear fits to the normalized friction losses for each engine. The fits take the form shown in Equation (139) and are shown in Table 33. The poor correlation coefficients for the 3W-28i and 3W-55i engines were the result of high variability in the measurement relative to the small change in delivery ratio. The fits in Figure 150 were influenced by two factors: the magnitude of friction at the WOT point and the rate at which viscous losses from the induction and exhaust of fresh charge decreased with throttle. As demonstrated previously, the magnitude of WOT friction losses can be tied to engine size. Given that at a fixed speed the power dissipated by friction with changing throttle appeared tied to the delivery ratio, it was proposed that throttled friction

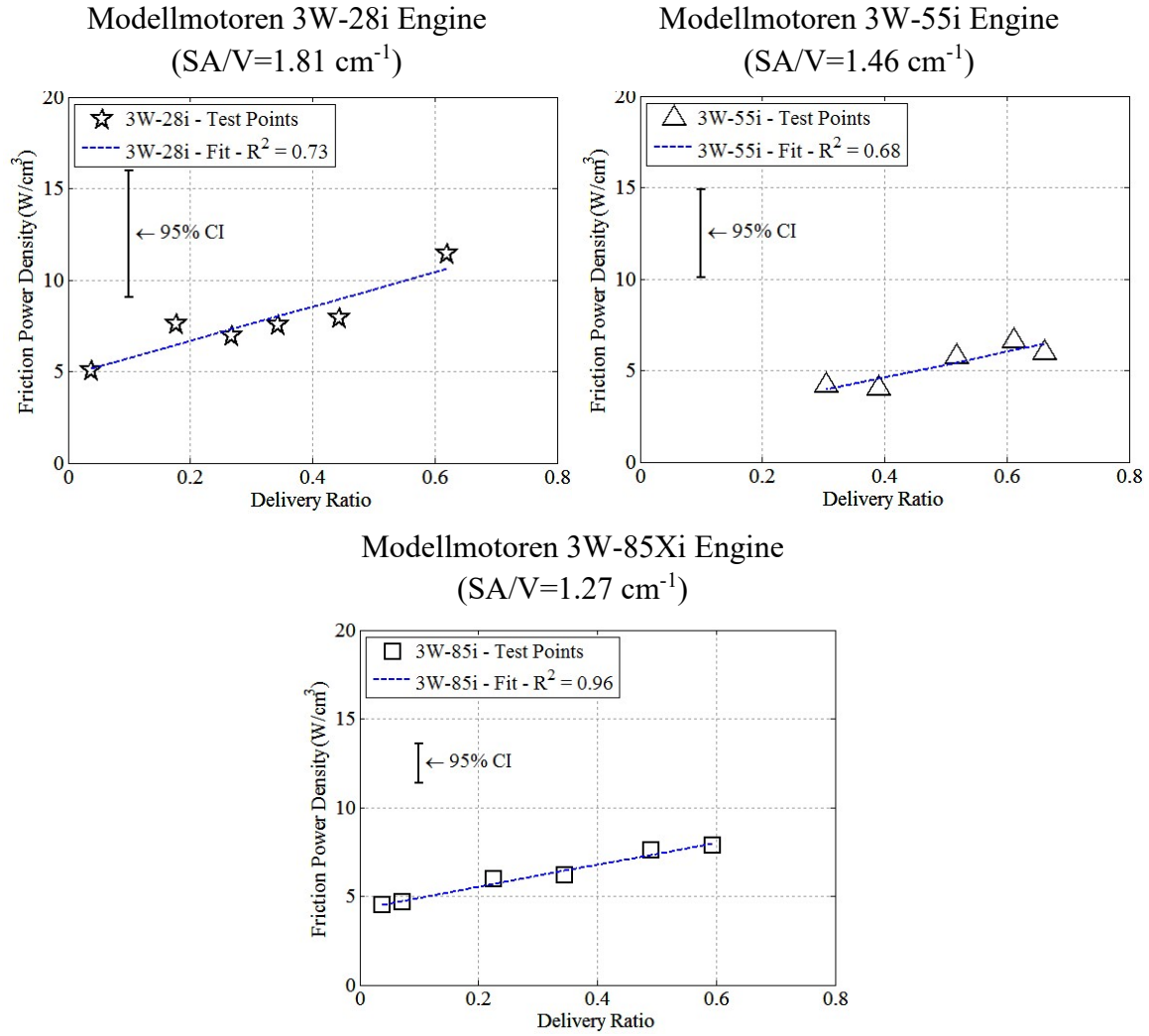


**Figure 150: Influence of throttle setting (normalized as delivery ratio) on engine friction losses at 6000 rpm. Fits created using linear least squares regression.**

losses could be predicted from WOT friction losses knowing the delivery ratio at both the throttled and WOT points. The proposed form of that relation is shown in Equation (140).

$$\frac{P_f}{V_d} [kW/cm^3] = C_1 + C_2 \lambda \quad (139)$$

$$\frac{P_f(\lambda)}{P_f|_{WOT}} = 1 - C_1(\lambda|_{WOT} - \lambda) \quad (140)$$

**Table 33: Best Fit Coefficients for Equation (139), Friction as a Linear Function of Delivery Ratio**

Engine	$C_1$ (W/cm <sup>2</sup> )	$C_2$ (W/cm <sup>2</sup> )	$R^2$
<b>3W-28i</b>	4.81±0.61	9.33±1.67	0.732
<b>3W-55i</b>	1.81±0.71	7.04±1.38	0.678
<b>3W-85Xi</b>	4.30±0.14	6.21±0.40	0.959

To determine an appropriate value for  $C_1$  in Equation (140), the results in Figure 150 were normalized by the peak friction loss for each engine and plotted against delivery ratio as shown in Figure 151. The fits are summarized numerically in Table 34. As in the raw data, the WOT delivery ratio and peak friction loss for each engine had a strong influence on the intercept of the linear fit. However, all of the linear fits have comparable slopes

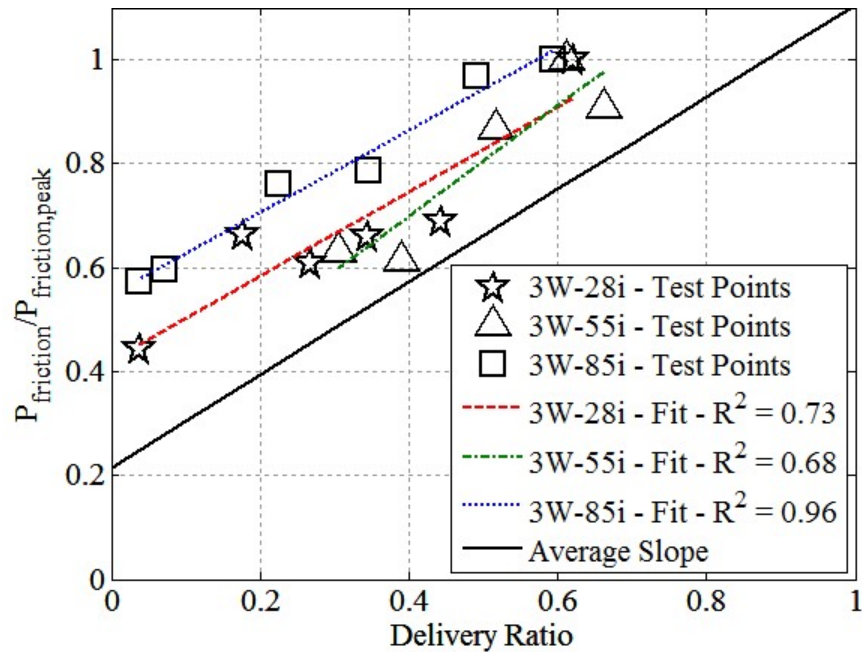


**Figure 151: Normalized friction results for the 3W-28i, 3W-55i, and 3W-85Xi engines and the resulting linear fits. Also included is a line of average slope describing the general relationship between friction power and delivery ratio.**

( $\pm 15\%$  of the average slope). Therefore, the results confirm that throttled friction losses may be predicted from knowledge of WOT friction losses and delivery ratio as proposed in Equation (140). Based on the data presented herein,  $C_1$  takes on a value  $0.89 \pm 0.30$ . It should be noted that the average slope of each of the lines is not the same as a single linear regression to all of the test points. The latter is inappropriate because the slope of the single correlation is influenced by the WOT power and delivery ratio of each engine. Dealing with the fact that those terms are engine and speed specific is the entire reason to use Equation (140).

**Table 34: Best Fit Coefficients for Equation (140), Friction as a Linear Function of Delivery Ratio**

Engine	$C_1$	$C_2$	$R^2$
<b>3W-28i</b>	$0.421 \pm 0.053$	$0.815 \pm 0.146$	0.732
<b>3W-55i</b>	$0.273 \pm 0.107$	$1.065 \pm 0.209$	0.678
<b>3W-85Xi</b>	$0.548 \pm 0.018$	$0.791 \pm 0.051$	0.959

### 3.3. Friction Modelling Summary

This section discussed modelling engine friction losses for Objective 2. Due to the motored friction testing method, only speed and throttle could be studied, and only results for speed were widely available in the literature for larger and smaller engines. Compared to larger engines where FMEP is typically best fit with a quadratic function of engine speed [21:722, 22:368], the studied engines had nearly constant values of FMEP similar to smaller glow fuel engines [16]. Normalized friction losses in the tested engines were generally lower than in automotive and larger scale engines since the tested engines had no accessory type losses (cooling pumps, valve trains in the case of four-stroke engines, and so forth). Noting that FMEP for small two-stroke engines was essentially constant over

the tested speed range, the data from the tested engines was combined with data from the literature for smaller (glow fuel) two-stroke engines with similar friction sources [16]. The results showed that friction losses scale with the surface area to volume ratio, and a suggested correlation is shown in Equation (141). The correlation is valid for crankcase scavenged two-stroke engines less than 100 cm<sup>3</sup> displacement.

$$FMEP[kPa] = (-0.5 \pm 17.8) + (62.5 \pm 9.2) \frac{SA}{V_d} [cm^{-1}] + (3.02 \pm 1.02) \left( \frac{SA}{V_d} \right)^2 [cm^{-2}] \quad (141)$$

The impact of throttle, normalized as delivery ratio, on friction was also investigated. Based on the three engines tested herein, friction losses during throttled operation may be predicted from the delivery ratio and friction losses at WOT using the form given in Equation (142). While the throttle data was collected at 6000 rpm, the strongly linear nature of friction power with speed indicates that this relationship would hold at other speeds, although confirmation of this result would require further testing.

$$\frac{P_f(\lambda)}{P_f|_{WOT}} = 1 - (0.89 \pm 0.30)(\lambda|_{WOT} - \lambda) \quad (142)$$

#### 4. Gas Exchange Modelling

While attempting to model gas exchange was outside of the scope of this effort, Objective 2 did include comparing the observed gas exchange to simple models to provide insight into how much improvement might be made in the scavenging process. The parametric studies accomplished for Objective 1 made it possible to evaluate the impact of each of the engine control parameters on the scavenging process. In this section, scavenging performance on the 3W-28i, 3W-55i, and 3W-85Xi engines is compared to the

perfect isothermal displacement and perfect isothermal mixing models, which are typically considered to bound scavenging performance in modern two-stroke engines. For a review of the models, the reader is referred to Chapter II, Section 5.3.1.1. Of the five control parameters, speed and throttle had the most significant impact on scavenging, and each will be discussed in its own subsection, Section 4.1 and Section 4.2, respectively. Equivalence ratio, combustion phasing, and engine cooling had minimal impacts on the scavenging process and their discussion is combined in to a single subsection, Section 4.3.

#### **4.1. Speed**

In the literature, scavenging performance is often presented as charging and trapping efficiency as functions of delivery ratio, making it easier to compare to models relating the three parameters. (Recall that short-circuiting is unity less trapping efficiency.) Figure 152 provides two such plots for each engine, and the perfect isothermal displacement and perfect isothermal mixing models are overlaid on each plot. The calculation of both delivery ratio and charging efficiency require a reference mass (volume) of the cylinder contents. The reference mass is almost universally calculated using the fresh charge conditions and the displacement volume of the engine [22:44]. The left hand plots use the displaced volume as the reference volume, consistent with convention. From a physics standpoint, this definition is somewhat misleading. Until the exhaust port closes, some of the charge will escape from the cylinder as the piston moves upwards. Thus, the effective displaced volume of the engine from a gas exchange standpoint will be somewhere between the geometric displacement and the trapped displacement, similar to the difference between the geometric compression ratio and the trapped compression ratio. Therefore, the plots on the right side in Figure 152 use the trapped volume as the reference volume.

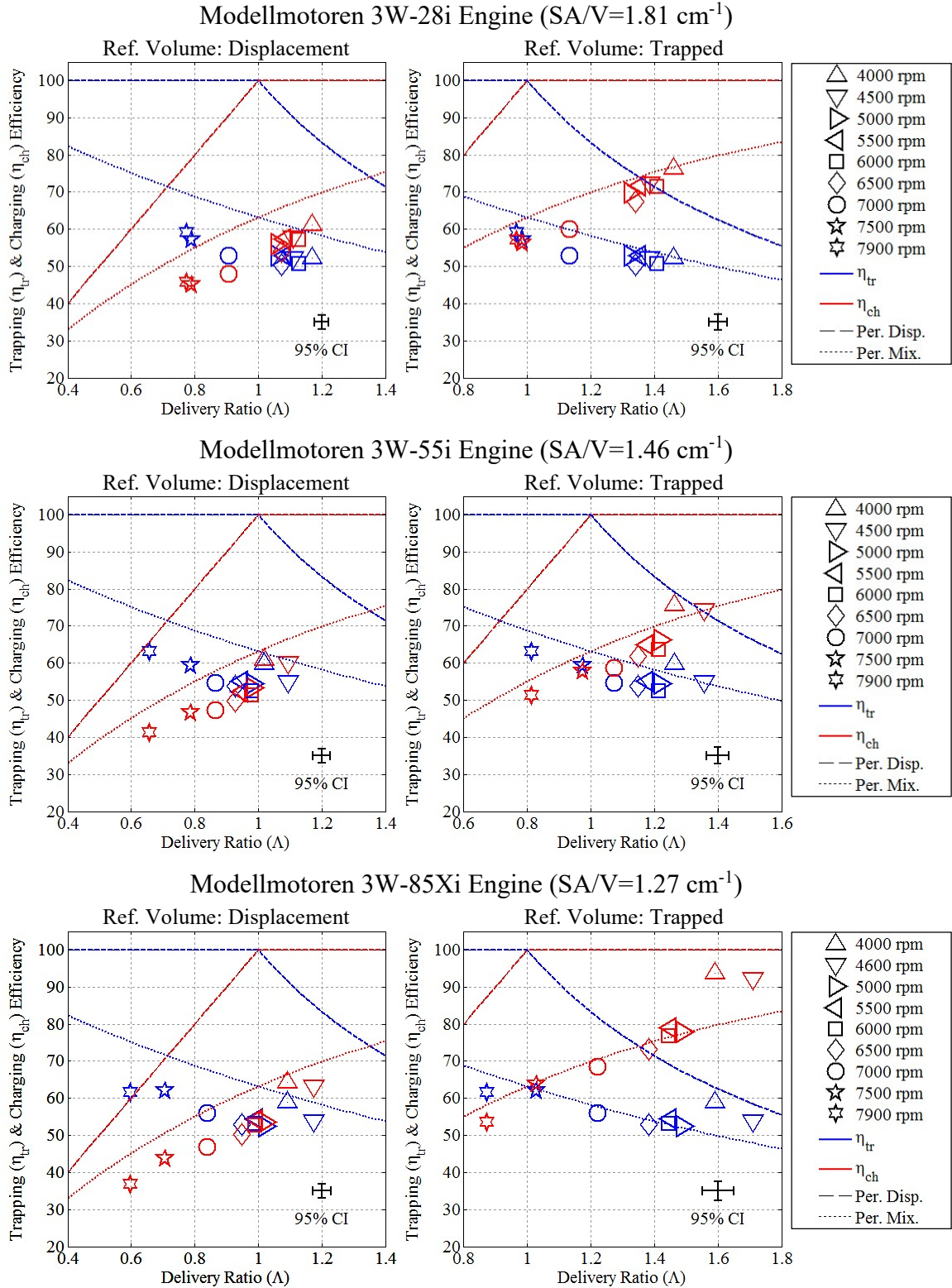


**Figure 152: Impact of speed on scavenging behavior for WOT,  $\phi=1.06\pm0.02$ , CA50=8 $\pm$ 0.5°aTDC, CHT=130 $\pm$ 2°C, for the 3W-28i, 3W-55i, and 3W-85Xi engines compared to perfect isothermal mixing and displacement models.**

Changing from the displaced volume to the trapped volume has no effect on the trapping efficiency (or short-circuiting) but will increase the value of the delivery ratio and charging efficiency by a factor of  $V_d/V_{tr}$ . The magnitude of that ratio will increase with port timing, and therefore the 3W-85Xi engine shows the largest difference between the two reference volumes. The following discussion will be based on the trapped volume results, as they are more representative of the underlying physics. The displaced volume results are included since that standard definition was used throughout the remainder of this work and because those results provide a basis for comparison to data reported using the standard literature definitions.

All three engines behaved comparably to the perfect isothermal mixing model across their tested speed ranges, slightly outperforming the model at low speeds and slightly underperforming the model at high speeds. The plots indicate two underlying issues with the scavenging performance of the engines in the COTS configuration. The first issue is that at WOT and the majority of operating conditions, the engines operated at delivery ratios in excess of unity, by more than 60% at some conditions. A delivery ratio of 1.6 means that there is not enough volume in the cylinder to hold the charge delivered (at its delivery conditions) to the engine and that 37.5% of the charge will short-circuit simply because there is not enough space in the cylinder (perfect isothermal displacement model).

There are a number of ways that an engine's delivery ratio may exceed unity. The assertion that the cylinder can hold a maximum of a delivery ratio of unity is predicated on three assumptions. The first is that the reference volume was appropriately selected. Using port closed volume as the trapped volume is a slight underestimate (as there will be some ram effect from the motion of the piston), but it is a much better estimate than the entire



displaced volume. The second is that nothing has been done to increase the fresh charge density before induction into the cylinder. Thus, turbocharged engines may trap charge in excess of a delivery ratio of unity. Crankcase compression will yield a slight density advantage, but since in-cylinder pressure is near ambient during gas exchange, the advantage is small. The third is that no heat is transferred from the burnt charge and cylinder walls to the fresh charge. Such heat transfer will lower the fresh charge density preventing the engine from even trapping charge equivalent to the delivery ratio of unity. Of those three assumptions, the isothermal assumption is the least valid, and as a result the delivery ratio above which charge must short-circuit due to insufficient space is likely less than unity on the studied engines. Therefore, the first issue with scavenging in the tested engines is the delivery of more charge than the engine can possibly trap.

The second issue is that engine scavenging behavior more closely aligns with the perfect isothermal mixing model than the perfect displacement model even when the delivery ratio is reduced to or below unity. If the problem were solely an excess of fresh charge, then reducing the delivery ratio should maintain charging efficiency (and power) while reducing short-circuiting losses. For changes in the delivery ratio at WOT driven by changes in speed, this was not the case. Actually throttling the engines resulted in slightly different behavior that is discussed in the next section. Therefore, even when the amount of charge delivered to the engines was more appropriate for the cylinder capacity, scavenging performance remained near the perfect isothermal mixing model. While short-circuiting decreased, a power penalty was also incurred.

The split of short-circuiting between that guaranteed by an excess of fresh charge (delivery ratio above unity) and that directly attributable to poor scavenging (behavior

similar to the perfect isothermal mixing model) may be estimated based on delivery ratio as shown in Equation (143), where  $\eta_{tr|per. disp.}$  is the trapping efficiency calculated using the perfect isothermal displacement model, which is a function of delivery ratio. The split varies with delivery ratio and is 0:100 at and below a delivery ratio of unity. Above unity the split is increasingly weighted toward excess charge, increasing to 40:60 at a delivery ratio of 1.2, 60:40 at a delivery ratio of 1.4, and 75:25 at a delivery ratio of 1.6.

$$\frac{SC_{\Lambda>1}}{SC_{scavenging}} = \frac{1 - \eta_{tr|per. disp.}}{\eta_{tr|per. disp.} - \eta_{tr}} \quad (143)$$

#### 4.2. Throttle

Figure 153 shows the impact of throttling the engines on scavenging performance. As in Figure 152, the left side shows results calculated using displaced volume as the reference volume and the right side shows the results calculated using the trapped volume as the reference volume. The plots confirm the behavior described during the discussion of throttle in the parametric study performed during Objective 1 (see Chapter IV, Section 3.4). As the engines were throttled, short-circuiting decreased more rapidly than charging efficiency. As each engine was throttled, performance improved from at or below the perfect isothermal mixing model to above the isothermal mixing model. In terms of overall engine performance, the result was a substantial increase in fuel conversion efficiency (up to 25%, relative) between WOT and half throttle. Chapter IV, Section 3.4 provided an example that suggested range and endurance could be improved on a fielded platform by using an oversized engine throttled at the cruise condition to reduce short-circuiting losses.

Even at throttled conditions, there is still plenty of room for improvement in the scavenging performance of small COTS two-stroke engines; there is potential to improve

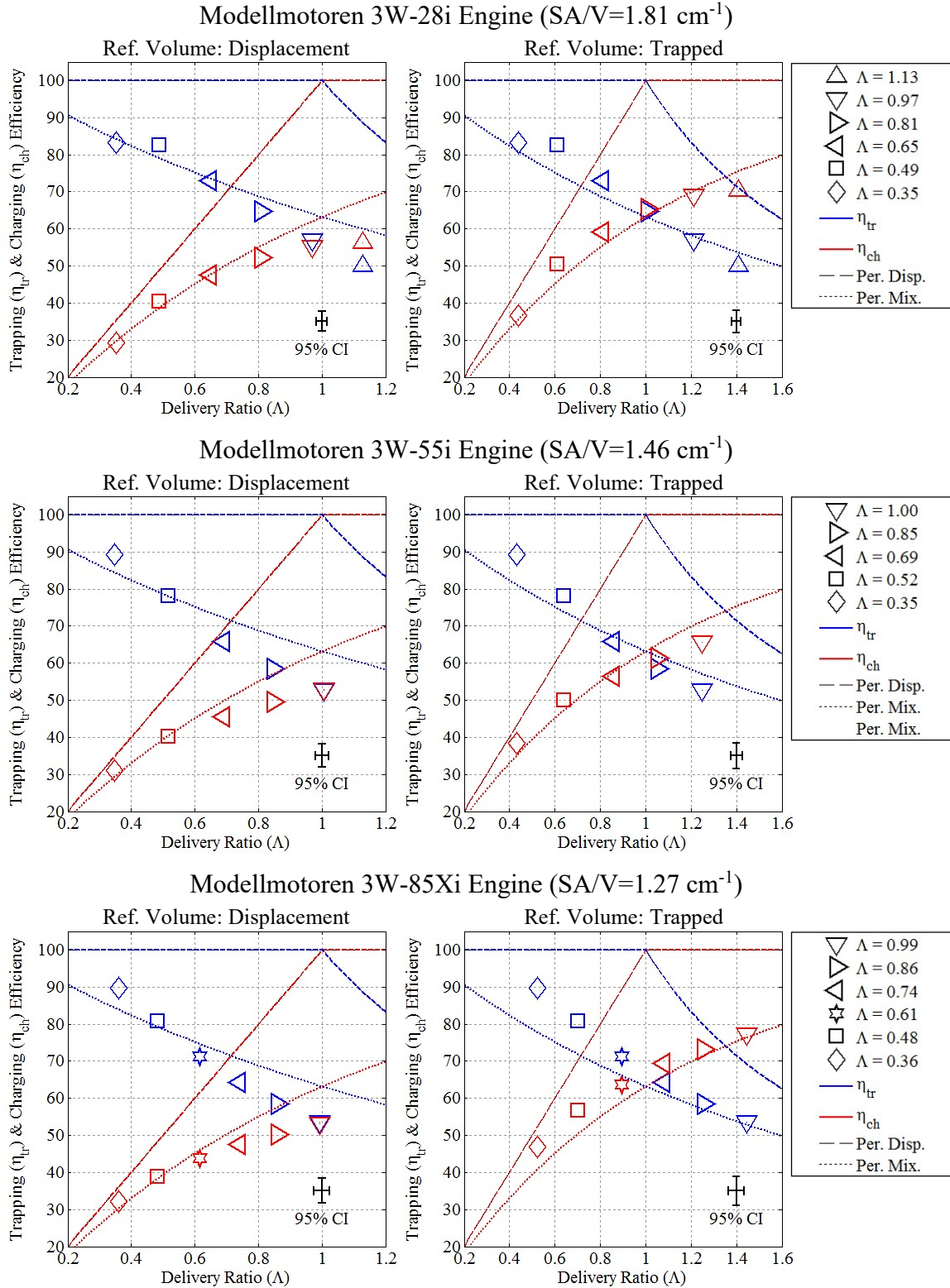


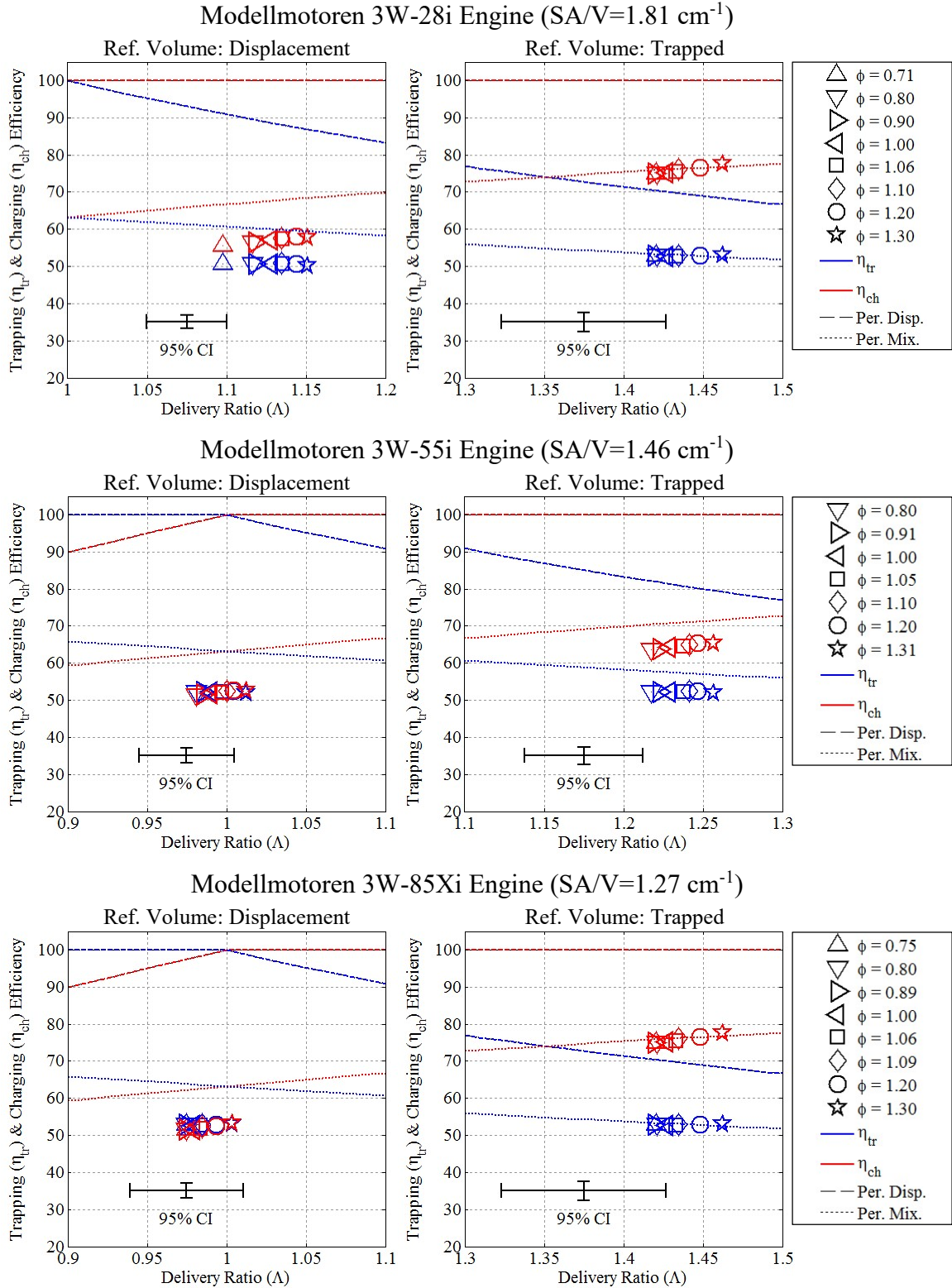
**Figure 153: Impact of throttle on scavenging behavior for 6000 rpm,  $\phi=1.06\pm0.02$ , CA50=8 $\pm$ 0.5°aTDC, CHT=130 $\pm$ 2°C, for the 3W-28i, 3W-55i, and 3W-85Xi engines compared to perfect isothermal mixing and displacement models.**

both charging efficiency and trapping efficiency. For example, at a delivery ratio of 0.6, there was at least a 10%-15% margin between the perfect isothermal displacement model and the actual charging efficiency. The WOT results show that the engines were capable of holding at least that much (10%-15% absolute) additional charge (leading to a corresponding reduction in short-circuiting), if the trapping to short-circuiting split were improved. Such improvements could be pursued through short-circuiting management as discussed in Chapter IV, Section 2.2. Those improvements would likely shift charging and trapping curves up, potentially moving the plateau of peak charging efficiency to the right. The power versus delivery ratio curves would also shift, tracking the charging efficiency.

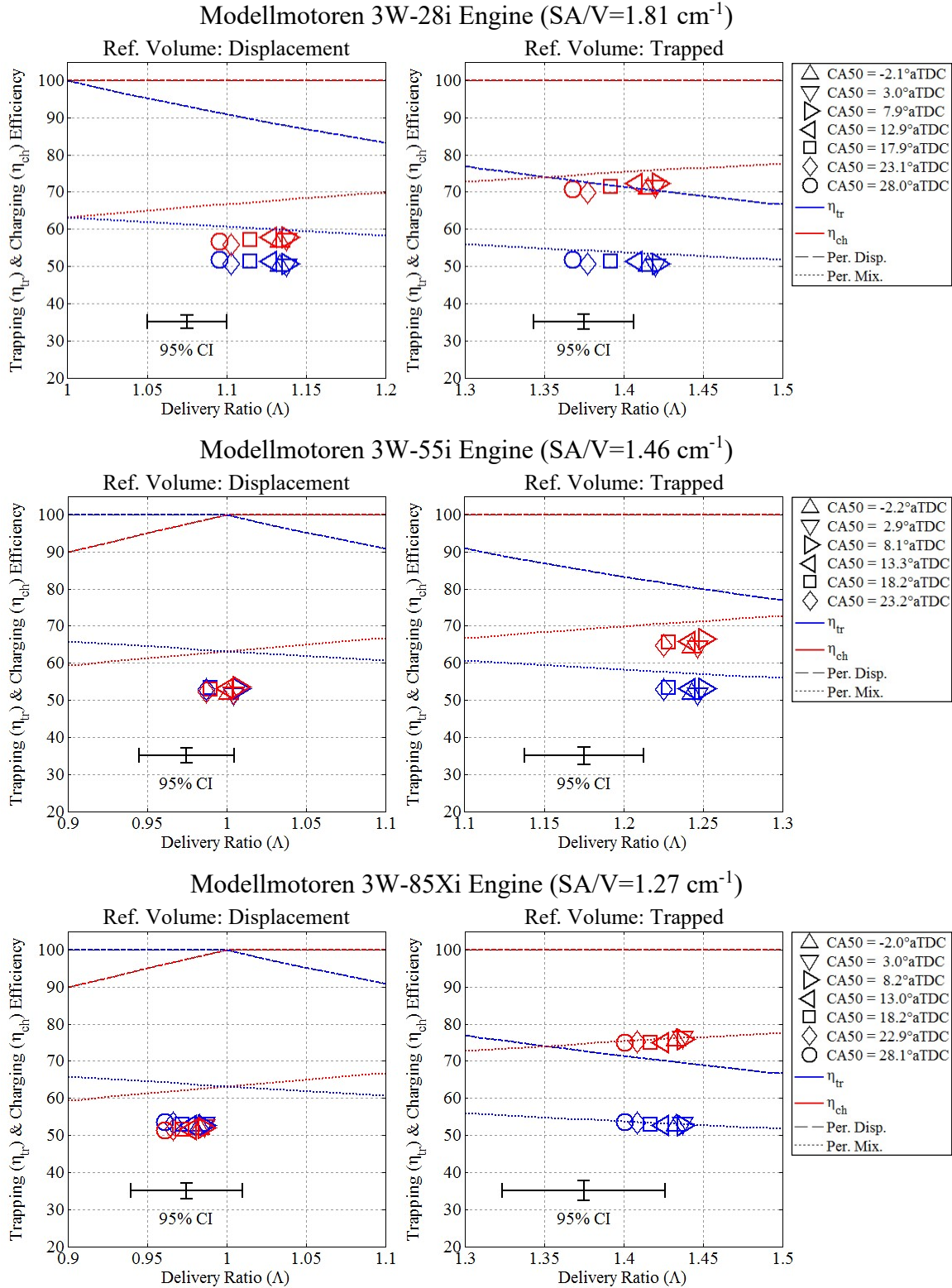
#### **4.3. Equivalence Ratio, Combustion Phasing, & Engine Head Temperature & Cooling**

Figure 154, Figure 155, and Figure 156 show the impact of equivalence ratio, combustion phasing, and engine cooling, respectively, on scavenging performance. Compared to speed and throttle, the impacts of equivalence ratio, combustion phasing, and engine cooling on scavenging were minimal, and the horizontal axes have been zoomed in compared to Figure 152 and Figure 153. Generally, performance in the three remaining cases closely tracked the perfect isothermal mixing model. Variations from the base cases tended to maintain the relative position to the models even as changes in equivalence ratio, combustion phasing, and engine cooling resulted in small changes in delivery ratio. This behavior was dissimilar to the trends observed in both speed and throttle where changes in engine speed and throttle setting improved or worsened performance relative to the model.

Increasing the equivalence ratio caused a slight charge cooling effect, increasing the delivery ratio and trapping efficiency at rich conditions. The preceding discussion regarding the loss of excess charge versus poor scavenging suggested that the improvement



**Figure 154: Impact of equivalence ratio on scavenging behavior for 6000 rpm, WOT, CA50=8±0.5°aTDC, CHT=130±2°C, for the 3W-28i, 3W-55i, and 3W-85Xi engines compared to perfect isothermal mixing and displacement models.**



**Figure 155: Impact of combustion phasing on scavenging behavior for 6000 rpm, WOT,  $\phi=1.06\pm0.02$ , CHT=130±2°C, for the 3W-28i, 3W-55i, and 3W-85Xi engines compared to perfect isothermal mixing and displacement models.**



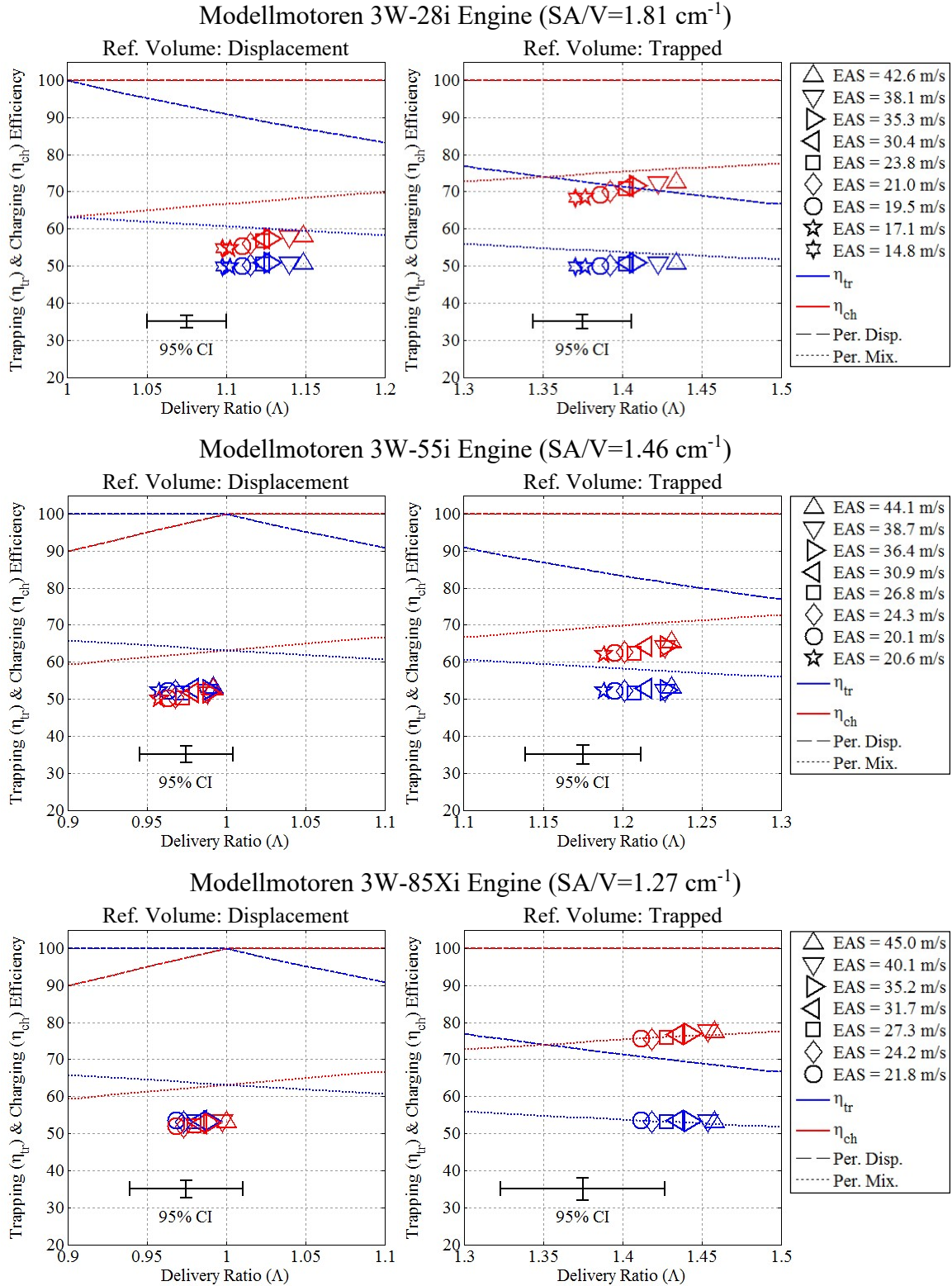


**Figure 156: Impact of cooling air speed on scavenging behavior for 6000 rpm, WOT,  $\phi=1.06\pm0.02$ , CA50=8 $\pm$ 0.5°aTDC, for the 3W-28i, 3W-55i, and 3W-85Xi engines compared to perfect isothermal mixing and displacement models.**

was from improved retention of excess charge. Retarding combustion phasing beyond MBT timing led to a small decrease in delivery ratio and trapping efficiency. Retarding the combustion phasing pushed the combustion event later into the cycle reducing the energy lost to heat transfer from the head as well as the energy converted to power. As a consequence the energy available for transfer to the fresh charge increased, lowering charge density and causing the opposite behavior of charge cooling from rich operation. Finally, increasing engine cooling reduced heat transfer to the fresh charge resulting in higher charge density as well as improved delivery ratio and trapping efficiency. The impacts of all of these changes on engine performance metrics including power and fuel conversion efficiency were discussed in Chapter IV, Section 3.

#### **4.4. Gas Exchange Modelling Summary**

While attempting to model gas exchange was outside of the scope of this effort, Objective 2 did include comparing the observed gas exchange to simple models to provide insight into how much improvement might be made in the scavenging process. The parametric studies accomplished for Objective 1 made it possible to evaluate the impact of each of the engine control parameters on the scavenging process. The scavenging performance of the 3W-28i, 3W-55i, and 3W-85Xi engines was compared to the perfect isothermal displacement and perfect isothermal mixing models, which are typically considered to bound scavenging performance in modern two-stroke engines. Over the entire operating range, the scavenging performance was comparable to the perfect isothermal mixing model  $\pm 10\%$ , absolute, generally taken as the worst case scenario for larger modern engines. For most operating conditions the engines slightly underperformed the model by less than 5%. Two factors drove the high short-circuiting observed in the



studied engines: excess fresh charge delivered to the engines beyond the cylinder capacity and poor scavenging performance comparable to the perfect isothermal mixing model even for delivery ratios below unity where the cylinder could accommodate the entire volume of delivered charge.

Of the five control parameters, speed and throttle had the most significant impacts on scavenging. Increasing engine speed tended to decrease delivery ratio, but also to improve trapping and charging, relative the perfect isothermal mixing model. Decreasing throttle had a similar effect. Equivalence ratio, combustion phasing, and engine cooling had minimal impacts on the scavenging process. For an aircraft designer seeking to model a 10-100 cm<sup>3</sup> displacement, two-stroke engine, the results of this work indicate that the perfect isothermal mixing model using the trapped volume as the reference volume would predict charging efficiency and trapping efficiency within  $\pm 10\%$  (absolute) at all conditions and with  $\pm 5\%$  (absolute) for most conditions. This assumes that no modifications have been made to the COTS engine to specifically improve scavenging performance. Moreover, it is likely that as larger scale engine technology, especially port design, permeates into the 10-100cm<sup>3</sup> displacement, two-stroke engine market that that the perfect isothermal mixing model will become a conservative estimate as it is for larger engines.

## **5. Summary: Objective 2**

The goal of Objective 2 was to investigate models for heat transfer and friction losses in small, 10-100 cm<sup>3</sup> displacement ICEs. While the objective did not include modelling gas exchange, it did included comparing the observed gas exchange to simple models to provide insight into how much improvement might be made in the scavenging process.

The remainder of this chapter was divided into three sections addressing heat transfer modelling, friction loss modelling, and gas exchange modelling.

The first section (Section 2) investigated heat transfer models for 10-100 cm<sup>3</sup> displacement, SI two-stroke engines. Due to limited equipment availability, only the 3W-28i and 3W-55i engines were included in the heat transfer study. Most models calculate in-cylinder temperature using the in-cylinder pressure, which is easier to measure than in-cylinder temperature. Two temperature models based on the ideal gas law, one based on a trapped mass that varied with changing engine operating condition and one that used an average trapped mass that did not change with operating condition, were compared to temperature results from a line-of-sight measurement through the combustion dome made using TLAS. Compared to the models, the temperature measured using TLAS exhibited an earlier, sharper, and higher peak caused by the flame front traversing the line-of-sight, as well as a more rapid drop due to localized cooling. In most cases the modelled temperatures captured the qualitative behavior of the measured temperature as engine controls were swept over their operational range. Key exceptions were the speed and throttle sweeps. The results demonstrated that it was difficult to calculate a consistent trapped mass as speed, temperature, and cooling all affected the in-cylinder temperature and pressure measurements used in the calculation. Provided the ability to estimate the effect of changing operating condition on the trapped mass, the variable mass model was more appropriate.

Working with the modelled temperatures as well as delayed availability of the TLAS system cut into the time and resources for heat transfer modelling. Therefore, the heat transfer modelling effort was limited to an initial evaluation of the spatially and temporally

averaged Taylor and Toong model, originally developed for automotive and larger scale engines. Of the two temperature models, the variable mass model provided a visually better fit, and that fit is reproduced in Equation (144). However, the correlation was relatively weak and the fit should only be used as an order-of-magnitude estimate. Based on the results, the Taylor and Toong model was not formulated to handle variations in throttle, speed, and cooling and was highly sensitive to the in-cylinder temperature, which was difficult to model in the first place. Additionally, coefficients provided in the literature for larger engines were not appropriate for the engines studied here. Future efforts could improve and adapt the model by improving the calculation of the trapped mass, including the characteristic velocity of the coolant, and adapting the characteristic velocity used in the Reynolds number to reflect engine operation speed in lieu of throttle setting.

$$Nu = (9.4 \pm 5.8)Re^{(0.31 \pm 0.1)} \quad (144)$$

The second section (Section 3) investigated friction loss modelling. Due to the motored friction testing methods, only speed and throttle could be studied. Compared to larger engines where FMEP is typically best fit with a quadratic function of engine speed [21:722, 22:368], the studied engines had nearly constant values of FMEP similar to smaller glow fuel engines [16]. Normalized friction losses in the tested engines were generally lower than in automotive and larger scale engines since the tested engines had no accessory type losses (cooling pumps, valve trains in the case of four-stroke engines, and so forth). The data from the tested engines was combined with data from the literature for smaller (glow fuel) two-stroke engines with similar friction sources [16]. The results showed that friction scales with surface area to volume ratio; a suggested correlation for crankcase scavenged two-stroke engines less than 100 cm<sup>3</sup> displacement is shown in Equation (145).

$$\begin{aligned}
FMEP[kPa] = & (-0.5 \pm 17.8) + (62.5 \pm 9.2) \frac{SA}{V_d} [cm^{-1}] \\
& + (3.02 \pm 1.02) \left( \frac{SA}{V_d} \right)^2 [cm^{-2}]
\end{aligned} \tag{145}$$

The impact of throttle, normalized as delivery ratio, on friction was also investigated. Friction losses during throttled operation may be predicted from delivery ratio and friction losses at WOT using the form given in Equation (146). The WOT friction losses could be predicted from surface area to volume ratio using Equation (145). The strongly linear nature of normalized friction losses with speed indicates that this relationship would hold at speeds other than the test speed (6000 rpm); confirmation would require further testing.

$$\frac{P_f(\Lambda)}{P_f|_{WOT}} = 1 - (0.89 \pm 0.30)(\Lambda|_{WOT} - \Lambda) \tag{146}$$

The third section (Section 4) compared gas exchange to historical models and discussed the scavenging performance observed in the studied engines. Attempting to model gas exchange was outside of the scope of this effort, so Objective 2 compared the observed gas exchange to simple models to provide insight into the scavenging process in 10-100 cm<sup>3</sup> displacement, COTS, two-stroke engines. The scavenging performance of the studied engines was compared to the perfect isothermal displacement and perfect isothermal mixing models, typically considered to bound scavenging performance in modern two-stroke engines. Over the operating range, the engine scavenging performance was comparable to the perfect isothermal mixing model, generally taken as the worst case scenario for larger modern engines. Two factors drove the high short-circuiting observed during Objective 1: excess fresh charge delivered to the engine beyond the cylinder capacity and poor scavenging performance comparable to the perfect isothermal mixing

model even for delivery ratios below unity. Of the five control parameters, speed and throttle had the most significant impacts on scavenging. Increasing engine speed tended to increase delivery ratio, but also to improve trapping and charging, relative the perfect isothermal mixing model. Decreasing throttle had a similar effect. Equivalence ratio, combustion phasing, and engine cooling all had minimal impacts on the scavenging process. For an aircraft designer seeking to model a 10-100 cm<sup>3</sup> displacement, two-stroke engine, the results of this work indicate that the perfect isothermal mixing model using the trapped volume as the reference volume would predict charging efficiency and trapping efficiency within about  $\pm 10\%$  (absolute) for essentially all conditions and  $\pm 5\%$  for most conditions. For most operating conditions, the engines underperformed the perfect isothermal mixing model. The applicability of the model assumes that no modifications have been made to the COTS engine to specifically improve scavenging performance. Moreover, as larger engine technology permeates into the 10-100 cm<sup>3</sup> displacement, two-stroke engine market the perfect isothermal mixing will likely become a conservative estimate as it is for larger two-stroke engines.

## VI Objective 3: Fuel AKI Relaxation

### 1. Chapter Overview

The goals of Objective 3 were to identify relationships between the fuel AKI requirement, loss mechanisms, and engine size, to quantify the performance impacts of switching from 98 ON fuel (manufacturer recommended) to approximately 20 ON, logistically supported fuel (JP-8, Jet A/Jet A-1, and diesel), and to determine which engine control parameters were most effective at controlling knock in 10-100 cm<sup>3</sup> displacement engines. While the logistically supported fuels have different additive packages, they are comparable from a knock standpoint. Low AKI fuels are often referred to as ‘heavy fuel’, describing the position of typical low AKI fuels as distillation products. Gasoline and other high AKI fuel fuels are described as ‘light fuels’ although such nomenclature is uncommon in engine literature. The results of Objective 3 are split into three sections. The first section (Section 2) examines KLIMEP, power, and burn angle for 10 different PRF blends ranging from 0 ON to 98 ON. Day to day variations in engine operating conditions made trends in burn angle and efficiency difficult to resolve, especially on the 3W-55i engine where testing was conducted over multiple weeks. Therefore, repeat tests of 98 ON and 20 ON were performed and the second section (Section 3) explores the impact of switching from 98 ON to 20 ON fuel on burn angle, power, and efficiency. Finally, the third section (Section 4) examines the impact of combustion phasing, equivalence ratio, and head temperature on the knock limit of each engine. Impacts on the knock limit are tied back to the parametric study on engine control parameters and losses from Objective 1.

## 2. Impact of Fuel AKI on KLIMEP, Power, and Burn Angle: All ONs

The first goal of Objective 3 was to establish the fuel AKI requirements for the engines, and determine the feasibility, from a combustion standpoint, of running COTS engines on low AKI fuel. It is important to note that the engine testing configuration used in this study employed throttle body fuel injection in lieu of the stock air carburetor. As a consequence, engine operation was closer to stoichiometric (equivalence ratio of 1.05 to 1.07) and more consistent than COTS operation. The impact of equivalence ratio on the knock limit is explored as part of Section 4.

From a combustion standpoint, the primary obstacle to lowering the fuel AKI for an SI engine is abnormal combustion, typically knock. For the purpose of this discussion, the term ‘knock’ is used to describe a specific subset of abnormal combustion: the ignition of the end-gas from a source other than the flame front initiated by the spark plug that results in rapid heat release and high frequency pressure waves inside the cylinder. To combat knock, engines may be throttled (the method used in this work, example Figure 157) or the spark timing may be retarded, in both cases incurring a power penalty. Therefore, knock-limited operation is typically described in terms of the KLIMEP, the maximum power that can be produced at a given condition. Figure 157 shows KLIMEP values for each of the engines on ten different PRF blends ranging from 0 ON-98 ON. Red points were knock-limited; orange points indicate that knock was observed in the pressure trace, but that it was insufficiently severe to warrant throttling the engine.

Recalling the Livengood-Wu integral (Chapter II, Section 2.6.3), the criteria for auto ignition (that can lead to knock) can be described as the integral of a function of mixture, temperature, and pressure over time, where autoignition occurs when the integral reaches

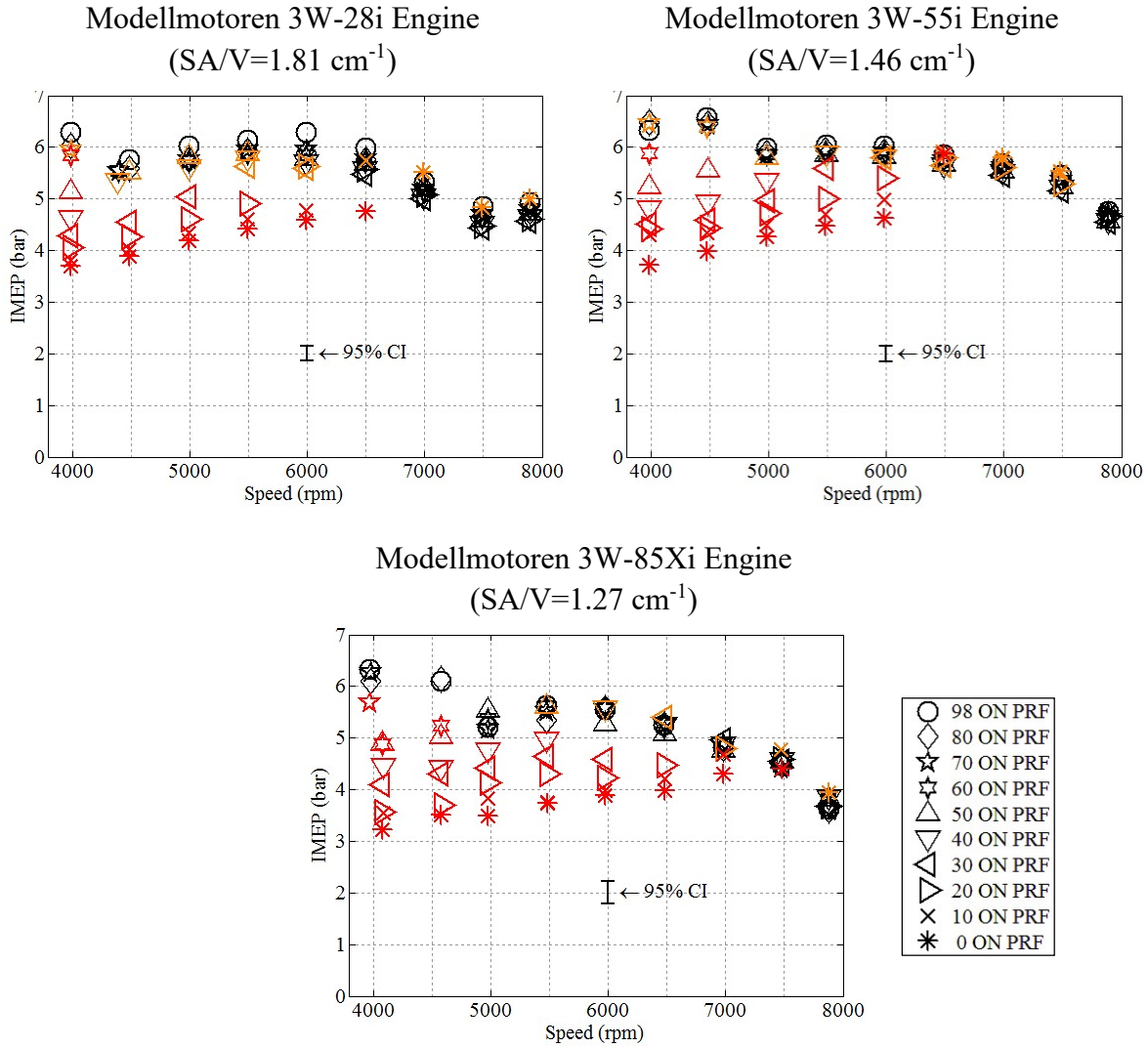


**Figure 157: Knock-limited IMEP for  $\phi=1.06\pm0.02$ , CA50=8 $\pm$ 0.5 $^\circ$ aTDC, & CHT=130 $\pm$ 2 $^\circ$ C. Red points were knock-limited. Orange points indicate the presence of abnormal combustion.**

unity. Obert offers a similar explanation that will be more illustrative for the proceeding discussion [282:105]. For any given fuel air mixture there exists a three-dimensional surface described by temperature, induction time, and density (pressure) as illustrated in Figure 158. For conditions above this surface, autoignition (abnormal combustion) occurs.



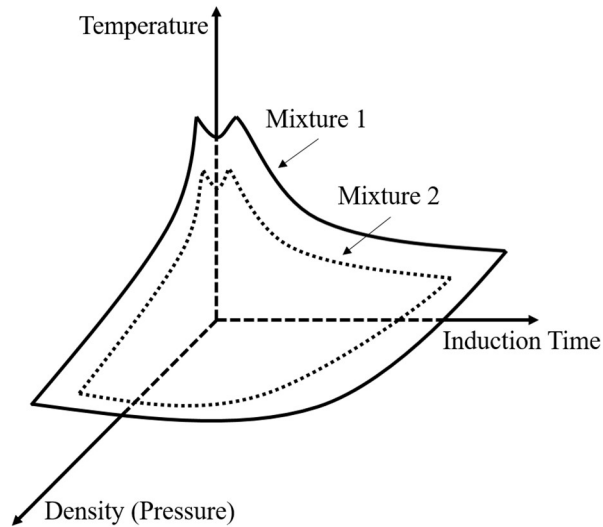


**Figure 158: Idealized autoignition criteria based on temperature, density (pressure), and induction time for two fuel air mixtures. Autoignition will occur for conditions above the surface for the fuel air mixture. Adapted from Obert [282:105].**

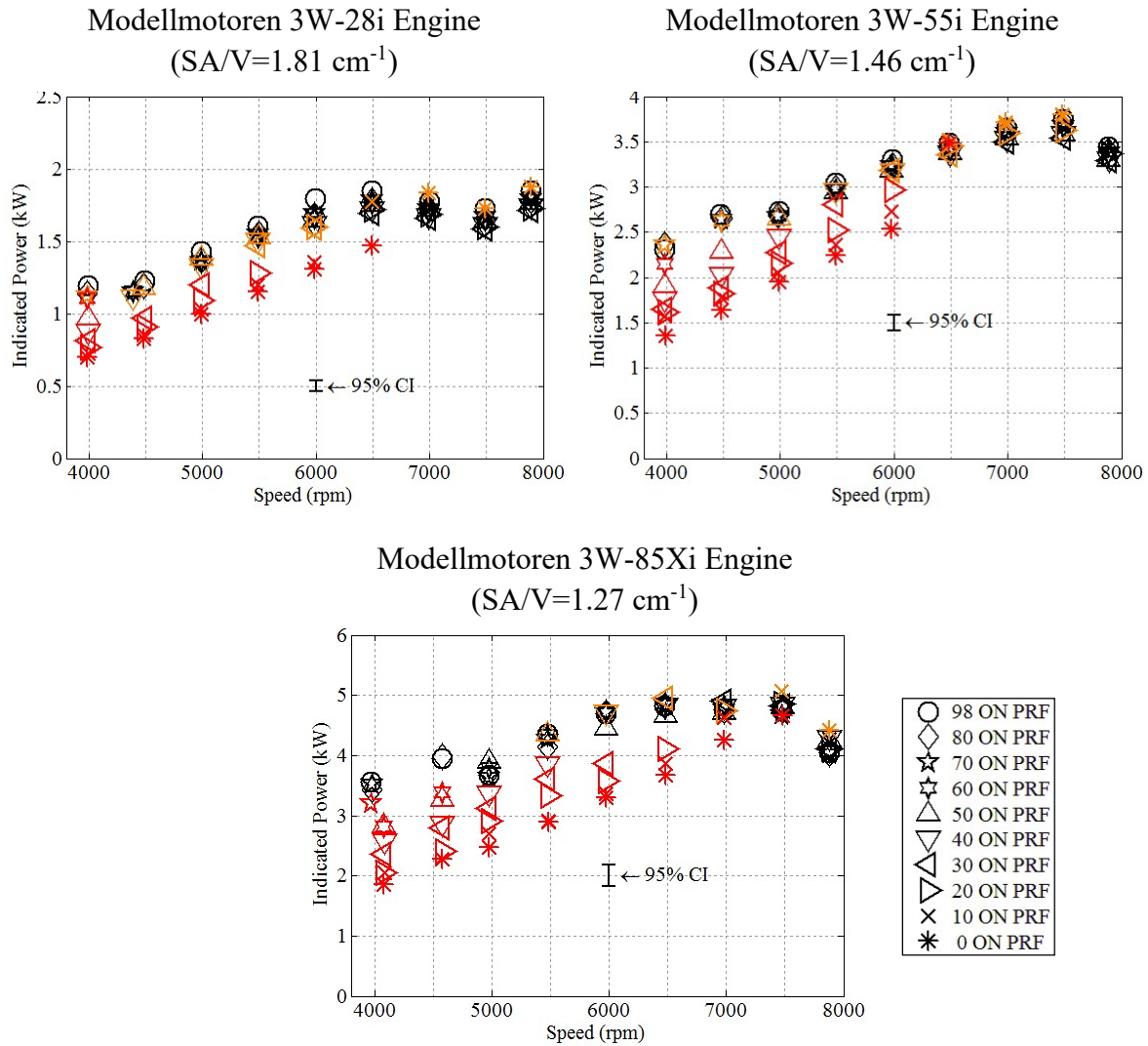
To prevent autoignition and in turn knock, one or more of the three conditions must be adjusted (reduced) so the final point lies below the autoignition surface.

Figure 157 shows that knock in these engines was strongly speed dependent. Increasing engine speed not only decreased the burn duration due to improved mixing, but it also decreased the residence time of the fresh charge in the cylinder prior to combustion, allowing normal combustion to occur prior to reaching the autoignition condition in the end gas. In addition to speed, engine size also impacted the observed knock limit. Comparing 20 ON PRF performance, the 3W-85Xi engine was knock-limited at and below 6500 rpm, while the 3W-55i and 3W-28i engines exhibited less restrictive limits of 6000 rpm and 5500 rpm, respectively. Similarly, knock was observed in the 3W-85Xi engine about 10 ON higher for each speed than in the other two engines. These observations support the hypothesis that decreasing engine size provides a margin against knock.

As described above, knock management is about preventing the fresh charge, specifically the end gas, from reaching its auto-ignition criteria by maintaining the operating point below the autoignition surface in Figure 158. For a given speed, the induction time (residence time) of the fresh charge in the warm cylinder was primarily a function of the scavenge (not exhaust) port timing, which was comparable for all three engines. Charge density and pressure were primarily functions of compression ratio. As discussed previously, the effective compression ratio decreased with increasing displacement, which would increase knock resistance. Therefore, for a given fuel blend (equivalence ratio was held constant during these tests), decreasing engine size increased knock resistance due to reduced heat transfer to and warming of the fresh charge. Heat transfer to the fresh charge is controlled by the gas exchange process and in turn the port timing, engine geometry, and throttle as well as heat rejection to the exhaust gas and through the cylinder head.

As discussed in Chapter IV, Section 2.3, increasing surface area to volume ratio with decreasing engine size shifted thermal loading from the exhaust gases to the cylinder head, reducing heat transfer to the fresh charge. Furthermore, while port design and geometry are not the traditional metrics one thinks of when discussing engine size, they are linked to engine size, at least for given classes of engines. For example, the larger volume of the 3W-85Xi engine drove the design decision to raise exhaust port timing compared to the smaller engines. Thus, based on KLIMEP data, for the studied engines decreasing engine size did increase the resistance to knock when operating on a low AKI fuel due to a variety of factors that reduced the end-gas temperature and the propensity to auto-ignite.

While IMEP provides a normalized metric to compare engines of different sizes (and operational speed ranges), a designer seeking to convert a COTS engine to heavy fuel for use on an aircraft might be more concerned about the impact on raw power. Figure 159 shows the knock-limited indicated power for the engines tested in this study. In each case, the engine was capable of developing peak power (as tested on 98 ON) running on 20 ON



**Figure 159: Knock-limited indicated power for  $\phi=1.06\pm0.02$ , CA50=8 $\pm0.5^\circ$ aTDC, & CHT=130 $\pm2^\circ$ C. Red points were knock-limited. Orange points indicate the presence of abnormal combustion.**

fuel (JP-8/diesel equivalent) since the peak power points tended to occur higher in the operational speed range. In the case of the 3W-85Xi engine the peak power occurred at 6500 rpm-7500 rpm; the lower end of this range was knock-limited on 20 ON PRF fuel, while abnormal combustion below the knock limit was observed in the upper end of the range. This underscores the IMEP results that indicated the larger 3W-85Xi engine was in fact less knock resistant than the smaller engines and would be more difficult to convert to low AKI fuel.

Based on the IMEP and power results, the feasibility of converting a small RPA propulsion system to heavy fuel is dependent on the intended operational speed range of the propeller or load, the power requirements, and to an extent engine size. At higher operational speeds (at and above 7000 rpm) conversion of a 10-100 cm<sup>3</sup> displacement, two-stroke engine appears feasible with minimal management of abnormal combustion. Lower speed operation would require knock mitigation strategies and below 4000 rpm, the degree of throttling required to mitigate knock may preclude producing useful power.

So far the discussion has focused on the abnormal combustion (specifically knock) aspect of low AKI fuel conversion, and has ignored a number of other aspects of conversion that deserve mention. First, the engines in this study were converted from air carburetors to a throttle body fuel injection systems. In the case of the highly volatile PRF blends used in this effort, fuel injection primarily provided repeatable, consistent fuel metering. For actual heavy fuels such as diesel and JP-8, fuel injection serves a second critical role. As noted in virtually every prior heavy fuel conversion effort (see Chapter II, Sections 6.3 & 6.4) one of the key challenges was vaporizing the fuel, especially at cold operating conditions. Carburetors designed for volatile fuels such as gasoline were simply

not up to the task, and as shown by both Cathcart *et al.* [15] and Duddy *et al.* [38], fuel injection overcomes this problem. Second, the engines in this study were also converted from stock ECUs with a linear timing map to an ECU with an adjustable timing map. As will be shown in Section 4, combustion phasing had the most significant control authority over abnormal combustion (compared to cooling and equivalence ratio), and thus the ability to manage combustion phasing is also critical to the conversion process. The third and final assumption was that the lubricity of the heavy fuel mixture was sufficient to lubricate the engine (at least as well as the recommended gasoline oil mixture). Based on the work of Lee *et al.* [260], 2% two-stroke oil (fortuitously, the study used the same oil utilized herein) was sufficient for proper lubrication. With these qualifications in mind, this study has shown that small two-stroke engines can be converted to run on low AKI fuel with minimal impact to peak power, that abnormal combustion is only a significant impediment at low operational speeds, and that smaller engines possess a greater resistance to abnormal combustion.

Figure 160 and Figure 161 show the total burn angle at each operating condition for the tested engines. Generally speaking, as engine speed increased combustion took longer in crank angle space (since the total time for 1 CAD of revolution decreased), but was shorter in time space due to improved mixing and turbulence. The 3W-28i engine displayed somewhat unusual behavior at and above 7000 rpm, where burn angle increased drastically in crank angle space and to a small extent in time space. As discussed in Chapter IV, Section 2.2 this engine experienced a significant drop in airflow (per cycle) at these operating conditions. The reduction of fresh charge and corresponding increase in residuals slowed the burn and increased the burn angle for all tested fuel blends at those

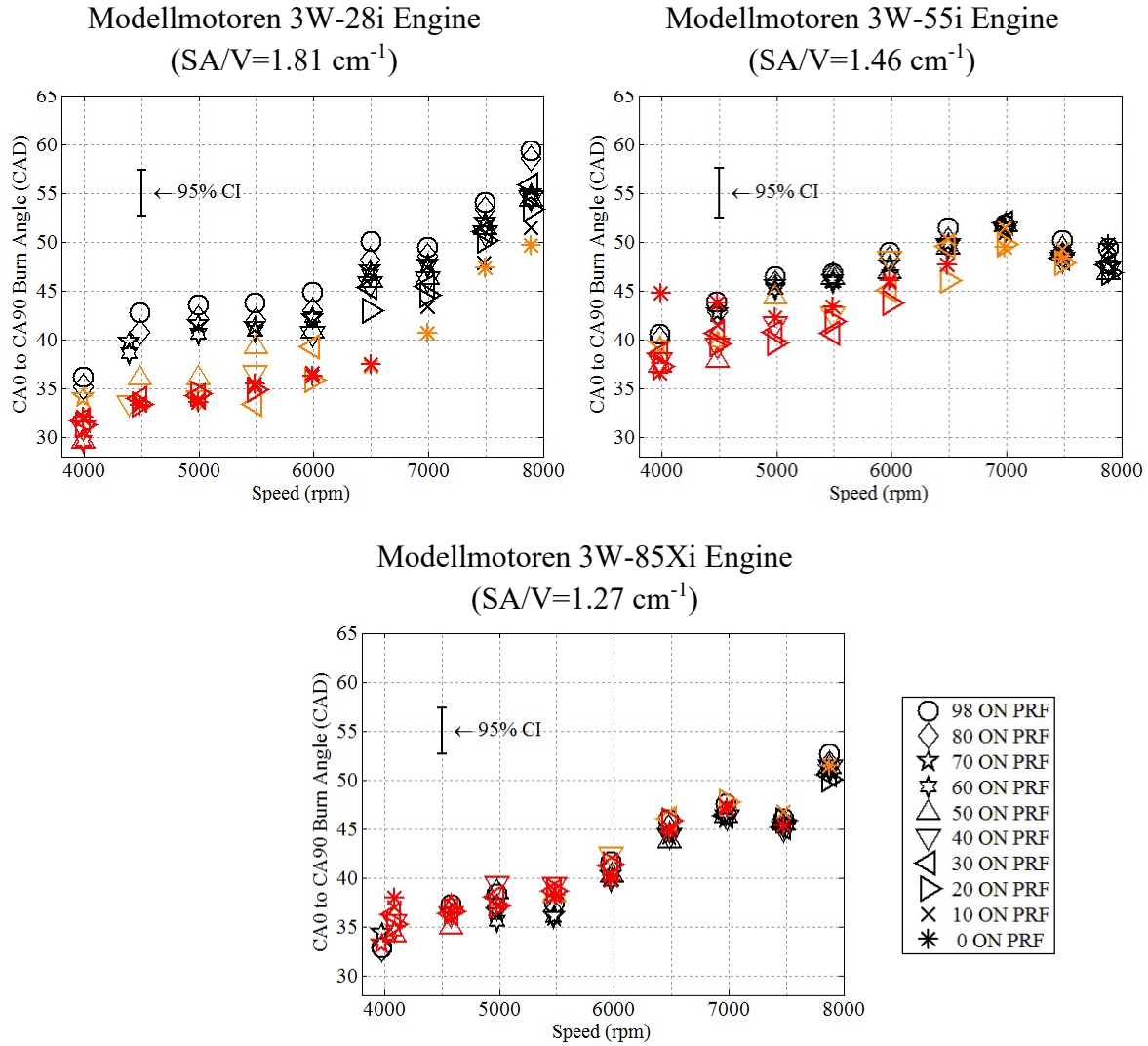


**Figure 160: Total burn angle (CA0-CA90) in CAD for  $\phi=1.06\pm0.02$ , CHT=130 $\pm$ 2°C, & CA50=8 $\pm$ 0.5°aTDC. Red points were knock-limited. Orange points indicate the presence of abnormal combustion.**

conditions. Similar comments apply to the breathing of the 3W-85Xi engine at high speeds, specifically at 7900 rpm.

Lower AKI fuels typically have shorter ignition delays [80] and higher laminar flame speeds [23] than higher AKI fuels. As a result, Wilson *et al.* [14] hypothesized that operation on low AKI fuel would shorten the burn angle and improve power/efficiency by

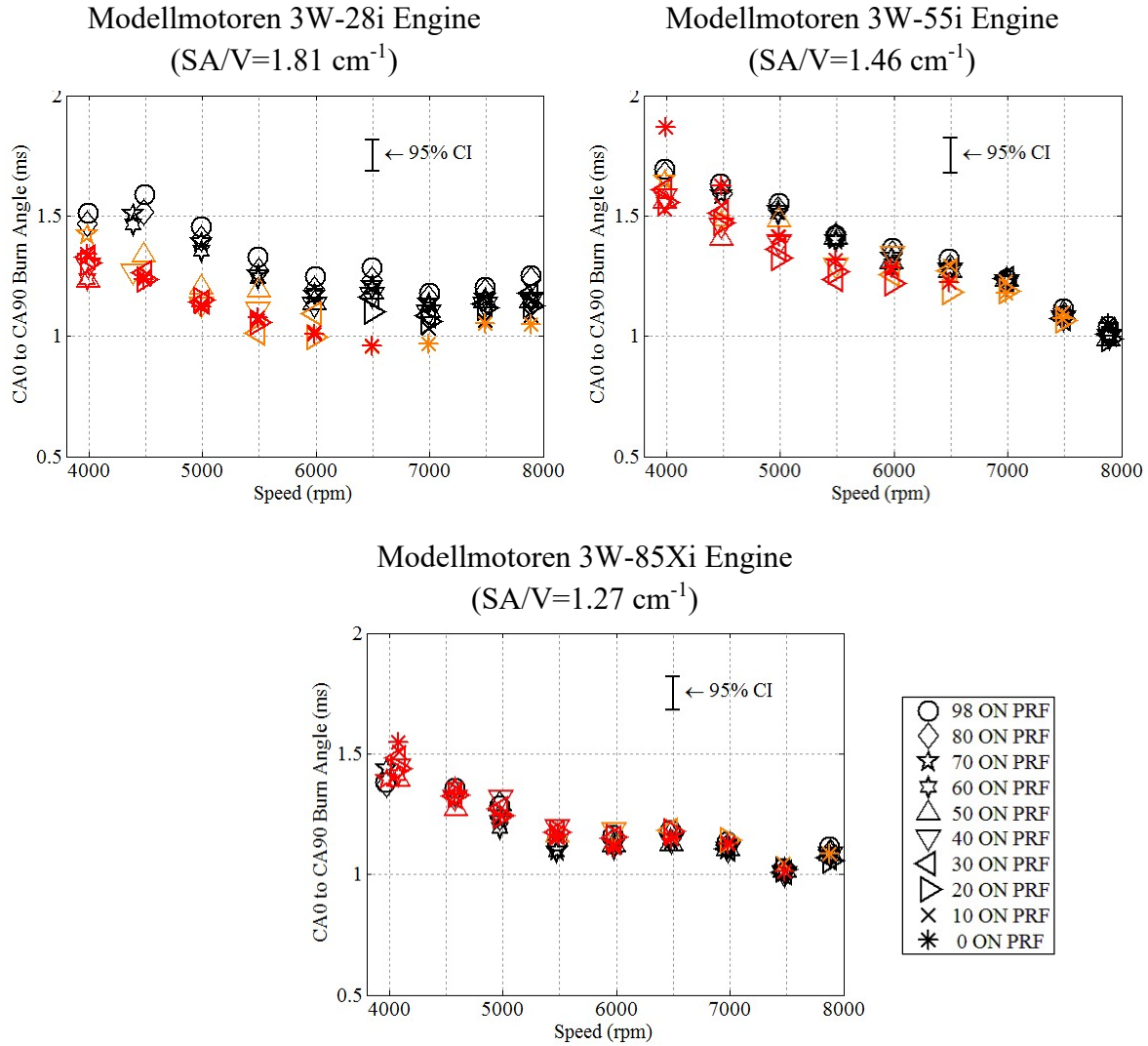


**Figure 161: Total burn angle (CA0-CA90) in milliseconds for  $\phi=1.06\pm0.02$ , CHT=130 $\pm$ 2°C, & CA50=8 $\pm$ 0.5°aTDC. Red points were knock-limited. Orange points indicate the presence of abnormal combustion.**

creating narrower, taller pressure peaks. Generally, all three engines exhibit such a trend, although it was somewhat noisy. Considering only knock free operating points, the CA0-CA90 (total) burn angle was reduced by about 5-6 CAD in the 3W-28i engine between 98 ON and 20 ON operation. Similar trends were observed in the 3W-55i engine and the 3W-85Xi engines, although the change in burn angle was less pronounced with

increasing engine size, dropping to about 3-4 CAD and 2-3 CAD, respectively. Figure 162 zooms in on the CA0-CA90 burn angle at 7900 rpm for each of the tested engines, and is indicative of the trends observed in knock free burn angles as fuel ON was reduced. Intuitively, one might expect the larger engine to exhibit the greatest reduction in burn angle from reducing the fuel ON. Indeed, higher flame speeds from lower AKI fuels should translate to a greater reduction in burn angle for larger cylinder volumes. Yet, the opposite trend was observed in these engines. The next section will examine the impact of fuel AKI on burn angle in greater detail, looking at the effects of changing from 98 ON PRF to 20 ON PRF on the spark timing as well as on the CA0-CA10 and CA10-CA90 burn angles.

In the interim, there are a number of intertwined factors that influence the total burn duration. Turbulence and mixing drive the creation of a flammable mixture as well as the

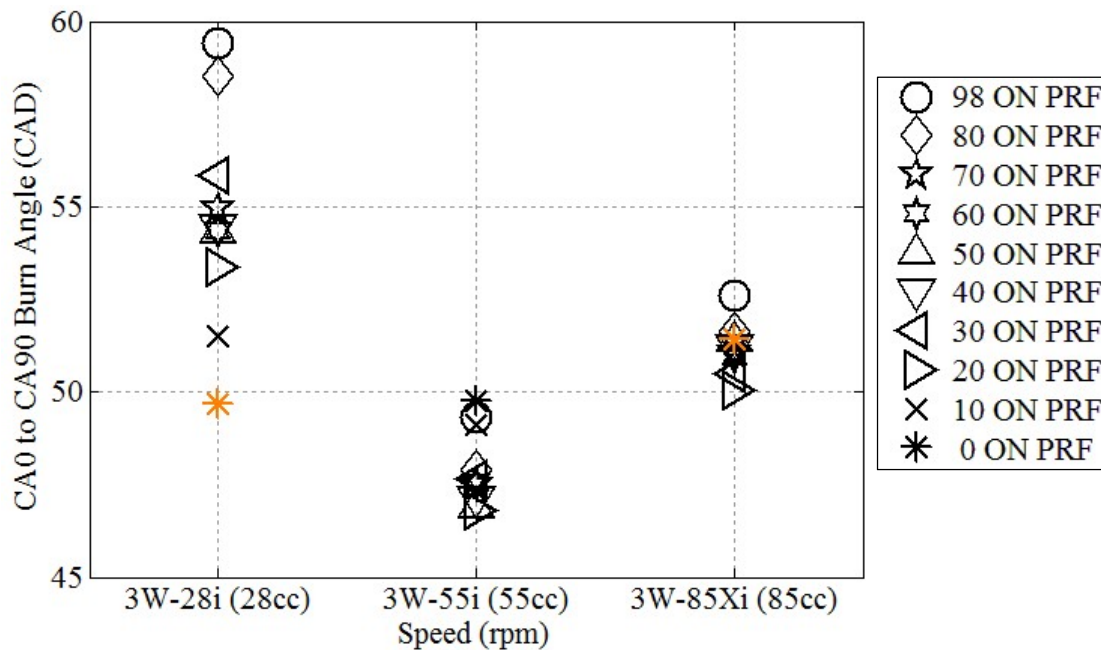


**Figure 162: Total burn angle (CA0-CA90) in CAD for 7900 rpm,  $\phi=1.06\pm0.02$ , CHT= $130\pm2^\circ\text{C}$ , & CA50= $8\pm0.5^\circ\text{aTDC}$ . Red points were knock-limited. Orange points indicate the presence of abnormal combustion.**



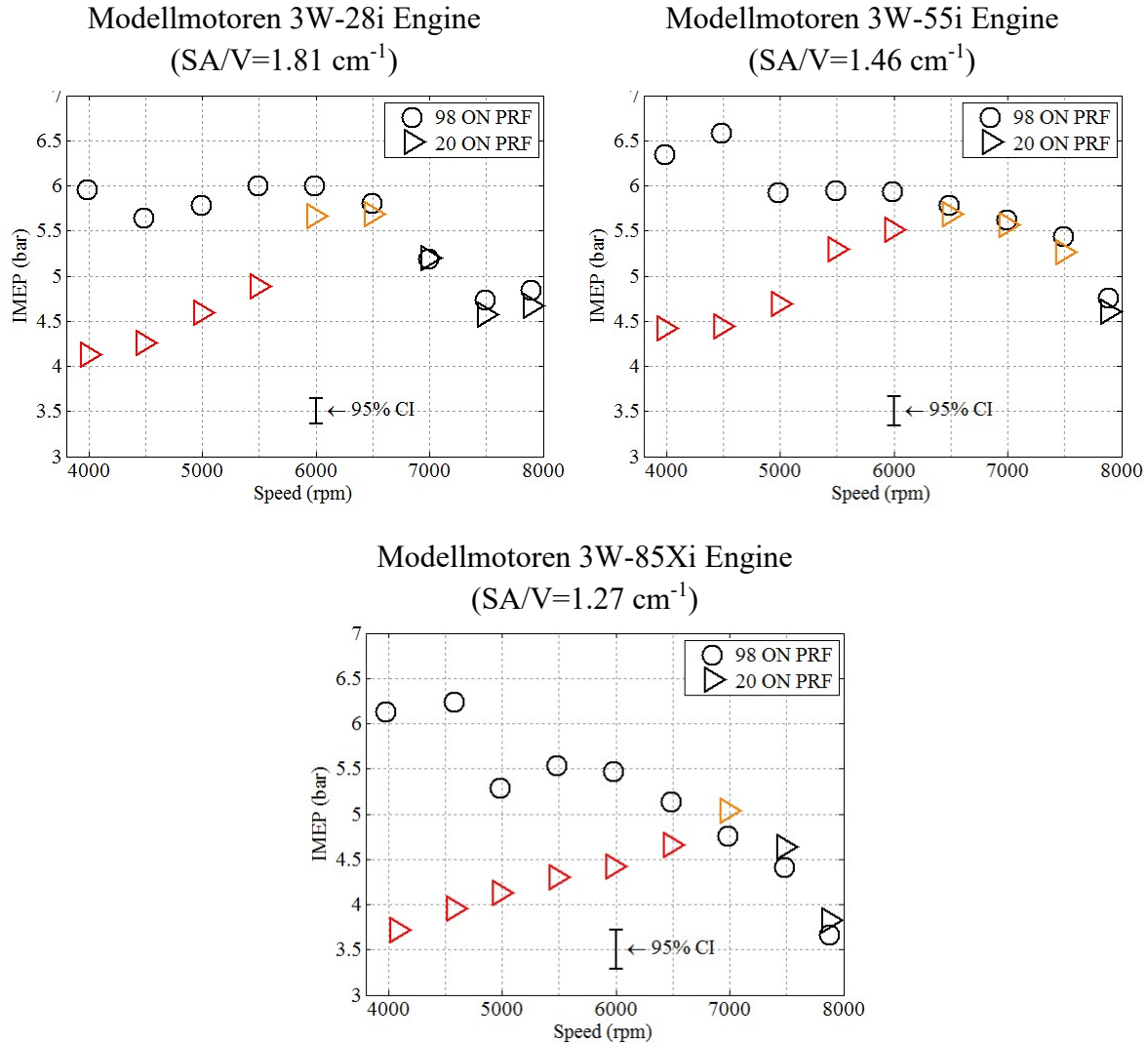
convective propagation of the flame. Temperature and pressure control pre-flame reactions (which enhance the burn rates of all fuels, not just those prone to knock) and ignition delays. Fuel type also influences the chemical delay (time to ignite the fuel) and the laminar flame speed. A full discussion of these interactions is outside the scope of this work (Obert [282:110-36] offers a thorough handling of the topic), but the key point is that enhancement of one factor may reduce the importance of another factor. For example, consider improved mixing and turbulence. Increased mixing propagates the flame through convection, allowing the flame to ignite many regions of gas simultaneously. In such an instance the chemical delays of each region proceed in parallel, reducing the impact of chemical delay relative to a less convective flame front where each subsequent region must wait on the preceding region to ignite before its chemical delay may commence. As a result, in an engine with robust mixing and turbulence, the impact of fuel AKI on burn angle may be less pronounced than on an engine with more quiescent cylinder contents.

The preceding discussion offers insight into the burn angle trends observed Figure 160 and Figure 161. As engine size increased, knock resistance decreased which indicates increasingly favorable conditions for pre flame reactions. Additionally, the 3W-85Xi engine had additional boost and scavenge ports and higher port timings, presumably enhancing turbulence and mixing in the cylinder. Thus, as engine size increased in the tested engines, improved mixing and increased pre-flame reactions reduced the impact of fuel AKI on the total burn angle. The following section will examine that reduction in greater detail in the context of converting a COTS engines from 98 ON PRF (manufacturer recommended) to 20 ON PRF (JP-8 and diesel equivalent).

### **3. Comparison of 98 ON and 20 ON PRF: KLIMEP, Burn Angle and Efficiency:**

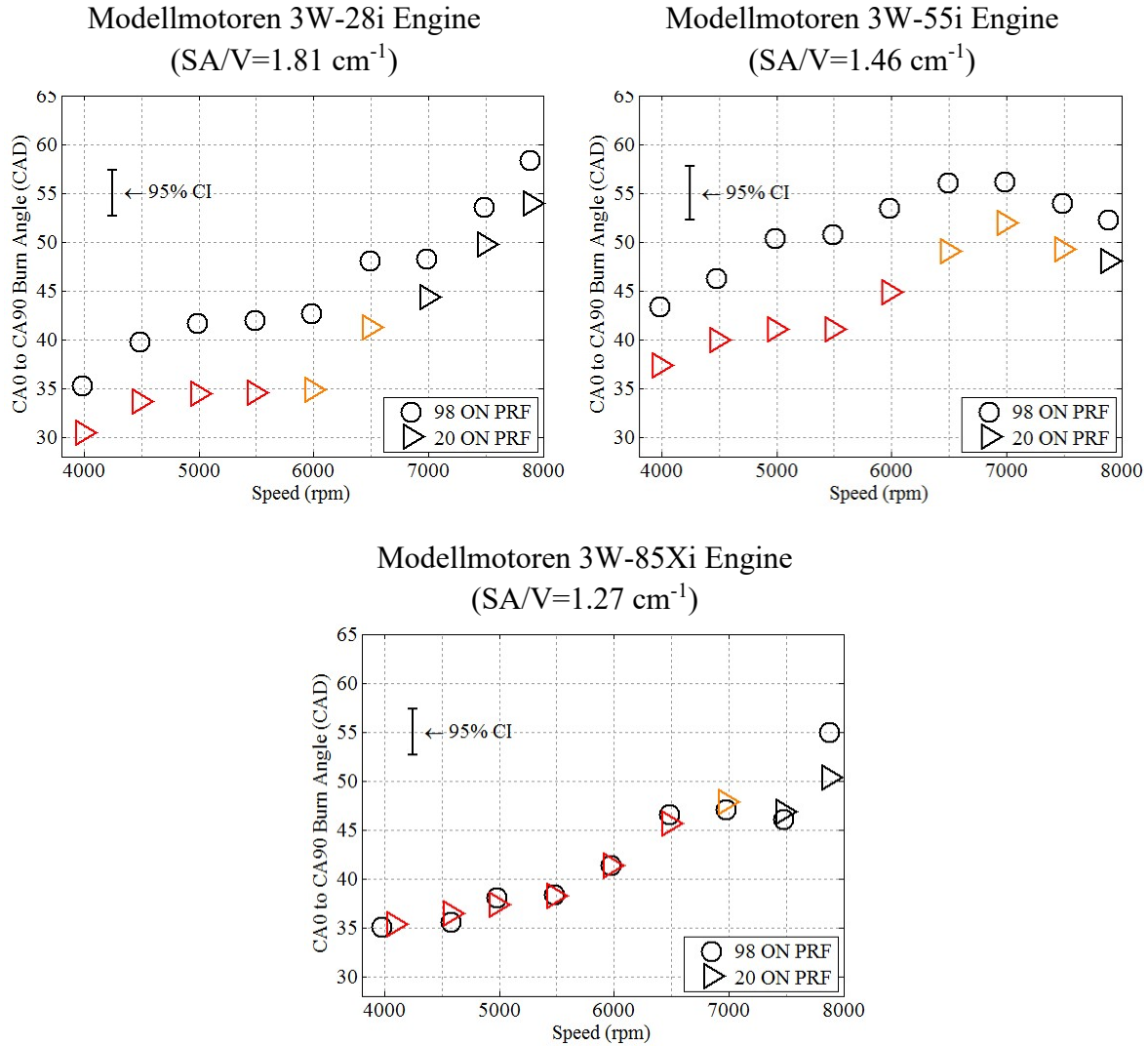
At the onset of the project, there were two motivations to pursue operation on heavy fuel: compliance with the single battlefield fuel initiative and improved fuel conversion efficiency due to reduced burn angle. As observed in the previous section, the changes between 10 ON increments were relatively small. Thus, to investigate the performance impacts of changing from 98 ON fuel as recommended by the manufacturer to 20 ON fuel representative of JP-8 and diesel, each sweep was repeated in triplicate (on different days) and averaged to better resolve differences between 98 ON and 20 ON performance.

Figure 163 and Figure 164 show the KLIMEP and CA0-CA90 burn angles for each of the three engines across the operational speed range. As noted above, the KLIMEP data showed decreasing knock resistance with increasing engine size, where the 3W-85Xi engine was knock-limited at and below 6500 rpm while the 3W-28i engine was only limited at and below 5500 rpm. For abnormal combustion free conditions, the 3W-28i and 3W-55i engines showed slight decreases in power (less than 2%), while the 3W-85Xi engine exhibited a 2% increase in power running non-knock limited on the 20 ON PRF blend. The small differences are well within the uncertainty bounds on IMEP, but the consistency of the observations (across all three independent trials) suggests that these differences were more than random observations. Moreover, the different trends between the 3W-85Xi engine and the smaller two engines suggests different underlying physical phenomena. The proceeding discussion will first address the observations in the 3W-85Xi engine and then discuss the differences that caused the opposite fuel AKI and power behavior in the remaining two engines.



**Figure 163: KLIMEP for  $\phi=1.06\pm0.02$ , CA50=8 $\pm$ 0.5 $^\circ$ aTDC, & CHT=130 $\pm$ 2 $^\circ$ C. Red points were knock-limited. Orange points indicate the presence of abnormal combustion.**

Theoretically, shortening the total burn angle, while maintaining combustion phasing would result in an increase in power. The shorter, more rapid burn would result in a higher, narrower pressure peak, resulting in less work against the upward motion of the piston and more work into the downward stroke (see Chapter II, Section 2.6.1). Figure 17 (page 79) shows how a faster burn could translate into a taller, narrower pressure peak. The timing data noted at the top of the figure suggests that combustion phasing was not adjusted to



**Figure 164: Total burn angle (CA0-CA90) for  $\phi=1.06\pm0.02$ , CA50=8 $\pm$ 0.5°aTDC, & CHT=130 $\pm$ 2°C. Red points were knock-limited. Orange points indicate the presence of abnormal combustion.**

maintain CA50, instead maintaining the spark timing. Noting that the area under the curve before TDC will work against the piston, with fixed spark timing the faster n-heptane burn may actually have reduced IMEP in Wilson's example [43:49]. In a more likely scenario, conversion to heavy fuel would dictate the use of variable spark timing to control knock, and at knock free conditions spark timing would be adjusted to maintain MBT timing (or

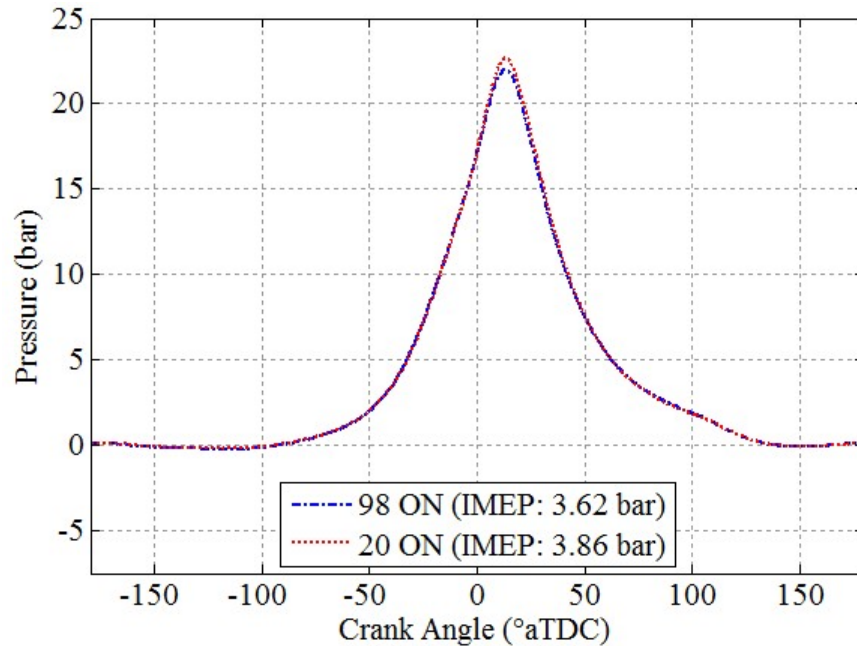


**Figure 165: Comparison of 400 cycle average in-cylinder pressure curves for the 3W-85Xi engine operating abnormal combustion free on 20 ON PRF and 98 ON PRF. Operating conditions: 7900 rpm,  $\phi=1.06\pm0.02$ , CA50= $8\pm0.5^\circ$ aTDC, & CHT= $130\pm2^\circ$ C.**

at least close to MBT timing), shifting the n-heptane curve to the right (and probably reducing its peak height). Figure 165 shows in-cylinder pressure traces for the 3W-85Xi engine operating at 7900 rpm. The traces are 400 cycle averages that correspond to the 7900 rpm points shown in Figure 163 and Figure 164. The timing shift in Figure 165 is so subtle (only a few degrees) that in terms of combustion phasing, the two traces appear on top of one another. However, the peak of the 20 ON trace is about a bar higher than the 98 ON trace, accounting for the 2-3% increase in power at 7900 rpm on 20 ON fuel.

Given that each of the non-knock-limited points for the 3W-85Xi engine show an improvement in power similar to 7900 rpm when changing from 98 ON PRF to 20 ON PRF, one would expect those points to show a similar reduction in burn angle. Returning to Figure 164, such a reduction does appear to occur. However, Figure 164 presents only

the total burn angle, which provides limited information on where the reduction in burn duration actually occurred. Therefore, Figure 166 shows the CA0, CA10, CA50, and CA90 combustion phasing for the 3W-85Xi engine (as well as the other two engines) running on 98 ON and 20 ON fuel. In the case of all three engines, running on 20 ON fuel shortened the CA0-CA10 burn angle as spark timing was retarded to maintain near MBT timing. Shortening the CA0-CA10 burn angle allowed the start of combustion to be delayed, while

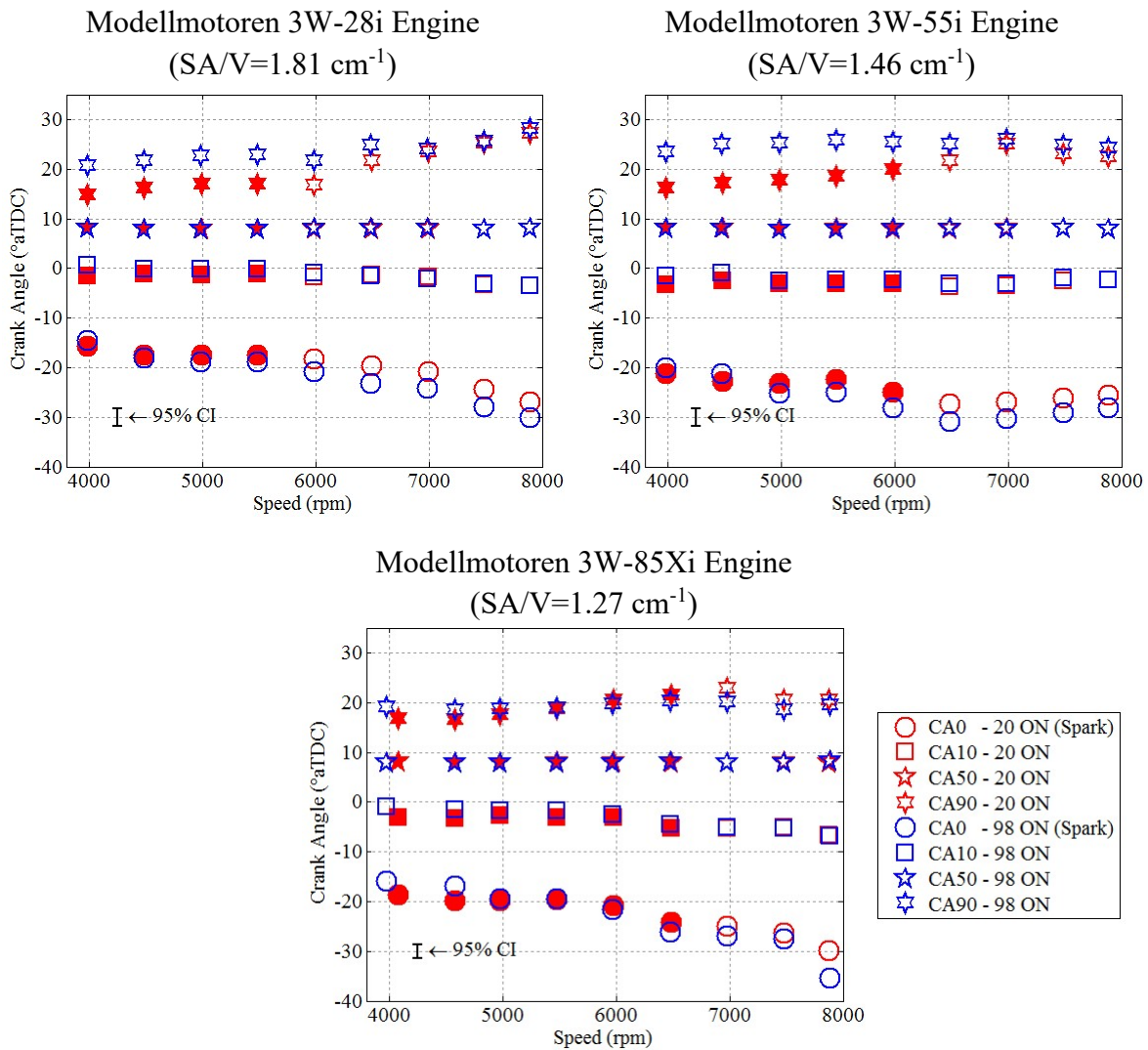


**Figure 166: Spark timing and mass fraction burned angles for  $\phi=1.06\pm0.02$ , CA50=8 $\pm$ 0.5°aTDC, & CHT=130 $\pm$ 2°C. Filled points were knock-limited.**

maintaining the location of CA50 and peak pressure. The result was a slightly narrower and taller pressure curve, such as that seen in Figure 165. For non-knock-limited operation of the 3W-85Xi engine, the reduction in CA0-CA10 burn angle was the greatest at 7900 rpm, however, a reduction did occur at the remaining non-knock-limited conditions. Spark timing was controlled to  $\pm 0.1$  CAD, which was much tighter than the uncertainty bands on the calculated mass fraction burn angles shown in Figure 166. Those reductions in burn angle were sufficiently small that variations in CA90, which is more difficult to measure, obscured the reduction in the CA0-CA90 burn angle at other speeds. Therefore, the approximately 2% improvement in power on 20 ON fuel in the 3W-85Xi engine may be attributed to an approximately 1-3 CAD reduction in the CA0-CA10 burn angle.

Before returning to the power trend observed in the smaller two engines, it is appropriate to make several other comments concerning the burn angles in Figure 166. First, for non-knock-limited conditions, both the 3W-55i engine and 3W-28i engine show shorter burn durations on 20 ON fuel than on 98 ON fuel. Like the 3W-85Xi engine, the reduction in burn duration was dominated by shortening of the CA0-CA10 burn angle by 3-5 CAD. Shortening the CA0-CA10 burn angle indicates that the initial development of the flame kernel from the spark was aided by the combustion properties of the 20 ON fuel. Thus, as one would expect, fuel AKI properties heavily influenced initial flame development. At the same conditions, the CA10-CA90 burn angles remained largely unchanged, shortening at some conditions (generally in the smaller two engines) and lengthening at others (generally in the 3W-85Xi engine). This indicates that fuel AKI properties played a less dominant role in the later portion of combustion. Therefore, while the lower chemical ignition delays and higher flame speeds had a measurable impact on the initiation and

development of the flame kernel, the travel of the flame front was largely dominated by other variables such as turbulence, mixing, and cylinder geometry. Considering that typical flames speeds in an SI engine are approximately 30 times faster than laminar flames [23, 282:99] due to convection, it is unsurprising that the 10% difference in laminar flame speed [23] had a minimal impact during the second half of the burn.

The observed reductions in burn angle were approximately half an order-of-magnitude smaller than Wilson *et al*'s [14] estimate, and the difference arises from the engine control scheme used in the studies. Wilson *et al.* [14] fixed the spark timing of the engine, using the manufacturer supplied ignition coil. As a result, neither the timing for iso-octane (100 ON PRF) nor n-heptane (0 ON PRF) was optimized. In the presented study, the timing was fixed near MBT at  $CA_{50}=8\pm0.5^{\circ}aTDC$ . It is presumed that conversion of a COTS engine to heavy fuel would also incorporate fuel injection, a custom ECU, and optimized spark timing. Thus, the comparison presented here is a realistic, direct comparison of the behavior of high and low AKI fuel; compared to previous studies, the effect of optimal combustion phasing was separated from the effect of fuel type.

At throttled conditions, lower fuel AKI resulted in shorter burn durations down to approximately 20 ON PRF, especially on the 3W-28i and 3W-55i engines. Similar to WOT, shorter chemical delays and higher laminar flame speeds aided in the initial development of the flame kernel. Throttled operation points generally required advancing the spark timing to maintain the combustion phasing as throttling negatively impacted mixture formation. Thus, gains in flame kernel development from switching to 20 ON fuel were partially countered by poorer mixture in the flame kernel development region.



Unlike WOT operation, throttled operation on 20 ON fuel showed a clear reduction in the CA50-CA90 burn angle. The reduction can be traced to two root causes. First, throttling a two-stroke engine reduces the intensity of mixing and turbulence in-cylinder, creating a less homogenous mixture and reducing convection of the flame. By reducing the contribution of convection to flame propagation, the relative impact of increased laminar flame speeds and low fuel AKI were amplified. Additionally, throttling the engines in this study caused a substantial reduction in short-circuiting (charge cooling). Short-circuiting (as a percentage of total airflow) decreased by 60% when the engine was throttled to 50% of WOT airflow. The reduction in charge cooling led to increased cylinder temperatures, contributing to the reduction in burn angle. At lower speeds on 20 ON fuel and for most knock-limited points on 0 ON and 10 ON fuel, the degree of throttling negatively impacted mixing and increased the residual contents of the cylinder sufficiently that the spark needed to be advanced to maintain timing. As a result, the total burn angle actually increased at such conditions.

The discussion now returns to the power behavior observed in Figure 163 for the 3W-28i and 3W-55i engines. Unlike the 3W-85Xi engine, for conditions not limited by knock, IMEP decreased by 1-2% on 20 ON fuel compared to 98 ON fuel. The same trend was observed in brake power. Yet, the fact that burn angles decreased by roughly 5 CAD over the same interval suggests that the opposite should have held true. Since the reduction in burn angle occurred primarily during the first half of combustion, spark timing was retarded from the 98 ON baseline to maintain combustion phasing near MBT timing. The completion of the burn (CA90) remained virtually unchanged. Thus the faster burn of the

lower AKI fuel should have resulted in a taller, narrow pressure peak, leading to improved IMEP. Yet the opposite occurred.

To investigate the discrepancy, the control variables were reexamined for a confounding variable, and the issue was traced to the reliance on WOT for the baseline condition. Figure 167 shows the impact of changing the fuel from a 98 ON PRF blend to a 20 ON PRF blend on delivery ratio. While the reduction at knock-limited points was clearly the result of throttling the engine to mitigate knock, the 4%-5% (absolute) reduction on the 3W-55i engine and the 2%-3% reduction on the 3W-28i engine at non-knock-limited conditions was more vexing. The order of the sweeps was varied, and the trends observed in Figure 167 were consistent, no matter which subset of sweeps were considered. Thus, the data actually suggest that the fuel ON changed the delivery ratio of those two engines. Based on data sets collected in Chapter IV, Section 3.4, the reduction in intake air flow would result in a 3%-6% decrease (depending on the engine) in indicated power and IMEP, indicating that lowering the fuel AKI would have increased power by 2%-3% if the intake air flow rate had remained unaltered. This is consistent with the behavior observed from the 3W-85Xi engine.

This poses a more troublesome question: how could fuel ON alter the airflow to the engine, which is largely a function of intake, engine, and exhaust geometry? The mechanism was identified (almost by accident) during a routine inspection of the intake system on the 3W-55i engine. At the beginning of the study, a manufacturing error was identified in the reed valve assembly of the 3W-55i engine. An example of the primary reed and reed carrier for each of the three engines is shown in Figure 168. The 3W-55i engines purchased for the study shipped with a single fiberglass reed, and reed failures

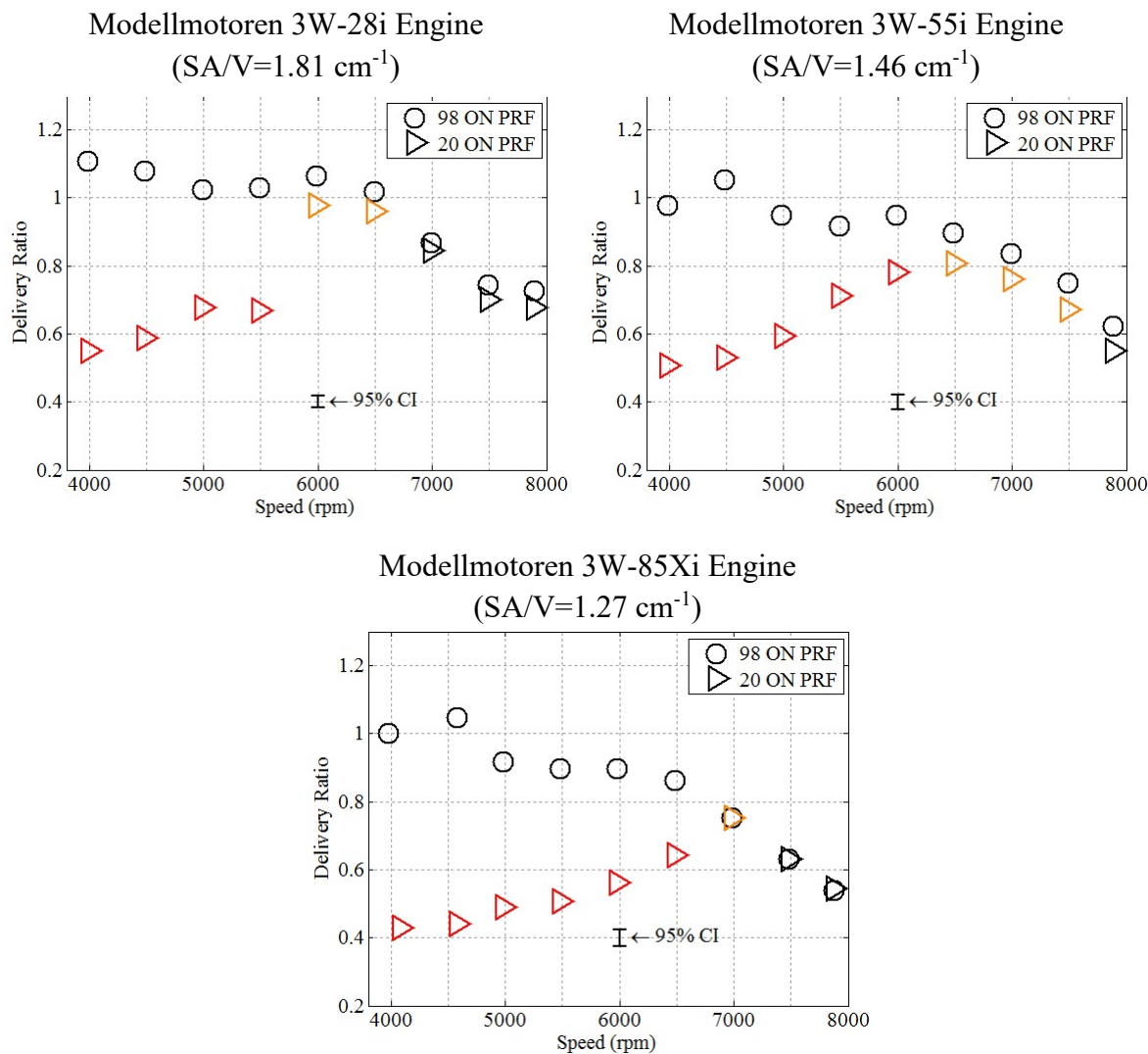


**Figure 167: Delivery ratio for  $\phi=1.06\pm0.02$ , CA50=8 $\pm$ 0.5°aTDC, & CHT=130 $\pm$ 2°C. Red points were knock-limited. Orange points indicate the presence of abnormal combustion.**

were occurring every 2-4 hours. After comparing the reed assembly to an earlier batch of engines and consulting with the U.S. distributor, it was determined that the engines were missing a second, half size reed that stiffens the primary reed preventing over deflection. After correcting the discrepancy, the reed assembly was inspected following each ON sweep to verify reed integrity. During these inspections, it was observed that oil deposition



**Figure 168: Reeds and reed carriers for the 3W-28i (left), 3W-55i (middle) and 3W-85Xi (right) engines.**

on the reeds changed with fuel AKI. For fuels composed primarily of iso-octane, the reeds were wetted with a film of oil, which formed a seal against the reed carrier. For fuels composed primarily of n-heptane, the reeds appeared dry and the upper half of the reed did not form a seal with the reed carrier. Failure to adequately seal against/ adhere to the reed carrier as the gas in the crankcase was compressed by the downward motion of the piston caused (increased) chatter and backflow through the reeds into the throttle body and intake runner. For a more comprehensive review of dynamic reed valve behavior see Fleck *et al.* [61]. To validate this theory, the reed petals were wetted with two-stroke oil and the engine was operated on 20 ON fuel and 7900 rpm, observing the air flow and IMEP. After the initial 120 second warm-up condition, the delivery ratio would drop from values observed on 98 ON PRF to the delivery ratio for 20 ON fuel seen in Figure 167 as the oil was stripped from the reed valves and not replaced by fresh deposition. The total process from engine start to steady state air flow took approximately 300 seconds. Similar behavior was

observed in the 3W-28i engine, although the extent was not as severe as in the 3W-55i engine. The 3W-85Xi engine exhibited no drop in airflow, and an excess of oil was observed both in the crankcase and on the reeds, even during operation on pure n-heptane. It was also the only engine that showed pooling of oil in the crankcase, and pooling occurred both on 20 ON and 98 ON fuel. Oiling during heavy fuel conversion has been addressed in the literature from a lubricity standpoint [260]. For future work, it is clear that the solubility of the oil in the intended fuel should be considered to ensure proper deposition of the oil in critical areas. Note that no abnormal wear was observed in bearings or piston ring cylinder interface from operation on lower AKI fuels and the issue seems to have been isolated to the reeds.

Figure 169 shows the impact of the switch from 98 ON fuel to 20 ON fuel on fuel conversion efficiency. Throttled, knock-limited points showed the largest improvement of up to 6.5%. However, the majority of the improvement was due to throttling the engine to mitigate knock. As previously mentioned, throttling these engines reduced short-circuiting more rapidly than power. As a result, the large improvements in efficiency at throttled points would be mostly realizable for the same throttle setting running 98 ON fuel.

For non-knock-limited points, the improvement in fuel conversion efficiency between 98 ON fuel and 20 ON fuel was lower, about 1% on the 3W-55i and 3W-85Xi engines and less than 1% on the 3W-28i engine. Moreover, both the 3W-55i and the 3W-28i engines were also influenced by the interactions of the fuel, engine oil, and reed valves causing the delivery ratio on 20 ON fuel to be lower than on 98 ON fuel even at WOT. The reduction in intake air flow behaved similarly to throttling the engine. Data on the relationship between delivery ratio and fuel conversion efficiency from Chapter IV, Section 3.4 made

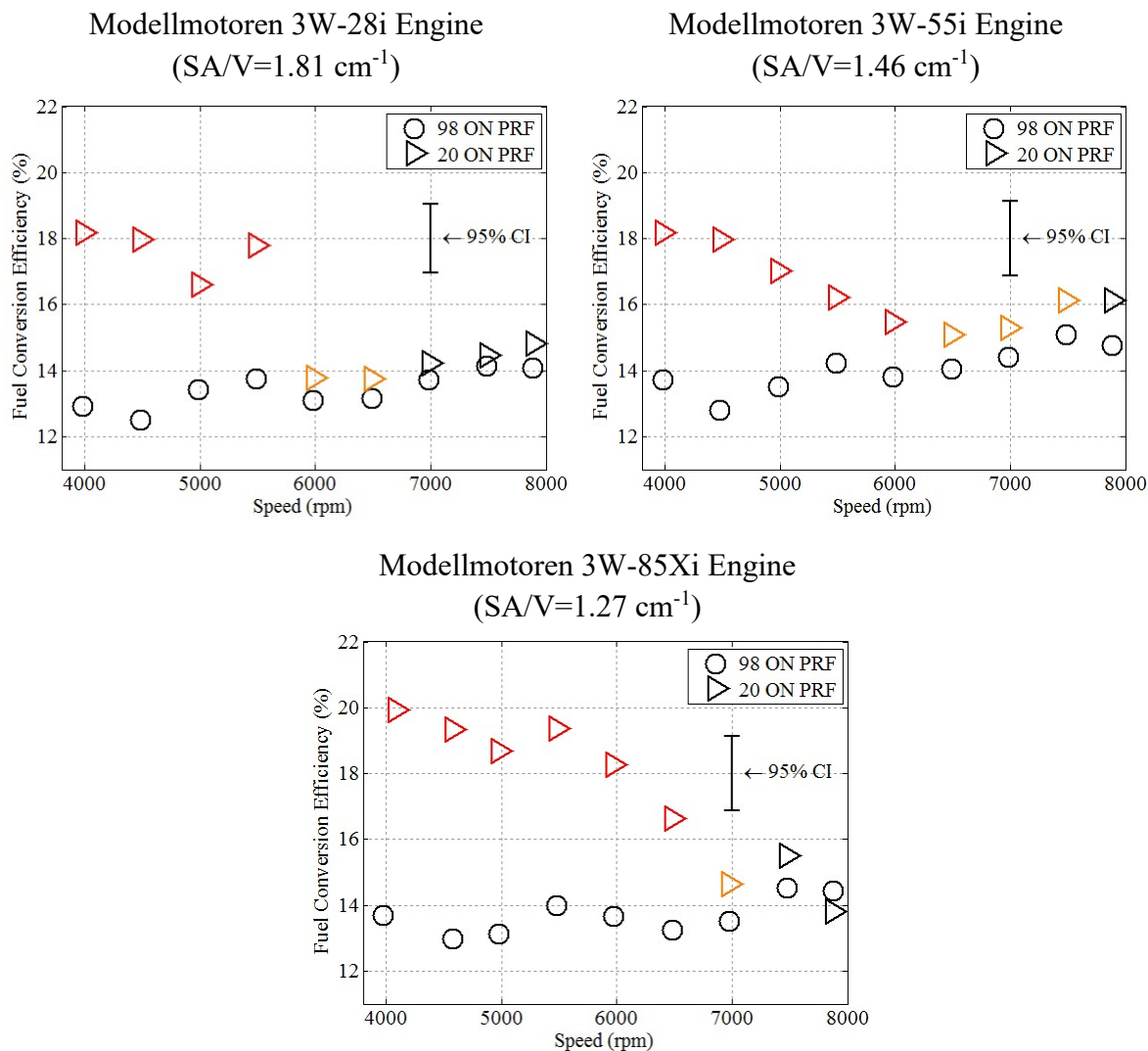


**Figure 169: Fuel conversion efficiency for  $\phi=1.06\pm0.02$ , CA50=8 $\pm$ 0.5 $^\circ$ aTDC, & CHT=130 $\pm$ 2 $^\circ$ C. Red points were knock-limited. Orange points indicate the presence of abnormal combustion.**

it possible to estimate how much of the improvement in fuel conversion efficiency could be attributed to the reduction in short-circuiting and how much could be attributed to the faster burn rate of the lower AKI fuel. For WOT points, about half of the improvement on the 3W-28i and 3W-55i and all of the improvement on the 3W-85Xi was the direct result of the combustion characteristics of the fuel, while the remainder on the smaller two

engines was the result of reductions in short-circuiting. Similarly, at the throttled points, about 0.5%-1% (absolute) of the improvement in fuel conversion efficiency was the result of changing the fuel composition, with the remainder accounted for by reductions in short-circuiting caused by throttling the engines. Given that the baseline WOT efficiencies of these engine were approximately 15%, switching to 20 ON fuel from 98 ON offers about a 6% improvement in range and endurance. Thus, while low AKI fuel did offer an efficiency benefit from reducing the burn angle, the steps taken to implement such a conversion (such as fuel injection, pre heating, modification of spark timing) will tend to dominate the changes in engine performance, explaining the otherwise conflicting observations of Cathcart *et al.* [15], Duddy *et al.* [38], and Wilson [14] (as well as the other studies noted in Chapter II, Section 6).

#### **4. Parametric Study of Engine Controls**

The previous section addressed the performance impact of switching from 98 ON, manufacturer recommend fuel to 20 ON fuel which simulates diesel or JP-8. This section will focus on the control aspects. During the parametric control study in Chapter IV, Section 3, there were five primary engine control variables: speed, throttle, equivalence ratio, combustion phasing, and head temperature. As explained in Chapter III, Section 5.3, in the fuel AKI study throttle was no longer an independent variable as it was the primary control to mitigate knock. The impact of speed on abnormal combustion was already discussed earlier in this chapter (Section 2). Therefore, there remained three independent engine control variables.

The parametric engine study aimed to answer three questions of interest to practical heavy fuel conversion for an aircraft application. First, if the engine is operating at a knock

free condition, can variation in the control parameters (combustion phasing, equivalence ratio, and head temperature) cause the engine to move into a knocking or knock-limited condition? Second, for operation where knock is observed but not severe enough to warrant mitigation, can variability of the control parameters lead to a knock-limited condition? Third, for operation in a knock-limited condition, can the controls be used to increase the knock-limited power, and if so, what is the penalty in terms of efficiency associated with that power increase? The following three sections present the answers to those questions, where engine speed was selected to create each condition (knock free, knock observed but not limited, and knock-limited) at the baseline settings. Each control variable was then swept similar to the parametric study in Chapter IV, Section 3.

#### **4.1. Equivalence Ratio**

Figure 170 shows the effect of equivalence ratio on knock at the three different speeds for each engine. While the particular speeds for each engine were chosen based on their knock characteristics at the baseline condition, the following general trend holds. The highest speed was knock free at the baseline condition and the slowest speed was knock-limited at the baseline conditions. The middle speed exhibited a degree of knock at the baseline condition, but was not knock-limited. At knocking conditions, it is not immediately clear from Figure 170 how much of the variation in IMEP was due to changing the equivalence ratio directly, and how much was due to adjusting the throttle to control knock. Therefore, Figure 171 shows the delivery ratio and fuel conversion efficiency for each operating point in Figure 170. The change in delivery ratio describes the change in throttle setting. Some small changes in the delivery ratio for WOT points were the result of changes in the engine control variables, in this case equivalence ratio. These small



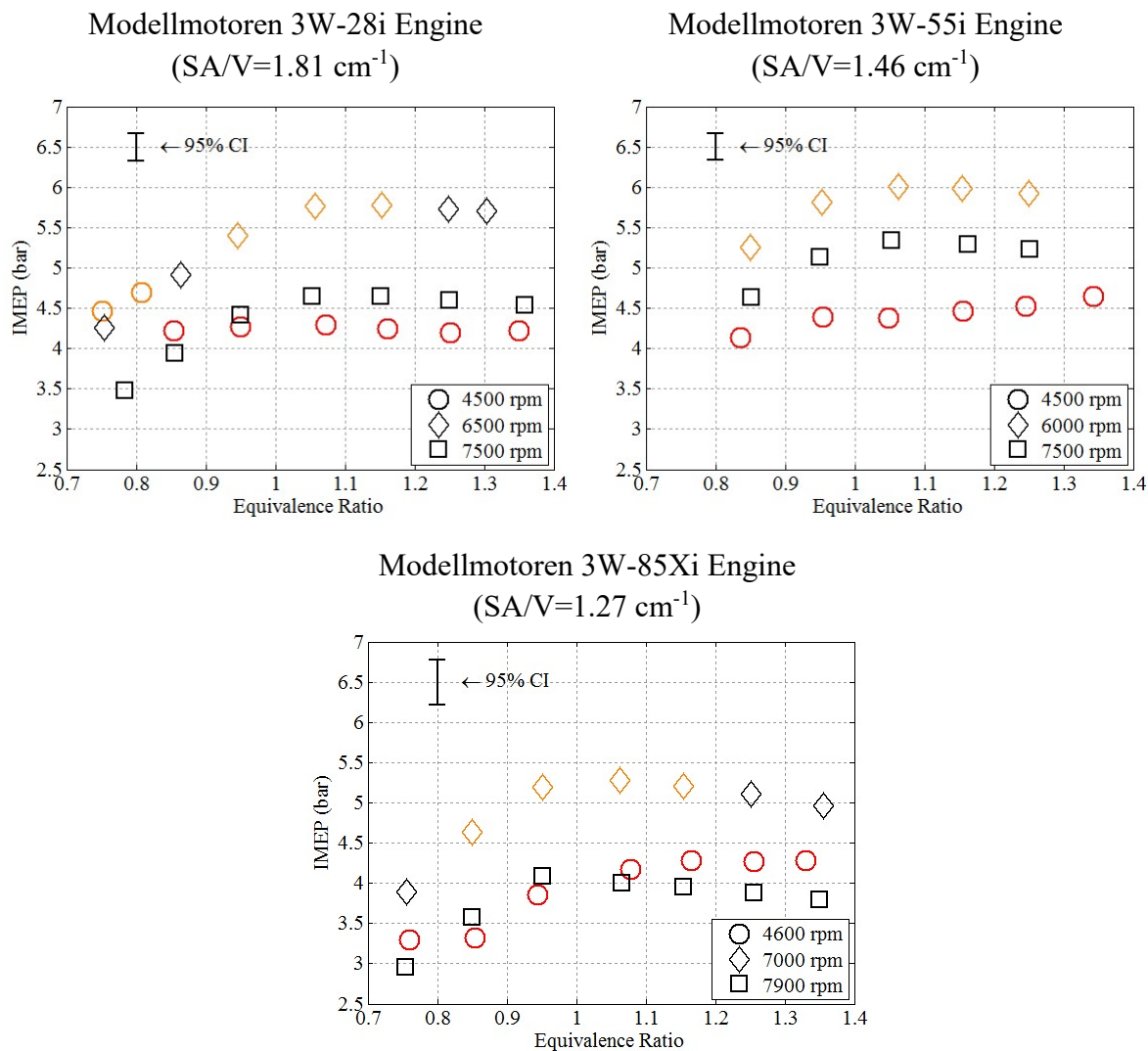


**Figure 170: Effect of equivalence ratio on knock and KLIMEP for CA50=8±0.5°aTDC, CHT=130±2°C, & 20 ON PRF blend. Red points were knock-limited. Orange points indicate the presence of abnormal combustion.**

changes were typically due to changes in the in-cylinder gas temperatures and gas exchange caused by changing the engine operating point.

Based on Figure 170, when the baseline condition was knock free, varying the equivalence ratio over a realistic range (0.8 to 1.3) for engine operation did not push the engine into a knocking condition. When the baseline condition exhibited signs of knock, but was not knock-limited, varying the equivalence ratio eliminated the knock at both the

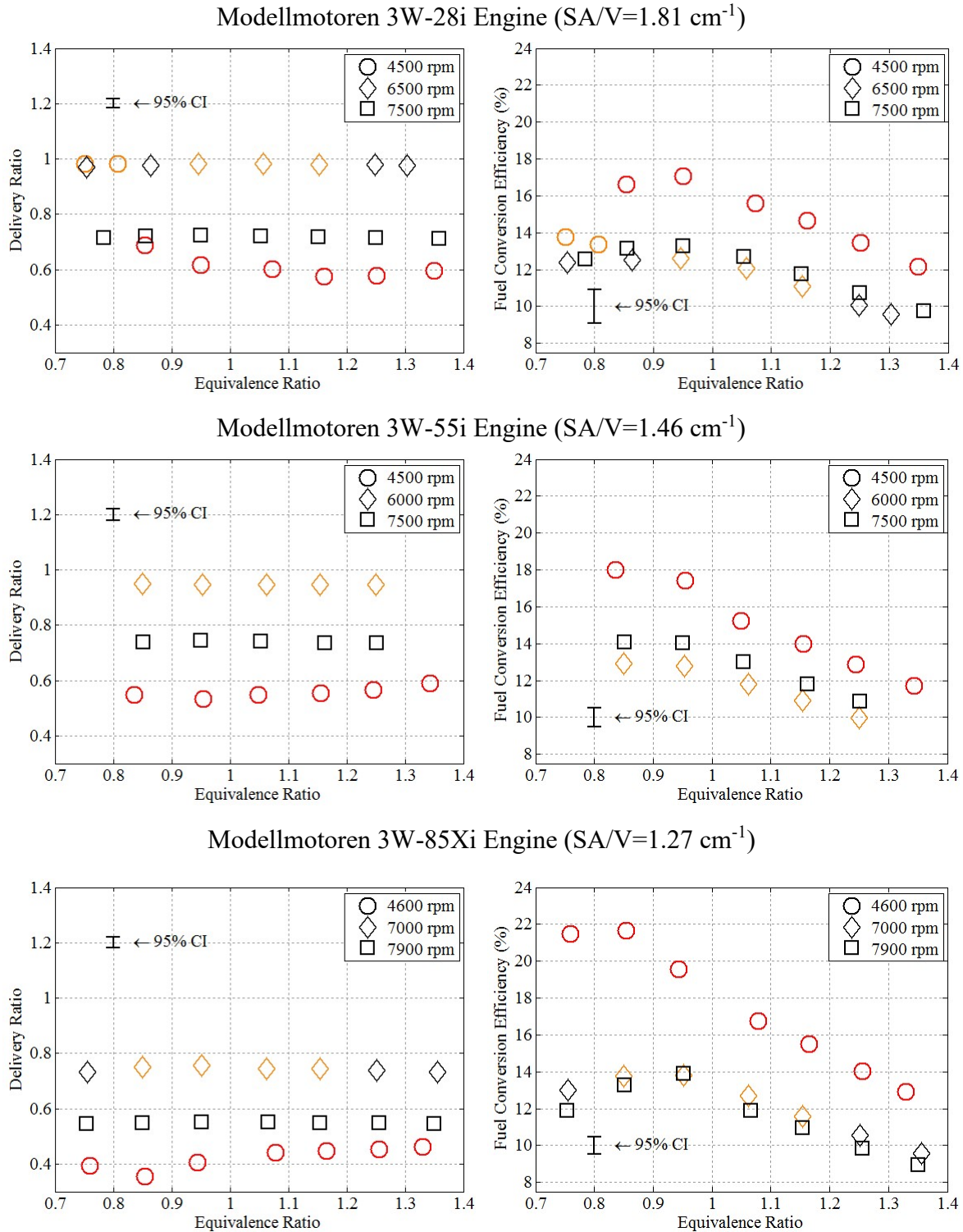


**Figure 171: Effect of equivalence ratio on delivery ratio, fuel conversion efficiency, and knock running on 20 ON PRF blend. The engines were operated at  $CA_{50}=8\pm0.5^\circ\text{aTDC}$ , &  $CHT=130\pm2^\circ\text{C}$ . Red points were knock-limited. Orange points indicate the presence of abnormal combustion.**

rich and lean extremes. At rich equivalence ratios, extra fuel provided a charge cooling effect as well as a mixture less prone to auto-ignition. Lean conditions reduced the amount of fuel available for combustion reducing the thermal load in the cylinder. This trend was not observed in the 3W-55i engine, partially because the stable equivalence ratio of the engine was more limited than the 3W-28i and 3W-85Xi engines. In all cases, for non-knock-limited conditions, varying the equivalence ratio did not cause the engine to enter into a runaway knock condition or require throttling to mitigate knock.

When the baseline was a knock-limited operating point, several different behaviors were observed. For the 3W-28i engine, reducing the equivalence ratio below unity increased the knock resistance of the engine, allowing the throttle to be opened. At the leanest operating conditions, the engine was no longer knock-limited, although poor combustion stability near an equivalence ratio of 0.75 would make running the engine at such a condition on a fielded platform impractical. At rich conditions, the throttle was relatively constant and richening the mixture above an equivalence ratio of 1.1 provided no notable improvement in power. This suggests that the reduction in in-cylinder temperature from lean operation was more significant than the reduction from charge cooling for a similar relative change in fuel delivery. This hypothesis was confirmed using plots of in-cylinder temperature as a function of delivery ratio seen in Chapter V, Section 2.1. For the 3W-55i engine, the lean limit of the engine was slightly lean of an equivalence ratio of 0.85, and no clear power or knock reduction benefit was observed for lean operation. For rich operation, increasing the equivalence ratio from 1.05 to 1.35 increased power by 6%-7% and allowed the throttle to be opened approximately 8%.

The charge cooling came at a high price in terms of fuel; fuel conversion efficiency decreased from 16% to 12%, with the majority of the decrease resulting from the additional fuel added to increase equivalence ratio. (See Chapter IV, Section 3.4 for plots showing how throttle and delivery ratio influence fuel conversion efficiency). Therefore, while rich operation did reduce the knock limit, the reduction came at almost twice the efficiency cost per unit of additional power as retarding the combustion phasing (discussed in the next section). On the 3W-85Xi engine, lean operation provided negligible throttle margin and knock resistance. As a result, knock-limited power responded to lean operation similar to power at WOT, with a lockstep decrease in equivalence ratio and power. For rich operation at an equivalence ratio of 1.05 to 1.35, charge cooling only provided about 5% additional power, for a 5% (absolute) decrease in fuel conversion efficiency.

These observations support the following conclusions regarding equivalence ratio and knock-limited operation. For a smaller, more inherently knock-resistant engine with a lower lean limit (such as the 3W-28i engine) the reduction in in-cylinder temperature from lean operation increased the knock resistance of the engine sufficiently to allow close to WOT operation. In this case, the increase in power from opening the throttle more than offset the loss in power from leaning the engine, leading to an improvement in knock-limited power (about 10%), but a decrease in fuel conversion efficiency (about 2% absolute) due to the increase in short-circuiting caused by opening the throttle. For larger engines, such as the 3W-55i and the 3W-85Xi engines, the reduction in thermal loading from leaning the engine had less of an impact on knock resistance, and the power penalty from lean operation led to minimal gains (or losses) in knock-limited power. For rich operation (from an equivalence ratio 1.05 to 1.35) in the larger engines, knock-limited

power could be increased by 5%-7% at the cost of a 4%-5% (absolute) or 25%-33% (relative) decrease in fuel conversion efficiency. Thus, while lean operation for a smaller engine may offer an efficient knock mitigation strategy, rich operation provides relatively little margin considering the incurred penalty.

#### **4.2. Combustion Phasing**

Figure 172 shows the impact of combustion phasing on knock and knock-limited IMEP, and Figure 173 shows the corresponding plots for the delivery ratio and fuel conversion efficiency. For knock free conditions, retarding the combustion phasing beyond MBT timing (roughly the baseline) had no measurable impact on abnormal combustion, and operation remained knock free. Advancing the combustion phasing beyond MBT timing caused knock below the established threshold, but did not push the engines into knock-limited or runaway conditions. Similarly, when the baseline condition exhibited knock, retarding the timing did not push the engine into knock-limited operation, and for more than 10 CAD of retard, knock disappeared entirely. Both the 3W-55i and 3W-85Xi engines had issues with combustion stability at some speed and retarded combustion phasing combinations. Those points were unable to be tested.

As with equivalence ratio, the results for the knock-limited baseline condition were more varied, although unlike equivalence ratio the trend was the same for all three engines. In each engine retarding the phasing from MBT timing resulted in increased knock resistance and increased knock-limited power. For the 3W-28i engine, the engine was no longer knock-limited at a CA50 of 23°aTDC and showed the characteristic decrease in power expected for further retardation of the phasing. In the 3W-55i engine, knock disappeared entirely at a CA50 of 28°aTDC, but since the timing was not further retarded,

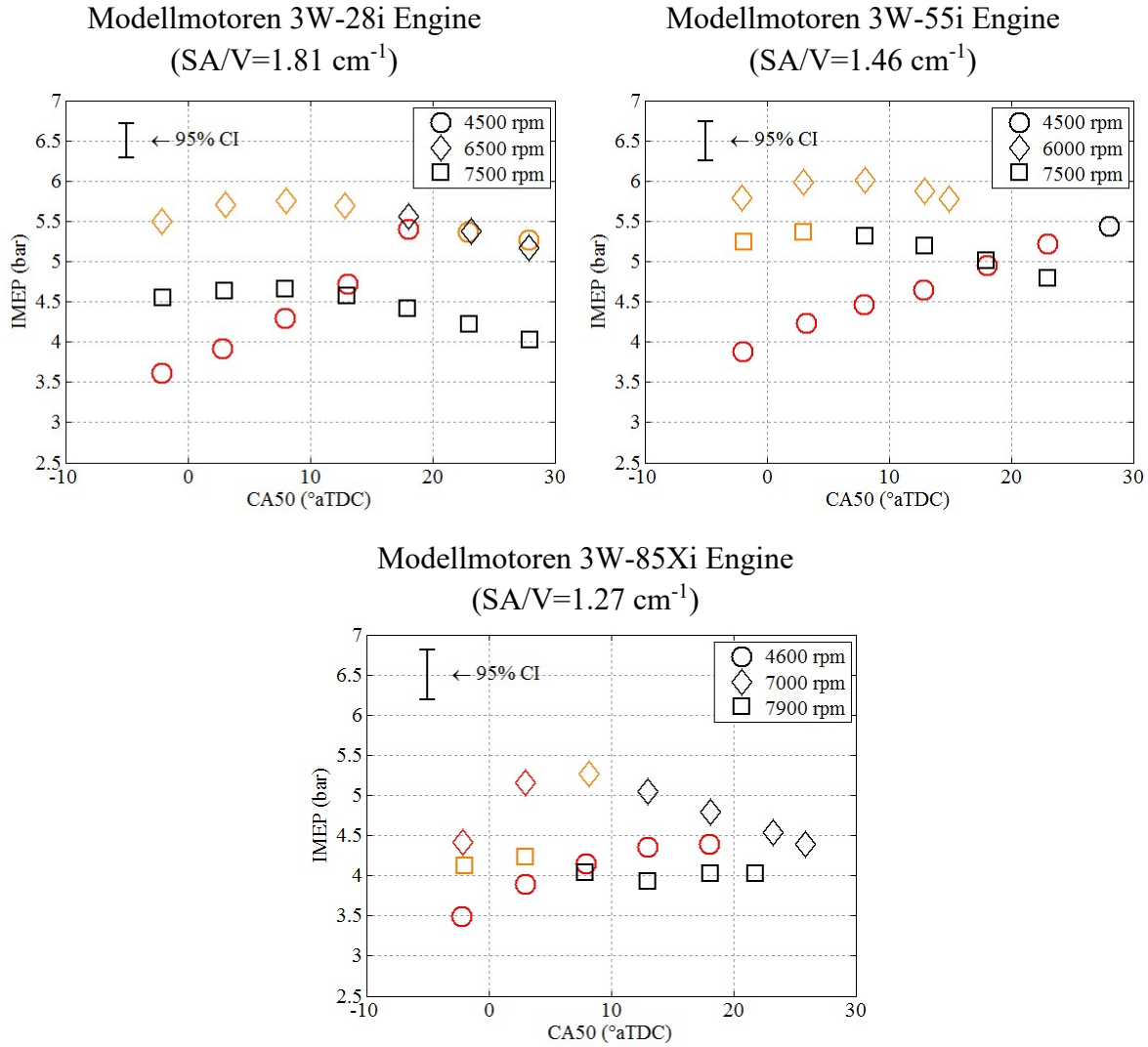


**Figure 172: Effect of combustion phasing on knock and KLIMEP for  $\phi=1.06\pm0.02$ , CHT=130 $\pm$ 2°C, & 20 ON PRF blend. Red points were knock-limited. Orange points indicate the presence of abnormal combustion.**

the increase in power from improving knock resistance was greater than the decrease in power from retarding timing at all tested points. The 3W-85Xi engine showed even more modest gains. All three engines showed the same trend as combustion phasing was advanced: decreased knock resistance and a decrease in knock-limited power. Fuel

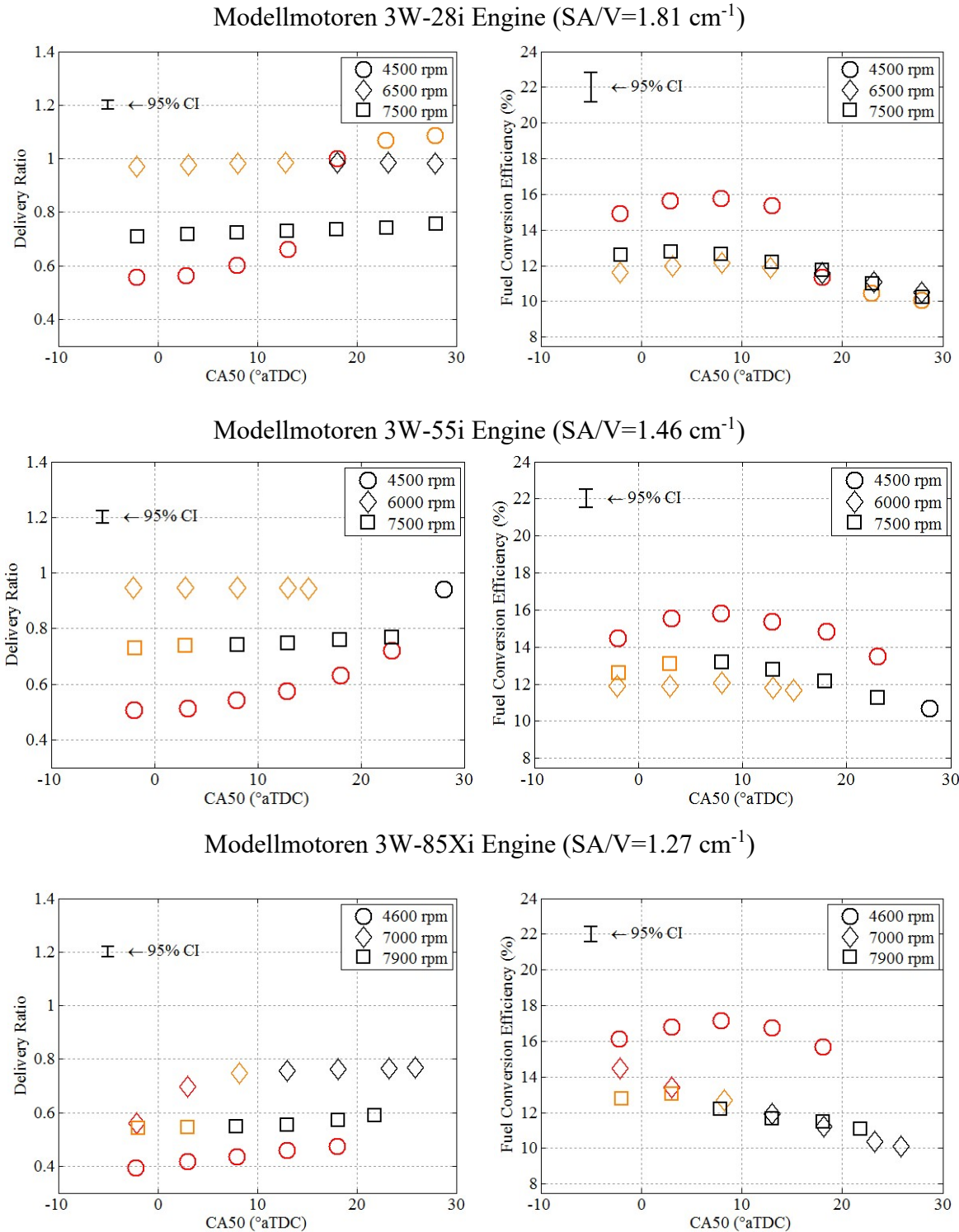


**Figure 173: Effect of combustion phasing on delivery ratio, fuel conversion efficiency, and knock running on 20 ON PRF blend. The engines were operated at  $\phi=1.06\pm0.02$ ,  $CHT=130\pm2^\circ\text{C}$ . Red points were knock-limited. Orange points indicate the presence of abnormal combustion.**

conversion efficiency was influenced by the impact of short-circuiting on throttle and by losses from advancing or retarding the phasing from near MBT timing.

Thus, the following conclusions may be drawn regarding the impact of combustion phasing on the knock limit. For most knock free and non-knock-limited operating conditions, variations in the spark timing from MBT timing are unlikely to cause the engine to shift to knock-limited or runaway knocking operation with one exception. For engines with lower knock resistance such as the 3W-85Xi, advancing the phasing from MBT timing did cause the engine to slip into knock limit operation. These results indicate that the temperature and pressure effects of varying the combustion phasing had a greater impact on knock than the timing of combustion itself. This is typical of automotive and larger scale engines, where advancing timing increases knock (as opposed to burning the fuel sooner, before reaching the autoignition criteria and in turn preventing knock).

For knock-limited baseline conditions, shifting the combustion phasing offered a significant control over knock as well as a means to develop additional power. The degree of control appeared to track with the engine's knock resistance. Shifting CA50 from 8°aTDC to 18°aTDC in the 3W-28i engine increased the knock-limited power by about 20%, while the same shift in the 3W-55i and 3W-85Xi engines led to increases of 11% and 9%, respectively. In the case of the 3W-28i and 3W-55i engines, the 3W-55i engine eventually caught up as the 3W-28i engine reached WOT at a more advanced phasing than the 3W-55i engine. The 3W-85Xi was sufficiently knock-limited that it never caught up, leveling off around 10% (with poor combustion stability). Of course, later phasing does negatively impact fuel conversion efficiency. Similar to equivalence ratio, the changes in fuel conversion efficiency between the knock-limited points were split between an increase



in short-circuiting from opening the throttle and shifting combustion phasing from MBT timing (see Chapter IV, Sections 3.2 & 3.4). Of the three parameters investigated, combustion phasing has the greatest potential for increasing knock-limited power and offers the most control authority relative to its impact on fuel conversion efficiency.

### **4.3. Engine Head Temperature & Cooling**

The third and final control parameter was the cylinder head temperature. Figure 174 shows the impact of head temperature and engine cooling on knock and knock-limited IMEP, while Figure 175 and Figure 176 show the corresponding delivery ratio and fuel conversion efficiency information. One of the hypotheses leading into this objective was that increasing the surface area to volume ratio and in turn heat transfer would play a pivotal role in the knock resistance of engines of 10-100 cm<sup>3</sup> displacement. Section 2 showed a clear link between engine size and knock limit. However, the influence of cylinder size on knock manifested only weakly in terms of heat transfer from the cylinder.

If the practical range of head temperature is taken to be 100°C to 150°C in accordance with manufacturer limits (and noting that the cooling system on the SERB had insufficient authority to reach 100°C on some engines at some conditions), then head temperature had no measurable impact or influence on the presence of knock or on knock-limited IMEP. Increasing head temperature did not cause knock to appear for a knock free baseline, appreciably worsen for a baseline with minor knock, or drive the engine into more knock-limited operation from a knock-limited baseline. The reduction in delivery ratio and IMEP were the result of hotter, less dense trapped charge as discussed in conjunction with Chapter IV, Section 3.3. Extending the tested range to 180°C on the 3W-28i and 3W°85Xi engines (testing on the 3W-55i was more conservative due to concerns unrelated to knock)

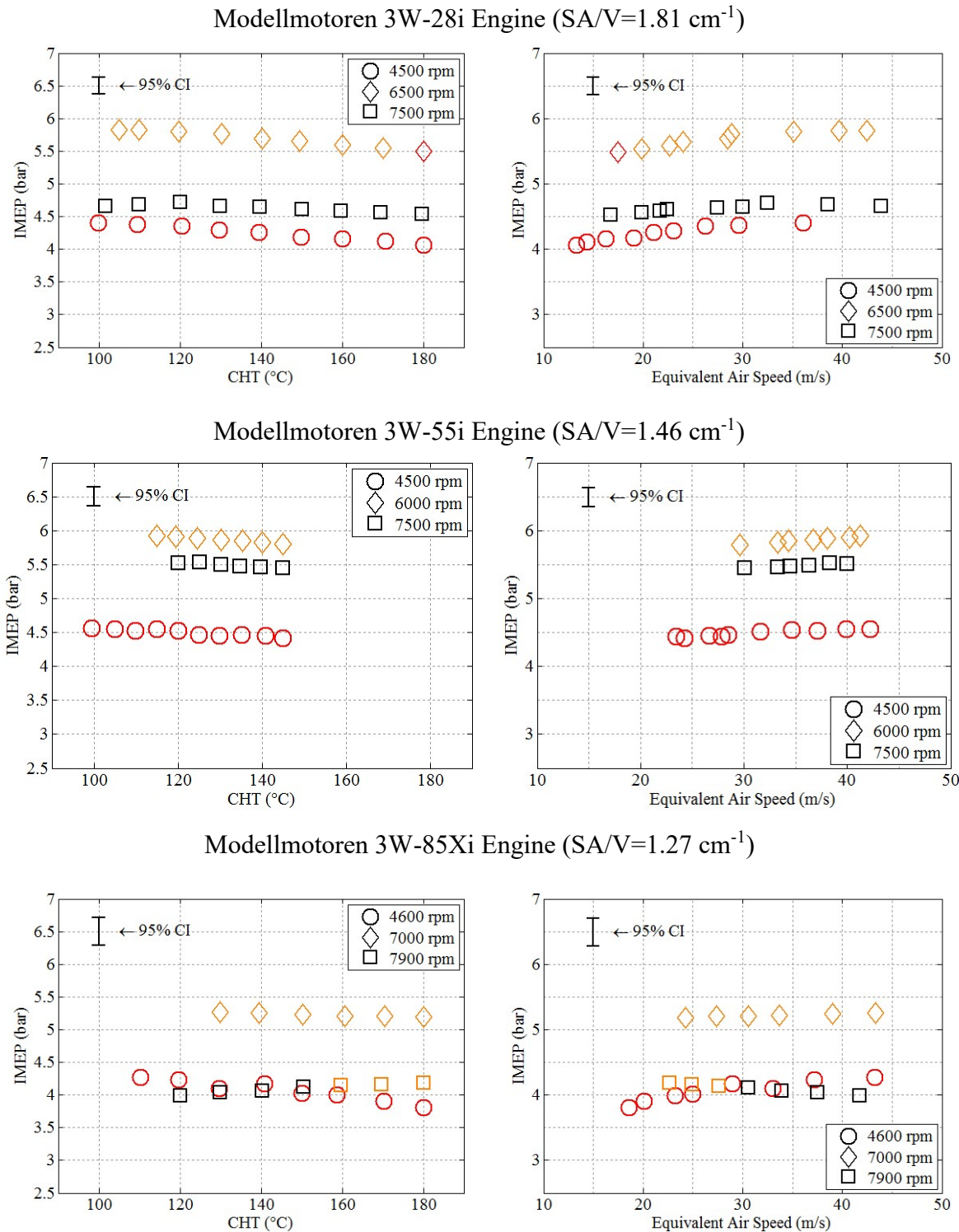
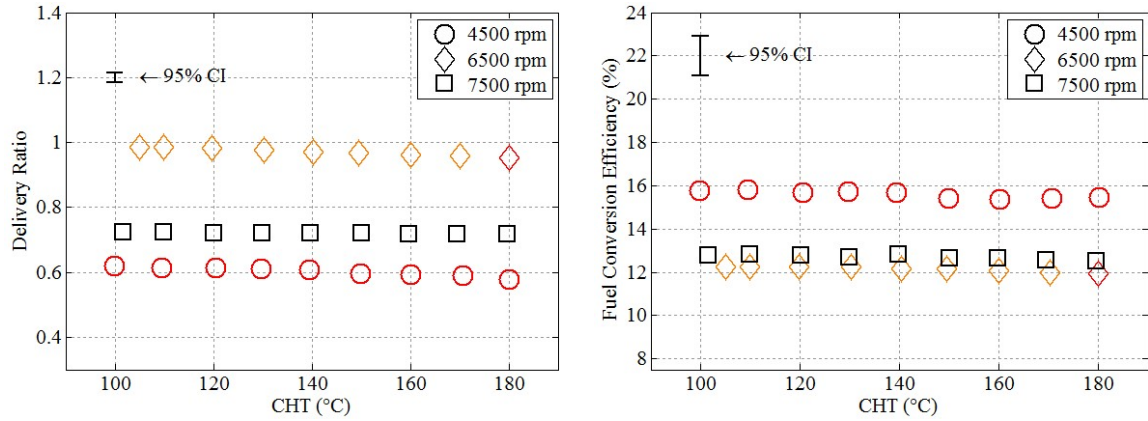
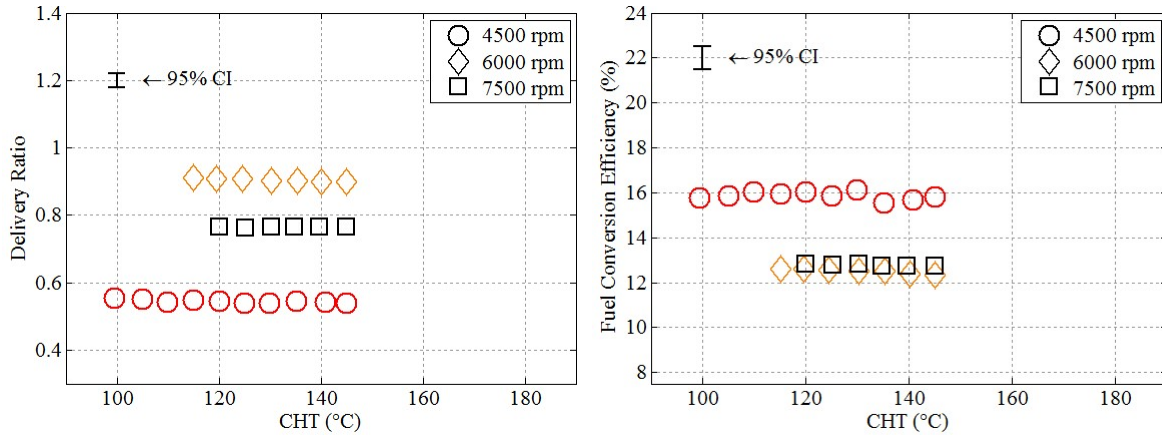


**Figure 174: Effect of head temperature and engine cooling on knock and KLIMEP for  $\phi=1.06\pm0.02$ ,  $CA_{50}=8\pm0.5^\circ\text{aTDC}$ , & 20 ON PRF blend. Red points were knock-limited. Orange points indicate the presence of abnormal combustion.**

### Modellmotoren 3W-28i Engine (SA/V=1.81 cm<sup>-1</sup>)



### Modellmotoren 3W-55i Engine (SA/V=1.46 cm<sup>-1</sup>)



### Modellmotoren 3W-85Xi Engine (SA/V=1.27 cm<sup>-1</sup>)

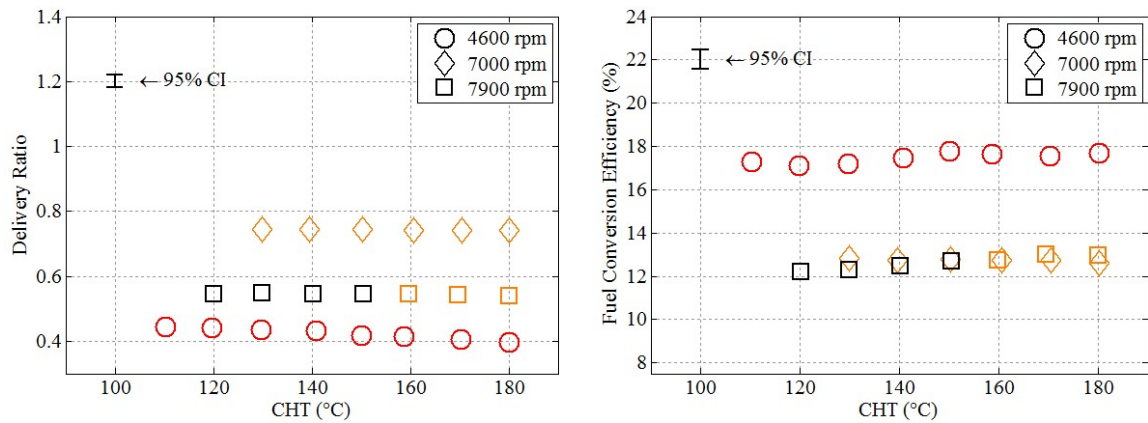


**Figure 175: Effect of head temperature on delivery ratio, fuel conversion efficiency, and knock running on 20 ON PRF blend. The engines were operated at  $\phi=1.06\pm0.02$ , CA50=8 $\pm$ 0.5°aTDC, & 20 ON PRF blend. Red points were knock-limited. Orange points indicate the presence of abnormal combustion.**

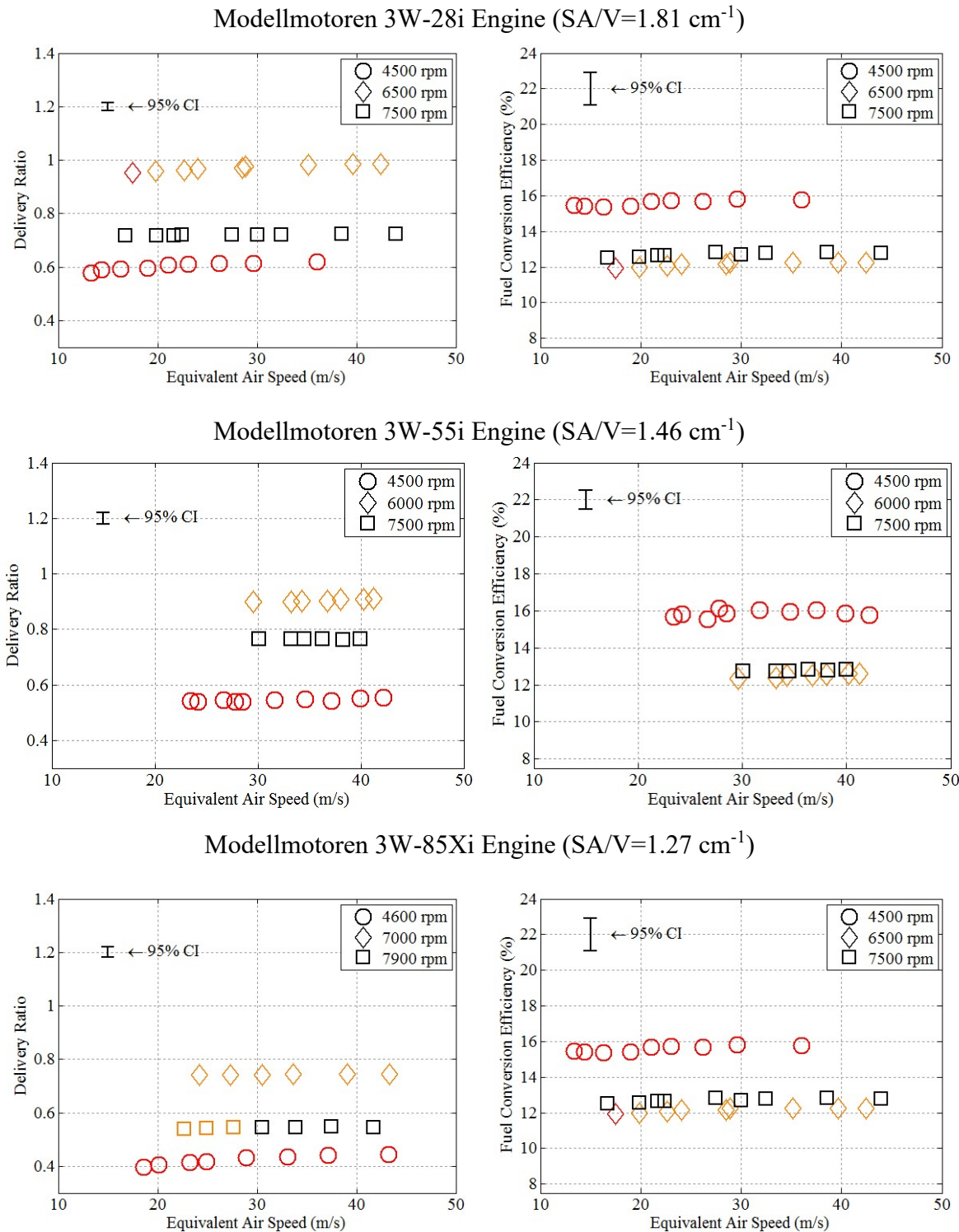


**Figure 176: Effect of engine cooling on delivery ratio, fuel conversion efficiency, and knock running on 20 ON PRF blend. The engines were operated at  $\phi=1.06\pm0.02$ ,  $CA_{50}=8\pm0.5^\circ\text{aTDC}$ , & 20 ON PRF blend. Red points were knock-limited. Orange points indicate the presence of abnormal combustion.**

showed only two minor exceptions to this observation. Above 150°C on the 3W-85Xi engine, barely detectable knock appeared in some of the pressure traces, and at 180°C the 3W-28i engine slipped from knock observed to very slightly knock-limited. Generally speaking however, provided the engine had sufficient cooling to meet the manufacturer's recommendations, external head temperature and cooling had no meaningful impact on the knock limit. This is in line with observations in Chapter V, Section 2.1 that showed cooling flow rate had little impact on in-cylinder temperatures and that other than preventing the engine from melting, external cooling was, generally, not the dominant segment of the heat transfer pathway.

## **5. Summary: Objective 3**

The goals of Objective 3 were to identify relationships between the fuel AKI requirement, loss mechanisms, and engine size, to quantify the performance impacts of switching from 98 ON fuel (manufacturer recommended) to 20 ON fuel (JP-8 and diesel), and to determine which engine control parameters were most effective at controlling knock in 10-100 cm<sup>3</sup> displacement engines. This chapter detailed the results of that investigation and was divided into three subsections. The first subsection (Section 2) examined KLIMEP, power, and burn angle for 10 different PRF blends ranging from 0 ON to 98 ON. The results indicated that knock was strongly dependent on rotational speed. Generally, once knock occurred the knock-limited speed range increased by 500 rpm for every 10 ON decrease in fuel ON. The results also showed a dependence on engine size, with the 3W-55i and 3W-85Xi engines being knock-limited about 500 rpm and 1000 rpm faster (or 10 ON and 20 ON higher) than the 3W-28i engine, respectively. Thus, for the studied engines decreasing engine size did increase the resistance to knock when operating on a low AKI

fuel due to a variety of factors that reduced the end-gas temperature and its propensity to auto-ignite. One of those factors was surface area to volume ratio. As discussed in Chapter IV, increasing surface area to volume ratio with decreasing engine size shifted thermal loading from the exhaust gases to the cylinder head, reducing heat transfer to the fresh charge and increasing knock resistance. When running on 20 ON fuel, which simulates operation on JP-8 and diesel, all engines were able to operate at WOT (i.e. not knock-limited) at the peak power conditions for 98 ON fuel, although the 3W-85Xi engine was substantially closer to its knock limit. Therefore, with attention to low speed operation, COTS conversion of a 10-100 cm<sup>3</sup> displacement, SI two-stroke engine is possible from an abnormal combustion standpoint, although the conversion becomes more difficult with increasing engine size.

To further quantify the implications of such a conversion, Section 3 directly compared power, burn angle, and efficiency for 98 ON and 20 ON operation. Switching from 98 ON fuel to 20 ON fuel led to a 2%-3% increase in power at non knock-limited conditions due to shortening of the CA0-CA10 burn angle. However, the power benefits were not realized on the 3W-28i and 3W-55i engines, which instead showed a 2% decrease in power. The decrease in power was traced to a decrease in intake air flow rate corresponding to operation on low AKI fuel, including the 20 ON PRF blend. Based on visual inspection of the reed valves, it was concluded that the low AKI fuel failed to deposit sufficient oil on the valves, which then failed to seal during compression of the crankcase contents and allowed backflow into the intake runner. When switching from 98 ON fuel to 20 ON fuel, burn angle reductions were on the order of 5 CAD, dominated by reductions in the CA0-CA10 burn angle. This indicates that fuel AKI played a critical role in initial flame

development, but was dominated by other factors such as convection and turbulence during flame propagation. After accounting for the impact of changing air flow rates (due to throttling and oiling of the reed valves), switching from 98 ON fuel to 20 ON fuel improved fuel conversion efficiency by 0.5%-1% (absolute). Considering the typical WOT fuel conversion efficiencies of these engines were about 15%, this translates to a 6% increase in range or endurance. Thus, while low AKI fuel did offer an efficiency benefit from reducing the burn angle, the steps taken to implement such a conversion (such as fuel injection, pre heating, modification of spark timing) will tend to dominate the changes in engine performance, explaining the conflicting observations of Cathcart *et al.* [15], Duddy *et al.* [38], and Wilson [14].

Section 4 evaluated the ability of equivalence ratio, combustion phasing, and head temperature to influence knock. The impact of equivalence ratio varied with the knock resistance of the engine. On the 3W-28i engine, lean operation at an equivalence ratio of 0.8 allowed the throttle to be fully opened (from a knocking baseline condition at 4500 rpm) resulting in a 10% increase in power. The 3W-55i and 3W-85Xi engines showed negligible change in knock-limited throttle setting with lean operation, and as a result, knock-limited power responded to lean operation similar to power at WOT, with a lockstep decrease in equivalence ratio and power. The lean results indicated that the effectiveness of reducing in-cylinder temperature through lean mixtures depends on engine size in the tested range. Richening the mixture beyond an equivalence ratio of 1.05 had a minimal effect except on the 3W-55i engine, where increasing the equivalence ratio from 1.05 to 1.35 increased power by 6%-7% but decreased fuel conversion efficiency from 16% to 12%. Therefore,

the charge cooling effect of extra fuel was generally ineffective and/or costly at mitigating knock in the studied engines.

Similar to equivalence ratio, the impact of varying combustion phasing correlated to the engine's resistance to knock. Advancing combustion phasing from near MBT timing (from  $CA_{50}=8^{\circ}aTDC$  to  $CA_{50}=-2^{\circ}bTDC$ ) could cause abnormal combustion to appear at knock free conditions in the 3W-28i and 3W-55i engines, but pushed the 3W-85Xi engine into a knock-limited condition. For knock-limited operation, retarding combustion phasing from  $CA_{50}=8^{\circ}aTDC$  to as late as  $CA_{50}=28^{\circ}aTDC$  reduced knock and for sufficiently late phasing allowed the engines to run closer to or at WOT. As engine size decreased the degree of retardation necessary to move from a knock-limited condition to WOT operation decreased. At 4500 rpm the 3W-28i engine was able to operate at WOT for  $CA_{50}$  greater than  $18^{\circ}aTDC$ , while such operation occurred at  $CA_{50}=28^{\circ}aTDC$  on the 3W-55i engine and not all on the 3W-85Xi engine. Thus, combustion phasing offered a significant control over knock as well as a means to develop additional power. The degree of control correlated to each engine's knock resistance. Shifting  $CA_{50}$  from  $8^{\circ}aTDC$  to  $18^{\circ}aTDC$  in the 3W-28i engine increased the knock-limited power by about 20%, while the same shift in the 3W-55i and 3W-85Xi engines led to increases of 11% and 9%, respectively. Of the three parameters investigated, combustion phasing had the greatest potential for controlling/ increasing knock-limited power, and offered the most control authority relative to its impact on fuel conversion efficiency.

Finally, cylinder head temperature had minimal impact on the knock limit or the presence of knock over the tested range from  $100^{\circ}C$  to  $150^{\circ}C$ . Despite the hypothesis that heat transfer would play a pivotal role in the knock resistance of 10-100  $cm^3$  displacement



engines, the influence of cylinder size on knock manifested only weakly in terms of heat transfer from the cylinder in the studied engines. Increasing head temperature to up to 150°C (manufacture limit) did not cause knock to appear for a knock free baseline, appreciably worsen for a baseline with minor knock, or drive the engine into more knock-limited operation from a knock-limited baseline. Above 150°C on the 3W-85Xi engine, barely detectable knock appeared in some of the pressure traces, and at 180°C the 3W-28i engine slipped from knock observed to very slightly knock-limited. Generally, provided an engine had sufficient cooling to meet the manufacturer's recommendations, external head temperature and cooling had no meaningful impact on the knock limit.

## VII Conclusions and Suggestions for Future Work

### 1. Chapter Overview

Effective in August of 2016, the Federal Aviation Administration's Small UAS Rule (Part 107) expanded access to the nation's skies for certified drone operators [283]. The policy was another step to meet the seemingly insatiable demand for remotely piloted aircraft. Even before the rule was released companies such as Amazon and WalMart were already seeking to use drones for deliveries [283]; local, state and federal emergency services were trying to expand laws to use drone over flights to aid disaster relief [283]. And of course, military demand keeps increasing as well; AFRL's Small Engine Research Lab has expanded from one fielded aircraft project at the start of this effort to at least four concurrent fielded aircraft programs in addition to its fundamental research programs. While the majority of small unmanned aircraft are short-endurance, electric powered vehicles, the superior specific power of hydrocarbon fuel relative to batteries (see Chapter I, Section 1) gives small ICEs a clear advantage in the extended range, long loiter category. This work has provided data and insight quantifying the behavior of COTS (as available at the time of writing), 10-100 cm<sup>3</sup> displacement, two-stroke, SI engines so that they may be more effectively employed on remotely piloted aircraft.

To that end, this work aimed to provide practical insight into the behavior and performance of 10-100 cm<sup>3</sup> displacement, two-stroke engines appropriate for Group 2 RPAs by studying three, geometrically similar as commercially possible COTS engines in that displacement range: the 3W-28i (28 cm<sup>3</sup>), the 3W-55i (55 cm<sup>3</sup>), and the 3W-85Xi (85 cm<sup>3</sup>). Chapter I identified three general issues with 10-100 cm<sup>3</sup> displacement ICEs, distilled those issues into problem statements, and then set forth to answer the problems

statements through three research objectives. Chapter II provided background on two-stroke engines, engine testing, and the specific topics involved in each objective. Chapter III described the experimental methodology to address each objective and Chapters IV-VI presented the results. This chapter concludes the document by mirroring Chapter I. It will first review the Objectives as set forth in Chapter I by linking the Objectives with their key conclusions (Section 2). Then it will tie the conclusions back to the practical problem statements that were the impetus for this effort (Section 3). It will also note a number of other results not directly tied to the research objectives that were delivered by this effort. The chapter will conclude with some general comments and suggestions for future work (Section 4).

## **2. Research Objectives and Key Conclusions**

The research objectives were originally presented in Chapter I, Section 3. This review will restate each of the Objectives, briefly describe the approach used to accomplish each Objective, and then restate the high level tasks. Following each high level task, a brief description of the key conclusion(s) will be offered to demonstrate its successful completion.

### **2.1. Objective 1**

*Investigate how loss pathways scale in 10-100 cm<sup>3</sup> displacement ICEs.*

This first objective established the order of importance for losses and how that order changes with engine size. The results were presented in Chapter IV.

**Approach:** The Small Engine Research Bench was designed to measure five energy pathways in 10-100 cm<sup>3</sup> displacement engines and validated for the 3W-28i (28 cm<sup>3</sup>), the 3W-55i (55 cm<sup>3</sup>), and the 3W-85Xi (85 cm<sup>3</sup>) engines studied herein. Those pathways were

brake power, heat transfer from the cylinder, short-circuiting of fresh charge, incomplete combustion, and sensible exhaust enthalpy. Based on the control volume around the engine, friction was measured as heat in the cooling load and exhaust sensible enthalpy. Brake power was measured using a dynamometer, and corrected for losses in the drive train. Heat transfer was measured as the enthalpy change of the cooling air in a control volume surrounding the engine. Short-circuiting and incomplete combustion were measured by analyzing bagged exhaust samples using gas chromatography in combination with thermal conductivity and flame ionization detectors as well as mass spectrometry. Fuel and air flow were also measured to verify closure of the energy balances. The bench was described in detail in Chapter III, Section 2, and the energy balance methodology was described in Chapter III, Section 3.

**Task 1:** Determine the relative contributions of the following losses in a family of geometrically similar, commercially available engines with displaced volumes ranging from 10-100 cm<sup>3</sup> (1-7 kW, manufacturer rated): heat transfer from the cylinder, short-circuiting of fresh charge, sensible enthalpy in the exhaust gases, incomplete combustion, and brake power, which is not a loss, but an energy pathway necessary for a full energy accounting.

**Approach 1:** Three two-stroke, spark-ignition COTS engines as geometrically similar as possible were selected and converted to variable spark timing and throttle body fuel injection using a custom ECU. The engines had displacement volumes of 28 cm<sup>3</sup>, 55 cm<sup>3</sup>, and 85 cm<sup>3</sup>. The engines were run at WOT throttle over their speed range of 4000 rpm to 8000 rpm to determine the maximum power point. The loss pathways were then quantified at peak power. The engines and test methodology were described in Chapter III, Section 3.

**Conclusion 1a:** Chapter IV, Section 2 presented energy balances for each of the studied engines and the scaling study that was the focus of Objective 1. The balances demonstrated a full accounting of the energy delivered to each of the three engines. Comparison to manufacturer data showed that performance of the tested engines was comparable to manufacturer expectations of the engines as well as performance of typical 10-100 cm<sup>3</sup> displacement, two-stroke engines. Energy balances and the comparison to manufacturer data were presented in Chapter IV, Section 2.2 and Chapter IV, Section 2.3, respectively.

**Conclusion 1b:** At the outset of this effort it was unclear which losses drove the efficiency in 10-100 cm<sup>3</sup> displacement, two-stroke, spark-ignition engines. The results showed that the primary losses were short-circuiting and incomplete combustion. At peak power, the loss pathways ranked by relative magnitude were: short-circuiting (40%-50%), sensible exhaust enthalpy (14%-18%), incomplete combustion (11%-17%), brake power (14%-15%), and heat loss from the cylinder (10%-11%).

**Task 2:** Determine which losses are responsible for the observed decrease in fuel conversion efficiency as engine displacement decreases.

**Approach 2:** Engine design parameters dominated the variation in the energy pathways between the tested engines. To draw conclusions about the scaling of loss pathways, the peak power energy balances for the tested engines were compared to energy balances for smaller micro glow fuel engines as well as automotive scale and larger spark-ignition and compression-ignition engines.

**Conclusion 2:** As displaced volume decreased from greater than 100 cm<sup>3</sup> to 10-100 cm<sup>3</sup>, short-circuiting and incomplete combustion losses drove the decrease in efficiency. When these losses were removed and only the energy released during combustion was considered

(thermal efficiency), the studied engines had thermal efficiencies comparable to conventional (automotive) scale engines (approximately 35%). Based on data for micro glow engines (less than 10 cm<sup>3</sup> displacement), as engine displacement further decreased to less than 10 cm<sup>3</sup>, heat transfer became increasingly important, driving down thermal efficiency more rapidly. Thus, the primary obstacle to improving performance in the 28-85 cm<sup>3</sup> displacement COTS two-stroke engines investigated herein was addressing short-circuiting, not heat transfer. To improve efficiency in small COTS, two-stroke engines, efforts should target reducing short-circuiting losses through exhaust tuning, lean operation, and direct injection. The scaling of loss pathways as well as methods for mitigating short-circuiting losses were discussed in Chapter IV, Section 2.4.

**Task 3:** Perform a parametric study of engine controls (speed, throttle, equivalence ratio, combustion phasing, and cylinder head temperature) to link losses with the mechanisms that cause them.

**Approach 3:** The design of the SERB (Chapter III, Sections 2 and 3) included five engine control variables: speed (4000 rpm to 8000 rpm), equivalence ratio (0.70–1.30), combustion phasing (CA50 = -2-28°aTDC), cooling (CHT = 130-180°C), and throttle (WOT to 1/3 throttle). Starting from a baseline condition of 6000 rpm, WOT,  $\Phi = 1.05-1.07$ , CA50 = 8°aTDC, and CHT = 130°C, each of the control variables was swept across its operational range to quantify the impact on power, efficiency, and the energy pathways.

**Conclusion 3:** The parametric study was presented in Chapter IV, Section 2.3 (speed) as well as Chapter IV, Section 3 (equivalence ratio, combustion phasing, head temperature, and throttle). The study discussed ways to improve engine performance over the COTS configurations. Operation at equivalence ratios between 0.8 and 0.9 increased fuel

conversion efficiency by up to 4% (absolute) from typical operation at an equivalence ratio between 1.1 and 1.2 with a power penalty of about 10%. The linear timing maps in the stock ECU were within  $\pm 5$  CAD of MBT timing between 4000 rpm and 8000 rpm, leading to a negligible (less than 5%) impact on power. However, the linear map in the stock ECU was too retarded at low starting speeds, making the engines difficult to start. A non-linear map with 20-30°bTDC spark timing at starting speeds could reduce starting time by up to 90%, especially in a motor-to-start configuration. Decreasing head temperature from 180°C to 120°C led to a 5%-10% increase in power and a 0.5% (absolute) increase in fuel conversion efficiency, indicating that more cooling is preferable. Finally, fuel conversion efficiency improved at throttled conditions by 4% to 6% (absolute) due primarily to decreased short-circuiting. This suggests that oversizing an engine and operating at throttled conditions would be an effective method to mitigate short-circuiting. As an example, using a heavier, throttled 3W-55i engine in place of a WOT 3W-28i engine would break even in terms of system weight at 2.5 hours, and save 5 g/min of fuel thereafter.

## 2.2. Objective 2

*Develop models/ correlations for thermal and friction losses  
for 10-100 cm<sup>3</sup> displacement ICEs.*

This objective aimed to employ the loss data collected for Objective 1 to develop appropriate overall heat transfer and friction loss models/correlations for 10-100 cm<sup>3</sup> displacement ICEs.

**Approach:** The SERB developed to complete Objective 1 was used to measure three loss pathways: heat transfer, friction, and short-circuiting (scavenging). The measurements described in Objective 1 were supplemented with measurements of in-cylinder gas

temperature for heat transfer. The data were then used to validate literature correlations for the studied engines and to propose new correlations where literature correlations proved inadequate. The methodology for Objective 2 was described in Chapter III, Section 4.

**Task 1:** Determine if the overall heat flux model proposed by Taylor and Toong [21:677-80] is appropriate for 10-100 cm<sup>3</sup> displacement, two-stroke, spark-ignition engines.

**Approach 1:** Heat transfer losses from 3W-28i and 3W-55i engines were measured using the methodology described in Objective 1. (Equipment availability precluded testing the 3W-85Xi engine). In-cylinder pressure data were used to calculate in-cylinder temperature profiles, which were then compared to in-cylinder temperature measurements made using TLAS. The modeled and measured data was used to evaluate the validity of Taylor and Toong's [21:677-80] spatially and temporally averaged model, which was originally developed for larger CI and SI engines ranging from 241 cm<sup>3</sup> to 3.3 L displacement, for heat transfer for the studied engines. Fits to Taylor and Toong's model provided by Annand [17] were also evaluated. The methodology for heat transfer modelling was described in detail in Chapter III, Section 4.1.

**Conclusion 1:** Taylor and Toong's heat flux model was not readily adaptable to the 3W-28i and 3W-55i engines, and provided only an order of magnitude estimate of the heat transfer. Equation (147) shows a fit of the model to data collected on the studied engines. Fits provided in the literature [17, 21:677-80] had Reynold's number exponents of 0.7 to 0.8, significantly higher than those for the 3W-28i and 3W-55i engines (0.3 to 0.4). Therefore, the literature fits developed for larger engines are not appropriate for engines in the 10-100 cm<sup>3</sup> displacement range. Heat transfer modelling results were presented in Chapter V, Section 2.



$$u = (9.4 \pm 5.8)Re^{(0.31 \pm 0.1)} \quad (147)$$

**Task 2:** Evaluate other quantities for inclusion in the model for the Nusselt number.

**Approach 2:** Similar to the parametric study in Objective1, each of the engine control variables (speed, equivalence ratio, combustion phasing, throttle, and cooling) was swept over its control range. The results were plotted with Nusselt number as the ordinate and Reynold's number as the abscissa to identify variations not captured/described by the terms in Taylor and Toong's [21:677-80] proposed form.

**Conclusion 2a:** Based on the results, the Taylor and Toong [21:677-80] model was not formulated to handle variations in throttle, speed, and cooling flow rate as observed in the studied engines. Therefore, the following terms should be considered in future efforts to model heat transfer in 10-100 cm<sup>3</sup> displacement, two-stroke, SI, air-cooled engines. In the original model, mass flow rate of charge through the engine was used to calculate the Reynold's number. As a result, engine speed had little effect on Reynold's number (but a notable impact on heat transfer) while throttle had a large effect on Reynold's number (but a small impact on Nusselt number). Therefore, it is suggested that the engine operational speed be included in the Reynold's number. One possible methodology is that proposed by Annand [17], where the Reynold's number is based on the mean piston speed (characteristic velocity) and bore (characteristic length scale). Additionally, the original model was primarily based on water cooled engines, and was therefore not formulated to handle the large changes in the coolant flow rate common on small air-cooled aircraft engines. Future modelling efforts should consider including a form of the coolant flow rate, non-dimensionalized as a Reynold's number.

**Conclusion 2b:** Most models calculate in-cylinder temperature using the in-cylinder pressure. Two temperature models based on the ideal gas law, one using a variable trapped mass and one using an average trapped mass, were compared to temperature results from a line-of-sight temperature measurement through the combustion dome made using TLAS. The temperature measured using TLAS exhibited an earlier, sharper, and higher peak caused by the flame front traversing the line-of-sight, as well as a more rapid drop due to localized cooling. In most cases the modelled temperatures captured the qualitative behavior of the measured temperature as engine controls were swept through their operational range. The results demonstrated that it was difficult to calculate a consistent trapped mass and that the calculated temperature profiles were highly sensitive to that mass. Provided the ability to estimate the effect of operating condition on the trapped mass, the variable mass model was more appropriate. More detail on the in-cylinder temperature measurement and modelling results can be found in Chapter V, Section 2.1.

**Task 3:** Compare friction loss data from the tested engines to the proposed friction loss correlation presented in Chapter I, Section 2.2.2.

**Approach 3:** In Objective 1 friction losses were lumped with the cooling load and exhaust sensible enthalpy. For the modelling effort, friction losses were measured in a motoring engine test conducted at operational engine temperatures. The motoring friction test setup was described in Chapter III, Section 3.3 and the test methodology was described in Chapter III, Section 4.2. Since a motoring test was used, only the effects of speed and throttle on friction losses were investigated. The results for speed were compared to the standard three term model common in the literature [22:722 22:368], and the influence of

surface area to volume ratio on friction losses was also investigated. Finally, the throttle results were used to develop a predictive correlation for engine friction.

**Conclusion 3:** Chapter V, Section 3 presented the friction loss modelling results. Compared to larger engines where FMEP is typically best fit with a quadratic function of engine speed [21:722, 22:368], the engines tested herein had nearly constant values of FMEP similar to smaller glow fuel engines [16]. Therefore, data from small glow fuel engines was used in conjunction with the data collected herein to develop a correlation between cylinder surface area to volume ratio and friction losses.

**Task 4:** Identify which coefficient(s) in the friction loss model scale with engine size and reconcile that information with engine design.

**Approach 4:** The data from the tested engines was combined with data from the literature for smaller (glow fuel) two-stroke engines [16]. The impact of throttle, normalized as delivery ratio, on friction was also investigated.

**Conclusion 4:** The results showed that friction scales with surface area to volume ratio; a suggested correlation valid for crankcase scavenged two-stroke engines less than approximately 100 cm<sup>3</sup> displacement is shown in Equation (148).

$$\begin{aligned}
 FMEP[kPa] = & (-0.5 \pm 17.8) + (62.5 \pm 9.2) \frac{SA}{V_d} [cm^{-1}] \\
 & + (3.02 \pm 1.02) \left( \frac{SA}{V_d} \right)^2 [cm^{-2}]
 \end{aligned}
 \tag{148}$$

Friction losses during throttled operation may be predicted using delivery ratio and the power to overcome friction losses at WOT using the form given in Equation (149). Additional detail on friction modelling may be found in Chapter V, Section 3.

$$\frac{P_f(\Lambda)}{P_f|_{WOT}} = 1 - (0.89 \pm 0.30)(\Lambda|_{WOT} - \Lambda) \quad (149)$$

**Task 5 (additional):** Compare scavenging performance to historical models.

**Approach 5:** Scavenging data collected during Objective 1 was compared to the perfect isothermal mixing and perfect isothermal displacement models. Results showing the effects of all five control variables (speed, equivalence ratio, combustion phasing, throttle, and cooling) were presented and discussed.

**Conclusion 5:** Chapter V, Section 4 compared gas exchange to historical models and discussed the scavenging performance observed in the studied engines. Over the operating range, engine scavenging performance was within  $\pm 5\%$  (absolute) at most points and  $\pm 10\%$  (absolute) at all points of the perfect isothermal mixing model using the trapped volume as the reference volume. At most operating conditions, the engines slightly underperformed the perfect isothermal mixing model, generally taken as the worst case scenario for larger modern engines. Two factors drove the high short-circuiting observed during Objective 1: excess fresh charge delivered to the engine beyond the cylinder capacity and poor scavenging performance comparable to the perfect isothermal mixing model even for delivery ratios below unity.

### 2.3. Objective 3

*Quantify the relationship between engine size, loss mechanisms, performance, and fuel AKI requirements in 10-100 cm<sup>3</sup> displacement ICEs.*

This objective investigated the relationship between loss pathways, engine size, and fuel AKI requirement.

**Approach:** Knock was measured in real time using the AVL Indismart Combustion Analyzer and an in-cylinder pressure transducer. The knock limit was defined as the more conservative of 5 bar MAPO or 5 bar/deg peak pressure rise rate for 1% of 400 consecutive cycles. Throttling the engine was the primary means of controlling knock. The testing methodology for the fuel AKI study was described in Chapter III, Section 5.

**Task 1:** Map the knock-limited indicated mean effective pressure for a family of geometrically similar engines in the 10-100 cm<sup>3</sup> displacement range, running primary reference blend fuels ranging from 0-100 ON.

**Approach 1:** The KLIMEP was mapped in 10 ON increments from 0 ON to 98 ON across the operational speed range for the 3W-28i, 3W-55i, and 3W-85Xi engines. The ON was established using PRF blends of iso-octane and n-heptane.

**Conclusion 1:** Chapter VI, Section 2 examined KLIMEP, power, and burn angle for 0 ON to 98 ON PRF blends from 4000-8000 rpm. Knock was strongly dependent on rotational speed. Generally, once knock occurred, the knock-limited speed range increased by 500 rpm for every 10 ON decrease. The results showed a dependence on engine size, with the 3W-55i (55 cm<sup>3</sup>) and 3W-85Xi (85 cm<sup>3</sup>) engines being knock-limited about 500 rpm and 1000 rpm faster (or 10 ON and 20 ON higher) than the 3W-28i (28 cm<sup>3</sup>) engine, respectively. Thus, for the 28-85 cm<sup>3</sup> two-stroke engines studied herein, decreasing engine size did increase the resistance to knock when operating on a low AKI fuel.

**Task 2:** Evaluate the performance impact (power, efficiency) of converting from 98 ON fuel to 20 ON fuel.

**Approach 2:** Repeat testing (three trials of each fuel) was conducted to quantify the effects of switching from a high AKI fuel (98 ON) such as gasoline to a low AKI fuel (20 ON) such as diesel or JP-8.

**Conclusion 2:** Chapter VI, Section 3 directly compared power, burn angle, and efficiency for 98 ON and 20 ON operation. Switching from 98 ON fuel to 20 ON fuel led to a 2%-3% increase in power at non knock-limited conditions due to shortening the CA0-CA10 burn angle. Switching from 98 ON fuel to 20 ON fuel, burn angle reductions were on the order of 5 CAD, dominated by reductions in the CA0-CA10 burn angle. This indicates that fuel AKI played a critical role in initial flame development, but was dominated by other factors such as convection and turbulence during flame propagation. Changing from 98 ON fuel to 20 ON fuel improved fuel conversion efficiency by 0.5%-1%. Considering the typical WOT fuel conversion efficiencies of these engines were about 15%, this translates to a 6% increase in range or endurance. Thus, while low AKI fuel did offer an efficiency benefit from reducing the burn angle, the steps taken to implement such a conversion will tend to dominate the changes in engine performance, which accounts for the conflicting heavy fuel conversion results reported in the literature [14, 15].

**Task 3:** Quantify the impact of engine control variables (speed, equivalence ratio, combustion phasing, and head temperature) on the knock limit. Link changes in losses and loss mechanisms (identified in Objective 1) and engine size to the observed trends in the fuel AKI requirement.

**Approach 3:** The effects of equivalence ratio, combustion phasing, and engine cooling on the knock limit were evaluated at knock free conditions, knock-limited conditions, and conditions where knock was present below the knock limit at the baseline condition. Each

of the control parameters was swept through its operational range to quantify its impact on the knock limit and its tendency to induce or worsen knock.

**Conclusion 3:** Chapter VI, Section 4 evaluated the ability of equivalence ratio, combustion phasing, and head temperature to influence knock. The impact of equivalence ratio varied with the knock resistance of the engine. The lean combustion results indicated that the effectiveness of reducing in-cylinder temperature through lean mixtures depends on engine size in the tested range. The charge cooling effect of extra fuel was generally ineffective and inefficient at mitigating knock in the studied 28-85 cm<sup>3</sup>, SI two-stroke engines. For knock-limited operation, retarding combustion phasing from CA50=8°aTDC to as late as CA50=28°aTDC reduced knock and for sufficiently late phasing allowed the engine to run at WOT. Of the three parameters, combustion phasing had the greatest potential for increasing knock-limited power, and offered the most control authority relative to its impact on fuel conversion efficiency. Cylinder head temperature had minimal impact on the knock limit and the presence of knock over the tested range from 100°C to 150°C. Despite the hypothesis that heat transfer would play a pivotal role in the knock resistance of engines of 10-100 cm<sup>3</sup> displacement, the influence of cylinder size on knock manifested only weakly in terms of heat transfer from the cylinder in the studied engines.

### **3. Problems Statements and Answers**

The three research objectives were developed to address practical questions about using 10-100 cm<sup>3</sup> displacement SI, two-stroke engines on Group 2 RPAs. This section revisits those practical questions and answers them using the conclusions for each research objective. It also includes a list of ‘answers’ to questions not posed in the original problem.

### 3.1. Scaling of Loss Pathways

An understanding of how loss pathways change with engine size is crucial to improving performance and fuel conversion efficiency and to determining if the mechanisms responsible for the efficiency drop permit an inherent (and useful) relaxation of fuel AKI requirement with engine size. Based on collected data and data available from the literature for larger [21:674] and smaller engines [6, 16], the drop in efficiency in 10-100 cm<sup>3</sup> engines relative to engines larger than 100 cm<sup>3</sup> displacement was driven by high short-circuiting losses and incomplete combustion. Thermal losses through the cylinder were not an issue until displacement dropped below 10 cm<sup>3</sup>. Therefore, based on the studied engines, efforts to improve 10-100 cm<sup>3</sup> displacement, two-stroke engine performance for Group 2 RPAs should focus on fuel delivery and charge retention. Approaches include throttle body or direct injection, intake and exhaust tuning, and port redesign depending on the number of production engines, the permissible unit cost, and the mission requirements. When no additional short-circuiting mitigation techniques are employed, running a larger engine at partial throttle could yield a weight savings for long endurance missions.

### 3.2. Loss Models

Models for loss pathways offer aircraft designers the ability to predict engine performance in the airframe early during the design phase without rigorous testing of the engine. Models for heat transfer (cooling requirements), friction (mechanical efficiency), and gas exchange (fuel consumption and emissions) were generally unavailable or not validated for 10-100 cm<sup>3</sup> displacement engines. For heat transfer, a spatially and temporally averaged model would provide an estimate of cooling requirements for an engine. Taylor and Toong's model was investigated for this purpose. Not only were the



coefficients used in this model inappropriate for small, two-stroke SI engines, the model was not well-suited to correlate variations in speed, throttle, and cooling flow. Further work is required to adapt the model for small two-stroke engines. Therefore, the fit provided in this work (Equation (147)) offers an order-of-magnitude estimate of the cooling requirement. The primary difference between the developed model and the literature model was the exponent on the Reynold's number. For the studied engines, that exponent was about half (0.3-0.4) of the exponent provided in the literature (0.7-0.75). In addition to improvements in the heat transfer model, the temperature model also needs a better methodology for estimating the trapped mass.

Friction reduces the mechanical efficiency of an engine. Generally speaking, friction losses in the tested engines were low compared to automotive and larger scale engines. Combining data from the engines studied in this work with data available in the literature for micro glow engines [16] showed that for two-stroke engines less than 100 cm<sup>3</sup> displacement, FMEP is relatively constant with speed compared to larger engines where FMEP is typically a quadratic with speed. Therefore, for two-stroke engines less than 100 cm<sup>3</sup> displacement, FMEP may be predicted using the surface area to volume ratio provided the engine in question has similar friction sources to those investigated in this work. The throttled friction may then be predicted using the WOT friction losses as a linear function of delivery ratio at a given speed.

For modelling gas exchange in a 10-100 cm<sup>3</sup> displacement, two-stroke engine, the results of this work indicate that the perfect isothermal mixing model using the trapped volume as the reference volume would predict charging efficiency and trapping efficiency within  $\pm 10\%$  (absolute) ( $\pm 5\%$  for most conditions). Note that the engines underperformed

the perfect isothermal mixing model at most operating conditions. The applicability of the perfect isothermal mixing model assumes that no modifications have been made to the COTS engine to specifically improve scavenging performance. Moreover, as automotive and larger scale engine technology permeates in to the 10-100 cm<sup>3</sup> displacement, two-stroke engine market, the perfect isothermal mixing will likely become a conservative estimate as it is for larger modern two-stroke engines.

### **3.3. Inherent Relaxation of Fuel AKI Requirement with Engines Size**

From the DoD's perspective there is an interest in running current (at the time of writing) COTS engines on low AKI fuel, which is more logistically supportable. However, the trade space and feasibility of such a conversion had not been systematically studied for 10-100 cm<sup>3</sup> displacement, two-stroke engines. Based on the surveyed literature, conversion to heavy fuel requires replacing the carburetor with a fuel injection system and replacing the stock ECU with an ECU capable of adjusting the spark timing. With those modifications, this effort demonstrated that all of the tested engines were able to make full power (as measured on 98 ON fuel) running on 20 ON fuel (similar to JP-8 and diesel) despite knock limitations at the lower end of the speed range. Therefore, with attention to low speed operation, COTS conversion of a 10-100 cm<sup>3</sup>, SI two-stroke engine solely through the addition of throttle body fuel injection and variable spark timing is possible from an abnormal combustion standpoint although the conversion becomes more difficult with increasing engine size. Furthermore, low AKI fuel did offer an efficiency (and power) benefit of 0.5%-1% (1%-2% in power) by reducing the burn angle, which translates to a 6% increase in range or endurance. Combustion phasing was the most effective control to mitigate abnormal combustion. Rich operation offered some margin but with a large fuel

conversion efficiency penalty. Engine cooling within the manufacturer recommended limits had little impact on the knock limit.

### **3.4. Answers beyond the Original Questions**

Beyond the posed research objectives and problem statements, there were a number of other results/recommendations that came out of this effort. They are listed below:

**Recommendation:** DoD systems should always consider replacing the stock carburetor with throttle body fuel injection. Throttle body fuel injection improves stability of engine operation, enables lean operation, and can reduce fuel burn by up to 30% with minimal impact on power compared to the stock carburetor.

**Recommendation:** For engines starting in mid-air or in a contested environment, the linear timing maps in the stock ECU should be replaced with optimized spark timing. Deviations between the linear timing maps and optimal timing at low speed and/or low throttle led to difficulties starting the engines and running at low power.

**Result:** A measurement technique for short-circuiting using GC-MS to quantify iso-octane and argon in the exhaust was validated. The methodology offers a measurement technique valid at lean operation when PRF fuel blends are used during engine testing.

**Result:** Measuring spark plug pressure transducers and flush mount pressure transducers were shown to be statistically interchangeable in small, two-stroke, SI engines. A spark plug pressure transducer may be used in small engine testing without concerns over the spark element or transducer adversely affecting the test results. Unlike a flush mount transducer, the spark plug transducer does not require modifying the engine head.

**Result:** This work provides a database of test data for 28-85 cm<sup>3</sup>, SI, two-stroke engines.

#### **4. Final Thoughts and Future Work**

The fact that short-circuiting rather than heat transfer was the dominant loss in the studied engines was perhaps one of the least expected outcomes of this research. The result disproved the original assumption that poor fuel conversion efficiency for 10-100 cm<sup>3</sup> displacement, two-stroke engines was driven by thermal losses from the cylinder. The result also showed that reducing short-circuiting losses through methods such as tuning, direct injection, and lean operation should be the first step to improving small two-stroke engine performance. At the same time, the short-circuiting results raised another question: if four-stroke engines of a comparable size are expected to have similar efficiencies yet very limited short-circuiting, then where does the excess energy go? The parametric study results and fuel AKI requirement results raise other systems engineering type questions regarding the tradeoffs between system cost, mission requirements, short-circuiting mitigation techniques, and the value of operation on logistically supported fuel. And, of course, more work could certainly be done for temporally resolved heat flux models. This work has provided a foundation to answer those questions, some directly through future efforts on AFRL's SERB. The small remotely piloted aircraft market is no longer a niche occupied solely by hobbyists and enthusiasts. It is a market that has the attention of companies, militaries, and governments all racing to field increasingly capable platforms that fly further, stay aloft longer, and carry out progressively complex missions. Ultimately, this document has provided insight into how to take inexpensive COTS propulsion systems designed primarily for hobbyist aircraft, understand the cost-performance trade space, and integrate them onto reliable, fielded systems.

## **Appendix A**

**Paper:** Development of Test Bench and Characterization of Performance in Small Internal Combustion Engines

**Presented at:** 2013 Small Engine Technology Conference in Taipei, Taiwan

**Citation:**

J. K. Ausserer, P. J. Litke, J. R. Groenewegen, A. Rowton, M. Polanka, and K. Grinstead, "Development of Test Bench and Characterization of Performance in Small Internal Combustion Engines," presented at the 19th Small Engine Technology Conference, Taipei, Taiwan, SAE Technical Paper 2013-32-9036, 15 October 2013, doi: 10.4271/2013-32-9036.

# Development of Test Bench and Characterization of Performance in Small Internal Combustion Engines

**Joseph K. Ausserer, Paul J. Litke**  
Air Force Research Laboratory, United States Air Force

**Jon-Russell Groenewegen**  
University of Dayton Research Institute

**Alexander Rowton, Marc Polanka**  
Air Force Institute of Technology

**Keith Grinstead**  
Innovative Scientific Solutions Incorporated

Copyright © 2013 SAE Japan and Copyright © 2013 SAE International

## ABSTRACT

Small internal combustion engines (ICEs), (<7.5 kW), possess low thermal efficiencies due to high thermal losses. As the surface area to volume ratio increases beyond 1.5 cm<sup>2</sup>/cc, the increase in thermal losses leads to a drop off of engine efficiency and power. This effort describes the development and validation of a test stand to characterize thermal losses of small ICEs, optimize combustion phasing, and eventually enable heavy fuel operation. The test stand measures torque, rotational speed, brake power, intake air mass flow, up to 48 temperatures (including ambient, intake, cylinder head, fuel, and exhaust), 8 pressures (including ambient, intake, and exhaust), throttle position, and fuel and air mass flows. Intake air temperature and cylinder head temperature are controlled and adjustable. Three geometrically similar engines with surface area to volume ratios near 1.5 cm<sup>2</sup>/cc were selected from 3W Modellmotoren. During bench validation the 3W 55i engine's power, torque, brake specific fuel consumption, efficiency, and equivalence ratio were mapped in the stock configuration. The engine developed a peak power output of 2.1 kW at 7000 rpm, 54% of its manufacturer rated power. Additional tuning of the exhaust or carburetor may achieve manufacturer rated performance.

## INTRODUCTION

Over the past two decades, routine uses of small ICEs in the 1 to 8 kW range have expanded from lawn tools and hobbyist aircraft to commercially produced RPAs. While these engines possess lower fuel conversion efficiencies than their larger counterparts [1], the high specific energy of fossil fuels relative to even the best battery technology on the market allows these small ICEs to offer RPAs improved range and endurance over competing, economically viable electric and hybrid solutions [2].

As a result of the rapid and chaotic growth of the small (less than 50 kg) RPA industry, most manufacturers have opted for COTS power plants due to their relatively low price. Designing and building an ideal solution is both time and cost prohibitive. Thus, these small ICEs have been adapted from low use, low reliability applications to a high use, high reliability application, with little focus on development or improvement of the engine itself. Small ICEs often lack the performance data required for design decisions, such as matching the speed and torque ranges of the engine and the propeller. Much of the available data is from hobbyist magazines [3, 4, 5, 6] and provides only torque, speed, and power data. Manufacturer data is often less complete. Small RPAs rarely employ variable pitch propellers due to the added weight, cost, and complexity. Instead, they employ fixed pitch propellers, which require knowledge of both the propeller and engine operating curves to match them into an efficient system [7].

Most small RPAs use hobbyist COTS propellers. For an engine such as the 3W 55i, such a propeller might be 50-80 cm diameter with 25-40 cm of pitch and designed to operate between 2000-8000 rpm to achieve viable propeller efficiency and mitigate propeller noise. Even at 8000 rpm, the 3W 55i operates with a mean piston speed of 9.3 m/s, far lower than even large diesel engines used in an 18-wheeler application. One significant advantage of decreasing engine size is that operational speed can be increased without increasing the inertial loads on the engine's components. The increasing of engine speed counteracts some of the negative scaling effects, such as thermal losses, from increased surface area to volume ratio and non-adiabatic frictional losses. For example, micro engines with displacements in the 3 cc to 15 cc range can run at operational speeds of 20,000-40,000 rpm and greater. When appropriately tuned, these engines can actually exhibit an increase in specific power with decreasing size. However, without a gearbox or improved propeller technology to permit increased operational speeds, the engines considered in this work (and

for many small RPA applications) are limited to speeds below 9,000 rpm. The consequence is that increasing losses and decreasing engine size with relatively fixed engine operational speeds causes an exponential drop-off in specific power.

Historically, COTS ICE's for hobbyist aircraft have operated on glow fuel (70% methanol and 30% nitro methane), which has a heat of combustion of about 16.5 kJ/cc (18.5 kJ/g). Glow fuel has a relatively low energy density relative to common fuels such as gasoline, which has a heat of combustion of 35.5 kJ/cc (47.3 kJ/g). Thus, glow fuel was a heavy and space intensive fuel to carry compared to gasoline. Glow fuel also has a very low air to fuel ratio compared to gasoline; methanol has an air to fuel ratio of 6.42:1, and gasoline is about 15:1. The low air to fuel ratio and energy density of glow fuel results in BSFC values for glow operated engines ranging from 1200 g/kW-hr, which was an extremely efficient glow fuel engine, to upwards of 4250 g/kW-hr compared to 500 g/kW-hr or less for a modern gasoline spark ignition engine.

Over the last two decades, small COTS engines have shifted from glow fuel to gasoline. Compared to glow fuel, a BSFC of 1000 g/kW-hr, which would be unacceptable in a commercial car, boat, or plane engine, is a dramatic increase in efficiency for the hobbyist market. For hobbyist aircraft, fuel tanks were no longer the limiting factor in flight duration. For long endurance RPAs however, decreasing BSFC below 500 g/kW-hr would significantly enhance mission performance compared to the ~1200 g/kW hour measured on the stock 3W 55i in this work.

Most small COTS ICEs operate on high AKI fuels. For example, the engines in this study run on 92 RON pump gasoline. High AKI fuels are not readily available worldwide, creating logistics and support challenges for operators such as the DoD. Engines that operate on low AKI fuels while maintaining power density and fuel efficiency would alleviate these logistical burdens. Combustion optimization and improved thermal management for knock mitigation are both potential methods to relax the high AKI fuel requirement for these SI engines.

Therefore, a test bench to obtain complete and reliable performance data would have several benefits. First, it would provide a platform to scientifically study small ICE performance to better understand the thermal phenomena that begin to dominate combustion and engine efficiency as engine size decreases. Second, it would provide a platform for testing modifications to improve engine performance and optimize combustion phasing. Combined, the thermal studies and combustion optimization offer a path forward for enabling low-AKI, logistically supportable fuels for small RPAs. Finally, the bench would provide the data necessary to match small ICEs to propellers for RPA applications, potentially improving RPA endurance and range by up to 40% [8].

## PREVIOUS WORK

Several similar small ICE test setups helped to guide the creation of the SETB. Menon and Moulton have at least two test beds, one designed for engines less than 1 kg and one SETC2013

designed for larger engines in the 10-50 kW range. [9, 10] The small bench was used to develop scaling relations for losses in engines less than 1 kg, and to study the quenching losses that begin to dominate thermal efficiency and combustion physics as engine size decreases and the surface area to volume ratio of the cylinder increases [9, 11]. While the study focused on engines with a mass less than 1 kg, it did encounter several issues relevant to the SETB, including accurate fuel flow measurement and the importance of maintaining a consistent fuel mixture. The second setup was designed for a 3W Modelmotoren 100 cc engine, a larger, two-cylinder version of the engine in this study [10]. Data collected on the rig indicates that the engine developed almost full manufacturer rated power at the rated speed. The thesis also describes the simulation and modeling of the engine's performance [10]. While the simulation numbers do not provide accurate magnitudes of the simulated variables, according to the author they do provide insight into possible performance enhancing modifications to the engine, such as the adjustment of the exhaust and scavenge port timings.

In addition to small lawn and garden tools, the hobbyist aircraft industry is a major consumer of small ICEs. Hobbyists desire reliable performance data to match propellers to engines to achieve sufficient power for flight. A good overview of matching power plants and propellers is available in [7] and an experimental study using a Fuji 34 cc engine is presented in [12]. In the early 1970s, Gierke published a series of three articles in *Flying Models*, describing his homemade torque reaction dynamometer and presenting complete power curves for a number of small ICEs [4, 5, 6]. While more complete than most manufacturer data, the information is still limited to torque, speed, and power.

Wiegand et al. described the setup of a micro-engine (less than 0.5 kW) test bench [13]. The electric motor cradle used as a dynamometer is of interest to the development of the SETB. Such a system (with slight modifications) could be used to measure frictional losses in both the engine and the SETB drive train; a planned experiment is described in the future work section of this paper.

## LOSSES & ENGINE SELECTION

A scaling study, of the increased impacts of thermal and frictional losses, with decreasing engine size, drove the selection of the engines. The selected engines, in turn, drove the sizing of many of the bench components. As the size of ICEs decrease, the surface area to volume ratio of the cylinder increases driving up the relative effects of thermal and frictional losses [14]. Increasing the cylinder's surface area, relative to its volume, provides more area for heat transfer out of the cylinder, quenching losses at the cylinder walls, and frictional losses relative to the energy released in the combustion volume. These losses decrease engine fuel conversion efficiency and eventually the thermal losses begin to dominate the combustion physics leading to a drop off in engine efficiency as engine size decreases. Previous authors have examined this phenomenon on the micro scale with engines less than 1 kg [8]. Figure 1 shows the results of a market survey of small ICEs, with the surface area to volume ratios of the engines plotted against their manufacturer reported maximum brake power outputs. The plot also shows



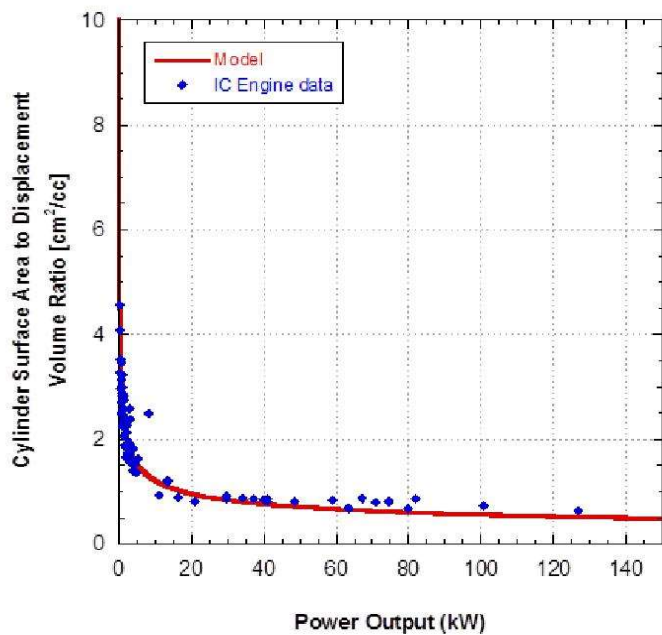


**Figure 1: Compilation of manufacturer engine data showing an exponential decrease in engine power output due to increasing effects of thermal and frictional losses as engine size decreases.**

a simple model that assumes a square engine and a volume to power ratio of 9.67 cc/kW [14]. The manufacturer data indicate that the losses begin to dominate combustion physics as the surface area to volume ratio of the cylinder increases above 1.5 cm<sup>2</sup>/cc. The intent of the scaling study is to quantify the losses in a family of small, geometrically similar ICEs to better understand which loss mechanisms influence this exponential drop off in power.

To examine the scaling effects in small ICEs, as many geometrical and manufacturing variables as possible should be held as constant. Therefore, selecting engines for the SETB necessitated finding a family of similar engines, in the appropriate size range, from a single engine manufacturer. German company 3W Modelmotoren specializes in small two-stroke engines. They have several different lines of engines in the 1-7 kW power class, including a single cylinder product line that comes in regular and competition versions. The difference between the competition and regular series is the compression ratio (1:10 for the regular version and 1:11 for the competition version) and in turn a slight difference in the maximum power output.

Since the SETB will eventually be used to characterize each engine, all engines were chosen prior to designing the test bench to provide design limits for the power train, dynamometer, and intake air system. Table 1 lists the relevant parameters for the selected 3W engines. All engines are air carbureted; the carburetor allows mixture tuning for maximum power and idle. The engines each have an electronic speed controller and ignition unit that advances timing based on the engine's rotational speed, which is provided by a magnetic encoder on the output shaft. The chosen engines lie on either side of the 1.5 cm<sup>2</sup>/cc cylinder surface area to volume ratio described previously as the point where losses begin to dominate engine performance.

**Table 1: Manufacturer reported key engine parameters for 3W engines selected for the SETB [15, 16, 17]**

Engine	3W-28i	3W-55i	3W-85Xi
Displacement (cc)	28	55	85
Power (kW)	2.5	3.9	6.9
Mass (kg)	1.21	1.94	2.40
Power density (kW/kg)	2.06	2.01	2.86
Bore (cm)	3.61	4.50	5.08
Stroke (cm)	2.79	3.51	4.09
Compression ratio	10:1	10:1	10:1
Cylinder surface area to volume ratio	1.86	1.48	1.24

## OBJECTIVE

This paper describes the setup and validation of an SETB designed to characterize the performance of ICEs in the 1-7 kW size class. In contrast to the available manufacturer and hobbyist data, the bench measures air and fuel mass flow rates, as well as key temperatures and pressures in addition to the standard torque, speed, and power measurements provided by the dynamometer. The SETB instrumentation was designed to provide reliable, repeatable performance data to enable future studies examining thermal and frictional losses, to develop scaling relationships for geometrically similar engines of varying sizes, and to identify and test methods for improving small ICE performance. While there are other groups that have constructed similar benches to study small engines, their efforts focus on either side of the size class (1-7kW) considered for the SETB.

## TEST BENCH SETUP

### DESIRED BENCH CAPABILITIES

To quantify engine performance the SETB must measure the torque and speed of the engine. The torque seen by the dynamometer is reduced by friction in both the engine and drive train and a future study will characterize those frictional losses. To quantify the combustion mixture, both intake fuel flow and air flow must be measured. The fuel flow rate measurement is complicated due to its low flow rate and pulsed flow; the air flow measurement is complicated by flow oscillations due to the scavenging nature of two-stroke engines.

There are a number of locations where both temperature and pressure should be measured: the intake air manifold, the exhaust gas, the fuel supply line, and the ambient conditions. In cylinder pressure allows quantification of IMEP, although the small size of the engines makes adding a pressure port difficult. Measuring the head temperature of the engine is also important to avoid overheating. These particular engines are designed to be cooled by the propeller wash in a hobbyist application, so bench cooling is a necessity. The measurement of air to fuel ratios using an oxygen sensor in the exhaust is complicated by the scavenging nature of two-stroke engines. Specifically, the COTS AFR measurement



devices for four stroke engines will not provide accurate results for two stroke engines. Future plans to add exhaust gas analysis to measure trapped efficiency and calculate the trapped air to fuel ratio are described in the future work section.

In addition to the measured quantities, there are several variables that should be controllable to maintain similar conditions between runs. First, the intake air temperature has a direct effect on engine performance and could confound the study of thermal effects if it is not controlled. Second, the temperature of the ambient air used to cool the engine will have a direct effect on heat losses and quenching at the cylinder walls. Thus, there should be a mechanism for holding the head temperature constant. Third, the fuel composition and pressure should be consistent.

## EQUIPMENT & INSTRUMENTATION

Figure 2 shows the SETB configured for testing the 3W 55i engine, with the instrumentation and controls installed. The bench is located in a test cell separated from the control room by a wall; the test cell is monitored from the control room using five closed circuit cameras.

### Power Train and Dynamometer

The dynamometer and power train are the most critical part of the system as they must withstand the vibration and torque spikes of the engine. The dynamometer is a Magtrol 1-WB-65 Eddy Current Dynamometer. It is water cooled, and has a maximum speed of 10,000 rpm, a maximum torque of 10 N-m, and a maximum continuous power sinking capacity of 6 kW with the capability to sink 25% additional power for short periods provided sufficient cooling. The dynamometer has a measurement accuracy of  $\pm 0.5\%$  of the full scale for both torque and speed.

The torque and speed signals from the dynamometer are filtered and conditioned using a Magtrol TSC 401 signal conditioning unit. The dynamometer is controlled by a Magtrol DSP 6001 High-Speed Dynamometer Controller. The control unit is connected to a computer via a National Instruments GPIB controller so that the dynamometer can be controlled from a data acquisition program written in National Instrument's LabVIEW. The excitation current for the dynamometer is provided by a Magtrol DES 311 Power

Supply. Figure 3 provides schematic of the dynamometer setup and interfaces.

The power train for the SETB consists of two separate shafts, one for the dynamometer and one for the engine. They are connected with a timing belt to ensure the rotational speed reported by the dynamometer matches that of the engine. The timing belt between the engine and dynamometer provides some damping of the torque spikes produced by the engine. When changing engines, the shaft attached to the dynamometer does not require adjustment, reducing the number of components that must be realigned when exchanging engines. Both shafts are supported by pillow blocks to eliminate radial loading of the engine and dynamometer by the belt.

The belt and pulleys for the drive train were designed using the Industrial Belt Design software provided by Gates Corporation. The Power Grip G2 belt series has a tooth shape designed specifically for high torque timing belt applications. A 15 mm wide, 750 mm long belt paired with two 60.5 mm pitch diameter pulleys were chosen to match the 305 mm distance between the dynamometer and engine drive shafts. The shafts are customized  $\frac{3}{4}$  in (19.05 mm) stainless steel precision ground shafts. The dynamometer shaft has keyways for the both the drive pulley and the coupler to the dynamometer, but is smooth along the rest of the length to facilitate the one-way clutch bearing on the starter motor. The starter motor is a 2AM-NCW-7B Lubricated Air Motor produced by GAST. It has a rated speed of 3000 rpm and a rated output of 0.70 kW. The starter motor is attached to the dynamometer drive shaft using an ANSI 25 roller chain. A one way clutch bearing that rides on the dynamometer shaft allows the starter motor to spin the engine, and then disengage from the system once it has been shut off. The air pressure to the starter (and thus its speed) is controlled using a Wilkerson ER1 electronic pressure regulator, which is set using a voltage signal provided by the NI DAQ program. The entire

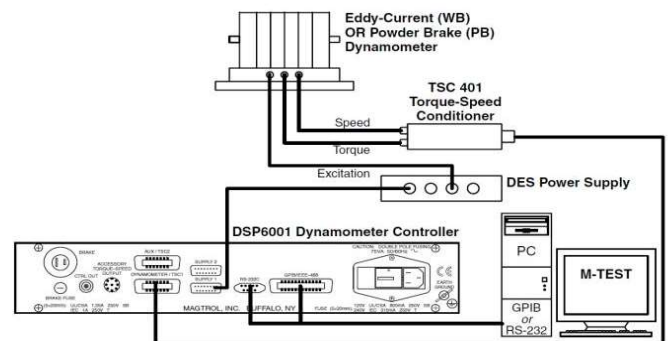


**Figure 3: Connection diagram for Magtrol Dynamometer system consisting of a 1 WB 65 Eddy Current Dynamometer, a DES 311 Power supply, a TSC401 Signal Conditioning Unit, and a DSP6001 High-Speed Dynamometer Controller. [20]**

drive train is secured to a two inch thick steel t-slotted bedplate, supported by a t-slot frame, to ensure a level surface for alignment of the power transmission shafts.

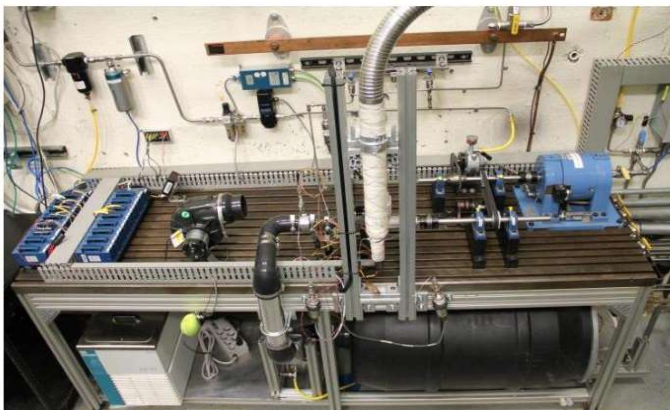


**Figure 2: SETB configured for the 3W Modelmotoren 55i engine.**



The dynamometer comes with an 18 mm diameter keyed shaft for coupling to the test system. A flange for a 0.75 in (19.05 mm) diameter shaft was manufactured to bolt to the propeller hub on the engine, allowing the engine to be coupled to the power train. The dynamometer and engine shafts are aligned using a sleeve bored to the shaft diameter for each component with a tolerance of  $+0.005''$  (0.0127 mm). To align the system the sleeve is slid over each shaft at least 1.25 in (31.75 mm) and the pillow blocks and components are secured, ensuring a misalignment of less than 0.01 in (0.024 mm) axially and  $0.5^\circ$  angularly. The sleeve is then removed from the shaft without loosening the pillow blocks, and a bellows coupler is inserted in its place. Both the engine and dynamometer couplings are Ruland BC32 Bellows Shaft Couplings with a rated load of 45 N-m and a rated speed of 10,000 rpm, well over the maximum speed of any of the 3W engines. Figure 4 shows the coupler used between the engine and the drive train. The couplers allow for a misalignment of up to 0.01 in (0.024 mm) and  $2^\circ$ , which is sufficient for the alignment method described above. The only difference between the dynamometer coupler and the engine coupler is the specification for the clamp diameter.

Figure 5 shows the fully assembled drive train with the 55i engine aligned and mounted. The robust nature of the power train may cause it to have frictional losses that are significant compared to the power output of the engine. Thus, one of the planned future studies for the SETB is to use an electric motor in a reaction cradle attached to the engine power shaft to determine the frictional losses in the power train [13].

### Intake Air Control

The intake air control system is the second most complicated part of the SETB. The system must allow for a reliable intake air flow measurement and be capable of holding a consistent intake air temperature. The air flow measurement system was designed first. Based on data for a similar two stroke engine, the maximum delivery ratio of the 85xi engine was estimated at 80% for 5000 rpm and falling to 60% by 7000 rpm [18]. This suggests a maximum intake air flow rate of 360 L/min at ambient conditions. A TSI 40211 High Performance Linear Mass Flow Meter was chosen to measure this flow rate. The flow meter uses a hot wire anemometer and a temperature correction thermocouple to provide a 0-5 V analog signal proportional to the flow rate through the device. The flow meter can also make an additional correction based on ambient pressure, but the feature is not currently in use. The flow meter has a scaling factor of 75 SLPM/V and an accuracy of 3% of the reading at  $21.1^\circ\text{C}$  and 1 atm. The hot wire type flow meter does have a drawback: it does not indicate which direction the flow is traveling through the meter, an issue since two-stroke engines can have back flow due to scavenging. Previous experience with other flow meters suggests that placing a baffle 20-50 times the displacement volume of the engine between the flow meter and carburetor can stabilize the flow oscillations and permit the use of a hot wire type device. A 209 L (55 gal.) drum was converted to a baffle, providing significantly more than 50 times the displacement volume of even the 85xi engine. During motored tests, presented later, there are no oscillations in the air flow measurements that indicate backflow from the engine. Additionally, the reed valve installed at the crankcase



**Figure 4: Ruland Bellows Shaft Coupler.**

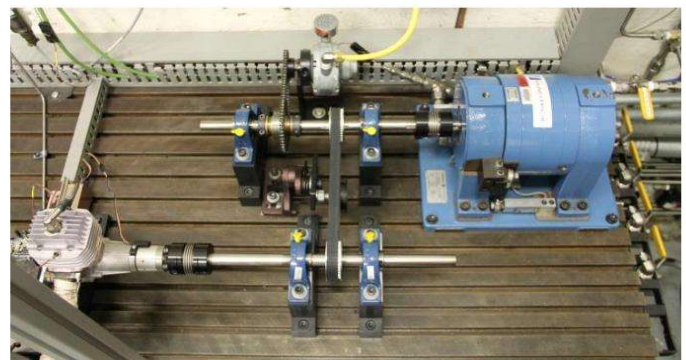


**Figure 5: Assembled drive train on SETB.**

intake of the 3W engines should also reduce back flow that could interfere with the air flow meter.

Since the TSI air flow meter's accuracy is sensitive to temperature, the intake air conditioning system is positioned downstream of the baffle between the baffle and the carburetor. A Frozen Boost heat exchanger was selected to condition the temperature of the intake air. No information on the efficiency of the heat exchanger was available from the manufacturer, although the device is designed for much higher heat loads and flow rates. To heat and cool the heat exchanger, a Thermo Neslab RTE-211 recirculating water bath unit was selected. The unit is monitored and controlled by the NI DAQ program. The RTE-211 provides 0.5 kW of cooling and 0.8 kW of heating from  $-25^\circ\text{C}$  to  $150^\circ\text{C}$ , although operating below freezing and above boiling requires a working fluid other than water. Based on the air flow rate numbers, a shift of  $50^\circ\text{C}$  in the intake air temperature at the maximum air flow rate estimated for the 3W 85 cc engine requires about 0.35 kW of heating or cooling, well within the unit's design range. Figure 6 shows the intake air system assembled and installed underneath the bed plate on the SETB.

### Engine Temperature Control

The temperature of the cylinder walls has a direct influence on the heat losses and combustion quenching physics of the engine. To isolate the effects of heat transfer to geometry and



engine size, the temperature of the cylinder walls should be held as constant as possible. The intake and exhaust port orientation as well as the motion of gasses within the cylinder cause the surface temperature of the engine to vary significantly depending on location. Therefore, two points were selected based on previous experience as control points for cylinder temperature. Both are located on the top fin of the engine; as close as possible to the cylinder volume. One point is directly above the exhaust port on the engine; the other directly opposite of the exhaust port. Class I Type J ring thermocouples are bolted to the engine with thermal paste between them and the underlying surface. Figure 7 shows the location of the two thermocouples on the cylinder head of the 55i engine. The thermocouple readings are fed back into the data acquisition program and used to control a cooling blower. A JABSCO 35440-Series blower was selected to provide cooling air. It can produce an air flow of over 7,000 SLPM at the exit. The 24 V blower is controlled using a Midwest Motion Products MMP 25A-24VD Motor Speed Controller, also controlled through the data acquisition program.

## Fuel System

There are two challenges when measuring the rate of fuel flow to the engine. First, the flow rates are relatively low, on the order of 10s of mL/min. Second, small engine carburetors tend to take in fuel in spurts as opposed to a constant flow; small Honda four-stroke engines frequently exhibit this characteristic due to the setup of the fuel sump in the carburetor. Therefore, a positive displacement flow meter made by Max Machinery was selected to make the measurement. The 213 Piston Flow Meter uses a rotary encoder to provide a square wave corresponding to 1000 pulse/rev, where each revolution is 0.89 cc of fluid. It has an accuracy of  $\pm 0.2\%$  of the reading and is rated for most

organic liquids. Note that while the Viton seals in the current unit are not compatible with methanol and nitro methane, TSI does make a similar model with (more expensive) compatible materials. The meter is equipped with an analog transmitter that converts the flow rate into a 0-10 V signal corresponding to a full scale of 0-1800 cc/min. To protect the flow meter from debris, there is a 40  $\mu\text{m}$  and a 7  $\mu\text{m}$  filter upstream of the device. To overcome the pressure drop in the flow meter and filter, the fuel tank is pressurized to 6.7 kPa using nitrogen, which is regulated by a high precision pressure regulator, accurate to  $\pm 670$  Pa.

The fuel mixture is a PRF blend of iso-octane and n-heptane. 3W recommends using a 92 Rated Octane Number (RON) fuel. Therefore, fuel for the engines was created using a mix of 92% octane and 8% heptane by volume. Two percent by volume of SAE 5W-20 synthetic oil was added to the fuel mixture as per the engine manufacturer's recommendation. The fuel density is 690 kg/m<sup>3</sup> at 18°C as measured using a hydrometer. The data acquisition uses that baseline density to calculate the actual fuel density based on a temperature correlation adapted from the Handbook of Aviation Fuel Properties [19]. The density is used to compute the fuel mass flow rate.

The intake air and mass flow rates provide enough information to calculate the air to fuel ratio of the fresh mixture. In addition to calculating the mixture based on the incoming air and fuel, an oxygen sensor is installed in the exhaust pipe of the engine. The Powerdex Air-Fuel Monitor by NGK Spark plugs outputs a 0-5 V analog signal that is inversely proportional to the equivalence ratio measured in the exhaust. For optimal performance, the sensor must be located at least 30 diameters upstream of the exhaust exit to the atmosphere and at least 12 inches from the exhaust port on the engine. The authors acknowledge that the measurements from the Powerdex Air-Fuel Monitor are inaccurate for two stroke engines due fresh charge short circuiting the combustion chamber during combustion. The sensor was included in the event a four stroke engine is tested in the future, and the results are reported in case they should be of some future value.

A stainless steel hose connects the engine exhaust pipe to the laboratory ventilation system. The exhaust pipe is a two inch diameter tube while the ventilation duct is a 6 inch diameter

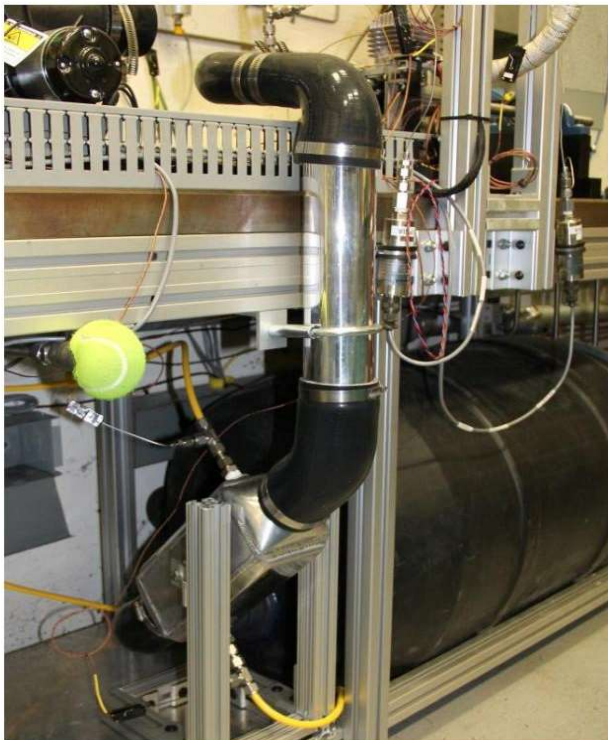


Figure 6: Intake air system on SETB.

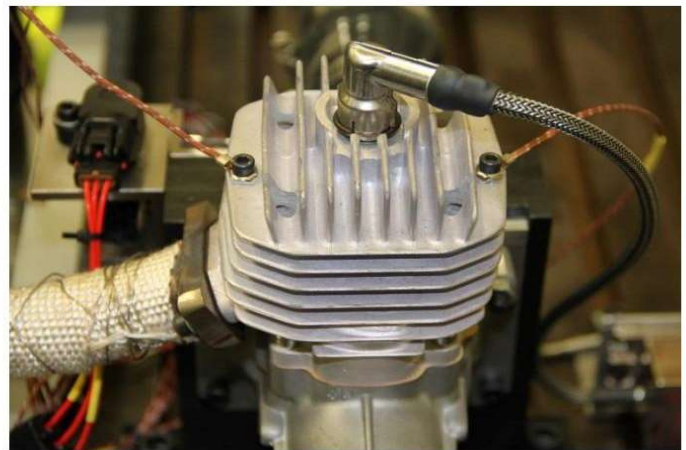


Figure 7: Cylinder head thermocouple locations on the 3W 55i engine.



tube. The mismatch allows the exhaust gas to mix with fresh air, cooling the exhaust. It also prevents the ventilation system from directly coupling to the exhaust pipe and drawing down the exhaust port pressure of the engine. Pulling a vacuum on the exhaust port of a two-stroke engine can lead to unstable operation due to the design and function of the scavenging system. Figure 8 shows the exhaust pipe and the location of the oxygen sensor.

Two stroke engines typically have tuned exhaust pipes to maximize their performance. The exhaust pipe is designed and sized to reflect pressure waves towards the exhaust port so an expansion wave reaches the exhaust port when it opens and a compression wave reaches the exhaust port when it closes. This prevents some of the short-circuiting of fresh charge, increasing the power output and reducing the BSFC of the engine. Since the objective of this work is to test the 55i engine in its stock configuration, the exhaust pipe leading from the engine to the laboratory exhaust system was modeled after the stock exhaust pipe supplied by manufacturer. Based on the constant cross section of the exhaust pipe, the manufacturer's exhaust pipe is not tuned.

### Temperatures and Pressures

All temperatures are measured using Class 1 Type J thermocouples. In addition to the temperatures already mentioned, the water line on both the intake air heat exchanger and the dynamometer cooling water are monitored for control, safety, and troubleshooting. Class 1 Type J thermocouples are accurate to  $\pm 1.5^{\circ}\text{C}$  from  $-40^{\circ}\text{C}$ - $375^{\circ}\text{C}$  with an additional  $\pm 0.004^{\circ}\text{C}$  per degree over  $375^{\circ}\text{C}$ . Table 2 list the thermocouples installed on the test bench.

Honeywell TJE pressure transducers were selected to provide

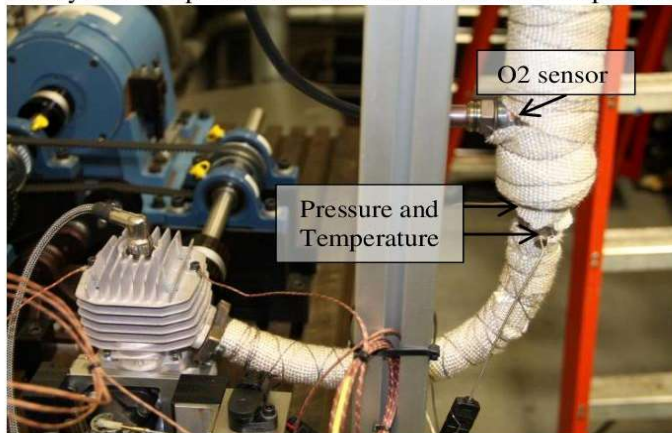


**Figure 8: Engine exhaust pipe showing the oxygen sensor and the pressure and temperature taps.**

pressure measurements for the SETB. Table 3 lists the pressure transducers, their locations, and their ranges. Each transducer has an internal amplifier that provides a 0-5 V analog output signal, which is read in the data acquisition system. The transducers have an accuracy of 0.1% of the full range. Some of the transducers are mounted remotely and connected to their pressure taps using a 1/16 in stainless steel tube. Remotely mounting the transducers reduces their exposure to heat and vibration, at the expense of damping high frequency oscillations in the pressure measurements.

Table 3 lists the pressure transducers, their ranges, and locations.

**Table 2: Listing of Thermocouple Names and Locations**

Name	Location
Intake air	Upstream of carburetor, downstream of intake air heat exchanger
Exhaust gas	Exhaust pipe, 30 cm downstream of exhaust port
Cylinder Head	Top fin of engine head, one over exhaust port, one opposite exhaust port
Ambient	Beneath bed plate, left hand side facing bench
Intake baffle	In intake baffle
Intake heat exchanger water inlet	In water bath line, upstream of intake air heat exchanger
Intake heat exchanger water outlet	In water bath line, downstream of intake air heat exchanger
Fuel	Fuel line downstream of fuel flow meter
Dyno cooling water inlet	Inlet of dynamometer cooling water line
Dyno cooling water outlet	Outlet of dynamometer cooling water line

**Table 3: Pressure transducers installed on the SETB**

Name	Location	Range (kPa)
SEB01	Exhaust pipe 12 in downstream of exhaust port. Remotely mounted.	0-344.7
SEB02	Fuel line, downstream of flow meter.	0-344.7
SEB03	Ambient, mounted under bed plate.	0-103.4
SEB04	Intake manifold, tap upstream of carburetor. Mounted remotely.	0-103.4

### Throttle Control

It is more difficult to set and measure the throttle setting of an air carbureted engine than an engine using PFI or DI. However, since one objective was to characterize the stock engines, a system to control and measure the throttle setting was developed. The throttle and choke are driven using a Hitec HS-85MG+ analog, metal gear micro servos. The servo was chosen for both its high torque and vibration resistance. It is designed specifically to drive throttles on hobbyist engines. The servos are controlled using PWM signals generated by the data acquisition system. The servos are connected to the control horns on the carburetor using a combination of ball and socket connectors, clevis connectors, and 2-56 threaded rod. Once attached to the carburetor, the operational range of the servo is adjusted to match the range of the control horn. A CTS Single Ear Rotary Position Sensor is attached to the throttle servo to provide a feedback signal to verify throttle position. Table 4 lists the servo settings corresponding to the open and closed positions for throttle and choke on the 3W 55i engine. Note that the percentages are inverted from common practice due to the setup in the



data acquisition program. Figure 9 shows the throttle and choke servos and their connection to the 55i engine.

**Table 4: Throttle and choke servo ranges for 3W 55i engine installed on the SETB.**

	Open Throttle	Closed Throttle	Open Choke	Closed Choke
Servo Setting	30%	80%	0%	80%
TPS (V)	2.120	0.207	n/a	n/a

## Data Acquisition

The data acquisition and control is carried out in a custom DAQ program written in National Instruments LabVIEW. From the program, the test engineer can monitor all of the instrumentation in real time and control the engine, the recirculating water bath, and the dynamometer. The majority of the data acquisition and control is carried out through two National Instruments cFP-1808 Field Point Ethernet and Serial Interface, 8-slot backplanes. Twelve of the sixteen slots are currently configured for use; the other four remain open for future needs.

### cFP-AI-118 - Analog Input Module (x1)

The cFP-AI-118 Analog Input Module provided inputs for analog signals requiring isolation from the common ground of the system. Currently only the oxygen sensor requires an isolated reference.

### cFP-AI-100 Analog Input Module (x2)

The system currently uses two cFP-AI-100 Analog Input Modules. The first module accepts the signals from the pressure transducers and fuel flow meter and provides the 24 V rail used to power them. The second module reads the throttle position sensor and the air flow meter and provides 5 V instrument power. The second module also reads the auxiliary torque and speed analog output provided by the dynamometer control unit. While torque and speed are read directly into the LabVIEW in the dynamometer control

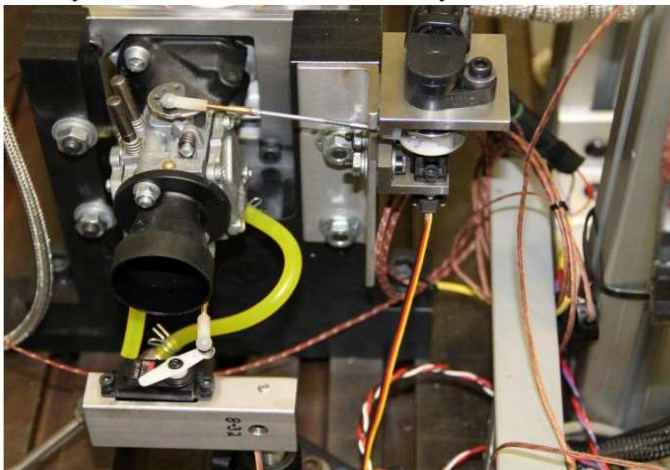


**Figure 9: Throttle and choke servos configured for the 3W 55i engine on the SETB.**

portion of the program, these signals provide a backup when the dynamometer is operated in manual mode through the DSP6001 controller instead of through LabVIEW.

### cFP-AO-210 Analog Output Module (x1)

The cFP-AO-210 Analog Output Module is used to control the cooling blower and the electronic pressure regulator for the starter motor. Each device has its own slider in LabVIEW that controls the voltages and in turn the set point of the device. The cooling blower can also be controlled using a PID loop to hold the temperature of the cylinder head, read by the cylinder head thermocouples, constant.

### cFP-PWM-520 (x1)

Initially an analog to PWM conversion circuit was used to produce a PWM signal from an analog signal provided by LabVIEW DAQ via the cFP-AO-210 module. However, National Instruments also sells a cFP-PWM-520 module designed to generate PWM signals. Two channels on this module were setup to provide a 50 Hz, 5V peak PWM signal with a variable 5%-10% duty cycle to control the throttle and choke servos. The poorly conditioned square wave from this module necessitated the use of analog servos, which are less sensitive to the PWM signal quality than their newer digital counterparts. Since the analog servos perform acceptably with the module, no further investigation has been done to determine the cause of the poorly conditioned signal.

### cFP-RLY-512 Relay Module (x1)

The cFP-RLY-512 Relay Module provides several switches accessible from the data acquisition program. One channel controls the air starter, allowing the user to start the engine from the data acquisition program. Three additional channels control power to the engine ECU, the oxygen sensor power, and the power to the choke and throttle servos.

### cFP-TC-120 Thermocouple (x6)

Six cFP-TC-120 Thermocouple modules are installed in the SETB data acquisition system, to provide a sufficient number of channels for the instrumentation anticipated for future thermal studies. Only the first two are currently in use. The thermocouple modules use an internal reference cold junction thermistor to compensate for ambient temperature effects.

## Other Data Acquisition

In addition to the controls and instrumentation that run directly through the cFP backplanes, several other pieces of equipment feed directly in the LabVIEW program. The DSP6001 Dynamometer controller links directly to DAQ PC via a GPIB interface, allowing the speed, torque, brake status, and PID values for the dynamometer to be controlled directly from the program. The recirculating water bath used to control intake air temperature is equipped with an RS-232 communication protocol. It too is hooked into the control program via a USB to serial cable, allowing control of its set point and PID values directly from the DAQ program.



## RESULTS AND DISCUSSION

### Motored Test: 3W 55i Engine

A 3W 55i engine, broken in according to the manufacturer specified procedure, was initially tested under motored conditions, using the air starter and the electronic pressure regulator to drive the system at various speeds. These tests were used to verify dynamometer function, break in the drive train, and check the intake air system. Figure 10 shows the results for the intake air system test. The recirculating water bath was set to 55°C and allowed to reach the set point. During the five minutes of testing shown, the intake air system held the intake air temperature in a 2°C range, less than the precision of the thermocouple used, while the engine speed varied from 1000 rpm to 3000 rpm. The intake air flow rate during the test varied 20 SLPM at 1500 rpm to 29 SLPM at 2800 rpm.

Increases and decreases in the speed of the engine, especially notable in the 2800 rpm to 3100 rpm range, are caused by the compressor providing air for the starter system. Even with the electronic pressure regulator at a set point, the speed of the system increases when the compressor engages and pressurizes the air tanks. The speed then gradually decreases as the tank pressure decreases until the compressor reengages. The air flow rate is limited by the supply line size. The air flow rate decreases as the tank pressure falls leading to the decreases in starter motor speed. This could be corrected by increasing the supply line size, but such a correction is unnecessary since the starter motor is primarily used to start the engine.

Figure 11 shows the intake air flow and delivery ratio of the engine measured during motored testing with the choke fully open. The delivery ratio is calculated as the ratio of the mass of fresh charge delivered to the cylinder per cycle to the mass

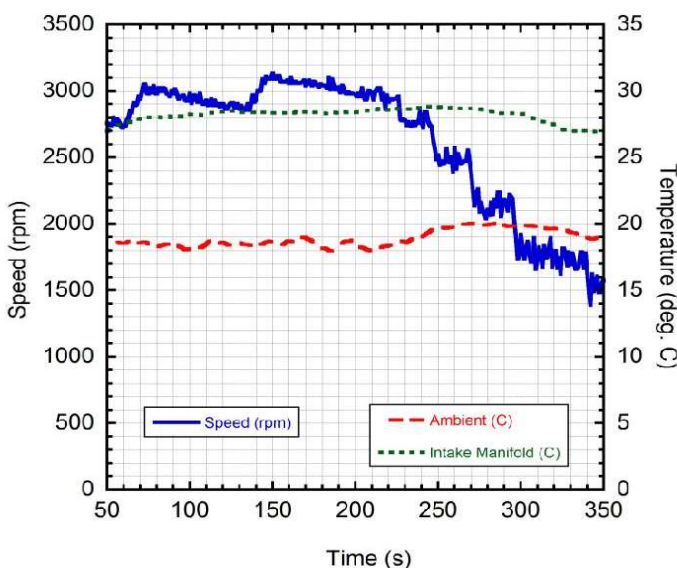


**Figure 10: Intake air temperature control demonstration for 3W Modellmotoren 55i engine, fully open choke. The recirculating water bath set point was 55°C. Engine was motored using the air starter, controlled using an electronic pressure regulator.**

of fresh charge that could fill the cylinder at intake conditions [18]. The delivered mass of fresh charge will be greater than the mass of fresh charge trapped in the cylinder at when the exhaust port closes due to short circuiting. The intake air flow rate increases steadily between 1500 rpm and 2800 rpm and appears to begin decreasing by 3000 rpm. While the data in Figure 11 are similar to data presented by Heywood and Sher [18] for a similar engine, firing the engine introduces numerous complex pressure and temperature interactions that dramatically affect the scavenging behavior of the engine, making it difficult to draw any meaningful conclusions about fired performance from the motored results alone. The data is presented to demonstrate the functionality of the air flow measurement system, based on its similarity to accepted literature.

### Fired Test: 3W 55i Engine

Following the motored test, the 3W 55i engine was run at four throttle settings: WOT,  $\frac{3}{4}$  throttle,  $\frac{1}{2}$  throttle, and  $\frac{1}{4}$  throttle. The throttle settings are equally spaced across the throttle's range of motion. The intake air temperature was held between 27°C and 30°C. The carburetor was tuned to the manufacturer recommended settings on both needles.

Figure 12 and Figure 13 show the torque and power maps, respectively, for the 3W 55i engine, based on two throttle sweeps. The torque curve exhibits the typical rise and then fall of torque as speed increases. The peak power for the engine also occurs at a higher speed than the peak torque, typical for ICEs. Both power and torque display an erratic increase at 3000 rpm. This increase may be due to the carburetor, which transitions from the low speed tuning mixture to the high speed tuning mixture between 2000 rpm and 4000 rpm. It could also be a poorly tuned operating range for the engine. There appears to be a second dip in power at 5000 rpm, although it is only pronounced at half throttle. The data also demonstrate a significant limitation of many air carburetors: the last 50% of the throttle offers very little

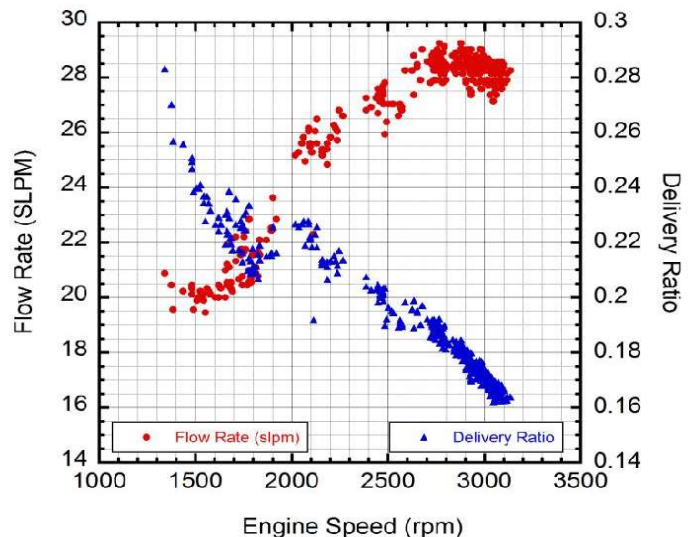


**Figure 11: Intake air flow and delivery ratio as a function of engine speed under motored test conditions for 3W Modellmotoren 55i engine. The engine was motored using the air starter, controlled using an electronic pressure regulator.**



control over the engine. Most of the control for small air carbureted engines is in the first 30% of the throttle range [16].

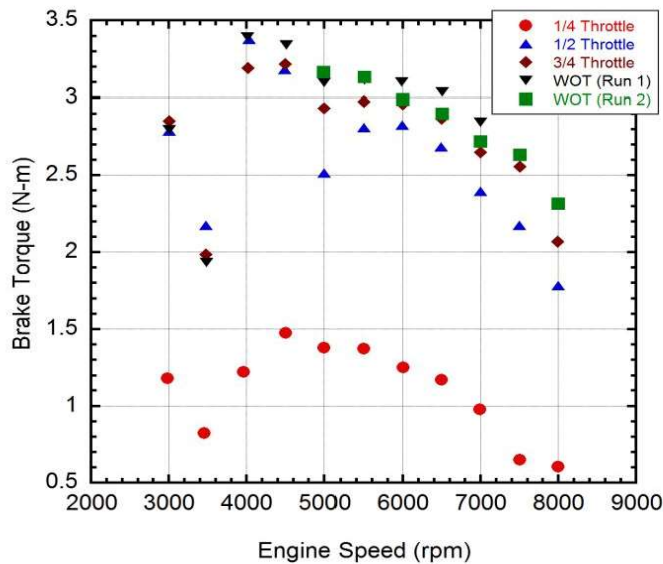
Based on the power curve, the engine is only developing 54% of its rated power in the current setup. Several factors may be at work here and further investigation is necessary before drawing any firm conclusions. While there are frictional losses in the drive train, these losses could not account for the whole 1.7 kW without significant heating to and ultimately damage of the drive train. Previous experience with similar small engines has shown that manufacturers often base the rated power output of the engine on the displacement volume, instead of bench testing data, leading to overstated

capabilities of many small engines. Small ICEs that only develop 50%-70% of their rated power are not uncommon [8]. However, Cadou et. al. tested the two cylinder version of this engine (3W 100i-B2) and it developed nearly its rated power of 6.9 kW at 8500 rpm [10]. It is highly likely that tuning the exhaust on the engine would significantly enhance the performance, possibly. It has been shown that exhaust tuning may double the delivery of fresh charge to the cylinder and in turn the power output of the engine. However, the goal of the test was to evaluate the engine in the manufacturer's stock configuration, which did not include a tuned exhaust. Therefore, while exhaust tuning should improve the performance of the engine, it does not justify the low power output of the engine compared to manufacturer claims. It is also possible that the carburetor requires additional tuning. This case is supported by the mixture data discussed below.

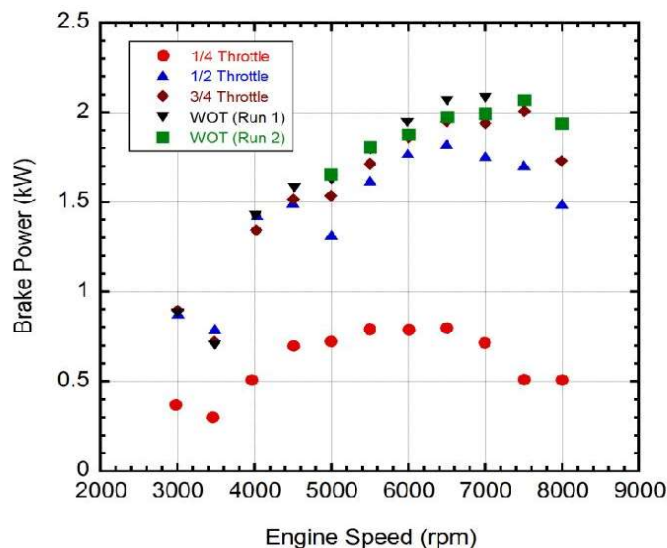
Normally, flow rate, mixture, and efficiency data would be presented as contours on a plot with speed as the abscissa and BMEP as the ordinate. However, the available data is too sparse to make a viable contour plots. Therefore, the data will be presented using contour of constant throttle setting, and tabulated at the end of the section along with BMEP.

Figure 14 shows the intake air flow rate for the 3W 55i engine, taken during the fired test described above. The air flow rate to the engine increases over nearly the whole speed range, only decreasing at 8000 rpm at the higher throttle settings. This indicates the delivery of fresh charge to the engine is not restricted by the port geometry until nearly the maximum speed of the engine. At the 1/4 throttle setting, the flow rate is essentially linear above 5000 rpm.

Figure 15 shows the delivery ratio for the 3W 55i engine, taken during the fired test. The delivery ratio data follows the same trend expected for a single cylinder, crankcase-compression engine with reed valves on the intake. The plots are similar in both the magnitude of the values and the trends, including the dip between 3500 rpm, and 4000 rpm, the peak near 5000 rpm, and the continual drop off of delivery ratio at lower throttle settings [17]. The plot indicates that the air flow into the engine does not increase as rapidly as the throughput required to maintain the delivery ratio as the speed increases beyond 5000 rpm at higher throttle settings. The more rapid drop beyond 7500 rpm results from a decrease in air flow coupled with an increase in speed. Monitoring the intake manifold pressure verified the flow restriction occurs in the engine and not in the intake air system.



**Figure 12: Torque map for 3W Modellmotoren engine run using 92 ON PRF blend, 26-28°C intake air temperature.**



**Figure 13: Power map for 3W Modellmotoren engine run using 92 ON PRF blend, 26-28°C intake air temperature.**

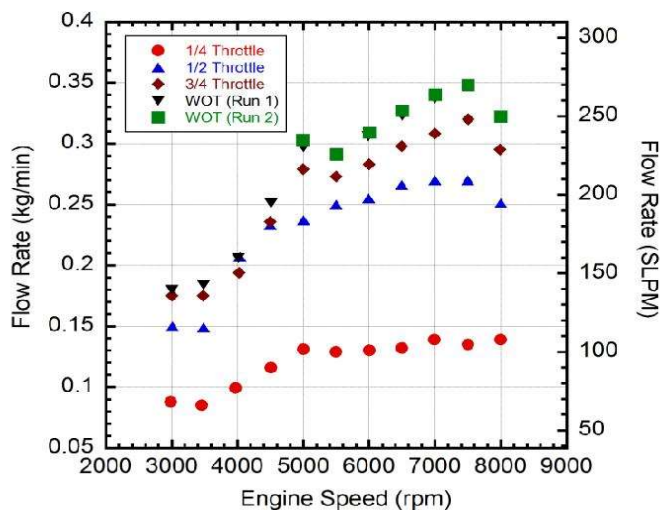


**Figure 14: Intake air flow for 3W Modellmotoren 55i engine run using 92 ON PRF blend, 26-28°C intake air temperature.**

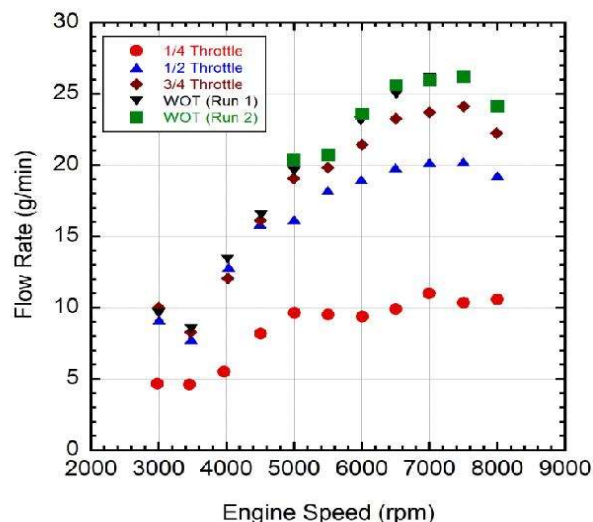


**Figure 16: Fuel flow rate for 3W Modellmotoren 55i engine run using 92 ON PRF blend, 26-28°C intake air temperature.**

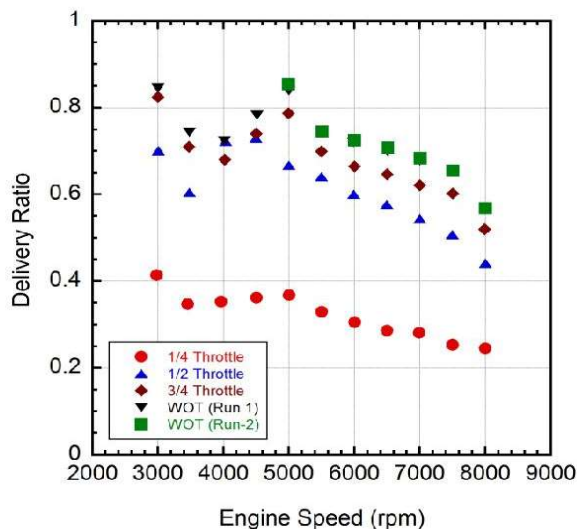


**Figure 15: Delivery ratio for 3W Modellmotoren 55i engine run using 92 ON PRF blend, 26-28°C intake air temperature.**

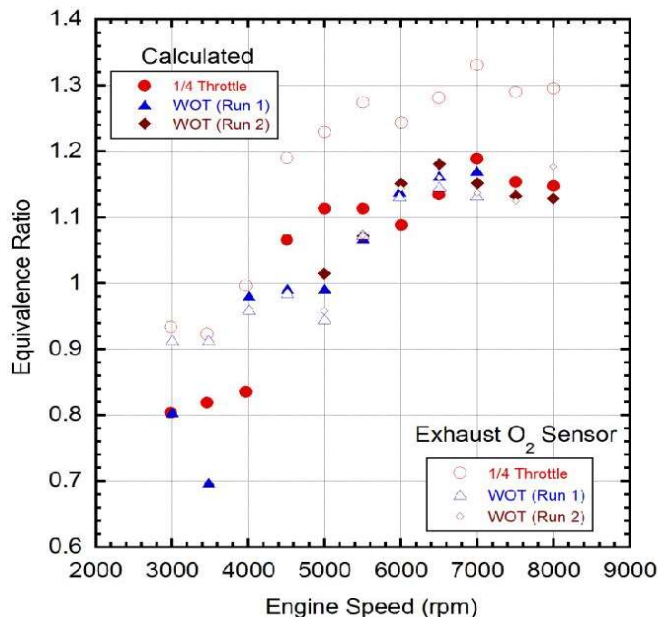


**Figure 17: Equivalence ratio for 3W Modellmotoren 55i engine run using 92 ON PRF blend, 26-28°C intake air temperature. Calculations are based on air and fuel flow rate measurements; measured values are from the exhaust oxygen sensor.**

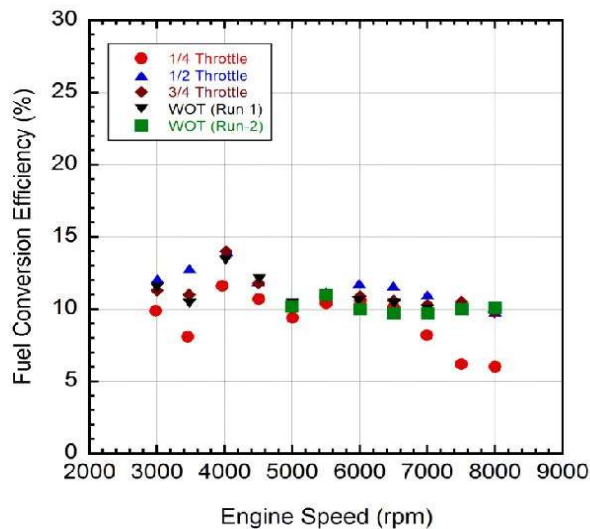
Figure 16 shows the fuel flow data for the 3W 55i during the fired test. The fuel flow follows the same trend as the air flow, indicating the carburetor may be capable of maintaining a relatively constant air to fuel ratio. Figure 17 plots the equivalence ratio measured by the exhaust oxygen sensor against the fresh charge equivalence ratio calculated using the air and fuel flow rates. The stoichiometric A/F ratio for the 92 ON PRF fuel blend is 15.05. At the low throttle setting, the exhaust sensor reads a substantially higher equivalence ratio than the calculated composition of the fresh charge delivered to the engine. One likely cause is the short circuiting of fresh charge into the exhaust, which is why AFR sensors are not intended for use on two-stroke engines. Another possibility is low turbulent mixing in the exhaust at low throttle settings, requiring additional spacing between the exhaust port and the sensor for an accurate reading [18]. At higher throttle settings, the exhaust oxygen sensor reads

within 0.05 points of the calculated equivalence ratio across the entire speed range.

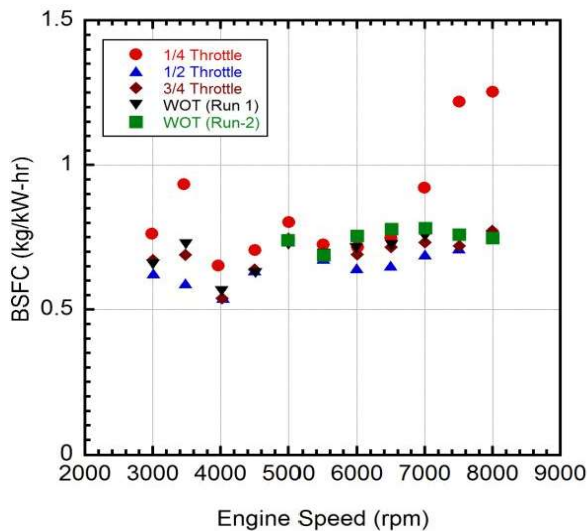
The rapid jump in equivalence ratio near 4000 rpm from lean to rich mixtures could indicate a tuning discrepancy between the low speed and high speed tuning needles, resulting in an abrupt transition between the two mixture settings. For this set of test runs, both needles were tuned to the manufacturer recommended settings. For future testing, the low speed needle should be richened to smooth the transition between low speed and high speed operation.



Figure 18 and Figure 19 and show the fuel conversion efficiency and BSFC, respectively, for the 3W 55i engine. The peak efficiency of the engine is 14% at 4000 rpm and 10% to 12% over the majority of the speed range above 5000 rpm. The falloff in efficiency corresponds to the mixture richness increasing as the carburetor transitions to the high speed tuning needle. Engine operation at leaner conditions is more fuel efficient than at rich conditions, although high speed operations at lean mixture conditions could present thermal management issues. The BSFC of the engine is about twice that of an efficient spark ignition ICE, most likely due to mixture control in the carburetor and no tuning of the exhaust. [14]. Table 5 summarizes the data along with speed and BMEP.



**Figure 19: Fuel conversion efficiency for 3W Modellmotoren 55i engine run using 92 ON PRF blend, 26-28°C intake air temperature.**



**Figure 18: BSFC for 3W Modellmotoren 55i engine run using 92 ON PRF blend, 26-28°C intake air temperature.**

**Table 5: Summary of data for 3W 55i run on 92 ON PRF, 26-28C intake air temperature**

BMEP (kPa)	Speed (rpm)	Air Flow ( $\frac{kg}{min}$ )	Fuel Flow ( $\frac{g}{min}$ )	$\Delta$ (%)	$\phi$	$\eta_f$ (%)	BSFC ( $\frac{kg}{kW-hr}$ )
1/4 Throttle							
135	3000	0.088	4.7	41.4	0.80	9.9	0.76
94	3500	0.085	4.6	34.7	0.82	8.1	0.93
140	4000	0.099	5.5	35.3	0.84	11.6	0.65
168	4500	0.116	8.2	36.2	1.07	10.7	0.71
158	5000	0.131	9.7	36.8	1.11	9.4	0.80
157	5500	0.129	9.5	33.0	1.11	10.4	0.72
143	6000	0.130	9.4	30.5	1.09	10.6	0.72
134	6500	0.132	9.9	28.6	1.13	10.1	0.75
112	7000	0.139	11.0	28.1	1.19	8.2	0.92
74	7500	0.135	10.4	25.3	1.15	6.2	1.22
69	8000	0.139	10.6	24.5	1.15	6.0	1.25
1/2 Throttle							
318	3000	0.150	9.2	70.1	0.92	12.1	0.63
248	3500	0.149	7.8	60.5	0.79	12.8	0.59
386	4000	0.207	12.9	72.3	0.94	14.0	0.54
363	4500	0.233	15.9	73.0	1.03	11.9	0.64
287	5000	0.237	16.2	66.7	1.03	10.3	0.74
321	5500	0.250	18.3	64.1	1.10	11.2	0.68
322	6000	0.255	19.0	60.0	1.12	11.8	0.64
307	6500	0.266	19.8	57.7	1.12	11.6	0.65
274	7000	0.270	20.2	54.4	1.13	11.0	0.69
248	7500	0.270	20.3	50.8	1.13	10.6	0.71
204	8000	0.251	19.3	44.2	1.16	9.8	0.78
3/4 Throttle							
325	3000	0.175	10.0	82.4	0.86	11.3	0.67
227	3500	0.175	8.3	71.0	0.71	11.0	0.69
364	4000	0.194	12.1	68.0	0.94	14.0	0.54
367	4500	0.236	16.1	74.0	1.03	11.8	0.64
335	5000	0.279	19.1	78.7	1.03	10.1	0.75
340	5500	0.273	19.8	69.9	1.10	10.9	0.69
338	6000	0.283	21.4	66.5	1.14	10.9	0.69
327	6500	0.298	23.3	64.6	1.18	10.6	0.72
303	7000	0.308	23.7	62.1	1.16	10.3	0.73
292	7500	0.320	24.1	60.2	1.13	10.5	0.72
236	8000	0.295	22.3	52.0	1.14	9.8	0.77
WOT -1							
320	3000	0.180	9.6	84.5	0.80	11.5	0.66
221	3500	0.184	8.5	74.4	0.70	10.4	0.73
388	4000	0.206	13.4	72.4	0.98	13.4	0.57
382	4500	0.251	16.5	78.3	0.99	12.1	0.63
354	5000	0.297	19.6	83.9	0.99	10.4	0.73
356	5500	0.292	20.7	74.9	1.07	10.9	0.69
354	6000	0.306	23.1	72.0	1.14	10.6	0.71
347	6500	0.323	25.0	70.0	1.16	10.4	0.72
325	7000	0.337	26.2	67.8	1.17	10.0	0.75
WOT -2							
264	5000	0.322	24.2	56.8	1.13	10.1	0.75
301	5500	0.348	26.2	65.5	1.13	10.0	0.76
310	6000	0.340	26.0	68.4	1.15	9.7	0.78
331	6500	0.327	25.6	70.8	1.18	9.7	0.78
341	7000	0.309	23.6	72.5	1.15	10.0	0.75
358	7500	0.291	20.7	74.5	1.07	11.0	0.69
362	8000	0.303	20.4	85.5	1.01	10.2	0.74

## FUTURE WORK

The setup and validation of the SETB is just the beginning of the planned work. The next step will be to characterize each of the 3W engines and create a performance baseline. At the same time, an electric motor mounted in a reaction cradle will be developed to measure the frictional losses in the drive train and to determine motored frictional and pumping losses in the

engines themselves. A Kistler in-cylinder pressure transducer attached to an AVL Indisart combustion analyzer will be installed to take in-cylinder pressure measurements and detect knock. The combustion analyzer will also require a high fidelity rotary encoder to track the crank angle of the engine. Emissions measurements of oxygen and carbon dioxide will also be added. The measurements will permit the calculation of trapping and scavenging efficiency.

After the baseline is created, the work splits into two research paths. The first path will focus on quantizing the thermal losses from the engine. The engine will be enclosed in a box, with air flow measurements at the cooling air inlet and temperature measurements at the cooling air inlet and outlet. The aim of the experiment will be to determine the amount of heat lost through the cylinder head relative to that lost in the exhaust and the energy that goes into producing useful shaft work. The second path will examine the mixing and injection methods for the engines, exploring the use of PFI and DI to improve combustion and fuel efficiency. Variable timing via a custom ECU may also be considered to improve engine performance.

The anticipated results of these experiments are three fold. First, the data will allow for the development of scaling relationships relating engine geometry to performance, efficiency, and losses. While there are several examples of similar scaling relationships [1, 14], the prior experiments lack relevant data in the 1-6 kW size class. Second, methods to improve small engine performance will be identified and more importantly quantified. While both PFI and DI techniques should create more controllable and consistent mixtures than air carburetors, the improvements to performance are largely un-quantified for this size class of engine. Third and finally, the results will aid in adapting the engine to run on low-AKI fuels, such as JP-8. The knock characteristics that preclude the use of low AKI fuels in many ICEs are the direct result of the thermal characteristics and combustion timing of the engine, whether it is hot end-gas, hot spots, or spark timing. The SETB will provide a platform for studying the onset of these effects as the AKI for the engine is relaxed.

## SUMMARY/CONCLUSIONS

The baseline test for the 3W 55i engine indicates that the bench as currently configured is functional, although several incremental improvements are necessary for it to reach full capability. These improvements include the addition of an AVL Indisart combustion analyzer to make in cylinder pressure measurements and modifications to the control system to allow PFI and DI techniques to replace the stock air carburetors once base line characterization of the engine is complete. Despite issues other similar benches encountered with air and fuel flow measurements, a comparison of those measurements during the high throttle testing to the corresponding measurements from the exhaust gas oxygen sensor indicates the fuel and air flow meter are providing reasonable values. A larger air flow meter may be required for the 3W 85xi engine based on the scavenging performance of the 3W 55i engine.

While the presented performance maps for the 3W 55i engine demonstrate bench function, the engine only developed a maximum power of 2.1 kW, 54% of its manufacturer rated power. Further work is necessary to determine if the discrepancy is a tuning problem with the carburetor, a manufacturer overstatement, or a combination of both. Additional work is also necessary to characterize the frictional losses in the drive train.

The testing demonstrated the ability of the bench to control the intake air temperature to a 3°C range over a wide range of air flow rates from 20 SLPM to 250 SLPM. The cooling blower was able to hold cylinder temperature constant at the majority of throttle and speed combinations, although more cooling may be necessary for higher speeds, full throttle, and larger engines. Imminent future testing will focus on tuning the 3W 55i engine and verifying its baseline before progressing to testing the other 3W engines and characterizing thermal losses.

## REFERENCES

- [1] C. Cadou, T. Sookdeo, N. Moulton and T. Leach, "Performance Scaling and Measurement for Hydrocarbon Fueled Engines with Mass Less Than 1 kg," *AIAA's 1st Technical Conference and Workshop on Unmanned Aerospace Vehicles*, 20-23 May 2002.
- [2] J. Ausserer and F. Harmon, "Integration, Validation, and Testing of a Hybrid-Electric Propulsions System for a Small Remotely-Piloted Aircraft," *10th International Energy Conversion Engineering Conference*, 30 July 2012.
- [3] S. Menon, N. Moulton and C. Cadou, "Development of a Dynamometer for Measuring Small Internal-Combustion Engine Performance," *Journal of Propulsion and Power*, vol. 23, no. 1, pp. 194-202, January-February 2007.
- [4] D. Gierke, "Part 1: Dynamometer and Engine Performance Analysis," *Flying Models*, pp. 21-25, June 1973.
- [5] D. Gierke, "Part 2: Dynamometer and Engine Performance and Analysis," *Flying Models*, pp. 38-47, July 1973.
- [6] D. Gierke, "Part 3: Dynamometer and Engine Performance Analysis," *Flying Models*, pp. 38-47, August 1973.
- [7] M. Drela, "QPROP Documents: DC Motor/Propeller Matching," Massachusetts Institute of Technology, Boston, MA, 2005.
- [8] C. Cadou and S. Menon, "Scaling of Losses in Small IC and Aero Engines with Engine Size," *42nd AIAA Aerospace Sciences Meeting and Exhibit*, 5-8 January 2004.
- [9] S. Menon, "Performance Measurement and Scaling in Small Internal Combustion Engines," University of Maryland, 2006.
- [10] N. Moulton, "Performance Measurement and Simulation of a Small Internal Combustion Engine," University of Maryland, 2007.



- [11] C. Cadou, N. Moulton and S. Menon, "Performance Measurement and Scaling in Small Internal Combustion Engines," *41st Aerospace Sciences Meeting and Exhibit*, 6-9 January 2003.
- [12] J. A. Baranski, M. H. Fernelius, J. L. Hoke, C. W. Wilson and P. J. Litke, "Characterization of Propeller Performance and Engine Mission Matching for Small Remotely Piloted Aircraft," *47th AIAA/ASME/SAE/ASEE Joint Propulsion Conference & Exhibit*, 2011.
- [13] A. Wiegand, S. Miers, J. Blough, D. Kowalski and A. Biske, "Development of a Micro-Engine Testing System," *SAE International*, 23 October 2012.
- [14] J. B. Heywood, *Internal Combustion Engine Fundamentals*, New York: McGraw-Hill, 1988.
- [15] 3W Modellmotoren, "Engine Manual 3W 85XI/85XI TS/CS - series," 2013. [Online]. Available: [www.modellmotoren.com](http://www.modellmotoren.com). [Accessed 5 April 2013].
- [16] 3W Modellmotoren, "Engine Manual 55i / 55i CS," 2013. [Online]. Available: [www.3w-modellmotoren.com](http://www.3w-modellmotoren.com). [Accessed 5 April 2013].
- [17] 3W Modellmotoren, "Engine Manual 24i-28i / CS," 2013. [Online]. Available: [www.3w-modellmotoren.com](http://www.3w-modellmotoren.com). [Accessed 5 April 2013].
- [18] J. B. Heywood and E. Sher, *The Two-Stroke Cycle Engine: Its Development, Operation, and Design*, New York, NY: Taylor and Francis Group, 1999.
- [19] Coordinating Research Council, Inc., "Handbook of Aviation Fuel Properties," Alpharetta, GA, 2003.
- [20] Magtrol, *WB and PS Series Eddy-Current and Magnetic Powder Dynamometers User's Manual*, 2009.
- BMEP – Brake Mean Effective Pressure  
 BSFC - Brake Specific Fuel Consumption  
 COTS – Commercial-off-the-Shelf  
 DAQ – Data Acquisition  
 DI – Direct Injection  
 DoD – Department of Defense  
 ICE – Internal Combustion Engine  
 IMEP – Indicated Mean Effective Pressure  
 NI – National Instruments  
 ON – Octane Number  
 PFI – Port Fuel Injection  
 PRF – Primary Reference Fuel  
 RON – Rated Octane Number  
 RPA – Remotely Piloted Aircraft  
 SETB – Small Engine Test Bench  
 SI – Spark Ignition  
 SLPM – Standard Liter Per Minute

## CONTACT INFORMATION

Lt Joseph Ausserer: [Joseph.Ausserer@wpafb.af.mil](mailto:Joseph.Ausserer@wpafb.af.mil), (937)-255-7664.

## ACKNOWLEDGMENTS

The authors would like to acknowledge the support of everyone who consulted and assisted with the fabrication of the Small Engine Test Bench. They would like to specifically thank Mr. Dave Burris for designing and coding the LabVIEW control and data acquisition program, and Mr. Rich Ryman and Mr. Ben Naguy for their assistance machining fixtures for the setup. Acknowledgement for funding is due to the Air Force Research Laboratory.

## SYMBOLS

$\eta_f$  – Fuel Conversion Efficiency  
 $\Lambda$  – Delivery Ratio  
 $\Phi$  – Equivalence Ratio

## DEFINITIONS/ABBREVIATIONS

AKI – Anti-Knock Index  
 SETC2013

## **Appendix B**

**Paper:** Preliminary Thermal Loss Measurements for a Small Internal Combustion Engine

**Presented at:** SciTech 2014 in National Harbor, Maryland

**Citation:**

J. A. Rittenhouse, A. K. Rowton, J. K. Ausserer, and M. D. Polanka, "Preliminary Thermal Loss Measurements for a Small Internal Combustion Engine," presented at the AIAA 52nd Aerospace Sciences Meeting, National Harbor, Maryland, AIAA 2014-0529, 13-17 January 2014, doi: 10.2514/6.2014-0529.

# Preliminary Thermal Loss Measurements for a Small Internal Combustion Engine

Joshua A. Rittenhouse\*, Alexander K. Rowton\*, Joseph K. Ausserer†, Marc D. Polanka‡

*Air Force Institute of Technology, WPAFB, OH, 45433, USA*

Paul J. Litke§

*Air Force Research Laboratories, WPAFB, OH, 45433, USA*

and

Keith D. Grinstead, Jr.¶

*Innovative Scientific Solutions Inc., Dayton, OH 45440, USA*

Three analysis techniques were used to measure the heat rejection of a 55 cc air-cooled two-stroke engine. This study was performed as part of a larger effort aimed at extending range and endurance limitations of Group 1 & 2 Remotely Piloted Aircraft (RPA). The engine selected for the study is a gasoline-fueled, carbureted, spark-ignition engine made by 3W and is representative of RPA engines in these groups. With a surface area to volume ratio of 1.48, the engine is in a size region where thermal losses begin to dominate engine efficiency and thermal efficiencies of less than 15% are common. The first method was to perform an energy balance between the fuel energy entering the system and the various avenues for energy to leave the system. The second method used an enclosure around the engine and measured the enthalpy increase of the air flowing past the cooling fins. The third method used heat flux gauges placed on the cylinder head to measure the heat flux at those locations. By quantifying the heat rejection, we can evaluate the effectiveness of thermal loss reduction techniques. The 55 cc engine tested achieved a maximum fuel conversion efficiency of 12.5% and a maximum brake power value of 3.0 kW, both at 7500 rpm.

## I. Introduction

THERMAL energy lost through engine cylinder walls is a major component of both overall engine efficiency and engine thermal management. Increased surface area within the cylinder allows for increased heat transfer to the cylinder walls. As cylinder size decreases, the ratio of surface area to volume increases resulting in increased thermal losses.<sup>1</sup> This phenomenon is shown in Figure 1 which shows the trend in power versus cylinder surface area to swept volume ratio for a range of IC engines. The points are manufacturer specified power values collected from over fifteen different manufacturers. The ratio was calculated using the engine stroke and bore size.

$$\frac{\text{SurfaceArea}}{\text{DisplacementVolume}} = \pi \text{Bore} \left( \frac{1}{2} \text{Bore} + \text{Stroke} \right) \quad (1)$$

For engine efficiency, thermal loss through the cylinder walls is a negative aspect in that the heat is energy not available as useful mechanical work. For thermal management, thermal loss is a positive aspect resulting in lower cylinder temperatures. Avoiding high cylinder temperatures can also aid in conversion to using low octane fuels or heavy fuels by minimizing preignition in addition to reducing material fatigue.<sup>2</sup> Quantifying

---

\*Aeronautical Engineering Masters Student

†Aeronautical Engineering PhD Student

‡Associate Professor of Aeronautical Engineering and AIAA Associate Fellow

§Senior Research Engineer and AIAA Senior Member.

¶Senior Research Engineer.

thermal losses is the first step toward controlling the thermal losses which could aid efforts to increase engine efficiency, convert to heavy fuels, and reduce engine fatigue.

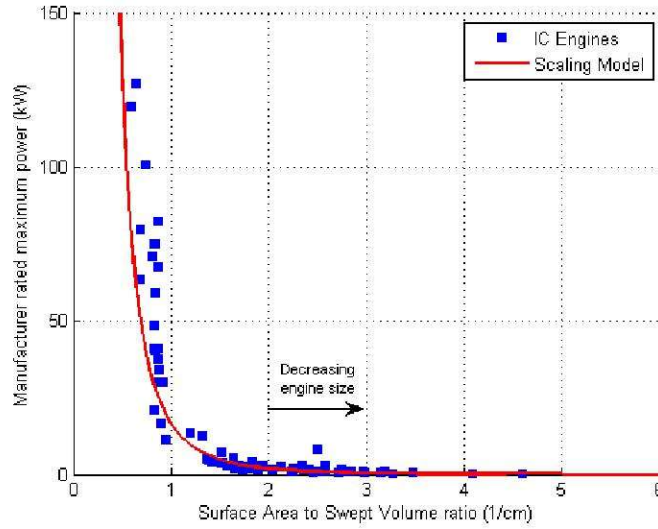


Figure 1: Manufacturer rated IC engine power vs. cylinder surface area to swept volume ratio

Maximum fuel conversion efficiency is limited by the idealized thermodynamic Otto cycle. Fuel conversion efficiency,  $\eta_f$  is calculated as the ratio of thermal energy input versus the work output.

$$\eta_f = \frac{W_b}{\dot{m}_f Q_{LHV}} \quad (2)$$

where  $W_b$  is the measured output of mechanical work from the system. The thermal energy is provided through the combustion of a given fuel as calculated by the product of fuel mass flow rate,  $\dot{m}_f$ , and the lower heating value,  $Q_{LHV}$ , of the fuel.

The Otto cycle defines the maximum fuel conversion efficiency of a spark-ignited reciprocating engine as a function of compression ratio,  $r_c$ , and specific heat ratio,  $\gamma$ . The specific heat ratio for air is 1.4 at standard conditions and decreases slightly as temperature rises through the compression and combustion process to as low as 1.3. The geometric compression ratio is set by engine geometry as the ratio between the combined volume of the cylinder and combustion chamber when at the bottom of the stroke (bottom-dead-center, BDC) versus the remaining volume of the combustion chamber when at the top of the stroke (top-dead-center, TDC). As the piston moves upward from BDC, the intake or exhaust ports may not be closed yet, therefore delaying compression. In this case, the more useful compression ratio is the effective compression ratio. Effective compression ratio is the adjusted ratio using the combined volume of the cylinder and combustion chamber once all ports are closed versus the volume of the combustion chamber at TDC. The governing efficiency equation is then:<sup>1</sup>

$$\eta_f = 1 - \frac{1}{r_c^{\gamma-1}} \quad (3)$$

For modern gasoline-fueled spark-ignition engines, compression ratios are normally around 10:1, but can be as high as 14:1. For a compression ratio of 10:1 and using an average  $\gamma$  of 1.35, the maximum theoretical efficiency is 55%.

Actual engine efficiencies are much lower than the theoretical maximum given by Equation 3. There are several reasons why this is the case. For one, the compression and expansion strokes are not isentropic. One of the largest contributors to less than ideal efficiency is thermal loss through the cylinder body, typically 20-36% of the fuel heating value.<sup>1</sup> Two-strokes suffer from an additional loss of efficiency known as short-circuiting. Short-circuiting is the escaping of fresh fuel/air mixture through the exhaust port during the gas



exchange process. Being able to quantify the loss mechanisms is a critical step to evaluating methods to improve overall efficiency.

As a positive aspect, thermal losses through the cylinder body allow engine components to cool and stay within acceptable operating ranges. Temperatures too high can cause fatigue cracking, deteriorate lubricating oil, and abnormal combustion.<sup>1</sup> Temperature distributions are not uniform throughout the cylinder body. Locations within the cylinder of consistently elevated temperatures with respect to the rest of the cylinder are referred to as hot spots. In addition to increased fatigue at these locations, hot spots can cause the fuel/air mixture to ignite locally in regions away from the spark plug. This could result in an abnormal combustion event, known as surface-ignition, and can cause engine knock.<sup>1</sup>

Gasoline fuels are rated for their ability to resist knock. The research octane rating (RON) is measured through a research method (ASTM D-2699) and the motor octane method (MON) measured under more severe operating conditions (ASTM D-2700).<sup>1</sup> Averaging these two ratings is the anti-knock index (AKI) seen at gas station pumps in the United States.

$$AKI = \frac{RON + MON}{2} \quad (4)$$

Using fuels with lower AKI values increases the risk of surface-ignition and subsequent knock. Effective techniques for avoiding knock are retarding ignition timing and reducing the intake air temperature.<sup>3</sup> One additional method to compensate for a low AKI is to reduce engine temperature in order to avoid surface-ignition prior to spark ignition. This conflicts however with the goal of improved efficiency through minimizing heat loss.

In-cylinder pressure data are valuable for determining indicated work over the operating cycle of an internal combustion engine. The indicated work per cycle is a measure of how compression, combustion, and expansion processes affect the power output of an engine. It is a sum of work available at the crankshaft and the work required to overcome engine friction and pumping power.<sup>1</sup> Conveniently, indicated measurements are not dependent on drivetrain components connected to the engine, so compensation for additional frictional loading is not necessary when recording data. The AVL IndiSmart combustion analyzer is designed to measure and record high speed pressure data during engine operation. This data, along with a high-resolution crank angle position signal, can yield indicated work per cycle via the following equation

$$W_{c,i} = \oint p dV \quad (5)$$

Subsequently, indicated power output can be obtained with the following equation

$$P_i = \frac{W_{c,i}N}{n_c} \quad (6)$$

In-cylinder pressure measurements are also used to signify the presence and severity of knock in an engine. During normal engine operation, a trace of in-cylinder pressure versus crank angle shows a smooth rise and fall over the engine's compression and expansion strokes. If an engine knocks however, the pressure trace will show sharp peaks and valleys in an oscillatory manner. These sharp pressure spikes can damage an engine's internal and structural components over time, so it is necessary to precisely determine the point of onset of knock in a particular engine in terms of fuel AKI or spark timing in spark-ignition engines.

The DOD uses small piston engines in Remotely Piloted Aircraft (RPA) applications and has been interested in the use of heavy fuels for both decreased Brake Specific Fuel Consumption (BSFC) and reduced fuel delivery logistics. Avoiding surface-ignition is difficult when converting an existing gasoline-fueled, spark-ignition engine to a low octane or heavy fuel. Heavy fuels have less resistance to compression ignition and are therefore already more prone to pre-ignite. However, certain engines with low compression ratios and high surface area to volume ratios can transition with minimal knock as shown by Wilson.<sup>2</sup> Conversely, running heavy fuel in a gasoline engine that is too cool will prevent the fuel from vaporizing to create a combustible air-fuel mixture. To overcome this scenario as seen in cold-starts, Groenewegen ran an engine initially on gasoline before switching to a heavy fuel.<sup>4</sup>

Many research efforts have focused on increasing overall efficiency, but less has been done to quantify the individual segments of thermal loss. Zhao, Collings, and Ma successfully utilized thermal imaging to measure cylinder head surface temperatures.<sup>5</sup> An infra-red scanner was used in cooperation with calibration and image processing equipment. They were able to achieve head temperatures that were in agreement with

thermocouples embedded into the cylinder head. However, this effort was focused on reading temperatures and not on quantifying heat loss.

Ajav, Singh, and Bhattacharya used a series of thermocouples in studying how ethanol-diesel blends affected thermal losses in a compression ignition engine. They categorized thermal loss into four areas: heat lost to the cooling water, heat lost to the exhaust gases, heat lost to the lubricating oil, and unaccounted for heat loss. Their emphasis was on how thermal losses for the blended fuel compared to losses with diesel fuel instead of accurately quantifying the thermal loss from the cylinder body.<sup>6</sup>

High thermal losses are being utilized in other ways besides minimizing knock and component fatigue. Martinez-Frias et al. showed how proper management of heat loss can be used to control a Homogeneous Charge Compression Ignition (HCCI) engine.<sup>7</sup> This type of engine uses a premixed charge like in gasoline engines but uses compression ignition as in diesel engines. The result is a highly efficient engine with low emissions. Through managing thermal losses, the point of ignition is controlled. Similarly, Mueller et al. demonstrated that proper thermal management can be used to reduce automotive engine emissions where engine operation duration is short.<sup>8</sup> Both of these applications would benefit from accurately quantifying thermal losses.

## II. Experimental Setup

The test bench used in studying the thermal loss techniques was developed by AFRL as part of a small engine research effort to study thermal and frictional losses with decreasing engine size.<sup>10</sup> An engine was selected near a cylinder surface area to displacement volume ratio of  $1.5\text{cm}^2/\text{cc}$ , the point where thermal and frictional losses begin to dominate combustion physics.<sup>1</sup> The 3W-55i from 3W Modelmotoren was chosen with a ratio  $1.48\text{cm}^2/\text{cc}$ . 3W Modelmotoren is a German manufacturer that specializes in engines for model aircraft. The engine is a carbureted two-stroke with mixture adjustment screws for idle and full throttle. Ignition is controlled through the manufacturer ignition module that advances timing as engine speed is increased. Additional engine parameters are specified in Table 1 including a compression ratio of 10:1.<sup>9</sup>

Table 1: Test Engine Parameters

Description	Value
Displacement	55 <i>cc</i>
Power	3.9 <i>kW</i>
Mass	1.94 <i>kg</i>
Power Density	2.79 $\frac{\text{kW}}{\text{kg}}$
Bore	4.50 <i>cm</i>
Stroke	3.51 <i>cm</i>
Compression Ratio	10:1
Cylinder surface area to volume ratio	0.54

The test bench shown in Figure 2 was designed to accurately test a family of 3W engines with minimal modifications between models. The engine is mounted to the table with cooling air provided by means of a blower to the left. The engine crankshaft is coupled to the drivetrain to the right. Intake air is routed through a baffling drum below the table, through a heat exchanger and then brought up to the tabletop and to the engine. Fuel is held in a tank off the table and pressurized with nitrogen to provide flow to the carburetor. A vertical exhaust stack is mounted to the side of the engine at the exhaust port. Data is recorded using a National Instruments FieldPoint system mounted on the bench and routed to a control computer located in an adjacent control room. Additional test bench details are in the following paragraphs with full details and verification results documented in Ausserer et al.<sup>10</sup>

The intake air control system was designed to compensate for fluctuating air flow and changing ambient air temperatures. A maximum anticipated intake air flow rate was calculated to be  $360 \frac{\text{L}}{\text{min}}$  based on similar engines and maximum delivery ratios for the series of 3W engines.<sup>10</sup> A TSI 40211 High Performance Linear Mass Flow Meter was used to measure the flow of intake air. An identical flow meter was later added in parallel to reduce intake air restrictions. The units used a hot wire anemometer and a temperature correction



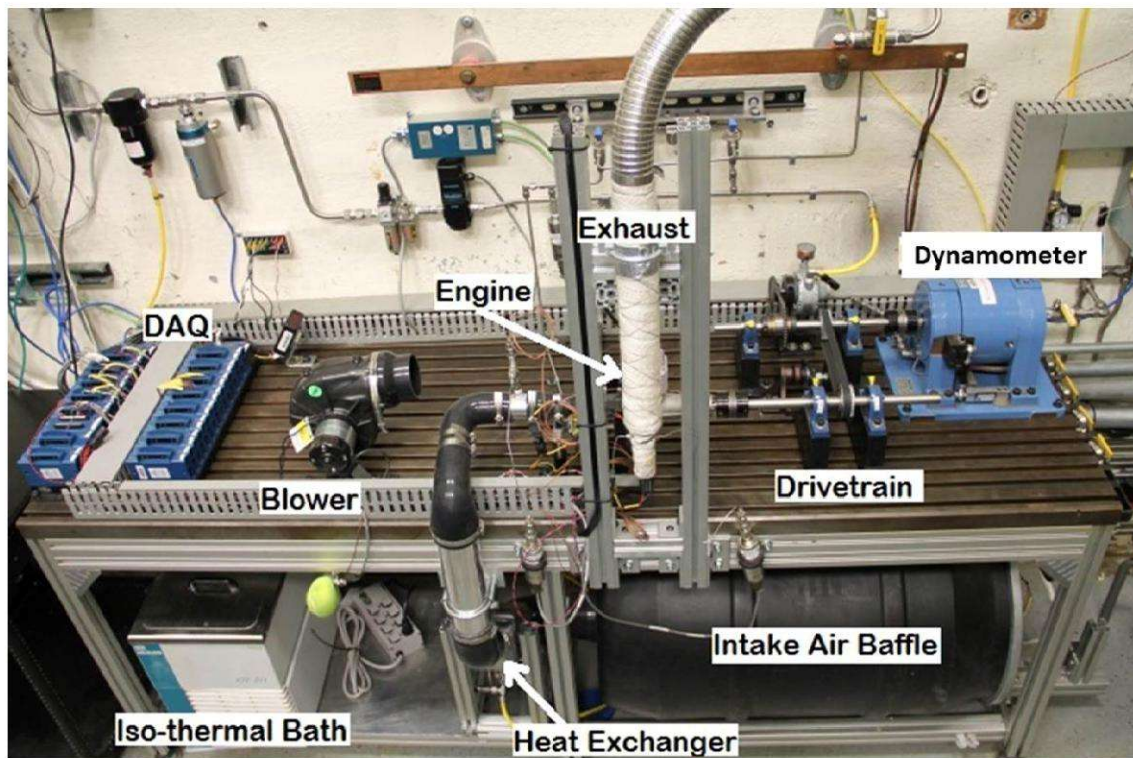


Figure 2: Small Engine Test Bench

thermocouple to provide a voltage to the DAQ that is proportional to the flow. A 209 L (55 gal.) drum was used as a baffle, isolating the flow meter from oscillating engine air flows. After the drum, air is routed through a Frozen Boost heat exchanger with water as the working fluid. Water temperature was controlled through the use of a Thermo Neslab RTE-211 recirculating isothermal bath. Temperature was measured just prior to the air entering the engine carburetor with a Type J thermocouple of  $2.2^{\circ}\text{C}$  or 0.75% accuracy. Pressure was also measured here using a Honeywell TJE pressure transducer with 0.10% accuracy. A 1.6 mm ( $\frac{1}{16}$  in) stainless steel tube was used as a pressure tap to reduce transducer exposure vibration.

Fuel flow was anticipated to be on the order of 10's of  $\frac{\text{mL}}{\text{min}}$  and was measured using a Max Machinery 213 Piston Flow Meter. The fuel used in this investigation is a Primary Reference Fuel (PRF) blend of 92% isooctane, 8% n-heptane, additionally 2% SAE 5W-20 synthetic oil by volume was added. The fuel tank is pressurized to approximately 6.7 kPa with nitrogen to provide flow through 40  $\mu\text{m}$  and 7  $\mu\text{m}$  fuel filters and the flow meter to the carburetor. The air to fuel ratio (AFR) can then be calculated using the measured air and fuel flow rates. A Powerdex Air-Fuel Monitor by NGK is mounted on the exhaust stack for real-time AFR readings and as a secondary measurement. Temperature and pressure was also measured on the exhaust stack. A Type J thermocouple was inserted into the exhaust stream for exhaust temperatures. Exhaust pressure was measured again using a stainless steel tube and Honeywell TJE pressure transducer.

The engine drives the drivetrain setup as shown in Figure 3. A Ruland bellows shaft coupler connects the engine crankshaft to the engine driveshaft. A timing belt pulley system is mounted on pillow block bearings and is used to transfer power to the dynamometer while minimizing vibration. A Magtrol 1 WB 65 eddy current dynamometer measures torque and speed. The dynamometer is capable of measuring up to 10 N-m of torque at up to 10,000 rpm with an accuracy of  $\pm 0.5\%$  of the full scale for both torque and speed. A Lubricated Air Motor from GAST is used with a one-way clutch bearing to start the engine by driving the dynamometer driveshaft.

The engine is configured with servo motors for throttle and choke controls. Hitec HS-85MG+ servos were chosen for their resistance to high torque and vibration. In operation, the engine would be cooled by airflow from the propeller moving past the cooling fins. On the test bench, cooling for the engine was initially accomplished by means of a JABSCO 35440 series blower directed at the cylinder body. The blower



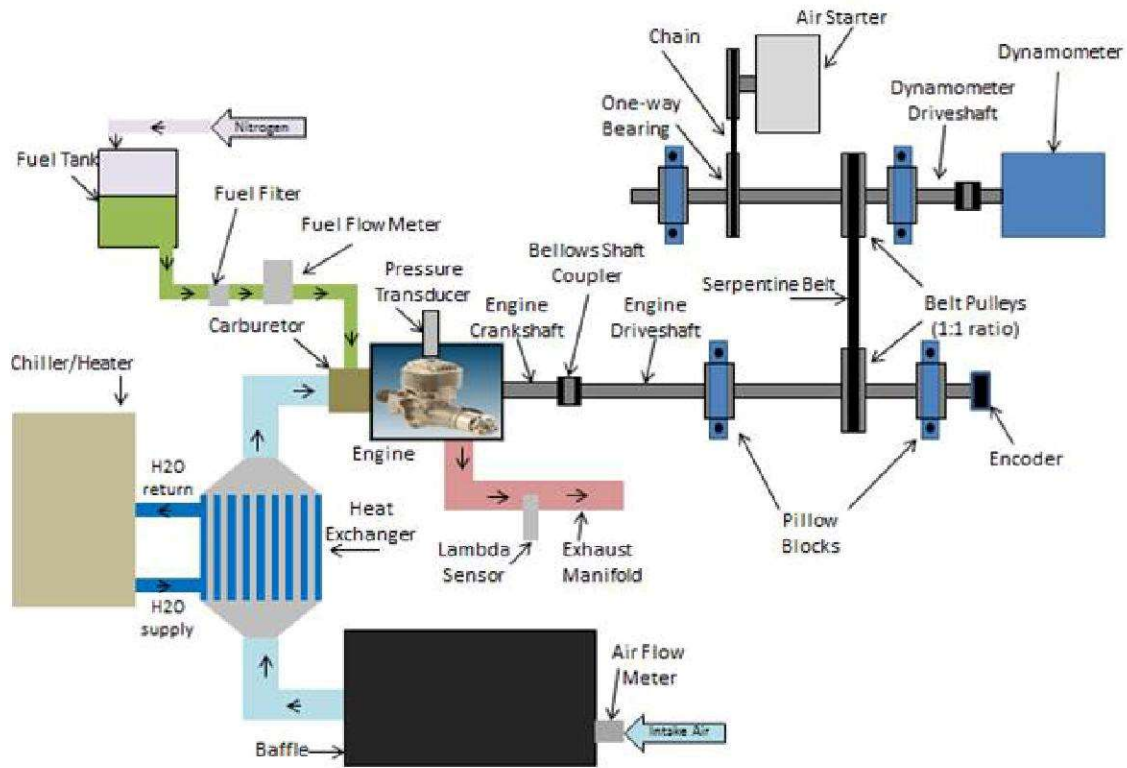


Figure 3: Flow of air, fuel, and power in the Small Engine Test Bench

was powered by 24V DC through the control of a Midwest Motion Products motor controller. A study of RPAs with engines of similar power ratings to the 3W 55i resulted in maximum speeds of  $30.5 \frac{m}{s}$  ( $100 \frac{ft}{s}$ ) or less. This speed was used as the maximum velocity for airflow directed at the engine. After the addition of ducting, the blower was found to be incapable of reaching desired flow rates and was replaced by a more capable 1.1 kW (1.5 hp) 480V AC motor/blower. This blower was controlled by means of a variable frequency drive (VFD) that used a 0-5V analog input from the DAQ for speed control.

Data acquisition was performed using a National Instruments FieldPoint system and custom LabVIEW programming. All data was recorded and time-correlated. The setup allowed for control and monitoring of the test rig from an adjacent control room for operator safety. For this experiment, the AVL system was configured to measure pressure inside the engine cylinder during operation using a Kistler type 6113B measuring spark plug. The Kistler pressure sensor can measure pressures from 0-200 bar with an accuracy of less than  $\pm 0.5\%$  within its operating temperature range of  $-20^{\circ}C$  to  $350^{\circ}C$ . The crank angle signal was measured using a US Digital E6-1800-750-IE-D-H-DB optical encoder. The encoder measures crank angle to within  $\pm 0.1^{\circ}$ . The AVL data acquisition system utilizes high speed cylinder pressure and crank angle data to calculate the average indicated mean effective pressure and coefficient of variance over 400 engine cycles. These data were used to determine the engine's indicated power output.

### III. Evaluated Measurement Techniques

This investigation aimed to quantify the heat rejection from the 55cc single cylinder, gasoline-fueled, spark-ignition, two-stroke engine shown in Figure 4. Three measurement techniques were used to capture the thermal losses of the cylinder body. The first method indirectly measured the loss through an energy balance into and out of the system. The second method measured the enthalpy increase of air flowing past the outside of the cylinder body and cooling fins. The third method used heat flux gauges at three locations on the cylinder body.

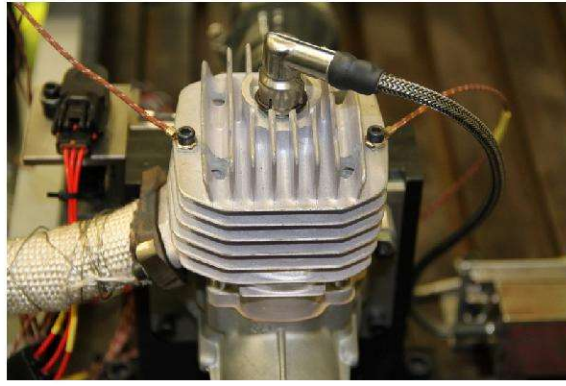


Figure 4: 3W-55i Test Engine

### A. Energy Balance

Energy is brought into the engine system through the combustion of fuel and air and leaves through a variety of different mechanisms. Through the measurement of total energy into the system and measuring the different mechanisms for energy leaving one can deduce an estimate for the amount of energy lost through heat rejection. The ideal or maximum amount of this energy that can be used is calculated from the Otto efficiency in Equation 3, the fuel flow rate, and the lower heating value.

$$E_t = \eta_{th} \dot{m}_f Q_{LHV} \quad (7)$$

The Indicated Mean Effective Pressure (IMEP) obtained from the AVL was used to measure the amount of power the engine produces before frictional and pumping losses. The indicated or IMEP-based power is then calculated by combining Equations 5 & 6.

$$P_i = \frac{\text{IMEP} * N * V_d}{n_c} \quad (8)$$

with  $N$  being the engine speed in revolutions per second,  $V_d$  is the engine displacement, and  $n_c$  is the number of revolutions per cycle (1 revolution per cycle for a 2-stroke). The difference between the ideal energy in Equation 3 and the indicated power is the energy lost due to thermal losses, short circuiting, and non-ideal combustion. This measurement provides an upper limit to the amount of heat rejected. A more accurate measurement of thermal loss can be obtained by minimizing or measuring short-circuiting and non-ideal combustion losses. Non-ideal combustion is minimized to less than 5% through proper tuning.<sup>1</sup> Short-circuiting losses are highest at low loads and can be reduced over a small range of engine speeds by utilizing a tuned exhaust pipe. Kumarappa and Prabhukumar saw a 9.1% increase in efficiency by implementing a direct injection fuel system to avoid any short-circuiting effects.<sup>11</sup> The short-circuiting losses could be quantified through the addition of emission instrumentation in the exhaust.

The brake power is the amount of usable mechanical energy available at the point of measurement on the shaft. Brake power was calculated by measuring the torque at the dynamometer and multiplying by the angular speed  $P_b = TN/2\pi$ . The difference between the IMEP and a Brake Mean Effective Pressure (BMEP) is the Friction Mean Effective Pressure (FMEP). FMEP accounts for the friction of internal engine components, pumping losses, and in this research the friction of the drivetrain linking the engine shaft to the dynamometer. Pumping losses are minimized by operating at wide-open-throttle (WOT) which minimizes air flow restrictions at the throttle plate.

### B. Measuring Heat Loss to External Engine Flow

The second technique measured the amount of heat transferred to air that flowed past the cylinder body. This configuration of the test bench is shown in Figure 5 with a closer view in Figure 6. An enclosure was built to contain the engine and measure the airflow ducted through. The enclosure was constructed of a clear polycarbonate to allow for visual engine monitoring during tests. Air at a measured temperature and



flow rate was then pumped into the container using the VFD and AC blower. Flow rates were representative of RPAs in flight with similar sized engines with a maximum of approximately  $30.5 \frac{m}{s}$  ( $100 \frac{ft}{s}$ ). The temperature of the airflow was then measured at the exit to calculate the amount of heat added to the air. This technique is similar to that used by Ajav with water as the working fluid.<sup>6</sup> The energy lost to the air is calculated by Equation 9.

$$\dot{Q} = \dot{m}_{air} c_p (T_{out} - T_{in}) \quad (9)$$

where  $\dot{Q}$  is the heat transfer rate,  $\dot{m}_{air}$  is the mass flow rate of the air into and out of the enclosure, and  $c_p$  is the specific heat of the working fluid. Radiative heat transfer effects were neglected.

The mass airflow was measured using an Omega FMA905A-V1 hot wire sensor inserted into the center of the duct upstream of the engine. An approximate ten diameters of duct was added upstream of the point of measurement along with five diameters downstream to accommodate flow profile development. The linear 0-5 V analog air speed output of the hot wire was measured with the DAQ and corrected for viscous effects at the wall of a circular duct to determine the bulk velocity. The mass airflow is then the product of the bulk velocity, duct cross-sectional area, and air density.

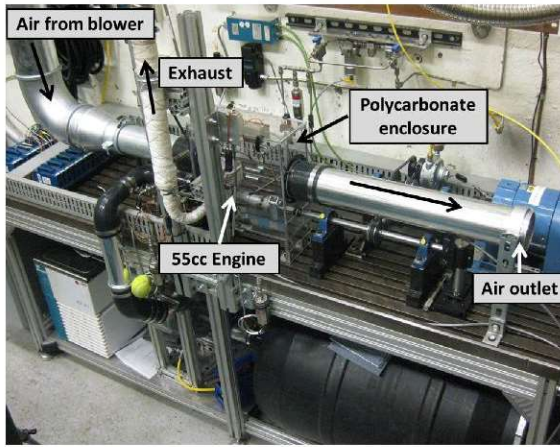


Figure 5: Overview of bench configured with ducted airflow through polycarbonate enclosure

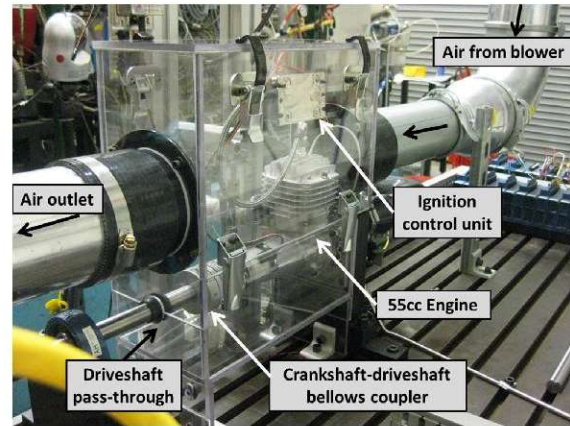


Figure 6: Engine within polycarbonate enclosure

### C. Thermal Imaging, Thermocouples, and Heat Flux Gauges

Direct measurement of heat loss was done by means of multilayer heat flux gauges. These heat flux gauges obtain a direct measurement of the heat flux by measuring the temperature difference between opposite sides of a thin layer of insulating substrate.<sup>12</sup> The frequency response of the gauge is increased as the thickness of the insulator is reduced. The gauge consisted of an upper and lower temperature-dependent platinum resistor similar to a resistance temperature detector (RTD). The change in resistance with temperature of the platinum is nearly linear. The temperature at each resistor element is calculated using

$$T = \frac{R_0 - R}{\alpha_R R_0} \quad (10)$$

where  $R$  is the measured resistance at temperature,  $R_0$  is the element resistance at a calibration temperature,  $\alpha_R$  is the temperature coefficient determined through calibration, and  $T$  is the measured temperature. A National Instruments 9217 24-Bit analog input module was used with internal excitation and Wheatstone bridge to capture the small changes in resistance as the temperature changed. Current values running through the bridge must be kept small to avoid heating the gauge element thus affecting the temperature and heat flux measurement. Once the temperature of the upper and lower elements are measured, the heat flux ( $\frac{W}{m^2}$ ) can then be calculated.

$$Q'' = -k \frac{(T_{upper} - T_{lower})}{dx} \quad (11)$$

The two elements are separated by Kapton with a conductivity of  $k = 0.179 \frac{W}{mK}$  and a thickness of  $dx = 51.1\mu m$ . The total energy the cylinder gives off as heat rejection is then the heat flux multiplied by the exterior surface area of the cylinder head. Due to the inability to cover the entire cylinder body with heat flux gauges, the accuracy of this method is limited. Energy loss calculations for this method used a heat flux value that was an average between three strategically placed gauges. The surface area was measured to be approximately  $640 \text{ cm}^2$  and will be compared to a value provided by a CAD model of the cylinder body during final calculations.

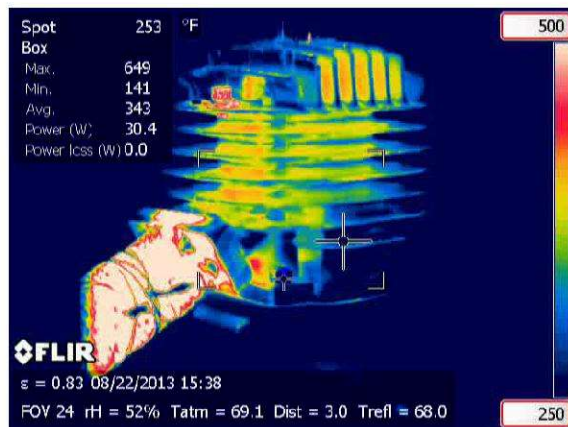


Figure 7: IR image used in evaluating temperature distribution

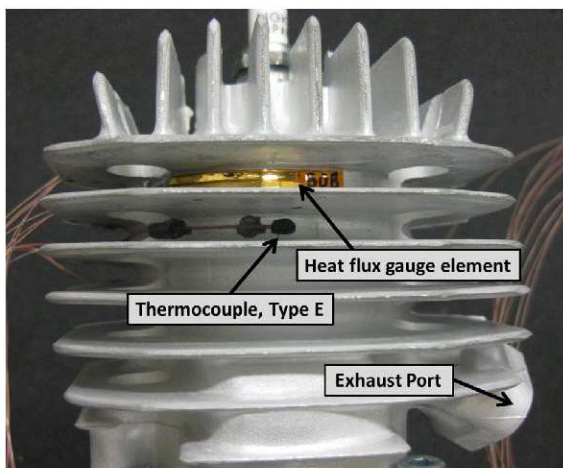


Figure 8: Thin-film heat flux gauge and thermocouple placement facing airflow

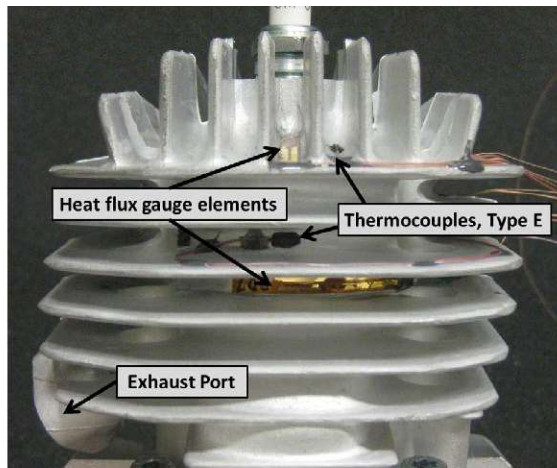


Figure 9: Second and third thin-film heat flux gauges and thermocouples, placed on side opposite the airflow

To aid in the placement of the heat flux gauges, a FLIR SC640 infrared (IR) camera was used to gather a continuous mapping of engine temperatures within the camera's field of view. This enabled the sensors to be strategically and non-invasively placed around the cylinder head at locations that would be representative of the cylinder body temperature. The IR camera also proved helpful in identifying potential hot spots. The IR image in Figure 7 shows higher temperatures on the exhaust side, at top of head, and near the base in between fins. Based on this and additional images, heat flux gauges were placed between fins on the cylinder body at three locations as shown in Figures 8 & 9. The first gauge was placed on the side facing the airflow, a second was placed on the side facing away from the airflow, and a third was placed at the top of the cylinder. Embedded E-type thermocouples were used to gather reference temperatures needed to calibrate the thermal IR images.



## IV. Results

The following are the results of the energy balance and the measured heat loss to external engine flow. The energy balance method provided a reasonable approximation of the amount of energy the 55 cc engine rejects through the cylinder body. The second method of external engine flow method provided a direct measurement of the heat rejection. The third method of using heat flux gauges is still ongoing.

### A. Energy Balance

Ideal fuel conversion efficiency for the test engine was calculated using Equation 3. Geometric compression ratio was 10:1 as specified by the manufacturer. Using an average specific heat ratio of 1.35 and the geometric compression ratio, the ideal fuel conversion efficiency of this engine was 55.3%. To account for open ports during a portion of the stroke, the ideal fuel conversion efficiency was also calculated using the effective compression ratio. The exhaust port was the last air passage to be covered as the piston travels towards TDC. Measuring the length of the remaining stroke from the point of closure resulted in an effective compression ratio of 7.1:1. To further examine if a small amount of compression exists prior to exhaust port closure, the engine was motored while monitoring in-cylinder pressure. An effective compression ratio of 7.2:1 was found through this analysis. With a 7.2:1 compression ratio, the ideal fuel conversion efficiency of the engine was 49.9%.

Actual fuel conversion efficiency was determined using Equation 2. Fuel flow rates and power measurements were taken from 4,000 rpm up to 8,000 rpm, the range at which the engine could consistently operate while at WOT. The lower heating value for the PRF was calculated to be  $44.4 \frac{MJ}{kg}$  using weighted values for the octane and heptane within the fuel. Total fuel energy and indicated power measurements are plotted in Figure 10. Also plotted in this figure is the exhaust enthalpy flux as calculated with engine air mass flow rate and exhaust temperature measurements. The decrease in total fuel energy near  $8 \frac{m}{s}$  was the result of decreased fuel flow most likely due to carburetor tuning. The indicated power line is a power value based on the IMEP obtained through the AVL DAQ. Figure f:powercurve shows a closer view of the various power curves over the engine speed range. Maximum indicated power was  $4.0 kW$  and maximum brake power was  $3.0 kW$ , both at  $8.8 \frac{m}{s}$  (7500 rpm). The dynamometer torque measurements were used to calculate the brake power line. The difference between the indicated power and brake power is the friction loss. As discussed earlier, this friction is a summation of engine friction, pumping losses, and drivetrain friction.

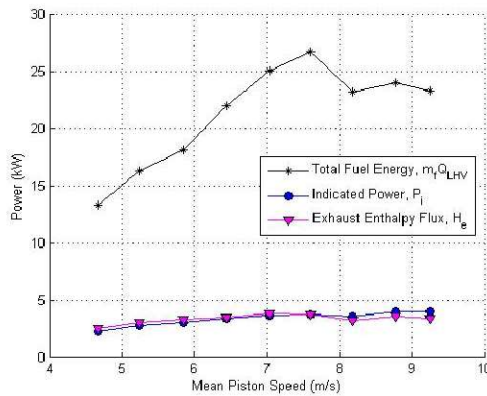


Figure 10: Total fuel energy, indicated power, and exhaust enthalpy flux of 55 cc engine at WOT

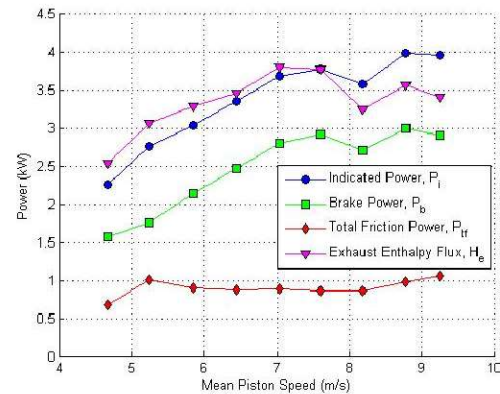


Figure 11: Power curves of 55 cc engine at WOT

An evaluation of power values as a percent of total energy is plotted over the speed range in Figure 12. The constant black line is the ideal Otto efficiency at 49.9%. The blue line is the indicated power efficiency with a maximum of 17.0% at  $9.2 \frac{m}{s}$  (7900 rpm). Maximum brake power efficiency in green was 12.5% at  $8.8 \frac{m}{s}$  (7500 rpm). The combined friction of the internal engine components, engine components, and pumping power remained relatively constant at approximately 5% of the fuel energy.

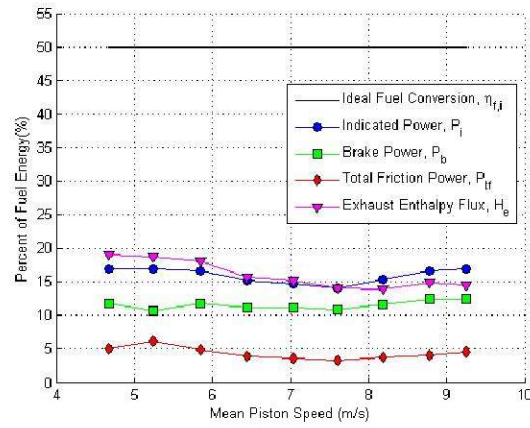


Figure 12: Power values as a percent of total fuel energy

Three repeatability runs were performed with the ideal, indicated, and brake power curves for each plotted in Figure 12. Run 1 shows slightly lower values for each of the three power types at 8000 rpm. A 16% drop in ideal power at this speed makes it apparent that fuel flow was reduced since the only variable changing in this curve is fuel flow.

The remaining unmeasured energy in the system is the difference between the total fuel energy and the sum of indicated power and exhaust enthalpy flux. This remaining energy is made up of thermal loss, short-circuiting, and non-ideal combustion. The thermal loss component can not be accurately determined without measuring the other two avenues for energy. The remaining energy does however provide a maximum limit for thermal loss. The remaining energy after accounting for indicated power and exhaust enthalpy flux while operating at full power was 65%. If incomplete combustion is assumed to be 5% and short-circuiting is assumed to be 10%, this approximates the heat rejection to be 50% of the total fuel energy.

## B. Measuring Heat Loss to External Engine Flow

Thermal losses were measured using the engine enclosure initially at full power and later at other power settings. Heat rejection measurements at full power are shown in Figure 13. The figure shows an approximation of 2 kW of energy is given off as heat from the cylinder body. The heat rejection increases slightly with engine speed with an increase of about 0.5 kW. At 2 kW of heat rejection, this represents 7-12% of the fuel energy as shown in Figure f:heatpercent. These percentages fall below the range mentioned in Heywood.<sup>1</sup> With the heat rejection measurements being lower than expected, additional improvements to the enclosure are planned to minimize heat transfer through the enclosure walls and to further reduce the amount of air escaping through locations other than the outlet.

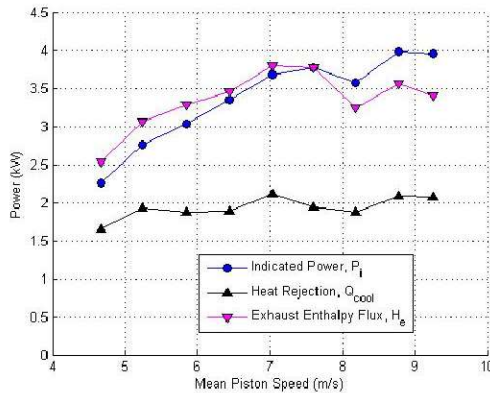


Figure 13: Heat rejection measurements at full power

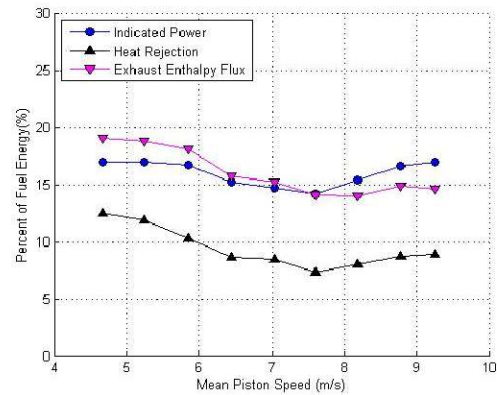


Figure 14: Energy values at full power as a percent of total fuel energy



Heat rejection was also measured at 75%, 50%, and 25% power settings. Figure 15 shows the heat rejection values with only slight differences between the power settings. There is however a consistent increase in heat rejection of about 0.5  $kW$  over the engine speed range. Figure 16 is an evaluating of these measurements as a percent of total fuel energy. The 25% power setting resulted in the largest heat rejection percentages at 18-31%. Maximum heat rejection percentages occurred at the slowest engine speeds (4000 rpm) for all power settings. At 4000 rpm, the heat rejection varied from 7-31% for all four power settings.

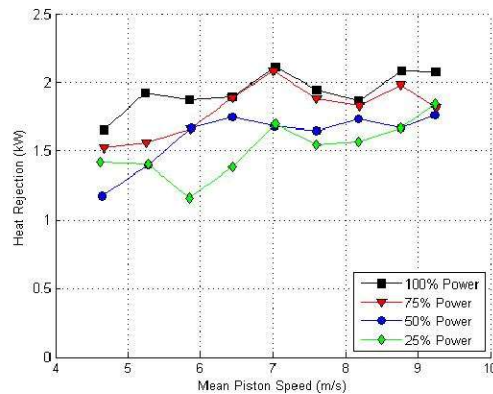


Figure 15: Heat rejection measurements at partial loading

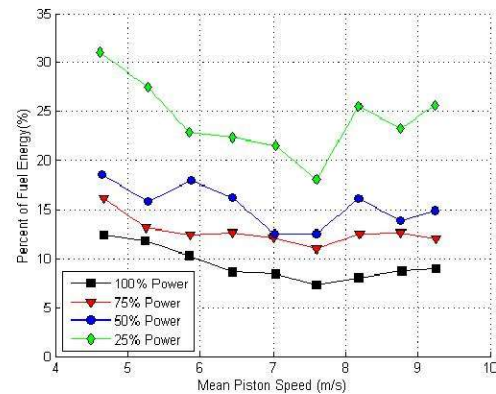


Figure 16: Heat rejection at partial loading as a percent of total fuel energy

## V. Conclusion

This effort focused on measuring thermal energy losses of a representative RPA engine using three measurement techniques. The engine chosen was a 55 cc 3W two-stroke spark-ignition engine with a surface area to displacement volume ratio of 1.48. The engine was found to have an effective compression ratio of 7.2:1 resulting in a maximum ideal fuel conversion efficiency of 49.9%. Actual maximum efficiency occurred at WOT and 7500 rpm with 12.5% with a brake power value of 3.0  $kW$ . A maximum amount of 6.2% of the total energy was required at 4500 rpm to overcome engine friction, drivetrain friction, and pumping losses. The energy balance method narrowed the heat rejection to approximately 50% of the total fuel energy. The heat rejection measured using the engine enclosure method resulted in 7.3-12.4% at full power with a maximum value of 31.1% at 25% power and 4000 rpm.

## Acknowledgments

The authors would like to acknowledge the support of all those who consulted and assisted with the development and execution of this research. The authors would like to thank all that aided in the construction and validation of the small engine test bench at the Small Engine Research Laboratory (SERL) at AFRL. They would like to specifically thank Mr. Rich Ryman for assisting in various aspects of setting up the test bench, Mr. Rob Free for instrumenting the heat flux gauges and thermocouples onto the engine, and Mr. Dave Burris for designing and coding the LabVIEW control and data acquisition program.

## References

- <sup>1</sup>Heywood, J. B., *Internal Combustion Engine Fundamentals*, McGraw-Hill, New York, 1988.
- <sup>2</sup>Wilson, C.W., "Performance of a Small Internal Combustion Engine Using N-Heptane and Iso-Octane", Thesis, Air Force Institute of Technology, WPAFB, Ohio, 2010.
- <sup>3</sup>Anderson, E.K., "Performance of Low-Octane Fuels in a Rotax 914 Engine with Advanced Knock Mitigation Strategies", Joint Propulsion Conference, AIAA 2011-5725, 2011.
- <sup>4</sup>Groenewegen, J. R., "The Performance and Emissions Characteristics of Heavy Fuels in a Small, Spark Ignition Engine", Thesis, University of Dayton, Dayton, Ohio, 2011.
- <sup>5</sup>Zhao, H., Collings, N., and Ma, T., "The Cylinder Head Temperature Measurement by Thermal Imaging Technique", SAE Technical Paper 912404, 1991.
- <sup>6</sup>Ajav, E., Singh, B., Bhattacharya, T., "Thermal balance of a single cylinder diesel engine operating on alternative fuels",



Energy Conversion & Management 41, 2000.

<sup>7</sup>Martinez-Frias, J., Aceves, S., Flowers, D., Smith, J. et al., "*HCCI Engine Control by Thermal Management*", SAE Technical Paper 2000-01-2869, 2000.

<sup>8</sup>Mueller, T., Hans, H., Krebs, W., Smith, S. et al., "*Thermal Management on Small Gasoline Engines*", SAE Technical Paper 2011-01-0314, 2011.

<sup>9</sup>3W Modellmotoren, *Engine Manual 55i / 55i CS*, 2013. [Online]. Available: [www.3w-modellmotoren.com](http://www.3w-modellmotoren.com). [Accessed 5 May 2013].

<sup>10</sup>Ausserer, J. K., Litke, P., Groenewegen, J. R., Rowton, A.R., Grinstead, K., "*Development of Test Bench and Characterization of Performance in Small Internal Combustion Engines*", Small Engine Technology Conference, SAE, 2013 (submitted for publication).

<sup>11</sup>Kumarappa, S. and Prabhukumar, G.P., "*Improving the Performance of Two Stroke Spark Ignition Engine by Direct Electronic CNG Injection*", Jordan Journal of Mechanical and Industrial Engineering, Vol. 2, No. 4, December 2008.

<sup>12</sup>Epstein, A., Guenette, G., Norton, R., and Yuzhang, C., "*High-frequency response heat-flux gauge*", Review of Scientific Instruments 57, April 1986.

## **Appendix C**

**Paper:** Measuring Scaling Effects in Small Two-Stroke Internal Combustion Engines

**Presented at:** 2014 Small Engine Technology Conference in Pisa, Italy

**Citation:**

A. K. Rowton, J. K. Ausserer, K. D. Grinstead, P. J. Litke, and M. D. Polanka, "Measuring Scaling Effects in Small Two-Stroke Internal Combustion Engines," presented at the 2014 Small Engine Technology Conference & Exposition, Pisa, Italy, SAE Technical Paper 2014-32-0010, 11 November 2014, doi: 20.4271/2014-32-0010.



# Measuring Scaling Effects in Small Two-Stroke Internal Combustion Engines

2014-32-0010

20149010

Published 11/11/2014

## Alexander K. Rowton

Air Force Research Laboratory

## Joseph K. Ausserer

Air Force Institute of Technology

## Keith D. Grinstead

Innovative Scientific Solutions Inc

## Paul J. Litke

Air Force Research Laboratory

## Marc D. Polanka

Air Force Institute of Technology

**CITATION:** Rowton, A., Ausserer, J., Grinstead, K., Litke, P. et al., "Measuring Scaling Effects in Small Two-Stroke Internal Combustion Engines," SAE Technical Paper 2014-32-0010, 2014, doi:10.4271/2014-32-0010.

## Abstract

As IC engines decrease in displacement, their cylinder surface area to swept volume ratio increases. Examining power output of IC engines with respect to cylinder surface area to swept volume ratio shows that there is a change in power scaling trends at approximately  $1.5 \text{ cm}^{-1}$ . At this size, it is suggested that heat transfer from the cylinder becomes the dominant thermal loss mechanism and performance and efficiency characteristics suffer. Furthermore, small IC engines ( $>1 \text{ cm}^{-1}$ ) have limited technical performance data compared to IC engines in larger size classes. Therefore, it is critical to establish accurate performance figures for a family of geometrically similar engines in the size class of approximately  $1.5 \text{ cm}^{-1}$  in order to better understand the thermal losses that contribute to lower efficiencies in small IC engines.

The engines considered in this scaling study were manufactured by 3W Modellmotoren, GmbH. In particular, they are the 3W-28i, 3W-55i, and 3W-85Xi engines, which have cylinder surface area to swept volume ratios of  $1.83 \text{ cm}^{-1}$ ,

$1.46 \text{ cm}^{-1}$ , and  $1.27 \text{ cm}^{-1}$  respectively. All three engines are two-stroke cycle, single cylinder, spark ignited, air cooled, and air carbureted. The engines have a similar gas exchange port design and utilize crank case compression and Schnuerle method scavenging. They have the same 10:1 geometric compression ratio. These engines were chosen due to their similarity in design while falling within the relevant size regime for evaluating thermal losses.

## Introduction

IC engines capitalize on the ability to convert the chemical energy in combustible fuel into work. This ability can be characterized and quantified by an engine's overall efficiency. Generally, engine size has a positive correlation to output power and it follows that an engine with lower mass will have a lower power output. However, as IC engines decrease in size, the ratio of cylinder surface area to swept volume increases, and there are several mechanisms that may result in increased losses for smaller engines. First, for a given engine rotational speed, heat transfer through the cylinder walls will increase



relative to the amount of fuel combusted due to an increased surface area to volume ratio. Incomplete combustion also plays a role on the small scale. As engine size decreases, engine speeds typically increase (speeds of 20,000 rpm in engines with displacement volumes less than 10 cm<sup>3</sup> are common). This results in decreased residence times, and fuel may not have sufficient time to burn completely before exiting the cylinder. Research carried out on glow fuel engines in the 1 cm<sup>3</sup> to 7.5 cm<sup>3</sup> size class has shown that incomplete combustion and thermal losses of this type dominate small engine performance [1]. Other researchers have suggested minimum burn times of 1 ms for hydrocarbons at 1 atm, and much shorter times at the pressures and temperatures found in cylinder [2]. Even at the maximum speed of 8000 rpm for the engines considered here, the residence time is still nearly 2.5 ms. Further investigation indicates that the OS 30X engine, with a 4.9 cm<sup>3</sup> combustion volume had sufficient time for complete combustion of the fuel at speeds over 10,000 rpm [3].

Another loss mechanism is quenching at the cylinder walls, which also increases relative to the combustion volume with decreasing engine size. Sher and Sher developed a model for predicting the theoretical limit of miniaturizing an IC engine [4]. The model suggests a minimum attainable displacement between 0.3 and 0.4 cm<sup>3</sup> for an HCCI engine, driven primarily by thermal losses through the wall and quenching losses at the wall [4, 5, 6]. The model also identified that this limit is strongly influenced by mechanical limits of the materials, which set the maximum engine speed and the piston to cylinder wall gap. One mechanism to offset heat losses from increased surface area to volume ratio is through increased engine speed and the burning of more fuel per unit time, effectively maintaining the ratio of combusted mass to surface area despite decreased combustion volume. Thus, if material limits set the maximum speed of the engine, this option becomes limited. While the minimum size limits suggested by [4] are not a hard rule, a similar analysis that suggests a minimum practical engine size of 0.1 cm<sup>3</sup> based on the rate of heat transfer from the cylinder exceeding the rate of heat generation by combustion [7].

Crevice and blow-by losses also present problems on the small scale. Frequently small engines have no piston rings, and several researchers have noted significant blow-by losses [4, 8]. Additionally, crevice volumes, especially in the spark plug, will increase relative to the combustion volume as engine size decreases [3, 9]. For example, all three engines considered in this study use the same spark plug, and the ratio of the spark plug crevice volume relative to the cylinder volume must therefore increase with decreasing engine size. The same is true of engines employing glow plugs where the same plug size is often common across a range of engines.

It would be difficult, if not impossible, to select a set of engines to study all of these effects at one time. Thus, this study will focus on the thermal losses due to heat transfer from the combustion chamber to the air flow used to cool the engine. It is speculated that as engine size decreases, the heat transfer to the cooling air as a fraction of the heat released during combustion will increase, consistent with the increased surface area to volume ratio.

Most of the effects discussed above, including the heat transfer at the center of this study, scale with cylinder area or volume. The cylinder surface area and swept volume are dictated by two spatial dimensions: bore and stroke. The ratio of cylinder surface area to swept volume is inversely proportional to bore and stroke as shown in Equation (1).

$$\frac{SA}{V_d} = \frac{\pi BL + \pi \frac{B^2}{2}}{\pi \frac{B^2}{4} L} = \frac{4}{B} + \frac{2}{L} \quad (1)$$

Typically, small to medium sized IC engines have a bore/stroke ratio ranging from 0.8 to 1.2, while large, slow speed IC engines can have a bore/stroke ratio as low as 0.5 [1]. One can hold a cylinder dimension fixed (bore or stroke) and change the other by varying the bore/stroke ratio to examine the change in cylinder surface area and swept volume with respect to the changing dimension. Figure 1 shows a plot of surface area to swept volume ratio as a function of bore to stroke ratio for various displacement volumes. It demonstrates how the surface area to swept volume ratio increases much more quickly with decreasing engine displacement than practical bore to stroke ratios.

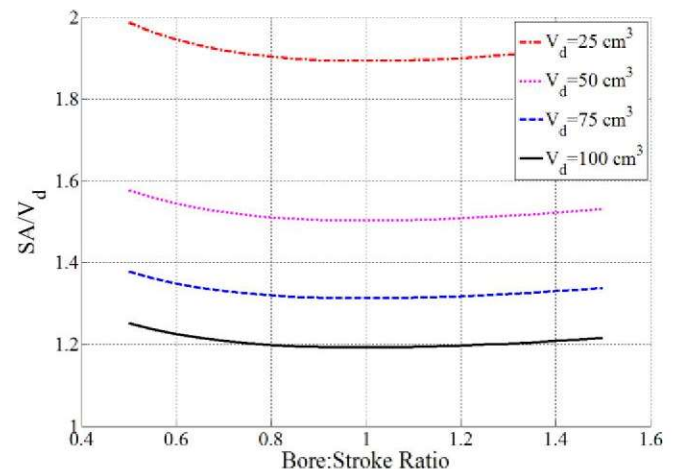


Figure 1. Surface area to swept volume ratio as a function of bore to stroke ratio for various displacement volumes

Furthermore, a cylinder's swept volume is more sensitive to dimensional change than surface area, and as engine size decreases, that surface area to volume ratio increases exponentially as the inverse of length scale, as seen in Figure 2. Therefore, volume based performance parameters like power output scale faster than surface area based performance parameters like thermal losses through the cylinder walls and surface friction. Thus, when IC engines are scaled down, power output falls off at a faster rate than loss mechanisms such as thermal losses and cylinder surface friction (for a fixed engine speed). Thus small IC engines generally have lower efficiencies than their larger counterparts.

Figure 3 shows a collection of IC engine power ratings as a function of cylinder surface area to swept volume ratio. Engines considered include two-strokes and four-strokes, SI and CI, carbureted and fuel-injected engine designs. In [10],



the authors describe a relationship between engine power output and the surface area to volume ratio. Assuming a square engine ( $B/L = 1$ ), the surface area to volume ratio becomes proportional to  $6/B$ . If a constant power density is assumed, then the engine power output becomes proportional to the swept volume, as in Equation (2).

$$P = \rho_{pwr} V_d = \rho_{pwr} \pi \frac{B^2}{4} L = \rho_{pwr} \pi \frac{B^3}{4} \quad (2)$$

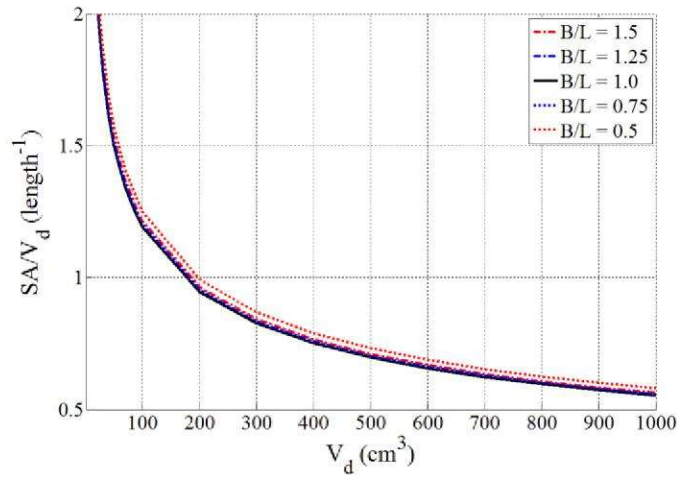


Figure 2. Surface area to swept volume ratio as a function of displacement volume for various bore to stroke ratios.

Thus, it is reasonable to suggest that power may scale according to Equation (3), where  $n \approx 3$ .

$$P = \frac{\rho_{pwr}}{4} \pi \left( \frac{SA}{V} \right)^{-n} \quad (3)$$

Based on Equation (3), a geometric curve was fit to manufacturer data [11, 12, 13, 14, 15, 16, 17, 18, 19, 20, 21], shown in Figure 3. The result of the fit is shown in Equation (4), where surface area in  $\text{cm}^2$  and displacement volume in  $\text{cm}^3$  yield power in kW.

$$P_{mfr} = 21.91 \left( \frac{SA}{V_d} \right)^{-3.1} [=] \text{ kW} \quad (4)$$

Both the leading constant and exponent were fit using least squares regression. The fit exponent is  $-3.1$ , very close to  $-3$ , as suggested by the rough derivation. Deviations are likely the result of the real engines being off square, and the wide range of engine sizes and types considered. This function is a potential model for describing the power scaling trends of IC engines across a wide range of sizes, and it suggests a power density of  $106 \text{ W/cm}^3$ .

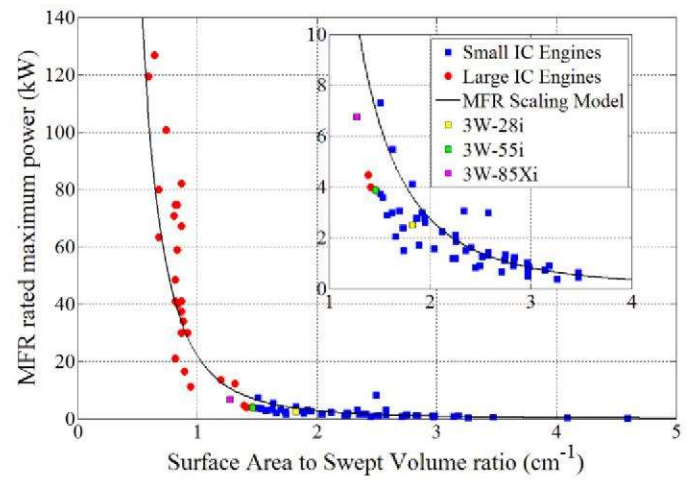


Figure 3. Manufacturer rated power as a function of cylinder surface area to swept volume ratio.

The delineation between large and small IC engines for the concern of this study is  $1.5 \text{ cm}^{-1}$ . Assuming a square engine, this equates to an engine swept volume of roughly  $50 \text{ cm}^3$ . Medium to large (approximately  $1000 \text{ cm}^3$  and up) IC engine size classes correspond to engines used commonly in the automotive, marine, and passenger aircraft industries all the way up to massive shipboard marine diesel IC engines. The widespread use of engines in these size classes has led to thorough technical investigations of many aspects of performance and loss characterization; there is a plethora of accurate technical performance data in the literature. Historically, as engines get smaller, their applications are focused primarily on hobbyist vehicles and handheld power equipment, although they are gaining an ever increasing hold in the unmanned aircraft market. Often, detailed test data for these engines is unavailable, proprietary, or focused on different aspects of engine performance than those considered here, such as meeting increasingly stringent emissions regulations. There is an increasing body of work being developed from groups working on small unmanned aircraft, but the available, relevant data in this size class remains limited.

In the realm of small remotely piloted aircraft (RPA) for intelligence, surveillance, and reconnaissance missions, these small, commercially available IC engines are used for propulsion. In this case, accurate performance data is critical for effective airframe design, payload designation, and mission capabilities. Recently, the demand for small RPAs has outpaced the development of propulsion systems. Often, RPAs use small two-stroke cycle IC engines that are commercially available off the shelf. Many of these engines were developed for use in hand-held tools or recreational model airplanes. The benefits of using commercial systems are their high availability and low cost. However, the detriments include system reliability and negative performance characteristics as altitude increases [22].

Furthermore, these commercially available engines are designed to operate on gasoline based fuels. In overseas military environments, there is a desire to utilize heavy, low volatility fuels such as JP-8, as they are more readily available in theater. Additionally, it has been shown that performance and fuel consumption improvements can be realized by operating



In the case of the 28 cm<sup>3</sup> and 55 cm<sup>3</sup> engines, intake air was drawn through two airflow meters in parallel to measure air flow rate. TSI model 40211 high performance linear mass flow meters capable of 0-300 SLPM with an accuracy of  $\pm 3\%$  of reading were used for measurement. The air flow meters were positioned upstream of a 208 L baffled chamber used to damp oscillations in the air flow. In order to maintain consistency over



several runs, intake air then passed through a shell and tube heat exchanger. The intake air flowed through the heat exchanger as the tube-side fluid. Water was utilized as the shell-side fluid. The water temperature was held at a constant value using a NESLAB RTE 211 heater/chiller unit. The heater/chiller unit can operate over a temperature range of 5°C to 100°C. Intake air temperature was measured downstream of the heat exchanger to assure consistent operating conditions despite changes in ambient temperature.

In the case of the 85 cm<sup>3</sup> engine, the aforementioned airflow configuration altered engine performance, so the TSI flow meters were replaced by an Omega Engineering air velocity transmitter. The transmitter is capable of measuring velocities from 0 m/s to 5.08 m/s with an accuracy of 2% of full scale. The air velocity was converted to a mass flow rate based on cross sectional area (in this case a #2 standard pipe) and concurrent ambient temperature and pressure readings. Temperature measurements were performed with Omega Engineering J-type 1.59 mm probe style thermocouples. The thermocouples are capable of temperature measurements from 0°C to 750°C with an accuracy of the greater of ±1.1°C or 0.4% of reading. Ambient pressure was measured with a Honeywell Model TJE pressure transducer capable of 0-103.4 kPa pressure measurements with an accuracy of ±0.10% of full scale.

In cylinder pressure measurements were taken using a Kistler type 6113B pressure measuring spark plug capable of detecting pressure from 0-200 bar with an accuracy of ±1%. Voltage signals from the pressure transducer were amplified with a Kistler 2852 Signal Conditioning Platform. Crank angle position was measured using a US Digital E6 optical encoder with 1800 counts per revolution. Pressure data and crank angle position were collected using an AVL Indisart combustion analyzer. The engine's throttle and choke were actuated remotely with Hitec HS-85MG+ analog metal gear servos. More information on the configuration of the Kistler pressure system can be found in Ausserer et al [24].

Thermal losses from heat rejection were measured by characterizing the temperature change and mass flow rate of cooling air as it passed over the cylinder head. In order to achieve these results, the engine was tested inside a custom insulated enclosure to isolate the cooling airstream from the environment. The enclosure was constructed of 6.35 mm polycarbonate and was insulated with 12.7 mm polystyrene foam. The cooling airstream velocity was varied to maintain a desired cylinder head temperature. Cylinder head temperatures were measured with a J-type ring style thermocouple bolted to the upper cooling fin on the cylinder head.

Figure 5 shows the interior of the insulated engine enclosure along with the locations of the cylinder head thermocouples and the pressure measuring spark plug. Cooling air flows from top to bottom in the view shown in Figure 5. Cooling air velocity was measured with an Omega Engineering air velocity

transmitter with a range capacity of 0 m/s to 50.8 m/s and an accuracy of 2% of full scale. Mass flow rates were derived similar to the method prescribed for the 85 cm<sup>3</sup> engine intake flow. Air temperatures were measured at locations upstream and downstream of the engine enclosure with probe style J-type thermocouples. Energy loss due to heat rejection to the cooling airstream was calculated based on a constant specific heat for air as shown in Equation (5).

$$Q = \dot{m}_{cool} c_{p,air} \Delta T \quad (5)$$

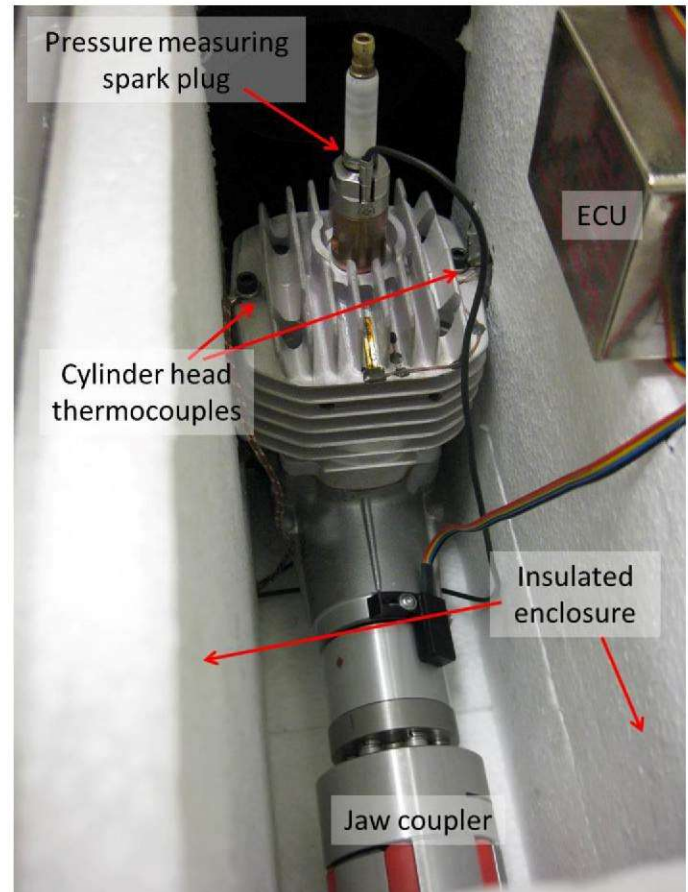


Figure 5. 3W-55i mounted on the test bench inside the insulated enclosure.

It is important to note that the engine and enclosure are mounted such that the carburetor, and thus the intake air stream are isolated from the cooling air flow. Exhaust gases exit the engine through a fiberglass insulated steel pipe that passes through a sealed port in the side of the enclosure to minimize mass flow losses and heat transfer. The engine exhaust system pipe is indirectly coupled to the laboratory exhaust system. The indirect coupling was designed to prevent the system from applying a vacuum to the engine exhaust port and altering performance. The exhaust system is also untuned, which matches the stock configuration. Figure 6 shows the engine enclosure during a typical test run.



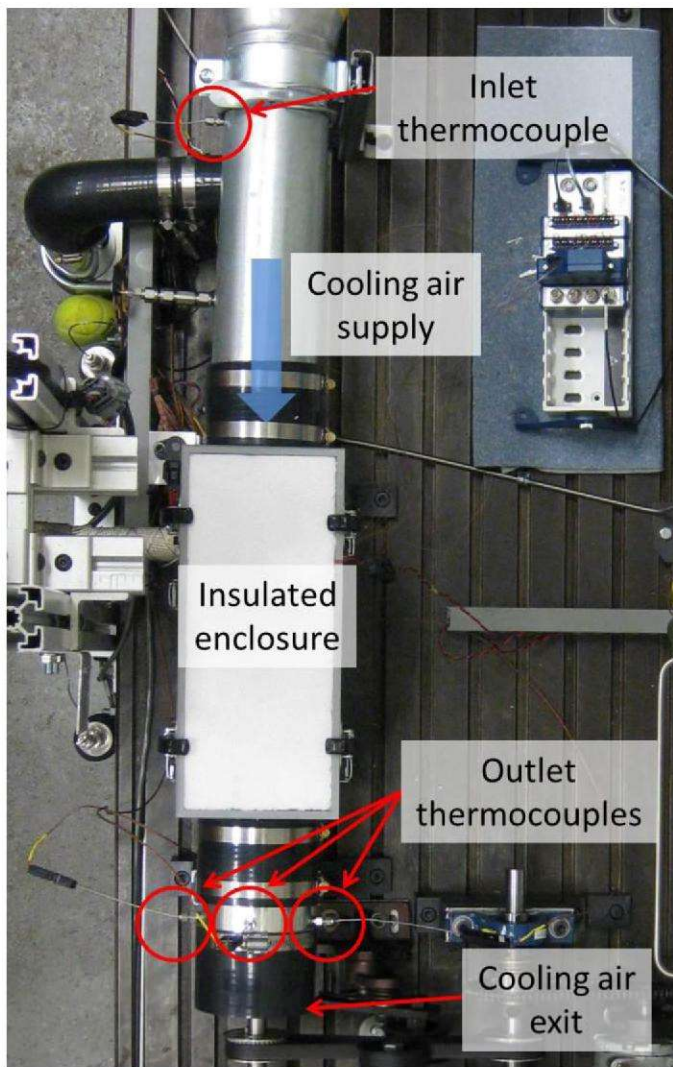


Figure 6. Test bench layout of the insulated engine enclosure and cooling air duct for measuring thermal losses

The driveshaft passes through a close-tolerance port in the enclosure with grommets on either side to reduce cooling air leakage. Cooling air inlet temperature is measured upstream of the enclosure with a J-type probe thermocouple. Outlet temperature is measured with a rake of three J-type probe thermocouples as shown in Figure 6. Using the uncertainty values supplied by the thermocouple manufacturer, heat rejection measurements would have had a measurement uncertainty of about 75%. According to Holman, however, when measuring a change in temperature instead of an absolute temperature, measurement accuracies are often much better than advertised [2]. This better accuracy was determined by placing the four thermocouples in a water bath. Temperature signals were reported as the water bath was swept from 5°C to 40°C. The maximum standard deviation of the four signals multiplied by three (for a 99% confidence interval) was then used as the thermocouple accuracy. This allowed the thermocouple accuracy to be narrowed from  $\pm 1.1^\circ\text{C}$  to  $\pm 0.214^\circ\text{C}$  which improved the heat rejection measurement error from 75% to 20%. More information on this measurement technique is outlined in Rittenhouse [3].

In an energy balance for an IC engine, exhaust enthalpy can account for a significant amount of energy loss. While the literature suggests 20% of fuel delivered in a given cycle is lost to short-circuiting as a rule of thumb for typical two-stroke engines [4], this approximation is simplistic and neglects the complex interaction between the fresh charge and exhaust gases during scavenging. To determine the scavenging and trapping efficiencies, exhaust gas analysis is typically used to investigate short circuited oxygen for rich mixtures, or unburnt hydrocarbons and fuel for lean mixtures (and in some cases rich mixtures as well). While exhaust gas analysis is part of future work planned for this setup, it was not available for this study. Therefore, the scavenging will be bounded by two models: perfect isothermal mixing and perfect displacement. Both models are described in detail in [25] and will be reviewed briefly here.

The perfect displacement model represents the best case scenario for scavenging; each volume of fresh charge displaces an equal volume of burnt mixture. The isothermal mixing model is considered a lower bound for modern engines (although virtually all modern engines outperform it [25]). The model assumes that during gas exchange the chamber is a well stirred reactor, so that as each unit of fresh charge enters, it displaces an equal volume of gas with composition as if the cylinder contents were homogenous. Both models require the calculation of the delivery ratio, shown in Equation (6).

$$\Lambda = \frac{\dot{m}_f + \dot{m}_a}{m_o \frac{N}{60}}$$

$$\text{where } m_o = \frac{P_{ref}}{RT_{ref}} V_d$$

(6)

The delivery ratio is then used to calculate the trapping efficiency, which is the portion of the fresh charge delivered to the engine that is retained in the cylinder to combust when the exhaust port closes. The calculation of trapping efficiency is shown in Equation (7) for the perfect mixing model and Equation (8) for the perfect displacement model. Measurements of fuel and air flow rates provide the fresh charge delivered to the engine, while the reference mass is the fresh charge composition required to fill the displaced cylinder volume at standard conditions. A careful examination of the wording in [25] does reveal that trapped volume may be more appropriate for the reference mass, but displaced volume is an acceptable substitute if its determination is less uncertain, as is the case in this work.

$$\eta_{tr} = \frac{1 - e^{-\Lambda}}{\Lambda}$$

(7)

$$\eta_{tr} = 1 \text{ for } \Lambda \leq 1$$

$$\eta_{tr} = \frac{1}{\Lambda} \text{ for } \Lambda > 1$$

(8)



From a combustion standpoint, approximately 5% of the mass of trapped fuel remains unburned at stoichiometric conditions [1]. For equivalence ratios greater than unity, the amount of unreleased heat increases as incomplete combustion occurs due to a lack of oxidizer. For lean conditions, a combustion efficiency of approximately 95% was used [26]. For rich conditions, it can be assumed that the trapped mass burns to perfect incomplete combustion products of water, carbon monoxide, and carbon dioxide. By applying one of the two aforementioned scavenging models in conjunction with an adjustment for combustion efficiency, the actual heat release for the engine may be estimated as in Equation (9).

$$\dot{Q}_{HR} = Q_{LHV} \dot{m}_f \eta_c \eta_{tr} \quad (9)$$

## Experimental Methods

Before performance data was acquired, all test engines were broken in according to the manufacturer's recommendation. Break-in for each engine consisted of 2 hours of total run time at moderate and varying speeds and loads (approximately 3000-5000 rpm and 25-50% throttle). Per the manufacturer recommendation, two stroke break-in oil with zinc additives was used at a fuel to oil ratio of 32:1.

The manufacturer supplies the same ECU with each of the test engines, so a single ECU was employed for all engines. Spark timing was measured using a Fluke Instruments induction current clamp. Induced voltage signals were processed with AVL Indicom combustion analysis software to obtain spark timing as a function of crank angle. The timing map is a linear function of speed changing from 12.5° BTDC at 4000 rpm to 32.2° BTDC at 7900 rpm. The ECU has a built-in speed limiter that activates at 8000 rpm. As a result, the maximum mean piston speeds achievable by the test engines scales with engine stroke only. This phenomenon leads to narrower performance envelopes as the engines decrease in size.

The data recorded for each engine consisted of a mean of three separate test runs. At a minimum, test runs were separated by a shutdown and inspection period to ensure data samples remained independent from one another. The test runs spanned operating conditions from 4000 rpm to 7900 rpm in 500 rpm increments at four throttle settings: wide open throttle (WOT), 75% throttle, 50% throttle, and 25% throttle. Data acquisition was limited to 7900 rpm in order to avoid non-firing cycles due to the ECU's speed limiting function. Operating conditions below 4000 rpm proved highly irregular in terms of combustion stability for the 28 cm<sup>3</sup> and 55 cm<sup>3</sup> engines (at least partially due to the retarded timing of the stock ECU), so the lower engine speed limit was imposed on the 85 cm<sup>3</sup> engine for consistency.

## Experimental Results

Engine performance baselines have been established for the engines in a stock configuration. Parameters recorded during these tests include torque, power, engine speed, fuel mass flow, air mass flow, ambient air pressure, intake air temperature

and pressure, exhaust temperature and pressure, cylinder head temperature, crank angle position, and in-cylinder pressure measurements. For each engine, a test run to determine the proper throttle settings was performed for the purpose of ensuring quality data distribution throughout each engine's performance envelope. Each engine's throttle index test was performed at a mean piston speed of 7 m/s. This equates to engine speeds of 7500, 6000, and 5100 rpm for the 3W-28i, 3W-55i, and 3W-85Xi engines, respectively. Mean piston speed,  $\bar{S}_p$ , can be calculated from engine speed and stroke as shown in Equation (10) [26].

$$\bar{S}_p = 2LN/60 \quad (10)$$

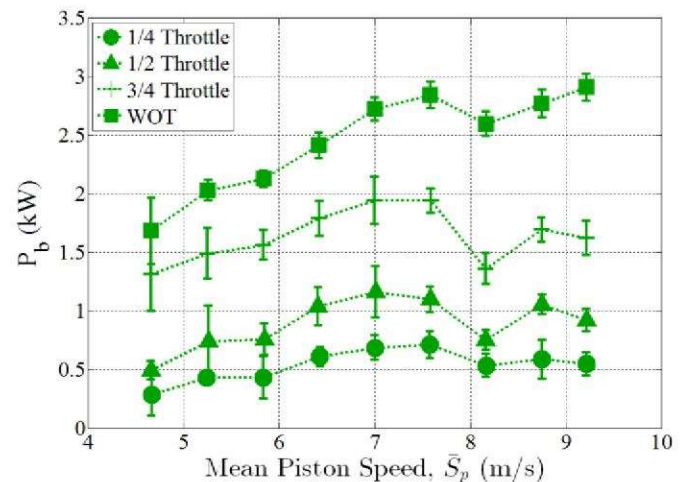


Figure 7. Brake power as a function of mean piston speed at four throttle settings for the 3W-55i engine.

The throttle was swept from idle to WOT at 7 m/s mean piston speed to obtain a brake power curve. A throttle setting index was established for each engine based on the resulting brake power data. Partial throttle settings that corresponded to full power, 75% power, 50% power, and idle (nominally 25%) power from the throttle index test run were used for each engine's subsequent data acquisition tests. A resultant plot of brake power as a function of mean piston speed for the four aforementioned throttle settings for the 55 cm<sup>3</sup> engine is shown in Figure 7. A common characteristic among the test engines is their tendency to exhibit dual power peaks. This behavior is most likely the result of gas dynamics within the exhaust, cylinder, and induction system. Many two stroke engines exhibit a dual power peak as the engine speed increases from the first harmonic of a tuned exhaust system to the second harmonic, experiencing a valley when the exhaust system is completely out of phase with the exhaust port timing. In the setup used for this work, there were no reflective surfaces in the exhaust to return a pressure wave to the engine, and thus exhaust tuning is likely not responsible for the behavior. However, it remains likely that a gas exchange dynamic is responsible for the dual peak.

The carburetor on each engine was tuned to maximum power at WOT and 6000 rpm. The speed closely matched the manufacturer rated speed (5750 rpm) and tuning at this speed provided stable operation of the engines from at least



4000 rpm to maximum speed at 8000 rpm. Once each engine was tuned, the carburetor mixing screws were kept stationary for the duration of the study.

Figure 7, Figure 8, Figure 9, Figure 10, Figure 11, Figure 12, Figure 13, Figure 14, Figure 15, Figure 16, Figure 17 show performance curves for each engine at WOT and 50% throttle as a function of mean piston speed. Table 2 provides the legend for the data in each figure. Each data set is an average of three separate test runs. In order to maintain consistency from run to run, cylinder head temperature was held to  $140^{\circ}\text{C} \pm 3^{\circ}\text{C}$ ; intake manifold air temperature was held to  $24^{\circ}\text{C} \pm 6^{\circ}\text{C}$ . The uncertainty consists of instrumentation error combined with error due to run to run variability at a 95% confidence interval.

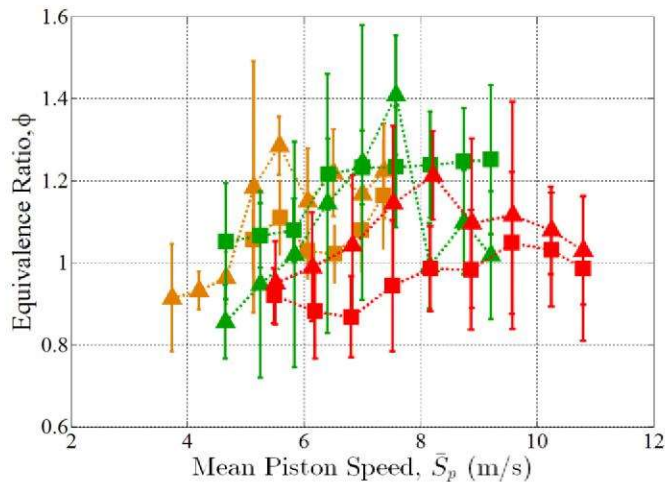


Figure 8. Equivalence ratio as a function of mean piston speed.

Table 2. Scaling study performance data legend

Engine	50% throttle	WOT
3W-28i	▲	■
3W-55i	▲	■
3W-85Xi	▲	■

Figure 8 shows the equivalence ratios for each engine as tested. Due to the unsteady nature of these small IC engines as well as their simple carburetors, repeatability of equivalence ratio from one test run to another was difficult to achieve. The error shown in Figure 8 is a combination of instrumentation uncertainty and run-to-run uncertainty for a 95% confidence interval. Uncertainty due to instrumentation was 5.4% while run-to-run variation yielded an uncertainty of 8.1%. The combined error averaged over all data points is 10.5%. The large swings in equivalence ratio make it clear that for future testing more refined control of the fuel air mixture is necessary.

The brake power was measured for the three engines and as shown in Figure 9, brake power scales with engine size as expected. Peak power values were 1.3 kW at 7000 rpm for the 28 cm<sup>3</sup> engine, 2.9 kW at 7900 rpm for the 55 cm<sup>3</sup> engine, and 3.9 kW at 6500 rpm for the 85 cm<sup>3</sup> engine. The overall

uncertainty in the measurement was 9.4%. The brake power measurements exhibit a 26% decrease in power for a 35% decrease in cylinder volume from the 85 cm<sup>3</sup> to the 55 cm<sup>3</sup>. From the 55 cm<sup>3</sup> to the 28 cm<sup>3</sup>, power drops by 55% for a 49% decrease in cylinder volume.

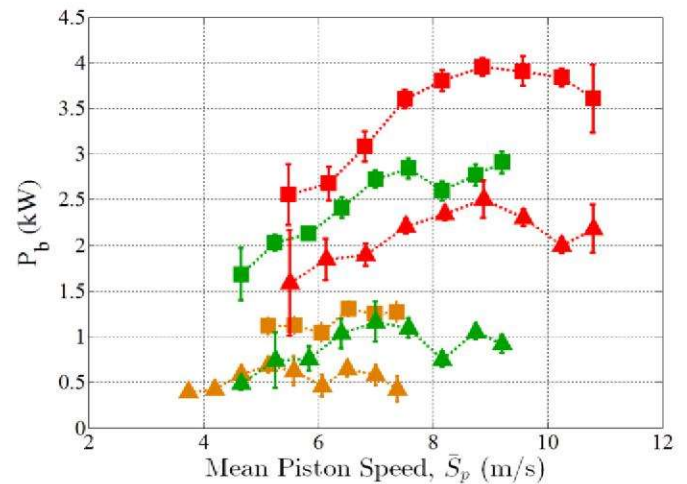


Figure 9. Brake power as a function of mean piston speed.

Fuel conversion efficiency,  $\eta_p$  is a measure of an engine's ability to convert a delivered mass of fuel into usable power. In the case of brake fuel conversion efficiency as shown in Equation (11), brake power is normalized by the total energy delivered to the engine as fuel.

$$\eta_{fb} = \frac{P_b}{\dot{m}_f Q_{LHV}} \quad (11)$$

Figure 10 indicates that as size decreases, an engine's ability to produce power with a given amount of energy diminishes. Peak fuel conversion efficiencies were 18%, 14%, and 12% for the 85 cm<sup>3</sup>, 55 cm<sup>3</sup>, and 28 cm<sup>3</sup> engines respectively. This is consistent with the reduction in cylinder volume.

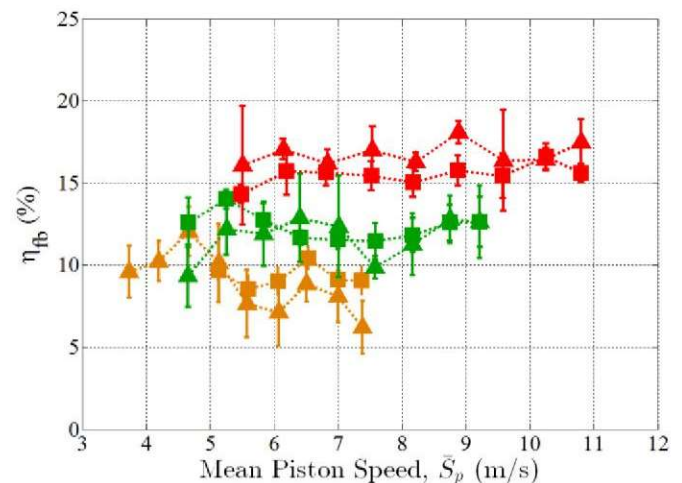


Figure 10. Brake fuel conversion efficiency as a function of mean piston speed.



Mean effective pressure is a more valuable metric to evaluate scaling effects on engine performance. When the data for the three engines were plotted in this fashion, the differences due to engine size collapsed and the effectiveness of the engines was discerned. As seen in [Figure 11](#), the IMEP is nearly identical for the three engines at WOT. The 55 cm<sup>3</sup> engine displays a lower IMEP at 50% throttle for lower piston speeds. The data in [Figure 8](#) indicate that the delivered equivalence ratio of the 55 cm<sup>3</sup> engine drops off by over 0.3 from 6.5 m/s to 4.5 m/s. Beginning at a  $\phi$  of 1.2 and dropping into lean operation below about 6 m/s, this decrease accounts for the 55 cm<sup>3</sup> engine's power decrease relative to the other engines.

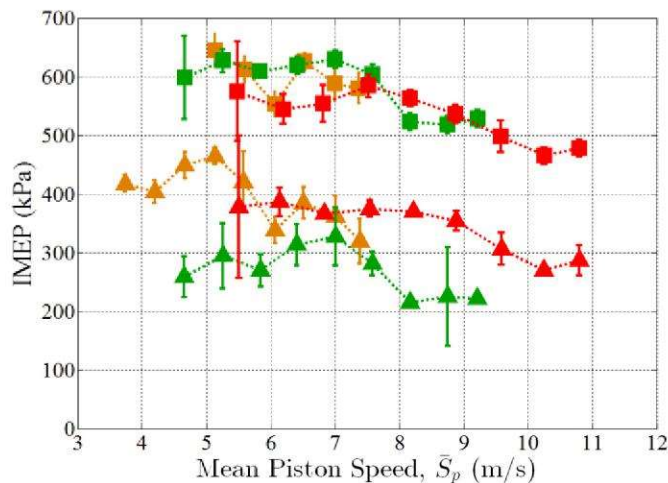


Figure 11. Indicated mean effective pressure as a function of mean piston speed.

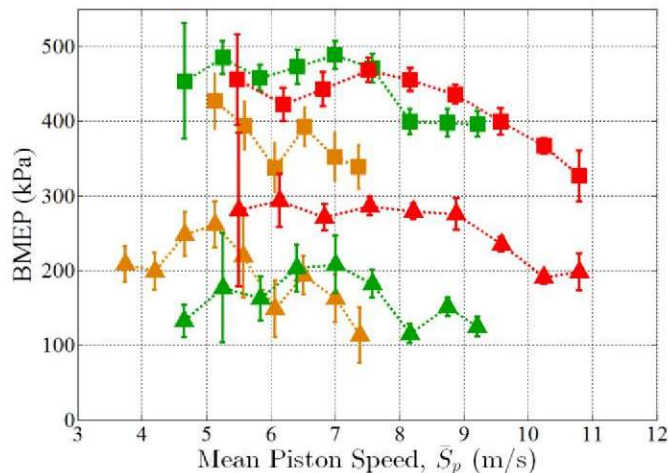


Figure 12. Brake mean effective pressure as a function of mean piston speed.

As shown in [Figure 12](#), there is a marked difference in BMEP as engine size is reduced below 55 cm<sup>3</sup> despite the similarities in design. The 55 cm<sup>3</sup> engine produced the highest WOT BMEP at 489 kPa while the 85 cm<sup>3</sup> and 28 cm<sup>3</sup> engines produced 466 kPa and 426 kPa respectively. Although the 85 cm<sup>3</sup> engine

was expected to produce a higher BMEP due to its lower surface area to swept volume ratio, two factors may have had an influence. First, the engine may have experienced more friction due to its second piston ring (the 55 cm<sup>3</sup> and 28 cm<sup>3</sup> only have one). Second, the 85 cm<sup>3</sup> and 55 cm<sup>3</sup> engines are equipped with the same size carburetor, possibly meaning the carburetor is under-sized for the larger engine. Its flow restricting characteristics would only be exhibited when the throttle plate is not acting as the primary flow restriction device; in other words, only when the throttle plate is at or near the fully-open position. As seen in [Figure 12](#), at 50% throttle the 85 cm<sup>3</sup> engine produces a higher BMEP across its operating range when compared to the 55 cm<sup>3</sup> engine and 28 cm<sup>3</sup> engine.

The lower BMEP values of the 28 cm<sup>3</sup> engine at WOT are an expected outcome due to the influence of the high surface area to swept volume ratio. In the case of the 50% throttle data, the 28 cm<sup>3</sup> engine outperforms the 55 cm<sup>3</sup> engine at mean piston speeds below 6 m/s. This can be attributed to the difference in actual engine speeds between the two engines and the associated variations in charging performance between the engines at those conditions. These variations as the result of gas exchange dynamics underline the need for scavenging and trapping quantification and the installation of exhaust gas analysis equipment in future work.

Friction losses were quantified by subtracting the indicated and brake performance of each engine. Thus the friction losses include the combined effects of friction in the engine, pumping losses through the intake and induction system, and friction losses in the drive train. A part of the future work for this setup is the creation and installation of a reaction cradle to quantify the friction in the engines and the drive train. [Figure 13](#) shows FMEP values for the scaling study engines. The 28 cm<sup>3</sup> engine has a maximum FMEP of 242 kPa. The 55 cm<sup>3</sup> engine has a maximum FMEP of 151 kPa and the 85 cm<sup>3</sup> engine has a maximum FMEP of 139 kPa. The data indicate that as size is decreased, an engine experiences more friction losses relative to power output. This frictional loss is in part dependent on the surface area of the cylinder. Therefore the frictional loss as a percent of total power is expected to increase based on the larger cylinder surface area to swept volume ratio as engine size decreases. The average increase in FMEP from the 85 cm<sup>3</sup> engine to the 55 cm<sup>3</sup> engine is 28 kPa and 19 kPa at WOT and 50% throttle, respectively. The average increase in FMEP from the 55 cm<sup>3</sup> engine to the 28 cm<sup>3</sup> engine was 90 kPa at WOT and 95 kPa at 50% throttle. All tests were performed over the same speed range (approximately 4000-8000 rpm), so each engine experiences the same friction loading from the rotational velocity of the drivetrain components. Therefore, the frictional losses within the engine itself must be increasing relative to power output as engine size decreases.



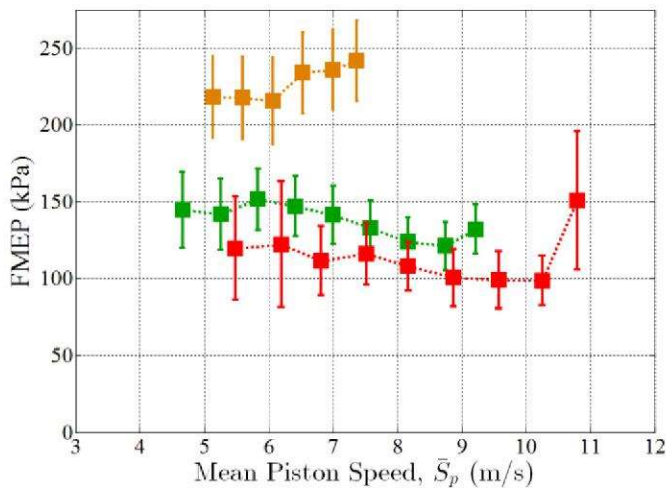


Figure 13. Friction mean effective pressure as a function of mean piston speed

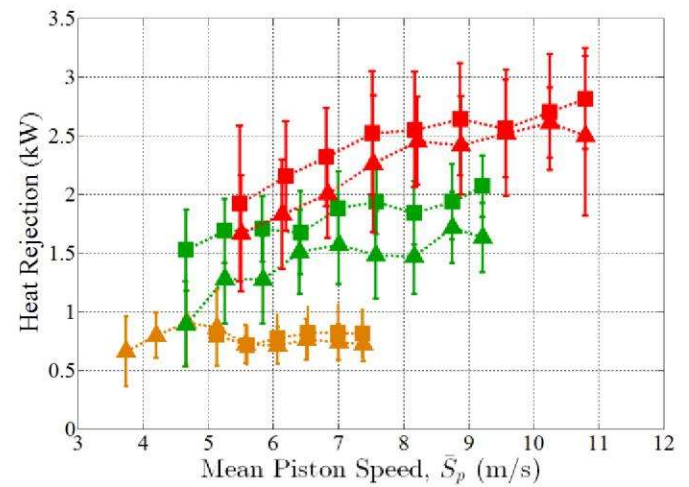


Figure 14. Heat rejection to cooling medium (air) as a function of mean piston speed

Figure 14 shows the heat rejection data from the engines. The dimensional data suggest that heat rejection scales with engine size, again consistent with more available energy and thus greater total losses. However, a more appropriate measure of heat rejection with respect to engine size would be to normalize the measured heat rejection value by the total heat released during combustion. The amount of heat release is the total fuel energy delivered, less the amount that short circuited, and reduced to comply with limited oxidizer and/or combustion efficiency as described in Equation (9). The scavenging models used in this work as bounding conditions were described previously, as was the use of a 95% combustion efficiency at lean points and incomplete combustion at rich points. Figure 15 shows the delivery ratio used in the calculation of the trapping efficiency for the scavenging models. Delivery ratio was calculated according to [25] (consistent with SAE J604) where the reference mass is the amount of fresh charge required to fill the displacement volume at standard conditions. The delivery ratio decreases with throttle setting due to blockage of the intake flow by the throttle plate. Thus Figure 15 provides a clear illustration of how merely throttling the engine negatively impacts the scavenging process. It is also interesting that delivery performance decreases with increasing speed for all engines, indicating that at higher speeds the engine may be ultimately port limited.

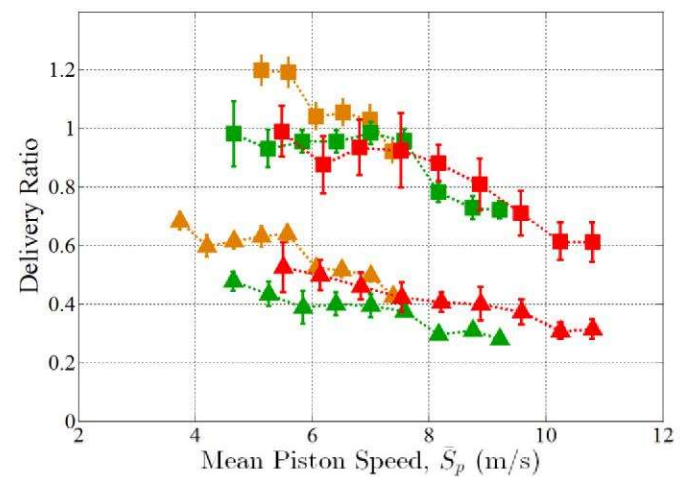


Figure 15. Delivery ratio as a function of mean piston speed

The corrected and normalized heat rejection values are shown in Figure 16 for the perfect mixing model and in Figure 17 for the perfect displacement model. The models form a bound for the heat rejected as a fraction of total heat released during combustion. The perfect mixing model will underestimate the amount of fuel trapped (trapping efficiencies between 58% and 87%) in the engine and thus underestimate the amount of heat released, leading to higher cooling fractions. Meanwhile, the pure displacement model overestimates the amount of trapped fuel (trapping efficiencies of 83% to 100%) and released heat, forming a lower bound for the thermal loss fraction.

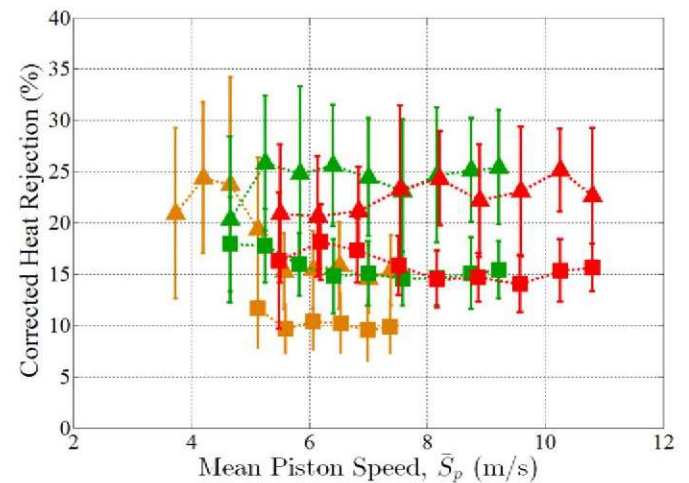


Figure 16. Heat rejection to cooling medium (air) normalized by total energy available for heat using the perfect isothermal mixing model.



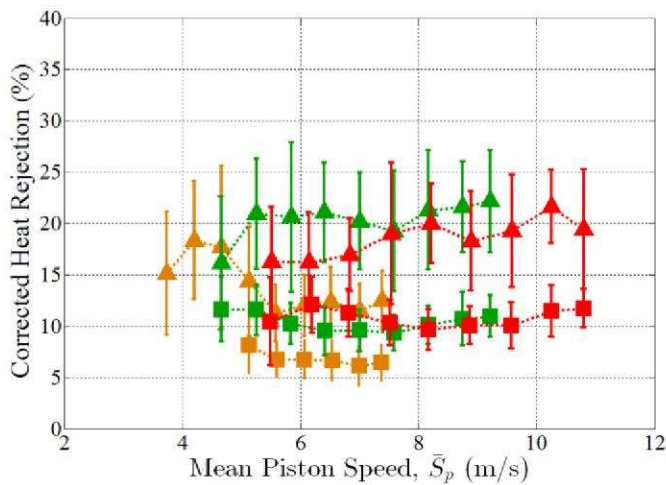


Figure 17. Heat rejection to cooling medium (air) normalized by total energy available for heat using the perfect displacement model.

Despite having a larger cylinder surface area to swept volume ratio, the smallest engine loses less energy in heat rejection with respect to available heat energy than the larger engines under both models. However, a word of caution is necessary in that this conclusion applies one of the two bounding models to all engines uniformly. In reality, the actual normalized heat rejection will lie between the two models at each point. The exact location between the two models is a function of the gas exchange dynamics, which is function of both the operating point and the engine. Furthermore, while it is used as a lower bound for modern conventional scale engines, the perfect mixing model may not be a true lower bound for the small scale engines considered here. Thus, the inclusion of exhaust gas sampling and analysis planned for future work will be critical to confirming the observed trend. Second, it is clear that the gas dynamics and the porting configurations of the engines (which do not scale cleanly with engine size, nor remain constant for these engines) play an important role in performance and thus the gas exchange behavior and must be accounted for more robustly in future studies.

It is also possible that an additional loss originating from the quenching of the combustion front in engine crevices inflated the overall losses for the smallest engine. As mentioned in the introduction, crevice volumes, especially those around the spark plug remain constant even as the combustion volume shrinks (one spark plug for three engines). Quenching in crevices would reduce engine efficiency, without a corresponding increase in thermal losses. Clearly, more analysis of crevice effects using detailed in cylinder pressure measurements is also warranted.

## Summary/Conclusions

This work sought to evaluate the baseline performance of three similarly designed IC engines that span a critical transition point in which power scaling trends change significantly with respect to cylinder surface area to swept volume ratio. The performance data indicate that engine friction becomes an increasingly important source of losses as engine size is reduced. An analysis of the thermal losses through the cylinder head revealed an unexpected trend. Typically, one expects that

the increase in cylinder surface area to swept volume ratio would result in an increase in thermal losses with decreasing engine size. However, this investigation found that as engine size decreases, the amount of heat rejected through the cylinder head as a fraction of the total heat released actually decreased with engine size. Clearly other losses are increasing as the engine size decreases faster than the thermal losses to account for the decrease in overall efficiency with decreasing engine size.

One possible loss is the short circuiting of fresh charge. The results make it clear that exhaust gas analysis is critical to isolating scaling effects from the gas transfer phenomena. Two exhaust analysis methods are planned in future work. The first will use FTIR at the exhaust port to resolve various species as a function of crank angle. The second will use gas chromatography and mass spectroscopy to quantify the exhaust gas composition and provide an accurate evaluation of the sensible exhaust enthalpy, short circuited fuel, and scavenging and trapping efficiencies. These analyses will enable a more complete understanding of scaling effects as IC engines become smaller.

There are two other projects currently planned. The first is to install an electric motor and torque cradle on the test bench to determine the friction in the drive train and in the engine. The second is to install a custom ECU to provide better controllability of the test bench. This would reduce the run to run variations in the equivalence ratio from the stock carburetor. A port fuel injection system would substantially reduce or eliminate the dependency of fuel flow on the intake air velocity, allowing more constant, controllable, and repeatable mixtures to be achieved across the operating range, and especially at low throttle settings.

These improvements and additions will provide a more refined picture of the loss mechanisms in the small IC engine (25-100 cm<sup>3</sup>) size regime. Quantification of these losses is a key to understanding the performance of these engines. With this knowledge an enhancement to the design, payload selection, and mission planning of future small unmanned aircraft can be accomplished.

## References

1. Menon S. and Cadou C., "Scaling of Miniature Piston Engine Performance Part 2: Energy Losses," *Journal of Propulsion and Power*, Vol. 29, pp. 788-799, July-August 2013, doi:10.2514/1.B34639.
2. Cadou C., Menon S., Moulton N., and Leach T., "Performance Scaling and Measurement for Hydrocarbon-Fueled Engines with Mass Less Than 1kg," presented at the AIAA's 1st Technical Conference and Workshop on Unmanned Aerospace Vehicles, Portsmouth, Virginia, 20-23 May 2002 2002.
3. Papac J. and Dunn-Rankin D., "Combustion in a Centimeter Scale Four Stroke Engine," presented at the Western States Section/The Combustion Institute Spring Meeting, UC Davis, Paper Number 04S-12, 29-30 March 2004.



4. Sher I., Levinzon-Sher D., and Sher E., "Minutization Limitations of HCCI Internal Combustion Engines," *Applied Thermal Engineering*, Vol. 29, pp. 400-411, 2009, doi:[10.1016/j.applthermaleng.2008.03.020](https://doi.org/10.1016/j.applthermaleng.2008.03.020).
5. Sher E. and Levinzon D., "Scaling-Down of Miniature Internal Combustion Engines: Limitations and Challenges," *Heat Transfer Engineering*, Vol. 26, pp. 1-4, 2005, doi:[10.1080/01457360591004780](https://doi.org/10.1080/01457360591004780).
6. Sher E. and Sher I., "Theoretical Limits of Scaling Down Internal Combustion Engines," *Chemical Engineering Science*, Vol. 66, pp. 260-267, 6 October 2011, doi:[10.1016/j.ces.2010.10.005](https://doi.org/10.1016/j.ces.2010.10.005).
7. Menon S. and Cadou C., "Scaling of Miniature Piston-Engine Performane Part 1: Overall Engine Performance," *Journal of Propulsion and Power*, Vol. 29, pp. 774-787, July-August 2013, doi:[10.2514/1.B34638](https://doi.org/10.2514/1.B34638).
8. Menon S., "The Scaling of Performance and Losses in Miniature Internal Combustion Engines," Ph.D. Aeronautical Engineering, Department of Aeronautical Engineering, University of Maryland, 2010.
9. Papac J. and Dunn-Rankin D., "In Cylinder Pressure and Combustion Measurements in a Minature Reciprocating Engine," presented at the 4th Joint Meeting of the U.S. Section of the Combustion Institute, Philadelphia, PA, 2005.
10. Ausserer, J., Litke, P., Groenewegen, J., Rowton, A. et al., "Development of Test Bench and Characterization of Performance in Small Internal Combustion Engines," 2013.
11. *3W Engines & Airplanes*. [Online] Available: [www.3w-modelmotoren.com](http://www.3w-modelmotoren.com) [Accessed: 19 April 2014].
12. *Centurion Aircraft Engines*. [Online] Available: [www.centurion.aero](http://www.centurion.aero) [Accessed: 19 April 2014].
13. *Compact Radial Engines*. [Online] Available: [www.compactradialengines.com](http://www.compactradialengines.com) [Accessed: 19 April 2014].
14. *DeltaHawk Diesel Engines*. [Online] Available: [www.deltahawkengines.com](http://www.deltahawkengines.com) [Accessed: 19 April 2014].
15. *Desert Aircraft*. [Online] Available: [www.desertaircraft.com](http://www.desertaircraft.com) [Accessed: 19 April 2014].
16. *Freedom Motors*. [Online] Available: [www.freedom-motors.com](http://www.freedom-motors.com) [Accessed: 19 April 2014].
17. *Kodiak Research Ltd*. [Online] Available: [www.kodiakbs.com](http://www.kodiakbs.com) [Accessed: 19 April 2014].
18. *O.S. Engine*. [Online] Available: [www.osengines.com](http://www.osengines.com) [Accessed: 19 April 2014].
19. *Recreational Power Engineering*. [Online] Available: [www.recpower.com](http://www.recpower.com) [Accessed: 19 April 2014].
20. *Super Tigre*. [Online] Available: [www.supertigre.com](http://www.supertigre.com) [Accessed: 19 April 2014].
21. *Zenoah*. [Online] Available: [www.zenoah.co.jp](http://www.zenoah.co.jp) [Accessed: 19 April 2014].
22. Husaboe T. D., Polanka M. D., Rittenhouse J. A., Litke P. J., and Hoke J. L., "Dependence of Small Internal Combustion Engine's Performance on Altitude," *Journal of Propulsion and Power*, 2014, doi:[10.2514/1.B35133](https://doi.org/10.2514/1.B35133).
23. Wilson C. W., "Performance of a Small Internal Combustion Engine Using N-Heptane and Iso-Octane," M.S. in Aeronautical Engineering, Department of Aeronautics and Astronautics, Air Force Institute of Technology, WPAFB, OH, 2010.
24. Ausserer, J., Rowton, A., Grinstead, K., Litke, P. et al., "Comparison of In-Cylinder Pressure Measurement Methods in a Small Spark Ignition Engine," SAE Technical Paper [2014-32-0007](https://doi.org/10.4271/2014-32-0007), 2014, doi:[10.4271/2014-32-0007](https://doi.org/10.4271/2014-32-0007).
25. Heywood J. B. and Sher E., *The Two Stroke Cycle Engine*. New York, NY: Taylor and Francis Group, 1999.
26. Heywood J. B., *Internal Combustion Engine Fundamentals*: McGraw Hill, 1988.

## Contact Information

Capt Alex K Rowton  
[alexander.rowton1@us.af.mil](mailto:alexander.rowton1@us.af.mil)  
 (719) 447-5640

## Acknowledgments

The authors would like to thank all involved with setting up and supporting the small engine test bench facility. The authors would specifically like to thank Mr. Rich Ryman for his machining expertise and support and Mr. Dave Burris for designing and supporting the LabVIEW engine control program.

## Definitions/Abbreviations

**B** - cylinder bore

**BMEP** - brake mean effective pressure

**BTDC** - before top dead center

**CAD** - crank angle degrees

**$c_{p,air}$**  - specific heat for air

**ECU** - engine control unit

**FMEP** - friction mean effective pressure

**IC** - internal combustion

**IMEP** - indicated mean effective pressure

**L** - engine stroke

**$\dot{m}_{cool}$**  - cooling air mass flow

**$\dot{m}_a$**  - air mass flow rate

**$\dot{m}_f$**  - fuel mass flow rate

**$m_o$**  - reference mass

**N** - engine speed

**P** - Engine power

**$P_{mfr}$**  - manufacturer rated power output

**$P_{ref}$**  - reference pressure

**Q** - heat rejection

**$\dot{Q}_{HR}$**  - heat release

**$Q_{LHV}$**  - lower heating value of fuel

**RPA** - remotely piloted aircraft

**SA** - cylinder surface area

$\bar{S}_p$  - mean piston speed

$\Delta T$  - change in temperature

$T_{ref}$  - reference temperature

$V_d$  - swept volume

**WOT** - wide open throttle

$\Lambda$  - delivery ratio

$\eta_c$  - Combustion efficiency

$\eta_{fb}$  - brake fuel conversion efficiency

$\eta_{tr}$  - trapping efficiency

$\rho_{pwr}$  - power density

---

The Engineering Meetings Board has approved this paper for publication. It has successfully completed SAE's peer review process under the supervision of the session organizer. This process requires a minimum of three (3) reviews by industry experts.

This is a work of a Government and is not subject to copyright protection. Foreign copyrights may apply. The Government under which this paper was written assumes no liability or responsibility for the contents of this paper or the use of this paper, nor is it endorsing any manufacturers, products, or services cited herein and any trade name that may appear in the paper has been included only because it is essential to the contents of the paper.

Positions and opinions advanced in this paper are those of the author(s) and not necessarily those of SAE International. The author is solely responsible for the content of the paper.

ISSN 0148-7191

<http://papers.sae.org/2014-32-0010>

## **Appendix D**

**Paper:** Comparison of In-Cylinder Pressure Measurement Methods in a Small Spark Ignition Engine

**Presented at:** 2014 Small Engine Technology Conference in Pisa, Italy

**Citation:**

J. K. Ausserer, A. Rowton, P. Litke, K. Grinstead, and M. Polanka, "Comparison of In-Cylinder Pressure Measurement Methods in a Small Spark Ignition Engine," presented at the 2014 SAE Small Engine Technology Conference, Pisa, Italy, SAE Technical Paper 2014-32-0007, 11 November 2014, doi: 10.4271/2014-32-0007.





## Comparison of In-Cylinder Pressure Measurement Methods in a Small Spark Ignition Engine

2014-32-0007

20149007

Published 11/11/2014

### Joseph K. Ausserer

Air Force Institute of Technology

### Alexander K. Rowton

Air Force Research Laboratory

### Keith D. Grinstead

Innovative Scientific Solutions Inc

### Paul J. Litke

Air Force Research Laboratory

### Marc D. Polanka

Air Force Institute of Technology

**CITATION:** Ausserer, J., Rowton, A., Grinstead, K., Litke, P. et al., "Comparison of In-Cylinder Pressure Measurement Methods in a Small Spark Ignition Engine," SAE Technical Paper 2014-32-0007, 2014, doi:10.4271/2014-32-0007.

## Abstract

In this work, in-cylinder pressure was measured in a 55 cc single cylinder, 4.4 kW, two stroke, spark ignition engine. In cylinder pressure measurements were taken using two different pressure transducers to determine if the performance differences between the two transducers are discernible in a small, spark ignition engine. A Kistler brand measuring spark plug was compared to a Kistler brand flush mount high temperature pressure sensor. Both sensors employ piezo-electric pressure sensing elements and were designed to measure indicated mean effective pressure as well as to detect knock at high temperature engine conditions. The pressure sensors were installed and adjusted to ensure cylinder volume after sensor installation matched the engine's original configuration within reasonable manufacturing tolerances.

A series of tests at four throttle settings ensued to determine if either device altered the combustion volume or the engine's performance. Performance measurements were obtained over a range of engine speeds from 4000 rpm to 6000 rpm. Run to run variation from randomness in the control variables results in a 2% to 5% variation in indicated mean effective pressure. The performance difference between the two spark plugs is less than that variation. Thus, the results indicate that, as a

spark plug, the Kistler measuring spark plug is not statistically different from the stock spark plug at the 95% confidence level. The results do indicate a statistically significant difference at the 95% confidence level between the pressure transducer in the measuring spark plug and the flush mount transducer. This difference, which amounts to 4% of indicated mean effective pressure, is the result of differences in the sensor linearity, likely arising from the factory calibrations. Finally, the results reveal a statistically significant difference in performance between the modified and unmodified engine heads above 6000 rpm at the 95% confidence level. This verifies the suppositions of other researchers who note that even a small modification to the combustion chamber of an engine this size could significantly impact the performance, measured in this instance as IMEP.

## Introduction

The need for in-cylinder pressure measurements has long been understood by engine developers. Shortly after Watt contrived his steam engine, he realized that the pressure in the combustion chamber was correlated to the performance of the device [1]. Early techniques for measuring the in-cylinder pressure involved a



mechanical linkage tied to a pressure port on an engine. Increasing engines speeds led to increasingly sophisticated mechanical techniques, such as the MIT method [2].

In 1956, Kistler published a paper on piezoelectric effect pressure transducers for in-cylinder pressure measurements. Piezo effect devices make use of the current induced by a pressure change on a crystal lattice. That current is converted into a voltage using a charge amplifier, and then read in a high speed analog data acquisition system. Despite their ability to tolerate the harsh conditions of the ICE combustion environment, the electrical amplification technology to make piezo devices precise and accurate was not developed until the 1970s and 1980s. Modern transistor technology, processors, and electrical component materials alleviated these issues and have made piezo effect devices the preferred choice for indicating measurements in most engine laboratories [3].

Currently, in-cylinder pressure measurements taken with piezo effect devices are now the cornerstone of combustion analysis in ICEs. With the in-cylinder measurements, heat release rates and burn angles can be calculated from zeroth order of thermodynamic models [2, 4]. Numerous technical papers have documented these results for larger, automotive sized engines (several notable papers cited for reference) [5, 6, 7, 8]. Yet, there is little documented information on the application and use of modern in-cylinder pressure measurement techniques in small ICEs in the 1-10kW (less than 100 cc displacement volume) size class.

Traditionally, small ICEs have run on glow fuel (a mixture of methanol, castor oil, and nitro methane) and their primary application has been small hobbyist aircraft, a market historically unable of supporting the cost of rigorous engine combustion analysis. Furthermore, until the development of stabilized crystals viable for uncooled sensors, the measurement technology was simply too large for these engines. Over the last two decades both factors have changed. The development of small gasoline fueled, spark ignited engines has expanded the market for small engines into hand held power tools and small RPAs, and reliable, uncooled piezo electric pressure transducers may be manufactured with diameters 5 mm and smaller [9].

Currently, small ICE research is largely being driven by emission standards in Europe and the demand for better endurance, longer range, and improved reliability for small RPAs and motor-generator sets. At the core of such research are measurements of cylinder pressure. Coupled with spark timing, injection timing, and mixture ratios, in-cylinder pressure measurements form the basis for optimizing combustion performance in any engine. Pressure sensing also permits the direct measurement and analysis of knock, a critical parameter in relaxing the fuel anti knock index. The criticality of in-cylinder pressure sensing for small engine research warrants the careful selection of an appropriate measurement technique.

This work focuses on a single aspect of that selection: the tradeoff between a sensor integrated within the spark plug, or modifying the engine head to install a standalone transducer.

## **Motivation and Objectives**

This project addresses the selection of an in-cylinder pressure measurement technique for small engines in the 1 to 10 KW class. These measurements are needed to supplement a parallel effort to characterize a set of geometrically similar small engines in order to develop an understanding of how thermal losses and octane requirements scale with engine size [10]. The effort described in this paper compared two options for making in-cylinder pressure measurements. The first method utilized a measuring spark plug, which combines the pressure transducer and spark plug. While this design eliminated the need to modify the cylinder head and simplified installation, the measuring spark plug is geometrically different than the stock spark plug (although both have the same spark gap). Therefore, its behavior was unknown compared to the stock plug. The second method was a flush mount pressure transducer, which required an additional access port to be added to the engine.

Thus, this work aims to answer the following question: are the stock spark plug and measuring spark plug interchangeable in terms of engine performance within the accuracy of the test setup? The answer will determine which transducers and modifications are employed in subsequent investigations and whether the engine characterization described in [10] can be performed without modifying each engine to accept a flush mount pressure transducer.

## **Previous Work**

While actual test data on small ICEs is sparse, relevant work has been accomplished by several researchers. Wiegand et al developed a test bench to study the conversion of an 11.5 cc glow fuel powered engine to JP-8 operation [11, 12]. To measure IMEP in both the stock and converted engine, a new head was manufactured to include a port for a flush mount pressure transducer. A portion of the research included modifying the head for other reasons, so there was little advantage in using a measuring spark in lieu of adding an additional port to the engine.

Cadou, Menon, and Moulton have published a significant volume of work on micro engines with power outputs less than 1 kW (select publications cited here) [13, 14, 15, 16]. Their work characterized nine glow fuel powered micro engines with displacement volumes from 7.5 cc to less than 1 cc. While their earlier work focused on dynamometer based engine characterization for developing scaling laws for micro engines [14, 15], their most recent work, involved modifying the heads of three OS engines to accept an optical pressure transducer [17]. The OS engines had cylinder volumes between 4.1 cc and 7.5 cc. The pressure data led Cadou *et al* to conclude that



combustion in these micro engines occurs across two different flame regimes and may vary from cycle to cycle. Since the OS engines run on glow fuel, modifying the head was the best option to install a pressure transducer; at the time there existed no commercially available glow plug transducer combinations in the required size. Cadou *et al* note that installation of the sensors did affect the cylinder geometry (especially due to the small size of the clearance volumes involved).

Papac and Dunn-Rankin also installed an optical pressure sensor in an OS FS-30-S engine to characterize combustion. They concluded that the lack of piston rings in the small engine severely limits the developed pressure and that the glow plug caused behavior and controllability issues similar to HCCI operation. They also determined that friction losses, calculated using IMEP from the in-cylinder pressure and power measured at a dynamometer, were more significant in small engines than in automobile scale engines [18].

To the best of the authors' knowledge, of the remaining researchers who have developed test stands and characterized similar small engines, none have included in-cylinder pressure measurements. Raine *et al*, who developed a small, low cost teaching engine test bench to provide hands-on testing opportunities to undergraduate engineering students, provides one potential reason [19]. He explains that the cost of such analysis is disproportionately large compared to the relative value of the engines and their end use products. Raine cites that the transducers can cost upwards of \$5000 before even considering the cost of the charge amplifier and combustion analyzer; significantly more than the cost of most of these small engines. Thus, as Wiegand notes, it is difficult to secure funding for such research systems in the context of small engine characterization [11].

## Methodology

This section is split into three subsections. The first section reviews the research bench used for this experiment, which is a modified version of the bench described in [10]. The second section describes equipment required to take in-cylinder pressure measurements and the modifications to the engine in order to accomplish this investigation. The third section explains the experimental procedure.

### Test Setup and Equipment

The engine selected for this work was the Modellmotoren 3W-55i engine. The engine has a displacement of 55 cc, a rated power of 3.9 kW, a bore of 4.50 cm, and a stroke of 3.51 cm. The engine's compression ratio is 10:1. For the IndiSmart Combustion Analyzer to determine the cylinder volume as a function of crank angle, the connecting rod length, which is not provided by the manufacturer, is required. The engine was partially disassembled and the connecting rod length was

measured at  $5.85 \pm 0.02$  cm. The engine was reassembled and tuned for maximum power at 6000 rpm, using the stock carburetor, ECU, and spark timing.

The bench was designed to test a series of geometrically similar engines ranging in manufacturer rated output power from 1-10 kW. The engine was loaded using a Magtrol brand, 1WB65 eddy current dynamometer rated to 10,000 rpm and 6 kW and possessing a full scale measurement accuracy of  $\pm 0.5\%$ . The dynamometer is coupled to the engine using a belt drive and elastomer spider couplers designed to minimize vibration. The dynamometer was controlled remotely through a DSP6001 dynamometer controller, wired into a data acquisition and control program written in National Instruments Labview. The engine was started using a lubricated air motor connected to the drive train using a clutch bearing on the dynamometer drive shaft. An overhead view of the bench showing the dynamometer, engine, and drive train is shown in Figure 1.

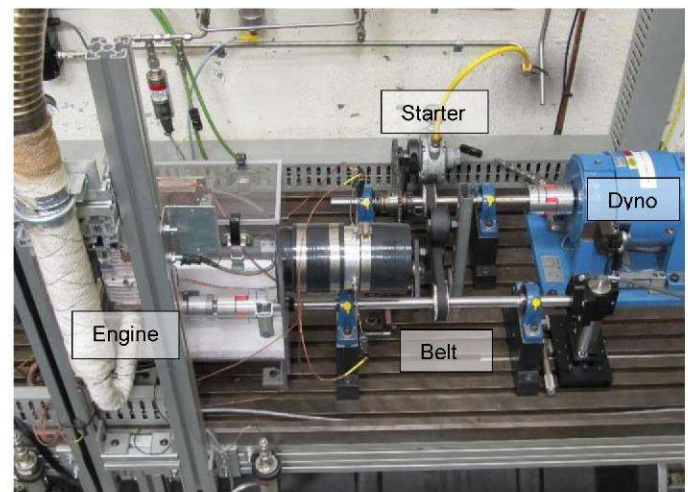


Figure 1. Overhead view of the test bench showing the dynamometer, engine, belt drive system, and starter motor.

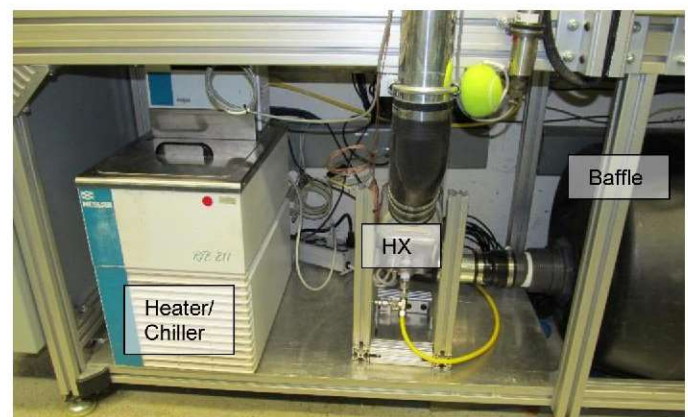


Figure 2. Side view of research bench showing the intake air system.

Intake air temperature was controlled by passing the intake air through an oversized performance heat exchanger. The other side of the heat exchanger was connected to a Thermo Neslab



RTE-211 recirculating water bath unit capable of delivering 0.5 kW of cooling and 0.8 kW of heating. Intake air flow was measured using a pair of TSI 40224 air flow meters, which can measure flow rates from 0 to 300 SLPM at an accuracy of  $\pm 3\%$  of the reading. The flow meters were isolated from the engine using a 55 gallon drum to damp out flow oscillations. The baffle size was based on heuristics in [20]. The entire intake air system is located under the test bench, as shown in Figure 2.

Engine temperature was controlled using a 2.25 kW blower, a significant change to the original setup discussed in [10]. The new blower configuration provides additional cooling authority to maintain control of engine head temperature at all operating conditions. The engine temperature was monitored using two thermocouples attached to the top fin of the engine at the cylinder centerline. One thermocouple was installed above the exhaust port and the second thermocouple was installed opposite of the exhaust port as shown in Figure 3. The VFD was wired into the DAQ program and could be run in either man in the loop mode or in a PID mode to hold engine temperature constant across set points. PID control is based solely on the thermocouple above the exhaust port, while man in the loop permits the operator to decide which combination of thermocouples to use.

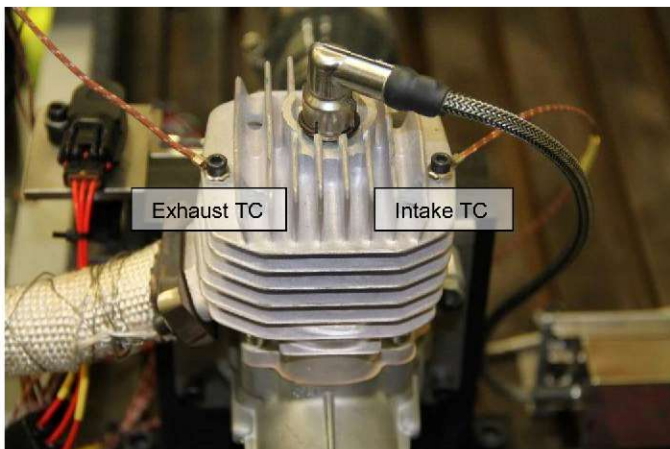


Figure 3. Location of engine temperature control thermocouples (ring) on 3W 55i engine.

The exhaust pipe was modeled after the manufacturer supplied pipe, which is not tuned. Thus the engine running in its stock configuration implies an un-tuned exhaust system. The engine's exhaust pipe was routed to the laboratory exhaust system, where it was indirectly coupled to prevent the exhaust system from drawing down on the exhaust port of the engine, which could lead to poor scavenging and increased short circuiting of fresh charge. Figure 4 shows the connection between the engine exhaust duct extension (5.08 cm diameter) and the laboratory exhaust system (15.24 cm diameter). The gap between the two pipes allows the exhaust system to draw ambient air and prevents the system from

pulling suction on the exhaust port of the engine. No difference in engine power output with the laboratory exhaust fans on and off has been observed.

Temperatures were measured using Class 1, Type J thermocouples. Pressures, except for the in-cylinder pressure, were measured using transducers accurate to 0.1% of full range. Both the thermocouples and pressure transducers used in the experiment are the same as those described in [10]. Engine throttle position and choke position were controlled using Hitec HS-85MG+ analog, metal gear servos driven by the DAQ program. Repeatability of the throttle servo settings was verified using a CTS Single Ear Rotary Position sensor. Control of the engine and test setup, as well as acquisition and recording of all signals (except for the in-cylinder pressure measurement) were performed in a DAQ program written in National Instruments' Labview.



Figure 4. Connection of engine exhaust pipe to laboratory exhaust system.

### ***In-Cylinder Pressure Measurement***

While there are several commercial options for in-cylinder pressure measurement systems, the AVL IndiSmart Combustion Analyzer was chosen for this effort. The IndiSmart system offers highly customizable and reliable hardware and software and is considered an industry standard for indicating engine measurements. The IndiSmart Combustion Analyzer serves as both a high speed signal processor and a data acquisition unit. Therefore, signals acquired through the IndiSmart are viewed, read, and recorded through AVL's proprietary program. For this effort, the data from the IndiSmart and the NI Labview control program were synchronized during analysis using a custom MatLab script.



In addition to the in-cylinder pressure signal, two additional signals were required to measure IMEP: engine crank angle and baseline pressure. Values calculated from the in-cylinder pressure are highly sensitive to the resolution of the crank angle (CA), and Rogers recommends a resolution of 0.2 CAD or better to resolve abnormal combustion and 1 CAD for pressure and heat release analysis [9]. While combustion optimization is not the subject of this investigation, it is planned for future work and thus an encoder capable of at least 1800 CPR was required. Most encoders recommend by AVL are not able to run above 6000 rpm and therefore were not suitable for this application. Thus, an open style E6 optical encoder was chosen from U.S. Digital. The 1800 CPR disk combined with the internal electronics permit 0.2 CAD resolution up to 10,000 rpm, and the pickup provides the quadrature output as well as the 1 CPR index to identify each new engine cycle. The output signals were conditioned and stepped down to 5V peak to peak using an optical isolator before transmission to the AVL IndiSmart. The encoder was installed on the driveshaft opposite of the engine to ensure any play in the belt did not affect the crank angle measurement.

The second required signal was a baseline pressure for the in-cylinder pressure measurement. Despite modern improvements in drift compensating electronics, AVL still recommends providing a pressure signal to baseline the in-cylinder pressure during each cycle to compensate for long term temperature effects on the transducer itself. In four-stroke engines, the intake air manifold pressure near BDC of the exhaust and intake stroke is commonly used. For a two stroke engine, such as the engine considered here, the window must be tightened to within 10 CAD of BDC, when both the intake port and the exhaust port are open. Since pressure variations during gas exchange are in the tenths of bars while pressures during a fired cycle are in the tens of bars, such a baseline will result in less than 1% error in the in-cylinder pressure. Furthermore, because this offset will be constant across an entire engine cycle, it will cancel out in the calculation of IMEP and introduce effectively no error to the IMEP value.

To convert the current from the in-cylinder pressure transducer to a voltage measurable by the IndiSmart combustion analyzer, a Kistler SCP charge amplifier was selected for this work. The system consists of two units. The chassis, model 2852A12, was fitted with a 5064C charge amplifier capable of processing two piezoelectric signals. The charge amplifier was configured for medium drift compensation based on prior experience and manufacturer recommendations. It is accurate to  $\pm 0.1\%$  of full scale.

Two different styles of in-cylinder pressure transducers from the same manufacturer were selected. The first style was a measuring spark plug, where the pressure transducer is integrated into a spark plug assembly. This design minimizes the modifications to the engine required to install the transducer. The second style was a flush mount pressure transducer. This style requires a hole be added to the top of the engine, but permits the use of the stock spark plug. The next two subsections describe each transducer and their respective installation procedures.

### Kistler Measuring Spark Plug

The 3W series of engines utilizes M10 $\times$ 1.00 spark plugs, which are smaller than standard automotive plugs. Thus, two measuring spark plugs, Type 6113B M10 $\times$ 1, were custom ordered with M10 $\times$ 1.00 threads. The pressure transducer in the measuring plug has a linearity of  $\pm 0.5\%$  of full scale and a sensitivity of  $\pm 1\%$  at 200 $\pm 50^\circ\text{C}$ . One of the custom spark plugs is shown alongside the stock plug in Figure 5. While the two plugs have the same spark gap and the same thread, they have significantly different geometries. Since the thread length of the measuring plug is significantly longer than the stock plug, a custom copper spacer was manufactured to keep the cylinder volume constant. Note that due to geometric differences between the measuring spark plug and the stock plug, the number of engaged threads is not the same for the two plugs, as can be seen in Figure 5. The copper spacer was machine finished to match the surface finish on the washer supplied by Kistler with the plug. Assuming the spacer is perfectly manufactured, the difference in cylinder volume between the two plugs is less than 0.03 $\pm$ 0.01 cc, which is less than 1% of the clearance volume. When compared to an increase in volume of 0.02 cc due to an extra 1/4 turn of either spark plug, this small difference is negligible. To ensure manufacturing error in the spacer did not alter the volume of the combustion chamber, the thickness tolerance was held to  $\pm 0.013$  cm, which is equivalent to an extra 1/8 turn of the spark plug.



Figure 5. Top: Custom Kistler Measuring spark plug with copper spacer washer installed. Middle: Stock CM-6 spark plug. Bottom: Kistler Flush Mount Pressure Transducer



## Kistler High Temperature Pressure Transducer

The high temperature pressure sensor, model 6052C, shown in Figure 5 is significantly smaller than the measuring spark plug. The high temperature pressure sensor has a linearity of  $\pm 0.3\%$  of full scale and a sensitivity of  $\pm 0.5\%$  at  $200 \pm 50^\circ\text{C}$  and  $\pm 2\%$  over the full temperature range. Unlike the measuring spark plug, whose location is determined by the plug location on the stock engine, the high temperature pressure sensor required a suitable installation location. This location was ultimately determined based on three requirements. Based on the work of Rogers [9], the transducer should be installed as close to the center of the head as possible to match the reading of the other transducer; pressure measurements will vary with cylinder location due to the movement of the flame front. Furthermore, the transducer needed to be angled so that it was flush with the wall in the combustion chamber. The creation of an extrusion or recess would change the cylinder volume and create potential hotspots. Finally, sufficient material to install the transducer was required.

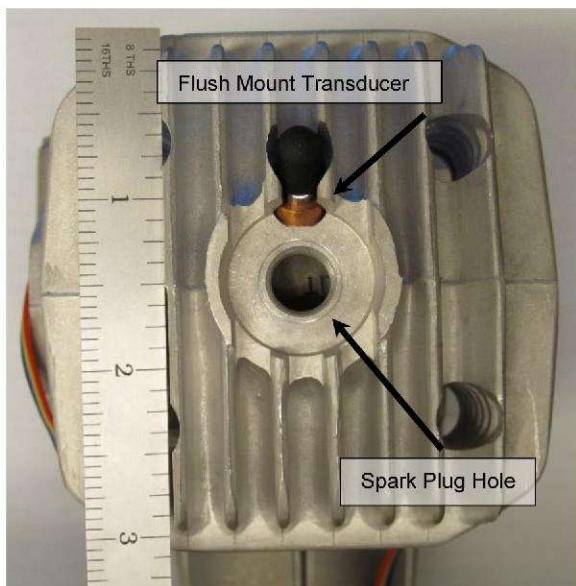


Figure 6. 3W-55i engine head showing installed Kistler high temperature flush mount pressure transducer.

Figure 6 shows the flush mount pressure transducer installed in the 3W-55i engine. When installed with the measuring spark plug, the distance between the two transducers is less than 0.6 cm, minimizing the potential for a pressure gradient between the two transducers. Such a gradient would manifest as an off-set in the peak pressures of the two signals. The maximum off-set was estimated as 0.5 CAD at 8000 rpm, assuming pressure waves propagate at the sonic velocity of the combusting gas and estimating the average gas temperature at  $700^\circ\text{C}$  during combustion. No such offset was observed in the experimental data. Like the measuring spark plug, a custom copper spacer was designed to avoid changing the cylinder volume. Noting the sensitivity of the transducer to sealing surface and installation torque, the both the washer and engine surface were finished with the manufacturer's provided tooling, and the specified installation torque of 1.5 N-m was observed. Type 1067 spark plug lubricant, provided by Kistler for use with both the flush mount sensor and the

measuring spark plug, was used during the installation. An extra full turn of the transducer during installation would result in a 0.01 cc change in cylinder volume (less than 1/3%), and the spacer machining tolerance results in a change of less than  $\pm 0.003$  cc ( $\sim 0.1\%$ ). Therefore, despite the addition of a hole to the engine, the impact from the flush mount transducer is even less than the measuring spark plug.

## Test Procedure

The engine was run in three different configurations. In the first configuration, only the measuring spark plug was installed on an unmodified head. In the second configuration, the flush mount high temperature pressure transducer was installed along with the stock spark plug using an identical, replacement head modified for the flush mount transducer. In the third configuration the measuring spark plug was run with the flush mount transducer. This configuration permitted the simultaneous measurement of pressure with both transducers, eliminating any run to run variation from their direct comparison.

The engine was initially tested at wide open throttle from 4000 rpm to 7900 rpm in increments of 500 rpm. (Note that the last increment was only 400 rpm). The engine was run through the speed range three times in each configuration, collecting a total of three independent samples at each operating point. Intake air temperature, engine head temperature, and fuel composition were controlled between runs. Timing was set at the factory default using the stock ECU. The intake air temperature was maintained between  $20^\circ\text{C}$  and  $25^\circ\text{C}$ . For each speed, head temperature was held at a set point  $\pm 5^\circ\text{C}$  for all configurations. These set points were speed dependent, ranging from  $270^\circ\text{C}$  at low speeds to  $300^\circ\text{C}$  at high speeds. The set points were selected based on manufacturer guidelines for maximum permissible and minimum recommended engine temperatures. The head temperature was measured at the exhaust side thermocouple.

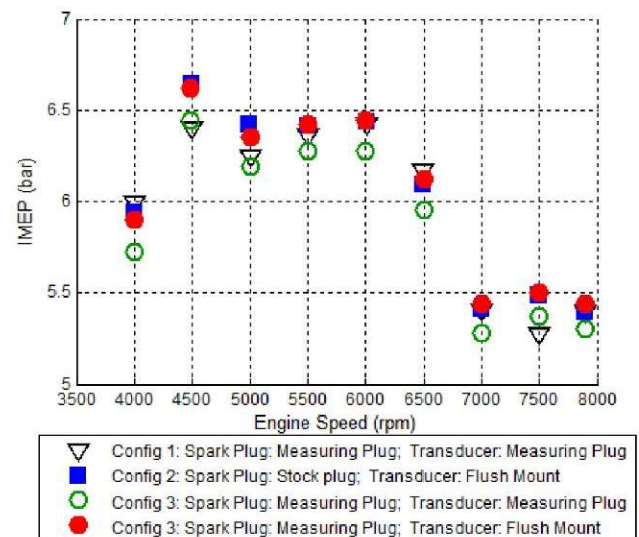


Figure 7. Average IMEP from three runs in each configuration at WOT.



Prior to each test, the TDC position of the engine was determined using a motored pressure trace and the thermodynamic algorithm within the AVL IndiSmart software. The TDC offset was verified between each run in case the encoder pickup was bumped or adjusted; the TDC measurement was repeatable with standard deviation of  $\pm 0.03$  CAD unless the encoder was intentionally adjusted. When both transducers were installed side by side, the TDC offset was taken from the measuring spark plug, although the TDC offset determined by the transducers agreed within  $\pm 0.1$  CAD, which is within the measurement uncertainty of the encoder.

The thermodynamic loss angle, which adjusts the thermodynamic TDC determination for heat loss and blow-by was set at 0.7 CAD based on recommendations in [9]. The determination of TDC creates an uncertainty of  $+1.3$  CAD  $-0.4$  CAD. During each test, the engine was held at the set point speed using the dynamometer and the blower was adjusted to set the head temperature. The engine was allowed to reach equilibrium (constant head temperature over a ten second window). Cylinder pressure data was then collected for 400 cycles using the AVL software.

## Results and Analysis

Data was subsequently collected at three other throttle settings. However, the results presented here will focus on the WOT data. Notable differences at other throttle settings are summarized in a subsequent section. The goal of this investigation was to determine if there are statistically significant differences between the spark plugs, pressure transducers, and modified and unmodified engine heads. [Figure 7](#) shows the average IMEP from three runs in each configuration taken at WOT on the 3W-55i engine. In the analysis, each source of uncertainty will be addressed separately, followed by a presentation of the total uncertainty. This will allow conclusions to be drawn about the significance of the observed differences in the configurations relative to each contribution to uncertainty. The contributions to uncertainty were grouped into three categories, all of which are expressed as 95% confidence intervals in the table and plots that follow.

### Comparison of Uncertainties

The first uncertainty, the COV of the mean of IMEP, represents the impact of cycle to cycle variability arising from changes in the gas exchange process, the trapped mixture composition, and the effect of those changes on the combustion process. The IMEP measured at each operating point in each configuration is the average of three separate test runs, and each test run is an average of 400 engine cycles. For statistical purposes, each engine cycle is assumed to be an independent event, and thus the IMEP values from the cycles are assumed to be normally distributed. This permits the calculation of the COV and the COV of the mean of IMEP. The COV represents the variation in IMEP due to cycle to cycle variability and quantifies the spread of IMEP for the 400 cycles relative to the run mean. Since the 400 cycles are only a sample of the engine performance at a given operating point during a given

run, the average IMEP from each run is only an approximation of the true IMEP. Thus the COV of the mean permits the calculation of a confidence interval surrounding the average IMEP for each run that indicates the range of probable values of the true mean with respect to cycle to cycle variability. Representative values of the COV uncertainty for each configuration at three speeds are shown in [Table 1](#). At all conditions, the contribution to uncertainty of the mean IMEP measurement from COV is less than 0.1%.

The second uncertainty, run to run variation, is the result of variation in the controlled parameters between the three runs that make up each operating point. These parameters include the intake air temperature, fuel temperature and composition, engine head temperature, small changes in the throttle setting, variation in equivalence ratio delivered by the carburetor, and any other variations in ambient conditions. Again, [Table 1](#) shows this uncertainty in term of a 95% confidence interval. With values on the order of 0.2% to 4.3%, the run to run variation is the largest random uncertainty in the experiment.

There are two potential avenues to reduce the run to run variation: increase the number of trials that make up the operating point, or improve control over the ambient conditions. Increasing the number of trials by two, from three to five, would tighten the confidence interval by a factor of  $\sqrt{2}$ , assuming the deviations of the additional trials from the mean are of comparable magnitude to the deviations of the first three trials.

A second method modifies the first method to reduce the required number of total trials. Instead of taking additional samples at every operating condition, several operating conditions could be selected as representative of the operating range. These conditions could be sampled a large number of times (at least 10) and used to provide run to run uncertainty for other similar operating conditions. This technique is consistent with uncertainty sampling techniques described in [21, 22].

Finally, run to run variability can also be reduced with improved control of the engine parameters. Of those control parameters, the equivalence ratio, controlled by the stock carburetor, is likely the best starting point. Even at a constant carburetor needle setting, engine speed, and intake air temperature, the delivered equivalence ratio was observed to vary by more than 0.2 at some conditions. Therefore, to reduce the run to run variability, the carburetor could be replaced with a more reliable fuel metering system, and the installation of throttle body injection on the test bench is planned for future work.

The third random uncertainty is the uncertainty in the instrumentation. Instrument uncertainty includes the accuracy of the pressure transducers, the angle encoder, and the charge amplifier as well as the uncertainty in the repeatable determination of TDC. Unlike cycle to cycle variability and the run to run variation, which are calculated from the raw data, the instrument uncertainty is calculated from the manufacturer specifications on the equipment. In some cases, instrument uncertainty can be reduced through *in situ* calibration for the installed operating range, should instrument uncertainty



dominate the overall uncertainty. Note that the assumed thermodynamic loss angle is a fixed bias, and therefore it is not included in the systematic uncertainty since it affects all measurements equally. Bias due to the selection of loss angle is discussed later in the paper. Shown in [Table 1](#), the uncertainty from the instrumentation is two to three times that of the cycle to cycle variability and half to 1/10<sup>th</sup> that of the uncertainty due to run to run variation.

Table 1. Representative uncertainties in IMEP

Config: Transducer (spark source)	Avg. IMEP (bar)	COV (bar) (%)	Run- Run (bar) (%)	Instr. (bar) (%)	Total (bar) (%)
4000 RPM					
1: Measuring plug (meas. spark plug)	5.99	<0.01 0.1	0.25 4.2	0.02 0.3	0.25 4.2
2: Flush mount (stock spark plug)	5.94	<0.01 0.1	0.10 1.7	0.02 0.3	0.10 1.7
3: Measuring plug (meas. spark plug)	5.72	0.01 0.2	0.17 3.0	0.02 0.3	0.17 3.0
3: Flush mount (meas. spark plug)	5.90	0.01 0.2	0.16 2.6	0.02 0.3	0.16 2.7
6000 RPM					
1: Measuring plug (meas. spark plug)	6.42	<0.01 <0.1	0.12 1.8	0.03 0.5	0.12 1.9
2: Flush mount (stock spark plug)	6.43	<0.01 <0.1	0.07 1.0	0.03 0.5	0.08 1.2
3: Measuring plug (meas. spark plug)	6.28	<0.01 <0.1	0.05 0.8	0.02 0.3	0.06 0.9
3: Flush mount (meas. spark plug)	6.45	<0.01 <0.1	0.04 0.6	0.02 0.3	0.05 0.7
7900 RPM					
1: Measuring plug (meas. spark plug)	5.40	<0.01 <0.1	0.09 1.7	0.03 0.6	0.10 1.8
2: Flush mount (stock spark plug)	5.40	<0.01 <0.1	0.03 0.6	0.03 0.7	0.05 0.9
3: Measuring plug (meas. spark plug)	5.30	<0.01 <0.1	0.01 0.2	0.01 0.2	0.02 0.3
3: Flush mount (meas. spark plug)	5.44	<0.01 <0.1	0.01 0.2	0.01 0.2	0.02 0.4

The fourth and final column in [Table 1](#) is the total uncertainty, propagated as a 95% confidence interval of the mean of IMEP. [Figure 8](#) provides a visual representation of how the 95% confidence interval compares to the difference in the average IMEP between the configurations. The empty symbols represent the modified and un-modified cylinder heads, configurations one and three, respectively. Based on the total calculated uncertainty interval, the difference between the two cylinder heads is statistically distinguishable at the 95% confidence level at 6500 rpm and 7000 rpm. At 6500 rpm and 7000 rpm, the modified and unmodified heads differed by 3.7% and 3.0%, respectively. From [Figure 8](#), 4000 and 6000 rpm have similar differences but larger uncertainty intervals. Thus the difference between the heads likely exists at all speed, but is only statistically resolvable within the run to run variation at some speeds. Thus, for smaller engine sizes, such as those examined in [12, 17, 18], there is a real impact on engine

performance, in this case IMEP, from installing a modified cylinder head. Therefore, for engines the same size and smaller than the engine considered here (55 cc), there is an advantage to using a pressure measurement technique that does not require a modified cylinder head.

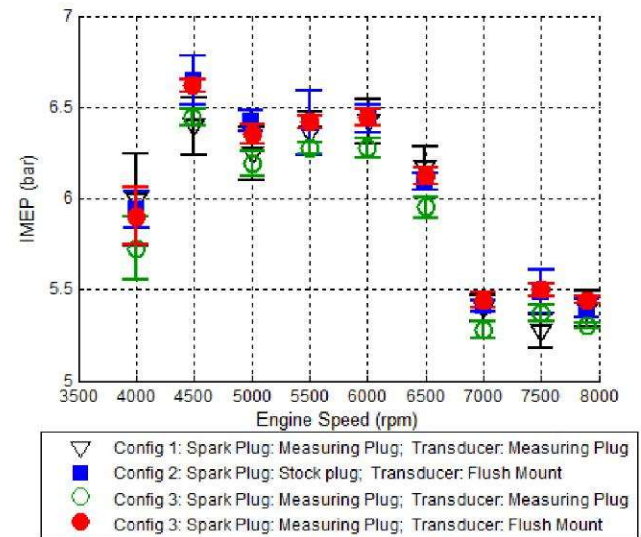


Figure 8. Combined uncertainty for combustion variability, run to run variation, and instrument uncertainty at WOT expressed as a 95% confidence interval.

### Comparison of Spark Plugs and Transducers

The filled symbols in [Figure 8](#) compare measurements taken with the flush mount pressure transducer with the stock spark plug on a modified head in Configuration 2, to the measuring spark plug in Configuration 3. At all speeds, the two values of IMEP are within 1%, and less than the total uncertainty at the 95% confidence level. Thus, any differences between the two spark plugs are not distinguishable within the uncertainty of the test setup at the 95% confidence level, and the plugs may be used interchangeably.

The circles in [Figure 8](#) compare the flush mount transducer and measuring spark plug transducer for the exact same engine cycles. The pressure transducer in the measuring spark plug reads consistently lower than the flush mount pressure transducer. Because there is no run to run variation for measurements taken in exactly the same cycle, [Figure 9](#) shows the simultaneous measurements again, this time with only the cycle to cycle variability and instrument uncertainty. The data demonstrate a conclusive difference between the measuring spark plug and the flush mount transducer as a pressure sensor. This difference between the two transducers amounts to a 4% difference in IMEP. Operationally both transducers are configured identically. When pressure traces from the two transducers were compared alongside one another during a motored engine run, shown in [Figure 10](#), (effectively eliminating thermal transient effects), the flush mount transducer displayed larger gain than the transducer in the measuring plug. Therefore, it can be concluded that there is a difference in the gain caused either by installation, or by the factory calibration.



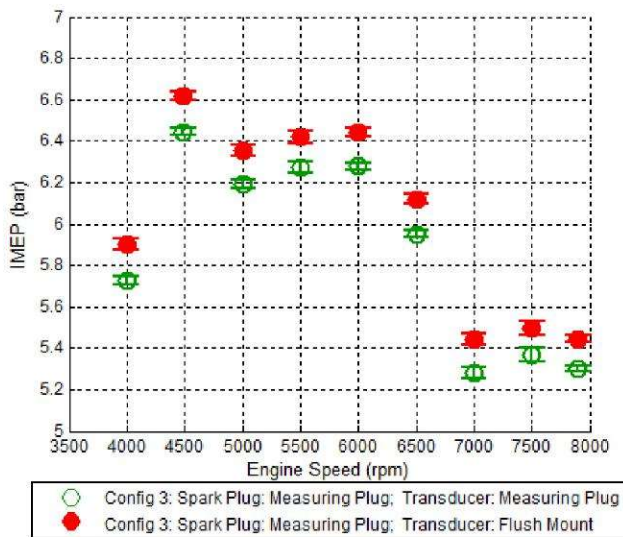


Figure 9. Comparison of measurements taken simultaneously with the measuring spark plug and flush mount transducers at WOT with run to run variation removed.

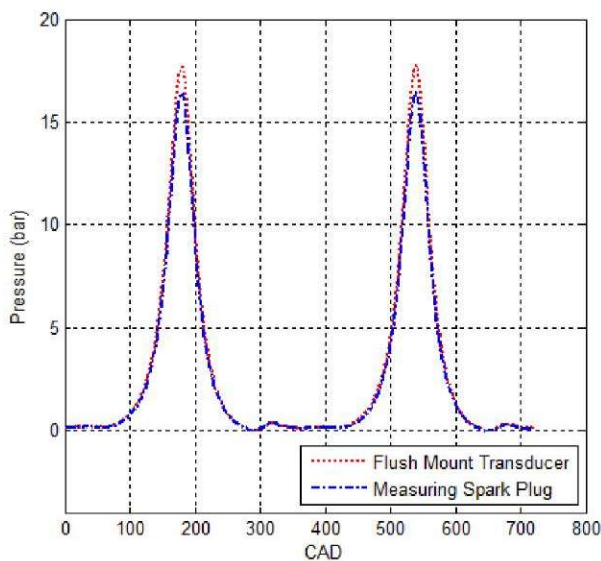


Figure 10. Motored comparison of transducers showing difference in gain.

The gain in question is used by the charge amplifier to convert the differential charge signal measured at the amplifier to a voltage that corresponds to the physical change in pressure at the transducer. That voltage is then measured as an analog signal by the data acquisition unit, in this case the AVL Indisart. Unlike a mechanical strain gauge, which produces a signal even under a static load, a piezoelectric device requires a dynamic load for calibration. For high speed devices such as in-cylinder pressure units, this calibration is difficult to perform without specialized equipment, which is why the factory calibration was used for both transducers. Those calibrations are highly sensitive to the installation torque, which was observed for the installation of the transducers in this work. In light of the data, it is clear that a correct calibration, at least in the case of these individual transducers, has a more significant impact on the overall results than the type of transducer, flush mount or measuring spark plug, used to take the measurement.

According to the manufacturer's data sheet, variability of the gain is primarily due to thermal effects. With the transducers between 150°C and 250°C that variation is  $\pm 1\%$ , and over the full operational temperature range from 23°C to 350°C it is  $\pm 2\%$ . Therefore, thermal effects on the sensitivity could account for the 4% difference in IMEP between the two transducers. Since the difference exists both under motored and fired conditions, it is unlikely thermal effects can account for the entirety of the difference between the transducers. Note that in the calculation of instrument uncertainty included in Figure 9, the thermal impact on the gain was not included.

The error associated with changing transducers is, based on these results, about 4% and the largest of the uncertainties observed in this experiment. Thus, when comparing the performance of multiple engines or configurations, using the same transducer and maintaining its temperature is as important as the other control variables.

### Impact of Thermal Loss Angle

The previous uncertainties only considered random events that could affect different runs and configurations. Sources of bias, which would have the same effect on all experiments and affect the absolute value of the results, were also considered. In this work, the dominant potential source of bias was the thermodynamic loss angle. The peak pressure of a motored engine cycle occurs slightly before geometric TDC due to blow by and thermal losses. To correct for these phenomena when using a thermodynamic determination of TDC, a thermodynamic loss angle is used. For conventional engines this angle can vary from 0.3 CAD to 2 CAD [9]. For this work, the angle was estimated as 0.7 CAD using data for small automobile engines [9], creating an uncertainty of +1.3 CAD to -0.4 CAD. This assumes the actual loss angle falls within the range of observed angles compiled from literature [9]. While this potential error in TDC is consistent for all runs, it does create an absolute error in IMEP. If the TDC using the loss angle is earlier than the actual TDC, IMEP will be higher than the actual value. For a TDC from the loss angle that trails the actual TDC, the calculated IMEP will be lower than actual IMEP. Based on the range of possible loss angles and pressures observed in the work, the loss angle bias is 1% to 4% of IMEP, depending on the operating condition.

Figure 11 shows the maximum bias that the choice of loss angle could impose on the results. The bias was calculated by determining the effect of a shift in TDC using the raw pressure data. This measurement bias is comparable to the total uncertainty shown in Figure 8. If one were interested in determining the error on the absolute value of IMEP, then this bias would add directly to the uncertainty above, giving an absolute error in IMEP of  $\pm 2\%$  to  $\pm 8\%$ , again depending on the operating condition.



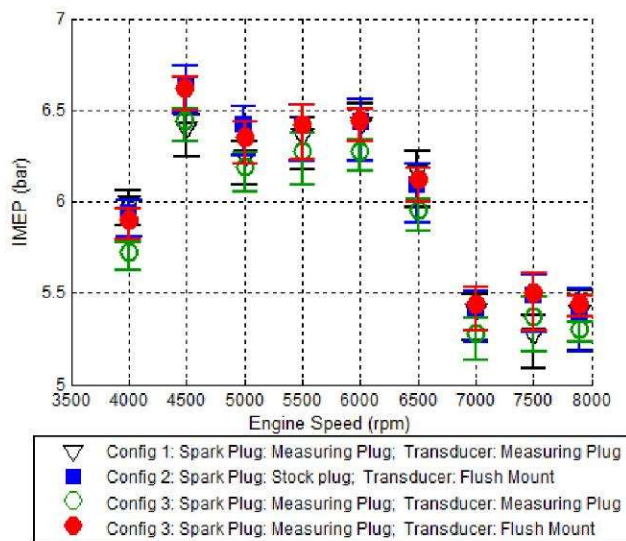


Figure 11. Potential impact of bias from the selection of thermodynamic loss angle at WOT.

Since this bias from loss angle selection is comparable to the random and instrument uncertainty, reducing it would improve the overall accuracy of the IMEP measurement. One method to improve the estimate involves motoring the engine in both directions and measuring the peak pressure. The true top dead center position will fall between the peaks, and the loss angle is half of the peak to peak distance. Until the completion of the friction measurement cradle for the bench, bi-directional motoring is unavailable.

There also exist several measurement techniques that do not require a thermodynamic loss angle. One such method is the use of a capacitive spark plug probe to determine TDC. Since the probe determines TDC using the proximity of the piston, it does not require a loss angle. In fact, it could be used to determine the loss angle by comparing the TDC position measured using the capacitive probe to the TDC position determined thermodynamically. Such an investigation is planned for future work to determine how loss angles for small engines compare to their larger counterparts.

### Results: $\frac{3}{4}$ , $\frac{1}{2}$ , and $\frac{1}{4}$ Throttle

The same data was collected for three other throttle settings, where the throttle position was determined as  $\frac{3}{4}$ ,  $\frac{1}{2}$ , and  $\frac{1}{4}$  of full power at 6000 rpm, respectively. Notable difference between the WOT throttle results already reported and the partial throttle results are summarized.

Typical values of the uncertainty in the mean value of IMEP due to cycle to cycle variability rise from less than 0.1% at WOT to 0.3% as throttle decreases to the  $\frac{1}{4}$  setting. This increase is partially due to lower IMEP values at lower throttle settings and partially due to increases in COV (0.2-0.4 bar). Table 2 shows the COV of IMEP (not the mean of IMEP at reported in Table 1). At low throttle settings, cycle to cycle variations are much higher than would be acceptable in a conventional automobile spark ignition engine. This performance is indicative of highly variable gas exchange and mixture preparation.

Table 2. Average COV values from the measuring spark plug transducer in an unmodified cylinder head.

Speed	WOT	$\frac{3}{4}$ Throttle	$\frac{1}{2}$ Throttle	$\frac{1}{4}$ Throttle
4000	2.0 %	3.3 %	24.4 %	24.9 %
4500	2.0 %	2.2 %	5.2 %	17.5 %
5000	1.4 %	2.2 %	17.9 %	20.7 %
5500	1.1 %	1.5 %	10.54 %	12.8 %
6000	1.1 %	1.6 %	4.0 %	11.7 %
6500	1.3 %	1.7 %	6.3 %	11.7 %
7000	1.8 %	3.7 %	11.6 %	15.6 %
7500	1.6 %	2.5 %	9.0 %	16.9 %
7900	1.5 %	2.5 %	13.2 %	26.2 %

Lower throttle settings also exhibit more run to run variation. At  $\frac{3}{4}$  throttle the run to run variation ranges from 0.3% to 6%. At  $\frac{1}{2}$  and  $\frac{1}{4}$  throttle run to run variation at most speeds ranges from 0.5% to 6%. However, some points exhibit exceptionally large run to run variation upwards of 30%. These points occur at low speeds (4000 rpm to 5000 rpm) and at high speeds (7900 rpm) and in all configurations. During operation, inconsistent engine operation between runs due to variable mixture preparation in the carburetor was observed, underlining the need for more reliable fuel metering for future testing in order to improve repeat-ability. Instrument uncertainty remains comparable to the WOT throttle results. Also, as at WOT, the total uncertainty at partial throttle is dominated by the run to run term.

Comparing the measuring spark plug and the stock plug as ignition sources, the two devices remain statistically indistinguishable across all speed ranges and throttle settings. Thus, a measuring spark may be used interchangeably with the stock plug. Statistically significant differences between the stock and modified engine heads are observable at  $\frac{3}{4}$  throttle and 5000 rpm, 5500 rpm, 7000 rpm to 7900 rpm, and at  $\frac{1}{2}$  throttle at 5000 rpm and 6500 rpm. Therefore, 25% of the test points, including two of the WOT points, exhibit a statistically significant difference between the two heads. This further indicates that the difference between the heads exists at all speeds, but is only statistically resolvable at some operating points due to large run to run uncertainty.

As the throttle setting decreases, so do peak pressures within the engine. As the peak pressures fall, the difference in IMEP between the measuring spark plug and flush mount transducer also decreases from 4% at WOT to between 1.5% and 2.5% at  $\frac{1}{4}$  throttle. Figure 12 shows the comparison of the two sensors at  $\frac{1}{4}$  throttle, similar to the WOT comparison in Figure 9. As the peak pressures in the cylinder decrease, the absolute differences between the two transducer signals also decrease. This result reinforces that a difference in linearity/gain is at the core of the disagreement between transducers. It remains unclear if the difference is the result of sensitivity to installation or the factory calibration, and which transducer is closer to the real value.



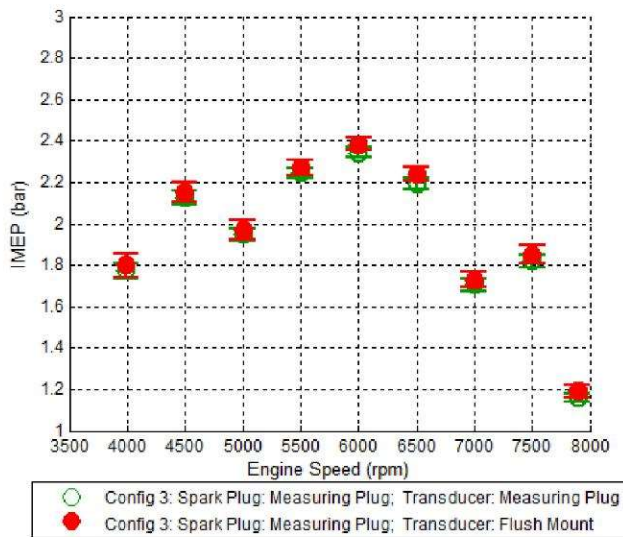


Figure 12. Comparison of measurements taken simultaneous with the measuring spark plug and flush mount transducers at  $\frac{1}{4}$  throttle with run to run variation removed.

## Summary/Conclusions

The results indicate that for the 3W-55i engine running at WOT in the stock configuration that cycle to cycle variability is less than 0.1%, insignificant compared to the run to run variation which is 1% to 4%. The instrument uncertainty, on the order of 0.5%, is also small compared to the run to run variation. Partial throttle tests yield typical run to run variations of 1% to 6%, with certain points exhibiting upwards of 30% run to run variation, while uncertainty from cycle to cycle variability remains less than 2% at 4000 rpm and less than 0.6% at higher speeds. In future work, uncertainty from run to run variation could be reduced using additional runs or by improving the control of engine equivalence ratio by installing a fuel injection system.

As a result, the performance differences in IMEP between the CM-6 stock spark plug that ships with the 3W-55i engine and the Kistler measuring spark plug are statistically insignificant compared the total uncertainty at the 95% confidence level. Thus, the two plugs may be interchanged without altering engine performance within the measurement capability of the setup. The performance differences between the head modified for a flush mount pressure transducer and the stock head are statistically different at 25% of the operating points, and likely persist at the remainder of the operating conditions despite being masked by run to run uncertainty. The statistically significant differences were observed speeds between 5000 rpm and 7900 rpm and  $\frac{1}{2}$  throttle to WOT. Thus, use of a modified engine head in this size class to accommodate a flush mount pressure transducer can have a significant impact on performance, even when careful attention is given to preserving the stock cylinder volume.

The results also show a 4% difference in IMEP as measured by the flush mount pressure transducer and the measuring spark plug transducer at WOT. This difference falls to the 1.5% to 2.5% level at  $\frac{1}{4}$  throttle. The difference is attributable to a calibration difference in the gain of the transducers. While there is insufficient data to assert which transducer is correct, one

may conclude that individual transducers could have as great of or more of an impact on the measurement accuracy as the run to run control variation of the test setup. The calibration difference could be further investigated through an in place calibration using a reference sensor.

Finally, the two largest sources of bias were identified as baselining the piezoelectric transducers and the selection of a thermodynamic loss angle. The former has no effect on the reported value of IMEP, although it will affect the absolute value of the peak pressure. Based on the pressures and speeds in this work and the range of possible loss angles, the selection of the loss angle could influence the measured value of IMEP by 1% to 4%. It will not affect the trends observed in this work since the same loss angle was used for all data reduction. Further work is planned to determine the relationship between the loss angle in small engines and their larger counter parts. The results of this work demonstrate that measuring spark plugs are comparable to the spark plugs for this small engine, and that they are preferable on the small scale to flush mount transducers, which require potentially performance modifying alterations to the cylinder head and combustion chamber.

## References

1. Bueno A. V., Velasquez J. A., and Milanez L. F., "Internal Combustion Engine Indicating Measurements," in *Applied Measurement Systems*, ed: InTech, 2012.
2. Taylor C. F., *The Internal Combustion Engine in Theory and Practice: Volume 1: Thermodynamics, Fluid Flow, Performance*, 2nd, revised ed. Vol. 1: First MIT Press, 1985.
3. Ferguson C. R. and Kirkpatrick A. T., *Internal Combustion Engines: Applied Thermosciences*. New York: John Wiley & Sons, Inc., 2000.
4. Heywood J. B., *Internal Combustion Engine Fundamentals*: McGraw Hill, 1988.
5. Brown, W., "Methods for Evaluating Requirements and Errors in Cylinder Pressure Measurement," SAE Technical Paper 670008, 1967, doi:10.4271/670008.
6. Foster, D., "An Overview of Zero-Dimensional Thermodynamic Models for IC Engine Data Analysis," SAE Technical Paper 852070, 1985, doi:10.4271/852070.
7. Lancaster, D., Krieger, R., and Lienesch, J., "Measurement and Analysis of Engine Pressure Data," SAE Technical Paper 750026, 1975, doi:10.4271/750026.
8. Pischinger R. and Krabnig G., "Problems of Pressure Indication in Internal Combustion Engines," in *COMODIA*, Tokyo, Japan, 1985.
9. Rogers, D.R., "Engine Combustion: Pressure Measurement and Analysis," (Warrendale, SAE International, 2010), doi:10.4271/R-388.
10. Ausserer, J., Litke, P., Groenewegen, J., Rowton, A. et al., "Development of Test Bench and Characterization of Performance in Small Internal Combustion Engines," 2013.



11. Wiegand, A., Miers, S., Blough, J., Kowalski, D. et al., "Development of a Micro-Engine Testing System," SAE Technical Paper [2012-32-0105](#), 2012, doi:[10.4271/2012-32-0105](#).
12. Wiegand A., "Conversion of a Micro, Glow-Ignition, Two-Stroke Engine from Nitromethane-Methanol Blend Fuel to Military Jet Propellant (JP-8)," M.S. in Mechanical Engineering, Michigan Technological University, 2012.
13. Menon S., Cadou C., and Moulton N., "Development of a Dynamometer for Measuring Small Internal-Combustion Engine Performance," *Journal of Propulsion and Power*, Vol. 23, pp. 194-202, 2007, doi:[10.2514/1.19825](#).
14. Menon S. and Cadou C., "Scaling of Miniature Piston Engine Performance Part 2: Energy Losses," *Journal of Propulsion and Power*, Vol. 29, pp. 788-799, July-August 2013, doi:[10.2514/1.B34639](#).
15. Menon S. and Cadou C., "Scaling of Miniature Piston-Engine Performance Part 1: Overall Engine Performance," *Journal of Propulsion and Power*, Vol. 29, pp. 774-787, July-August 2013, doi:[10.2514/1.B34638](#).
16. Menon S., "The Scaling of Performance and Losses in Miniature Internal Combustion Engines," Ph.D. Aeronautical Engineering, Department of Aeronautical Engineering, University of Maryland, 2010.
17. Menon S. and Cadou C., "Investigation of Combustion Processes in Miniature Internal Combustion Engines," *Combustion Science and Technology*, Vol. 185, pp. 1667-1695, 2013, doi:[10.1080/00102202.2013.829720](#).
18. Papac J. and Dunn-Rankin D., "In Cylinder Pressure and Combustion Measurements in a Miniature Reciprocating Engine," presented at the 4th Joint Meeting of the U.S. Section of the Combustion Institute, Philadelphia, PA, 2005.
19. Raine R. R., Moyle K., Otte G., and Robertson J., "A Cost-Effective Teaching and Research Dynamometer for Small Engines," *International Journal of Engineering Education*, Vol. 18, pp. 50-57, 2002, doi:[0949-149X/91](#).
20. Taylor C. F., *The Internal Combustion Engine in Theory and Practice: Volume 2: Combustion, Fuels, Materials, Design*, Revised ed. Vol. 2: MIT First Press, 1985.
21. Kline S. J. and McClintock F. A., "Describing Uncertainties in Single Sample Experiments," *Mechanical Engineering*, January 1953.
22. Moffat R. J., "Describing the Uncertainties in Experimental Results," *Experimental Thermal and Fluid Science*, pp. 3-17, 1988.

## Contact Information

Capt Joseph Ausserer  
[Joseph.Ausserer@wpafb.af.mil](mailto:Joseph.Ausserer@wpafb.af.mil)  
 (937)-904-4834

## Acknowledgments

The authors would like to acknowledge the support of everyone who consulted and assisted with the fabrication of the Small Engine Test Bench. They would like to specifically thank Mr. Dave Burris for designing and coding the LabView control and data acquisition program, and Mr. Rich Ryman for his assistance machining fixtures for the setup. Acknowledgement for funding is due to the Air Force Research Laboratory.

## Definitions/Abbreviations

**AKI** - anti-knock index  
**BSFC** - brake specific fuel consumption  
**BDC** - bottom dead center  
**CAD** - crank angle degree  
**CPR** - counts per revolution  
**DAQ** - data acquisition program  
**ECU** - engine control unit  
**GPB** - general purpose interface bus  
**HCCI** - homogenous charge compression ignition  
**ICE** - internal combustion engine  
**IR** - infrared  
**IMEP** - indicated mean effective pressure  
**PWM** - Pulse Width Modulation  
**RPA** - remotely piloted aircraft  
**SCP** - signal conditioning platform  
**SLPM** - standard liter per minute  
**TDC** - top dead center  
**VFD** - variable frequency drive  
**WOT** - wide open throttle

---

The Engineering Meetings Board has approved this paper for publication. It has successfully completed SAE's peer review process under the supervision of the session organizer. This process requires a minimum of three (3) reviews by industry experts.

This is a work of a Government and is not subject to copyright protection. Foreign copyrights may apply. The Government under which this paper was written assumes no liability or responsibility for the contents of this paper or the use of this paper, nor is it endorsing any manufacturers, products, or services cited herein and any trade name that may appear in the paper has been included only because it is essential to the contents of the paper.

Positions and opinions advanced in this paper are those of the author(s) and not necessarily those of SAE International. The author is solely responsible for the content of the paper.

ISSN 0148-7191

<http://papers.sae.org/2014-32-0007>

## **Appendix E**

**Paper:** Dynamic Friction Measurements on a Small Engine Test Bench

**Presented at:** SciTech 2015 in Kissimmee, Florida

**Citation:**

K. P. Horn, J. K. Ausserer, M. D. Polanka, P. J. Litke, and K. D. Grinstead, "Dynamic Friction Measurements on a Small Engine Test Bench," presented at the AIAA 53rd Aerospace Sciences Meeting, Kissimmee, Florida, AIAA 2015-1473, 5-9 January 2015.

# Dynamic Friction Measurements on a Small Engine Test Bench

Kevin P. Horn, \* Joseph K. Ausserer, <sup>†</sup> and Marc D. Polanka, <sup>‡</sup>

*Air Force Institute of Technology, WPAFB, OH 45433*

Paul J. Litke <sup>§</sup>

*Air Force Research Laboratory, WPAFB, OH 45433*

Keith D. Grinstead, Jr. <sup>§</sup>

*Innovative Scientific Solutions Inc., Dayton, OH 45440*

Research has shown that efficiency drops off as internal combustion engine size decreases due to thermal quenching losses. At a critical engine size, thermal quenching losses dominate in the combustion process, decreasing the amount of work produced produced by the combustion process. In small remotely piloted aircraft, engines are currently adapted from commercial off the shelf lawn-tool engines or hobbyist model airplane engines. The mission-specific needs of remotely piloted aircraft are demanding lighter, more efficient engines with increased performance from their propulsion systems. This results in a need for more accurate characterization of scaling models that predict engine efficiency for engines of this size class. This research effort seeks to characterize losses that influence engine scaling effects of three small two-stroke, single-cylinder internal combustion engines with displacements between 28 cc and 85 cc. The specific engines cover the critical transition region where thermal quenching losses are expected to dominate in the combustion process. Previously, IMEP, brake power and thermal loss data was collected for each of the three engines. A substantial difference was observed in mechanical efficiency between the engines suggesting significant friction losses in the system. New data was collected to quantify friction losses present in the drivetrain that measured brake power. The drivetrain friction was quantified by subtracting power produced by an electric motor spinning the drivetrain from power measured by the dynamometer. A linear fit model revealed the drivetrain absorbs 78.8 Watts per 1000 RPM across the entire speed range. This power draw was converted to a mean effective pressure for each of the three engines tested for direct comparisons of output normalized for engine size and power. Finally, brake power, fuel conversion efficiency and brake specific fuel consumption data was corrected for each engine and compared. The revised output data showed mechanical efficiencies for the 28 cc, 55 cc and 85 cc engines were 92.4%, 91.3% and 89.7%, respectively. Maximum fuel conversion efficiency for the three engines was calculated to be 14.9%, 15.4% and 18.3% at peak power, respectively.

## Nomenclature

$\dot{E}_{e,k}$	exhaust kinetic energy flux
$\dot{H}_e$	exhaust gas enthalpy flux
$\dot{H}_{e,ic}$	exhaust chemical enthalpy flux due to incomplete combustion
$\dot{H}_{e,s,a}$	exhaust sensible enthalpy entering through atmosphere

---

\*Masters Student in Aeronautical Engineering and AIAA Student Member.

<sup>†</sup>PhD Student in Aeronautical Engineering and AIAA Student Member.

<sup>‡</sup>Associate Professor of Aeronautical Engineering and AIAA Associate Fellow.

<sup>§</sup>Senior Research Engineer and AIAA Senior Member.

$\dot{m}_f$	fuel mass flow rate
$\dot{Q}_w$	heat transfer rate to combustion chamber wall
$\dot{Q}_{c,e}$	heat rejection rate to coolant in exhaust ports
$\dot{Q}_{cool}$	heat rejection rate to coolant
$\dot{Q}_{e,r}$	heat flux radiated from exhaust system
$\dot{Q}_{misc}$	sum of remaining energy fluxes and transfers
$\eta_f$	fuel conversion efficiency
$\eta_m$	mechanical efficiency
$\tau$	torque
$BMEP$	brake mean effective pressure
$BSFC$	brake specific fuel consumption
$C$	drivetrain friction slope coefficient
$F$	force
$FMEP$	friction mean effective pressure
$ICE$	internal combustion engine
$IMEP$	indicated mean effective pressure
$L$	stroke
$m_f$	mass of fuel
$MEP$	mean effective pressure
$N$	engine speed
$n_R$	engine cycles per power cycle
$P_b$	brake power
$P_i$	indicated power
$p_i$	indicated cylinder pressure
$P_{drivetrain}$	power lost to dynamometer drivetrain
$P_{pf}$	piston friction power
$P_{tf}$	total friction power
$PMEP$	pumping mean effective pressure
$PWM$	pulse width modulation
$Q_{LHV}$	fuel lower heating value
$r$	radial distance
$RPA$	remotely piloted aircraft
$t$	time
$TFMEP$	total friction mean effective pressure
$V_d$	displaced volume
$WOT$	wide open throttle

## I. Introduction

The internal combustion engine (*ICE*) operates on its ability to convert chemical potential energy in combustible fuel to usable work. This ability can be characterized and quantified by an engine's overall efficiency. Typically engine size has a positive correlation to output power. It follows that an engine with lower displacement will have a lower power output. The mass of similar engines will follow the displacement so that a smaller engine will have less mass. Efficiency of an engine will decrease with displacement as well. The power of a smaller engine will be reduced by both the decreased displacement and also increased losses. In the realm of aerospace propulsion, engine mass versus power produced is important to the design of a vehicle with mission specific capabilities. There exists a need to understand and characterize the losses that cause efficiency to diminish as engine size decreases. Models have been developed to predict engine performance and efficiency for engines with larger displacements but accurate models for engines of this size class do not exist. Effort needs to be made to adapt and validate these models for smaller engines.

Recently, the demand for small remotely piloted aircraft (*RPA*) has outpaced the development of propulsion systems. Typically, these small *RPA* use small two-stroke cycle *ICEs* that are commercially available off the shelf. These engines are often derived from hand-held lawn tools like weed trimmers or recreational model aircraft. The benefits of using commercial systems is their high availability and low cost although

system reliability and overall performance will decrease at higher altitudes typical of modern missions, limiting effectiveness.<sup>1</sup> Using these small engines in application they were not designed for leaves room for improvement in terms of performance and reliability. Furthermore, these commercially available engines are designed to operate on gasoline. In overseas environments, there is a desire to utilize heavy fuels such as JP-8 as they are more readily available in theater.<sup>1</sup> Therefore, there is a need to convert these small engines to run reliably and efficiently on heavier fuels.

Figure 1 shows how the fuel energy takes different routes through the engine.<sup>2</sup> This figure is notional but shows the complex interactions between the different energy forms. It becomes especially important to consider these energy pathways when analyzing the performance and losses in internal combustion engines. Improving loss determination does not involve discovering new forms of losses, but improving measurement and accounting of the energy pathways shown in this figure.

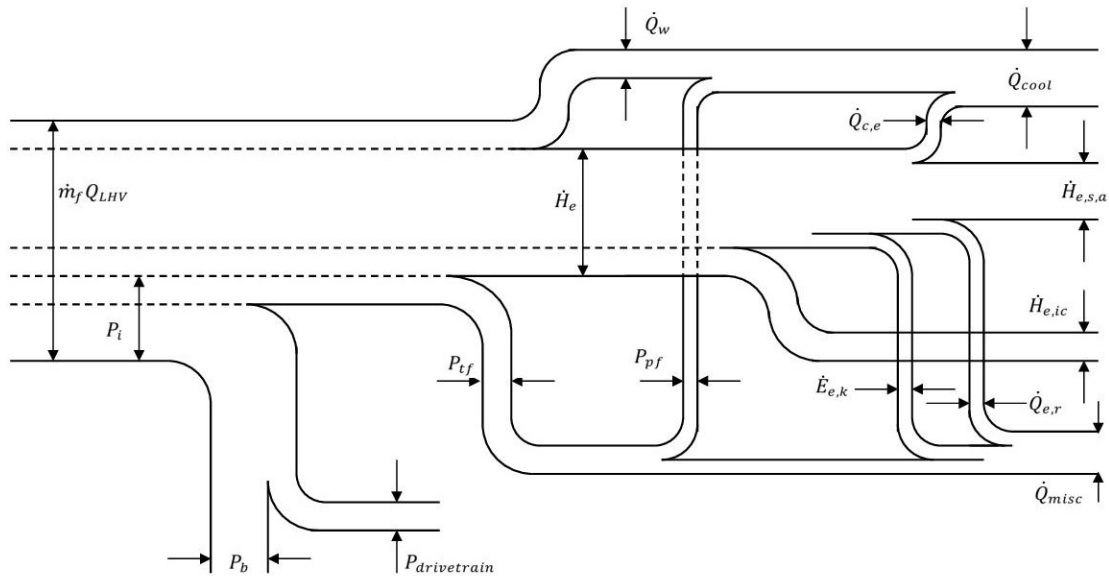


Figure 1: Diagram showing pathways taken by energy through the engine. (modified from Heywood<sup>2</sup>)

Each of the arrows on this figure represents a possible location to measure these energy pathways. Brake power is the useful power output and is represented on the figure as brake power ( $P_b$ ) which comes from indicated power ( $P_i$ ). In the test setup used here,  $P_b$  is further split by power lost to dynamometer drivetrain ( $P_{drivetrain}$ ) which is a parasitic power loss in the test setup. The rest of the energy in the engine is split and recombined to ultimately be released as heat rejection rate to coolant ( $\dot{Q}_{cool}$ ), exhaust sensible enthalpy entering through atmosphere ( $\dot{H}_{e,s,a}$ ), exhaust chemical enthalpy flux due to incomplete combustion ( $\dot{H}_{e,ic}$ ) and the sum of remaining energy fluxes and transfers ( $\dot{Q}_{misc}$ ). Some of these states can be measured easily and others prove more of a challenge. Understanding the relative magnitudes of each of these energy pathways and how they change as engine size decreases is required to develop improvements in small engine efficiency. It is known that fuel conversion efficiency of engines decreases with displacement however the mechanisms behind this phenomenon are not known as well as their interactions and what influences them.

Other groups have investigated performance and scaling of small and micro internal combustion engines. Cadou et al. from the University of Maryland have created a small engine dynamometer and used it to measure the performance and efficiency of small two stroke engines from 7.5 cc to 0.16 cc displacement.<sup>3</sup> They also investigated thermal loss pathways in these small two stroke engines. An apparatus was constructed that could motor the engine to determine friction mean effective pressure ( $FMEP$ ) while the engine was at operating conditions. They determined that engine friction power was a linear function dependent only on speed and developed a correlation to predict the power lost due to internal friction of an engine.<sup>4</sup> This represents some of the most comprehensive work in the literature on the subject of small engines, however the engines of interest to Cadou et al. all fall below the range of displacements investigated in this effort.

Table 1 shows the specifications and measured performance of three two stroke engines with displacements of 28 cc to 85 cc as collected by Rowton.<sup>5</sup> These engines were run on a dynamometer with in cylinder pressure measurements to determine mean effective pressure ( $MEP$ )s for each engine. Large differences



between the total friction mean effective pressure ( $TFMEP$ ) was seen between the engines despite similar design and construction. The differences between  $TFMEP$  in these engines indicates there may be other factors influencing the measurements.

Table 1: Engine geometric and performance parameters<sup>5</sup>

Engine	3W-28i	3W-55i	3W-85Xi
Displacement (cc)	28	55	85
Rated power (kW)	2.5	3.9	6.8
Mass (kg)	1.21	1.94	2.40
Bore (cm)	3.6	4.5	5.1
Stroke (cm)	2.8	3.5	4.1
Compression Ratio	10:1	10:1	10:1
$IMEP$ (kPa)	645	630	584
$BMEP$ (kPa)	426	489	468
$TFMEP$ (kPa)	219	141	116
$\eta_m$	68.1%	77.6%	80.1%

Previous work has sought to track the energy through the engine with the goal of accounting for all of the energy as it enters and exits the engine. Efforts have been made to measure each of the energy pathways shown in Figure 1. One such attempt was accomplished by Rittenhouse<sup>6</sup> and is shown in Figure 2. The study quantified several of the pathways, but needed to make assumptions about many to complete the analysis. Even with the assumptions, the summation of these paths does not reach 100%. This indicates that not all of the fuel energy entering the engine was accounted for. As seen in Figure 2, upwards of 20% of the energy is unaccounted for. Some of this energy is likely found in higher scavenging losses than estimated and in higher levels of incomplete combustion for these small engines than indicated in Figure 2. The data shown was taken from estimates for these values from the literature, originally developed for larger engines.

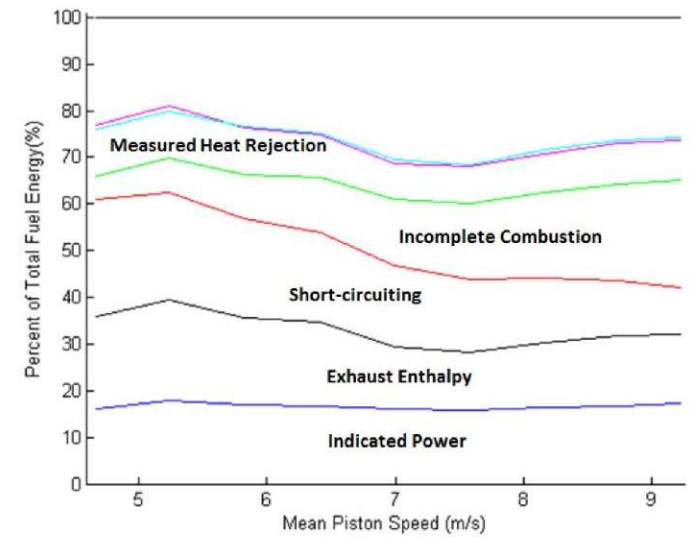


Figure 2: Plot showing estimates of total energy leaving the engine versus mean piston speed for a 55 cc two stroke engine.<sup>6</sup>

This work attempts to quantify the friction losses in the drivetrain in an attempt to generate an improved understanding of how indicated power is converted to brake power in the engine. It was hypothesized that a significant amount of friction existed due to the spinning components in the dynamometer drivetrain. In

Figure 1, this frictional loss would be envisioned as an additional power extraction from the brake power output before the measurement point as denoted by  $P_{drivetrain}$ . The power lost in the drivetrain should be similar between the three engines and would therefore have a larger effect on smaller engines. Refinement of brake power measurements will not move the sum of the energy pathways towards 100% since  $P_i$  is not affected, but it will improve efficiency and power output estimates. One specific issue to be addressed is that in Table 1, the total friction mean effective pressure decreases with increasing engine size. Specifically, the 28 cc engine has a  $TFMEP$  that is 89% larger than that of the 85 cc engine. If a large amount of power is lost in the drivetrain, one would expect the true values of  $TFMEP$  without drivetrain friction to be smaller and roughly equivalent between three similar engines. Quantifying this parasitic power draw will allow the true brake power of the engine to be known. With this additional information, the revised brake power estimates and the analysis of the thermal losses from previous works will be revisited supporting the goal of understanding scaling effects in small internal combustion engines. Improvements in thermal efficiency will only be made possible through careful analysis of the loss mechanisms present and their interactions. The next phase of research attempted to quantify losses present in the dynamometer-drivetrain system to ensure measurements made were representative of the brake power produced by the engine.

### I.A. Quantifying Friction

To understand performance, it is desired to recast engine performance parameters into values that can be directly compared between engines without having to account for displacement differences. The typical parameter used for this type of comparison in engines is brake mean effective pressure ( $BMEP$ ), which is defined in Equation (1).<sup>2</sup>

$$BMEP = \frac{P_b n_R}{V_d N} \quad (1)$$

where  $P_b$  is brake power,  $n_R$  is the number of engine revolutions per cycle,  $V_d$  is displaced volume and  $N$  is engine speed. Indicated mean effective pressure ( $IMEP$ ) is defined as the mean cylinder pressure over one complete cycle. Cylinder pressure is directly measured via either a spark plug pressure transducer or a flush mount pressure probe. Average pressure is calculated numerically in Equation (2).

$$IMEP = \frac{\sum_{k=1}^n p_i}{n} \quad (2)$$

where  $p_i$  is indicated cylinder pressure. Finally,  $FMEP$  can be calculated in Equation (3).<sup>7</sup>

$$FMEP = IMEP - (BMEP + PMEP) \quad (3)$$

Therefore,  $FMEP$  represents the work lost due to friction in the engine and pumping mean effective pressure ( $PMEP$ ) represents pumping losses in the intake system. For two stroke engines, the power lost during crankcase compression of the fresh charge and its transfer into the cylinder.  $PMEP$  is actually higher with increasing throttle, which is why the most efficient point for a two-stroke is often at throttled conditions, and why friction losses in a two stroke may decrease when the engine is throttled. With these equations,  $FMEP$  can be calculated using brake power from the dynamometer and the in-cylinder pressure measurements. The losses due to  $PMEP$  are functionally similar to  $FMEP$  in that they both reduce the power output of the engine, so the  $TFMEP$  in Equation (4) includes  $PMEP$ .<sup>8</sup>

$$TFMEP = IMEP - BMEP \quad (4)$$

Finally we can define mechanical efficiency as the ratio of  $BMEP$  and indicated mean effective pressure ( $IMEP$ ) in equation (5).<sup>2</sup>

$$\eta_m = \frac{BMEP}{IMEP} \quad (5)$$

Two more terms can be used to understand an engine's ability to extract energy from fuel. An engine's brake specific fuel consumption ( $BSFC$ ) is the amount of fuel burned to produce a unit power for a unit time and is defined in Equation (6).<sup>2</sup> It is useful when comparing engines of different sizes since it can be

calculated easily from experimental data and can be used to estimate fuel requirements when an engine is scaled.

$$\text{BSFC} = \frac{\dot{m}_f}{P_b t} \quad (6)$$

where  $m_f$  is mass of fuel and  $t$  is time. Finally, fuel conversion efficiency ( $\eta_f$ ) is the ratio of power produced to fuel energy consumed by the engine and is defined in Equation (7).<sup>2</sup>

$$\eta_f = \frac{P_b}{\dot{m}_f Q_{LHV}} \quad (7)$$

where  $\dot{m}_f$  is the fuel mass flow rate and  $Q_{LHV}$  is the fuel lower heating value.

## I.B. Modeling Friction

Losses inherent in two stroke engines have been previously investigated in literature. Blair created a simple two-stroke engine performance modeling code that sought to predict equilibrium conditions in 250 cc and 380 cc single cylinder two-stroke motorcycle engines.<sup>7</sup> In this model, the work done on the piston was represented by *MEP*. The losses are encapsulated in *FMEP* as shown in Equation (8).

$$\text{FMEP} = \frac{6LN}{1000} \quad (8)$$

where units are  $lb/in^2$  and  $L$  is stroke in inches. This simple model estimates *FMEP* as a linear function dependent only on speed. It is important to note this model provides data for engines roughly ten times larger than those that are being studied and may not necessarily apply to engines under 100 cc.

Heywood and Sher choose to represent *FMEP* here as *TFMEP* which includes *PMEP*. Through an analysis of published engine friction data, a quadratic model for *TFMEP* was proposed as a function of speed for an engine at a given load<sup>8</sup>

$$\text{TFMEP} = a + b\left(\frac{N}{1000}\right) + c\left(\frac{N}{1000}\right)^2 \quad (9)$$

where a, b and c are calibration constants for a specific engine and load setting. Calibration constants are available for two and four stroke engines with displacements of 325 cc to 4250 cc.<sup>8</sup> Cadou and Menon also have developed calibration constants for two stroke spark ignition and glow engines under 15 cc.<sup>4</sup> These models assume a mixture of surface friction and hydrodynamic friction from lubrication. The amount of friction would be dependent on amount of surface area of the friction surfaces and the displacement of the engine. The ratio of these changes with displacement so the coefficients developed for larger engines would not scale directly with either displacement or swept area in the engine. Again, there remains a need to collect data at smaller displacements to develop friction models that can be applied to the small two stroke engines studied here.

## II. Test Setup

An engine test bench has been built to characterize the performance and scaling relationships among internal combustion engine sized in the critical surface area to volume ratio regime where losses start to dominate. The bench has demonstrated the capability to accurately measure critical operating parameters to determine an engine's performance and efficiency. These parameters include engine speed, torque, brake power, air and fuel flow rates, air intake temperature and pressure, exhaust gas temperature and pressure, ambient air pressure, and in-cylinder combustion pressure measurements. Figure 3 depicts the various components used in the test bench. The fuel system design (shown in green) is pressurized with an external nitrogen supply. The fuel used to run the engine is a primary reference fuel; a blend of 92:8 iso-octane to n-heptane by volume for an overall octane rating of 92. A primary reference fuel provides a constant, predictable octane rating while virtually eliminating the possibility of additives or contaminants. Lubricating oil is added to the fuel mixture in a 1:100 ratio. In order to maintain consistency over several runs, intake air temperature can be modulated via an air-to-water heat exchanger. The water temperature is held constant at 25° C using a chiller/heater.





offset force will not sum to a moment, however the vibrations did introduce significant noise into the data collected. This noise had a peak to peak magnitude greater than the torque measured.

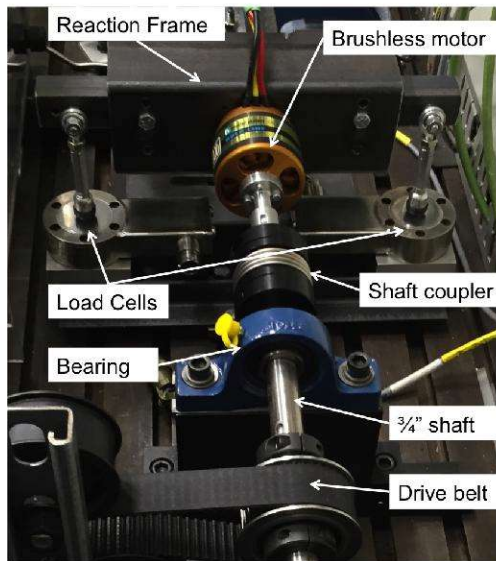


Figure 4: First generation reaction cradle showing load cells and connection linkages.

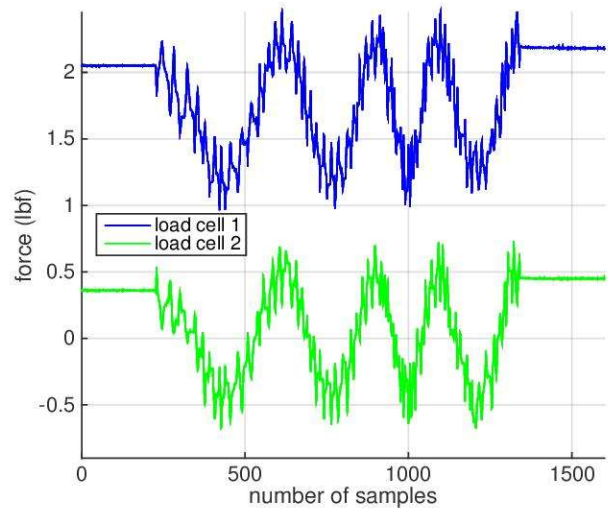


Figure 5: Plot of force measurements showing torque potential in motor poles and cyclic static loading.

With a better understanding of the challenges posed by the vibrational nature of the motor, shaft, and the difficulties of measuring a torque, a new device was designed to prevent the load cell from measuring translational motion in the vertical direction. A diagram of the friction testing setup is shown in Figure 6 and a picture of the setup showing the detail of the motor, load cell and linkage in Figure 7. The motor was rigidly mounted on a stationary shaft secured by two pillow block bearings to fix the motor except in axial rotation. Finally, a single load cell with a  $\pm 10$  lbf capacity, connected via an arm to the motor, was placed 6" from the centerline of rotation. The torque of the spinning motor was resisted by a reaction force measured in the load cell. Combined with the speed information from the dynamometer, the power applied to the drivetrain was calculated. Figure 8 shows the reduced cyclic loading due to vertical displacement. It is important to note that the torque due to the motor poles has a larger effect since that torque was resisted by only one load cell instead of two in the previous setup.

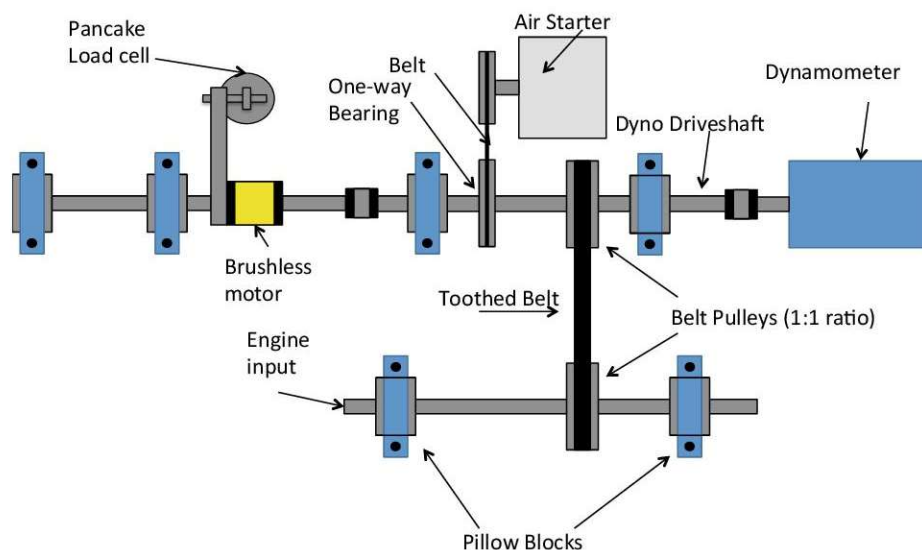


Figure 6: Small engine test bench showing friction testing setup.



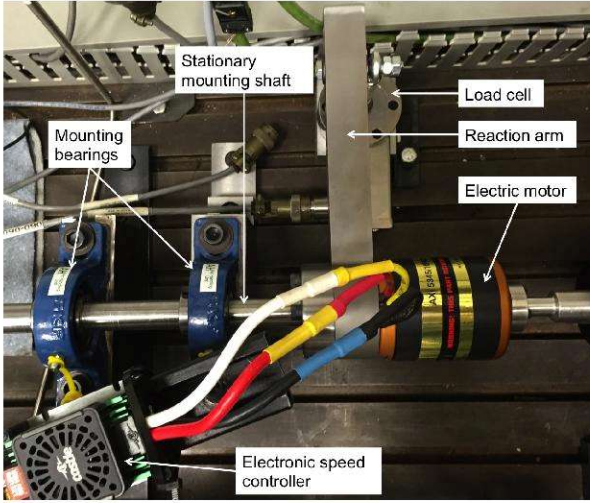


Figure 7: Second generation reaction cradle showing load cell and connection linkage.

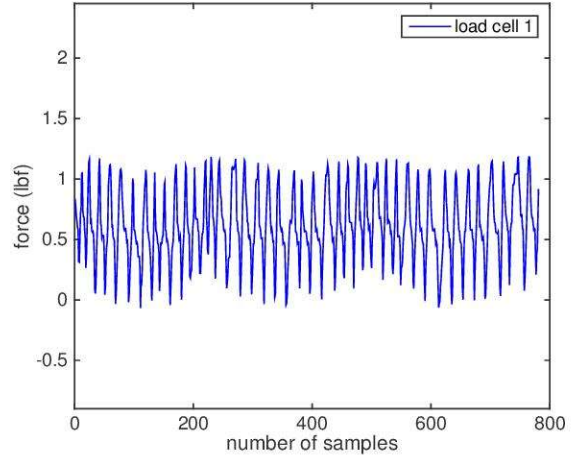


Figure 8: Plot of force measurements showing torque potential in motor poles on redesigned hardware.

The torque ( $\tau$ ) of the motor is calculated in Equation (10)

$$\tau = \mathbf{F}_{\text{loadcell}} \times \mathbf{r} \quad (10)$$

where  $\mathbf{r}$  is the length of the lever arm, in this case 1/2 foot. Power is calculated in Equation (11).

$$\mathbf{P}_{\text{motor}} = \frac{\tau \mathbf{N}}{5252} \quad (11)$$

The result is given in units of horsepower where speed is measured by the dynamometer as RPM. With motor power determined, the difference in power measured at the electric motor and the dynamometer can be found. Units were converted to SI after data collection for the analysis.

Testing was conducted to be consistent with the procedure used to collect data when operating *ICEs*. Each data point represents the average of 10 seconds of operation at a constant speed, governed by the dynamometer. Motor load is determined by a pulse width modulation (*PWM*) servo signal sent to the motor controller. A setting of 90% duty cycle was typical. Lithium polymer chemistry with a 4.2 volt nominal voltage per cell were used to power the motor. The optimum operating speed of the brushless motor is battery voltage dependent so combinations of batteries were used to reach the desired speed. Battery packs made of 4, 5 and 6 Lithium polymer cells were used, which could combined as pairs for 8, 10 and 12 cell packs.

### III. Results

Testing was conducted from 3000 RPM to 7000 RPM. This encompasses nearly the entire operation range of the 3W engines on the test bench. Data was recorded at 10 Hz, producing 100 samples which were then averaged. The difference in measured power between the electric motor and dynamometer is shown in Figure 9.

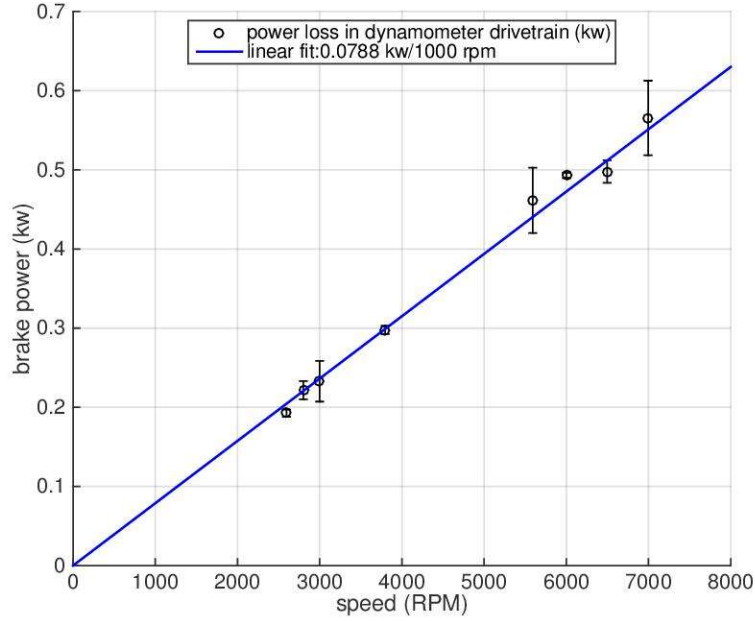


Figure 9: Plot showing power difference between electric motor and dynamometer with trend line.

A linear fit crossing at the origin was found by dividing the sum of the power values by the sum of the speed values. This produced a slope of 78.8 Watts per 1000 RPM. This curve quantifies friction in the drivetrain; it does not represent internal friction of an engine. A linear, zero crossing function was expected since this friction was largely due to rolling friction in the bearings. It was suspected that there may be some second order effects due to hydrodynamic friction from the heavy grease used to lubricate the bearings but this was not observed. Data points with larger error bars were generally taken at points of higher vibration. Some aliasing occurred due to the high frequency of the vibration so additional tests were conducted.

With a simple function that determines friction power losses with respect to speed, a correction can be applied to data previously collected for the 3W engines. Recalling Equation (1),  $MEP$  is a linear function of power and speed for any given engine. Friction mean effective pressure can be considered to be any frictional losses that are not measured as brake power. We can therefore recast  $FMEP$  for an engine of known type and displacement in terms of the measured drivetrain loss as seen in Equation (12).

$$FMEP_{\text{drivetrain}} = \frac{C n_R}{V_d} \quad (12)$$

Where the value  $C$  is the slope of the curve fit line seen in Figure 9 and  $n_r$  is 1 for two-stroke engines. Calculating a friction mean effective pressure in this manner reduces the power loss in the drivetrain for a given engine to a single value for all operating speeds. The  $FMEP_{\text{drivetrain}}$  value would have been previously captured as  $TFMEP$  but now should be added to engine  $BMEP$  to increase measured power output. Table 2 shows the  $FMEP_{\text{drivetrain}}$  values calculated for each engine. The values for  $IMEP$  are carried over from Table 1 and the drivetrain friction is subtracted from the previous  $TFMEP$  values to determine a new  $TFMEP$  for each engine.

Table 2: Engine mean effective pressures recalculated with drivetrain friction included

Engine	3W-28i	3W-55i	3W-85Xi
$FMEP_{drivetrain}$ (kPa)	153	78	50
$IMEP$ (kPa)	645	630	584
$BMEP$ (kPa)	595	575	524
$TFMEP$ (kPa)	49	55	60
$\eta_m$	92.4%	91.3%	89.7%
<i>Improvement</i>	39.8%	17.7%	11.9%

Utilizing the new friction correction, mechanical efficiency is approximately 91% for all three engines compared to those values in Table 1 where  $TFMEP$  decreased with engine size. Mechanical efficiency is expected to be similar for three similar engines. These engines do not have accessories to drive like water pumps, oil pumps, or alternators so mechanical efficiency is a measure of the internal friction of the engine. The trend of increasing  $TFMEP$  agrees with the model presented in Equation (8) in that  $FMEP$  increases with increasing stroke, assuming pumping losses are minimal.

Correcting data already recorded for the three engines involves applying the correction as a function of engine speed at each data point. Engine power was corrected in Equation (13) using the correction factor  $C$  previously found.

$$P_b(N) = P_b(N) + CN \quad (13)$$

Figure 10 shows the corrected and uncorrected brake power values for all three engines across the operating range. It should be noted that the magnitude of increase for each engine is the same as the other engines at the same speed. The correction as a percentage of measured power is much larger for the 28 cc engine than the 85 cc engine.

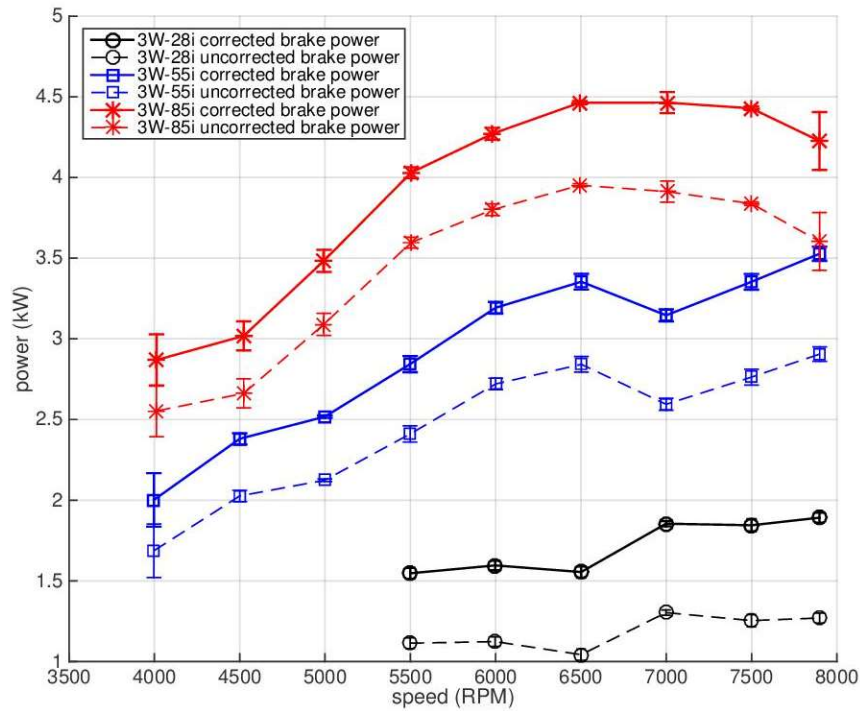


Figure 10: Brake power for three 3W two stroke engines showing corrected and uncorrected values.



Fuel conversion efficiency allows better insight into the effect of the correction on each engine's performance data. Since this value is a measure of the brake power over the fuel consumed, a ratio of corrected brake power to uncorrected brake power can be applied to the data to correct it at every point, as in Equation (14).

$$\eta_f(\mathbf{N}) = \eta_f(\mathbf{N})(\text{uncorrected}) \times \frac{\mathbf{P}_b(\mathbf{N})(\text{corrected})}{\mathbf{P}_b(\mathbf{N})(\text{uncorrected})} \quad (14)$$

Brake fuel conversion efficiency will be higher at every point and the magnitude of correction depends on the percentage of power absorbed by the drivetrain at a given speed. Figure 11 shows corrected and uncorrected brake fuel conversion efficiency for each of the three engines across the operating range. The 28 cc and 55 cc engines overlap at 6500 and 7000 RPM where they did not before the correction. On average the 28 cc engine is less efficient than the 55cc engine but after the correction was applied, the deficit shrank significantly. Again this is attributed to the magnitude of increase that was applied to brake power numbers for the 28 cc engine. The 85 cc engine had the highest efficiency.

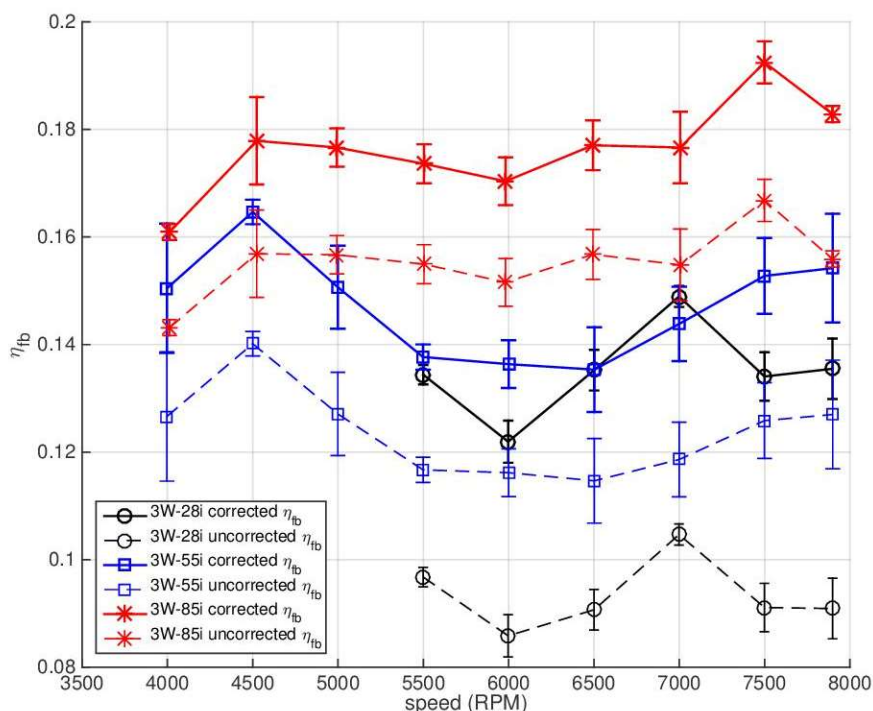


Figure 11: Fuel conversion efficiency for three 3W two stroke engines showing corrected and uncorrected values.

Brake specific fuel consumption can also be corrected, but the inverse must be applied as shown in Equation (15).

$$\text{BSFC}(\mathbf{N}) = \text{BSFC}(\mathbf{N})(\text{uncorrected}) \times \left[ \frac{\mathbf{P}_b(\mathbf{N})(\text{corrected})}{\mathbf{P}_b(\mathbf{N})(\text{uncorrected})} \right]^{-1} \quad (15)$$

Figure 12 reveals similar trends where the improved *BSFC* results in lower value for the corrected cases. The 28 cc engine had a minimum *BSFC* of 545  $g/(kW - hr)$ , the 55 cc engine had a minimum *BSFC* of 493  $g/(kW - hr)$  and the 85 cc engine had a minimum *BSFC* of 423  $g/(kW - hr)$ .

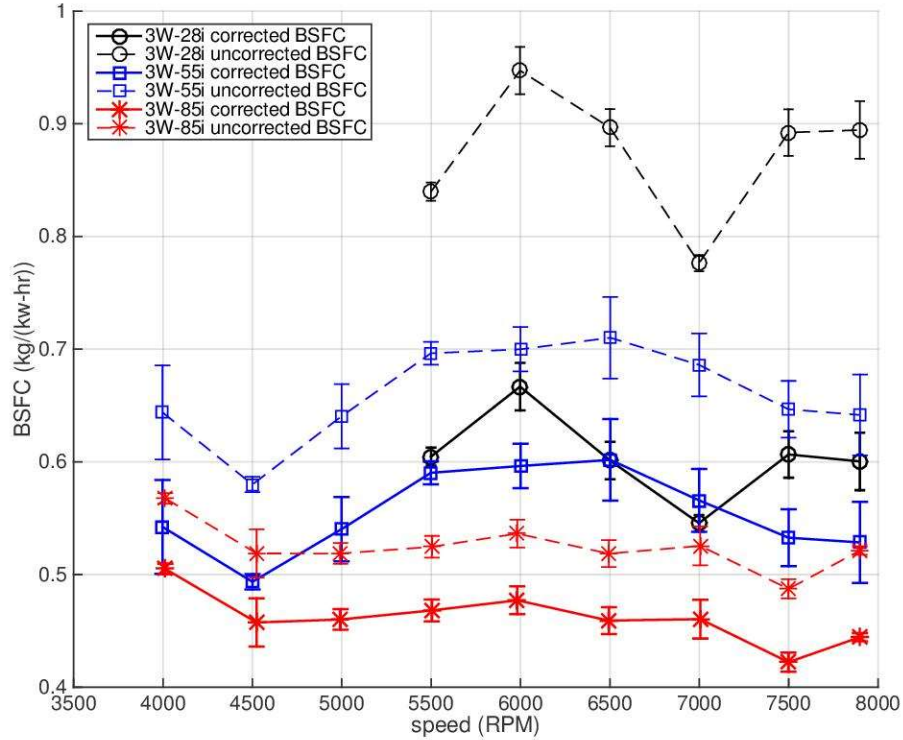


Figure 12: Brake specific fuel consumption for three 3W two stroke engines showing corrected and uncorrected values.

## IV. Conclusion

A friction measurement device was designed to quantify losses present in an engine test bench designed to measure performance of small two stroke engines. A brushless electric motor was mounted to a fixture that fixed it in all axes except axial rotation. The rotation was resisted by a load cell which measured a torque. Power produced by the electric motor was calculated and subtracted from the power measured at the dynamometer to determine the power lost in the drivetrain. The power required to spin the shafts was significant and a power correction factor was developed. The corrected data now reflects that these three engines are geometrically similar. Mechanical efficiency for the three engines are all very close, averaging 91% where before they ranged from 68% to 80%. Measured brake power, brake fuel conversion efficiency and brake specific fuel consumption improved at all operating speeds. This updated data and correction factor, when applied to future testing, will allow better understanding of the performance of these small two stroke engines. This investigation has eliminated one of the unknown energy pathways enabling an accurate measurement of brake power.

Future work will focus on the remaining areas where the losses have not been fully quantified in this size class such as short circuiting and incomplete combustion. Testing will be conducted to quantify these phenomena by analyzing exhaust gas species using a variety of methods. Gas chromatography-mass spectroscopy and Fourier transform infrared spectroscopy will be applied to determine precise species concentrations in the exhaust gas flow on both time-averaged and crank angle degrees resolved measurements.

## Acknowledgments

The authors would like to thank all involved with setting up and supporting the small engine test bench facility. The authors would specifically like to thank Mr. Rich Ryman for his machining expertise and

support, Mr. Dave Burris for designing and supporting the LabVIEW engine control program, Mr. Jacob Baranksi for use of his test supplies and equipment, and the AFRL/RQT machine shop for producing hardware ahead of schedule on short notice.

## References

- <sup>1</sup>Wilson, C. W., *Performance of a Small Internal Combustion Engine Using N-Heptane and Iso-Octane*, Master's thesis, Air Force Institute of Technology, March 2010.
- <sup>2</sup>Heywood, J., *Internal Combustion Engine Fundamentals*, Automotive technology series, McGraw-Hill Education, 1988.
- <sup>3</sup>Menon, S. and Cadou, C., "Scaling of Miniature Piston-Engine Performance, Part 1: Overall Engine Performance," *Journal of Propulsion and Power*, Vol. 29, No. 4, 2013.
- <sup>4</sup>Menon, S. and Cadou, C., "Scaling of Miniature Piston Engine Performance Part 2: Energy Losses," *Journal of Propulsion and Power*, Vol. 29, No. 4, 2013.
- <sup>5</sup>Rowton, A. K., *Measuring Scaling Effects in Small Two-Stroke Internal Combustion Engines*, Master's thesis, Air Force Institute of Technology, June 2014.
- <sup>6</sup>Rittenhouse, J. A., *Thermal Loss Determination for a Small Internal Combustion Engine*, Master's thesis, Air Force Institute of Technology, March 2014.
- <sup>7</sup>Blair, G., "Prediction of two-cycle engine performance characteristics," Tech. rep., SAE Technical Paper, 1976.
- <sup>8</sup>Heywood, J. B. and Sher, E., *The two stroke cycle engine, its development, operation and design*, Taylor and Francis, 1999.
- <sup>9</sup>Ausserer, J. K., Litke, P. J., Groenewegen, J.-R., Rowton, A., Polanka, M. D., and Grinstead, K., "Development of Test Bench and Characterization of Performance in Small Internal Combustion Engines," Tech. rep., SAE Technical Paper, 2013.
- <sup>10</sup>Rowton, A. K., Ausserer, J. K., Grinstead, K., Litke, P. J., and Polanka, M. D., "Measuring Scaling Effects in Small Two-Stroke Internal Combustion Engines," Tech. rep., SAE Technical Paper, 2014.

## **Appendix F**

**Paper:** Quantification of Short-Circuiting and Trapping Efficiency in a Small Internal Combustion Engine by GC-MS and GC-TCD

**Presented at:** SETC 2015 in Osaka, Japan

**Citation:**

J. K. Ausserer, K. P. Horn, M. D. Polanka, P. J. Litke, and K. D. Grinstead, "Quantification of Short-Circuiting and Trapping Efficiency in a Small Internal Combustion Engine by GC-MS and GC-TCD," presented at the 2015 SAE Small Engine Technology Conference, Osaka, Japan, SAE Technical Paper 2015-32-0716, 17 November 2015, doi: 10.4271/2015-32-0716.

# Quantification of Short-Circuiting and Trapping Efficiency in a Small Internal Combustion Engine by GC-MS and GC-TCD

Joseph K. Ausserer, Kevin P. Horn, Marc D. Polanka

Air Force Institute of Technology

Paul J. Litke

Air Force Research Laboratory

Keith D. Grinstead Jr.

Innovative Scientific Solutions Incorporated

Copyright © 2015 SAE Japan and Copyright © 2015 SAE International

## ABSTRACT

Loss mechanisms in 1-10 kW spark-ignition, two-stroke engines may be grouped into five categories: thermal losses, frictional losses, sensible enthalpy in the exhaust gases, incomplete combustion, and short-circuiting of fresh fuel and air mixture. These loss mechanisms cause small two-stroke engines to have fuel conversion efficiencies 50%-70% lower than similar larger engines. Previous studies of loss scaling in small engines have estimated the short-circuiting using heuristics derived for larger engines or grouped it with other combustion losses to complete the energy balance. This work describes and compares two methods for measuring short-circuiting on a commercially available, two-stroke, naturally aspirated, spark ignition engine with 55 cm<sup>3</sup> displacement. One method used oxygen as an analyte (the Watson method), nitrogen as an internal standard, and gas chromatography with a thermal conductivity detector for quantification. While the Watson method is historically proven, it only works under globally rich combustion conditions. The other method, selected for its potential to work under lean combustion conditions, used iso-octane as an analyte, argon as an internal standard, and gas chromatography for separation with mass spectrometry for identification and quantification. The iso-octane method yielded results within 4% of the Watson method, a difference that is statistically indistinguishable at the 95% confidence level. Therefore, despite the larger uncertainty of the iso-octane method (10%-15% versus 3%-5% for Watson's method), the iso-octane method offers a valid method for determining short-circuiting under lean combustion conditions.

## INTRODUCTION

The fuel conversion efficiency of an internal combustion engine [ICE] represents its ability to convert raw fuel into useful work. The fuel conversion efficiency in conventional automotive engines typically ranges from 30%-40% [1:842]. However, for small ICEs, measured efficiencies are often at SETC2015

least 50-70% lower than conventional engines [2] and some micro glow engines have efficiencies as low as 3%-5% [3]. As discussed in Rowton *et al* [2], loss mechanisms such as heat transfer, friction, and incomplete combustion (due to quenching of the flame) will scale with the surface area of the combustion chamber while the released energy will scale with the combustion volume. It follows that these loss mechanisms as a percentage of fuel energy will increase relative to the energy released during combustion with decreasing engine size. Other loss mechanisms such as short-circuiting are driven primarily by engine design. To complete the energy balance and understand the loss pathways in an engine, quantification of both types of loss mechanisms is necessary.

Data available in the literature indicates not only that the relative impact of losses increase with decreasing size, but also that the dominant loss mechanisms also change. Menon and Cadou [4] investigated the loss mechanisms in nine micro glow engines less than 750 W and compared the results to data available from Heywood [1:674] for conventional automotive engines. They determined that the largest loss was incomplete combustion, followed by heat transfer, sensible exhaust enthalpy, and friction. In the study, short-circuiting was lumped in with incomplete combustion losses. Meanwhile losses calculated from the automotive engine data followed a nearly opposite trend, with sensible exhaust enthalpy being the largest loss, followed by heat transfer from the engine, friction, and finally incomplete combustion. The three engines considered herein are larger than those considered by Menon and Cadou, but smaller than the conventional size automotive engines in Heywood. Thus they offer an opportunity to understand what happens to these losses in the transitional size regime.

## RESEARCH OBJECTIVES

This work is part of a larger effort to quantify the loss mechanisms in a family of geometrically similar 1-10 kW



two-stroke engines. An understanding of how loss mechanisms scale across the 1-10kW size class will offer insight into what mechanisms drive the observed decrease in fuel conversion efficiency and how/if the losses may be managed or mitigated. As a loss mechanism, short-circuiting in two-stroke engines is more dependent on engine and port design than size. Nevertheless, it is necessary to understand the short-circuiting losses both to complete the energy balance and to disentangle it from other loss mechanisms such as incomplete combustion. Previous efforts have measured the engine brake power [2], thermal losses [2, 5] and engine friction [2, 6]. The objective of this work is to develop and validate the capability to refine the existing energy balances on the selected engines by measuring the short-circuiting as well as the identification and quantification of the losses associated with the primary unburned hydrocarbons (UHCs) in the exhaust. Therefore, this work utilized a combination of gas chromatography (GC) for separation, and mass spectrometry (MS), a thermal conductivity detector (TCD), and a flame ionization detector (FID) for identification and quantification.

## PREVIOUS WORK

Historically, tracer gas methods have been a common technique for measuring short-circuiting in two-stroke engines. A tracer gas method relies on a substance that is added in a known quantity in the fresh charge and either destroyed completely during combustion or created in proportion to combustion. It also assumes that the tracer is resistant to decomposition between the exhaust port and the analytic instrument. By comparing the amount of tracer in the fresh charge and the exhaust, the amount of fresh charge lost to short-circuiting may be determined. Watson developed what is arguably the first gas tracer method in 1908 [7]. In Watson's method, the engine was operated rich and oxygen, though native to the charge, was used as the "tracer" gas. Due to the rich operating condition, all of the oxygen present in the exhaust was assumed to come from short-circuited charge. Measuring the mole fraction of oxygen in the exhaust ( $y_{O_2,ex}$ ) allows the calculation of trapping efficiency as in Equation (1), provided the molecular mass of the fresh charge ( $MW_{fc}$ ) and exhaust ( $MW_{ex}$ ) may be estimated or calculated.

$$\eta_{tr} = 1 - \frac{y_{O_2,ex} MW_{fc}}{y_{O_2,fc} MW_{ex}} \quad (1)$$

If the molecular weight of the fresh charge and exhaust gases are approximately equal then Equation (1) reduces to Equation (2), as described by Heywood and Sher [8:90].

$$\eta_{tr} = 1 - \frac{y_{O_2,ex}}{y_{O_2,fc}} \quad (2)$$

An alternative is to measure the oxygen concentration relative to an inert, internal standard, such as nitrogen or argon. In the case of the former, Equation (1) becomes Equation (3).

$$\eta_{tr} = 1 - \frac{\left(\frac{y_{O_2,ex}}{y_{N_2,ex}}\right)}{\left(\frac{y_{O_2,fc}}{y_{N_2,fc}}\right)} \quad (3)$$

Oxygen, however, works as an analyte for short-circuiting only during rich combustion. In lean combustion, there is no way to distinguish oxygen trapped in the cylinder and not consumed during combustion from short-circuited oxygen. Additionally, oxygen may continue to react in the exhaust manifold and sampling system [8:90-91].

Traditionally, small ICE's have operated globally rich for combustion stability and cooling. Recently, more stringent emissions regulations and a desire to develop more fuel efficient engines have driven research into lean operation in such engines [9]. The larger effort this work is a part of includes an interest in lean operation to extend the range and endurance of remotely piloted aircraft. Thus while, Watson's method offers a historically proven method for rich conditions, a second method for lean conditions is also required.

To handle lean operation, researchers have developed a number of other approaches. Some methods utilize a pair of analytes such as CO<sub>2</sub> and O<sub>2</sub> for lean and rich combustion conditions, respectively [10, 11]. Others introduce a trace quantity of a chemical such as monomethylamine [12-14] that is distinct from the fuel, destroyed entirely during combustion, and stable in exhaust. For any analyte destroyed during combustion Equations (1)-(3) will work, where the oxygen is simply replaced with the analyte of interest.

The quantity of analyte in the fresh charge is typically available from measurements of intake air and fuel flow rates. Measurement of the exhaust composition presents three challenges: separation, positive identification, and finally, quantification. Measuring the UHCs in the exhaust (for the calculation of exhaust gas composition and properties) presents similar challenges.

GC has been utilized extensively in ICE research to separate exhaust gases. However, GC is only a separation method and must be combined with a detector to identify and/or quantify the effluent. Most GC detectors such as flame ionization detectors (FID) and thermal conductivity detectors (TCD) only quantify the effluent without additional separation. Identification is limited to matching the retention time of the compound(s) against a standard. A mass selective detector (MSD) provides quantitation, identification and additional separation if analytes simultaneously elute from the GC.

GC methods have been used extensively in automotive exhaust research. As early as 1958 Hurn *et al* [15] recognized the potential of GC to improve vehicle emissions measurements. By 1967 Papa [16] applied GC-FID to measure hydrocarbon emissions in the parts per billion. Recent work has focused on reducing the run time for complex emissions separations. Rudlein *et al* [17] utilized cryogenic traps, column switching, and two different parallel columns to separate C2-C12 compounds in an ICE exhaust in less than 35 minutes. Otsuki *et al* [18] took this one step further using 4 parallel columns and ovens to separate and identify C2-C12 compounds in about 5 minutes, and Olson *et*

al [19, 20] developed a ‘fast’ GC technique and applied it to CI engine exhaust to identify 160 organic, ozone forming compounds in the exhaust of an automotive ICE.

Increasingly stringent emissions regulations in Europe and the United States have driven emissions research on small engines by manufacturers [21] and third parties [22, 23]. However, the required measurements from an emissions reduction standpoint differ from those required for an energy accounting on the engine. Emissions measurements to meet government regulation focus on levels of regulated species, typically  $\text{NO}_x$ ,  $\text{SO}_x$ , CO, and total UHCs (typically measured by ppm carbon using an FID). Meanwhile, determining the energy lost to short-circuiting and incomplete combustion for an energy balance requires the separation, identification, and quantification of a tracer or the major UHCs. The concentration of  $\text{NO}_x$  and  $\text{SO}_x$ , while critical to meet emissions standards, are generally a small proportion of the overall incomplete combustion energy compared to UHCs. Moreover, exhaust work on small engines often measures total hydrocarbons using FID directly on the exhaust (see for example [22]), sufficient for regulatory requirements, but insufficient to quantify short-circuiting, as a gross UHC analysis does not specifically quantify an analyte or tracer. This work describes the application of GC-MS, GC-TCD, and GC-FID techniques to measure short-circuiting and estimate incomplete combustion on one of three geometrically similar engines as part of a larger effort to understand loss pathways and in turn which loss pathways drive the observed decrease in engine efficiency in 1-10 kW size range.

## METHODOLOGY

This section is split into four subsections. The first subsection reviews the research bench used for this experiment, which is a modified version of the bench described in [2, 24]. The second and third subsections explain the two methods used to measure short-circuiting. The final subsection describes the methodology for measuring the UHCs in the exhaust.

### SMALL ENGINE RESEARCH BENCH

The small engine research bench (SERB) was designed for testing 1-10 kW engines to study how loss mechanisms such as thermal losses and friction varied with engine size and surface area to volume ratio in the 1-10 kW size range [2, 24]. It is described in detail in [2, 24, 25]. Key aspects and modifications are reviewed here. The engine for this effort was selected as part of that larger effort. For that effort, a family of engines that was commercially available and as geometrically similar as possible was chosen. Specifications for the three engines are listed in Table 1. This work focuses on measurements on the 55i engine.

The engines were loaded using a Magtrol brand, 1WB65 eddy current dynamometer rated to 10,000 rpm and 6 kW with a full scale measurement accuracy of  $\pm 0.5\%$ . The dynamometer was connected to the engines using a belt drive and was controlled remotely using the Low Speed Data Acquisition (LSDAQ) system with control software written in National Instrument LabVIEW. The engines were started using an air motor coupled to the system with a clutch bearing. A schematic of the drivetrain as well as an overhead view highlighting the dynamometer, engine enclosure, and drivetrain are shown in Figure 1. Drivetrain losses were measured at 78.8 W/krpm and a description of the testing methodology is available in [6]. These losses are combined with the brake power measured at the dynamometer to yield the brake power of the engine.

Air intake temperature was controlled by passing the intake air through a heat exchanger with the second circuit connected to a Thermo Neslab RTE-211 recirculating water bath. Intake air flow was measured using an Omega brand FMA900 series hot anemometer with a range of 0-5.08 m/s

Table 1: Engine Specifications

Engine	28i	55i	85Xi
Displacement (cc)	28	55	85
Power (kW)	2.5	3.82	6.76
Mass (kg)	1.21	1.94	2.39
Power Density (kW/kg)	2.07	1.97	2.83
Bore (cm)	3.61	4.50	5.08
Stroke (cm)	2.84	3.51	4.09
Compression Ratio (geometric)	10:1	10:1	10:1
Cylinder Surface Area to Volume Ratio (1/cm)	1.81	1.46	1.28
Exhaust Port Opening ( $^\circ$ ATDC)	107	103	103* 97**
Exhaust Port Area (cm <sup>2</sup> )	1.90	2.15	2.83
Exhaust Area/ Intake Area	0.59	0.62	0.74
*Main exhaust port			
**Auxiliary exhaust ports			

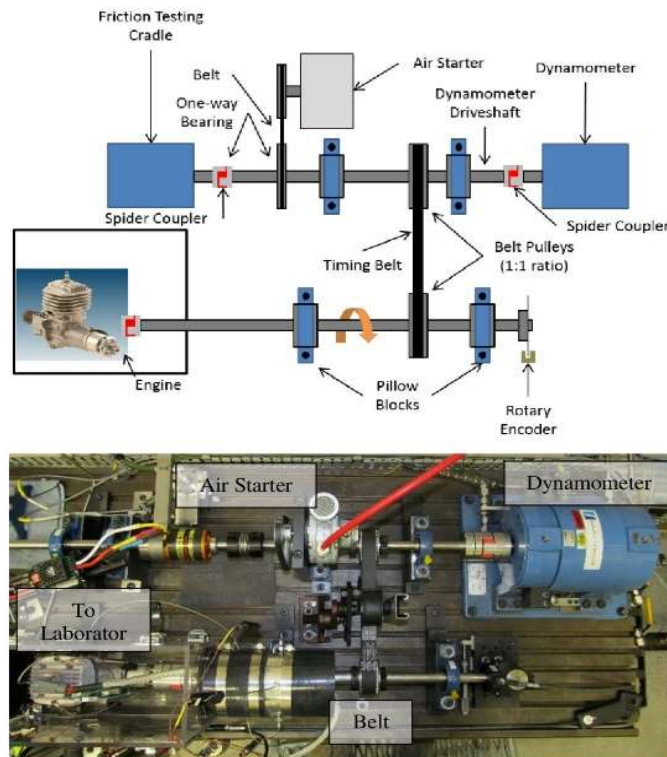


Figure 1: Top: Schematic of SERB drivetrain. Bottom: Overhead view of test bench showing the dynamometer, engine enclosure, and drivetrain.

SETC2015



and an accuracy of  $\pm 2\%$  of full scale. The hotwire was installed upstream of a 55 gallon baffle to damp out flow oscillations, with 10 diameters of straight runner both upstream and downstream. The baffle size was based on heuristics in [26]. For the engine in this study, intake air flow rates varied from 1 m/s to 2.7 m/s depending speed and throttle. The Reynolds number in the intake duct was on the order of  $10^4$ - $10^5$  indicating a fully turbulent flow. The volumetric flow rate was calculated using a  $1/7^{\text{th}}$  power law for turbulent flow [27:340] and verified using a sonic nozzle. The  $1/7^{\text{th}}$  power law results agreed with the measurement made using the sonic nozzle within  $\pm 5\%$  over the full operating range of the engine, making the measurements statistically indistinguishable at the 95% confidence level.

Engine cooling was provided using a 2.25 kW blower. Each engine was mounted inside of an enclosure (visible in Figure 1) and the blower could provide up to 25 m/s of air flow through the enclosure to simulate installation on a pusher configuration aircraft. Blower speed was varied from 60-100% to maintain the external head temperature of the engine at 128-130°C on the exhaust side. The flow rate of air through the cooling enclosure was measured upstream of the enclosure using an Omega brand FMA900 series hotwire anemometer with a range of 0-50.8 m/s and an accuracy of  $\pm 2\%$  of full scale. Temperature at the inlet and outlet of the box was measured using three Class A, 100  $\Omega$  platinum RTDs at each location. Temperature and flow rate measurements were used to calculate engine cooling load. Engine temperature was monitored using Class 1, Type J thermocouples mounted to the engine above the exhaust and boost ports.

The stock carburetor on the engine was replaced with a Currawong throttle body and throttle body injection system. The fuel injector was a Siemens Deka 60LB 630 cc High Impedance Fuel Injectors with a modified flow plate to reduce the fuel flow rates to those required by the engine. The throttle plate was controlled using a HiTec high torque digital servo. Both the throttle servo and the fuel injector were controlled using an in-house engine ECU and control program described in [28]. Testing revealed that the timing of the fuel injection (as opposed to the width of the injection) had no observable effect on the operation of the engine. This observation is consistent with the work of Grasas-Alsina *et al* who found that “timing of injection into the inlet duct was of little, if any, consequence” [29]. Fuel flow was measured with a Max Machinery 213 Piston Type flow meter with a range of 0-1800 cc/min and an accuracy of 0.2% of the reading. The delivered equivalence ratio was then calculated using the intake air and fuel flow rates and monitored by the operator to adjust the fuel injector pulse width to achieve the desired equivalence ratio. The engines were run on a primary reference fuel blend of 98% (of 99% pure) iso-octane and 2% (of 99% pure) n-heptane. Two percent by volume of AMSOIL SABER Professional synthetic two-stroke oil was added for lubrication.

The SERB was also equipped with an AVL Indismart combustion analyzer for measuring in-cylinder pressure and calculating IMEP, CA50 burn angle, and monitoring spark and injection timing. Engine crank angle was measured using a US Digital brand E6 optical encoder with 1800 counts per revolution. A Kistler 6113B measuring spark plug was

installed in place of the stock spark plug to measure in-cylinder pressure. The in-cylinder pressure signal was conditioned using a Kistler SCP charge amplifier, chassis model 2852A12 and amplifier model 5064C. During each cycle the baseline of the in-cylinder pressure sensor was set using a 0-103.4 kPa pressure transducer accurate to 0.1% of full scale. The pressure transducer was located in the intake runner approximately 5 cm upstream of the throttle plate.

Figure 2 shows a schematic of the exhaust system on the SERB. The system consisted of three separate pieces. The first piece was an adapter that joined the engine to the exhaust sampling runner. The adapter was a 10.2 cm long section of 2.5 cm diameter tube. Each engine run on the SERB uses its own adapter (of equal length) allowing the remainder of the exhaust system to remain consistent for all engines tested. The exhaust system was not tuned, and instead emulates a straight pipe configuration. It is acknowledged that tuning of the exhaust runner for a specific speed (and thus a specific application) will decrease short-circuiting and increase engine power. Since there is no specific platform identified in this work, all engines were operated in an un-tuned configuration with the understanding they could be later tuned for use on a specific platform.

The exhaust sampling runner consisted of a 30.4 cm tube welded to a 45.7 cm section of 5.1 cm diameter tube, with seven sampling ports. The spacing of those ports is shown in Figure 2. Attached to the end of the sampling runner was a 2 m section of flexible steel tube that connected the exhaust sampling runner to the laboratory exhaust system. The annulus between the laboratory exhaust system and the flexible portion of the exhaust runner was open to the atmosphere. This indirect coupling prevented the laboratory exhaust fans from pulling a vacuum on the engine exhaust port. The setup also kept the back pressure on the engine at the end of the runner consistent across all engines tested. All exhaust gas sampling locations are located at least 0.5 m from the outlet of the exhaust runner to the laboratory exhaust system, consistent with best practices described in SAE Standard J254 [30] for preventing unintended dilution of exhaust gas samples with ambient air. Pressure and temperature taps were located opposite of the sampling port at the Port 1 location.

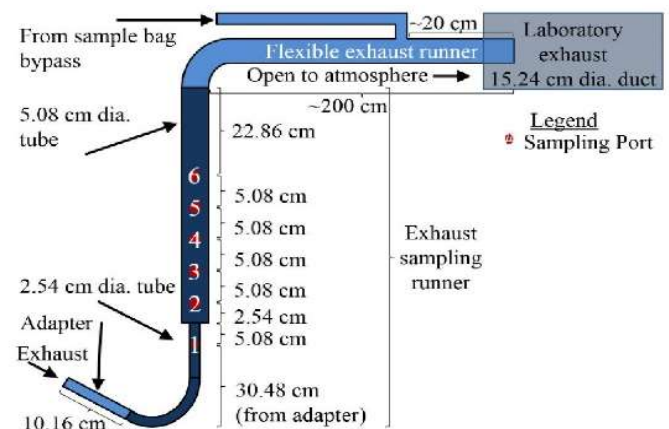


Figure 2: SERB exhaust system schematic showing sampling port location. Diagram is not draw to scale.



The exhaust was sampled by inserting a probe into sampling port 6, while leaving the other ports sealed. The sampling probe was built from 6 mm (0.25 in) stainless steel tube, consistent with the best practices recommend in the SAE J254 [30]. A photograph of the probe is shown Figure 3. The tapered end of the probe was oriented such that the opening was pointed downstream in the flow, again, consistent with recommend practices documented in SAE Standard J254 [30]. As discussed by Heywood and Sher [8:91], locating the sampling port too close to the engine can result in an axial spatial dependence of exhaust composition on the probe's location. Therefore, the exhaust sampling location must be far enough downstream from the engine to provide a sufficiently large mixing volume so that the time stratification and in turn the spatial stratification of the exhaust is eliminated. One may empirically determine the point at which the exhaust becomes well mixed by measuring the change in oxygen concentration axially along the runner, to see where it stabilizes. For the engine used in the work, the exhaust was sampled at each of the six ports at the same operating condition, 6000 rpm and WOT (the highest mass flow rate condition). Figure 5 shows a plot of oxygen concentration as a function of exhaust sampling port. The samples taken at ports 3-6 showed no statistically significant difference in oxygen concentration. Therefore Port 6 was used in this work.

A schematic of the sampling system is shown in Figure 4. The exhaust sample was drawn from the runner by a Dia-Vac inert sampling pump, model R254-AT-AA1. Before reaching the sampling pump, the sample passed through a cold trap that was chilled in an ice water bath to remove unburnt two stroke oil and water. Valves allowed the operator to pull fresh air from the laboratory through the pump when it was not collecting samples. After the exhaust sample passed through the pump, it was pushed into a 2 L Supel-Inert Foil Gas Sampling Bag. A regulator between the pump and sample bag split the flow between the bag and a return line that returned the extra exhaust flow to the flexible exhaust runner approximately 20 cm from the coupling to laboratory exhaust system as shown in Figure 2. The sampling bag fill rate was approximately 2 L/min and the bypass rate was approximately 12 L/min.

During validation of the setup, samples taken using the routing depicted in Figure 4 were compared to samples collected using a warm sample line and no cold trap. The iso-octane (the heaviest hydrocarbon observed in the exhaust) contents of the samples from the two systems were statistically indistinguishable, and thus the cold trap was used to prevent engine oil and water from accumulating in the sampling pumps, bags, and instruments. A sample of exhaust was extracted through the sampling system bypassing the cold trap to determine its impact on hydrocarbon content (most importantly iso-octane) in the exhaust. The iso-octane contents of the two samples were indistinguishable at the 95% confidence level. Since iso-octane was, essentially, the least volatile hydrocarbon in the fuel (neglecting lubricating oil) and thus the exhaust, the use of the cold trap to remove water and two-stroke oil from the sampling system did not interfere with the measurement of short-circuiting using iso-octane as an analyte.



Figure 3: Sampling probe used on the SERB.

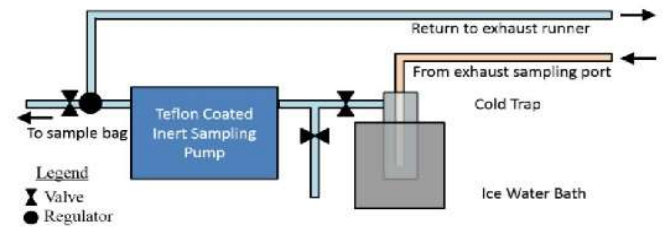


Figure 4: Schematic of the SERB exhaust sampling system.

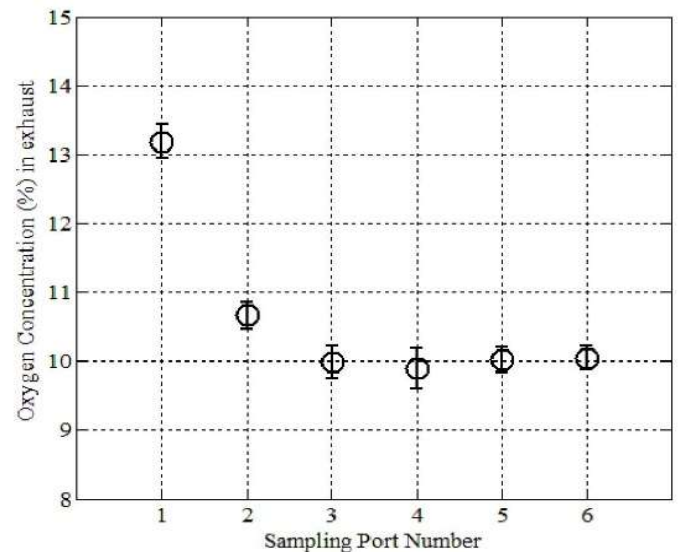


Figure 5: Oxygen in Exhaust Sample as a function of sampling port. For exhaust geometry and sampling port location see Figure 2.

For engine testing, the engine was operated utilizing the control variables outlined in Table 2. The engine was operated at WOT from 4000 rpm to 7900 rpm. A stable operating condition was reached when the engine reached the

Table 2: Operating Condition Control Variables

Fuel Type	98 ON PRF Blend
Fuel Pressure	4.14 bar (absolute)
Spark Timing	Variable – set for CA50 burn angle at $7.0 \pm 0.5^\circ$ ATDC
Fuel Injection (EOI)	$180^\circ$ ATDC
Intake Air Temperature	$26\text{--}28^\circ\text{C}$
Head Temperature	$128\text{--}130^\circ\text{C}$ (exhaust side, external)
Phi	1.1 at WOT 1.3 at PT (to reduce COV IMEP)



Table 3: Engine control limits for a stable operating condition.

Parameter	Typical Values	Limits
IMEP (400 cycle moving average)	4-6 bar at WOT	±0.2 bar
CA50 (400 cycle moving average)	8°ATDC	±0.5°
Equivalence Ratio (10 second running average)	1.05-1.10	±0.02
Engine Head Temperature (exhaust side TC)	130°C	±2°C
Exhaust Temperature (Opposite port 1)	360°C-490°C	±5°C

stable operating parameters listed in Table 3 within the listed limits for at least 2 minutes. Then, the valve allowing the sampling pump to pull engine exhaust (Figure 4, valve 1) was opened and the atmospheric bypass valve (Figure 4, valve 2) was closed. The exhaust system was allowed to purge for 90 seconds. Once purged, data was collected for 30 seconds while an exhaust sample was collected in a 2 L inert, foil sampling bag. The extracted exhaust was then tested using three different methods: two to calculate the short-circuiting and one to determine the UHCs in the exhaust.

As previously stated, the flow rate through the sampling system was approximately 12L/min compared to the 0.21 L volume of the system itself. Therefore, 90 seconds was deemed sufficient to completely purge the system and fill it with exhaust representative of the engine's operating condition. While the system was purging, the engine operating parameters listed in Table 3 were monitored for changes induced by engaging the exhaust sampling system. Following the addition of the sampling pump bypass, which returned most of the flow to the exhaust runner, there were no observable changes in engine performance induced by engaging the sampling system. Additionally, exhaust pressure was monitored using a Kulite ETL-DC-375-25A pressure transducer with a range of 0-25 psia and an accuracy of ±0.5% of the reading. The probe was installed at the junction of the adapter and the exhaust sampling runner (see Figure 2) and connected to the AVL IndiSmart to provide crank angle resolved pressure measurements. Based on those measurements, the sampling system had no observable effect on the pressure in the exhaust runner.

Directly across from sampling port 1, a Class 1, Type K thermocouple was installed to measure exhaust temperature, which was then used to calculate the sensible enthalpy in the exhaust using an estimate of exhaust composition. The exhaust composition was estimated using perfect incomplete combustion of the trapped charge to form CO, CO<sub>2</sub>, and H<sub>2</sub>O and by assuming the short-circuited charge was unreacted. The exhaust runner was insulated between the engine and the sampling port.

## METHOD 1: ISO-OCTANE AND ARGON

The first method to determine short-circuiting used the iso-octane in the PRF blend as an analyte and argon as an internal standard. Iso-octane meets the aforementioned requirements for trapping efficiency measurements if it is assumed that at

the right combustion conditions ( $\phi < 1.3$ ) the iso-octane is broken down into smaller hydrocarbons, even if combustion is globally incomplete. Adapting Equation (3) for these choices yields Equation (4) for the trapping efficiency.

$$\eta_{tr} = 1 - \frac{\left( \frac{y_{iso-octane,ex}}{y_{Ar,ex}} \right)}{\left( \frac{y_{iso-octane,fc}}{y_{Ar,fc}} \right)} \quad (4)$$

As described previously, the fuel volumetric flow rate was measured using a piston type flow meter. The volumetric flow rate of the fuel was converted to a mass flow rate using the fuel temperature, pressure and tabulated properties for iso-octane [31] and n-heptane [32]. It was assumed that the 2% of two-stroke oil had properties identical to the PRF blend. The hotwire in the intake air duct was positioned at the duct centerline. The air volumetric flow rate was then calculated using the 1/7<sup>th</sup> power law velocity profile for turbulent flow [27:340], as discussed in the Methodology: Small Engine Research Bench section. The volumetric flow rate was converted to a mass flow rate using the density calculated with pressure and temperature. The mass flow rates of fuel and air were used to determine the iso-octane to air ratio delivered to the engine, which is the denominator in Equation (4).

In Method 1, the collected exhaust was analyzed using an Agilent 7890 GC and an Agilent 5975 EI MSD with a triple axis detector. The GC was operated with a split inlet set at a 100:1 split ratio. For the separation an HP5-MS (5%-phenyl)-polysiloxane column was used. Additional details about the column and temperature profiles are listed in Table 4. While the HP5-MS column excelled at separating hydrocarbons by size, permanent gases eluted in a single peak. Therefore, the MSD was operated in SIM/Scan mode. Selective Ion Mode (SIM) permitted the quantification of specific ions of interest, while Scan mode provided a coarse spectra for the purpose of identifying compounds. SIM mode was used to detect the 40 AMU/e<sup>-</sup> peak from argon (distinct from all other permanent gases) and the 99 AMU/e<sup>-</sup> peak from iso-octane. The full spectra was used to confirm the identity of the iso-octane peak.

The GC-MS was calibrated using samples of air with a known concentration of the same iso-octane that was used to create

Table 4: GC-MS Parameters for Iso-Octane and Argon Separation and Quantification

Carrier Gas	Helium
<b>Oven:</b>	
Initial Temperature	40°C
Ramp Speed	15°C/min
Ramp Start Time	2 min
Final Oven Temperature	120°C
<b>Column (Agilent):</b>	PN: 19091S-433 25 m x 250µm
Flow Rate	1 mL/min
<b>Inlet:</b>	
Split Ratio	100:1
Purge Flow	4 mL/min
Temperature	120°C



the PRF fuel blend. To create each sample, 1 L of air was added to a clean exhaust sampling bag using a gas syringe accurate to  $\pm 10$  mL ( $\pm 1\%$ ). Then iso-octane was added to the bag using a 50  $\mu$ L gas tight syringe accurate to  $\pm 0.25 \mu$ L. Six bags were created using volumes of iso-octane ranging from 0  $\mu$ L to 80  $\mu$ L in 20  $\mu$ L increments. The sample bags were sealed and then heated to  $57.5 \pm 2.5^\circ\text{C}$ . For each calibration point, 10  $\mu$ L of sample was withdrawn from the bag using a 50  $\mu$ L gas tight syringe accurate to  $\pm 0.25 \mu$ L which was heated in the oven along with the bags. The sample was then injected into the GC. Each calibration sample was injected six times; the resulting calibration curve is shown in Figure 6. The resulting linear fit is shown in Equation (5) with uncertainty values for a 95% confidence interval.

$$\left(\frac{A_{\text{iso-octane}}}{A_{\text{Ar}}}\right)_{\text{SIM}} = (0.652 \pm 0.041) \left(\frac{y_{\text{iso-octane}}}{y_{\text{Ar}}}\right)_{\text{mol}} - (0.001 \pm 0.03) \quad (5)$$

Exhaust samples were processed in the same fashion as the calibration samples, but injected three times instead of six. The iso-octane/argon ratio from the SIM response was used to calculate the molar iso-octane to argon ratio in the exhaust using the calibration curve in Equation (5). The result was divided by the molar ratio calculated from the intake to yield the trapping efficiency as shown previously in Equation (4).

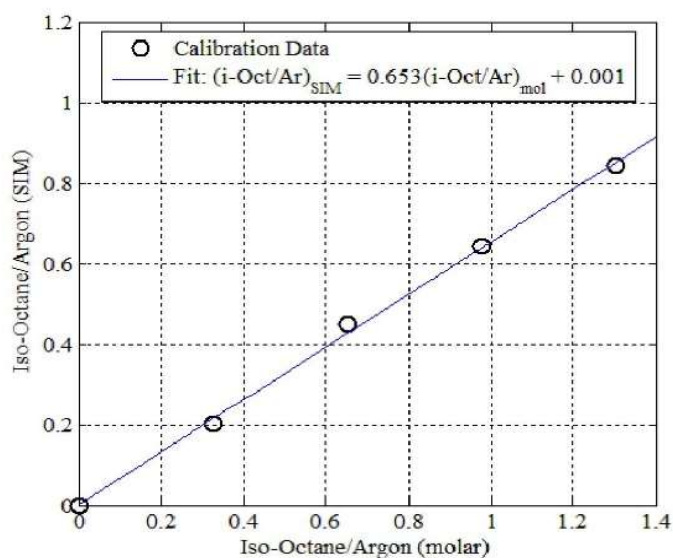


Figure 6: Calibration curve for the GC-MS. SIM mode was used to quantify the argon 40 AMU/e<sup>-</sup> ion and the iso-octane 99 AMU/e<sup>-</sup> electron.

## METHOD 2: OXYGEN AND NITROGEN (WATSON METHOD)

Concern over precipitation of iso-octane in the sampling lines and in the sample bag as well as the possibility that iso-octane in the fresh charge could decompose when short-circuiting into the high temperature exhaust duct led the authors to pursue a historically proven method of measuring short-circuiting to validate the method using iso-octane as the short-circuiting analyte. The second technique applied the method developed by Watson in 1908 using oxygen as an analyte at a rich combustion condition and nitrogen as an internal standard. The GC-MS used for Method 1 could not separate nitrogen and carbon monoxide (which both have a molecular

ion peak of 28 AMU/e<sup>-</sup>) so a second instrument capable of permanent gas separation was employed. To separate and quantify oxygen and nitrogen an HP 6890 GC with an Agilent brand HP-MOLSIV column was used. The column outlet was connected to a thermal conductivity detector, and relevant method parameters are listed in Table 5.

Table 5: GC-TCD Parameters for Oxygen and Nitrogen Separation and Quantification

Carrier Gas	Argon
Oven:	
Temperature	35°C
Column (Agilent):	PN: 19095P-MSOE 30 m x 530 $\mu$ m Film: 50 $\mu$ m
Flow Rate	25 mL/min
Inlet:	
Split Ratio	Splitless
Purge Flow	4 mL/min
Temperature	120°C
TCD:	
Temperature	150°C
Reference Flow	20 mL/min (Ar)
Makeup Flow	3 mL/min (N <sub>2</sub> )

The oxygen, nitrogen, and hydrogen responses of the detector were calibrated using 100  $\mu$ L samples made from mixtures of air and hydrogen. The hydrogen calibration is included since it was used to estimate hydrogen concentration in the exhaust samples. The calibration samples ranged from 0%-100% air in 10% increments. The calibrations for oxygen, nitrogen, and hydrogen are shown in Figure 7, Figure 8, and Figure 9, respectively. The calibration curves with a 95% confidence interval are shown in Equations (6), (7), and (8). Due to the low concentration of hydrogen in the exhaust relative to the calibration samples, the calibration was forced through zero to determine the detector's response factor (slope). The hydrogen response of a background of air was subtracted from the hydrogen response for each exhaust sample. The detector response of carbon monoxide was calibrated using an 8.6% carbon monoxide calibration gas standard, diluted using nitrogen. As with the other TCD calibrations, 100  $\mu$ L

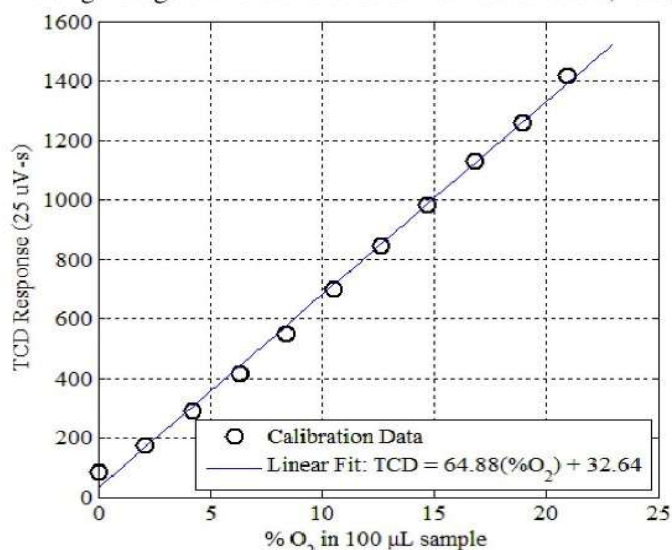


Figure 7: Calibration of TCD O<sub>2</sub> Response for a 100  $\mu$ L sample of air and hydrogen.



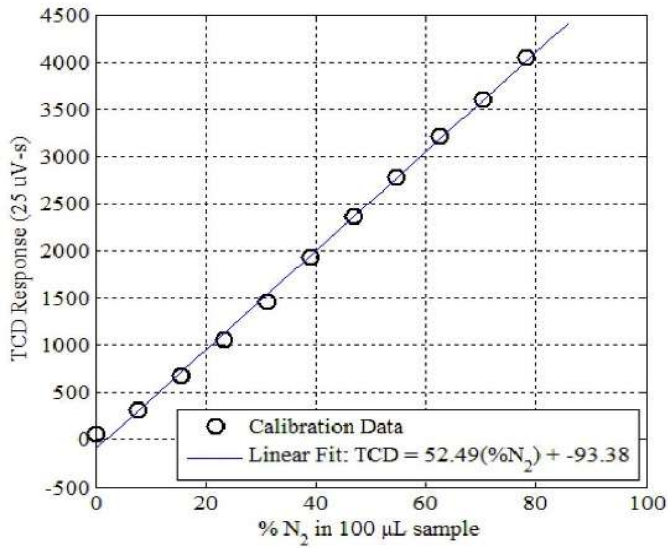


Figure 8: Calibration of TCD  $N_2$  Response for a 100  $\mu\text{L}$  sample of air and hydrogen.

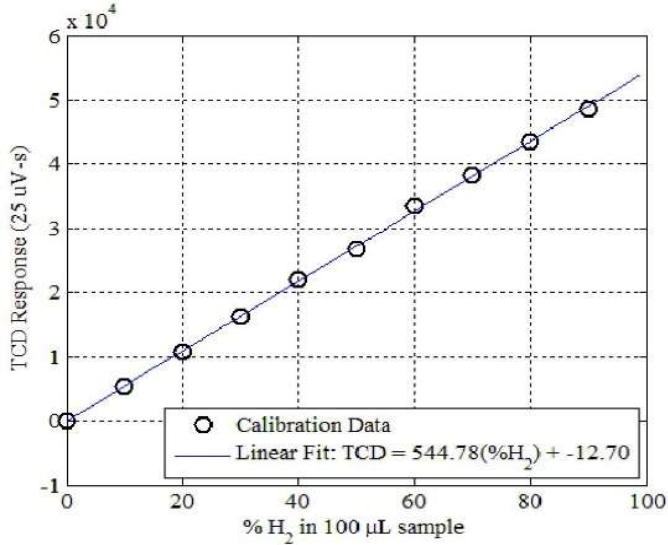


Figure 9: Calibration of TCD  $H_2$  Response for a 100  $\mu\text{L}$  sample of air and hydrogen.

samples were used. The carbon monoxide calibration is shown in Figure 10 and the calibration curve is shown in Equation (9).

To analyze the exhaust and determine short-circuiting a

$$y_{i,ex} = y_{iso-octane,ex} \left( \frac{A_i}{A_{iso-octane}} \right) \left( \frac{C_{iso-octane}}{C_i} \right) \zeta \quad (11)$$

100  $\mu\text{L}$  sample was injected onto the column. The calibration curves were used to determine the percentage (and thus mole fraction) of oxygen and nitrogen gases and the results were used to calculate the numerator of Equation (3). Fresh charge composition was calculated using the standard dry atmospheric composition adjusted for ambient humidity and was then combined with the exhaust measurement to determine the short-circuiting as shown in Equation (3).

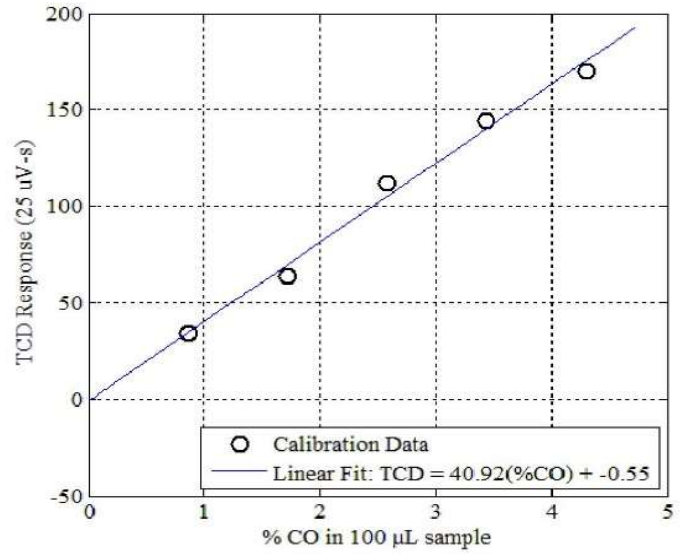


Figure 10: Calibration of TCD  $CO$  Response for a 100  $\mu\text{L}$  sample of carbon monoxide and nitrogen.

$$(A_{O_2})_{TCD} = (64.9 \pm 2.5)(\%O_2)_{molar} + (33.4 \pm 29.9) \quad (6)$$

$$(A_{N_2})_{TCD} = (52.5 \pm 1.8)(\%N_2)_{molar} - (94.5 \pm 86.0) \quad (7)$$

$$(A_{H_2})_{TCD} = (544.6 \pm 4.2)(\%H_2)_{molar} \quad (8)$$

$$(A_{CO})_{TCD} = (50.9 \pm 5.3)(\%CO)_{molar} - (0.6 \pm 15.2) \quad (9)$$

## UHCS, CO, AND $H_2$ : GC-FID AND GC-TCD

The primary UHCs in the exhaust samples were identified using the scan data collected from Method 1 by matching a spectra for each UHC to the NIST database. To quantify the UHCs, GC-FID was used. Like Method 2 for short-circuiting, an HP 6890C GC was employed, this time a J&W Scientific 115-3532 alumina column installed in the GC with helium as the carrier gas. The relevant method parameters are listed in Table 6. The elution order was verified with a C1-C10 alkane standard.

Equation (10) proposes that the area response of the FID ( $A_i$ ) is a function of the number of carbon atoms in the molecule ( $C_i$ ), the concentration of the component ( $[i]$ ), and a sensitivity factor ( $\zeta$ ) that accounts for difference in the FID response to alkanes, alkenes, alkynes, and aromatics.

$$[i] = [i - octane] \left( \frac{A_i}{A_{iso-octane}} \right) \left( \frac{C_{iso-octane}}{C_i} \right) \zeta \quad (10)$$

Equation (10) may also be expressed in terms of mole fraction since iso-octane acts as an internal standard for the other hydrocarbons, and that expression is shown in Equation (11). The sensitivity factors were approximated from data compiled by Zhao and Ladommatos [33:118] and are shown in Table 7. The mole fraction of each UHC was then used to estimate the quantity of that hydrocarbon in the exhaust based on the quantification of iso-octane from Method 1.

The flow rate of iso-octane in the exhaust was calculated as the product of short-circuiting, the flow rate of fuel delivered to the engine, and the percent of iso-octane in the fuel.

Table 6: GC-FID Parameters for Iso-Octane and Argon Separation and Quantification

Carrier Gas	Argon
<b>Oven:</b>	
Temperature	35°C
Ramp Speed	10°C/min
Final Temperature	180°C
Final Hold Time	5 min
<b>Column (J&amp;W Scientific):</b>	PN: 115-3532 30 m x 530 µm
Flow Rate	25 mL/min
<b>Inlet:</b>	
Split Ratio	Splitless
Purge Flow	4 mL/min
Temperature	120°C
<b>FID:</b>	
Temperature	250°C
Hydrogen Flow	40 mL/min
Air Flow	450 mL/min
Makeup Flow	6 mL/min (He)

Table 7: FID Sensitivity Relative to Hydrocarbon Family as Compiled by Zhao and Ladommatos [33:118].

Hydrocarbon Family	Response Relative to Alkanes
Alkane	1.00
Alkenes	0.95
Alkynes	1.30
Aromatics	1.00

That flow was then used to determine the flow rate of each of the UHCs as shown in Equation (12).

$$\dot{m}_i = \left( \frac{y_{i,ex}}{y_{iso-octane,ex}} \right) \frac{(\dot{m}_{fuel})(x_{iso-octane,fuel})}{MW_{iso-octane}} MW_i \quad (12)$$

Both carbon monoxide and hydrogen were measured using the GC-FID described previously. The flow rate of hydrogen in the exhaust was determined using the hydrogen calibration (shown in Figure 9 and Equation (8)) and nitrogen as an internal standard. The relevant formula is shown in Equation (13).

$$\dot{m}_{H_2} = \left( \frac{\%H_2}{\%N_2} \right) \frac{(\dot{m}_{air})(x_{N_2})}{MW_{N_2}} MW_{H_2} \quad (13)$$

Then the amount of CO in the exhaust flow was determined using nitrogen as an internal standard, as in Equation (14).

$$\dot{m}_{CO} = \left( \frac{\%CO}{\%N_2} \right) \frac{(\dot{m}_{air})(x_{N_2})}{MW_{N_2}} MW_{CO} \quad (14)$$

For all of the partially combusted products, the chemical enthalpy was calculated using the respective heats of combustion on a mass basis.

## RESULTS & ANALYSIS

The results and analysis are split into three subsections. The first section compares the short-circuiting results from

Method 1 and Method 2. The second section combines the short-circuiting data with delivery ratio and trapping efficiency to provide a complete picture of engine performance. The third section presents the UHCs observed in the exhaust and estimates of incomplete combustion enthalpy.

### METHOD 1 AND METHOD 2 COMPARISON

Figure 11 and Figure 12 shows two sets of short-circuiting measurements calculated using both Method 1 and Method 2 for the 3W-55i engine along with error bars representing a 95% confidence interval. The first data set in Figure 11 was collected at sample Port 2, which based on Figure 5 is one port too close to the engine to guarantee the exhaust is well-mixed. Figure 13 represents the same data at Port 6 where the exhaust gases are well mixed. However, since both Method 1 and Method 2 measure short-circuiting using components in the fresh charge, the slight sampling bias introduced by the use of Port 2 should not affect the measurement methods relative to one another. The assumption that the fresh charge is well mixed (not stratified) by the time it reaches the cylinder for throttle body injection has been investigated and verified in the literature, for example [29].

Perhaps the most significant difference between the two figures is the difference in short-circuiting, especially at low speed. Based on measurements of air flow to the engine, the highest mass flow rates occur near 4000 rpm and 6000 rpm at WOT, making these points the most susceptible to sampling bias from poorly mixed exhaust. Based on the data in Figure 5, at 6000 rpm the sampling bias results in about a 10% over sampling of the short-circuited charge (or a 10% under sampling of the trapped charge) by volume, which agrees with the 10% over prediction of short-circuiting observed at 6000 rpm in Figure 11 relative to Figure 12. Therefore, while Figure 11 is useful from the standpoint of comparing the effectiveness of the methods, Figure 12 and data taken at sampling Port 6 will be used for all further discussions of engine performance.

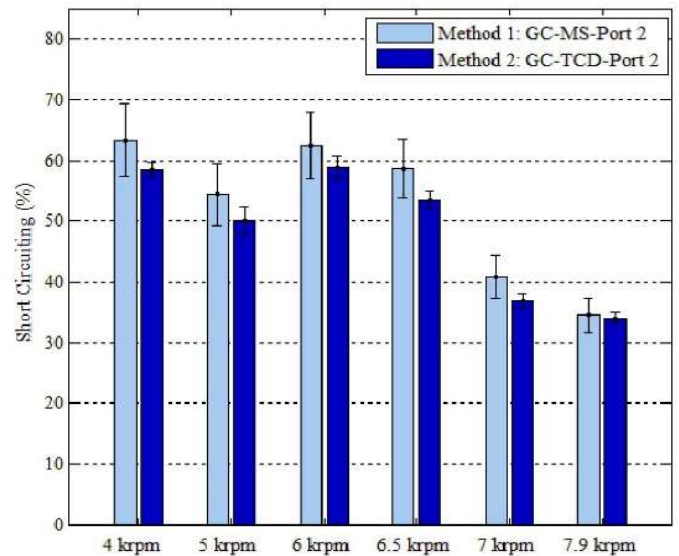


Figure 11: Short-circuiting measured at sampling port 2 using GC-MS and GC-TCD for the 3W-55i engine.



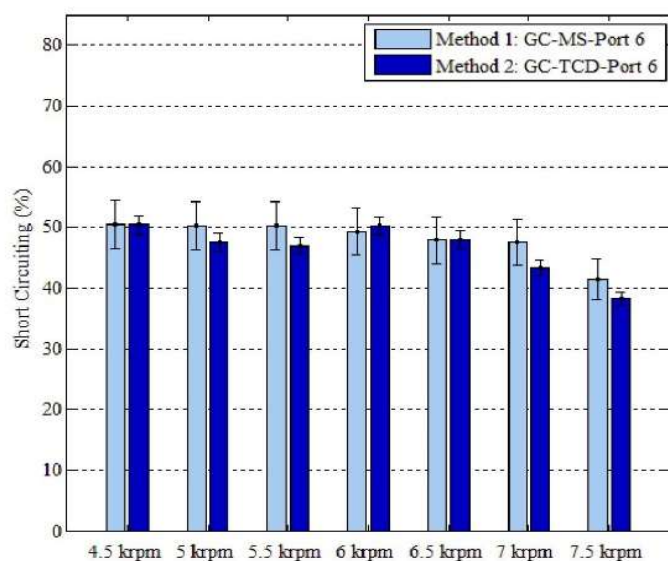


Figure 12: Short-circuiting measured at sampling port 6 using GC-MS and GC-TCD for the 3W-55i engine.

For samples taken at either port, the differences between the iso-octane method using GC-MS and the Watson method using GC-TCD are not statistically significant at the 95% confidence level. However, the iso-octane method consistently measured 4-5% higher short-circuiting for samples collected at sampling Port 2 than the Watson method. To a lesser degree, Figure 12 shows a similar, but less pronounced bias (4 points high, two points equal, only one point slightly less than the Watson method). In both cases, the bias causes the iso-octane method to report higher short-circuiting values than the Watson method. There are three possible explanations for a bias between methods: loss of analyte between the exhaust port and the sampling bag, reaction of short-circuited oxygen in the exhaust, and a systematic error introduced by one of the calibration curves. It has already been noted that sampling bias due to location of the sampling probe for the data shown in Figure 5 would affect both methods equally, and thus is not the cause.

The first explanation involves loss of analyte between the exhaust runner and the sampling port. At the onset of this effort, the primary concern was condensation of the iso-octane in the sampling system. Indeed, SAE exhaust sampling techniques (example [34]) have explicit requirements for heating sample lines to avoid the condensation of heavy hydrocarbons. However, the primary reference fuel combusted in this study yielded no hydrocarbons larger than octane (as observed by GC-MS and GC-FID), and based on the vapor pressure of octane at ambient pressure, the amount of octane present in the stoichiometric mixture should not have condensed even if cooled to freezing (0°C), especially once diluted with exhaust. Furthermore, exhaust samples extracted using the cold trap showed no statistical difference from those collected using a warm sample line with the cold trap bypassed. If iso-octane was deposited in the sampling system, it should cause the iso-octane method to under-report short-circuiting compared to the Watson method, which is not the behavior observed in either Figure 11 or Figure 12.

Therefore, the results indicate that iso-octane is sufficiently stable to act effectively as an analyte when used as a primary

fuel component. It remains effective even when the exhaust is cooled prior to analysis, which is useful for removing oil and water from the exhaust to prevent them from contaminating sensitive instrumentation. Thus, in studies where a PRF blend is run as a fuel, the iso-octane may be used as an analyte, preventing the additional burden of adding a tracer to track short-circuiting during lean combustion (where the Watson method will not work due to excess trapped oxygen).

The second explanation for the difference in the methods is the reaction of oxygen in the exhaust. As noted by Heywood and Sher [8:91], the exhaust oxygen concentration varies downstream of the exhaust port and can be altered by reaction of short-circuited oxygen in the fresh charge with incomplete combustion products in the hot exhaust. While care was taken to locate the exhaust sampling port sufficiently downstream of the engine to ensure the burnt and short-circuited charge were well-mixed, it is possible that oxygen reacted during the mixing. Indeed, analysis of the exhaust contents on the GC-TCD indicated high levels of CO and hydrogen at the sampling port (on the order of 5,000 – 30,000 ppm). Both the water hydrogen shift reaction and the combustion of carbon monoxide could consume short-circuited oxygen as the burnt and fresh charge mix at the beginning of the gas-exchange process. The lower oxygen concentration would then cause the Watson method to report lower short-circuiting than the iso-octane method.

A third explanation for the consistent difference between the two methods is a bias caused by one of the calibration curves. The confidence intervals on the calibration curves presented in Equations (5)-(9) only provide the random and instrument uncertainty in those calibrations, they do not account for how that calibration might change if repeated on a different day. If one of the calibrations displayed significant day to day drift, the variation present in the chosen calibration would effectively bias all results from that method.

To explore this possibility, calibrations for the GC-TCD and GC-MS were repeated, and the results were compared to the calibrations presented above. The GC-TCD calibrations for oxygen, nitrogen, hydrogen, and carbon monoxide were repeatable within  $\pm 1\%$ , indicating their confidence intervals in Equations (6)-(9) reasonably capture the uncertainty in the calibration. However, calibrations performed on the GC-MS (using the same sample bags on different days) varied by  $\pm 5\%$ , which is a variation not captured by the confidence interval in Equation (5). That variation is included in Figure 11 and Figure 12 where the two methods agree within a 95% confidence interval. Unlike the contribution to uncertainty from each sample, any error in the calibration curve affects all points calculated using that curve. Therefore, while it appears there is a consistent difference between the two methods, especially in Figure 11, the difference is simply an artifact of the GC-MS calibration for the iso-octane method.

The preceding discussion underscores the primary tradeoffs of the two methods. The iso-octane method offers a viable methodology for measuring short-circuiting in a globally lean environment, but as implemented herein is subject to large variability and uncertainty. After accounting for variability introduced by the calibration, the iso-octane method has



substantially more variability (approximately 10%-15%) than Watson's method (approximately 4%-5%). Table 8 shows the primary uncertainty contributors for both methods at a single speed (now as a percent of short-circuiting). (Note: The total uncertainties were calculated using the methodology outlined in ASME PTC19.1). For the Watson method, essentially all of the uncertainty comes from the quantification of oxygen and nitrogen with the GC-TCD. The response of the TCD used for this work was highly repeatable day to day (less than 1%), allowing a single calibration to be used for multiple tests. To obtain even reasonable repeatability on the GC-MS, the instrument had to be calibrated after every tune, and the instrument has to be tuned on a weekly basis. Even with frequent tuning, the exhaust composition as measured using the GC-MS has approximately three times the uncertainty of the GC-TCD.

The iso-octane method also depended on measurements of the intake air flow and fuel flow rates; the Watson method did not because the oxygen and nitrogen composition of the atmosphere is well known and essentially constant. The small, oscillatory nature of the engine made the intake flow rates difficult to measure, and the difficulty would increase in future testing when flow rates decrease with reduced throttle. Thus, while the Watson method cannot be employed at lean conditions, its lower uncertainty offers an advantage over the iso-octane method (as implemented herein) at rich conditions. The Watson method also offers distinct advantages for micro engines, where low fuel and air flow rates are difficult to measure, as noted by other researchers (example Cadou *et al* [35]).

## ENGINE PERFORMANCE ANALYSIS

For clarity, the short-circuiting results from the Watson method collected at Port 6 will be used for the remainder of the results and analysis. As shown in Figure 12, short-circuiting at WOT reached nearly 50% at some operating conditions, which is high for even a two-stroke engine. To verify the short-circuiting measurements, energy balances were performed for several operating points. The balances account for brake power, thermal losses, sensible exhaust enthalpy, and short-circuiting. The test setup for brake power, thermal losses, and sensible exhaust enthalpy was

Table 8: Primary contributors to 95% CI uncertainty for Iso-Octane and Watson Methods

Condition	6000 rpm, WOT	
	Iso-Octane	Watson
<b>Total</b>	9.4%	4.1%
Exhaust Measurement	7.7%	3.1%
Intake Air Flow	4.9%	n/a
Intake Fuel Flow	2.5%	n/a

described briefly in the Methodology section above. For additional details and information on the proposed energy balance see Rittenhouse *et al* [5], Rowton *et al* [2], and Horn *et al* [6]. Friction and pumping losses were grouped with thermal losses, which encompass all heat rejected from the engine other than the exhaust flow. The energy balances also include the chemical exhaust enthalpy, discussed in the next subsection. The energy balances are shown in Figure 13 for 4500 rpm through 7500 rpm. All energy balances account for all of the energy delivered to the engine within the uncertainty

limits, validating the short-circuiting measurement of the iso-octane method.

The most notable energy pathway, especially at WOT is the short-circuiting. In their scaling study of nine micro two-stroke glow engines, Cadou *et al* [4] estimated "combustion losses" of 50%-65% of the total fuel energy. The analysis calculated combustion losses as the energy that remained after considering brake power, thermal losses, sensible exhaust enthalpy, and friction. However, the analysis did not distinguish between losses due to incomplete combustion (due to factors such as residence time and trapped equivalence ratio) and short-circuiting. Cadou *et al* concluded that improvements to small and micro engine should start with addressing these combustion losses. The data in Figure 13 indicate that of the two losses, addressing the short-circuiting of fresh charge is the more critical avenue. As an illustrative example, if short-circuiting were eliminated from the 55cc engine at 5500 rpm and WOT, brake fuel conversion efficiency would jump from 14% to nearly 23% (assuming rather optimistically, that the remaining pathways maintained the same magnitude of energy).

Figure 14 shows the gas exchange performance of the engine as a function of engine speed at WOT. At WOT the charging efficiency remains almost constant, while the delivery ratio drops above 6500 rpm leading to a corresponding decrease in short-circuiting losses. The low pressure drop across the throttle plate and large port time areas at low speed and WOT are likely the cause of the high delivery ratios observed below 6000 rpm. However, it appears that most of the charge is then lost straight to the exhaust.

While plotting the gas exchange performance parameters as a function of engine speed makes it clear how the engine's ability to induct fresh charge is impacted by higher operating speeds, additional insight may be gleaned by comparing the engine's performance to what are consider to be bounding models for gas exchange: the perfect isothermal displacement model and the perfect isothermal mixing model. The perfect

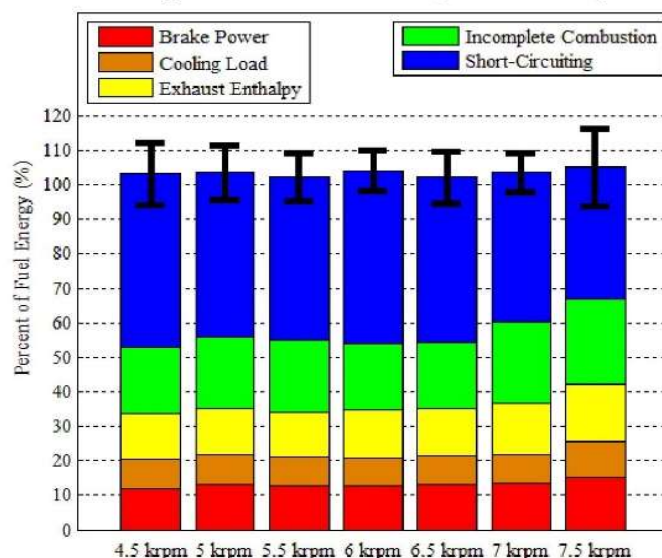


Figure 13: Energy balance performed at WOT on the 3W-55i engine. The uncertainty on each complete balance is provided at the 95% confidence level.



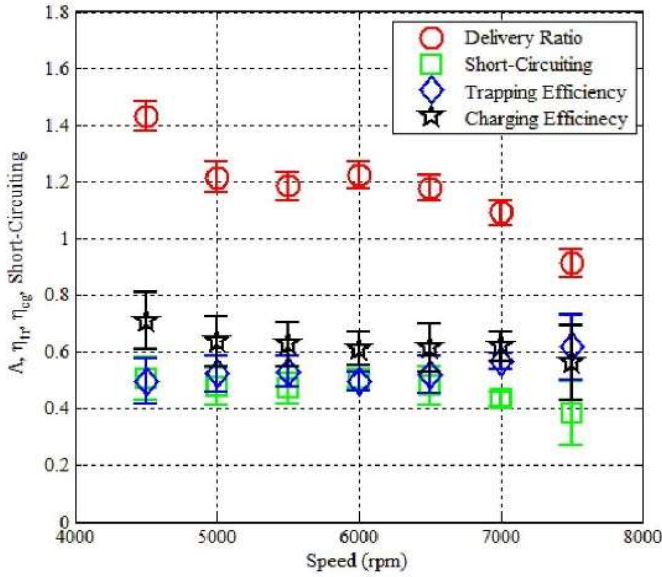


Figure 14: Gas exchange performance at WOT on a 3W-55i (55 cc) engine with un-tuned exhaust.

isothermal displacement model assumes that each unit of fresh charge displaces an equal unit of burnt charge without any mixing, until the entire cylinder had been scavenged. It is therefore a best case for gas exchange. The perfect isothermal mixing model assumes that each unit of fresh charge mixes instantaneously with the cylinder contents. The perfect isothermal mixing model is not a worst case for the gas exchange process; pure short-circuiting is less desirable. However, most modern engines exceed the performance of the model and it is considered to be a lower bound [8:47]. The perfect isothermal displacement model is shown in Equations (15) and (16). The perfect isothermal mixing model is shown in Equations (17) and (18).

$$\eta_{tr} = 1 \text{ for } \Lambda \leq 1$$

$$\eta_{tr} = \frac{1}{\Lambda} \text{ for } \Lambda > 1$$
(15)

$$\eta_{ch} = \Lambda \text{ for } \Lambda \leq 1$$

$$\eta_{ch} = 1 \text{ for } \Lambda > 1$$
(16)

$$\eta_{tr} = \frac{1 - e^{-\Lambda}}{\Lambda}$$
(17)

$$\eta_{ch} = 1 - e^{-\Lambda}$$
(18)

Figure 15 shows the trapping and charging efficiencies of the engine plotted against the delivery ratio at WOT. Also included on the plot are lines for the perfect isothermal mixing and displacement models. At WOT, both the charging and trapping efficiencies fall slightly below the perfect isothermal mixing model. One key difference between the isothermal models and actual engine operation is that during engine operation the fresh charge is heated by the cylinder wall and burnt gas, which decreases the trapping and charging efficiencies. Taking that into consideration, the scavenging performance of the engine was comparable to the perfect mixing model, the standard lower benchmark for conventional engines.

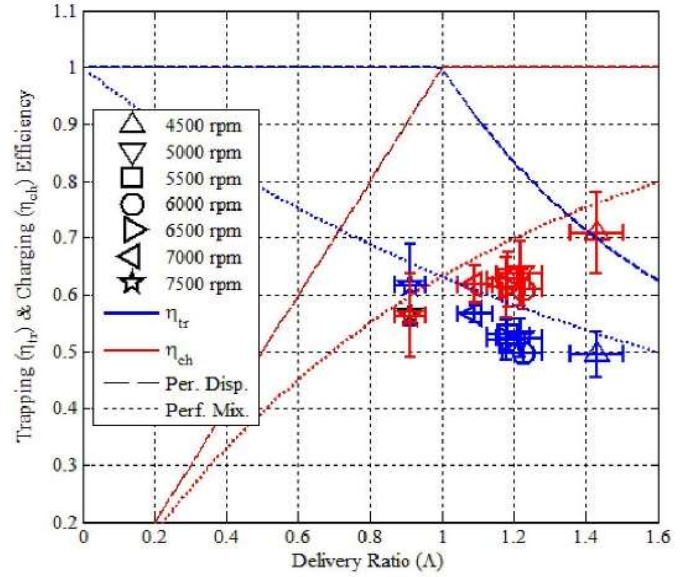


Figure 15: Gas exchange performance at WOT on a 3W-55i (55 cc) engine with un-tuned exhaust compared to the perfect isothermal displacement and mixing models. Uncertainty bars are for a 95% confidence interval.

The fact that engine performs similar to the perfect mixing model at WOT conditions does not inherently mean that the underlying physics occurring in the cylinder replicate that model. For example, consider the three zone model offered by Maekawa [36]. The model consists of a fresh charge zone, a mixing zone, and a short-circuiting zone. In the right balance these zones could have the same charging efficiency, trapping efficiency, and delivery ratio as the perfect mixing model with drastically different implications for the underlying gas physics in the cylinder. Any further discussion of the gas exchange process would require additional measurements, preferably crank angle resolved composition measurements of the gas in the cylinder or at the exhaust port. Such measurements are planned for future efforts. Regardless of the underlying physics, the results indicate that there is room for improvement in the scavenging performance of small two-stroke engines.

## INCOMPLETE COMBUSTION ANALYSIS

Figure 16 shows the exhaust chemical enthalpy losses as a fraction of total fuel energy delivered to the engine resulting from UHCs, hydrogen, and carbon monoxide. Of the loss pathways, carbon monoxide is the largest, followed by hydrogen. Both hydrogen and carbon monoxide are products indicative of rich combustion or inefficient combustion. Figure 17 shows the measured equivalence ratio for the same engine operating points shown in Figure 16. The slight richening of the mixture at 5000 rpm and 5500 rpm corresponds to an increase in both carbon monoxide and hydrogen emissions at those speeds. However, no appreciable change in equivalence ratio occurs at 7000 rpm and 7500 rpm to explain the jump in emissions at those operating conditions. One potential answer lies in the data in Figure 14. Both 7000 rpm and 7500 rpm show a decrease in delivery ratio and charging efficiency. A consequence of such a decrease is a corresponding increase in residual gases



in the cylinder and in turn a decrease in combustion efficiency.

Figure 18 shows the primary exhaust products, this time expressed in g/kW-hr. Volckens *et al* conducted an emissions study on 23 two stroke engines from 17 cm<sup>3</sup> to 59 cm<sup>3</sup> used in handheld power equipment produced from 1981 through 2003 [22]. Engine testing was weighted at 90% for full torque at rated speed, and 10% at idle. For engines produced after 2002 (regulated by US EPA Phase-2 emissions standards), typical CO emissions levels ranged from 350-450 g/kW-hr. These CO levels are comparable to those observed from the engine tested here. UHC emissions reported in Figure 18 do not include short-circuited fuel, and are considerably lower than the 50 g/kW-hr to 100 g/kW-hr reported by Volckens *et al*. Including the short-circuited fuel would increase HC emissions to 500-650 g/kW-hr across the tested speed range, high even compared to engines that predate EPA control measures (250-350 g/kW-hr) for small engines in the United States.

Figure 19 shows the breakdown of UHCs in the exhaust, with iso-octane and n-heptane from the short-circuited fuel not included. The plot is weighted by the relative amount of energy. While the plot was made with results from 7000 rpm and WOT, the same trends hold across the range of tested speeds at WOT. Pentane (mostly iso-pentane) is the primary component, accounting for over 50% of the energy. This makes sense as it is an early intermediate in the combustion of iso-octane. By energy, propylene is the other major contributor.

Figure 20 shows UHCs for the same operating condition as Figure 19, this time weighted by mole fraction in exhaust. Again, iso-octane and n-heptane from short-circuited charge are omitted. The result of weighting by mole fraction instead of energy content shows the influence of the increase in energy per molecule as the size of the number or carbon atoms increase. It also shows that on a per molecule basis, methane, ethane, and ethylene play a much larger roles in the exhaust than they do on an energy weighted basis.

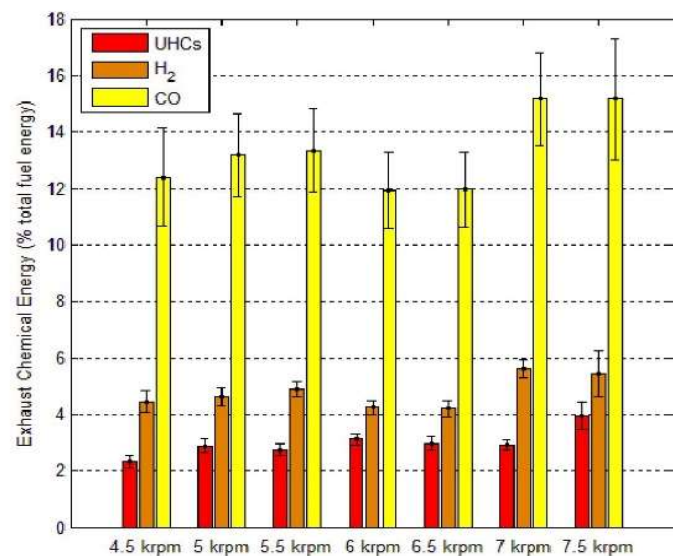


Figure 16: Incomplete combustion enthalpy on a 3W-55i (55cc) engine at WOT. Uncertainty bars represent a 95% confidence

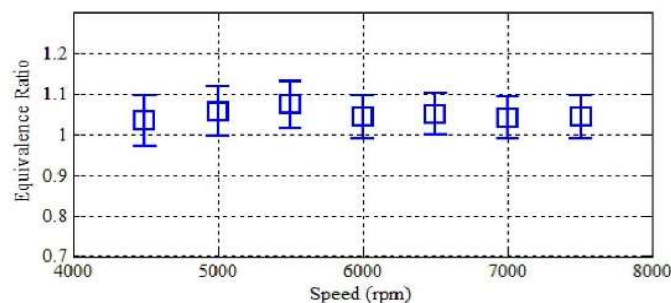


Figure 17: Equivalence ratio for all engine operating conditions

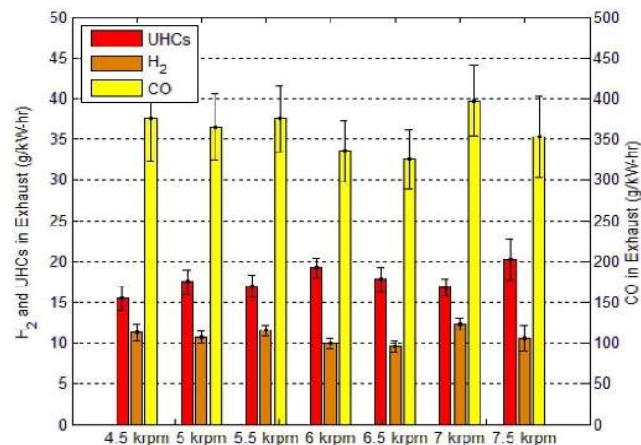


Figure 18: Emissions on a 3W-55i (55cc) engine at WOT. Uncertainty bars represent a 95% confidence interval. UHCs are calculated as g/kW-hr propane and do not include short-circuited fuel.

## SUMMARY/CONCLUSIONS

This work is part of a larger effort to quantify the loss mechanisms in a family of geometrically similar 1-10 kW two-stroke engines. The objective of this work was to develop and validate short-circuiting measurement techniques to refine the existing energy balances on the

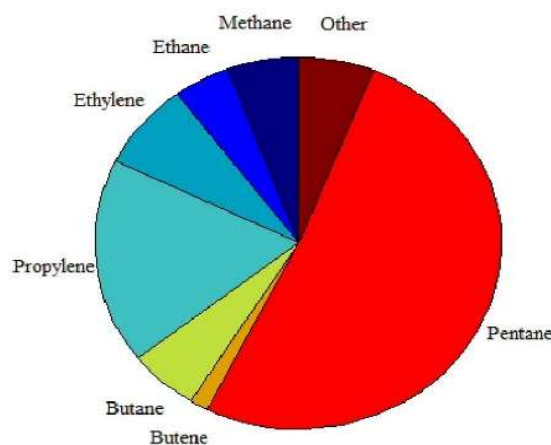


Figure 19: UHCs in 3W-55i exhaust at WOT and 7000 rpm, weighted by chemical energy content. Iso-octane and n-heptane from short-circuited fuel are not included



engines, and to identify and quantify of the losses associated with the primary unburned hydrocarbons (UHCs) in the exhaust.

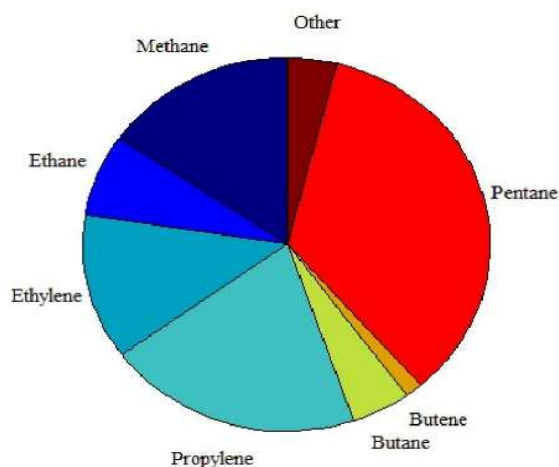


Figure 20: UHCs in 3W-55i exhaust at WOT and 7000 rpm, weighted by mole fraction in the exhaust. Iso-octane and n-heptane from short-circuited fuel are not included.

Two different measurement techniques, each using a different analyte and internal standard were examined. The first used iso-octane as the analyte and argon as the internal standard. The second, known as the Watson method, used oxygen as the analyte and nitrogen as the internal standard. The results show that iso-octane is sufficiently immune to decomposition in the exhaust and functions as an analyte. The short-circuiting results determined using the iso-octane method overlapped those from the Watson method within a 95% confidence interval. As implemented, the iso-octane method was subject to significant experimental uncertainty (10%-15%) due primarily to variability in the response of the GC-MS, and secondarily to measurements of the intake air and fuel flow rates. The Watson method had much lower uncertainties (3%-5%). Both methods are useful tools in their own right for small engine testing. The iso-octane method offers a solution for lean combustion in engines already being tested on a PRF blend. The Watson method offers a solution of rich combustion, and it is not dependent on fuel and air flow rates which can be difficult to measure on small 1-10 kW engines.

A 55cc engine was tested in the manufacturer's stock configuration (un-tuned exhaust) with the exception of an aftermarket throttle body and fuel injector that replaced the stock carburetor. Short-circuiting was measured at 35%-50% at WOT from 4500 rpm to 7500 rpm. The short-circuiting measurements were confirmed using an energy balance that closed to 100% at a 95% confidence level. The scavenging performance of the engine was comparable to the perfect isothermal mixing model. Coupled with previous studies of micro engines, the results indicate that short-circuiting should be the first loss pathway addressed to improve small engine fuel conversion efficiency. Options include exhaust tuning and direct injection, techniques already common on conventional scale engines.

Finally, the exhaust chemical enthalpy was quantified using GC-TCD and GC-FID based methods with short-circuited iso-octane acting as a reference for UHCs and nitrogen acting as an internal standard for carbon monoxide and hydrogen. Carbon monoxide was the primary loss pathway, accounting for approximately 60-70% of incomplete combustion losses, followed by hydrogen at 20-25%. The remainder of the incomplete combustion pathway consisted of UHCs. The primary UHCs by energy were methane, ethane, ethylene, propylene, and pentane, with pentane accounting for about 50% of the energy.

## REFERENCES

- [1] J. B. Heywood, *Internal Combustion Engine Fundamentals*. New York: McGraw-Hill, 1988.
- [2] A. K. Rowton, J. K. Ausserer, K. D. Grinstead, P. J. Litke, and M. D. Polanka, "Measuring Scaling Effects in Small Two-Stroke Internal Combustion Engines," presented at the 2014 Small Engine Technology Conference & Exposition, Pisa, Italy, SAE Technical Paper 2014-32-0010, 11 November 2014, doi: 10.4271/2014-32-0010.
- [3] S. Menon and C. Cadou, "Scaling of Miniature Piston-Engine Performance Part 1: Overall Engine Performance," *Journal of Propulsion and Power*, vol. 29, pp. 774-787, July-August 2013, doi: 10.2514/1.B34638.
- [4] S. Menon and C. Cadou, "Scaling of Miniature Piston-Engine Performance Part 2: Energy Losses," *Journal of Propulsion and Power*, vol. 29, pp. 788-799, July-August 2013, doi: 10.2514/1.B34639.
- [5] J. A. Rittenhouse, A. K. Rowton, J. K. Ausserer, and M. D. Polanka, "Preliminary Thermal Loss Measurements for a Small Internal Combustion Engine," presented at the SciTech 2014, National Harbor, MD, AIAA 2014-0529, 13-17 January 2014, doi: 10.2514/6.2014-0529.
- [6] K. P. Horn, J. K. Ausserer, M. D. Polanka, P. J. Litke, and K. D. Grinstead, "Dynamic Friction Measurements on a Small Engine Test Bench," presented at the SciTech 2015, Kissimmee, Florida, AIAA 2015-1473, 5-9 January 2015.
- [7] G. P. Blair, *Design and Simulation of Two-Stroke Engines*. United States of America: Society of Automotive Engineers, 1996.
- [8] J. B. Heywood and E. Sher, *The Two-Stroke Cycle Engine*. New York: Taylor & Francis Group, 1999.
- [9] A. Trattner and H. Grassberger, "Advantages and Challenges of Lean Operation of Two-Stroke Engines for Hand-Held Power Tools," *SAE International Journal of Engines*, vol. 8, pp. 101-119, SAE Paper Number 2014-32-0009, 11 November 2014, doi: 10.4271/2014-32-0009.
- [10] E. Hashimoto, T. Tottori, and S. Terata, "Scavenging Performance Measurements of High Speed Two-Stroke Engines," presented at the SAE International Congress & Exposition, Detroit, MI, SAE Technical Paper 850182, 25 February - 1 March 1985, doi: 10.4271/850182.
- [11] B. J. Tobis, R. Meyer, J. Yang, D. D. Brehob, and R. W. Anderson, "Scavenging of a Firing Two-Stroke Spark Ignition Engine," presented at the SAE

- International Congress & Exposition, Detroit, MI, 940393, 1 March 1994 1994, doi: 10.4271/940393.
- [12] P. H. Schweitzer and F. DeLuca, "The Tracer Gas Method of Determining the Charging Efficiency of 2-Stroke Cycle Engine," NACA Technical Note 838, January 1942.
- [13] C. F. Taylor and A. R. Rogowski, "Scavenging the 2-Stroke Engine," *SAE Transactions*, vol. 62, pp. 487-502, SAE Technical Paper 540258, 1954, doi: 10.4271/540258.
- [14] D. B. Olsen, G. C. Hutcherson, B. D. Willson, and C. E. Mitchell, "Development of the Tracer Gas Method for Large Bore Natural Gas Engines - Part 1: Method Validation," *ASME Transactions*, vol. 124, p. 8, 2002, doi: 10.1115/1.1454116.
- [15] R. W. Hurn, K. J. Hughes, and J. O. Chase, "Application of Gas Chromatography to Analysis of Exhaust Gas," presented at the SAE Annual Meeting, Detroit, Michigan, SAE Technical Paper 580259, 13-17 January 1958, doi: 10.4271/580259.
- [16] L. J. Papa, "Gas Chromatography - Measuring Hydrocarbons Down to Parts Per Billion," presented at the Mid-Year Meeting, Chicago, Illinois, SAE Technical Paper 670494, 15-19 May 1967, doi: 10.4271/670494.
- [17] N. Rudlein, W. Geiger, N. Peiz, and J.-J. Scherrbacher, "Development of a Single Run Method for the Determination of Individual Hydrocarbons (C2-C12) in Automotive Exhaust by Capillary Gas Chromatography," presented at the International Congress & Exposition, Detroit, Michigan, SAE Technical Paper 940827, 28 February - 3 March 1994, doi: 10.4271/940827.
- [18] S. Otsuki, T. Oie, and K. Ishida, "Hydrocarbon Speciation of Automotive Emissions Using High Speed Gas Chromatography," presented at the SAE International Congress and Exposition, Detroit, Michigan, SAE Technical Paper 950513, 27 February - 2 March 1995, doi: 10.4271/950513.
- [19] K. L. Olson, J. F. Loo, and P. A. Mulawa, "Rapid Hydrocarbon Speciation and Exhaust Reactivity Measurements using High Speed, High Resolution Gas Chromatography," presented at the International Fuels and Lubricants Meeting, Paris, France, SAE Technical Paper 2000-01-2950, 16 October 2000, doi: 10.4271/2000-01-2950.
- [20] J. E. Farrugia and K. L. Olson, "Speciation of Hydrocarbons in Exhaust from Low-Emission, Gasoline-Fueled Vehicles by High-Speed and Standard Gas Chromatography Models," presented at the SAE World Congress & Exposition, Detroit, Michigan, SAE Technical Paper 2007-01-0305, 16-19 April 2007, doi: 10.4271/2007-01-0305.
- [21] T. Gegg, A. Kölmel, and K. W. Beck, "Combustion Analysis on Small Two-Stroke SI-Engines for Handheld Power Tools," presented at the 2010 Small Engine Technology Conference, Linz, Austria, SAE Technical Paper 2010-32-0062, 28 September 2010, doi: 10.4271/2010-32-0062.
- [22] J. Volckens, J. Braddock, R. F. Snow, and W. Crews, "Emissions Profile from New and In-Use Handheld, 2-Stroke Engines," *Atmospheric Environment*, vol. 41, pp. 640-649, 17 August 2006, doi: 10.1016/j.atmosenv.2006.08.033.
- [23] W. Welch and T. D. Durbin, "Emissions and Demonstration of an Emission Control Technology for Small Two Stroke Utility Engines," *Journal of the Air and Waste Management Association*, vol. 54, pp. 200-206, February 2004.
- [24] J. K. Ausserer, P. J. Litke, J.-R. Groenewegen, A. Rowton, M. Polanka, and K. Grinstead, "Development of Test Bench and Characterization of Performance in Small Internal Combustion Engines," presented at the 19th Small Engine Technology Conference, Taipei, Taiwan, SAE Technical Paper 2013-32-9036, 15 October 2013, doi: 10.4271/2013-32-9036.
- [25] J. K. Ausserer, M. Polanka, J. Rittenhouse, A. Rowton, P. Litke, and K. Grinstead, "Comparison of In-Cylinder Pressure Measurement Methods in a Small Spark Ignition Engine," presented at the 2014 SAE Small Engine Technology Conference, Pisa, Italy, SAE Technical Paper 2014-32-0007, 2014.
- [26] C. F. Taylor, *The Internal Combustion Engine in Theory and Practice: Volume 2: Combustion, Fuels, Materials, Design*, Revised ed. vol. 2: MIT First Press, 1985.
- [27] Y. A. Çengel and J. M. Cimbala, *Fluid Mechanics: Fundamentals and Applications*, 2nd ed. New York, New York: McGraw Hill Science/ Engineering/ Math, 2006.
- [28] J. Baranski, "Experimental Investigation of Octane Requirement in a Turbocharged Spark-Ignition Engine," M.S. in Mechanical Engineering, School of Engineering, University of Dayton, Dayton, Ohio, 2013.
- [29] C. Grasas-Alsina, E. Freixa, P. Esteban, and J. Massó, "Low-Pressure Discontinuous Gasoline Injection in Two-Stroke Engines," presented at the International Congress and Exposition, Detroit, Michigan, SAE Technical Paper 860168, 24-28 February 1986, doi: 10.4271/960168.
- [30] "Surface Vehicle Information Report: Instrumentation and Techniques for Exhaust Gas Emissions Measurements," SAE International, J254, 2011.
- [31] A. A. H. Pádua, J. M. N. A. Fareleira, and J. C. G. Caldo, "Density and Viscosity Measurements of 2,2,4-Trimethylpentane (Isooctane) from 198K to 348K and up to 100 MPa," *Journal of Chemical Engineering Data*, vol. 41, pp. 1488-1494, 1996.
- [32] D. Pecar and V. Dolecek, "Temperature and Pressure Dependence of Volumetric Properties for Binary Mixtures of n-heptane and n-octane," *Acta Chimica Slovenica*, vol. 54, pp. 538-544, 2007.
- [33] H. Zhao and N. Ladommatos, *Engine Combustion and Diagnostics*. Warrendale, Pennsylvania: Society of Automotive Engineers, 2001.
- [34] "Surface Vehicle Information Report: Constant Volume Sampler System for Exhaust Emissions Measurement," J1094, 2011.
- [35] C. Cadou, N. Moulton, and S. Menon, "Performance Measurement and Scaling in Small Internal Combustion Engines," presented at the 41st Aerospace Sciences and Exhibit, Reno, NV, 6-9 January 2003 2003.
- [36] M. Maekawa, "Text of Course," *Japanese Society of Mechanical Engineers*, p. 23, 1957.



## CONTACT INFORMATION

Capt Joseph Ausserer  
[Joseph.Ausserer@wpafb.af.mil](mailto:Joseph.Ausserer@wpafb.af.mil)  
(937)-904-4834

## ACKNOWLEDGMENTS

The authors would like to acknowledge the support of everyone who consulted and assisted with the fabrication of the Small Engine Test Bench. They would like to specifically thank Mr. Rich Striebich for his assistance with setting up and operating the gas chromatography and mass spectrometry equipment, as well as Mr. Rich Ryman for his assistance machining fixtures for the setup. Acknowledgement for funding is due to the Air Force Research Laboratory.

## NOMENCLATURE

[·]	concentration, species [mol/L]
% <i>i</i>	percent of species <i>i</i> (listed in subscripts)
<i>Λ</i>	delivery ratio
<i>A</i>	peak area
<i>A/F</i>	air to fuel ratio
<i>C</i>	carbon atoms
<i>ṁ</i>	flow rate, mass [g/s]
<i>MW</i>	molecular weight [g/mol]
<i>ṅ</i>	flow rate, molar [mol/s]
<i>x</i>	mass fraction
<i>y</i>	mole fraction
<i>η</i>	efficiency
<i>ζ</i>	sensitivity factor

### Subscripts

<i>adj</i>	adjusted
<i>air</i>	air
<i>Ar</i>	argon
<i>ch</i>	charging
<i>CO</i>	carbon monoxide
<i>ex</i>	exhaust
<i>fc</i>	fresh charge
<i>fuel</i>	fuel
<i>H<sub>2</sub></i>	hydrogen
<i>i</i>	generic species
<i>iso – octane</i>	iso-octane
<i>O<sub>2</sub></i>	oxygen
<i>N<sub>2</sub></i>	nitrogen
<i>tr</i>	trapping

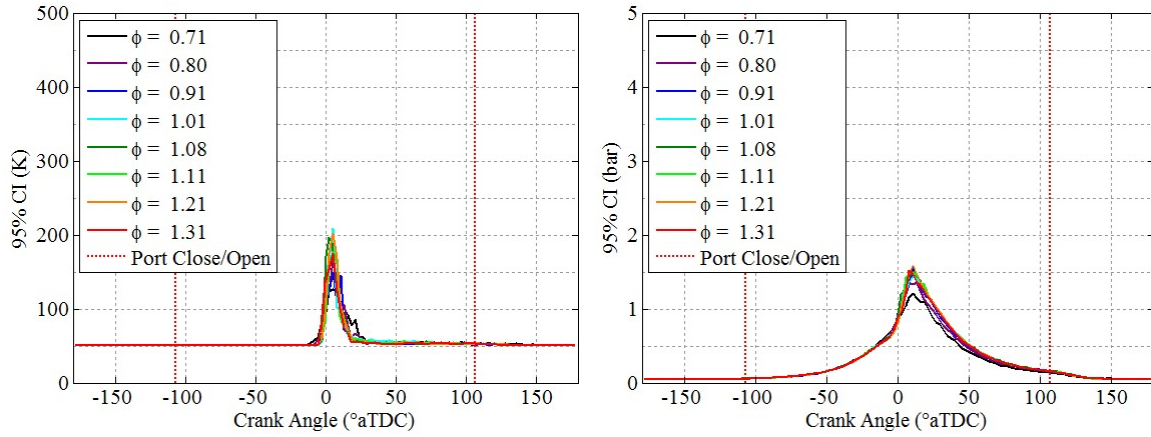
## DEFINITIONS/ABBREVIATIONS

<b>ATDC</b>	after top dead center
<b>CA50</b>	crank angle 50%
<b>COV</b>	coefficient of variance
<b>DI</b>	direct injection
<b>ICE</b>	internal combustion engine
<b>RPA</b>	remotely piloted aircraft
<b>FID</b>	flame ionization detector
<b>GC</b>	gas chromatography/ chromatograph
<b>IMEP</b>	indicated mean effective pressure
<b>MS</b>	mass spectrometry/spectrometer
<b>MSD</b>	mass selective detector
<b>ON</b>	octane number
<b>PRF</b>	primary reference fuel
<b>PT</b>	partial throttle
<b>SERB</b>	Small Engine Research Bench
<b>SIM</b>	Selective Ion Mode
<b>SOI</b>	start of injection
<b>TCD</b>	thermal conductivity detector
<b>UHCs</b>	unburned hydrocarbons
<b>WOT</b>	wide open throttle

## **Appendix G**

This appendix serves as a supplement to Chapter V, Section 2. It contains additional plots showing the crank angle resolved, 95% confidence intervals on the in-cylinder temperature and pressure measurements. Since the extra figures more than a half page each, the figures begin on the following page.

### Modellmotoren 3W-28i Engine (SA/V=1.81 cm<sup>-1</sup>)



### Modellmotoren 3W-55i Engine (SA/V=1.46 cm<sup>-1</sup>)

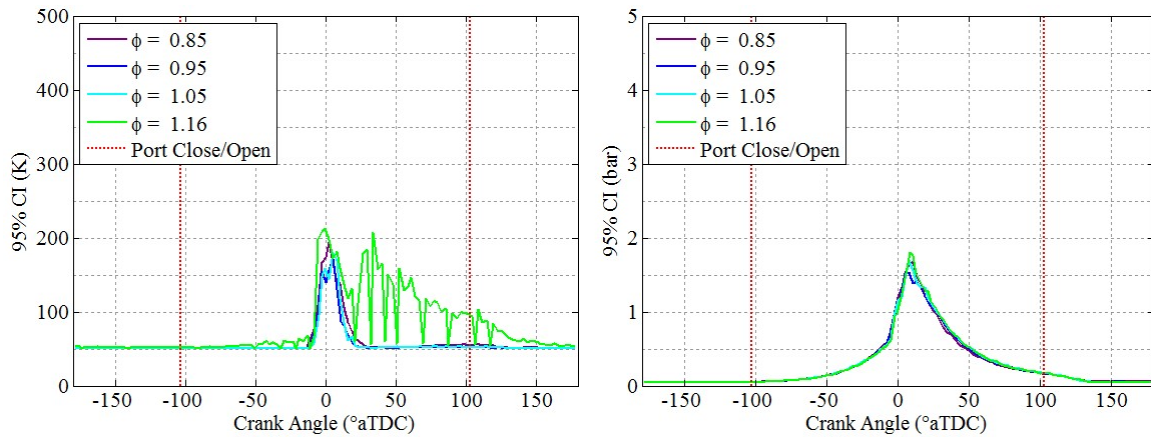
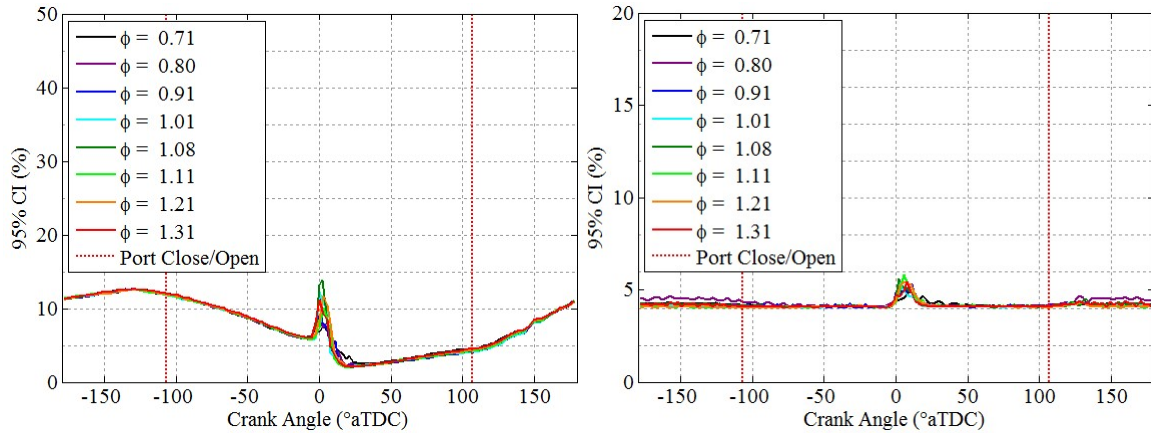


**Figure 177: 95% confidence interval on measured temperature and pressure expressed in absolute units for equivalence ratio sweep results in Figure 117.**

Modellmotoren 3W-28i Engine (SA/V=1.81 cm<sup>-1</sup>)



Modellmotoren 3W-55i Engine (SA/V=1.46 cm<sup>-1</sup>)

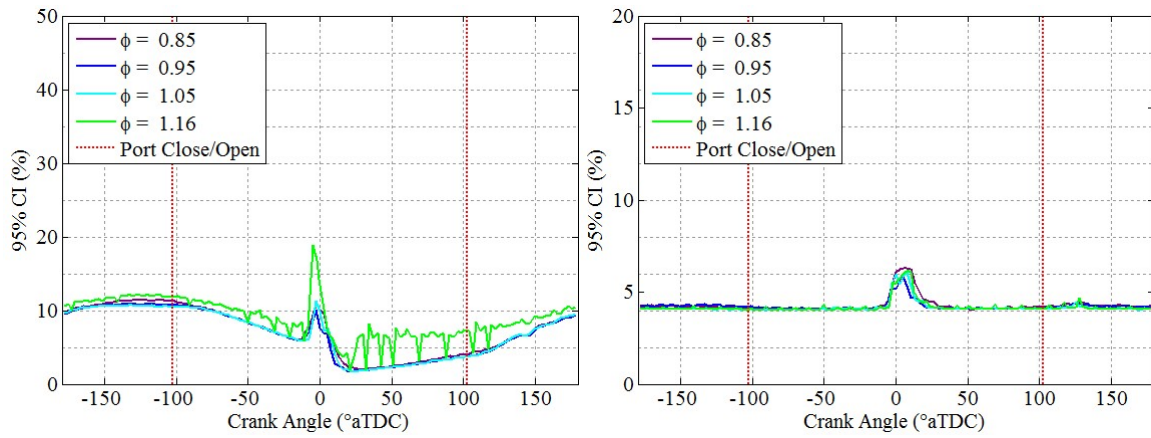
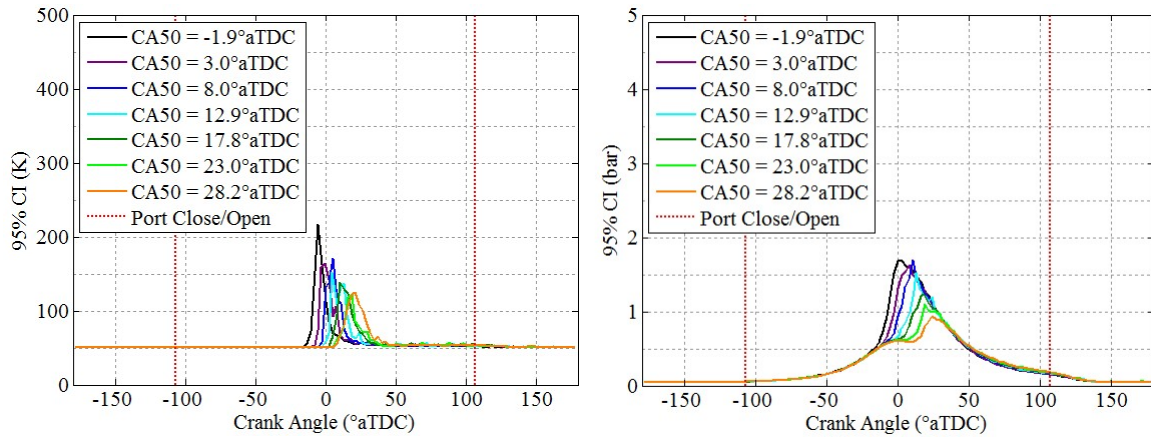


**Figure 178: 95% confidence interval on measured temperature and pressure expressed as a percentage for equivalence ratio sweep results in Figure 117.**

### Modellmotoren 3W-28i Engine (SA/V=1.81 cm<sup>-1</sup>)



### Modellmotoren 3W-55i Engine (SA/V=1.46 cm<sup>-1</sup>)

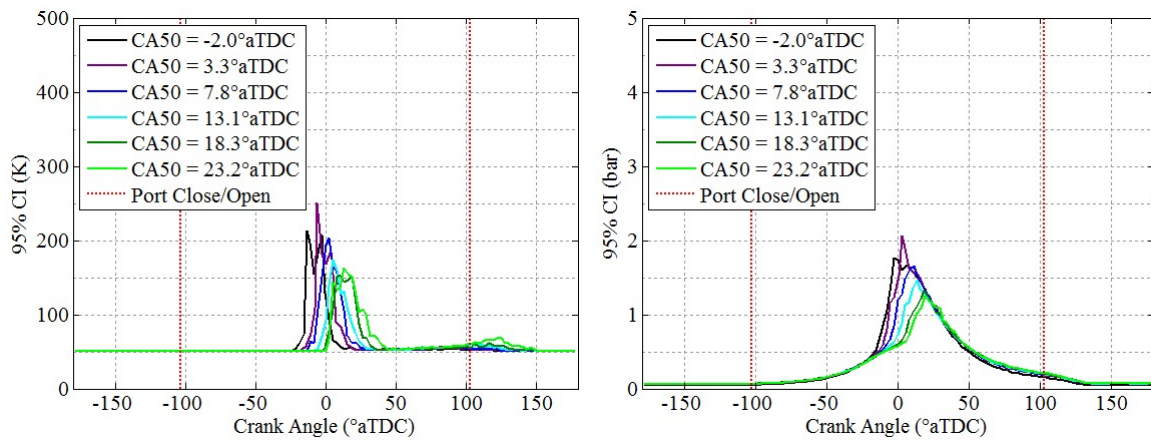
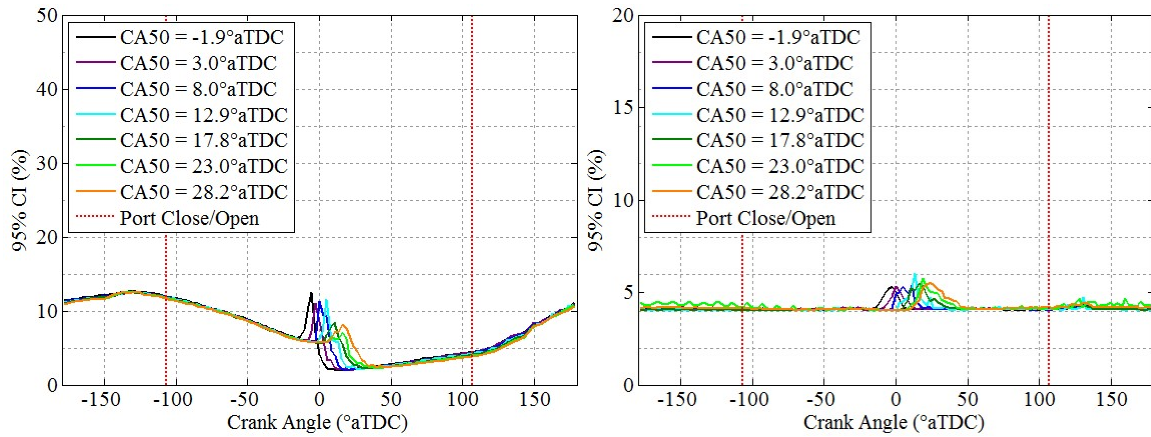


**Figure 179: 95% confidence interval on measured temperature and pressure expressed in absolute units for combustion phasing sweep results in Figure 122.**



### Modellmotoren 3W-28i Engine (SA/V=1.81 cm<sup>-1</sup>)



### Modellmotoren 3W-55i Engine (SA/V=1.46 cm<sup>-1</sup>)

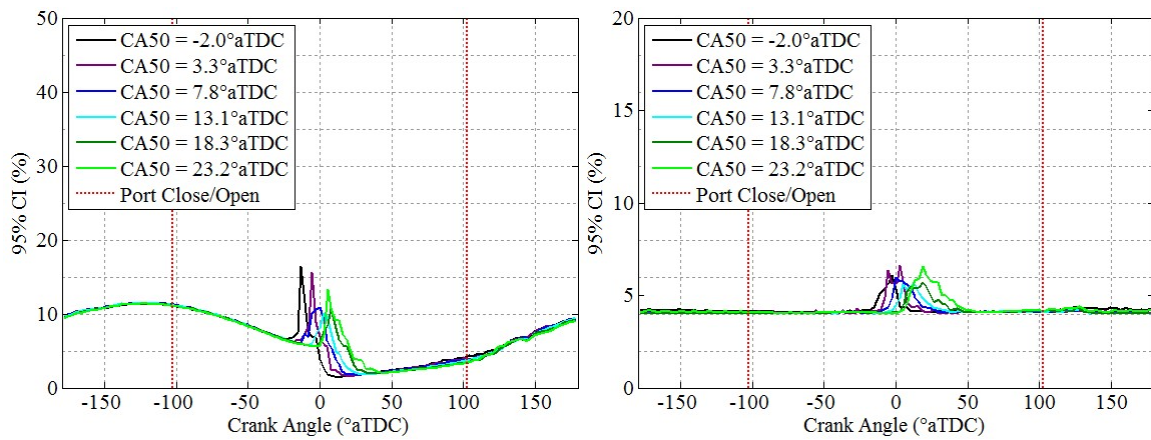
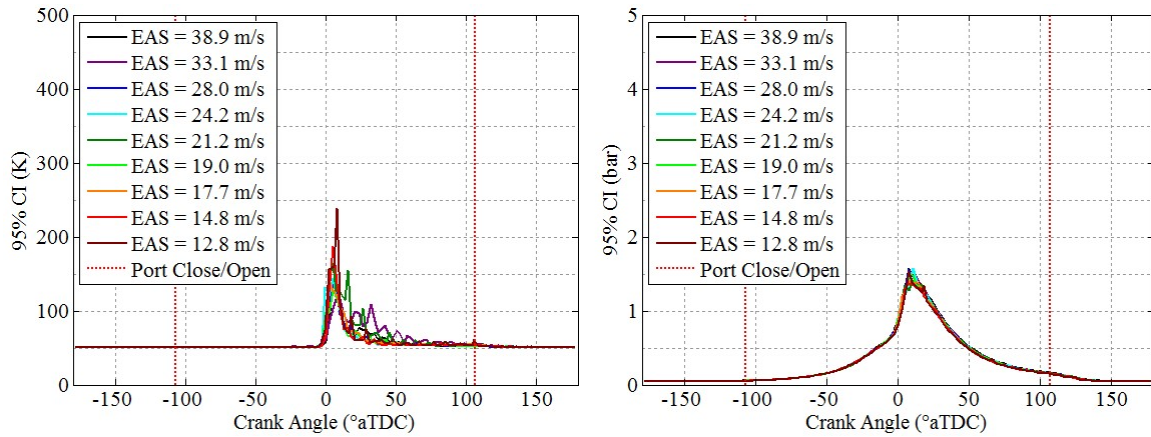


**Figure 180: 95% confidence interval on measured temperature and pressure expressed as a percentage for combustion phasing sweep results in Figure 122.**

### Modellmotoren 3W-28i Engine ( $SA/V=1.81 \text{ cm}^{-1}$ )



### Modellmotoren 3W-55i Engine ( $SA/V=1.46 \text{ cm}^{-1}$ )

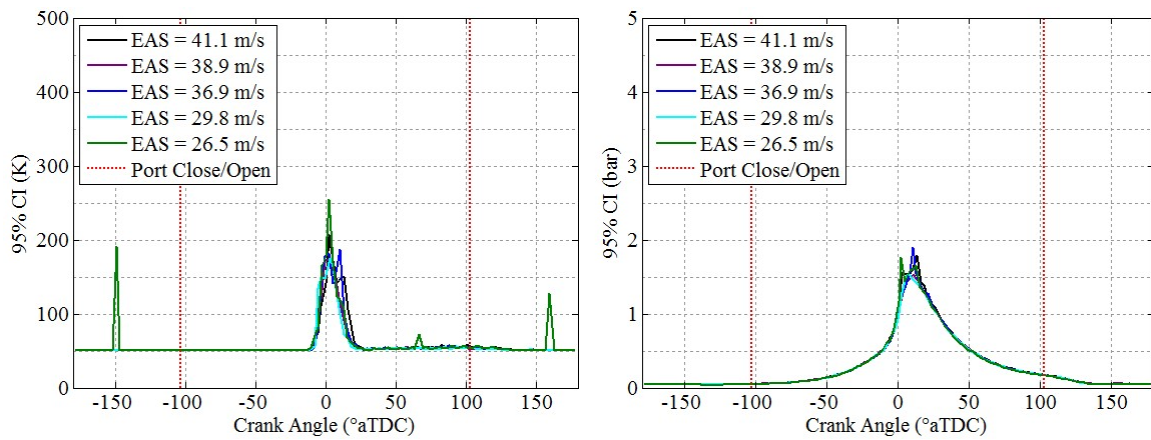
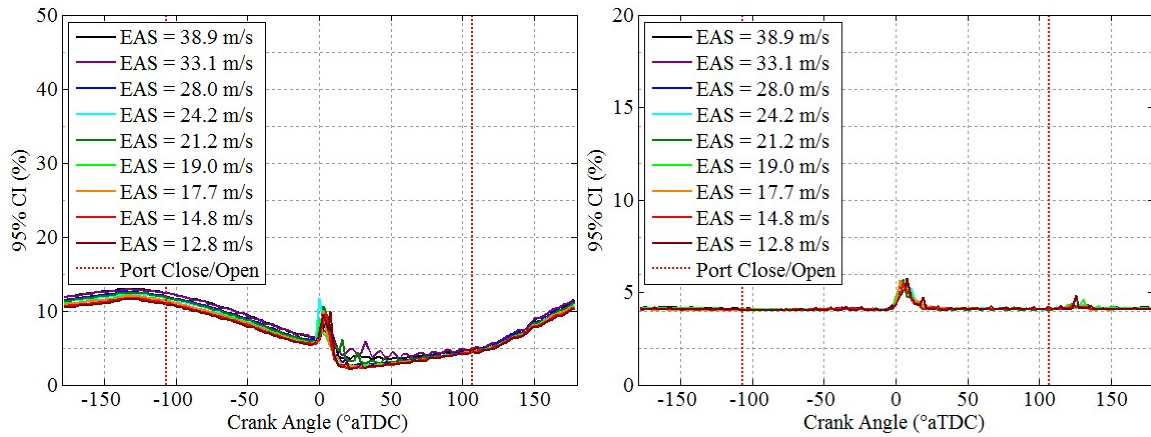


**Figure 181: 95% confidence interval on measured temperature and pressure expressed in absolute units for cooling sweep results in Figure 127.**

### Modellmotoren 3W-28i Engine ( $SA/V=1.81 \text{ cm}^{-1}$ )



### Modellmotoren 3W-55i Engine ( $SA/V=1.46 \text{ cm}^{-1}$ )

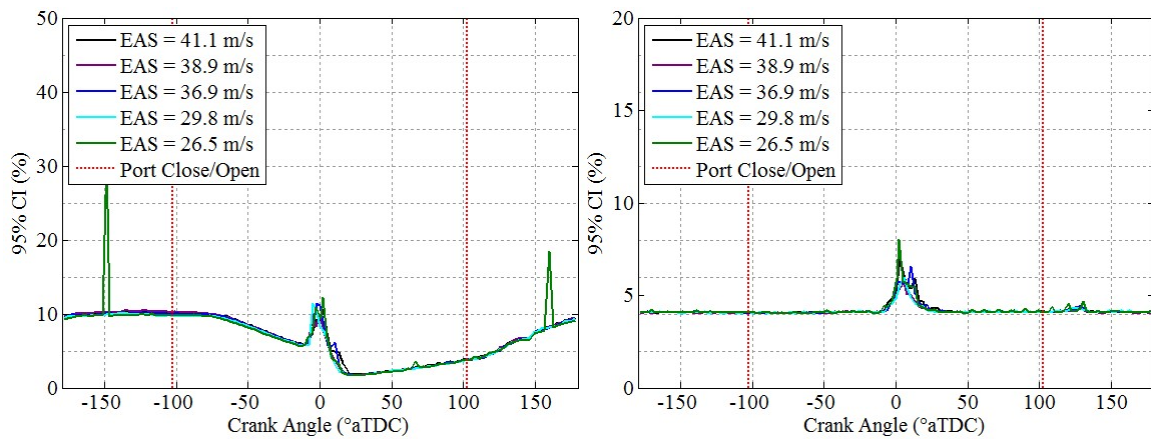
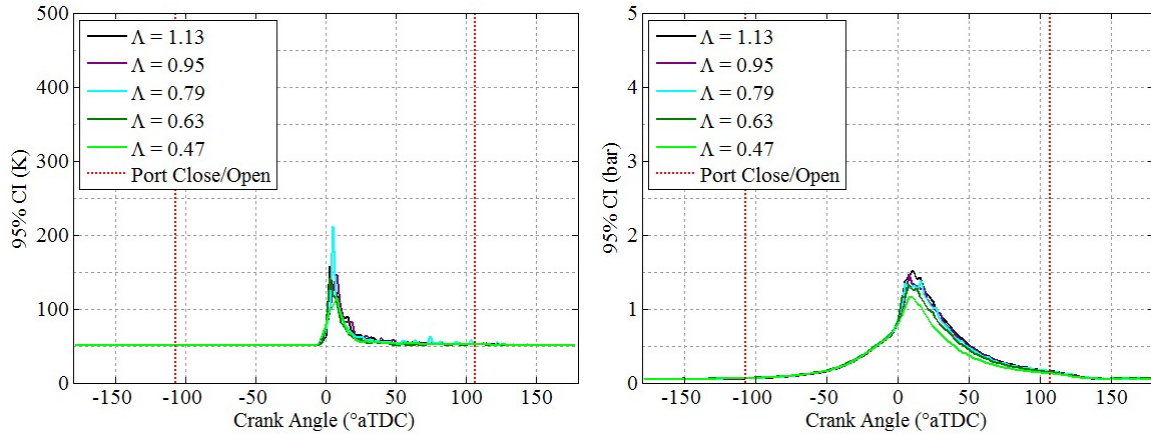


**Figure 182: 95% confidence interval on measured temperature and pressure expressed as a percentage for cooling sweep results in Figure 127.**

### Modellmotoren 3W-28i Engine ( $SA/V=1.81 \text{ cm}^{-1}$ )



### Modellmotoren 3W-55i Engine ( $SA/V=1.46 \text{ cm}^{-1}$ )

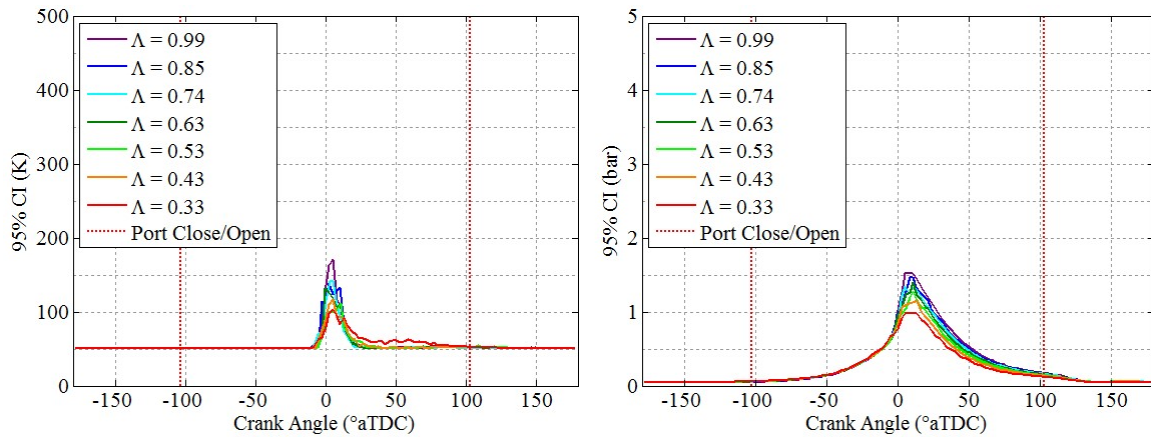
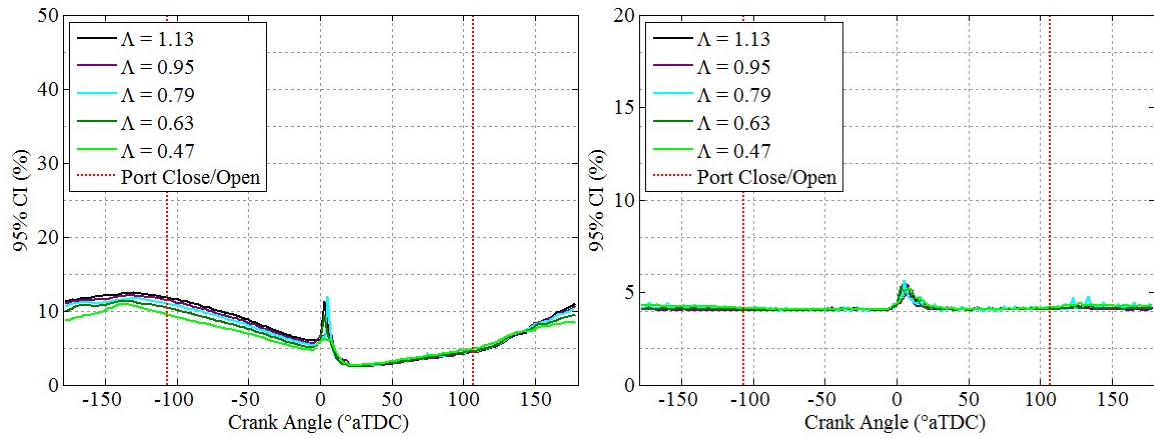


**Figure 183: 95% confidence interval on measured temperature and pressure expressed in absolute units for throttle sweep results in Figure 132.**

### Modellmotoren 3W-28i Engine (SA/V=1.81 cm<sup>-1</sup>)



### Modellmotoren 3W-55i Engine (SA/V=1.46 cm<sup>-1</sup>)

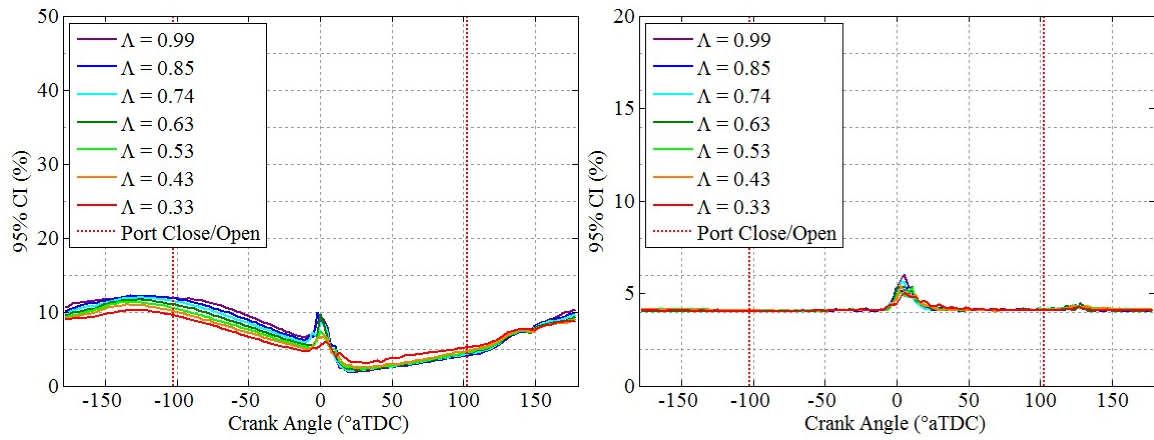


**Figure 184: 95% confidence interval on measured temperature and pressure expressed as a percentage for throttle sweep results in Figure 132.**

## Bibliography

- [1] D. Jenkins and B. Vasigh, "The Economic Impact of Unmanned Aircraft Systems Integration in the United States," Association for Unmanned Vehicle Systems International, Arlington, Virginia, March 2013.
- [2] S. Menon, "The Scaling of Performance and Losses in Miniature Internal Combustion Engines," Ph.D. Aeronautical Engineering, Department of Aeronautical Engineering, University of Maryland, 2010.
- [3] J. R. Wilson. (2007, May) UAVs: A World Wide Roundup. *Aerospace America*. pp. 30-35.
- [4] C. Cadou, S. Menon, N. Moulton, and T. Leach, "Performance Scaling and Measurement for Hydrocarbon-Fueled Engines with Mass Less Than 1 kg," presented at the AIAA's 1st Technical Conference and Workshop on Unmanned Aerospace Vehicles, Portsmouth, Virginia, 20-23 May 2002.
- [5] A. K. Rowton, J. K. Ausserer, K. D. Grinstead, P. J. Litke, and M. D. Polanka, "Measuring Scaling Effects in Small Two-Stroke Internal Combustion Engines," presented at the 2014 Small Engine Technology Conference & Exposition, Pisa, Italy, SAE Technical Paper 2014-32-0010, 11 November 2014, doi: 20.4271/2014-32-0010.
- [6] S. Menon and C. Cadou, "Scaling of Miniature Piston-Engine Performance Part 1: Overall Engine Performance," *Journal of Propulsion and Power*, vol. 29, pp. 774-787, July-August 2013, doi: 10.2514/1.B34638.
- [7] C. Cadou, N. Moulton, and S. Menon, "Performance Measurement and Scaling in Small Internal Combustion Engines," presented at the 41st Aerospace Sciences Meeting and Exhibit, Reno, Nevada, 6-9 January 2003.
- [8] S. Menon, "Performance Measurement and Scaling in Small Internal Combustion Engines," M.S. Aeronautical Engineering, Department of Aeronautical Engineering, University of Maryland, 2006.
- [9] C. F. Taylor, *The Internal Combustion Engine in Theory and Practice: Volume 1: Thermodynamics, Fluid Flow, Performance*, 2nd revised ed. vol. 1. Cambridge, Massachusetts: First MIT Press, 1985.
- [10] J. K. Ausserer, P. J. Litke, J. R. Groenewegen, A. Rowton, M. Polanka, and K. Grinstead, "Development of Test Bench and Characterization of Performance in Small Internal Combustion Engines," presented at the 19th Small Engine Technology Conference, Taipei, Taiwan, SAE Technical Paper 2013-32-9036, 15 October 2013, doi: 10.4271/2013-32-9036.
- [11] A. Wiegand, "Conversion of a Micro, Glow-Ignition, Two-Stroke Engine from Nitromethane-Methanol Blend Fuel to Military Jet Propellant (JP-8)," M.S. Mechanical Engineering, Michigan Technological University, 2012.
- [12] P. Wolfowitz, "Department of Defense Directive Number 4140.25," 2004.
- [13] J. Baranski, E. Anderson, K. Grinstead, J. Hoke, and P. Litke, "Control of Fuel Octane for Knock Mitigation on a Dual-Fuel Spark-Ignition Engine," presented at the SAE World Congress, Detroit, Michigan, SAE Technical Paper 2013-01-0320, 8 April 2013, doi: 10.4271/2013-01-0320.
- [14] C. W. Wilson, P. I. King, J. L. Hoke, and F. R. Schauer, "The Effects of Varied Octane Rating on a Small Spark Ignition Internal Combustion Engine," presented

- at the 48th AIAA Aerospace Sciences Meeting Including the New Horizons Forum and Aerospace Exposition, Orlando, Florida, 4-7 January 2010.
- [15] G. Cathcart, G. Dickson, and S. Ahern, "The Application of Air-Assist Direct Injection for Spark-Ignited Heavy Fuel 2-Stroke and 4-Stroke Engines," presented at the Small Engine Technology Conference and Exposition, Bangkok, Thailand, SAE Technical Paper 2005-32-0065, 12 October 2005, doi: 10.4271/2005-32-0065.
  - [16] S. Menon and C. Cadou, "Scaling of Miniature Piston-Engine Performance Part 2: Energy Losses," *Journal of Propulsion and Power*, vol. 29, pp. 788-799, July-August 2013, doi: 10.2514/1.B34639.
  - [17] W. J. D. Annand, "Heat Transfer in the Cylinders of Reciprocating Internal Combustion Engines," *Proceedings of the Institution of Mechanical Engineers*, vol. 177, pp. 973-991, 1 June 1963, doi: 10.1243/PIME\_PROC\_1963\_177\_069\_02799.
  - [18] W. Nusselt, "Die Wärmeübergang in den Verbrennungs-kraftmaschinen," *Zeitschrift des Vereines Deutscher Ingenieure*, vol. 67, pp. 696-708, 1923.
  - [19] G. Borman and K. Nishiwak, "Internal Combustion Engine Heat Transfer," *Progress in Energy and Combustion Science*, vol. 13, pp. 1-46, 1987.
  - [20] D. E. Foster, "An Overview of Zero-Dimensional Thermodynamic Models of IC Engine Data Analysis," presented at the International Fuels and Lubricants Meeting and Exposition, Tulsa, Oklahoma, SAE Technical Paper 852070, 21-24 October 1985, doi: 10.4271/852070.
  - [21] J. B. Heywood, *Internal Combustion Engine Fundamentals*. New York, New York: McGraw-Hill, 1988.
  - [22] J. B. Heywood and E. Sher, *The Two-Stroke Cycle Engine*. New York, New York: Taylor & Francis Group, 1999.
  - [23] K. Kumar, J. E. Freech, C. J. Sung, and Y. Huang, "Laminar Flame Speeds of Preheated iso-Octane/O<sub>2</sub>/N<sub>2</sub> and n-Heptane/O<sub>2</sub>/N<sub>2</sub> Mixtures," *Journal of Propulsion and Power*, vol. 23, pp. 428-436, March 2007, doi: 10.2514/1.24391.
  - [24] C. F. Taylor, *The Internal Combustion Engine in Theory and Practice: Volume 2: Combustion, Fuels, Materials, Design*, Revised ed. vol. 2. Cambridge, Massachusetts: MIT First Press, 1985.
  - [25] W. W. Pulkrabek, *Engineering Fundamentals of the Internal Combustion Engine*. Upper Saddle River, New Jersey: Prentice Hall, 1997.
  - [26] R. Stone and J. K. Ball, *Automotive Engineering Fundamentals*. Warrendale, Pennsylvania: SAE International, 2004.
  - [27] G. P. Blair, *Design and Simulation of Two-Stroke Engines*. Warrendale, Pennsylvania: Society of Automotive Engineers, 1996.
  - [28] C. R. Ferguson and A. T. Kirkpatrick, *Internal Combustion Engines: Applied Thermosciences*. New York, New York: John Wiley & Sons, Inc., 2000.
  - [29] D. G. Wilson and T. Korakianitis, *The Design of High-Efficiency Turbomachinery and Gas Turbines*. Upper Saddle River, New Jersey: Prentice Hall, 1998.
  - [30] D. Jeffrey. (2014). *Lecture 5: Heat Engines, Refridgerators, and the Carnot Engine*. [Online] Available: [http://www.nhn.ou.edu/~jeffery/course/c\\_energy/energy/lec005.html](http://www.nhn.ou.edu/~jeffery/course/c_energy/energy/lec005.html) [Accessed: 30 September 2014].
  - [31] A. Trattner, S. Schmidt, R. Kirchberger, H. Eichlseder, A. Kölmel, M. Raffenberg, et al., "Future Engine Technology in Hand-Held Power Tools," *SAE International*



- Journal of Engines*, vol. 5, pp. 1-18, SAE Technical Paper 2012-32-0111, 23 October 2012, doi: 10.4271/2012-32-0111.
- [32] D. T. Falkowski, D. L. Abata, and P. Cho, "The Performance of a Spark-Ignited Stratified-Charge Two Stroke Engine Operating on a Kerosine Based Aviation Fuel," presented at the International Off-Highway & Powerplant Congress & Exposition, Milwaukee Wisconsin, SAE Technical Paper 972737, 8-10 September 1997, doi: 10.4271/972737.
  - [33] I. Sher, D. Levinzon-Sher, and E. Sher, "Miniaturization Limitations of HCCI Internal Combustion Engines," *Applied Thermal Engineering*, vol. 29, pp. 400-411, 18 March 2009, doi: 10.1016/j.applthermaleng.2008.03.020.
  - [34] V. Manente, "Characterization of Glow Plug and HCCI Combustion in a Small Volume at High Engine Speed," Licentiate in Engineering M.S., Department of Energy Sciences, Lund University, 2007.
  - [35] J. Chang, O. Güralp, Z. Filipi, D. A.-W. Kuo, P. Najt, and R. Rask, "New Heat Transfer Correlation for an HCCI Engine Derived from Measurements of Instantaneous Surface Heat Flux," presented at the 2004 Powertrain & Fluid Systems Conference & Exhibition, Tampa Bay, Florida, SAE Technical Paper 2004-01-2996, 25 October 2004, doi: 10.4271/2004-01-2996.
  - [36] C. Cadou and S. Menon, "Scaling of Losses in Small IC Aero Engines with Engine Size," presented at the 42nd AIAA Aerospace Sciences Meeting and Exhibit, Reno, Nevada, 5-8 January 2004.
  - [37] N. Moulton, "Performance Measurement and Simulation of a Small Internal Combustion Engine," M.S. Aeronautical Engineering, Department of Aeronautical Engineering, University of Maryland, 2007.
  - [38] B. Duddy, J. Lee, M. Walluk, and D. Hallbach, "Conversion of a Spark-Ignited Aircraft Engine to JP-8 Heavy Fuel for Use in Unmanned Aerial Vehicles," presented at the SAE 2011 World Congress & Exhibition, Detroit, Michigan, SAE Technical Paper 2011-01-0145, 12 April 2011, doi: 10.4271/2011-01-0145.
  - [39] S. C. Crosbie, "Increasing Reliability of a Small 2-Stroke Internal Combustion Engine for Dynamically Changing Altitudes," M.S. Aeronautical Engineering, Department of Aeronautics and Astronautics, Air Force Institute of Technology, WPAFB, Ohio, 2012.
  - [40] S. C. Crosbie, M. D. Polanka, P. J. Litke, and J. L. Hoke, "Increasing Reliability of a Two-Stroke Internal Combustion Engine for Dynamically Changing Altitudes," *Journal of Propulsion and Power*, vol. 30, pp. 87-95, 2014, doi: 10.2514/1.B34753.
  - [41] (2014). *Currawong Engineering*. [Online] Available: <http://www.currawongeng.com/> [Accessed: 31 May 2016].
  - [42] P. J. Suhy, E. Morgan, L. W. Evers, and J. E. Wank, "The Feasibility of a Kerosene Fueled Spark Ignited Two-Stroke Engine," presented at the International Off-Highway & Powerplant Congress & Exposition, SAE Technical Paper 911846, 1 September 1991, doi: 10.4271/911846.
  - [43] C. W. Wilson, "Performance of a Small Internal Combustion Engine Using N-Heptane and Iso-Octane," M.S. Aeronautical Engineering, Department of Aeronautics and Astronautics, Air Force Institute of Technology, WPAFB, Ohio, 2010.

- [44] J. R. Groenewegen, "The Performance and Emissions Characteristics of Heavy Fuels in a Small Spark Ignition Engine," M.S. Mechanical Engineering, School of Engineering, University of Dayton, Dayton, Ohio, 2011.
- [45] (2014). *FlexDI - Flexible Direct Injection*. [Online] Available: <http://www.orbitalcorp.com.au/businesses/intellectual-propertyflexdi.html> [Accessed: 18 August 2014].
- [46] G. D. Tankaria and B. B. Ghosh, "Some Studies on Use of Kerosene and Petrol Blends in Spark-Ignition Engine," *Journal of the Institution of Engineers (India)*, vol. 57, June 1974.
- [47] B. Gupta and V. Ganesan, "Experimental Investigation on Performance Characteristics of a Small Four-Stroke SI Engine with Different Fuel Blends," *Journal of the Institution of Engineers (India)*, vol. 64, pp. 147-152, January 1984.
- [48] (2009). *Daves Tuning Alternatives*. [Online] Available: [http://www.davestuning.com/index.php?p=1\\_11\\_Fuel-Injector-Sizing](http://www.davestuning.com/index.php?p=1_11_Fuel-Injector-Sizing) [Accessed: 8 October 2014].
- [49] A. Kinnen, W. Layher, and H. Daschner, "Electronically Controlled Batteryless Injection System for Small Two-Stroke SI Engines," presented at the SAE Small Engine Technology Conference, Madison, Wisconsin, SAE Technical Paper 2012-32-0118, 23 October 2012, doi: 2012-32-0118.
- [50] (2014). *Ecotrons: Fuel Injection and Engine Controls*. [Online] Available: [http://www.ecotrons.com/products/small\\_engine\\_fuel\\_injection\\_kit/](http://www.ecotrons.com/products/small_engine_fuel_injection_kit/) [Accessed: 8 October 2014].
- [51] (2014). *Motech Engine Management & Data Acquisition Systems*. [Online] Available: <http://www.motec.com/> [Accessed: 8 October 2014].
- [52] (2014). *Haltech Software*. [Online] Available: <http://www.haltech.com/product/software/> [Accessed: 23 August 2016].
- [53] J. Baranski, "Experimental Investigation of Octane Requirement in a Turbocharged Spark-Ignition Engine," M.S. Mechanical Engineering, School of Engineering, University of Dayton, Dayton, Ohio, 2013.
- [54] H. Dueker, K. H. Friese, and W. D. Haecker, "Ceramic Aspects of the Bosch Lambda-Sensor," SAE Technical Paper 750223, 1 February 1975, doi: 10.4271/750223.
- [55] E. Hamann, H. Manger, and L. Steinke, "Lambda-Sensor with Y2O3-Stabilized ZrO2-Ceramic for Application in Automotive Emission Control Systems," SAE Technical Paper 770401, 1 February 1977, doi: 10.4271/770401.
- [56] H. Zhao and N. Ladommatos, *Engine Combustion and Diagnostics*. Warrendale, Pennsylvania: Society of Automotive Engineers, 2001.
- [57] R. Bosch, *Automotive Handbook, 7th English Edition*. Stuttgart: Robert Bosch GmbH, 2007.
- [58] M. Greiner, P. Romann, and U. Steinbrenner, "BOSCH Fuel injectors - New Developments," presented at the SAE International Congress & Exposition, Detroit, Michigan, SAE Technical Paper 870124, 23-27 February 1987, doi: 10.4271/870124.
- [59] C. D. Gierke, *Two Stroke Glow Engines for R/C Aircraft*. Wilton, Connecticut: Air Age Inc., 1994.

- [60] R. Fleck, G. P. Blair, and R. A. R. Houston, "An Improved Model for Predicting Reed Valve Behaviour in Two-Stroke Cycle Engines," presented at the International Off-Highway & Powerplant Congress & Exposition, Milwaukee, Wisconsin, SAE Technical Paper 871654, 14-17 September 1987, doi: 10.4271/871654.
- [61] R. Fleck, A. McGregor, and P. A. Harrington, "Evaluation of Reed Valves in High Performance Two-Stroke Engines," presented at the Motorsports Engineering Conference & Exposition, SAE Technical Paper 942528, 1 December 1994, doi: 10.4271/942528.
- [62] C. F. Taylor, A. R. Rogowski, A. Hagen, and J. Koppernaes, "Loop Scavenging Versus Through Scavenging of Two-Stroke Engines," SAE Technical Paper 580044, 1 January 1958, doi: 10.4271/580044.
- [63] "Surface Vehicle Standard: Engine Power Test Code - Spark Ignition and Compression Ignition - Gross Power and Torque Rating," SAE International, J1995, 2014.
- [64] H. M. Cheung and J. B. Heywood, "Evaluation of a One-Zone Burn-Rate Analysis Procedure Using Production SI Engine Pressure Data," presented at the International Fuels & Lubricants Meeting & Exposition, Philadelphia, Pennsylvania, SAE Technical Paper 932749, 1 October 1993, doi: 10.4271/932749.
- [65] J. K. Ball, R. R. Raine, and C. R. Stone, "Combustion Analysis and Cycle-by-Cycle Variations in Spark Ignition Engine Combustion Part 1: An Evaluation of Combustion Analysis Routines by Reference to Model Data.," *Proceedings of the Institution of Mechanical Engineers, Part D: Journal of Automobile Engineering*, vol. 212, pp. 381-399, 1 May 1998, doi: 10.1243/0954407981526046.
- [66] Y. Y. Wu, B. C. Chen, and F. C. Hsieh, "Heat Transfer Model for Small-Scale Air-Cooled Spark-Ignition Four-Stroke Engines," *International Journal of Heat and Mass Transfer*, vol. 49, pp. 3895-3905, 27 June 2006, doi: 10.1016/j.ijheatmasstransfer.2006.03.043.
- [67] Y. Y. Wu, B. C. Chen, F. C. Hsieh, and C. T. Ke, "Heat Transfer Model for Small-Scale Spark-Ignition Engines," *International Journal of Heat and Mass Transfer*, vol. 52, pp. 1875-1886, 8 December 2008, doi: 10.1016/j.ijheatmasstransfer.2008.10.015.
- [68] Y. Wu, B. Chen, H. Hsieh, and C. Ke, "Heat Transfer Model for Scooter Engines," presented at the SAE World Congress and Exposition, Detroit, Michigan, SAE Technical Paper 2008-01-0387, 14-17 April 2008, doi: 10.4271/2008-01-0387.
- [69] J. Abraham, F. A. Williams, and F. V. Bracco, "A Discussion of Turbulent Flame Structure in Premixed Charges," presented at the International Congress & Exposition, Detroit, Michigan, SAE Technical Paper 850345, 1 February 1985, doi: 10.4271/850345.
- [70] S. R. Turns, *An Introduction to Combustion: Concept and Applications*. Boston, Massachusetts: McGraw Hill, 2000.
- [71] S. Menon and C. Cadou, "Investigation of Combustion Processes in Miniature Internal Combustion Engines," *Combustion Science and Technology*, vol. 185, pp. 1667-1695, 7 October 2013, doi: 10.1080/00102202.2013.829720.
- [72] A. V. Bueno, J. A. Velasquez, and L. F. Milanez, "Internal Combustion Engine Indicating Measurements," in *Applied Measurement Systems*: InTech, 2012.

- [73] D. R. Rogers, *Engine Combustion: Pressure Measurement and Analysis*. Warrendale, Pennsylvania: SAE International, 2010.
- [74] K. J. Roth, A. Sobiesiak, L. Robertson, and S. Yates, "In-Cylinder Pressure Measurements with Optical Fiber and Piezoelectric Pressure Transducers," presented at the SAE 2002 World Congress, Detroit, Michigan, SAE Technical Paper 2002-01-0745, 4 March 2002, doi: 10.4271/2002-01-0745.
- [75] J. K. Ausserer, A. Rowton, P. Litke, K. Grinstead, and M. Polanka, "Comparison of In-Cylinder Pressure Measurement Methods in a Small Spark Ignition Engine," presented at the 2014 SAE Small Engine Technology Conference, Pisa, Italy, SAE Technical Paper 2014-32-0007, 11 November 2014, doi: 10.4271/2014-32-0007.
- [76] D. Bradley and G. T. Kalghatgi, "Influence of Autoignition Delay Time Characteristics of Different Fuels on Pressure Waves and Knock in Reciprocating Engines," *Combustion and Flame*, vol. 156, pp. 2307-2318, 8 October 2009, doi: 10.1016/j.combustflame.2009.08.003.
- [77] C. D. Miller, "Relation Between Spark-Ignition Engine Knock, Detonation Waves, and Autoignition as Shown by High-Speed Photography," National Advisory Committee on Aeronautics Report 855, 1946.
- [78] C. Livengood and P. C. Wu, "Correlation of Autoignition Phenomena in Internal Combustion Engines and Rapid Compression Machines," *Symposium (International) on Combustion*, vol. 5, pp. 347-356, 1955, doi: 10.1016/S0082-0784(55)80047-1.
- [79] H. Zhao, *Advanced Direct Injection Combustion Engine Technologies and Development, Volume 1: Gasoline and Gas Engines*. Boca Raton, Florida: CRC Press LLC, 2010.
- [80] K. C. Tucker, "A Flash Vaporization System for Detonation of Hydrocarbon Fuels in a Pulse Detonation Engine," Ph.D. Aeronautical Engineering, Department of Aeronautics and Astronautics, Air Force Institute of Technology, WPAFB, Ohio, 2005.
- [81] E. Galloni, "Dynamic Knock Detection and Quantification in a Spark Ignition Engine by Means of a Pressure Based Method," *Energy Conservation and Management*, vol. 64, pp. 256-262, 26 September 2012, doi: 10.1016/j.enconman.2012.05.015.
- [82] X. Zhen, Y. Wang, S. Xu, Y. Zhu, C. Tao, T. Xu, *et al.*, "The Engine Knock Analysis - An Overview," *Applied Energy*, vol. 92, pp. 628-636, 20 December 2011, doi: <http://dx.doi.org/10.1016/j.apenergy.2011.11.079>.
- [83] W. P. Attard, H. Blaxill, E. Anderson, and P. J. Litke, "Knock Limit Extension with a Gasoline Fueled Pre-Chamber Jet Igniter in a Modern Vehicle Powertrain," *SAE International Journal of Engines*, vol. 5, pp. 1-15, SAE Technical Paper 2012-01-1143, 16 April 2012, doi: 10.4271/2012-01-1143.
- [84] E. K. Anderson, A. C. Brown, J. A. Baranski, J. L. Hoke, P. J. Litke, and F. R. Schauer, "Performance of Low-Octane Fuels in a Rotax 914 Engine with Advanced Knock Mitigation Strategies," presented at the 47th AIAA/ASME/SAE/ASEE Joint Propulsion Conference & Exhibit, San Diego, California, 31 July - 3 August 2011.
- [85] W. P. Attard, E. Toulson, F. Hamori, and H. C. Watson, "Combustion System Development and Analysis of a Downsized Highly Turbocharged PFI Small

- Engine," *SAE International Journal of Engines*, vol. 3, pp. 511-528, SAE Technical Paper 2010-32-0093, 28 September 2010, doi: 10.4271/2010-32-0093.
- [86] T. Edwards, "Liquid Fuels and Propellants for Aerospace Propulsion: 1903-2003," *Journal of Propulsion and Power*, vol. 19, pp. 1089-1107, November-December 2003, doi: 10.2514/2.6946.
  - [87] G. T. Kalghatgi, "Auto-Ignition Quality of Practical Fuels and Implications for Fuel Requirements of Future SI and HCCI Engines," presented at the 2005 SAE World Congress, Detroit, Michigan, SAE Technical Paper 2005-01-0239, 11 April 2005, doi: 10.4271/2005-01-0239.
  - [88] B. Hamilton. (1996). *What Do Fuel Octane Requirements Really Indicate?* [Online] Available: <http://www.faqs.org/faqs/autos/gasoline-faq/part3/> [Accessed: 24 October 2014].
  - [89] S. Russ, "A Review of the Effect of Engine Operating Conditions on Borderline Knock," presented at the SAE International Congress & Exposition, Detroit, Michigan, SAE Technical Paper 960497, 1 February 1996, doi: 10.4271/960497.
  - [90] M. L. Monaghan, "Future Gasoline and Diesel Engines - Review," *International Journal of Automotive Technology*, vol. 1, pp. 1-8, 2000.
  - [91] J. A. Topinka, M. D. Gerty, J. B. Heywood, and J. C. Keck, "Knock Behavior of a Lean-Burn, H<sub>2</sub> and CO Enhanced, SI Gasoline Engine Concept," presented at the SAE World Congress and Exposition, Detroit, Michigan, SAE Technical Paper 2004-01-0975, 8 March 2004, doi: 10.4271/2004-01-0975.
  - [92] A. Cairns, H. Blaxill, and G. Irlam, "Exhaust Gas Recirculation for Improved Part and Full Load Fuel Economy in a Turbocharged Gasoline Engine," presented at the SAE World Congress & Exposition, Detroit, Michigan, SAE Technical Paper 2006-01-0047, 3 April 2006, doi: 10.4271/2006-01-0047.
  - [93] A. Swarts, A. Yates, C. Viljoen, and R. Coetzer, "A Further Study of Inconsistencies between Autoignition and Knock Intensity in the CFR Octane Rating Engine," presented at the SAE Brazil Fuels & Lubricants Meeting, Rio de Janeiro, Brazil, SAE Technical Paper 2005-01-2081, 11 May 2005, doi: 10.4271/2005-01-2081.
  - [94] A. D. B. Yates, A. Swarts, and C. L. Viljoen, "Correlating Auto-Ignition Delays And Knock-Limited Spark-Advance Data For Different Types Of Fuel," presented at the SAE Brazil Fuels & Lubricants Meeting, Rio de Janeiro, Brazil, SAE Technical Paper 2005-01-2083, 11 May 2005, doi: 10.4271/2005-01-2083.
  - [95] K. Okamoto, T. Ichikawa, K. Saitoh, K. Oyama, K. Hiraya, and T. Urushihara, "Study of Antiknock Performance Under Various Octane Numbers and Compression Ratios in a DISI Engine," presented at the 2003 JSAE/SAE International Spring Fuels and Lubricants Meeting, Tokohama, Japan, SAE Technical Paper 2003-01-1804, 19 May 2003, doi: 10.4271/2003-01-1804.
  - [96] "ASTM Standard D2699-13b: Standard Test Method for Research Octane Number of Spark-Ignition Engine Fuel," American Society for Testing and Materials International, 2013.
  - [97] "ASTM Standard D2700-14: Standard Test Method for Motor Octane Number of Spark-Ignition Engine Fuel," American Society for Testing and Materials International, 2014.

- [98] G. T. Kalghatgi, "Fuel Anti-Knock Quality - Part 1. Engine Studies," presented at the International Fall Fuels and Lubricants Meeting and Exposition, San Antonio, Texas, SAE Technical Paper 2001-01-3584, 24 September 2001, doi: 10.4271/2001-01-3584.
- [99] V. Mittal and J. B. Heywood, "The Shift in Relevance of Fuel RON and MON to Knock Onset in Modern SI Engines Over the Last 70 Years," *SAE International Journal of Engines*, SAE Technical Paper 2009-01-2622, 2 November 2009, doi: 10.4271/2009-11-02.
- [100] K. D. Edwards, R. M. Wagner, J. Tom E. Briggs, and T. J. Theiss, "Defining Engine Efficiency Limits," presented at the 17th DEER Conference, Detroit, Michigan, 2011.
- [101] R. R. Raine, K. Moyle, G. Otte, and J. Robertson, "A Cost-Effective Teaching and Research Dynamometer for Small Engines," *International Journal of Engineering Education*, vol. 18, pp. 50-57, 2002, doi: 0949-149X/91.
- [102] A. Wiegand, S. Miers, J. Blough, D. Kowalski, and A. Biske, "Development of a Micro-Engine Testing System," presented at the 2012 Small Engine Technology Conference & Exposition, Madison, Wisconsin, SAE Technical Paper 2012-32-0105, 23 October 2012, doi: 10.4271/2012-32-0105.
- [103] (2008). *Sonex Two-Stroke Heavy Fuel Engine Technology*. [Online] Available: <http://www.sonexresearch.com> [Accessed: 31 May 2016].
- [104] M. L. Smith, J. Owen E. Buxton, and K. Y. Tang, "Study of Miniature Engine-Generator Sets," The Ohio State University Research Foundation, 1956.
- [105] D. Gierke. (1973) Part I: Dynamometer: An Engine Performance Analysis. *Flying Models*. pp. 21-25.
- [106] D. Gierke. (1973) Part II: Dynamometer: An Engine Performance Analysis. *Flying Models*. pp. 43-51.
- [107] D. Gierke. (1973) Part III: Dynamometer: An Engine Performance Analysis. *Flying Models*. pp. 38-47.
- [108] S. Menon and C. Cadou, "Experimental and Computational Investigations of Small Internal Combustion Engine Performance," presented at the 5th US Combustion Meeting, San Diego, California, 25-28 March 2007.
- [109] D. M. Chon and J. B. Heywood, "Performance Scaling of Spark-Ignition Engines: Correlation and Historical Analysis of Production Engine Data," presented at the SAE 2000 World Congress, Detroit, Michigan, SAE Technical Paper 2000-01-0565, 6-9 March 2000.
- [110] R. R. Raine and H. Thorwarth, "Performance and Combustion Characteristics of a Glow Ignition Two-Stroke Engine," presented at the 2004 SAE World Congress, Detroit, Michigan, SAE Technical Paper 2004-01-1407, 8-11 March 2004, doi: 10.4271/2004-01-1407.
- [111] Y. Shin, S.-H. Chang, and S.-O. Koo, "Performance Test and Simulation of a Reciprocating Engine for Long Endurance Miniature Unmanned Aerial Vehicles," *Journal of Automobile Engineering*, vol. 219, pp. 573-581, 6 October 2005, doi: 10.1243/095440705X11013.
- [112] J. Papac and D. Dunn-Rankin, "Combustion in a Centimeter Scale Four Stroke Engine," presented at the Western States Section/The Combustion Institute Spring Meeting, UC Davis, Paper Number 04S-12, 29-30 March 2004.

- [113] J. Papac and D. Dunn-Rankin, "In Cylinder Pressure and Combustion Measurements in a Minature Reciprocating Engine," presented at the 4th Joint Meeting of the U.S. Section of the Combustion Institute, Philadelphia, Pennsylvania, 2005.
- [114] T. Ogawa and Y. Kawaguchi, "Performance Testing of 5cc Glow-Ignition Four-Stroke Engine," presented at the 2007 ASME-JSME Thermal Engineering and Summer Heat Transfer Conference, Vancouver, British Columbia, Canada, 8-12 July 2007.
- [115] M. D. Kass, M. W. Noakes, B. Kaul, D. Edwards, T. Theiss, L. Love, *et al.*, "Experimental Evaluation of a 4-cc Glow Ignition Single Cylinder Two-Stroke Engine," presented at the SAE 2014 World Congress & Exhibition, Detroit, Michigan, SAE Technical Paper 2014-01-1673, 1 April 2014, doi: 10.4271/2014-01-1673.
- [116] J. D. Anderson, *Aircraft Performance and Design*. Boston, Maryland: McGraw Hill, 1999.
- [117] M. Mataczynski, J. Hoke, D. Paxson, and M. D. Polanka, "Design, Simulation, and Testing of a Pressure Wave Supercharger for a Small Internal Combustion Engine," presented at the SAE 2014 Aerospace Systems and Technology Conference, Cincinnati, Ohio, SAE Technical Paper 2014-01-2136, 16 September 2014, doi: 10.4271/2014-01-2136.
- [118] "Engine Power Test Code, Spark Ignition and Compression Ignition, Net Power Rating: SAE International, J1349, 1995.
- [119] T. D. Husaboe, M. D. Polanka, J. A. Rittenhouse, P. J. Litke, and J. L. Hoke, "Dependence of Small Internal Combustion Engine's Performance on Altitude," *Journal of Propulsion and Power*, September–October 2014, doi: 10.2514/1.B35133.
- [120] J. R. Groenewegen, S. S. Sidhu, J. L. Hoke, C. W. Wilson, and P. J. Litke, "The Performance and Emissions Effects of Utilizing Heavy Fuels and Algae Based Biodiesel in a Port-Fuel-Injected Small Spark Ignition Internal Combustion Engine," presented at the 47th AIAA/ASME/SAE/ASEE Joint Propulsion Conference & Exhibit, San Diego, California, July 31 - 03 August 2011.
- [121] J. A. Rittenhouse, A. K. Rowton, J. K. Ausserer, and M. D. Polanka, "Preliminary Thermal Loss Measurements for a Small Internal Combustion Engine," presented at the AIAA 52nd Aerospace Sciences Meeting, National Harbor, Maryland, AIAA 2014-0529, 13-17 January 2014, doi: 10.2514/6.2014-0529.
- [122] K. P. Horn, J. K. Ausserer, M. D. Polanka, P. J. Litke, and K. D. Grinstead, "Dynamic Friction Measurements on a Small Engine Test Bench," presented at the AIAA 53rd Aerospace Sciences Meeting, Kissimmee, Florida, AIAA 2015-1473, 5-9 January 2015.
- [123] J. K. Ausserer, K. P. Horn, M. D. Polanka, P. J. Litke, and K. D. Grinstead, "Quantification of Short-Circuiting and Trapping Efficiency in a Small Internal Combustion Engine by GC-MS and GC-TCD," presented at the 2015 SAE Small Engine Technology Conference, Osaka, Japan, SAE Technical Paper 2015-32-0716, 17 November 2015, doi: 10.4271/2015-32-0716.
- [124] *3W Engines & Airplanes*. [Online] Available: [www.3w-modelmotoren.com](http://www.3w-modelmotoren.com) [Accessed: 19 April 2014].



- [125] *Centurion Aircraft Engines*. [Online] Available: [www.centurion.aero](http://www.centurion.aero) [Accessed: 19 April 2014].
- [126] *Compact Radial Engines*. [Online] Available: [www.compactradialengines.com](http://www.compactradialengines.com) [Accessed: 19 April 2014].
- [127] *DeltaHawk Diesel Engines*. [Online] Available: [www.deltahawkengines.com](http://www.deltahawkengines.com) [Accessed: 19 April 2014].
- [128] *Desert Aircraft*. [Online] Available: [www.desertaircraft.com](http://www.desertaircraft.com) [Accessed: 19 April 2014].
- [129] *Freedom Motors*. [Online] Available: [www.freedom-motors.com](http://www.freedom-motors.com) [Accessed: 19 April 2014].
- [130] *Kodiak Research Ltd*. [Online] Available: [www.kodiakbs.com](http://www.kodiakbs.com) [Accessed: 19 April 2014].
- [131] *O.S. Engine*. [Online] Available: [www.osengines.com](http://www.osengines.com) [Accessed: 19 April 2014].
- [132] *Recreational Power Engineering*. [Online] Available: [www.recpower.com](http://www.recpower.com) [Accessed: 19 April 2014].
- [133] *Super Tigre*. [Online] Available: [www.supertigre.com](http://www.supertigre.com) [Accessed: 19 April 2014].
- [134] *Zenoah*. [Online] Available: [www.zenoah.co.jp](http://www.zenoah.co.jp) [Accessed: 19 April 2014].
- [135] A. K. Rowton, "Measuring Scaling Effects in Small Two-Stroke Internal Combustion Engines," M.S. Aeronautical Engineering, Department of Aeronautics and Astronautics, Air Force Institute of Technology, WPAFB, Ohio, 2014.
- [136] E. Sher and D. Levinzon, "Scaling-Down of Miniature Internal Combustion Engines: Limitations and Challenges," *Heat Transfer Engineering*, vol. 26, pp. 1-4, 2005, doi: 10.1080/01457360591004780.
- [137] E. Sher and I. Sher, "Theoretical Limits of Scaling Down Internal Combustion Engines," *Chemical Engineering Science*, vol. 66, pp. 260-267, 6 October 2011, doi: 10.1016/j.ces.2010.10.005.
- [138] C. F. Taylor and T.-Y. Toong, "Heat Transfer in Internal Combustion Engines," presented at the ASME-AIChE Heat Transfer Conference, University Park, Pennsylvania, 57-HT--17, 11-15 August 1957.
- [139] C. A. Finol and K. Robinson, "Thermal Modelling of Modern Engines: A Review of Empirical Correlations to Estimate the In-Cylinder Heat Transfer Coefficient," *Journal of Automobile Engineering*, vol. 220, p. 17, 4 August 2006, doi: 10.1243/09544070JAUTO202.
- [140] A. Franco and L. Martorano, "Methods to Evaluate In-Cylinder Heat Transfer and Thermal Load in the Small Internal Combustion Engines," presented at the International Congress and Exposition, Detroit, Michigan, SAE Technical Paper 1999-01-1252, 1-4 March 1999, doi: 10.4271/1999-01-1252.
- [141] G. Woschni, "A Universally Applicable Equation for the Instantaneous Heat Transfer Coefficient in the Internal Combustion Engine," SAE Technical Paper 670931, 1 February 1967, doi: 10.4271/670931.
- [142] N. Watson and M. S. Janota, *Turbocharging the Internal Combustion Engine*. London, Great Britain: Macmillan Publishers LTD, 1982.
- [143] K. Sihling and G. Woschni, "Experimental Investigation of the Instantaneous Heat Transfer in the Cylinder of a High Speed Diesel Engine," SAE Technical Paper 790833, 1 February 1979, doi: 10.4271/790833.

- [144] S. B. Han, Y. J. Chung, Y. J. Kwon, and S. Lee, "Empirical Formula for Instantaneous Heat Transfer Coefficient in Spark Ignition Engine," presented at the International Fall Fuels & Lubricants Meeting & Exposition, Tulsa, Oklahoma, SAE Technical Paper 972995, 13-16 October 1997, doi: 10.4271/972995.
- [145] W. J. D. Annand and T. H. Ma, "Instantaneous Heat Transfer Rates to the Cylinder Head Surface of a Small Compression Ignition Engine," *Proceedings of the Institution of Mechanical Engineers*, vol. 185, pp. 976-987, 10 November 1970.
- [146] G. Sitkei and G. Ramanaiah, "A Rational Approach for Calculation of Heat Transfer in Diesel Engines," presented at the Automotive Engineering Conference, Detroit, Michigan, SAE Technical Paper 720027, 10-14 January 1972, doi: 10.4271/720027.
- [147] G. F. Hohenberg, "Advanced Approaches for Heat Transfer Calculations," SAE Technical Paper 790825, 1 February 1979, doi: 10.4271/790825.
- [148] Y. T. Wu, B. C. Chen, and A. T. Tran, "Application of Semi-Direct Injection for Spark Ignition Engine," *International Journal of Vehicle Design*, vol. 54, pp. 356-370, 2010.
- [149] C. C. J. French, "Taking the Heat Off the Highly Boosted Diesel," SAE Technical Paper 690463, 1 February 1969, doi: 10.4271/690463.
- [150] N. J. Owen, K. Robinson, and N. S. Jackson, "Quality Assurance for Combustion Chamber Thermal Boundary Conditions - A Combined Experimental and Analytical Approach," presented at the Vehicle Thermal Management Systems Conference, Columbus, Ohio, SAE Technical Paper 931139, 1 April 1993, doi: 10.4271/931139.
- [151] T. LeFeuvre, P. S. Myers, and O. A. Uyehara, "Experimental Instantaneous Heat Fluxes in a Diesel Engine and Their Correlation," presented at the Mid-Year Meeting, Chicago, Illinois, SAE Technical Paper 690464, 19-23 May 1969, doi: 10.4271/690464.
- [152] J. Dent and S. Sulaiman, "Convective and Radiative Heat Transfer in a High Swirl Direct Injection Diesel Engine," presented at the International Automotive Engineering Congress and Exposition, Detroit, Michigan, SAE Technical Paper 770407, 28 February - 4 March 1977, doi: 10.4271/770407.
- [153] J. A. Rittenhouse, "Thermal Loss Determination for a Small Internal Combustion Engine," M.S. Aeronautical Engineering, Department of Aeronautics and Astronautics, Air Force Institute of Technology, WPAFB, Ohio, 2014.
- [154] B. P. Boyce, J. K. Martin, A. Poehlman, and D. Shears, "Effects of Ignition Timing and Air-Fuel Ratio on In-Cylinder Heat Flux and Temperature in a Four-Stroke, Air Cooled, Homogenous Charge Engine," presented at the International Congress and Exposition, Detroit, Michigan, SAE Technical Paper 1999-01-0284, 1-4 March 1999, doi: 10.4271/1999-01-0284.
- [155] J. Demuynck, "A Fuel Independent Heat Transfer Correlation for Premixed Spark Ignition Engines," Ph.D., Department of Flow, Heat and Combustion Mechanics, Gent University, 2012.
- [156] O. Spitsov, "Heat Transfer Inside Internal Combustion Engine: Modelling and Comparison with Experimental Data," M.S. Energy Technology, Lappeenranta University of Technology, 2013.

- [157] T. Gegg, A. Kölmel, and K. W. Beck, "Combustion Analysis on Small Two-Stroke SI-Engines for Handheld Power Tools," presented at the 2010 Small Engine Technology Conference, Linz, Austria, SAE Technical Paper 2010-32-0062, 28 September 2010, doi: 10.4271/2010-32-0062.
- [158] M. C. Burrows, S. Shimizu, P. S. Myers, and O. A. Uyehara, "The Measurement of Unburned Gas Temperatures in an Engine by an Infrared Radiation Pyrometer," *SAE Transactions*, vol. 69, pp. 514-528, SAE Technical Paper 610042, 1 January 1961, doi: 10.4271/610043.
- [159] H. Takagi, T. Ohno, and T. Asanuma, "Temperature Measurements of Combustion Gas in a Spark Ignition Engine by Infrared Monochromatic Pyrometry," presented at the International Congress and Exposition, Detroit, Michigan, SAE Technical Paper 900483, 26 February - 2 March 1990, doi: 10.4271/900483.
- [160] G. M. Rassweiler and L. Withrow, "Flame Temperatures Vary with Knock and Combustion-Chamber Position," *SAE Journal*, vol. 26, pp. 125-133, SAE Technical Paper 350091, 1 January 1935, doi: 10.4271/350091.
- [161] W. G. Agnew, "End Gas Temperature Measurement by a Two-Wavelength Infrared Radiation Method," *SAE Transactions*, vol. 68, pp. 495-513, SAE Technical Paper 610042, 1 January 1961, doi: 10.4271/610042.
- [162] M. Bach, J. Reissing, and U. Spicher, "Temperature Measurement and NO Determination in SI Engines Using Optical Fiber Sensors," presented at the International Fall Fuels & Lubricants Meeting & Exposition, San Antonio Texas, SAE Technical Paper 961922, 14-17 October 1996, doi: 10.4271/961922.
- [163] S. K. Chen, N. J. Beck, O. A. Uyehara, and P. S. Myers, "Compression and End-Gas Temperatures from Iodine Absorption Spectra," *SAE Transactions*, vol. 62, pp. 503-513, SAE Technical Paper 540259, 1 January 1954, doi: 10.4271/540259.
- [164] W. Ma, L. I. Leviticus, and F. G. Ullman, "On-Line Measurement of Formaldehyde in Tailpipe Emissions by Tunable Diode Laser Spectroscopy," presented at the International Off- Highway & Powerplant Congress & Exposition, Milwaukee, Wisconsin, SAE Technical Paper 941702, 12-14 September 1994, doi: 10.4271/941702.
- [165] J. C. Hill and R. F. Majkowski, "Time-Resolved Measurement of Vehicle Sulfate and Methane Emissions with Tunable Diode lasers," presented at the Congress and Exposition, Detroit, Michigan, SAE Technical Paper 800510, 25-29 February 1980, doi: 10.4271/800510.
- [166] J. Bechara, D. R. Karecki, G. I. Mackay, H. I. Schiff, and S. Nadler, "Chemical Analysis of Gases with Tunable Diode Lasers," presented at the International Congress and Exposition, Detroit, Michigan, SAE Technical Paper 940824, 28 February - 3 March 1994, doi: 10.4271/940824.
- [167] M. J. Deutsch, J. K. Ausserer, M. D. Polanka, P. J. Litke, A. W. Caswell, K. D. Grinstead, *et al.*, "Gas Temperature Measurement Using FTIR Spectroscopy in Small Internal Combustion Engines," presented at the AIAA 54th Aerospace Science Meeting, San Diego, California, AIAA 2016-0765, 2 January 2016, doi: 10.2514/6.20-2016-0765.
- [168] K. D. Rein, "High-Resolution Spectroscopic Measurement of Small Molecules in Combustion," Ph.D. Mechanical Engineering, Department of Mechanical Engineering, University of Wisconsin - Madison, Madison, Wisconsin, 2014.

- [169] D. Santavicca, "Temperature and Concentration Measurements in an Internal Combustion Engine Using Laser Raman Spectroscopy," presented at the 18th Thermophysics Conference, Montreal, Canada, AIAA 83-1551, 1-3 June 1983, doi: 10.2514/6.1983-1551.
- [170] J. R. Smith, "Temperature and Density Measurements in an Engine by Pulsed Raman Spectroscopy," presented at the Congress and Exposition, Detroit, Michigan, SAE Technical Paper 800137, 25-29 February 1980, doi: 10.4271/800137.
- [171] A. Bräumer, V. Sick, J. Wolfrum, V. Drewes, M. Zahn, and R. Maly, "Quantitative Two-Dimensional Measurements of Nitric Oxide and Temperature Distributions in a Transparent Square Piston SI Engine," presented at the Fuels & Lubricants Meeting & Exposition, Toronto, Ontario, SAE Technical Paper 952462, 16-19 October 1995, doi: 10.4271/952462.
- [172] T. Nakada, T. Itoh, and Y. Takagi, "Application of CARS to Development of High Compression Ratio Spark Ignition Engine," presented at the Fuel and Lubricants Meeting and Exposition, Philadelphia, Pennsylvania, SAE Technical Paper 932644, 18-21 October 1993, doi: 10.4271/932644.
- [173] C. R. Stone, E. P. Lim, P. Ewart, G. Lloyd, and R. B. Williams, "Temperature and Heat Flux Measurements in a Spark Ignition Engine," presented at the SAE 2000 World Congress, Detroit, Michigan, SAE Technical Paper 2001-01-1214, 6-9 March 2000, doi: 10.4271/2000-01-1214.
- [174] D. Klick, K. A. Marko, and L. Rimai, "Temperature and Concentration Measurements by CARS Spectroscopy in a Firing Single-Cylinder Engine," presented at the International Congress and Exposition, Detroit, Michigan, SAE Technical Paper 810227, 23-27 February 1981, doi: 10.4271/810227.
- [175] A. Roller, A. A. Paul, M. Decker, V. Sick, J. Wolfrum, W. Hentschel, *et al.*, "Non-intrusive Temperature Measurements during the Compression Phase of a DI Diesel Engine," presented at the Fuels & Lubricants Meeting & Exposition, Toronto, Ontario, SAE Technical Paper 952461, 16-19 October 1995, doi: 10.4271/952461.
- [176] S. Einecke, C. Schulz, V. Sick, A. Dreizler, R. Schießl, and U. Maas, "Two-Dimensional Temperature Measurements in an SI Engine Using Two-Line Tracer LIF," presented at the International Fuels and Lubricants Meeting and Exposition, San Francisco, California, SAE Technical Paper 982468, 19-22 October 1998, doi: 10.4271/982468.
- [177] B. C. Smith, *Fundamentals of Fourier Transform Infrared Spectroscopy*. Boca Raton, Florida: CRC Press, 1996.
- [178] P. R. Griffiths and J. A. d. Haseth, *Fourier Transform Infrared Spectroscopy*, 2nd ed. Hoboken, New Jersey: John Wiley & Sons, Inc., 2007.
- [179] P. R. Shore and R. S. deVries, "On-Line Hydrocarbon Speciation Using FTIR and CI-MS," presented at the International Fuels and Lubricants Meeting and Exposition, San Francisco, California, SAE Technical Paper 922256, 19-22 October 1992, doi: 10.4271/922246.
- [180] S. E. Stein, "IR Spectra," in *NIST Chemistry WebBook, NIST Standard Reference Database Number 69*, P. J. Linstrom and W. G. Mallard, Eds., Gaithersburg, Maryland: National Institute of Standards and Technology, 2011 [Online] Available: <http://webbook.nist.gov/> [Accessed: 21 October 2014].

- [181] L. A. Kranendonk, A. W. Caswell, and S. T. Sanders, "Robust Method for Calculating Temperature, Pressure, and Absorber Mole Fraction from Broadband Spectra," *Applied Optics*, vol. 46, pp. 4117-4124, 1 July 2007.
- [182] M. J. Deutsch, "Spectroscopic Measurement of Gas Temperature in Small Internal Combustion Engines," M.S. Aeronautical Engineering, Department of Aeronautics and Astronautics, Air Force Institute of Technology, WPAFB, Ohio, 2016.
- [183] W. Thiel, W. Hübner, R. Grisar, W. J. Riedel, and H. Wolf, "Dynamic Laser Analysis of Exhaust Gas," presented at the International Congress and Exposition, Detroit, Michigan, SAE Technical Paper 940825, 28 February - 3 March 1994, doi: 10.4271/940825.
- [184] G. Lenaers and M. Van Poppel, "A Tunable Diode Laser Measurement Technique for the On-Board Evaluation of Tail Pipe Ammonia Emissions," presented at the 7th International Conference on Engines for Automobiles, Naples, Italy, SAE Technical Paper 2005-24-018, 11-16 September 2005, doi: 10.4271/2005-24-018.
- [185] J. T. Pisano, C. Sauer, T. Durbin, and G. Mackay, "Measurement of Low Concentration NH<sub>3</sub> in Diesel Exhaust using Tunable Diode Laser Adsorption Spectroscopy (TDLAS)," presented at the SAE World Congress & Exhibition, Detroit, Michigan, SAE Technical Paper 2009-01-1519, 20 April 2009, doi: 10.4271/2009-01-1519.
- [186] P. K. Goenka, R. S. Paranjpe, and Y. R. Yeng, "FLARE: An Integrated Software Package for Friction and Lubrication Analysis of Automotive Engines - Part I: Overview and Applications," presented at the SAE International Congress and Exposition, Detroit, Michigan, SAE Technical Paper 920487, 1 February 1992, doi: 10.4271/920487.
- [187] I. N. Bishop, "Effect of Design Variables on Friction and Economy," *SAE Transactions*, vol. 73, pp. 334-358, SAE Technical Paper 640807, 1 January 1965, doi: 10.4271/640807.
- [188] K. J. Patton, R. G. Nitschke, and J. B. Heywood, "Development and Evaluation of a Friction Model for Spark-Ignition Engines," *SAE Transactions*, vol. 98, SAE Technical Paper 890836, 1 February 1989, doi: 10.4271/890836.
- [189] R. H. Thring, "Engine Friction Modelling," presented at the SAE International Congress and Exposition, Detroit, Michigan, SAE Technical Paper 920482, 1 February 1992, doi: 10.4271/920482.
- [190] K. Hamai, T. Masuda, T. Goto, and S. Kai, "Development of a Friction Prediction Model for High Performance Engines," *Journal of Lubrication Engineering*, vol. 47, pp. 567-573, 1991.
- [191] R. Harari and E. Sher, "Measurements of Engine Friction Power by Using Inertia Tests," *SAE Transactions*, vol. 104, SAE Technical Paper 950028, 1 February 1995, doi: 10.4271/950028.
- [192] M. I. L. Galdo and C. G. R. Vidal, "Simulation of Scavenging Process in Two-Stroke Engines," in *Numerical Modelling*, P. Miidla, Ed.: InTech, 2012.
- [193] S. Cagin, X. Fischer, N. Bouraba, E. Dealcourt, C. Morin, and C. D., "A Methodology for a New Qualified Numerical Model of a 2-Stroke Diesel Engine Design," in *Proceedings of the International Conference on Advances in Civil, Structural and Mechanical Engineering*, 2014.

- [194] G. P. Merker and M. Gerstle, "Evaluation on Two Stroke Engines Scavenging Models," presented at the SAE International Congress & Exposition, Detroit, Michigan, SAE Technical Paper 970358, 24-27 February 1997, doi: 10.4271/970358.
- [195] B. Hopkinson, "The Charging of Two-Cycle Internal-Combustion Engines," *Journal of the American Society for Naval Engineers*, vol. 26, pp. 974-985, 1914, doi: 10.1111/j.1559-3584.1914.tb00330.x.
- [196] E. Sher, "Scavenging the Two-Stroke Engine," *Progress in Energy and Combustion Science*, vol. 16, pp. 95-124, 1990, doi: 10.1016/0360-1285(90)90045-5.
- [197] H. S. Foudray, "Scavenging Measurements in a Direct Injection Two-Stroke Engine," M.S. Mechanical Engineering, Department of Mechanical Engineering, University of Wisconsin - Madison, 2002.
- [198] M. Maekawa, "Text of Course," *Japanese Society of Mechanical Engineers*, p. 23, 1957.
- [199] R. S. Benson and P. T. Brandham, "A Method for Obtaining a Quantitative Assessment of the Influence of Charging Efficiency on Two-Stroke Engine Performance," *International Journal of Mechanical Sciences*, vol. 11, pp. 303-312, 1969, doi: 10.1016/0020-7403(69)90048-4.
- [200] F. J. Wallace and P. R. Cave, "Experimental and Analytical Scavenging Studies on a Two-Cycle Opposed Piston Diesel Engine," presented at the Automotive Engineering Congress, Detroit, Michigan, SAE Technical Paper 710175, 11-15 January 1971, doi: 10.4271/710175.
- [201] R. S. Benson, "A New Gas Dynamic Model for the Gas Exchange Process in Two Stroke Loop and Cross Scavenged Engines," *International Journal of Mechanical Sciences*, vol. 19, pp. 693-711, 1977, doi: 10.1016/0020-7403(77)90056-X.
- [202] E. Sher, "A New Practical Model for the Scavenging Process in a Two-Stroke Cycle Engine," presented at the SAE International Congress & Exposition, Detroit, Michigan, SAE Technical Paper 850085, 25 February - 1 March 1985, doi: 10.4271/850085.
- [203] E. Sher and R. Harari, "A Simple and Realistic Model for the Scavenging Process in a Crankcase-Scavenged Two-Stroke Cycle Engine," *Journal of Power and Energy*, vol. 205, pp. 129-137, May 1991, doi: 10.1243/PIME\_PROC\_1991\_205\_019\_02.
- [204] A. Jante, "Scavenging and Other Problems of Two-Stroke Cycles Spark-Ignition Engines," SAE Technical Paper 680468, 1 February 1968, doi: 10.4271/680468.
- [205] J. F. Bryan, R. Fleck, R. J. Kee, and D. J. Thornhill, "The Evaluation of Discharge Coefficients in the Cylinders of High Performance Two-Stroke Engines," presented at the 2003 SAE/JSAE Small Engine Technology Conference & Exhibition, Madison, Wisconsin, 15-18 September 2003.
- [206] J. B. Ghandhi and J. K. Martin, "Velocity Field Characteristics in Motored Two-Stroke Ported Engines," presented at the International Congress & Exposition, Detroit, Michigan, SAE Technical Paper 920419, 24-28 February 1992, doi: 10.4271/920419.
- [207] D. S. Sanborn, G. P. Blair, R. G. Kenny, and A. H. Kingsbury, "Experimental Assessment of Scavenging Efficiency of Two-Stroke Cycle Engines," presented at

- the International Off-Highway Meeting and Exposition, Milwaukee, Wisconsin, SAE Technical Paper 800975, 8-11 September 1980, doi: 10.4271/800975.
- [208] M. E. G. Sweeney, R. G. Kenny, G. B. G. Swann, and G. P. Blair, "Single Cycle Gas Testing Method for Two-Stroke Engine Scavenging," presented at the International Congress & Exposition, Detroit, Michigan, SAE Technical Paper 850178, 25 February - 1 March 1985, doi: 10.4271/850178.
  - [209] B. J. Tobis, R. Meyer, J. Yang, D. D. Brehob, and R. W. Anderson, "Scavenging of a Firing Two-Stroke Spark Ignition Engine," presented at the SAE International Congress & Exposition, Detroit, Michigan, SAE Technial Paper 940393, 1 March 1994, doi: 10.4271/940393.
  - [210] T. Gegg, A. Jager, J. Tribulowski, M. Mugele, U. Spicher, and H. Roskamp, "Analysis of Mixture Conditions in a Small Two Stroke Engine Using a Gas Sampling Valve," presented at the Small Engine Technology Conference, Kyoto, Japan, SAE Technical Paper 2002-32-1836, 29 October 2002, doi: 10.4271/2002-32-1836.
  - [211] T. Asanuma and S. Yanagihara, "Gas Sampling Valve for Measuring Scavenging Efficiency in High-Speed Two-Stroke Engines," SAE Technical Paper 620540, 1962, doi: 10.4271/620540.
  - [212] D. B. Olsen, G. C. Hutcherson, B. D. Willson, and C. E. Mitchell, "Development of the Tracer Gas Method for Large Bore Natural Gas Engines - Part 1: Method Validation," *ASME Transactions*, vol. 124, p. 8, 2002, doi: 10.1115/1.1454116.
  - [213] P. H. Schweitzer and F. DeLuca, "The Tracer Gas Method of Determining the Charging Efficiency of 2-Stroke Cycle Engine," NACA Technical Note 838, January 1942.
  - [214] C. F. Taylor and A. R. Rogowski, "Scavenging the 2-Stroke Engine," *SAE Transactions*, vol. 62, pp. 487-502, SAE Technical Paper 540258, 1 January 1954, doi: 10.4271/540258.
  - [215] K. Hori, "A Method of Measuring Scavenging Efficiency and Its Application," *Bulletin of the Japanese Society of Mechanical Engineers*, vol. 5, pp. 327-334, 1962.
  - [216] K. Hori, "The Influence of Volume and Period of Gas-Sampling upon the Accuracy of the Measurements of Scavenging Efficiency," *Bulletin of the Japanese Society of Mechanical Engineers*, vol. 6, pp. 289-296, 1963.
  - [217] V. Bazika and J. Rodig, "A New Method of Determining the Scavenging Efficiency of Oil Engine Cylinders," *The Engineers' Digest*, vol. 24, 1963.
  - [218] H. Miyabe and T. Shimomura, "Measurement of Trapping Efficiencies of a Two-Stroke Engine," *Bulletin of the Japanese Society of Mechanical Engineers*, vol. 6, pp. 297-307, 1963.
  - [219] S. Isigami, "On Scavenging of the Crank Compression Type Two-Stroke Cycle Diesel Engine," *Bulletin of the Japanese Society of Mechanical Engineers*, vol. 6, pp. 531-539, 1963.
  - [220] S. Isigami, Y. Tanaka, and M. Tamari, "The Trapping Efficiency Measurement of a Two-Stroke Engine," *Bulletin of the Japanese Society of Mechanical Engineers*, vol. 6, pp. 524-539, 1963.
  - [221] M. Oggero, "FIAT Research Methods for the Experimental Study of Large Bore Diesel Engines," *FIAT Technical Bulletin*, vol. 21, pp. 86-92, 1968.



- [222] S. Ohigashi and Y. Hamamoto, "Cylinder Gas Composition of Small 2-Stroke Cycle Gasoline Engine," presented at the Automtoive Engineering Congress, Detroit, Michigan, SAE Technical Paper 710143, 11-15 January 1971, doi: 10.4271/710143.
- [223] E. W. Huber, "Measuring the Trapping Efficiency of Internal Combustion Engines Through Continuous Exhaust Gas Analysis," *SAE Transactions*, vol. 80, SAE Technical Paper 710144, 1 February 1971, doi: 10.4271/710144.
- [224] G. P. Blair and M. C. Ashe, "The Unsteady Gas Exchange Characteristics of a Two-Cycle Engine," presented at the Off-Highway Vehicle Meeting, Milwaukee, Wisconsin, SAE Technical Paper 760644, 13-16 September 1976, doi: 10.4271/760644.
- [225] E. Hashimoto, T. Tottori, and S. Terata, "Scavenging Performance Measurements of High Speed Two-Stroke Engines," presented at the SAE International Congress & Exposition, Detroit, Michigan, SAE Technical Paper 850182, 25 February - 1 March 1985, doi: 10.4271/850182.
- [226] M. Nuti and L. Martorano, "Short-Circuit Ratio Evaluation in the Scavenging of Two-Stroke S.I. Engines," presented at the SAE International Congress & Exposition, Detroit, Michigan, SAE Technical Paper 850177, 25 Ferbruary - 1 March 1985, doi: 10.4271/850177.
- [227] K. Sato, H. Ukawa, and M. Nakano, "A Two-Stroke Cycle Gasoline Engine with Poppet Valves in the Cylinder Head - Part II," presented at the SAE International Congress and Exposition, Detroit, Michigan, SAE Technical Paper 920780, 24-28 February 1992, doi: 10.4271/920780.
- [228] T. Murayama, Y. Sekiya, B. Sugiarto, and T. Chikahisa, "Study on Exhaust Control Valves and Direct Air-Fuel Injection for Improving Scavenging Process in Two-Stroke Gasoline Engines," presented at the SAE International Congress & Exposition, Detroit, Michigan, SAE Technical Paper 960367, 26-29 February 1996, doi: 10.4271/960367.
- [229] D. B. Olsen, G. C. Hutcherson, B. D. Willson, and C. E. Mitchell, "Development of the Tracer Gas Method for Large Bore Natural Gas Engines - Part II: Measurement of Scavenging Parameters," *ASME Transactions*, vol. 124, p. 9, 2002, doi: 10.1115/1.1454117.
- [230] W. Welch and T. D. Durbin, "Emissions and Demonstration of an Emission Control Technology for Small Two Stroke Utility Engines," *Journal of the Air and Waste Management Association*, vol. 54, pp. 200-206, February 2004.
- [231] J. Volckens, J. Braddock, R. F. Snow, and W. Crews, "Emissions Profile from New and In-Use Handheld, 2-Stroke Engines," *Atmospheric Environment*, vol. 41, pp. 640-649, 17 August 2006, doi: 10.1016/j.atmosenv.2006.08.033.
- [232] (2014). *Reducing Air Pollution - ARB Programs*. [Online] Available: <http://www.arb.ca.gov/html/programs.htm> [Accessed: 21 October 2014].
- [233] "Clean Air Act of 1963," in *42 U.S.C. 7401 P.L. 88-206*. United States of America, 1963.
- [234] "M700 Manual Version 5," Enerac, 2013.
- [235] "Surface Vehicle Information Report: Instrumentation and Techniques for Exhaust Gas Emissions Measurements," SAE International, J254, 2011.
- [236] "Introduction to Fourier Transform Infrared Spectroscopy," Thermo Nicolet, 2001.

- [237] S. R. Lowry, J. Roberts, J. Lindner, and D. Munday, "The Measurement of Exhaust Emissions from Oxygenated Fuel Blends by Fourier Transform Infrared Spectroscopy," presented at the International Congress and Exposition, Detroit Michigan, SAE Technical Paper 950220, 2 March 1995, doi: 10.4271/950220.
- [238] B. Daham, G. E. Andrews, H. Li, R. Ballesteros, M. C. Bell, J. Tate, *et al.*, "Application of a Portable FTIR for Measuring On-Road Emissions," presented at the SAE 2005 World Congress & Exposition, Detroit, Michigan, SAE Technical Paper 2005-01-0676, 11 April 2005, doi: 10.4271/2005-01-0676.
- [239] (2014). *Organic Chemistry at UC Boulder; Spectroscopy*. [Online] Available: <http://orgchem.colorado.edu/Spectroscopy/MS/inletsys.html> [Accessed: 21 October 2014].
- [240] "Agilent J&W GC Column Selection Guide," Agilent Technologies, 2014.
- [241] S. Otsuki, T. Oie, and K. Ishida, "Hydrocarbon Speciation of Automotive Emissions Using High Speed Gas Chromatography," presented at the SAE International Congress and Exposition, Detroit, Michigan, SAE Technical Paper 950513, 27 February - 2 March 1995, doi: 10.4271/950513.
- [242] R. W. Hurn, K. J. Hughes, and J. O. Chase, "Application of Gas Chromatography to Analysis of Exhaust Gas," presented at the SAE Annual Meeting, Detroit, Michigan, SAE Technical Paper 580259, 13-17 January 1958, doi: 10.4271/580259.
- [243] L. J. Papa, "Gas Chromatography - Measuring Hydrocarbons Down to Parts Per Billion," presented at the Mid-Year Meeting, Chicago, Illinois, SAE Technical Paper 670494, 15-19 May 1967, doi: 10.4271/670494.
- [244] N. Rudlein, W. Geiger, N. Peiz, and H. J. Scherrbacher, "Development of a Single Run Method for the Determination of Individual Hydrocarbons (C2-C12) in Automotive Exhaust by Capillary Gas Chromatography," presented at the International Congress & Exposition, Detroit, Michigan, SAE Technical Paper 940827, 28 February - 3 March 1994, doi: 10.4271/940827.
- [245] E. W. Landen and J. M. Perez, "Some Diesel Exhaust Reactivity Information Dervied by Gas Chromatography," presented at the Combined Commercial Vehicle and Fuels & Lubricants Meetings, Chicago, Illinois, SAE Technical Paper 740530, 17-21 June 1974, doi: 10.4271/740530.
- [246] J. Arning, T. Ramsander, and N. Collings, "Analysis of In-Cylinder Hydrocarbons in a Multi-Cylinder Gasoline HCCI Engine Using Gas Chromatography," presented at the SAE 2009, San Antonio, Texas, SAE Technical Paper 2009-01-2698, 2 November 2009, doi: 10.4271/2009-01-2698.
- [247] (2014). *GC Detectors*. [Online] Available: <http://www.srigc.com/documents.htm> [Accessed: 22 October 2014].
- [248] S. E. Stein, "Mass Spectra," in *NIST Chemistry WebBook, NIST Standard Reference Database Number 69*, P. J. Linstrom and W. G. Mallard, Eds., Gaithersburg, Maryland: National Institute of Standards and Technology, 2011 [Online] Available: <http://webbook.nist.gov/> [Accessed: 21 October 2014].
- [249] U. Elghawi, J. Misztal, A. Tsolakis, M. L. Wyszynski, and H. M. Xu, "GC-MS Speciation and Quantification of 1,3 Butadiene and Other C1-C6 Hydrocarbons in SI / HCCI V6 Engine Exhaust," presented at the SAE World Congress and

- Exhibition, Detroit, Michigan, SAE Technical Paper 2008-01-0012, 14 April 2008, doi: 10.4271/2008-01-0012.
- [250] J. E. Farrugia and K. L. Olson, "Speciation of Hydrocarbons in Exhaust from Low-Emission, Gasoline-Fueled Vehicles by High-Speed and Standard Gas Chromatography Models," presented at the SAE World Congress & Exposition, Detroit, Michigan, SAE Technical Paper 2007-01-0305, 16-19 April 2007, doi: 10.4271/2007-01-0305.
  - [251] K. L. Olson, J. F. Loo, and P. A. Mulawa, "Rapid Hydrocarbon Speciation and Exhaust Reactivity Measurements using High Speed, High Resolution Gas Chromatography," presented at the International Fuels and Lubricants Meeting, Paris, France, SAE Technical Paper 2000-01-2950, 16 October 2000, doi: 10.4271/2000-01-2950.
  - [252] (2014). *3W Modellmotoren: 2-Stroke Heavy Fuel & Gasoline Engines*. [Online] Available: <http://www.3w-international.com/> [Accessed: 31 May 2016].
  - [253] J. Lawton, "Development of a Heavy Fuel Engine for an Unmanned Air Vehicle," presented at the AIAA/SAE/ASME/ASEE 26th Joint Propulsion Conference, Orlando, Florida, AIAA 90-2170, 1990, doi: 10.2514/6.1990-2170.
  - [254] Z. Rosenberg. (2012). *Textron Unveils Modified Aerosonde*. [Online] Available: <http://www.flightglobal.com/news/articles/textron-unveils-modified-aerosonde-366807/> [Accessed: 18 August 2014].
  - [255] D. Cordon, M. Walker, S. Beyerlein, and J. Steciak, "Catalytically Assisted Combustion of JP-8 in a 1 kW Low-Compression Genset," presented at the Small Engine Technology Conference & Exposition, San Antonio, Texas, SAE Technical Paper 2006-32-0024, 13 November 2006, doi: 10.4271/2006-32-0024.
  - [256] (2014). *EU1000i*. [Online] Available: <http://powerequipment.honda.com/generators/models/eu1000i> [Accessed: 31 May 2016].
  - [257] W. P. Attard, M. Bassett, P. Parsons, and H. Blaxill, "A New Combustion System Achieving High Drive Cycle Fuel Economy Improvements in a Modern Vehicle Powertrain," presented at the SAE 2011 World Congress & Exhibition, Detroit, Michigan, SAE Technical Paper 2011-01-0664, 2011, doi: 10.4271/2011-01-0664.
  - [258] "ASTM Standard D6078-04 (2010): Standard Test Method for Evaluating Lubricity of Diesel Fuels by the Scuffing Load Ball-on-Cylinder Lubricity Evaluator," American Society for Testing and Materials International, 2010.
  - [259] "ASTM Standard D6079-11: Standard Test Method for Evaluating Lubricity of Diesel Fuels by the High-Frequency Reciprocating Rig," American Society for Testing and Materials International, 2011.
  - [260] J. H. Lee, B. Duddy, M. Thurston, D. Beardslee, and R. Enyeart, "Increasing the Lubricity of JP-8 to Fuel Two-stroke Spark Ignition Engines for Midsized Unmanned Aerial Vehicles," presented at the SAE World Congress, Detroit, Michigan, SAE Technical Paper 2011-01-0332, 2011, doi: 10.4271/2011-01-0332.
  - [261] (2016). *Power4Flight*. [Online] Available: <http://power4flight.com/> [Accessed: 31 May 2016].
  - [262] (2016). *iPower (Compression Wave Injection)*. [Online] Available: <http://www.hirth-engines.de/index.php/en/services/66-uav-en/205-ipower-english> [Accessed: 4 August 2016].

- [263] (2016). *Products*. [Online] Available: <http://www.hirth-engines.de/index.php/en/products> [Accessed: 4 August 2016].
- [264] "WB and PB Series Eddy-Current and Magnetic Power Dynamometers: User's Manual," Magtrol, 1st ed, 2009.
- [265] Y. A. Çengel and J. M. Cimbala, *Fluid Mechanics: Fundamentals and Applications*, 2nd ed. New York, New York: McGraw Hill Science/ Engineering/ Math, 2006.
- [266] A. A. H. Pádua, J. M. N. A. Fareleira, and J. C. G. Caldo, "Density and Viscosity Measurements of 2,2,4-Trimethylpentane (Isooctane) from 198K to 348K and up to 100 MPa," *Journal of Chemical Engineering Data*, vol. 41, pp. 1488-1494, 1996.
- [267] D. Pecar and V. Dolecek, "Temperature and Pressure Dependence of Volumetric Properties for Binary Mixtures of n-heptane and n-octane," *Acta Chimica Slovenica*, vol. 54, pp. 538-544, 2007.
- [268] K. Rein, S. Roy, S. T. Sanders, A. W. Caswell, F. R. Schauer, and J. R. Gord, "Measurements of Gas Temperatures at 100-kHz Within the Annulus of a Rotating Detonation Engine," *Applied Physics*, 2016 [under review].
- [269] L. S. Rothman, I. E. Gordon, Y. Babikov, A. Barbe, D. C. Benner, P. F. Bernath, *et al.*, "The HITRAN2012 Molecular Spectroscopic Database," *Journal of Quantitative Spectroscopy & Radiative Transfer*, vol. 130, pp. 4-50, 12 July 2013, doi: 10.1016/j.jqsrt.2013.07.002.
- [270] G. Schulze, A. Jirasek, M. M. L. Yu, A. Lim, R. F. B. Turner, and M. W. Blades, "Investigation of Selected Baseline Removal Techniques as Candidates for Automated Implementation," *Applied Spectroscopy*, vol. 59, pp. 545-574, 2005, doi: 10.1366/0003702053945985.
- [271] J. J. Olivero and R. L. Longbothum, "Empirical Fits to the Voigt Line Width: A Brief Review," *Journal of Quantitative Spectroscopy & Radiative Transfer*, vol. 17, pp. 233-236, January 1977, doi: DOI: 10.1016/0022-4073(77)90161-3.
- [272] L. S. Rothman, I. E. Gordon, R. J. Barber, H. Dothe, R. R. Gamache, A. Goldman, *et al.*, "HITEMP, the High-Temperature Molecular Spectroscopic Database," *Journal of Quantitative Spectroscopy & Radiative Transfer*, vol. 111, pp. 2139-2150, 2010, doi: 10.1016/j.jqsrt.2010.05.001.
- [273] K. P. Horn, "Exhaust Composition in a Small Internal Combustion Engine Using FTIR Spectroscopy," M.S. Aeronautical Engineering, Department of Aeronautics and Astronautics, Air Force Institute of Technology, WPAFB, Ohio, 2015.
- [274] (2015). *3W International*. [Online] Available: <http://www.3w-international.com/> [Accessed: 9 November 2015].
- [275] M. Garg, D. Kumar, M. Syed, and S. Nageswara, "CFD Modelling of a Two Stroke Engine to Predict and Reduce Short Circuit Losses," presented at the 2015 Small Engine Technology Conference, Osaka, Japan, SAE Technical Paper 2015-32-0702, 17 November 2015, doi: 20.4271/2015-32-0702.
- [276] J. Paur. (2009). *Boeing's Best Selling Aircraft Fits on Your Shoulder*. [Online] Available: <http://www.wired.com/2009/08/boeing-uav/> [Accessed: 23 November 2015].
- [277] L. Romani, F. Balduzzi, G. Vichi, and G. Ferrara, "An Experimental Methodology for the Evaluation of the Trapped Air-Fuel Ratio of a Small 2S LPDI Engine,"

- presented at the 2015 Small Engine Technology Conference, Osaka, Japan, SAE Technical Paper 2015-32-0762, 17 November 2015, doi: 20.4271/2015-32-0762.
- [278] F. Winkler, R. Oswald, O. Schögl, A. Abis, S. Krimplstätter, and R. Kirchberger, "Layout and development of a 300 cm<sup>3</sup> high performance 2S-LPDI engine," presented at the 2015 Small Engine Technology Conference, Osaka, Japan, SAE Technical Paper 2015-32-0832, 17 November 2015, doi: 20.4271/2015-32-0832.
  - [279] C. Grasas-Alsina, E. Freixa, P. Esteban, and J. Massó, "Low-Pressure Discontinuous Gasoline Injection in Two-Stroke Engines," presented at the International Congress and Exposition, Detroit, Michigan, SAE Technical Paper 860168, 24-28 February 1986, doi: 10.4271/960168.
  - [280] (2015). *AXI Model Motors*. [Online] Available: <http://www.modelmotors.cz> [Accessed: 9 November 2015].
  - [281] D. F. Davidson, M. A. Oehlschlaeger, and R. K. Hanson, "Methy Concentration Time-Histories During iso-Octane and n-Heptane Oxidation and Pyrolysis," *Proceedings of the Combustion Institute*, vol. 31, pp. 321-328, January 2007, doi: 10.1016/j.proci.2006.07.087.
  - [282] E. F. Obert, *Internal Combustion Engines and Air Pollution*. New York, New York: Harper & Row, Publishers, 1973.
  - [283] D. Lee. (2016, 3 July). Drone Industry Delight at New US Rules. *BBC News*. Available: <http://www.bbc.com/news/technology-36584515>

## **Vita**

Capt Ausserer earned Bachelor of Science degrees in Mechanical Engineering and Chemical Engineering from Rose-Hulman Institute of Technology, Terre Haute, IN in 2010. He also received his Air Force commission in 2010 from Air Force ROTC Detachment 218, Indiana State University, Terre Haute, IN. From 2010 to 2012, Capt Ausserer was assigned to the Air Force Institute of Technology where he earned a Master of Science degree in Aeronautical Engineering, focusing on hybrid electric propulsion systems for small remotely piloted aircraft. From 2012 to 2013 Capt Ausserer served as a research engineer for the Air Force Research Laboratory's (AFRL) Aerospace Systems Directorate at Wright Patterson Air Force Base, OH, where he conducted and oversaw research on propulsion systems for remotely piloted aircraft. Capt Ausserer then returned to the Air Force Institute of Technology to earn a PhD in Aeronautical Engineering collaborating on small propulsion system research with AFRL.

REPORT DOCUMENTATION PAGE				Form Approved OMB No. 074-0188	
<p>The public reporting burden for this collection of information is estimated to average 1 hour per response, including the time for reviewing instructions, searching existing data sources, gathering and maintaining the data needed, and completing and reviewing the collection of information. Send comments regarding this burden estimate or any other aspect of the collection of information, including suggestions for reducing this burden to Department of Defense, Washington Headquarters Services, Directorate for Information Operations and Reports (0704-0188), 1215 Jefferson Davis Highway, Suite 1204, Arlington, VA 22202-4302. Respondents should be aware that notwithstanding any other provision of law, no person shall be subject to a penalty for failing to comply with a collection of information if it does not display a currently valid OMB control number.</p> <p><b>PLEASE DO NOT RETURN YOUR FORM TO THE ABOVE ADDRESS.</b></p>					
1. REPORT DATE (DD-MM-YYYY) 16-09-2016		2. REPORT TYPE Dissertation		3. DATES COVERED (From – To) Sept. 2013 – Sept. 2016	
TITLE AND SUBTITLE  The Scaling of Loss Pathways and Heat Transfer in Small Scale Internal Combustion Engines				5a. CONTRACT NUMBER	
				5b. GRANT NUMBER	
				5c. PROGRAM ELEMENT NUMBER	
6. AUTHOR(S)  Ausserer, Joseph K., Captain, USAF				5d. PROJECT NUMBER	
				5e. TASK NUMBER	
				5f. WORK UNIT NUMBER	
7. PERFORMING ORGANIZATION NAMES(S) AND ADDRESS(S) Air Force Institute of Technology Graduate School of Engineering and Management (AFIT/ENY) 2950 Hobson Way, Building 640 WPAFB OH 45433-8865				8. PERFORMING ORGANIZATION REPORT NUMBER  AFIT-ENY-DS-16-S-055	
9. SPONSORING/MONITORING AGENCY NAME(S) AND ADDRESS(ES) Air Force Research Laboratory, Aerospace Systems Directorate 2130 8 <sup>th</sup> St. WPAFB, OH 45433 937-904-4807 ATTN: Paul Litke				10. SPONSOR/MONITOR'S ACRONYM(S)  AFRL/RHIQ (example)	
				11. SPONSOR/MONITOR'S REPORT NUMBER(S)	
12. DISTRIBUTION/AVAILABILITY STATEMENT DISTRIBUTION STATEMENT A. APPROVED FOR PUBLIC RELEASE; DISTRIBUTION UNLIMITED.					
13. SUPPLEMENTARY NOTES This material is declared a work of the U.S. Government and is not subject to copyright protection in the United States.					
14. ABSTRACT The growing use of small unmanned aircraft has increased interest in 10-100 cm <sup>3</sup> displacement internal combustion engines (ICEs). Prior literature indicates fuel conversion efficiency and normalized power deteriorate increasingly rapidly with decreasing displacement, but does not fully reveal the driving losses. The literature also suggested that increasing losses relax the required fuel anti-knock index (AKI), but offered conflicting conclusions on the performance impact. This comprehensive experimental study of three, 28 cm <sup>3</sup> to 85 cm <sup>3</sup> displacement, commercial-off-the-shelf (COTS), two-stroke ICEs identified short-circuiting as having the most deleterious impact on COTS engine performance in this size range. Heat transfer losses were comparable to larger engines for displaced volumes greater than 10 cm <sup>3</sup> . An engine friction model was developed that uses the surface area to volume ratio, speed, and throttle to predict friction losses; a heat transfer model was also validated. The impact of reducing fuel AKI on performance was systematically investigated. The results showed a dependence on engine size; the fuel AKI requirement decreased 20 octane number between 85 cm <sup>3</sup> and 28 cm <sup>3</sup> displacement. Switching from 98 ON (manufacturer recommended) to 20 ON (JP-8, diesel equivalent) fuel increased power 2%-3% and fuel conversion efficiency by 0.5%-1% at non knock-limited conditions.					
15. SUBJECT TERMS internal combustion engine, scaling, loss pathways, fuel anti-knock index, heat transfer model					
16. SECURITY CLASSIFICATION OF:			17. LIMITATION OF ABSTRACT  UU	18. NUMBER OF PAGES  629	19a. NAME OF RESPONSIBLE PERSON Marc D. Polanka, AFIT/ENY
a. REPORT  U	b. ABSTRACT  U	c. THIS PAGE  U			19b. TELEPHONE NUMBER (Include area code) (937) 255-6565, ext 4714 (NOT DSN) (Marc.Polanka@afit.edu)

Standard Form 298 (Rev. 8-98)  
Prescribed by ANSI Std. Z39-18